Using Geochemical Data

This textbook is a complete rewrite and expansion of Hugh Rollinson's highly successful 1993 book *Using Geochemical Data: Evaluation, Presentation, Interpretation*. Rollinson and Pease's new book covers the explosion in geochemical thinking over the past three decades, as new instruments and techniques have come online. It provides a comprehensive overview of how modern geochemical data are used in the understanding of geological and petrological processes. It covers major element, trace element, and radiogenic and stable isotope geochemistry. It explains the potential of many geochemical techniques, provides examples of their application, and emphasizes how to interpret the resulting data. Additional topics covered include the critical statistical analysis of geochemical data, current geochemical techniques, effective display of geochemical data, and the application of data in problem solving and identifying petrogenetic processes within a geological context. It will be invaluable for all graduate students, researchers and professionals using geochemical techniques.

Hugh Rollinson is Emeritus Professor of Earth Sciences at the University of Derby. His particular interest is in the application of geochemistry to the early history of the Earth, and he has published on the geochemistry of Archaean rocks from Scotland, Sierra Leone, Zimbabwe, India, west Greenland and Russia.

Victoria Pease is Professor of Tectonics and Magmatism at Stockholm University. Her research focuses on unravelling Arctic tectonics. She sits on a number of international committees and is a chief editor of *Precambrian Research*.

From a review of the First Edition:

"... a well-balanced, clearly written account of how to deal with geochemical data ... Students, researchers, academic and industrial professional geologists will need to have this manual at their elbow when dealing with geochemical data."

Mineralogical Magazine

Praise for the Second Edition:

"The new edition of *Using Geochemical Data* is not only an excellent text for a geochemistry course, but it also provides an easy source to find geochemical information, especially for a non-specialist. The chapter on analysing geochemical data is outstanding and the information in this chapter is not generally available in other geochemical texts. The chapters on major and trace elements are not only useful in geochemistry, but are also important in igneous and sedimentary petrology courses: most petrology texts do not cover the valuable information in these chapters. For a non-specialist, it is easy to look up specific geochemical diagrams in the book, see how they are constructed, and what the limitations are for their applications. The discussion of trace elements in evaluating various magmatic processes and tectonic settings in Chapters 4 and 5 is clearly in a league of its own when compared to other geochemistry textbooks. And the worked problems in Chapter 6 (radiogenic isotopes) are very helpful for students. I strongly recommend the book as both a geochemical textbook and as an easy-to-use reference for geochemists and non-geochemists alike."

Kent C Condie, New Mexico Institute of Mining & Technology

"This welcome second edition combines geochemical approaches in the tackling of geological problems, with descriptions of widely used techniques. It ranges from major and trace element geochemistry, to geochemical discriminant diagrams, and radiogenic and stable isotopes, ensuring that it will be a key resource for those seeking to utilise the breadth of geochemistry now available. For me, the strength of this textbook is the combination of the breadth of topics covered in one place, providing a resource that people can dip into and learn how to apply different approaches."

Chris Hawkesworth, University of Bristol

"The new Rollinson and Pease version of *Using Geochemical Data* is a very welcome second edition of the classic original ... This revised and much expanded text is very well illustrated and covers many new developments in geochemistry ... It will be of great value to petrology undergraduates as well as to postgraduate students starting to use their own data."

Stephen Daly, University College, Dublin

"Geochemists of a certain vintage and with petrological inclinations usually have at least one much-used copy of Rollinson (1993). This second edition is an impressive distillation of the classic and the current, carefully updated and expanded. It is still, at its heart, a pragmatic "how to do it" guide anchored in numerical and a new statistical rigour, and so will take pride of place on many a geochemical bookshelf."

Mike Fowler, University of Portsmouth

"From A-F-M to Zr/Y, this timely update to a classic textbook provides an accessible introduction to geochemical data analysis, accompanied by numerous practical recipes, and built on solid statistical foundations. Rollinson and Pease have created an essential reference for a new generation of geochemists."

Pieter Vermeesch, University College London

"This thoroughly contemporary revamp of Rollinson's text - with updates and additions on analytical methods, data analysis, and modern interpretations - reinforces the critical role of this authoritative practical reference for robust use of geochemical data across a broad swathe of solid Earth geochemistry."

Peter Reiners, University of Arizona

"After having broken apart several copies of the first edition of *Using Geochemical Data* from extensive use, it is great to see a thoroughly updated version of the book, which will again see much use as a shelf reference and for graduate-level coursework. The second edition follows a similar format as the first, but completely modernised to include more on advanced instrumental and data analysis techniques followed by dedicated sections that centre on how to understand and illustrate major- and trace-element data, as well as radiogenic and stable isotope data. Unlike most books that would be specifically geared to rock type, *Using Geochemical Data* focuses discussion on explaining how and why different geochemical approaches apply to the study of different rock types. This approach not only does an excellent job of explaining how and why certain elemental groups are used and illustrated, but also allows readers to build an understanding of the geochemical connections between different fields of geosciences."

Chris Fedo, University of Tennessee, Knoxville

Using Geochemical Data

to Understand Geological Processes

Hugh Rollinson
University of Derby

Victoria Pease
Stockholm University

CAMBRIDGE
UNIVERSITY PRESS

CAMBRIDGE
UNIVERSITY PRESS

University Printing House, Cambridge CB2 8BS, United Kingdom

One Liberty Plaza, 20th Floor, New York, NY 10006, USA

477 Williamstown Road, Port Melbourne, VIC 3207, Australia

314–321, 3rd Floor, Plot 3, Splendor Forum, Jasola District Centre, New Delhi – 110025, India

79 Anson Road, #06–04/06, Singapore 079906

Cambridge University Press is part of the University of Cambridge.

It furthers the University's mission by disseminating knowledge in the pursuit of education, learning, and research at the highest international levels of excellence.

www.cambridge.org
Information on this title: www.cambridge.org/9781108745840
DOI: 10.1017/9781108777834

First published 1993
Second edition published 2021

Printed in the United Kingdom by TJ Books Limited, Padstow Cornwall

A catalogue record for this publication is available from the British Library.

Library of Congress Cataloging-in-Publication Data
Names: Rollinson, Hugh R. (Hugh Richard), 1949- author. | Pease, Victoria, author.
Title: Using geochemical data : to understand geological processes / Hugh Rollinson, University of Derby, Victoria Pease, Stockholm University.
Description: Second edition. | Cambridge, UK ; New York, NY : Cambridge University Press, 2021. | Includes bibliographical references and index.
Identifiers: LCCN 2020055279 (print) | LCCN 2020055280 (ebook) | ISBN 9781108745840 (paperback) | ISBN 9781108777834 (epub)
Subjects: LCSH: Geochemistry.
Classification: LCC QE515 .R75 2021 (print) | LCC QE515 (ebook) | DDC 551.9–dc23
LC record available at https://lccn.loc.gov/2020055279
LC ebook record available at https://lccn.loc.gov/2020055280

ISBN 978-1-108-74584-0 Paperback

Using Geochemical Data

This textbook is a complete rewrite and expansion of Hugh Rollinson's highly successful 1993 book *Using Geochemical Data: Evaluation, Presentation, Interpretation*. Rollinson and Pease's new book covers the explosion in geochemical thinking over the past three decades, as new instruments and techniques have come online. It provides a comprehensive overview of how modern geochemical data are used in the understanding of geological and petrological processes. It covers major element, trace element, and radiogenic and stable isotope geochemistry. It explains the potential of many geochemical techniques, provides examples of their application, and emphasizes how to interpret the resulting data. Additional topics covered include the critical statistical analysis of geochemical data, current geochemical techniques, effective display of geochemical data, and the application of data in problem solving and identifying petrogenetic processes within a geological context. It will be invaluable for all graduate students, researchers and professionals using geochemical techniques.

Hugh Rollinson is Emeritus Professor of Earth Sciences at the University of Derby. His particular interest is in the application of geochemistry to the early history of the Earth, and he has published on the geochemistry of Archaean rocks from Scotland, Sierra Leone, Zimbabwe, India, west Greenland and Russia.

Victoria Pease is Professor of Tectonics and Magmatism at Stockholm University. Her research focuses on unravelling Arctic tectonics. She sits on a number of international committees and is a chief editor of *Precambrian Research*.

From a review of the First Edition:

"... a well-balanced, clearly written account of how to deal with geochemical data ... Students, researchers, academic and industrial professional geologists will need to have this manual at their elbow when dealing with geochemical data."

Mineralogical Magazine

Praise for the Second Edition:

"The new edition of *Using Geochemical Data* is not only an excellent text for a geochemistry course, but it also provides an easy source to find geochemical information, especially for a non-specialist. The chapter on analysing geochemical data is outstanding and the information in this chapter is not generally available in other geochemical texts. The chapters on major and trace elements are not only useful in geochemistry, but are also important in igneous and sedimentary petrology courses: most petrology texts do not cover the valuable information in these chapters. For a non-specialist, it is easy to look up specific geochemical diagrams in the book, see how they are constructed, and what the limitations are for their applications. The discussion of trace elements in evaluating various magmatic processes and tectonic settings in Chapters 4 and 5 is clearly in a league of its own when compared to other geochemistry textbooks. And the worked problems in Chapter 6 (radiogenic isotopes) are very helpful for students. I strongly recommend the book as both a geochemical textbook and as an easy-to-use reference for geochemists and non-geochemists alike."

Kent C Condie, New Mexico Institute of Mining & Technology

"This welcome second edition combines geochemical approaches in the tackling of geological problems, with descriptions of widely used techniques. It ranges from major and trace element geochemistry, to geochemical discriminant diagrams, and radiogenic and stable isotopes, ensuring that it will be a key resource for those seeking to utilise the breadth of geochemistry now available. For me, the strength of this textbook is the combination of the breadth of topics covered in one place, providing a resource that people can dip into and learn how to apply different approaches."

Chris Hawkesworth, University of Bristol

"The new Rollinson and Pease version of *Using Geochemical Data* is a very welcome second edition of the classic original ... This revised and much expanded text is very well illustrated and covers many new developments in geochemistry ... It will be of great value to petrology undergraduates as well as to postgraduate students starting to use their own data."

Stephen Daly, University College, Dublin

"Geochemists of a certain vintage and with petrological inclinations usually have at least one much-used copy of Rollinson (1993). This second edition is an impressive distillation of the classic and the current, carefully updated and expanded. It is still, at its heart, a pragmatic "how to do it" guide anchored in numerical and a new statistical rigour, and so will take pride of place on many a geochemical bookshelf."

Mike Fowler, University of Portsmouth

"From A-F-M to Zr/Y, this timely update to a classic textbook provides an accessible introduction to geochemical data analysis, accompanied by numerous practical recipes, and built on solid statistical foundations. Rollinson and Pease have created an essential reference for a new generation of geochemists."

Pieter Vermeesch, University College London

"This thoroughly contemporary revamp of Rollinson's text - with updates and additions on analytical methods, data analysis, and modern interpretations - reinforces the critical role of this authoritative practical reference for robust use of geochemical data across a broad swathe of solid Earth geochemistry."

Peter Reiners, University of Arizona

"After having broken apart several copies of the first edition of *Using Geochemical Data* from extensive use, it is great to see a thoroughly updated version of the book, which will again see much use as a shelf reference and for graduate-level coursework. The second edition follows a similar format as the first, but completely modernised to include more on advanced instrumental and data analysis techniques followed by dedicated sections that centre on how to understand and illustrate major- and trace-element data, as well as radiogenic and stable isotope data. Unlike most books that would be specifically geared to rock type, *Using Geochemical Data* focuses discussion on explaining how and why different geochemical approaches apply to the study of different rock types. This approach not only does an excellent job of explaining how and why certain elemental groups are used and illustrated, but also allows readers to build an understanding of the geochemical connections between different fields of geosciences."

Chris Fedo, University of Tennessee, Knoxville

Using Geochemical Data

to Understand Geological Processes

Hugh Rollinson
University of Derby

Victoria Pease
Stockholm University

CAMBRIDGE
UNIVERSITY PRESS

CAMBRIDGE
UNIVERSITY PRESS

University Printing House, Cambridge CB2 8BS, United Kingdom

One Liberty Plaza, 20th Floor, New York, NY 10006, USA

477 Williamstown Road, Port Melbourne, VIC 3207, Australia

314–321, 3rd Floor, Plot 3, Splendor Forum, Jasola District Centre, New Delhi – 110025, India

79 Anson Road, #06–04/06, Singapore 079906

Cambridge University Press is part of the University of Cambridge.

It furthers the University's mission by disseminating knowledge in the pursuit of education, learning, and research at the highest international levels of excellence.

www.cambridge.org
Information on this title: www.cambridge.org/9781108745840
DOI: 10.1017/9781108777834

First published 1993
Second edition published 2021

Printed in the United Kingdom by TJ Books Limited, Padstow Cornwall

A catalogue record for this publication is available from the British Library.

Library of Congress Cataloging-in-Publication Data
Names: Rollinson, Hugh R. (Hugh Richard), 1949- author. | Pease, Victoria, author.
Title: Using geochemical data : to understand geological processes / Hugh Rollinson, University of Derby, Victoria Pease, Stockholm University.
Description: Second edition. | Cambridge, UK ; New York, NY : Cambridge University Press, 2021. | Includes bibliographical references and index.
Identifiers: LCCN 2020055279 (print) | LCCN 2020055280 (ebook) | ISBN 9781108745840 (paperback) | ISBN 9781108777834 (epub)
Subjects: LCSH: Geochemistry.
Classification: LCC QE515 .R75 2021 (print) | LCC QE515 (ebook) | DDC 551.9–dc23
LC record available at https://lccn.loc.gov/2020055279
LC ebook record available at https://lccn.loc.gov/2020055280

ISBN 978-1-108-74584-0 Paperback

Using Geochemical Data

This textbook is a complete rewrite and expansion of Hugh Rollinson's highly successful 1993 book *Using Geochemical Data: Evaluation, Presentation, Interpretation*. Rollinson and Pease's new book covers the explosion in geochemical thinking over the past three decades, as new instruments and techniques have come online. It provides a comprehensive overview of how modern geochemical data are used in the understanding of geological and petrological processes. It covers major element, trace element, and radiogenic and stable isotope geochemistry. It explains the potential of many geochemical techniques, provides examples of their application, and emphasizes how to interpret the resulting data. Additional topics covered include the critical statistical analysis of geochemical data, current geochemical techniques, effective display of geochemical data, and the application of data in problem solving and identifying petrogenetic processes within a geological context. It will be invaluable for all graduate students, researchers and professionals using geochemical techniques.

Hugh Rollinson is Emeritus Professor of Earth Sciences at the University of Derby. His particular interest is in the application of geochemistry to the early history of the Earth, and he has published on the geochemistry of Archaean rocks from Scotland, Sierra Leone, Zimbabwe, India, west Greenland and Russia.

Victoria Pease is Professor of Tectonics and Magmatism at Stockholm University. Her research focuses on unravelling Arctic tectonics. She sits on a number of international committees and is a chief editor of *Precambrian Research*.

From a review of the First Edition:

"... a well-balanced, clearly written account of how to deal with geochemical data ... Students, researchers, academic and industrial professional geologists will need to have this manual at their elbow when dealing with geochemical data."

Mineralogical Magazine

Praise for the Second Edition:

"The new edition of *Using Geochemical Data* is not only an excellent text for a geochemistry course, but it also provides an easy source to find geochemical information, especially for a non-specialist. The chapter on analysing geochemical data is outstanding and the information in this chapter is not generally available in other geochemical texts. The chapters on major and trace elements are not only useful in geochemistry, but are also important in igneous and sedimentary petrology courses: most petrology texts do not cover the valuable information in these chapters. For a non-specialist, it is easy to look up specific geochemical diagrams in the book, see how they are constructed, and what the limitations are for their applications. The discussion of trace elements in evaluating various magmatic processes and tectonic settings in Chapters 4 and 5 is clearly in a league of its own when compared to other geochemistry textbooks. And the worked problems in Chapter 6 (radiogenic isotopes) are very helpful for students. I strongly recommend the book as both a geochemical textbook and as an easy-to-use reference for geochemists and non-geochemists alike."

Kent C Condie, New Mexico Institute of Mining & Technology

"This welcome second edition combines geochemical approaches in the tackling of geological problems, with descriptions of widely used techniques. It ranges from major and trace element geochemistry, to geochemical discriminant diagrams, and radiogenic and stable isotopes, ensuring that it will be a key resource for those seeking to utilise the breadth of geochemistry now available. For me, the strength of this textbook is the combination of the breadth of topics covered in one place, providing a resource that people can dip into and learn how to apply different approaches."

Chris Hawkesworth, University of Bristol

"The new Rollinson and Pease version of *Using Geochemical Data* is a very welcome second edition of the classic original ... This revised and much expanded text is very well illustrated and covers many new developments in geochemistry ... It will be of great value to petrology undergraduates as well as to postgraduate students starting to use their own data."

Stephen Daly, University College, Dublin

"Geochemists of a certain vintage and with petrological inclinations usually have at least one much-used copy of Rollinson (1993). This second edition is an impressive distillation of the classic and the current, carefully updated and expanded. It is still, at its heart, a pragmatic "how to do it" guide anchored in numerical and a new statistical rigour, and so will take pride of place on many a geochemical bookshelf."

Mike Fowler, University of Portsmouth

"From A-F-M to Zr/Y, this timely update to a classic textbook provides an accessible introduction to geochemical data analysis, accompanied by numerous practical recipes, and built on solid statistical foundations. Rollinson and Pease have created an essential reference for a new generation of geochemists."

Pieter Vermeesch, University College London

"This thoroughly contemporary revamp of Rollinson's text - with updates and additions on analytical methods, data analysis, and modern interpretations - reinforces the critical role of this authoritative practical reference for robust use of geochemical data across a broad swathe of solid Earth geochemistry."

Peter Reiners, University of Arizona

"After having broken apart several copies of the first edition of *Using Geochemical Data* from extensive use, it is great to see a thoroughly updated version of the book, which will again see much use as a shelf reference and for graduate-level coursework. The second edition follows a similar format as the first, but completely modernised to include more on advanced instrumental and data analysis techniques followed by dedicated sections that centre on how to understand and illustrate major- and trace-element data, as well as radiogenic and stable isotope data. Unlike most books that would be specifically geared to rock type, *Using Geochemical Data* focuses discussion on explaining how and why different geochemical approaches apply to the study of different rock types. This approach not only does an excellent job of explaining how and why certain elemental groups are used and illustrated, but also allows readers to build an understanding of the geochemical connections between different fields of geosciences."

Chris Fedo, University of Tennessee, Knoxville

Using Geochemical Data

to Understand Geological Processes

Hugh Rollinson
University of Derby

Victoria Pease
Stockholm University

CAMBRIDGE
UNIVERSITY PRESS

CAMBRIDGE
UNIVERSITY PRESS

University Printing House, Cambridge CB2 8BS, United Kingdom

One Liberty Plaza, 20th Floor, New York, NY 10006, USA

477 Williamstown Road, Port Melbourne, VIC 3207, Australia

314–321, 3rd Floor, Plot 3, Splendor Forum, Jasola District Centre, New Delhi – 110025, India

79 Anson Road, #06–04/06, Singapore 079906

Cambridge University Press is part of the University of Cambridge.

It furthers the University's mission by disseminating knowledge in the pursuit of education, learning, and research at the highest international levels of excellence.

www.cambridge.org
Information on this title: www.cambridge.org/9781108745840
DOI: 10.1017/9781108777834

First published 1993
Second edition published 2021

Printed in the United Kingdom by TJ Books Limited, Padstow Cornwall

A catalogue record for this publication is available from the British Library.

Library of Congress Cataloging-in-Publication Data
Names: Rollinson, Hugh R. (Hugh Richard), 1949- author. | Pease, Victoria, author.
Title: Using geochemical data : to understand geological processes / Hugh Rollinson, University of Derby, Victoria Pease, Stockholm University.
Description: Second edition. | Cambridge, UK ; New York, NY : Cambridge University Press, 2021. | Includes bibliographical references and index.
Identifiers: LCCN 2020055279 (print) | LCCN 2020055280 (ebook) | ISBN 9781108745840 (paperback) | ISBN 9781108777834 (epub)
Subjects: LCSH: Geochemistry.
Classification: LCC QE515 .R75 2021 (print) | LCC QE515 (ebook) | DDC 551.9–dc23
LC record available at https://lccn.loc.gov/2020055279
LC ebook record available at https://lccn.loc.gov/2020055280

ISBN 978-1-108-74584-0 Paperback

Using Geochemical Data

This textbook is a complete rewrite and expansion of Hugh Rollinson's highly successful 1993 book *Using Geochemical Data: Evaluation, Presentation, Interpretation*. Rollinson and Pease's new book covers the explosion in geochemical thinking over the past three decades, as new instruments and techniques have come online. It provides a comprehensive overview of how modern geochemical data are used in the understanding of geological and petrological processes. It covers major element, trace element, and radiogenic and stable isotope geochemistry. It explains the potential of many geochemical techniques, provides examples of their application, and emphasizes how to interpret the resulting data. Additional topics covered include the critical statistical analysis of geochemical data, current geochemical techniques, effective display of geochemical data, and the application of data in problem solving and identifying petrogenetic processes within a geological context. It will be invaluable for all graduate students, researchers and professionals using geochemical techniques.

Hugh Rollinson is Emeritus Professor of Earth Sciences at the University of Derby. His particular interest is in the application of geochemistry to the early history of the Earth, and he has published on the geochemistry of Archaean rocks from Scotland, Sierra Leone, Zimbabwe, India, west Greenland and Russia.

Victoria Pease is Professor of Tectonics and Magmatism at Stockholm University. Her research focuses on unravelling Arctic tectonics. She sits on a number of international committees and is a chief editor of *Precambrian Research*.

From a review of the First Edition:

"... a well-balanced, clearly written account of how to deal with geochemical data ... Students, researchers, academic and industrial professional geologists will need to have this manual at their elbow when dealing with geochemical data."

Mineralogical Magazine

Praise for the Second Edition:

"The new edition of *Using Geochemical Data* is not only an excellent text for a geochemistry course, but it also provides an easy source to find geochemical information, especially for a non-specialist. The chapter on analysing geochemical data is outstanding and the information in this chapter is not generally available in other geochemical texts. The chapters on major and trace elements are not only useful in geochemistry, but are also important in igneous and sedimentary petrology courses: most petrology texts do not cover the valuable information in these chapters. For a non-specialist, it is easy to look up specific geochemical diagrams in the book, see how they are constructed, and what the limitations are for their applications. The discussion of trace elements in evaluating various magmatic processes and tectonic settings in Chapters 4 and 5 is clearly in a league of its own when compared to other geochemistry textbooks. And the worked problems in Chapter 6 (radiogenic isotopes) are very helpful for students. I strongly recommend the book as both a geochemical textbook and as an easy-to-use reference for geochemists and non-geochemists alike."

Kent C Condie, New Mexico Institute of Mining & Technology

"This welcome second edition combines geochemical approaches in the tackling of geological problems, with descriptions of widely used techniques. It ranges from major and trace element geochemistry, to geochemical discriminant diagrams, and radiogenic and stable isotopes, ensuring that it will be a key resource for those seeking to utilise the breadth of geochemistry now available. For me, the strength of this textbook is the combination of the breadth of topics covered in one place, providing a resource that people can dip into and learn how to apply different approaches."

Chris Hawkesworth, University of Bristol

"The new Rollinson and Pease version of *Using Geochemical Data* is a very welcome second edition of the classic original ... This revised and much expanded text is very well illustrated and covers many new developments in geochemistry ... It will be of great value to petrology undergraduates as well as to postgraduate students starting to use their own data."

Stephen Daly, University College, Dublin

"Geochemists of a certain vintage and with petrological inclinations usually have at least one much-used copy of Rollinson (1993). This second edition is an impressive distillation of the classic and the current, carefully updated and expanded. It is still, at its heart, a pragmatic "how to do it" guide anchored in numerical and a new statistical rigour, and so will take pride of place on many a geochemical bookshelf."

Mike Fowler, University of Portsmouth

"From A-F-M to Zr/Y, this timely update to a classic textbook provides an accessible introduction to geochemical data analysis, accompanied by numerous practical recipes, and built on solid statistical foundations. Rollinson and Pease have created an essential reference for a new generation of geochemists."

Pieter Vermeesch, University College London

"This thoroughly contemporary revamp of Rollinson's text - with updates and additions on analytical methods, data analysis, and modern interpretations - reinforces the critical role of this authoritative practical reference for robust use of geochemical data across a broad swathe of solid Earth geochemistry."

Peter Reiners, University of Arizona

"After having broken apart several copies of the first edition of *Using Geochemical Data* from extensive use, it is great to see a thoroughly updated version of the book, which will again see much use as a shelf reference and for graduate-level coursework. The second edition follows a similar format as the first, but completely modernised to include more on advanced instrumental and data analysis techniques followed by dedicated sections that centre on how to understand and illustrate major- and trace-element data, as well as radiogenic and stable isotope data. Unlike most books that would be specifically geared to rock type, *Using Geochemical Data* focuses discussion on explaining how and why different geochemical approaches apply to the study of different rock types. This approach not only does an excellent job of explaining how and why certain elemental groups are used and illustrated, but also allows readers to build an understanding of the geochemical connections between different fields of geosciences."

Chris Fedo, University of Tennessee, Knoxville

Using Geochemical Data

to Understand Geological Processes

Hugh Rollinson
University of Derby

Victoria Pease
Stockholm University

CAMBRIDGE
UNIVERSITY PRESS

CAMBRIDGE
UNIVERSITY PRESS

University Printing House, Cambridge CB2 8BS, United Kingdom

One Liberty Plaza, 20th Floor, New York, NY 10006, USA

477 Williamstown Road, Port Melbourne, VIC 3207, Australia

314–321, 3rd Floor, Plot 3, Splendor Forum, Jasola District Centre, New Delhi – 110025, India

79 Anson Road, #06–04/06, Singapore 079906

Cambridge University Press is part of the University of Cambridge.

It furthers the University's mission by disseminating knowledge in the pursuit of education, learning, and research at the highest international levels of excellence.

www.cambridge.org
Information on this title: www.cambridge.org/9781108745840
DOI: 10.1017/9781108777834

First published 1993
Second edition published 2021

Printed in the United Kingdom by TJ Books Limited, Padstow Cornwall

A catalogue record for this publication is available from the British Library.

Library of Congress Cataloging-in-Publication Data
Names: Rollinson, Hugh R. (Hugh Richard), 1949- author. | Pease, Victoria, author.
Title: Using geochemical data : to understand geological processes / Hugh Rollinson, University of Derby, Victoria Pease, Stockholm University.
Description: Second edition. | Cambridge, UK ; New York, NY : Cambridge University Press, 2021. | Includes bibliographical references and index.
Identifiers: LCCN 2020055279 (print) | LCCN 2020055280 (ebook) | ISBN 9781108745840 (paperback) | ISBN 9781108777834 (epub)
Subjects: LCSH: Geochemistry.
Classification: LCC QE515 .R75 2021 (print) | LCC QE515 (ebook) | DDC 551.9–dc23
LC record available at https://lccn.loc.gov/2020055279
LC ebook record available at https://lccn.loc.gov/2020055280

ISBN 978-1-108-74584-0 Paperback

Contents

Preface to the Second Edition

It is now more than 25 years since the publication of the first edition of *Using Geochemical Data* and in that time the field of geochemistry has expanded exponentially. In part this is because the application of the Earth Sciences has also expanded but in addition geochemistry now touches every aspect of the Earth sciences and overflows into related disciplines such as geomorphology and archaeology. Geochemistry itself has grown and now has well established subdisciplines such as cosmochemistry, environmental geochemistry, biogeochemistry and exploration geochemistry.

In this new and expanded edition of *Using Geochemical Data* our primary focus is still petrological, although we have sought to be inclusive of the new areas of geochemistry that have developed over the past 25 years. In particular we have sought to accommodate the vast array of new technological developments that have taken place in geochemistry, and these are briefly reviewed below.

The development of new technologies and the improvement of existing technologies now provide better quality geochemical data, for a wider range of elements and isotope systems, more rapidly than before and at high spatial resolution. We now have routine access to inductively coupled plasma-based analytical tools, in particular, inductively coupled plasma mass spectrometry which has contributed massively to the increase in high-quality trace element and isotope data. In addition, a range of high-resolution in-situ microbeam methods have been developed to include ion probes and laser probes which allow the detailed within-grain mapping of trace elements and isotopes.

The development of new geochemical techniques. Since the first edition of this book a number of isotopic techniques have moved from the domain of a few highly specialised laboratories to being much more widely used. In part this can be attributed to some of the new technologies now available as mentioned above. We now routinely see radiogenic isotope data from the Re-Os and Lu-Hf systems reported, and results for the short-lived radiogenic Nd and W isotopes are widely used in early Earth studies. The field of stable isotope geochemistry has expanded to include nitrogen and a vast array of what have been termed the 'non-traditional' stable isotope systems. The field of zircon isotope geochemistry has exploded from being an area of minority interest within geochronology to being a major contributor to geochemical models of crustal growth and in which individual zircon grains are mined for the isotopic and trace element information that they hold.

An expanded experimental and theoretical understanding of geochemical data. Our understanding of how geochemical processes operate has continued to grow through the contribution of the results of experimental petrology. Alongside this there has been a growth in the thermodynamic modelling of geochemical systems, built on the results of experimental petrology, but expanded into areas that have previously not been experimentally investigated. This approach has been applied across the field of geochemistry to include the behaviour of major and trace elements in melts, the partitioning of trace elements between minerals and melt, the understanding of metamorphic reactions and fluid chemistry. These approaches have a great predictive power and allow models of physical processes to be built which replicate measured geochemical data.

Better approaches to the statistical treatment of geochemical data. As was emphasised in the first edition of this book, the way in which geochemists use their data, particularly major element chemical data, is a source of great concern to statisticians. In this edition we discuss the more robust approaches to using geochemical data in the light of advances in the field of geostatistics. We also review the misapplication of tectonic discrimination diagrams and seek to put the users of geochemical data back on track.

A revolution in computing technology. The first edition of this book was written without any access to the internet. In the intervening years the explosion in computing technologies has meant the emergence of large geochemical databases, the growth of 'big data' and a huge increase in the number of software packages available, which have allowed massive progress in the rapid processing of analytical data and the analysis of geochemical data sets. With relatively easy

access to large data sets we find ourselves in the 'big data' era: an area of geochemistry which has probably not yet reached full maturity and in our view requires some careful management.

An explosion in the geochemical literature. Coupled with the rise in computer technology and the wide access to the geochemical literature online has come an increase in the volume of geochemical literature. In the intervening years there have been two editions of *The Treatise on Geochemistry*, other online encyclopaedias, new journals and an array of specialist textbooks.

So where does this book fit in? We have modified the title slightly to reflect what we would argue is the focus of all modern geochemistry: an understanding of processes. Nevertheless, the principal purpose of the book remains the same and is a guide to the user of geochemical data to obtain meaning from their data. Albeit expanded, the basic principles of geochemistry remain the same; the focus is primarily petrological, reflecting the background of the authors; and previous users of the book will recognise that the basic structure of the book remains the same. However, the book is longer, is better illustrated and, as indicated, is updated in every area with extensive reference to the modern literature. There are a number of detailed and specialist geochemical texts, to which we refer and acknowledge with gratitude, but this text is deliberately broad and aimed at the graduate student to assist in the manipulation and interpretation of their data and to assist in the process of obtaining geological meaning from geochemical data. Our experience tells us that this text has also been widely used by professional geologists and geochemists in many disciplines as a guide to areas of geochemistry which are not their specialisation. We hope that this will continue to be the case.

At a personal level we are grateful to the many individuals who have assisted in this revision. In particular, VP wishes to thank colleagues who generously answered what must have seemed to be apparently random questions (A. Hoffman, W. White, A. Kemp, C. Fedo) and a special thanks to M. Whitehouse who got the brunt of these. At Cambridge University Press we appreciate Matt Lloyd's enthusiasm and support for this project, without which it might have floundered, and we appreciate Sarah Lambert's patience. We are also grateful to colleagues at the Faraday Institute for Science and Religion in Cambridge through whom we had access to the University of Cambridge library, and for a visiting fellowship for VP to St Edmund's College Cambridge and to colleagues at CASP for an office and administrative support during VP's fellowship period in Cambridge. VP thanks Hugh for allowing her to be a part of this endeavour – 'as a heavy user of the first edition, I am looking forward to the second!'

HR wishes to thank his co-author Victoria Pease for the encouragement to both begin and complete this revised edition. The observant reader of the first edition might wonder what became of A, E, O and P in the intervening years and so it is pleasing to report that each has found success in life without any reference to geochemistry. P remains my constant source of encouragement and I cannot express enough my thanks for her support over these many months.

Preface to the First Edition

Pascal once wrote 'the last thing that we discover in writing a book is to know what to put at the beginning'. In my case this is particularly so, for what excuse have I as a single author for venturing into the fields of so many experts in an attempt to explain the methodologies of the main subdisciplines of geochemistry. This same problem was acknowledged by Goldschmidt in the preface to his classic 1954 text on geochemistry. Today of course the problem is compounded, for geochemistry has a multitude of relatively new and comparatively narrow fields. We find experts in X-ray fluorescence and plasma emission techniques, those who specialise in the lead isotopes of zircon and the isotope systematics of argon. This specialisation is necessary for the technologies of such techniques are complex. Nevertheless, for some there needs to be an overview of the main range of techniques, for there are many workers who wish to understand the potential of geochemical techniques and intelligently interpret the results. That such an overview does not exist is my chief defence. This text is not original in the ideas that it conveys, rather it is original in the sense that it brings together a wide range of ideas and methods from the geochemical literature.

The principal emphasis in this book is on 'whole-rock' chemistry and the equally large area of mineral chemistry has only been touched upon tangentially. Furthermore, it has not been possible to cover some of the more novel and esoteric techniques currently being applied to geochemical investigations.

This text was conceived as a work to be put into the hands of a graduate student embarking upon a geochemical project. As it has evolved however, it has become apparent that it serves many more purposes. It may, for example, be used as a text in final-year and graduate-student geochemistry courses. It will be useful to the professional geochemist who has worked chiefly in one subdiscipline of the subject and needs to look more broadly at a problem. It will also be of use to the non-geochemist, whether in academia, industry or a geological survey, who has access to geochemical data and needs to interpret it.

This book has therefore two main goals. The first is to put into the hands of a non-expert, who needs to make use of geochemical data, a summary of the methods and techniques currently used in geochemistry. And yet a text which will enable the user to obtain something of geological significance from the data. The second goal is to put within one cover the disparate techniques and methodologies currently in use by geochemists. Thus, this text may be read at two levels. First, it may be read by a geochemist with data who wishes to evaluate and interpret that data. Second, it may be read by a geologist or geochemist who wants to understand some of the current geochemical jargon and make sense of the geochemical literature.

The reader will detect a number of biases in this text which are an inevitable consequence of the author's geological interests. The first bias is towards examples chosen from the Archaean, which is the area of geology in which the author has principally worked and evident also from the place of writing. The second bias is towards igneous and metamorphic petrology, which again is the author's field of interest, but also the area in which many of the methods described were first applied.

I am grateful to many colleagues for their assistance during the preparation of this book. Particular thanks go to Jan Kramers, Gordon Lampitt, Alex Woronow, David Lowry, Ken Eriksson, Kevin Walsh and my late colleague Thorley Sweetman for reading various sections of the text. Final thanks must go to Patricia my wife for her tolerance of the back of my head for so many months whilst seated at this keyboard and to Amy, Oliver and Edward for their patient encouragement of 'how many chapters to go Dad?'

May 1992, University of Zimbabwe

Abbreviations

AAS	atomic absorption spectrophotometry
AFC	assimilation and fractional crystallisation
AFM	triangular variation diagram showing Alkalis (Na_2O + K_2O), FeO and MgO
AI	alkalinity index
ASI	aluminium saturation index
BAB	back-arc basin basalt
BE	the composition of the bulk Earth
BSE	bulk silicate Earth (the composition of the bulk Earth without the core)
CAB	calc-alkaline basalt
CHUR	chondritic uniform reservoir (chondritic model for the composition of the bulk earth)
CIA	chemical index of alteration (a measure of the degree of chemical weathering)
CIPW	Cross, Iddings, Pearsson and Washington (the originators of the norm calculation)
CLM	continental lithospheric mantle (also SCLM)
CMAS	projection into CaO-MgO-Al_2O_3-SiO_2 space
D	distribution or partition coefficient (previously Kd)
DM	depleted mantle
EDS	energy dispersive spectrometer
EDXRF	energy dispersive XRF
EMI, EM2	enriched mantle source(s) 1 and 2
E-MORB	enriched-MORB
EPMA	electron probe microanalysis
ES	the composition of average European shale
FA	factor analysis
fO_2	oxygen fugacity
Ga	billion (10^9) years
GLOSS	global subducting sediment
GMWL	Global Meteoric Water Line
GOE	Great Oxidation Event (c. 2.34 Ga)
HFS(E)	high field strength trace element
HIMU	high μ mantle source region
HREE	heavy REE
HSE	highly siderophile element
IAB	island arc basalt
ICP	inductively coupled plasma
ICP-MS	ICP mass spectrometry
ICP-OES	ICP optical emission spectrometry
ID-MS	isotope dilution mass spectrometry
INAA	instrumental neutron activation analysis
Kd	distribution or partition coefficient (now D)
KDE	kernel density estimate
LA-ICP-MS	laser ablation ICP-MS
LA-MC-ICP-MS	laser ablation multi-collector ICP-MS
LFS(E)	low field strength element
LIL(E)	large ion lithophile element
LOI	loss on ignition
LREE	light REE
Ma	million (10^6) years
MALI	modified alkali-lime index
MC-ICP-MS	multi-collector ICP-MS
MC-SIMS	multi-collector SIMS
MDS	multidimensional scaling
MELTS	igneous modelling software
MORB	mid-ocean ridge basalt
MREE	middle REE
MS	mass spectrometry
MSWD	mean squares of weighted deviates
NASC	North American shale composite (an average shale composition)
NHRL	Northern Hemisphere Reference Line (for Pb isotopes in basalts)
NIST	National Institute of Standards and Technology (US)
N-MORB	normal-MORB
OIB	ocean island basalt
OLS	ordinary least squares
ORG	ocean ridge granite
PAAS	post-Archaean Australian shale (average)
PCA	principal component analysis
PDC	probability density curves
PDF	probability density function

PGE	platinum group element
PGM	platinum group metal
PM	primitive mantle
ppb	part per billion (1 in 10^9)
ppm	part per million (1 in 10^6)
ppt	part per trillion (1 in 10^{12})
PREMA	prevalent mantle reservoir (for oceanic basalts)
PUM	primary uniform mantle reservoir
REE	rare earth element
RMA	reduced major axis
RTF	a periodically replenished, periodically tapped and continuously fractionated magma chamber
S-CHUR	supra-chondritic
SCLM	sub-continental lithospheric mantle (see CLM)
S-COLG	syn-collisional granite
SEM	scanning electron microscope
SHRIMP	sensitive high-resolution ion microprobe
SIMS	secondary ion mass spectrometry
SSMS	spark source mass spectrometry
TAS	total alkalis silica diagram
T_c	closure temperature
TIMS	thermal ionisation mass spectrometry
TTG	granitoids of the tonalite, trondhjemite granodiorite group
VAB	volcanic arc basalt
VAG	volcanic arc granite
VPDB	Vienna Peedee belemnite
VSMOW	Vienna Standard Mean Ocean Water
WPB	within plate basalt
WPG	within plate granite
wt.%	weight percent
WDXRF	wave-length dispersive XRF
XANES	X-ray absorption near-edge structure
XRF	X-ray fluorescence (spectrometry)
μ (mu)	the isotopic ratio $^{238}U/^{204}Pb$

1 Geochemical Data

1.1 Introduction

This book is about geochemical data and how they can be used to obtain information about geological processes. The major focus of this book is petrological, and the principal themes are the applications of geochemical data to igneous, sedimentary and metamorphic petrology. Minor themes include the application of geochemical data to cosmochemistry and the study of meteorites and to mineral exploration geochemistry. This book does not cover the topics of organic chemistry, hydro-geochemistry, solution chemistry or gas geochemistry and touches only briefly on the subject of environmental geochemistry. For a detailed discussion of these subdisciplines of geochemistry, the reader is referred elsewhere.

Conventionally geochemical data are subdivided into four main categories; these are the major elements, trace elements, radiogenic isotopes and stable isotopes and these four types of geochemical data each form a chapter in this book. Each chapter shows how the particular form of geochemical data can be used and how it provides clues to the processes operating in the suite of rocks in question. Different methods of data presentation are discussed and their relative merits evaluated.

The *major elements* (Chapter 3) are the elements which predominate in any rock analysis. In silicate rocks they are normally Si, Ti, Al, Fe, Mn, Mg, Ca, Na, K and P, and their concentrations are expressed as a weight percent (wt.%) of the oxide (Table 1.1). Major element determinations are usually made only for cations and it is assumed that they are accompanied by an appropriate amount of oxygen. Thus, the sum of the major element oxides will total to about 100% and the analysis total may be used as a rough guide to its reliability. Iron may be determined as FeO and/or Fe_2O_3, but is frequently expressed as 'total Fe' and given as Fe_2O_3(tot), Fe_2O_3(t) or Fe_2O_{3T}. Anions are not routinely determined.

Trace elements (Chapter 4) are defined as those elements which are present at less than the 0.1 wt.% level and their concentrations are expressed in parts per million (ppm) or more rarely in parts per billion (10^{-9} = ppb) of the element (Table 1.1). Convention is not always followed, however, and trace element concentrations exceeding the 0.1 wt.% (1000 ppm) level are sometimes cited. The trace elements of importance in geochemistry are shown in Figure 4.1.

Some elements behave as major elements in one group of rocks and as a trace element in another group of rocks. An example is the element K, which is a major constituent of rhyolites, making up more than 4 wt.% of the rock and forming an essential structural part of minerals such as orthoclase and biotite. In some basalts, however, K concentrations are very low and there are no K-bearing phases. In this case K behaves as a trace element.

Volatiles such as H_2O, CO_2 and S can be included in the major element analysis. Water combined within the lattice of silicate minerals and released above 110°C is described as H_2O+. Water present simply as dampness in the rock powder and driven off by heating to 110°C is quoted as H_2O- and is not an important constituent of the rock. Most frequently the total volatile content of the rock is determined by ignition at 1000°C and is expressed as loss on ignition (LOI) as in Table 1.1 (Lechler and Desilets, 1987).

Isotopes are subdivided into radiogenic and stable isotopes. *Radiogenic isotopes* (Chapter 6) include those isotopes which decay spontaneously due to their natural radioactivity and those which are the final daughter products of such a decay scheme. They include the parent-daughter element pairs K-Ar, Rb-Sr, Sm-Nd, Lu-Hf, U-Pb and Re-Os. They are expressed as ratios relative to a non-radiogenic isotope such as $^{87}Sr/^{86}Sr$ (Table 1.1) in which ^{87}Sr is the radiogenic isotope. *Stable isotope* studies in geochemistry (Chapter 7) concentrate on the naturally occurring isotopes of light elements such as H, O, C, S and N and a wide range of metallic elements (see Figure 7.29) which may be fractionated on the basis of mass differences between the isotopes of the element. For example, the isotope ^{18}O is 12.5% heavier than the isotope ^{16}O and the two are fractionated during the evaporation of water. Stable isotopes contribute significantly to an understanding of fluid and volatile species in geology. They are expressed as

Table 1.1 Geochemical data for peraluminous granites from the North Qilian suture zone, China (after Chen et al., 2014)

Sample	09QL-01	09QL-03	11QL-32	11QL-35
Major elements (wt.%)				
SiO_2	70.82	71.35	69.17	72.57
TiO_2	0.38	0.32	0.61	0.37
Al_2O_3	14.27	14.43	14.38	13.33
Fe_2O_{3T}	2.89	2.55	4.07	2.46
MnO	0.04	0.05	0.06	0.05
MgO	1.23	0.86	1.42	0.78
CaO	1.10	2.01	3.31	2.57
Na_2O	3.50	2.49	1.60	1.66
K_2O	4.52	4.67	3.37	4.23
P_2O_5	0.09	0.08	0.12	0.07
LOI	1.03	1.08	1.06	1.08
Total	99.87	99.89	99.17	99.16
Major elements (wt.%) recalculated dry				
SiO_2	71.56	72.13	69.92	73.37
TiO_2	0.38	0.32	0.62	0.37
Al_2O_3	14.42	14.59	14.54	13.48
Fe_2O_3t	2.92	2.58	4.11	2.49
MnO	0.04	0.05	0.06	0.05
MgO	1.24	0.87	1.44	0.79
CaO	1.11	2.03	3.35	2.60
Na_2O	3.54	2.52	1.62	1.68
K_2O	4.57	4.72	3.41	4.28
P_2O_5	0.09	0.08	0.12	0.07
Total	99.87	99.89	99.17	99.17
Radiogenic isotopes				
$^{87}Rb/^{86}Sr$	4.5490	4.7470	2.5920	3.0480
$^{87}Rb/^{86}Sr$	0.7640	0.7780	0.7541	0.7598
$^{147}Sm/^{144}Nd$	0.1260	0.1230	0.1190	0.1250
$^{147}Sm/^{144}Nd$	0.5121	0.5120	0.5121	0.5121

Trace elements (ppm)	09QL-01	09QL-03	11QL-32	11QL-35
Li	10.30	37.10	9.10	10.30
P	393.00	305.00	527.00	307.00
Be	1.62	1.93	nd	nd
Sc	9.33	6.81	10.30	6.72
Ti	2300.00	1754.00	3930.00	2356.00
V	37.60	20.10	50.60	28.40
Cr	10.80	10.40	11.70	7.80
Mn	322.00	368.00	389.00	289.00
Co	4.62	2.97	5.65	2.46
Ni	6.81	7.24	5.99	2.75
Cu	10.10	4.05	17.20	4.48
Zn	56.50	46.30	47.10	32.70
Ga	14.90	16.40	16.30	14.30
Rb	126.00	170.00	113.00	115.00
Sr	80.50	104.00	127.00	110.00
Y	37.70	36.80	36.70	33.60
Zr	166.00	149.00	233.00	175.00
Nb	14.40	12.10	22.90	18.90
Mo	0.24	0.15	2.89	1.48
Cs	1.27	2.86	2.37	0.78
Ba	602.00	468.00	697.00	523.00
La	27.40	28.70	40.20	27.90
Ce	57.90	58.40	80.90	54.50
Pr	6.65	6.61	9.03	6.23
Nd	23.70	23.70	33.40	23.20
Sm	4.94	4.82	6.56	4.79
Eu	0.74	0.78	1.22	0.93
Gd	5.05	4.92	6.53	4.98
Tb	0.86	0.84	1.07	0.85
Dy	5.63	5.38	6.82	5.65
Ho	1.15	1.11	1.38	1.18
Er	3.56	3.30	4.03	3.63
Tm	0.53	0.49	0.57	0.54
Yb	3.46	3.30	3.65	3.67
Lu	0.48	0.47	0.52	0.53
Hf	3.93	3.50	5.83	4.76
Ta	0.90	0.80	3.17	1.74
Pb	13.80	13.20	9.80	15.20
Th	10.30	8.60	10.20	7.30
W	nd	nd	1.91	2.60

a nd, not determined; data not reported using significant figures.

ratios relative to a standard using the δ-notation (see Section 7.2.1.1).

An example of a typical geochemical dataset is given in Table 1.1 for a suite of peraluminous biotite monzogranites from the Chaidanuo batholith from the North Qilian suture zone in central China from the study by Chen et al. (2014). This dataset shows the major elements with Fe given as Fe_2O_{3T} and the volatiles as LOI (Section 3.1.1). The data are also recalculated dry, that is, volatile free. In this study the major elements were determined by inductively coupled plasma optical-emission spectroscopy (ICP-OES). The trace elements reported in Table 1.1 were measured by

inductively coupled plasma mass spectrometry (ICP-MS) and this long list of trace elements shows the range of trace elements readily determined using this method. Where a particular element is not measured it is designated 'nd' (not determined) and where it cannot be determined because it is below the limits of detection of the analytical method used it may be reported as 'bd'. The radiogenic isotopes of Sr and Nd were measured using thermal ionisation mass spectrometry (TIMS).

The major part of this book discusses the four main types of geochemical data outlined above and shows how they can be used to identify and understand geochemical processes. In addition, Chapter 5 shows the way in which trace and major element chemistry is used to determine the tectonic setting of some igneous and sedimentary rocks. Chapter 2 discusses some of the particular statistical problems which arise when analysing geochemical datasets and some recommendations are made about permissible and impermissible methods of data presentation.

In this introductory chapter we consider three topics:

(1) The geochemical processes which are likely to be encountered in nature and their geochemical signatures.
(2) The interaction between geological fieldwork and the interpretation of geochemical data.
(3) The different analytical methods currently used in modern geochemistry.

1.2 Geological Processes and Their Geochemical Signatures

A major purpose of this text is to show how geochemical data can be used to identify and interpret geological processes. In this section, therefore, we review the main processes which have taken place during the formation and differentiation of our rocky planet and which have subsequently shaped it into the form that we recognise today.

It is conventional in geochemistry to distinguish between those processes which take place at high temperatures, deep in the Earth, from the low-temperature processes which operate at or near the Earth's surface. We will follow this pattern here, and so first we review those processes which took place during the formation of the Earth and the subsequent magmatic processes which have led to its differentiation and its reworking during metamorphism. We then discuss those processes which operate at low temperatures at the Earth's surface and in which there are interactions between rocks and the Earth's atmosphere, hydrosphere and those living organisms that inhabit them and ultimately lead to the formation of sedimentary rocks. In each case our primary purpose is to seek to identify those geological processes which have a distinctive geochemical signature and which can be recognised through the collection and interpretation of geochemical data. We point the readers to those sections of this book where these processes are described in greater detail.

1.2.1 Processes Which Control the Formation and Differentiation of Planetary Bodies

Any full understanding of our planet must address the question of its origin and its relationship to its planetary neighbours. The answer to this question comes primarily from a knowledge of the overall composition of the Earth, often expressed as the bulk Earth composition. Our principal source of the information on the composition of the Earth comes from the study of meteorites – in particular the most primitive meteorites, chondritic meteorites. Chondritic meteorites are thought to have formed during the condensation of the solar nebula, and so the study of meteorite chemistry takes us into the domain where fields of cosmochemistry and geochemistry overlap (see Section 4.1.1).

After the Big Bang the majority of the chemical elements were formed by the processes of stellar nucleosynthesis during star formation. The distribution of elements in our star – the Sun – as obtained from spectroscopy and the study of meteorites is shown in Figure 1.1 and their relative concentrations provides details about the processes of nucleosynthesis. Chondritic meteorites formed from the condensation of the gas and dust of the solar nebula, and their chemistry and mineralogy provide information about processes in the solar nebula. The cosmochemical processes operating during the condensation of a solar nebula are very different from those of geochemistry for they are largely controlled by the relative volatility of the elements and compounds in the solar nebula (see Table 4.10). In the later stages of condensation

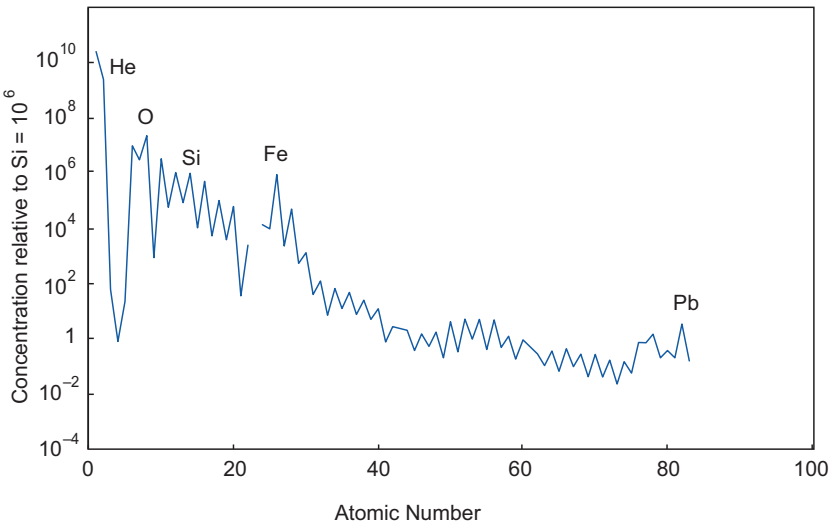

Figure 1.1 The abundances of elements in the sun, by atomic number, relative to the solar value Si = 10^6. (Data from Anders and Grevesse, 1989)

planetary bodies formed by the accretion of dust and rocky fragments and as these early planetary bodies grew they melted and differentiated into a metallic core and silicate mantle.

The chemical study of primitive meteorites illuminates our study of geochemistry in three important ways:

1. Knowing the chemical composition of the materials from which the Earth formed provides a geochemical baseline for measuring the differentiation of the Earth and the fractionation process that take place on the Earth. Typically, trace elements and isotopes are expressed relative to the *chondritic composition* of the Earth (Sections 4.3.2.2 and 6.2.2) as a measure of the original *bulk Earth composition (BE)*. Alternatively, trace element abundances and isotope ratios may be expressed relative to the Earth's primordial or *primitive mantle (PM)* which is the composition of the Earth after the separation of the core and represents the *bulk silicate Earth (BSE)* (see Sections 3.1.3, 4.4.1.2 and 6.2.2).
2. Some primitive meteorites contain information about processes in the solar nebula and more rarely about even earlier processes. Pre-solar grains of refractory minerals such as diamond and SiC can predate the solar nebula itself and stable isotope studies of elements such as Cr and Mn can provide information about the distribution of nucleosynthetic products in the early solar system (Section 7.4.4.3). Hydrogen isotope ratios are now available for a range of solar system objects and together with measurements made in meteorites are thought to indicate where in the solar system planets and other solar system objects formed (Section 7.3.2.2, Figure 7.7).
3. Meteorites also provide information about the large-scale differentiation of the Earth and the process of core formation. A knowledge of the mantle concentrations of those trace elements which have a high affinity for metallic iron, the highly siderophile elements (Section 4.5), coupled with experimental studies on their metal silicate partition coefficients (Table 4.10), provides information on the process of core formation. In a similar way, it is thought that carbon was sequestered into the Earth's core, and so the mass balance of carbon isotopes in the Earth's mantle also contributes to our understanding of this process (Section 7.3.3.2).

1.2.2 Processes Which Control the Chemical Composition of Igneous Rocks

The processes which control the composition of igneous rocks are summarised in Figure 1.2 and are illustrated for basaltic rocks.

1.2.2.1 Processes Which Take Place in the Mantle Source

Basaltic rocks may be extracted by partial melting from a range of mantle source compositions the most primitive of which – the primitive mantle – is the product of the very early differentiation of the Earth. This process involved the separation of the core and maybe formed during the magma-ocean stage of early Earth history. Subsequent partial melting and mixing events have

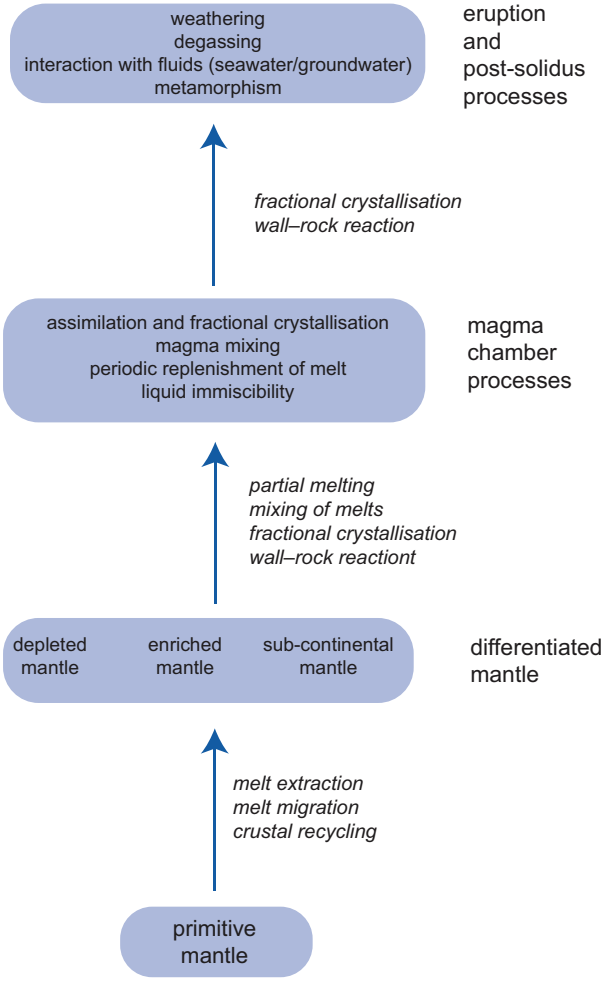

Figure 1.2 A flow diagram showing the main geochemical processes which operate during the genesis and eruption of basaltic rocks; the diagram is indicative of the geochemical processes which operate more generally in igneous rocks.

created the modern upper mantle which is differentiated into domains that are chemically depleted and enriched. Two main processes control the enrichment and depletion of the mantle. These are the extraction, migration and recrystallisation of partial melts, formed at different depths and representing different degrees of partial melting, and the recycling into the mantle of crustal materials through the process of subduction. Modern lavas derived from a source that has escaped later modification and so represents the Earth's primitive mantle are extremely rare. One example is the 61 Ma picrites from Baffin Island in north-eastern Canada which represent a relatively high melt fraction of deep mantle and have a primitive isotopic signature (McCoy-West et al., 2018).

Characterising the chemical composition of a mantle source region and thereby understanding those processes which take place in the source region is best achieved by measuring its radiogenic isotope composition (Section 6.2) and using selected trace element ratios, sometimes known as canonical trace element ratios, because these ratios are not modified during partial melting and subsequent magma chamber processes (Section 4.6.1.3).

1.2.2.2 Partial Melting Processes

Unmodified melts produced by the partial melting of the mantle are known as primary magmas. Their chemical composition is controlled by two main factors. The first controls are those of the chemical composition of the source and its mineralogy. The composition of the source will reflect whether or not it is chemically enriched or depleted, and the mineralogy of the source is a measure of the depth of melting. The second set of controls are the physical conditions of melting, that is, the temperature and depth of melting, the precise mechanism of melting and the degree of partial melting (Section 4.2.2.2). In some instances, the oxygen fugacity of the mantle is also an important control. After the initial melting stage, the primary magma may be modified as it migrates through the mantle through mixing with melts from other sources and through crystallisation and wall–rock reaction processes. The major element, trace element and radiogenic isotope chemistry are all important in unravelling the origins of primary magmas.

1.2.2.3 Magma Chamber Processes

Most basaltic rocks are filtered through a magma chamber prior to their emplacement at or near the surface. These magma chambers may be located at the base of the crust or at various levels within the crust. They are fed by what is known as the *parental magma*, which may or may not be the same as a primary magma. A wide variety of magma chamber processes modify the chemical composition of the parental magma. These include fractional crystallisation, assimilation of the country rock and associated fractional crystallisation, the mixing of magmas from more than one source, the separation of melts through liquid immiscibility or a dynamic mixture of several of these processes (Sections 3.3.4.1, 4.2.2.3 and 6.3.5). Magma chambers are best thought of as dynamic systems into which melt is fed and is differentiated, in which cumulate rocks form and from which melt is erupted. Resolving the chemical effects of these different processes requires the full

range of geochemical tools: major and trace element studies coupled with the measurement of both radiogenic and stable isotope compositions.

1.2.2.4 Post-solidus Processes

Following the emplacement or eruption of basaltic rocks they may be further chemically modified by the processes of outgassing or by interaction with a fluid such as seawater or groundwater. The outgassing or degassing of the dissolved gases in basaltic melts is the product of pressure release at the Earth's surface, and the effects are often seen in their stable isotope geochemistry, for this process readily fractionates isotopes on the basis of mass differences (Section 7.3.4.2). Hydrothermal processes operate at a range of temperatures, from several hundred degrees where seawater or groundwater interact with a magma chamber to the much lower temperatures of chemical weathering. Depending upon the temperature, these processes will modify the mineralogy of the parent rock through the development of clay minerals, and both major and trace elements may be mobilised (Sections 3.1.2 and 4.2.2.1). This is seen in igneous plutonic bodies where on emplacement hydrothermal ground-water circulation in the surrounding country rocks is initiated leading to the chemical alteration of the igneous pluton itself and sometimes the formation of ore bodies through the enhanced concentration of elements which have been mobilised. In addition to using major and trace elements, hydrothermal activity can be monitored by the use of radiogenic and stable isotopes, particularly those of strontium, oxygen and hydrogen, to measure the extent of fluid–rock interaction (Sections 6.3.5.2 and 7.3.2.7).

1.2.3 Processes Which Control the Chemical Composition of Metamorphic Rocks

The principal control on the chemical composition of a metamorphic rock is the composition of the protolith, that is, the composition of the rock prior to its metamorphism. Metamorphism is frequently accompanied by deformation, and at high metamorphic grades there may be the mechanical mixing of different protolith compositions through tectonic interleaving, which can give rise to metamorphic rocks of mixed parentage.

Metamorphic recrystallisation is the result of chemical reactions which take place in the solid state by the process of diffusion. These reactions occur during the burial and heating of the protolith and during cooling. They may be isochemical, but most commonly there is a change in chemical composition. This chemical change is related to the mineralogical reactions which take place and the extent to which those elements found in the minerals in the protolith can be accommodated in the new minerals of the metamorphic rock. Most commonly, these mineralogical changes are also controlled by the movement of fluids in the rock. For this reason, the ingress and expulsion of water during metamorphism, chiefly as a consequence of metamorphic hydration and dehydration reactions, exerts the major control on element mobility during metamorphism. These processes are controlled by the composition of the fluid phase, most commonly H_2O and CO_2, its temperature and the ratio of the volume of metamorphic fluid to that of the host rock. The extent to which major and trace elements are mobile during metamorphism can sometimes be assessed by reference to the composition of the unmetamorphosed parent rock. Reactions between crustal fluids and metamorphic rocks and the relative volume of the fluids involved can be measured using the stable isotopes of hydrogen and oxygen (Section 7.3.2.7).

At high metamorphic grades, and frequently in the presence of a hydrous fluid, melting may occur. The segregation and removal of a melt phase will differentiate the parental rock into two compositionally distinct components: the melt and the unmelted component, known as the restite. In this case, the precise nature of the chemical change is governed by the melting reaction and the degree of melting (Section 3.4.3).

1.2.4 Low-Temperature Processes in the Earth's Surficial Environment

Low-temperature processes in the Earth's surficial environment include the wide array of interactions between the atmosphere, the hydrosphere, and rocks and soils at the Earth's surface. These interactions are often summarised in diagrams representing geochemical cycles and can be represented by box models which show the mass balance for a particular element between the different Earth reservoirs. Examples of geochemical cycles quantified using stable isotope ratios are given in Chapter 7; see Figure 7.22 for the

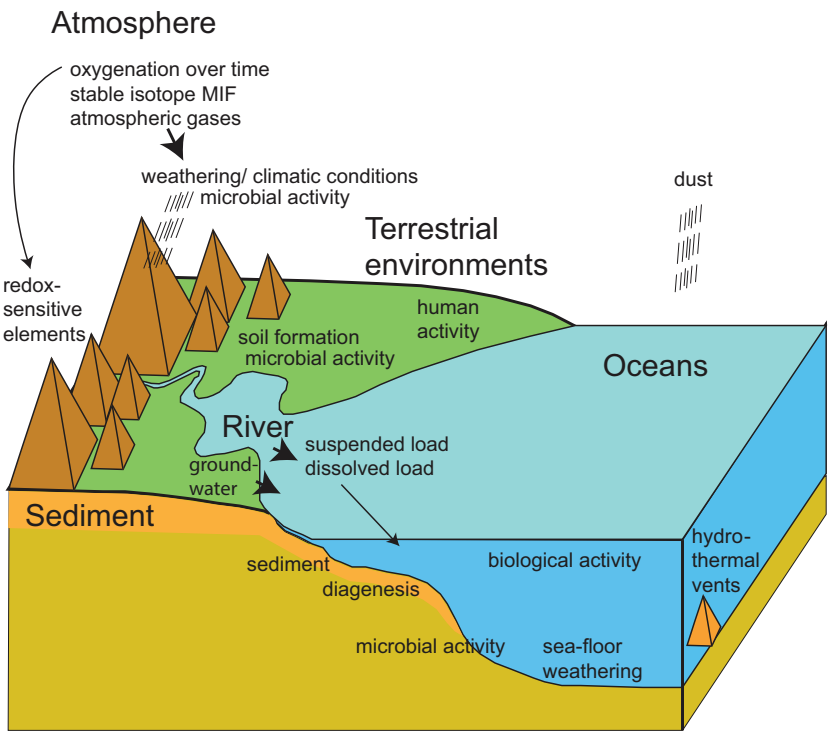

Figure 1.3 Cartoon diagram showing the interconnecting processes which operate at the Earth's surface in the atmosphere, in terrestrial environments and in the oceans. (Figure adapted from Frank et al., 2020. With permission from Elsevier)

elements sulphur, carbon and oxygen, and Figure 7.27 for nitrogen. A cartoon diagram summarising the main surficial processes discussed here is given in Figure 1.3.

1.2.4.1 Atmospheric Processes

A detailed discussion of geochemical processes occurring in the Earth's atmosphere is beyond the scope of this book. However, there is one aspect of atmospheric geochemistry which is relevant to the petrological processes discussed here, for over geological time the chemical composition of the Earth's atmosphere has become increasingly oxygenated. This change in the level of oxygen in the atmosphere has a direct bearing on the oxygenation of the oceans and on weathering processes. Thus, those elements which are redox sensitive at the Earth's surface can play an important role in identifying the different levels of oxygenation in the oceans and other bodies of surface water. Particularly important are the redox sensitive trace elements (Section 4.2.1.3) and the stable isotopes of the transition metals, nitrogen and sulphur (Sections 7.4.4.3 and 7.4.5.3). The process of mass independent fractionation of sulphur isotopes plays a particularly important role in the detecting the earliest oxygenation of the Earth's atmosphere (Section 7.3.4.4).

1.2.4.2 Weathering Processes

The interaction between the atmosphere and hydrosphere in the terrestrial environment leads to the development of a weathering profile and the formation of soils. This process is often biologically mediated and involves chemical reactions in which silicate minerals are converted into clays. These reactions are governed by the surface temperature and in some circumstances may be used to infer former climatic conditions. The intensity of chemical weathering has been quantified using the chemical index of alteration calculated from major element geochemistry (Section 3.3.1.5) and from the fractionation of the stable isotopes of lithium and silicon (Sections 7.4.1.3 and 7.4.3.2). The temperature of formation of the clay minerals kaolinite and smectite in the weathering environment has been estimated using hydrogen and oxygen isotopes (Section 7.3.2.4).

In the marine environment the interaction between seawater and the rocks of the ocean floor leads to the seafloor weathering of basalts. In some cases the isotopic composition of weathered ocean floor basalts is sufficiently different from that of unaltered basalt that this signature may be used to track the recycling of the altered basalts back into the Earth's mantle. This is particularly pertinent for Li isotopes (Section 7.4.1.1) and Os isotopes (Section 6.3.3.4).

1.2.4.3 Water Chemistry

The chemical composition of river water is expressed in terms of its dissolved load and its suspended load of particulate matter. Different elements behave in different ways and some may be present in solution; others are adsorbed onto particulate matter. These two components are a consequence of the particular weathering environment, and because of this the chemical composition of rivers from across the globe is very variable. In some weathering environments the fractionation of stable isotopes during the formation of clay minerals is extreme and this geochemical signature can be transferred to river water and in the case of Li isotopes gives it a very distinctive isotopic composition (Section 7.4.1.3). In a similar way the stable isotopes of Mg, Si, Cr and Fe are also highly fractionated in river water relative to silicate rocks (Figures 7.32, 7.33, 7.35 and 7.36).

The chemical composition of seawater is influenced by the input of river water, groundwater, atmospheric dust, hydrothermal fluids, sea-floor weathering and biological activity (Figure 7.3). Ultimately, the elements present in seawater are taken up in to sediments, but the average length of time they remain in the seawater is highly variable. This time interval is known as the *residence time*. For a given element the length of the residence time is a measure of how well mixed the oceans are for that particular element. This is illustrated for the rare earth elements (REE) in Section 4.3.3.2 and radiogenic isotopes in Section 6.3.2.3. The geochemistry of the oceans is not the main focus of this book, although there are two themes which are of petrological interest. These are the interactions between seawater and the rocks of the ocean floor, and the way in which the composition of seawater has changed over time (Figure 6.13). Seawater–rock interactions have been monitored using the stable isotopes of hydrogen and oxygen (Section 7.3.2.7) and these have great relevance to the formation of mineral deposits. The changing composition of seawater can be evaluated in the changing isotopic composition of marine sediments such as those carbonates which are precipitated directly from seawater. The stable isotope ratios of carbon (Section 7.3.3.5) and lithium (Section 7.4.1.3) and the radiogenic isotope ratios of strontium and osmium (Section 6.3.2.3) are particularly sensitive.

1.2.4.4 The Impact of Human Activity on the Earth's Surface Environment

The impact of anthropogenic activity is increasingly important in environmental geochemistry. Although beyond the scope of this book, two examples are pertinent. Recent work on nitrogen isotopes has shown that it is possible to fingerprint polluting anthropogenic nitrates (Section 7.3.5.3) and in a similar way the remediation of toxic Cr^{6+} in groundwater can be monitored using the stable isotopes of Cr (Section 7.4.4.3).

1.2.5 Processes Which Control the Chemical Composition of Sedimentary Rocks

1.2.5.1 Provenance

The geochemical make-up of the rocks constitutes the provenance which influences the composition of sediments. In immature sediments there is a direct geochemical link between the major and trace element composition of the sediment and its provenance (Section 5.5). The provenance of fine-grained, clay-rich sediments such as shale can be determined from selected trace elements and isotopes (Sections 4.2.2.4, 5.5.3 and 6.2.3.2). Provenance studies may also be used to determine the original tectonic setting of the basin in which fine-grained sediment formed (Section 5.5).

1.2.5.2 Weathering

Weathering conditions leave their signature in the resultant sediment and, as discussed above, major element and stable isotope studies of sedimentary rocks indicate that former weathering conditions can be recognised in the chemical composition of the sediments. Significant chemical changes may also take place during sediment transport, for some trace elements become concentrated in the clay fraction; others are concentrated in a heavy mineral fraction; while others are diluted in the presence of a quartz-rich fraction. To a large extent these processes are dependent upon the length of time the sediment spends between erosion and deposition.

1.2.5.3 Processes in the Depositional Environment

The chemical changes that occur during the deposition of sediments are governed by the nature of the depositional environment. This in turn is influenced by the subsidence rate and the attendant thermal conditions of the sedimentary basin. The temperature-

dependent fractionation of oxygen isotopes can be used to calculate the geothermal gradient during diagenesis and allows some control on the burial history of the rock (Sections 7.2.5 and 7.3.1.2). In the case of chemical sediments the chemical and biochemical processes controlling the solubility of particular elements coupled with thermal and redox conditions are also important. Post-depositional, fluid-related diagenetic processes are best investigated using stable isotopes. The stable isotopes of oxygen and hydrogen are important tracers of different types of water (Section 7.3.2.3) and the combined application of carbon and oxygen isotopes are important in the study of limestone diagenesis (Section 7.3.3.9).

1.2.6 Biogeochemical Processes

Microbial life is abundant at the surface of the Earth and can leave a geochemical fingerprint in its stable isotope signature. This is because many microbially mediated chemical reactions cause mass fractionation in particular stable isotope systems. For example, the kinetics of the conversion of inorganic carbon into living carbon entails the preferential concentration of the light carbon isotope in the living carbon (Section 7.3.3.6). Isotopic signatures of this kind open up the possibility of identifying specific microbial reactions which may relate to particular metabolic pathways which may be found in both modern environments and in the ancient sedimentary record. Other examples of elements which are essential to life and whose stable isotopes are fractionated by microbial activity are sulphur and nitrogen. In the marine environment sulphur isotopes are fractionated during the reduction of seawater sulphate by anaerobic bacteria (Section 7.3.4.2) and nitrogen isotopes are fractionated during the reduction of nitrate to atmospheric nitrogen through the metabolic processes of denitrification and anammox (Section 7.3.5.2). Magnesium is also an essential element in the biosphere and there is evidence that Mg isotopes are fractionated in plants during photosynthesis (Section 7.4.2.3). Iron isotopes are fractionated during both anaerobic bacterial iron reduction and photosynthetic iron oxidation operating under anaerobic conditions (Section 7.4.5.2).

1.2.6.1 The Search for Early Life on Earth

The preservation of microbially driven stable isotope fractionations in the geological record has been used a means of identifying the presence of life on Earth from the earliest stages of Earth history. One of the first studies was by Schidlowski (1988), who showed that the study of carbon isotopes can be used to trace ancient biological activity through the geological record back as far as 3.7 Ga (Section 7.3.3.7). Subsequent studies used the large negative sulphur isotope values in the sedimentary record as a means of exploring the processes of microbial sulphate reduction in the geological past (Section 7.3.4.6). It has also been suggested that the extreme iron isotope fractionations in Archaean sediments are, in part, the product of microbial activity, although as with other stable isotope systems it is important to establish whether or not similar fractionations could have been produced by abiotic processes (Section 7.4.5.3).

1.3 Geological Controls on Geochemical Data

The most fruitful geochemical investigations are those that test a particular model or hypothesis. This ultimately hinges upon a clear understanding of the geological relationships in the rock suite under investigation. Thus, any successful geochemical investigation must be based upon a proper understanding of the geology of the area. It is not sufficient to carry out a 'smash and grab raid', returning to the laboratory with large numbers of samples, if the relationships between the samples are unknown and their relationship to the regional geology is unclear. It is normal to use the geology to interpret the geochemistry. Rarely is the converse true, for at best the results are ambiguous.

In some instances this is self-evident, for example, when samples are collected from a specific stratigraphic sequence or lava pile or from drill core data, and there is a clear advantage in knowing how geochemical changes take place with stratigraphic height and therefore over time. A more complex example would be a metamorphosed migmatite terrain in which several generations of melt have been produced from a number of possible sources. A regional study in which samples are collected on a grid pattern may have a statistically accurate feel and yet will provide limited information on the processes in the migmatite complex. What is required in such a study is the mapping of the relative age relationships between the components present, at the appropriate scale, followed by the careful sampling of each domain. This then allows chemical variations within the melt

and restite components to be investigated and models tested to establish the relationships between them.

A further consideration comes from the different scales on which geochemical data are collected. With the advent of microbeam analytical techniques and the continuation of programmes such as the ocean drilling or continental drilling programmes it is possible to measure geochemical data from the micro to macro scales. For example, the mapping of trace element or isotopic data in a single mineral grain may be used to illuminate processes such as fractionation in an igneous melt, diffusion in a metamorphic rock or changing fluid conditions during sediment diagenesis. This was illustrated in the study of the zonation of iron isotopes in olivines from Kīlauea Iki lava lake in Hawai'i by Sio et al. (2013). Equally, the mapping of isotopic variations in ocean floor basalts can be used to identify geographically specific compositional reservoirs in the Earth's mantle. Hart (1984) mapped the southern hemisphere DUPAL anomaly in this way on the basis of anomalous Sr- and Pb-isotopic compositions. At an intermediate scale, the mapping of the distribution of Pb in stream sediments over a large area of eastern Greece has relevance for both environmental pollution and mineral exploration (see figure 2 in Demetriades, 2014).

A fundamental tenet of this book therefore is that if geochemical data are going to provide information about geological processes, then geochemical investigations must always be carried out in the light of a clear understanding of the geological relationships. This normally means that careful geological fieldwork is a prerequisite to a geochemical investigation. This approach leads naturally to the way in which geochemical data are presented. In the main this is as bivariate (and trivariate) plots in which the variables are the geochemical data. The interpretation of these plots forms the basis for understanding the geological processes operating.

1.3.1 Sample Collection

It is important that any new geochemical investigation has a well-developed sampling strategy. The key parameters are discussed in detail by Ramsay (1997) and for environmental applications by Demetriades (2014). A brief summary is given here.

- Sample size tends to be governed by the grain size of the rock. The overriding principle is that the sample must be representative of the rock. In addition, the portion of the sample used in geochemistry must be fresh and therefore an allowance must be made for any weathered material present which will be removed later. It is also important to retain part of the sample for future research and/or the preparation of a thin section.
- Sampling will normally be done using a hammer. Occasionally, precise sampling or sampling from a difficult surface may be carried out using a coring drill. In either case care must be taken to establish that rock sampling is permitted at the site in question and that sampling is carried out as discretely as possible.
- The number of samples is normally governed by the nature of the problem being solved. Relevant are the geographic extent of the study area and whether or not there are spatial or temporal aspects to the research project. If the research question is very specific a relatively small number (10–20) of well-chosen samples may suffice. Often many more samples than this are required. A further consideration is whether there is the opportunity to return to the field area. If not, then selecting a larger number of samples makes good sense.
- The careful labelling of samples in the field, at the site of collection, is perhaps obvious. A geological description of the site is important, accompanied by photographs and the precise GPS location. This will allow the researcher or their successor to return to the precise sample site if necessary, and such information is often important in the future publication of the results.

1.4 Analytical Methods in Geochemistry

In this section the more widely used analytical methods are reviewed in order to provide a guide for those embarking on geochemical analysis. This text is not principally a book about analytical methods in geochemistry and excellent summaries are given by Gill (1997), Rouessac and Rouessac (2007) and in the second edition of volume 15 of the *Treatise on Geochemistry* (McDonough, 2014b). First, however, it is necessary to consider the criteria by which a particular analytical technique might be evaluated (Figure 1.4). In this book, in which geochemical data are used to infer geochemical processes, it is the quality of the data which is important. Data quality may be measured in terms of precision, accuracy and detection limits.

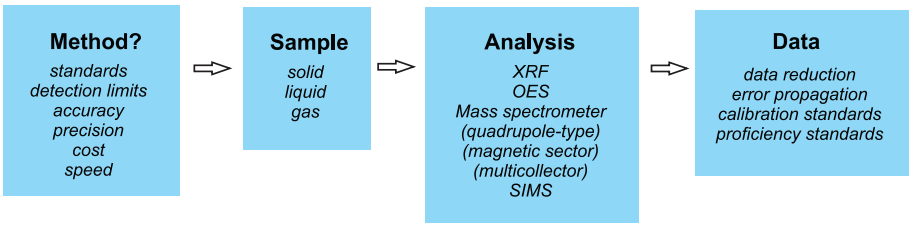

Figure 1.4 Obtaining geochemical data. A summary of the key issues to be considered when collecting geochemical data and in selecting an appropriate method of analysis.

Precision refers to the repeatability of a measurement. It is a measure of the reproducibility of the method and is determined by making replicate measurements on the same sample. The limiting factor on precision is the counting statistics of the measuring device used. Precision can be defined by the coefficient of variation which is 100 times the standard deviation divided by the mean (Till, 1974), also known as the relative standard deviation (Jarvis and Williams, 1989). A common practice, however, is to equate precision with one standard deviation from the mean (Norman et al., 1989). It can be helpful to distinguish between precision during a given analytical session (repeatability) and precision over a period of days or weeks (reproducibility).

Accuracy is about getting the right answer. It is an estimate of how close the measured value is to the true value. Knowing the true value can be very difficult, but it is normally done using recommended values for international geochemical reference standards (see Section 1.6.4). It is of course possible to obtain precise but inaccurate results.

The *detection limit* is the lowest concentration which can be 'seen' by a particular method and is a function of the level of background noise relative to the sample signal (Norish and Chappell, 1977). Where concentrations of a particular element are below the levels of detection for a particular analytical method, this is often reported in data tables as 'bd' (below the limits of detection; see Table 1.1).

1.4.1 Sample Preparation

In the laboratory, rock samples must be reduced to a fine powder for fusion or dissolution prior to geochemical analysis. This normally follows a number of stages. These include the splitting of the rock and the removal of any remaining weathered material; the crushing of the sample, often in a hardened steel jaw crusher; and then the pulverising of the sample to a fine powder in a ball mill or disc mill. Two key principles must be followed. First, the whole sample must be reduced to a powder and so the sample should not be sieved. Second, the chemical composition of the machinery used in the pulverisation of the rock sample must be chosen with the sample geochemistry in mind. It would be unwise to use a tungsten-carbide mill if tungsten is an element of interest because it is very probable that the sample will become contaminated with W during sample preparation.

1.4.2 Sample Dissolution

Many of the analytical methods describe below require the bulk rock sample to be in solution. Given the insoluble nature of silicate rocks this requires a number of acid dissolution, digestion and/or fusion techniques. It is essential that the entire rock, including resistant insoluble phases such as zircon or chromite, is completely dissolved and that the dissolution process is done in an ultra-clean environment so that the sample is not contaminated during the digestion process. A comprehensive review of the full range of dissolution techniques for analytical geochemistry is given by Hu and Qi (2014). The main analytical methods currently in use in geochemistry are briefly described below.

1.4.3 X-Ray Fluorescence (XRF)

X-ray fluorescence spectrometry (XRF) was the workhorse of early-modern geochemistry and was widely used for the determination of major and trace element concentrations in rock samples. It is still widely used in mining geology and exploration geochemistry. The method is versatile: it can analyse up to 80 elements over a wide range of sensitivities detecting concentrations from 100% down to a few ppm and is rapid so that large numbers of precise analyses can be made in a relatively short space of time. Good reviews of the older applications of the XRF method are given by Leake et al.

(1969), Norrish and Chappell (1977), Ahmedali (1989) and Fitton (1997) and there is a comprehensive recent review by Nakayama and Nakamura (2014).

1.4.3.1 Wavelength Dispersive X-Ray Fluorescence Spectrometry (WDXRF)

X-ray fluorescence spectrometry is based upon the excitation of a sample by X-rays. A primary X-ray beam excites secondary X-rays (X-ray fluorescence) which have wavelengths characteristic of the elements present in the sample. The intensity of the secondary X-rays is proportional to the concentration of the element present and is used to determine the concentrations of the elements present by reference to calibration standards. In most XRF spectrometers the X-ray source is an X-ray tube in which the X-rays are generated by the bombardment of a target with electrons. For the analysis of geological samples, the target element, or anode of the X-ray tube, is Rh as the X-rays from Rh are capable of exciting a very wide range of elements. However, in some instances W, Au, Cr and Mo tubes may also be used. The intensity of the secondary X-rays is analysed in a wavelength dispersive spectrometer using either a gas proportional counter or a scintillation counter. In detail instruments vary in precisely how the analyses are made. In some a relatively small number of elements are measured simultaneously, in others a larger number of elements are measured sequentially.

1.4.3.2 Energy Dispersive X-Ray Fluorescence (EDXRF)

A more recent application of X-ray fluorescence technology is the development of energy dispersive X-ray fluorescence in which the X-ray *energy* is measured using a solid-state silicon drift detector (Potts et al., 1990). This method allows the simultaneous measurement of a large number of elements and in principle can measure almost every element between Na to U at concentrations from a few ppm to nearly 100% within a few seconds. The detector identifies the radiation from the different elements present in the sample and analyses the energy on a multi-channel pulse height analyser.

The range of elements that may be detected during X-ray fluorescence analysis varies according to the type of instrument. In WDXRF the element range is from Be to U, whereas in EDXRF it is from Na to U. The limits of detection depend upon the element and the sample matrix, but generally the heavier elements have better detection limits. The better peak resolution of WDXRF means that there will be fewer spectral overlaps and the background noise is reduced so that detection limits and sensitivity are improved over EDXRF. In terms of speed of analysis and therefore cost, a spectrum is collected very rapidly in EDXRF, whereas with WDXRF the elements are analysed in sequence or in batches and therefore each analysis takes longer. Samples for trace element analysis are prepared as a pressed disc of the rock powder (Leake et al. 1969); for major element analysis a glass bead is made from a fusion of the powdered sample with a lithium metaborate or tetraborate flux.

New developments in XRF technology have led to the recent development of micro-XRF and portable XRF analysers. Micro-XRF uses the energy-dispersive method of detection and a narrow X-ray beam as an imaging tool to map microscopic particles and build high-resolution elemental maps of geological materials. Portable XRF analysers also use the energy-dispersive method of detection. They are capable of measuring a wide range of elements from Mg (some include Na) upwards in the periodic table and have detection limits of a few ppm to a few tens of ppm for trace elements of geological interest. Applications include the analysis of clean rock surfaces and drill core. Rowe et al. (2012) discuss the application of portable XRF in the analysis of mudrocks.

1.4.4 Instrumental Neutron Activation Analysis (INAA)

Instrumental neutron activation analysis has been used in the past as a non-destructive technique for the determination of trace elements, particularly the REE. Instrumental neutron activation analysis (INAA) uses a about 100 mg of powdered rock or mineral sample; the sample is placed in a neutron flux in a neutron reactor and irradiated. The neutron flux gives rise to new, short-lived radioactive isotopes of the elements present which emit gamma radiation and are measured using a Ge detector (Hoffman, 1992). Instrumental neutron activation analysis has now been superseded by more rapid and more accurate methods of trace element analysis and is no longer widely used.

1.4.5 Atomic Absorption Spectrophotometry (AAS)

Atomic absorption spectrophotometry (AAS) has been used in the past for major and trace element analysis.

The method is based upon the observation that atoms of an element can absorb electromagnetic radiation when the element is atomised. A lowering of response in a detector during the atomisation of a sample in a beam of light as a consequence of atomic absorption can be calibrated and is sensitive at the ppm level (Price, 1972). However, this technique allows only one element to be analysed at a time, and so has been superseded by more rapid methods of silicate analysis and now is rarely used for geochemical analysis.

1.4.6 Mass Spectrometry

Mass spectrometry is an analytical technique which is particularly suited to the measurement of isotopes in geological samples (Figure 1.5). It offers very high precision, low levels of detection and may be applied to very small samples. Often, however, it requires extensive sample preparation which may involve the chemical separation of the element of interest. In this section we consider the techniques of thermal ionisation mass spectrometry (TIMS), gas source mass spectrometry and the isotopic method of isotope dilution mass spectrometry. In Section 1.4.7 we will consider inductively coupled plasma mass spectrometry (ICP-MS) and in Section 1.4.9 secondary ion mass spectrometry (SIMS). In each case, however, the principles are the same. All rely on the generation of a beam of charged ions which is fired along a curved tube through a powerful electromagnet in which the atoms are separated according to their mass in response to the forces operating in the magnetic field. A mass spectrum is produced in which the lighter ions are deflected with a smaller radius of curvature than heavy ions. The quantitative detection of the signal allows isotope ratios to be calculated. The main difference between these mass spectrometric techniques is the manner in which the sample is ionised.

1.4.6.1 Thermal Ionisation Mass Spectrometry (TIMS)

In thermal ionisation mass spectrometry the sample is ionised on a glowing filament made of a high-melting-point metal, often Re. The method is particularly relevant to elements that have a high capacity for thermal ionisation and whose isotope systems are of interest. In geochemistry this includes Mg, Cr, Ti, Sr, Ba, Nd, Re, Os, W and Pb (Carlson, 2014). Most elements of interest ionise as positive ions, but Re and Os are more efficiently ionised as negative ions. In his detailed review Carlson (2014) summarises the main strengths and weaknesses of the TIMS method. He shows that the main advantages of TIMS are the following: for those elements that ionise easily the ionisation is highly efficient; the molecular interference spectrum is quite simple; the thermal ionisation produces ions with a small energy spread allowing good mass resolution; and the potential for sample to sample cross contamination is small. Disadvantages are that for some elements of geological interest the ionisation efficiency is low and so the technique is unsuitable for Hf, W and positive Os ions; the chemical preparation of samples is complex and time-consuming; and corrections have to be made for the mass fractionation between isotopes during the process of thermal ionisation.

1.4.6.2 Gas Source Mass Spectrometry

Gas source mass spectrometry is used to measure the traditional stable isotopes (H, O, C, S and N) as described by Sharp (2014) and the noble gases (Wieler, 2014). In stable isotope geochemistry rock samples are converted into a gas before the element of interest is introduced into the mass spectrometer: hydrogen as H_2, oxygen and carbon as CO_2, sulphur as SO_2 or SF_6 and nitrogen as N_2. The chemistry can be complex, as is the process of gas purification. The gas is introduced into the mass spectrometer using either a

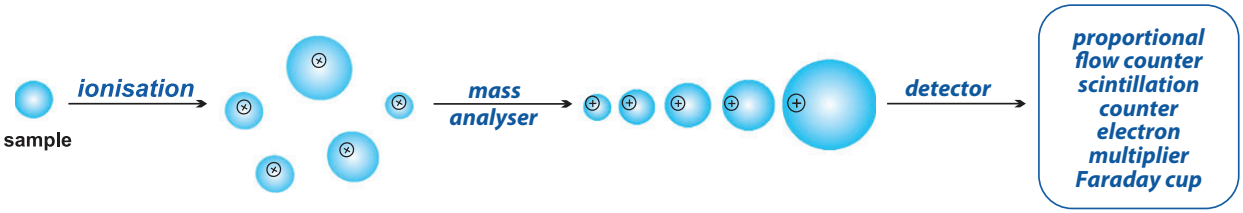

Figure 1.5 The essentials of mass spectrometry. The sample material is ionised and introduced into the mass spectrometer which is under vacuum. The ionised materials travel through the mass analyser, where ions are separated according to their charge to mass ratio, and then on to the detector where they are counted.

dual-inlet system or a continuous flow. In the dual-inlet system there is either the rapid switching between the sample and a standard reference gas or a dynamic inlet system in which the sample gas is constantly refreshed. In the continuous flow method a pulse of the sample gas is entrained in a helium stream, passed through a gas chromatographic column for purification, and into the mass spectrometer. The continuous flow method is popular, although there are isotope fractionations during the combustion of samples which must be accounted for in the data processing. Once in the mass spectrometer the sample gas is ionised by the impact of high-energy electrons from a tungsten filament.

1.4.6.3 Laser Fluorination Gas Source Mass Spectrometry

The in situ analysis of traditional stable isotopes (C, O, S, N) may be carried out using laser fluorination gas source mass spectrometry (Arevalo, 2014). This method has a very high spatial resolution for the analysis of mineral grains and permits the in situ analysis of individual micron-scale fluid and melt inclusions.

1.4.6.4 Isotope Dilution Mass Spectrometry

Isotope dilution mass spectrometry is the most accurate and most sensitive of all trace element analytical techniques and is particularly suited to measuring very low concentrations of trace elements to very high levels of accuracy and precision. The method is described in detail by Stracke et al. (2014) and is applicable to the different mass spectrometric methods described above. Isotope dilution depends upon the addition of a known quantity of an element with a non-natural isotopic composition (known as a 'spike') to a known quantity of the sample. The isotopic composition of the spike–sample mixture is then measured by mass spectrometry, and from the known isotopic compositions of the sample and the spike it is possible to calculate the concentration of the element. The detail of the calculations is given in Stracke et al. (2014). The method is applicable to any element which has two or more naturally occurring isotopes and has been particularly useful in geochronology and in determining the abundances of trace elements at very low concentrations. The main advantage of isotope dilution is that the method does not depend upon any external calibration, for element concentrations are determined directly from the masses of the sample and the spike and the measured isotopic compositions of the sample, spike and sample–spike mixture. Further, unlike other mass spectrometric methods isotope dilution does not depend upon the quantitative recovery of the element from the sample.

Double-spike isotope dilution methods require the addition of two spike isotopes and the analysis of four or more isotopes. This method uses two independently measured isotope ratios to determine two unknowns and is used to separate natural isotope fractionations from those induced by chemical processing or fractionations which occur during analytical measurements such as instrumental mass fractionation.

1.4.7 Inductively Coupled Plasma (ICP) Spectrometry

Inductively coupled plasma (ICP) spectrometry is an analytical method in which the sample is introduced into a plasma source in which the energy is supplied by electrical currents produced by electromagnetic induction. The inductively coupled plasma is a stream of argon atoms, heated by the inductive heating of a radio frequency coil and ignited by a high-frequency Tesla spark. The sample dissociates in the argon plasma into a range of atomic and ionic species. Samples are prepared in solution using the standard methods of silicate dissolution. There are two main applications of ICP spectrometry: the older technique of ICP-optical emission spectrometry and the more recently developed and now widely used technique of ICP-mass spectrometry.

1.4.7.1 ICP-Optical Emission Spectrometry (ICP-OES)

ICP optical emission spectrometry (ICP-OES), also known as ICP-atomic emission spectrometry (ICP-AES), is a light-source technique with a plasma temperature in the range 6000–10,000 K. A sample solution is passed as an aerosol from a nebuliser into an argon plasma. The sample dissociates in the argon plasma and a large number of atomic and ionic spectral lines are excited. Emission rays that correspond to photon wavelengths are measured and the element type and concentration is determined from the position and intensity of the photon rays, respectively. The spectral lines are detected by a range of photomultipliers; these are compared with calibration lines, and their intensities converted into concentrations. The ICP-OES method is capable of measuring most elements in the periodic table with low detection limits and good precision over several orders of magnitude. Elements are

measured either simultaneously or sequentially. When measured simultaneously a complete analysis can be made in the space of about 2 minutes, making it an extremely rapid analytical method. A full description of the method and its application is given by Walsh and Howie (1980) and Thompson and Walsh (1983).

1.4.7.2 ICP-Mass Spectrometry (ICP-MS)

ICP mass spectrometry is now widely used as a means of elemental and isotopic analysis, for the detection limits are extremely low and may be in the parts per trillion (ppt, ngl^{-1}) range. A review of the methodology and instrumentation is given by Olesik (2014). There are now a number of different types of mass spectrometer which are used in ICP analysis. These include the following:

- Quadrupole mass spectrometers. Quadrupole instruments are widely used, for they are able to rapidly and sequentially measure the different atomic masses. However, it is necessary to use instrumental and/or mathematical corrections in the data processing to accommodate spectral overlaps.
- Sector field mass spectrometers. These measure masses sequentially and can be used for isotope ratio measurements as well as elemental chemical analysis. They provide a much higher sensitivity or, alternatively, a much higher mass resolution than quadrupole instruments. Sector field mass spectrometers are more complex than quadrupole instruments and use a double focusing design to achieve the higher sensitivity or mass resolution. This means that ions with the same mass to charge ratio but different kinetic energies are focussed into a single location in the focal plane.
- Multi-collector instruments (MC-ICP-MS). These use sector field mass spectrometry but with multiple detectors to measure isotopes simultaneously in order to determine isotope ratios with extremely high precision. However, multi-collector instruments require the chemical separation of the element of interest from the sample matrix.

1.4.7.3 Laser Ablation ICP Mass Spectrometry (LA-ICP-MS)

Laser ablation mass spectrometry is an in situ analytical method which can be used for measuring elemental concentrations down to very low abundances and radiogenic and non-traditional stable isotope ratios. The details of the methodology are given by Arevalo (2014). The benefits of the LA-ICP-MS method are that it provides rapid, high-precision analysis, minimal sample processing and high spatial resolution of the data. The sample is ablated using either a pulsed Nd:YAG (Nd-doped yttrium aluminium garnet) laser system or an excimer laser system which employs gas mixtures of a noble gas and a halogen. The ablated material is then introduced into an ICP mass spectrometer. Issues of concern in the application of this technology are elemental fractionations which may take place during the ablation process or non-stoichiometric ablation. These may be accommodated using a range of operational protocols as outlined by Arevalo (2014). The reduction in LA-ICP-MS data is carried out using a variety of software packages, and a recent study showed that different users can obtain significantly different results from the same raw data. For this reason, Branson et al. (2019) recently proposed a new data-reduction package which provides some consistency in this field and allows for the reproducible reduction of LA-ICP-MS data.

1.4.8 Electron Probe Micro-analysis (EPMA)

Electron probe analysis is a microbeam technique which is principally used in the analysis of minerals and glasses. The method is reviewed by Reed (1994). The sample is excited by a highly focused beam of electrons and X-rays are generated. The quantitative analysis of the sample is obtained by the analysis of the X-rays and as with X-ray fluorescence analysis these may be analysed in two ways. They may be analysed according to their wavelength or by their energy spectrum. In electron microprobe wavelength dispersive analysis, using a wavelength dispersive spectrometer (WDS), the X-rays are analysed in a series of element-specific detectors in which the peak area is counted relative to a standard, and intensities converted into concentrations after making appropriate corrections for the matrix (Long, 1994). There are a variety of software packages which process the data. Energy-dispersive electron microprobe analysis, using an energy dispersive spectrometer (EDS), utilises an energy versus intensity spectrum and allows the simultaneous determination of the elements of interest. The spectrum is collected using a solid-state silicon drift detector. EDS analysis may also be made using a scanning electron microscope (SEM) with an attached solid-state detector and can be used for quantitative

analysis provided it is calibrated with suitable standards. WDS is the more precise of the two methods and the speed of analysis is governed by the number of spectrometers on the instrument – often around 3 minutes for a ten-element analysis. EDS analysis prefers speed (about 1 minute to collect a spectrum) over very high levels of precision.

During the interaction between the electron beam and the sample secondary electrons and backscattered electrons are generated. These may be used, with the appropriate detectors, to provide an electron image of the sample and so guide the EPMA user to suitable 'spots' on the sample for analysis. Images may also be used for element mapping, in which the distribution pattern of a particular element is displayed within a mineral grain, and so is important in demonstrating features such as element zoning or exsolution.

The chief merit of the electron microprobe is that it has excellent spatial resolution and commonly employs an electron beam of 1–5 microns in diameter. This means that extremely small sample areas can be analysed and individual mineral grains can be analysed in great detail. Elements from B to U can be analysed, but most laboratories analyse only the major elements on a routine basis. Most geological applications are in the analysis of minerals and natural and synthetic glasses. The analysis of silicate glass is of particular importance in the analysis of tephra and the experimental charges in experimental petrology; less commonly fused discs of rock powder are analysed for major elements using this method (Staudigel and Bryan, 1981). In glass analysis a wider, defocussed electron beam is normally used to minimise the problems of sample volatilisation during analysis and inhomogeneity in the glass.

The development of field emission electron probe instruments (FE-EPMA), in which the microprobe is equipped with a thermal field emission gun electron source, has provided even better imaging and analytical resolution. FE-EPMA instruments can provide accurate quantitative analyses of individual grains as small as 300–400 nm and have the X-ray imaging capacity of down to 200 nm (Armstrong et al., 2013). Samples for EPMA are prepared for analysis by making a polished thin section of a rock slice or grain mount in epoxy resin. The polished surface is then sputter coated with a thin conductive layer of carbon or gold.

1.4.9 The Ion Microprobe (SIMS)

The ion microprobe, or ion-probe as it is also known, combines the analytical accuracy and precision of mass spectrometry with the very fine spatial resolution of the electron microprobe. It is widely used in the fields of geochronology, stable isotope geochemistry and trace element analysis. Reviews of the method and its application are given by Hinton (1994) and Ireland (2014). There are two principal instruments available, the SHRIMP (sensitive high-resolution ion microprobe) family of instruments from the Australian National University and Cameca instruments which include the NanoSIMS with nanometer resolution.

Ion microprobe technology employs a finely focussed beam of ions to bombard an area of the sample (typically 10–25 microns in diameter) and causes a fraction of the target area to be ionised and emitted as secondary ions. The ionisation process, known as sputtering, drills a small hole in the surface of the sample a few microns in depth. Samples are prepared as polished thin sections or grain mounts coated with carbon or gold. Before analysis, samples are normally characterised using conventional geological microscopy and electron imaging in order to determine the best sample area for analysis. Ion-probe analysis is non-destructive, highly sensitive and is capable of producing many analyses from a very small amount of material – important when multiple analytical methods on a single location are desired.

The primary ion beam is most commonly made up of either Cs or oxygen ions. Cs^+ is used for non-metals such as O or S, and oxygen for metals such as Pb^+. There is a trade-off during analysis between spatial resolution and precision – the larger the spot size, the larger the mass sputtered which typically results in better precision, but at the cost of spatial resolution. The spectrum of the secondary ions is analysed using a sector mass spectrometer to determine the isotopic composition of the sample – hence the term 'secondary ion mass spectrometry' (SIMS).

Ion probe analysis is used in both trace element and isotopic analysis. It can be used in the determination of the abundance of volatile species H, O, S, N, C, F and Cl and the analysis of traditional and non-traditional stable isotopes. It is often used in geochronology and applied to the U-Th-Pb and Hf isotope systems. A particular application is the U-Pb geochronology of zircon grains, for these contain measurable quantities of U and Th but not Pb. Ion probe analysis may

also be used in exploring diffusion profiles in minerals through the sequential sputtering of a grain during depth profiling.

The development of nanoSIMS allows a much finer spatial resolution than conventional SIMS instruments and operates with spot sizes as low as 50 nm for a caesium beam and 200 nm for an oxygen beam (Ireland, 2014). Zhang et al. (2014) measured sulphur isotopes at the submicron scale in pyrite and sphalerite using a ~0.7 pA Cs^+ beam of ~100 nm diameter and scanning over areas of 0.5 × 0.5 μm^2. They documented external reproducibility (1 SD) of better than 1.5‰ for both $\delta^{33}S$ and $\delta^{34}S$.

1.4.10 Synchrotron X-Ray Spectroscopic Analysis

A synchrotron is a charged particle accelerator which generates intense radiation. Of interest here is the application of synchrotron radiation in the X-ray part of the spectrum to geochemical analysis. One such microbeam method is X-ray absorption fine structure (XAFS) spectroscopy. This method can provide a detailed picture of the average electronic and molecular energy levels associated with multivalent elements, and allows the determination of valence state, coordination number and nearest neighbour bond lengths (Sutton and Newville, 2014). An important application of XAFS spectra to geochemistry is the X-ray absorption near-edge structure (XANES) energy region. The micro-version of this application (μ-XANES) spectroscopy has been used to determine in situ the $Fe^{3+}/\Sigma Fe$ ratio in basaltic glasses. The detail of the methodology is given in Kelley and Cottrell (2009).

1.5 Selecting an Appropriate Analytical Technique

Choosing an analytical technique in geochemistry depends entirely upon the nature of the problem to be solved with the ultimate goal of understanding the processes that have taken place in a given suite of rocks. In part this requires selecting the right samples in the field. For example, consider a suite of basaltic lavas derived from a mantle source. In their journey to the surface the magmas will have experienced a wide range of fractionation and mixing processes which will have modified the composition of the original primitive mantle melt. In order to characterise the composition of the original melt this sequence of interactions must be progressively removed. A helpful way of doing this is to follow the flow diagram in Figure 1.2 backwards. This means at the sample selection stage those samples that show any evidence of fluid interaction during weathering, hydrothermal alteration or metamorphism are eliminated from the sample set. The remaining samples are examined using major and trace element geochemistry to identify magma chamber processes and the composition of the primary melt which fed the magma chamber. This then allows the identification of what is normally a small suite of the least fractionated and least contaminated samples which might be primary magmas and can be used reflect processes operating in the mantle source region. These samples can be further investigated using trace element and isotope geochemistry in order to understand the processes operating in the source region.

A similar sequence of sample selection may be followed for a suite of granitic rocks, although in this case identifying the nature of the source – crust or mantle – may be more complex. Further, the solidified rock may be a crystal-laden melt, and so it is sometimes necessary to identify those samples which represent true melt compositions. Further, the distribution of some trace elements may be governed by the presence of minor phases such as monazite, which is rich in P and the light REE, and phases of this type must be identified using petrography. It may also be important to know the age of the granite, in which case the isotopic analysis of its zircon is a commonly used technique. The oxygen and Hf isotope composition of the zircon may also provide further constraints on the composition and age of the source.

The choice of analytical technique also depends upon the nature of the material to be investigated. For example, a sample that is already in solution such as seawater or river water is amenable to analysis by ICP methods – ICP-OES or ICP-MS – immediately after dilution or pre-concentration. On the other hand, a rock sample crushed to a powder can be analysed by XRF after being made into a pressed powder pellet or fused into a glass disc; otherwise, it has to be turned into a solution using a ranging of fluxing and acid treatments. Once in solution it is then amenable to analysis by ICP methods – ICP-OES or ICP-MS. If samples are to be analysed by TIMS or INAA, then analysis must be preceded by sample digestion and the chemical separation of the element(s) of interest. The stable isotope analysis of a rock powder using gas

source mass spectrometry requires that the sample is converted to a gas and undergoes sample purification for the element of interest. The non-destructive analysis of solid samples can be carried out using in situ methods such as the electron microprobe for major element and some trace element analysis, and the ion microprobe or laser ablation ICP-MS for trace elements and isotopes. These methods require a relatively small amount of sample preparation and can also function with very small samples.

Further considerations are the number of samples to be analysed and so the amount of sample preparation time involved, the speed of chemical analysis, the cost of the analysis and the precision required. In general terms XRF and ICP-OES and ICP-MS methods are rapid and can cope with large numbers of samples at relatively low cost, although both methods require the rock to be in powder form and so there is a certain amount of sample preparation involved. Other isotope methods – TIMS, isotope dilution mass spectrometry and gas source mass spectrometry – involve much greater sample preparation but isotope dilution offers the best possible precision. In some cases it is possible to screen a large number of samples using techniques such as quadrupole ICP-MS or in the case of in situ analysis LA-ICP-MS and then carry out high-precision analysis of a selected number of samples using either much longer counting times or very precise methods such as SIMS or isotope dilution.

1.6 Sources of Error in Geochemical Analysis

Normally, if samples are collected carefully and if sample preparation is carried out in a clean environment following conventional analytical protocols, the geochemical data are safe to use. However, there are a number of ways in which the results of geochemical analysis can be in error and it is important for the user to be alert to these possibilities. They are briefly reviewed below.

1.6.1 Contamination

The user of geochemical data must always be alert to the possibility that samples have become contaminated. This is known to have happened in sometimes the most bizarre circumstances such as when petrol spilt on rock samples in a boat resulted in spurious Pb isotope analyses, or the more avoidable convergence of Pb isotope compositions of a suite of igneous rocks with that of Indian Ocean seawater, when the samples were collected from a beach on the Indian Ocean.

More subtle is the contamination which may take place during sample preparation. This can occur during crushing and grinding and may arise either as cross-contamination from previously prepared samples or from the grinding apparatus itself. Cross-contamination can be eliminated by careful cleaning and by pre-contaminating the apparatus with the sample to be crushed or ground. For the highest precision analyses samples should be ground in agate, although this is delicate and expensive and even agate may introduce occasional contamination (Jochum et al., 1990). Tungsten carbide, a commonly used grinding material in either a shatter box or a ring mill, can introduce sizeable tungsten contamination, significant Co, Ta and Sc and trace levels of Nb (Nisbet et al., 1979; Hickson and Juras, 1986; Norman et al., 1989; Jochum et al., 1990). Chrome steel introduces sizeable amounts of Cr, Fe, moderate amounts of Mn and trace amounts of Dy and high carbon steel significant Fe, Cr, Cu, Mn, Zn and a trace of Ni (Hickson and Juras, 1986).

Other sources of laboratory contamination may occur during sample digestion and arise from impure reagents or from the laboratory vessels themselves. This therefore requires ultra-clean laboratory procedures and the use of ultra-pure chemicals. A measurement of the level of contamination from this source can be made by analysing the reagents themselves in the dilutions used in sample preparation and determining the composition of the 'blank'.

Natural contamination of samples may occur through the processes of weathering or through contact with natural waters. This may be remedied by removing all weathered material from the sample during sample slitting and leaching the rock chips with 1 M HCl for a few minutes after splitting but before powdering.

1.6.2 Calibration

Most of the methods of analysis described above measure concentrations relative to international standards of known composition or to a calibration curve derived therefrom. Calibration curves are drawn on the basis of standards of known

composition and are used to convert counts per second in the instrument to ppm or wt.% in the sample. Standards used in the construction of calibration curves are either ultra-pure chemical reagents or international reference samples, as well as so-called in-house standards. Where matrix effects are important, such as with LA-ICPMS, standards should be of similar composition to the unknowns being investigated. Clearly, the accuracy of the final analysis of the unknown depends upon the accurate analysis of the standards used in calibration. It is possible for systematic errors to be introduced and these can be minimized if standard samples are interspersed and analysed as unknowns throughout the analytical session.

1.6.3 Peak Overlap

In most geochemical analytical techniques there is little attempt to separate the element to be analysed from the rest of the rock or mineral sample. Given that current analytical methods are generally a form of spectrometry, there is the possibility of interference between spectral lines or mass peaks so that the value measured is spuriously high due to overlap from a subsidiary peak of another element present in the rock. The effects of these interferences must be calculated and removed mathematically and in some cases minimised in the design of the instrument.

1.6.4 Detecting Errors in Geochemical Data

Errors in one's own data can be detected by routinely running well-analysed in-house or international standards as unknowns through the sample preparation and analytical system. This will alert the user to calibration errors. It is also important to know about potential peak overlaps for elements of particular interest. Errors may be detected if samples have anomalous compositions. In this case the hand specimen and thin section of the sample should be investigated carefully to determine the reason for the anomalous nature of the sample and whether or not it has a real geological explanation, or whether it is an artefact of the analytical process. Anomalously low concentrations of certain elements relative to those expected for a particular rock type might reflect the incomplete dissolution of the sample during sample preparation.

Errors are minimised by using international reference materials and certified reference materials. These are essential for instrument calibration, method validation and quality control, and form the basis of inter-laboratory comparisons. A thorough review of reference materials in geochemical and environmental research is given by Jochum and Enzweiler (2014) and up-to-date information can be obtained from the GeoReM database at http://georem.mpch-mainz.gwdg.de/ and in the academic journal *Geostandards and Geoanalytical Research*.

2 Analysing Geochemical Data

2.1 Introduction

The last 50 years have seen the growth of a large body of literature on the statistical treatment of geochemical data. Some of this literature is in the form of warnings to the geochemical community that their practices are not sufficiently statistically rigorous. Other articles are concerned with improving the statistical techniques current amongst geochemists and provide methods which are more appropriate to some of the peculiar properties of geochemical data. Further aspects of geostatistics are very specialised and apply particularly to the fields of ore reserve estimation and exploration geology (see, for example, Clark and Harper, 2007). These are not considered here.

However, many statisticians are not practising geochemists and, similarly, many geochemists are unfamiliar with the statistical literature. This may in part be because this literature is specific to mathematical geology and is written for other mathematicians rather than for geochemists. The net effect is that geostatisticians have been advising geochemists in the practice of their art for many years and yet rarely have the two communities come together to fully address their common concerns.

The purpose of this chapter, therefore, is to draw the attention of geochemists to some of the issues which our statistician colleagues have raised and to evaluate these in the context of presenting and interpreting geochemical data. This is not intended as a review of statistics as applied to geochemistry. There are excellent books for that purpose; see, for example, Waltham (2000), Davis (2002) and Reimann et al. (2008), and as well as the web-based reference *NIST/SEMATECH e-Handbook of Statistical Methods*. Rather, this chapter presents a discussion of some areas of statistics which directly relate to geochemistry. We assume an introductory level of statistical knowledge. See Box 2.1 for brief definitions of the statistical terms used.

Many of the statistical calculations described in this text can be carried out in an Excel spreadsheet using the data analysis 'Add-In' and the *Real Statistics Using Excel* 'Add-In' (available at www.real-statistics.com/). There are also commercial statistical packages that run in Excel and shareware packages that run on other platforms such as the java-based *Stacato*. Alternatively, more sophisticated analyses can be carried out in bespoke statistical packages such as SPSS (statistical package for the social sciences, officially IBM SPSS Statistics); there are also applications in *STATISTICA* (by Dell), Python, Matlab and R (see Van den Boogaart and Tolosana-Delgado, 2013; Janousek et al., 2016).

The central problem which geochemists have to address when considering the analysis of geochemical data is the unusual nature of geochemical data. Composition is expressed as a part of a whole, either as a percentage or parts per million. This type of data is 'constrained' or 'closed' and is not amenable to standard statistical analysis, which is generally designed for unconstrained data. The particular nature of geochemical data raises all sorts of uncomfortable questions about the application of standard statistical methods in geochemistry. These issues are addressed in Sections 2.2 and 2.7. Geochemical data also has 'outliers' which geochemists typically exclude but which statistics can now address, for example, Pernet et al. (2013). In addition, geochemical data are often derived from samples collected from limited outcrop in specific locations over a limited amount of time and yet the statistical 'validity' of the sampling process is seldom considered.

With these caveats in mind, let us turn to the application of selected statistical techniques which are widely used in geochemistry. Typically, geochemical data are multivariate; that is, many measurements are made on each sample (e.g., wt.% oxide data, trace element data and isotopic data are all measured on the same sample). For this reason it is necessary to use multivariate statistical methods such as those discussed in Section 2.8; these include correlation matrices, covariance matrices, principal component and factor analysis, and discriminant analysis. Sometimes, however, it is necessary to use multiple bivariate comparisons where only two of the many variables are compared at any one time, as for example in the use of correlation coefficients (Section 2.4) or regression analysis (Section 2.5). Univariate statistics such as the mean, median, mode and standard deviation, as well as

Box 2.1 Some statistical terms

Arithmetic mean (Section 2.3.2)
The arithmetic mean of a sample $\bar{x}$ (μ for the population) is the sum of the measurements divided by the number of measurements n:

$$\bar{x} = (x_1 + x_2 + \ldots + x_n)/n, \text{ or } \Sigma\, x/n$$

Chi-square (χ^2) (Section 2.3.5)
Evaluates the 'goodness of fit' between an empirical and theoretical data distribution

Closed array (Section 2.2.2.1)
A data array with individual varables that are not independent of each other but are related by, for example, being expressed as a percentage

Coefficient of variation (Section 2.6)
The ratio of the standard deviation s to the mean $\bar{x}$

Compositional data (Section 2.2.2)
Compositional data form a closed array and are expressed as part of a whole, such as percentages or parts per million.

Correlation coefficient (Section 2.4)
Pearson's product moment coefficient of linear correlation ρ measures the strength of the linear relationship between two variables x and y in a population.
An estimate of the same correlation coefficient r is given by:

$$r = \frac{\text{covariance}\,(x, y)}{\sqrt{[\text{variance}(x) * \text{variance}(y)]}}$$

The Spearman rank coefficient of correlation r_s is calculated from the difference in rank order of the variables (Eq. 2.3).

Covariance (Section 2.4.1)
The product of the deviation from the mean for two variables x and y averaged over the dataset:

$$S_{xy} = \frac{\Sigma(x - \bar{x})(y - \bar{y})}{n - 1}$$

Covariance matrix (Section 2.7.1)
The covariance of an entire dataset is represented by a covariance matrix.

Cumulative distribution function (Section 2.3.4)
The cumulative probabilty (up to 100%) of a particular value occurring in a population

Data transformation (Section 2.7)
Transforming the reference frame of constrained or closed data for better statistical evaluation, for example, the additive, centred or isometric log-ratio transformation

Degrees of freedom (Section 2.2.2.3)
The number of 'free' available observations (the sample size n) minus the number of parameters estimated from the sample

Geometric mean (Section 2.3.2)
The nth root of the product of positive values $X_1, X_2, \ldots, X_n$:

$$\bar{x}_G = (X_1 \times X_2 \times X_3 \times \ldots \times X_n)^{1/n}$$

Heteroscedasticity
Non-uniform error

Kernel density estimate (Section 2.3.3)
An approximation of the density function which does not require binning.

Log-(ratio) transformation (Section 2.7.1)
The isometric logarithmic transformation of non-Gaussian multivariate data (such as geochemical data) for proper statistical handling and better data visualisation

Median (Section 2.3.2)
The median value divides the area under a distribution curve into two equal parts. An estimate of the median is the value in the sequence of

Continued

Box 2.1 (cont.)

	individual values, ordered according to size, which divides the sequence in half. When the distribution is normal the median and the mean are the same.
Mode (Section 2.3.2)	For unimodal distributions, the mode is the value of the measurement which has the greatest frequency. When there is a normal distribution, the mode is the same as the mean.
Normal distribution (Section 2.3.1)	The normal or *Gaussian* distribution of samples is characterized by a symmetrical bell shape on a frequency diagram.
Null hypothesis (Sections 2.3.5 and 2.4.1)	The hypothesis that two populations agree with regard to some parameter is called the null hypothesis. The hypothesis is usually evaluated for rejection at a given level of probability.
Null value (Section 2.6)	The value assigned to a parameter in the null hypothesis
Outlier (Section 2.2.2.4)	A data point distant from the main distribution of the data
Probability density function (Section 2.3.3)	Provides the likelihood of a continuous random variable assuming a certain value
Probability distribution function (Section 2.3.3)	Provides the likelihood of a discrete random variable assuming a certain value
Population (Section 2.2.2.4)	A set of measurements of a specified property of a group of objects. Normally a sample of the population (*sub-population*) is studied. The symbols representing the population are given by Greek letters whereas those relating to the sub-population are given in Roman letters.
Regression (Section 2.5)	A measure of the intensity of the relationship between two variables. It is usually measured by fitting a straight line to the observations.
Robust test (Section 2.2.3)	A test is robust relative to a certain assumption if it provides sufficiently accurate results even when this assumption is violated.
Significance test (Sections 2.3–2.5)	A measure of the probability level at which a null hypthesis is accepted or rejected, usually at the 5% (0.05) or 1% (0.01) level
Skewed distribution (Section 2.2.2.4)	A non-normal or non-Gaussian distribution of data; a *tailed* distribution
Spurious correlation (Sections 2.3.5 and 2.6)	A false correlation resulting from too small datasets or incorrect handling of the data
Standard deviation (Section 2.3.2)	The spread of values about the mean. It is calculated as the square root of the variance and for a sample is denoted s: $s = \sqrt{\Sigma(x - \bar{x})^2/(n-1)}$ In a normally distributed set of numbers 68.26% of them will lie within one standard deviation of the mean and 95.46% will lie within two standard deviations from the mean. The standard deviation of a population is denoted σ.
Sub-composition (Section 2.2.2)	In compositional data analysis a sub-composition is a part of the composition.
Variance (Section 2.3.2)	A measure of the deviation of individual values about the mean: $s^2 = \Sigma(x - \bar{x})^2/(n-1)$ The variance is the square of the standard deviation.

probability functions (Section 2.3), are also needed to describe the distribution of the data.

2.2 A Statistical Approach?

2.2.1 Geochemical Investigation versus Statistical Trials

It should be acknowledged at the outset that a geochemical investigation may be constrained by funding, location, time available at the study area, the number and types of samples that are collected, the limited spatial distribution of those samples and the type of geochemical analyses that can be performed, so that structuring a study as a proper 'statistical trial' is unlikely. Geochemists do not work from carefully controlled trials, but from their often limited observations. Consequently, from inception, geochemical investigations may be regarded as somewhat statistically handicapped because the project may be constrained by small sample numbers and limited sample diversity. This contributes to the statistical limitations associated with geochemical data described in Section 2.2.2.

2.2.2 Statistical Limitations Associated with Geochemical Data

There are several important issues associated with geochemical data that complicate their statistical analysis. To varying degrees these apply to all geochemical studies and include the following:

- Constrained data
- Data with variable (non-uniform) errors
- Small datasets
- Outliers.

2.2.2.1 Constrained or Closed Data and the Constant Sum Problem

Data expressed as part of a whole (percentages or parts per million) are known as *compositional data*. Geochemists are used to expressing the major element compositions of rocks and minerals as percentages, so that the sum of the major elements will always be about 100% (a *constant sum*). This has to be in order to compare one chemical analysis with another. This standard form, which is universally used by geochemists for both rock and mineral analyses, is a source of concern to statisticians who for 60 years have been informing geochemists that they are working in a minefield of spurious correlations and that their interpretation of major and trace element chemistry is potentially unsound.

In brief, the problem with compositional data is as follows. Percentages are complex ratios containing variables in their denominators which represent all the constituents being examined. Thus, components of percentage data are not free to vary independently. As the proportion of one component increases, the proportion of one or more other components must decrease. These properties were more formally summarised by Pawlowsky-Glahn and Egozcue (2006), who showed that compositional data:

- convey only relative information
- are always positive, thus
- are not free to range between +/− infinity (in statistical terms they are *constrained* rather than *unconstrained*)
- are parts of a composition that sum to a constant (in statistical terms they form a *closed dataset*)
- are therefore not amenable to standard statistical tests which are generally devised for open datasets with unconstrained variables in the range +/− infinity.

The consequences of these properties for compositional data in geochemistry are the following:

- The summing of analyses to 100% forces a correlation between components of the dataset because the loss or gain of any component causes a change in the concentration of *all* the other components. The problem is illustrated by Meisch (1969), who demonstrated that an apparently significant correlation between two oxides may have arisen through the closure process from an actual correlation between two other oxides. These induced correlations may or may not conceal important geological correlations. In terms of correlation theory, the usual criterion of independent variables does not hold nor is variance and covariance within the dataset independent.
- There is a negative bias in correlations. If one component has a significantly higher value than all the other components – such as SiO_2 in silicate rocks – then bivariate graphs of SiO_2 and the other components will show a marked negative tendency. This attribute of percentage data is fully explored by Chayes (1960) and is illustrated in Figure 3.13.
- Data subsets or sub-compositions, as frequently used in triangular diagrams such as the AFM diagram (Section 3.3.3), do not reflect the variation

present in the 'parent' dataset. Aitchison (1986, Table 3.1) showed that the correlation coefficient between pairs of variables changes substantially in data subsets and that there is no apparent pattern to the changes. In addition, data subsets can show different rank orderings from the parent dataset. For example, in the AFM data subset (Na_2O + K_2O, FeO_T, MgO) the variance may be A > F > M, but in the parent dataset the variance may be F > A > M.

- The means of compositional datasets have little significance. Woronow (1990) and Woronow and Love (1990) have argued that because of the closure problem the means of percentage (and ppm) data have no interpretative value. They show that an infinite number of possible changes can explain an observed change in the mean of compositional data such that it is impossible to produce a meaningful statistical test to evaluate the similarities between means of compositional data. This observation has important implications for approaches frequently used in geochemistry such as discriminant analysis (Section 2.8.2).

It should be noted that the problem of closure is not eliminated when the data are transformed by some scaling process (Whitten, 1995), nor is it removed when the problem is presented in graphical rather than statistical form. Attempts to sidestep closure by relating all samples to a given reference curve as in the 'sliding normalisation diagrams' of Liegeois et al. (1998) or the 'delta diagrams' of Moyen et al. (2009) do not avoid the fundamental issues outlined above. Furthermore, the closure problem remains even when the constituents of an analysis do not sum exactly to 100%, due to analytical error or incomplete analysis, for there is always the category of 'others' (i.e., the missing data) which can be used to produce a sum of 100%. A more detailed discussion of how these problems have been approached in the geo-statistical community is given in Section 2.7.

2.2.2.2 Non-uniform Errors (Heteroscedasticity)

The statistical analysis of geochemical data depends on the errors associated with the variables (oxides and elements). In the context of geochemical analysis, error means the combined systematic and random error (the uncertainty) that is associated with an analytical measurement. All geochemical analyses have associated errors but these are not the same for all the components of a single analysis for the magnitude of the error depends upon what is being measured and the analytical method(s) used. For example, analytical errors associated with XRF analysis vary as a function of both the element mass and the concentration of the element and therefore different elements will have different associated errors. Further, in a comparison of data from one laboratory with another the errors associated with each lab will be different. In some instances data measured in different ways are used together, giving rise to different scales of error. An example would be the measurement of major elements by XRF and trace elements by mass spectrometry. This variability in the nature of the errors associated with geochemical data means that it is necessary to select the statistical approach which is most appropriate to the data.

2.2.2.3 Small *n*

Many statistical functions are dependent on the number (*n*) of variables involved because they assume a *normal or Gaussian distribution*. This often takes the form of the *Student's t-distribution*, which is used, for example, when determining statistical significance of the difference between two means, the confidence interval of the difference between two means, and in linear regression analysis. In a statistical calculation the term *degrees of freedom* refers to the number of variables that are free to vary; for example, in bivariate plots there are two degrees of freedom because there are two variables. As the number of degrees of freedom increases, the *t-distribution* approaches a normal distribution. However, a specific variable in a small sample set (*n*) may not be normally distributed and so violates the assumption of many statistical approaches.

2.2.2.4 Outliers

Many geochemical datasets contain outliers, that is, single values completely outside the range of the other measured values. Outliers can occur by chance in any distribution, but they often indicate a measurement error, the combination of unrelated sub-populations, or that the population has a *spurious* (non-Gaussian) distribution.

2.2.3 Can We Address These Limitations?

The following steps can be taken to address the limitations that geochemists face with their data. These are explored in detail in this chapter but are summarised here:

- *Constrained* geochemical data, in which the standard deviation of the error is not constant with respect to the variables involved, may be explored using *weighting* (Section 2.5) and *data transformation* (Section 2.7). Both methods work well and often provide similar results.
- Choosing a statistical method appropriate for the type of data involved requires knowledge of the types of errors associated with the data and whether these are variable or constant errors.
- Many statistical tests are designed for larger datasets. At a fundamental level statistical analysis generally works best above some nominal minimum number of samples or analyses, and so increasing n will increase the statistical options.
- All datasets need to be assessed for outliers and there are various tests that help to recognize them (Sections 2.3 and 2.4); once recognized, appropriate steps can be taken.
- Robust statistical methods are those which work even when the original assumptions of the test are not strictly fulfilled, such as non-Gaussian data, small n, variable errors and the presence of outliers, and these can be applied to minimise the effect of these assumptions.

2.3 Histograms, Averages and Probability Functions

2.3.1 Histograms

The histogram is a common way to show how data are distributed relative to the number of samples and shows the *density* of the data distribution. A histogram quickly and easily shows whether the data distribution is Gaussian or non-normal, symmetrical or skewed, uni-, bi- or multi-modal. However, this is in part a function of the way in which the data are allocated to intervals or 'bins' in the histogram. As general rule bin width $= \sqrt{n}$, where n is the number of samples in the dataset. It is clear that bin widths reduce in size the larger the dataset and as n increases the histogram 'steps' are eventually so small that the plot appears to have a smooth, step-free pattern. This is the *density function* shown as the blue line in Figure 2.1a and discussed in Section 2.3.3.

2.3.2 Averages

Geochemists frequently use 'average values' in order to present their data in summary form. Also, average rock compositions are sometimes used as a reference by which to assess the composition of other rock compositions. For example, the average values of mid-ocean ridge basalts or of chondritic meteorites are frequently used as normalising values in trace element studies (see, e.g., Table 4.7). Averages are also used in analytical geochemistry where a signal is measured several times and then an average of the measurements taken.

Rock (1987, 1988) has drawn attention to the way in which geochemists calculate average values and has shown that the methods most frequently used are inadequate. The most commonly used summary statistic is the *arithmetic mean*, with the *standard deviation* sometimes quoted as a measure of the spread of the data. The *geometric mean*, the *median*, the *mode*, and *variance* are less frequently used. These terms are defined in Box 2.1.

However, when averaging geochemical data the *arithmetic mean* is an inappropriate choice for three reasons. First, it assumes that the sample population is either normally or log-normally distributed (Figure 2.1a, b). For many geological datasets this is not the case, nor is there any a priori reason why it should be so. Therefore, the *normality* of geochemical data should never be assumed. Second, many geochemical datasets contain *outliers* that can cause extreme distortion to an arithmetic mean if not recognised and excluded. Furthermore, as argued by Woronow (1990) and Woronow and Love (1990), the arithmetic mean of compositional data has no interpretative value. Similar problems can occur with estimates of the standard deviation and with the geometric mean. Rock (1988) emphasised that in the statistical literature, of the various methods used to assess average values, the 'mean and standard deviation consistently performed the worst'. For this reason the *median* is a more *robust* measure of the average (Figure 2.1b) and is to be preferred. Rock (1988) also showed that the calculation of several robust estimates can identify outliers in the dataset from the inconsistencies that arise from between the calculated values.

2.3.3 Probability Functions and Kernel Density Estimates

Probability functions address either *continuous* or *discrete* random variables in a dataset and provide a means of assessing the likelihood of a certain random variable assuming a certain value. The probability *density* function (PDF) is for *continuous* random variables, where the area under the probability density curve or trace indicates the *interval* in which a variable will fall within

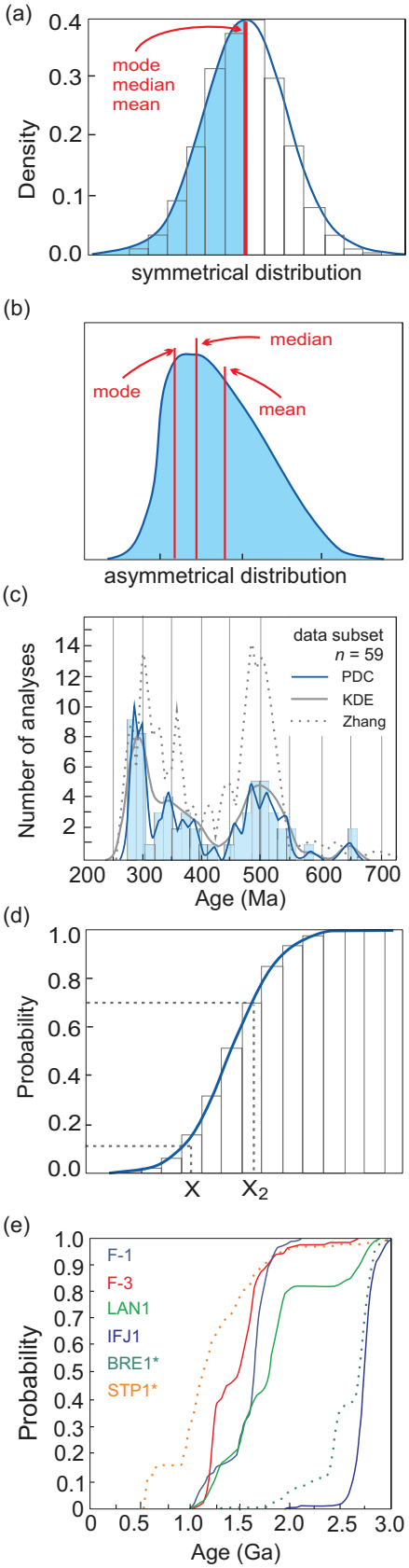

Figure 2.1 Histograms, density functions, and probabilities. (a) The density function (blue line) is the context of a set of continuous random variables. The probability density function can also be expressed as a *cumulative* probability or *cumulative* distribution (see Section 2.3.4). The *p* function is for *discrete* random variables and represents the relative probability of a (random) variable having a particular value; in this case the probability is measured at a single point.

The Kernel density estimate (KDE) is an approximation of the density function and its main advantage is that it is a continuous function that does not require binning. The KDE is calculated from the data using a specified bandwidth combined with a weighting (kernel) function. The KDE is a smoothed and continuous curve that is sensitive to bandwidth and the kernel function

Figure 2.1 (*cont.*) defined by the observations shown in the histogram; the area under the curve is equal to 100%. The blue shaded region represents 50% of the density function. The mode, median and mean are identical for symmetrical normally distributed datasets, where the mode is the most frequent number; the median is the middle number in the data list, and the mean is the average of all numbers. (b) The mode, median and mean are different for asymmetrical, non-normally distributed data. (c) Histogram, probability density curves (PDCs) and kernel density estimate (KDE) for Permian sandstones from the New Siberian Islands of Russia (from Pease et al., 2015; with permission from the Geological Society of London). The histogram of detrital zircon U-Pb ages (light blue rectangles; bin sizes = 15 Ma, maximum 2σ from dating method) and the PDCs for these data (blue line). The KDE for the same data is shown by the solid grey line and should mimic the histogram. The PDC of Permian sandstone from Taimyr (grey dotted line; data from Zhang et al., 2013) shows a strong similarity to that of the New Siberian Island data. (d) The cumulative probability function sums each of the observations in all bins up to the value of the bin specified. If the histogram has a normal distribution, the cumulative probability function will have a typical symmetrical, sigmoidal shape (blue line). On this plot the probability of obtaining a value of $\leq$X is 0.1 (or 10%) and the probability for obtaining a value $\leq X_2$ is 70%. (e) Cumulative probability curves (CPCs) for samples from different Caledonian Nappes showing similarity of samples (F-1 and F-3) within the Gaisa Nappe (after Zhang et al., 2016, with permission from Elsevier). Note the two datasets were generated at the same analytical facility using the same methods and have similar analytical errors.

used (Gaussian, uniform or triangular). KDEs are well suited to comparing the data distribution of multiple samples because multiple KDEs are easily plotted on a single diagram. The KDE can be calculated in Excel using the NumXL add-in and most statistical software packages. Java-based freeware for plotting KDEs is also available (Vermeesch, 2012).

Probability functions and KDEs are commonly used in the presentation of detrital zircon U-Pb age data in sediment provenance analysis. Such data may be displayed as probability density curves (PDCs) (Figure 2.1c). PDCs are similar to PDFs, but they are not equivalent (see the discussion in Vermeesch, 2018a). PDCs represent the sum of a number of Gaussian distributions (one for each datum) whose means and standard deviations correspond to the individual ages and their analytical uncertainties. Consequently, a PDC graph favours precise data (sharp peaks) over imprecise data (smooth lows) as illustrated in Figure 2.1c.

Pease et al. (2015) compared PDC patterns of Permian sandstones from the New Siberian Islands and Taimyr, Arctic Russia, and used their similarity to suggest that both samples represented part of the same foreland basin of the Uralian Orogen in Arctic Russia (Figure 2.1c). The PDC and KDE for the New Siberian Island sample are similar and mimic the histogram of the detrital zircon U-Pb age data. We recommend that PDCs or KDEs are displayed with a histogram of the data as this validates the data handling and allows any irregularities in the dataset to be identified. However, it should be noted that PDCs lack a firm theoretical basis and that *large* or *highly precise datasets* can produce counter-intuitive results (Vermeesch, 2012).

2.3.4 Cumulative Distribution Function

The probability density function (PDF) can also be expressed as a *cumulative* probability or *cumulative* distribution (Figure 2.1d). This makes it possible to determine the probability of a particular value occurring within a population. The cumulative distribution function (CDF) represents the probability that a random variable will have a value less than or equal to another value and can be used as a measure of the cumulation of probability up to a given value. It is useful, for example, to quantify the percentage of samples plotting above or below a certain value. In addition, multiple datasets can be combined on a single graph to allow a visual assessment of sample similarity. This method is commonly applied in sediment provenance analysis and was used by Zhang et al. (2016) to distinguish between different Caledonian Nappe complexes (Figure 2.1e).

2.3.5 Chi-Square (χ^2) 'Goodness of Fit' Test

The Pearson's chi-square test assesses the 'goodness of fit' between a theoretical distribution (such as normal, binomial or Poisson) and the empirical data distribution. It can be applied to any *univariate* dataset for which the cumulative distribution function (Section 2.3.4) can be calculated. The chi-square test is applied to data separated into intervals, or 'binned'. For non-binned data it is necessary first to calculate a histogram or frequency table before performing the chi-square test. In its simplified form the equation for χ^2 is:

$$\chi^2 = \frac{\sum(O-E)^2}{E} \tag{2.1}$$

where χ^2 = chi-squared, O = the observed value, and E = the expected value. The χ^2 test assumes that the data are a random sampling of binned data and it is sensitive to sample size. If the number of points in the bin interval is too small (<5) or the total number of observations is too small (<10), spurious results can be obtained (Koehler and Larnz, 1980).

χ^2 tests the null hypothesis against the alternative hypothesis with respect to an associated degree of freedom at some level of significance or probability (Table 2.1). The null hypothesis (H_0) typically assumes that there is *no significant* difference between the observed and expected values (the alternative hypothesis would then be that there is a *significant* difference between the observed and expected values). The probability that H_0 holds true may be estimated for different levels of *significance*, usually at the 5% (0.05) level or the 1% (0.01) level. Alternatively, these values may be expressed as *confidence limits*, in this case 95% or 99%, respectively. The probability values in Table 2.1 represent the *minimum* values needed to reject H_0. When χ^2 is greater than the table value, H_0 is rejected; when χ^2 is less than the table value, H_0 is accepted; small values for χ^2 generally lead to acceptance of H_0. The Pearson chi-square test is a standard function available in Excel and most statistical packages.

2.4 Correlation

One of the most important tasks for the geochemist using geochemical data is to determine whether or not

Table 2.1 Significance, chi-square test[a, b]

	Probability of a larger value of χ^2		
DF	0.99	0.95	0.90
1	0.00	0.004	0.016
2	0.020	0.011	0.211
3	0.115	0.352	0.584
4	0.297	0.711	1.064
5	0.554	1.145	1.61
6	0.872	1.635	2.204
7	1.239	2.167	2.833
8	1.647	2.733	3.49
9	2.088	3.325	4.168
10	2.558	3.940	4.865
11	3.053	4.575	5.578
12	3.571	5.226	6.304
13	4.107	5.892	7.042
14	4.66	6.571	7.79
15	5.229	7.261	8.547
16	5.812	7.962	9.312
17	6.408	8.672	10.085
18	7.015	9.39	10.865
19	7.633	10.117	11.651
20	8.26	10.815	12.443

[a] Values for χ^2 above which it is considered statistically significant (at the 1%, 5% or 10% level) for the specified degrees of freedom (DF).
[b] Data modified from *NIST/SEMATECH e-Handbook of Statistical Methods*, https://doi.org/10.18434/M32189.

there are associations between the oxides or elements. For example, in the list of analyses of tonalitic and trondhjemitic gneisses in Table 2.2, do the oxides CaO and Al_2O_3 vary together? Is there a linear relationship between K_2O and Na_2O? This type of question is traditionally answered using the statistical technique of *correlation*.

2.4.1 The Pearson Linear Correlation Coefficient (*r*)

Correlation may be defined as a measure of the strength of association between two variables measured on a number of individuals and is quantified using the Pearson product-moment coefficient of linear correlation, usually known as the *correlation coefficient* (r). Thus, the calculation of the correlation coefficient between CaO and Al_2O_3 or K_2O and Na_2O can provide an answer to the questions asked above. When, as is normal in geochemistry, only a sample of the total population is measured, the sample correlation coefficient (r) is calculated using the expression:

$$r = \text{covariance}\,(x, y)/\sqrt{[\text{variance}\,(x) * \text{variance}\,(y)]} \quad (2.2)$$

where there are n values of variable x ($x_1 \ldots x_n$) and of variable y ($y_1 \ldots y_n$).

2.4.1.1 The Significance of the Correlation Coefficient

The sample correlation coefficient (r) is an estimate of the population correlation coefficient (ρ), the correlation that exists in the total population of which only a sample has been measured. It is important to know whether a calculated value for r represents a statistically significant relationship between x and y. That is, does the relationship observed in the sample hold for the population? The probability that this is the case is made with reference to a table of r values (Table 2.3). For a given number of degrees of freedom (the number of samples minus the number of variables, which in the case of a bivariate plot = 2), r is tabulated for different significance levels. These r values represent the *minimum* value needed to reject the *null hypothesis* (H_0). In this case, the null hypothesis is that the correlation coefficient of the population is zero ($\rho = 0$) at the specified level of significance.

$H_0 : \rho = 0$	null hypothesis
$H_1 : \rho \neq 0$, ***or***	two-sided hypothesis
$H_1 : \rho > 0$ or $\rho < 0$	one-sided hypothesis

Two sets of tables are provided to account for both positive and negative r values. A one-sided test is used when the *alternative hypothesis* (H_1) is either $\rho > 0$ or $\rho < 0$ (the region of rejection lies in a single direction). The two-sided test is used when the alternative hypothesis is $\rho \neq 0$ (the region of rejection occurs in two directions). For example, the dataset in Table 2.2 contains 31 samples and the calculated correlation coefficient between CaO and Al_2O_3 is $r = 0.568$ (Table 2.4a). The tabulated values for r (assume a one-sided test) shows that at the 5% significance level and 29 degrees of freedom ($n - 2$), the tabulated value for $r = 0.301$ (Table 2.3a). Since the calculated value (0.568) is greater than the tabulated value (0.301), the correlation coefficient in the sample is statistically *significant at the 5% level.* That is, there is 95% chance that the relationship observed in the sample also applies to the population. Hence, the null hypothesis that $\rho = 0$ is rejected.

Table 2.2 Major element data for tonalitic and trondhjemitic gneisses from the north marginal zone, Limpopo belt, Zimbabwe[a]

Rock No.	1	2	3	4	5	6	7	8	9	10	11	12	13	14	15	16
SiO_2	61.50	62.15	62.58	62.59	62.82	63.19	63.62	63.71	66.67	67.18	67.31	67.63	67.68	67.89	68.00	68.55
TiO_2	0.61	0.75	0.56	0.58	0.61	0.82	0.61	0.66	0.72	0.77	0.31	0.47	0.41	0.37	0.78	0.47
Al_2O_3	15.88	18.35	18.10	16.02	17.46	16.66	16.87	15.81	15.41	16.08	18.37	15.47	14.72	15.72	11.70	16.20
Fe_2O_3	7.96	4.69	5.34	6.64	5.96	6.16	5.22	5.53	5.61	4.87	2.77	4.44	3.99	2.45	7.50	3.73
MnO	0.15	0.05	0.09	0.12	0.08	0.10	0.08	0.07	0.09	0.07	0.03	0.08	0.07	0.03	0.10	0.03
MgO	3.60	1.61	1.71	2.56	2.36	1.98	1.82	2.49	1.32	1.24	0.93	1.60	1.16	0.64	1.94	1.13
CaO	4.96	4.01	4.38	5.50	5.70	5.21	4.24	5.01	4.79	3.99	4.23	4.38	4.51	2.66	5.33	4.24
Na_2O	4.42	5.57	6.01	4.79	4.19	4.77	4.94	3.32	4.03	4.73	5.75	4.22	4.01	4.86	3.43	4.47
K_2O	0.82	1.89	1.30	1.22	0.87	1.28	1.70	1.99	1.05	1.44	1.21	1.02	1.06	3.18	0.54	1.31
P_2O_5	0.28	0.19	0.20	0.15	0.22	0.27	0.17	0.19	0.17	0.30	0.10	0.09	0.09	0.10	0.16	0.13
SUM	100.18	99.26	100.27	100.17	100.27	100.44	99.27	98.78	99.86	100.67	101.01	99.40	97.70	97.90	99.48	100.26

Rock No.	17	18	19	20	21	22	23	24	25	26	27	28	29	30	31
SiO_2	70.05	70.13	70.91	71.11	71.34	71.47	71.87	72.81	73.68	74.08	74.25	75.62	75.45	77.88	78.44
TiO_2	0.32	0.34	0.39	0.28	0.26	0.25	0.37	0.39	0.33	0.15	0.18	0.13	0.12	0.19	0.14
Al_2O_3	15.93	15.49	15.11	16.83	15.68	14.82	15.48	14.15	14.33	14.63	13.96	13.32	13.80	11.04	11.04
Fe_2O_3	2.88	3.52	3.88	1.92	2.64	3.04	2.42	3.16	2.28	1.49	1.53	1.95	1.40	3.08	3.14
MnO	0.03	0.05	0.09	0.00	0.05	0.04	0.02	0.06	0.02	0.04	0.03	0.05	0.04	0.04	0.05
MgO	0.82	1.36	0.92	0.35	0.68	0.63	0.45	0.68	0.83	0.39	0.32	0.20	0.06	0.01	0.01
CaO	3.11	3.49	3.52	2.94	3.51	3.22	3.26	3.41	2.87	2.38	2.17	1.39	1.09	1.36	1.04
Na_2O	5.06	4.65	4.80	5.69	4.77	5.16	5.00	3.90	4.57	4.50	4.15	4.23	4.76	4.78	4.71
K_2O	1.95	1.42	1.39	1.60	1.46	1.04	1.32	1.75	2.83	2.97	2.76	2.98	3.25	1.23	1.75
P_2O_5	0.12	0.12	0.15	0.03	0.11	0.04	0.14	0.10	0.07	0.06	0.05	0.04	0.04	0.01	0.07
SUM	100.27	100.57	101.16	100.75	100.50	99.71	100.33	100.41	101.81	100.69	99.40	99.91	100.01	99.62	100.39

[a]Data from Berger and Rollinson (1997).

Table 2.3 Significance, correlation coefficient (r)

(a) Pearson[a]	Two-sided		One-sided test		(b) Spearman[b]	One-sided test		
DF	5%	1%	5%	1%	n	10%	1%	0.1%
1	0.997	0.999	0.988	0.999	4	1.000		
2	0.950	0.990	0.900	0.980	5	0.800	1.000	
3	0.878	0.959	0.805	0.934	6	0.657	0.943	
4	0.811	0.917	0.729	0.882	7	0.571	0.893	1.000
5	0.754	0.875	0.669	0.833	8	0.524	0.833	0.952
6	0.707	0.834	0.621	0.789	9	0.483	0.783	0.917
7	0.666	0.798	0.582	0.750	10	0.455	0.745	0.879
8	0.632	0.765	0.549	0.715	12	0.406	0.687	0.818
9	0.602	0.735	0.521	0.685	14	0.367	0.626	0.771
10	0.576	0.708	0.497	0.658	16	0.341	0.582	0.729
12	0.532	0.661	0.457	0.612	18	0.317	0.550	0.695
14	0.497	0.623	0.426	0.574	20	0.299	0.520	0.662
16	0.468	0.590	0.400	0.543	25	0.265	0.466	0.598
18	0.444	0.561	0.378	0.516	30	0.240	0.425	0.549
20	0.423	0.537	0.360	0.492	35	0.222	0.394	0.510
25	0.381	0.487	0.323	0.445	40	0.207	0.368	0.479
30	0.349	0.449	0.296	0.409	45	0.194	0.347	0.453
35	0.325	0.418	0.275	0.381	50	0.184	0.329	0.430
40	0.304	0.393	0.257	0.358	60	0.168	0.300	0.394
50	0.273	0.354	0.231	0.322	70	0.155	0.278	0.365
60	0.250	0.325	0.211	0.295	80	0.145	0.260	0.342
70	0.232	0.302	0.195	0.274	90	0.136	0.245	0.323
80	0.217	0.283	0.183	0.257	100	0.129	0.233	0.307
90	0.205	0.267	0.173	0.242	n	20%	2%	0.2%
100	0.195	0.254	0.164	0.230		Two-sided test		
150	0.159	0.208	0.134	0.189				
200	0.138	0.181	0.116	0.164				
300	0.113	0.148	0.095	0.134				
400	0.098	0.128	0.082	0.116				
500	0.088	0.115	0.074	0.104				

[a] Values for the correlation coefficient (r) above which it is considered statistically significant (at the 1% or 5% level) for a given number of degrees of freedom (DF). Data from Sachs (1984).
[b] Significance values for sample size n, at the 10%, 1% and 0.1% significance levels (one-sided test) and the 20%, 2% and 0.2% significance levels (two-sided test). Data from Sachs (1984).

2.4.1.2 Assumptions Associated with the Correlation Coefficient

The Pearson product-moment coefficient of linear correlation is based upon the following assumptions:

1. The units of measurement are equidistant for both variables.
2. There is a linear relationship between the variables.
3. Both variables should be normally or nearly normally distributed.

The Pearson correlation coefficient is vulnerable to data outliers of any kind, high and low, as well as deviations from the main trend of the data array. Assumption (iii) is regarded as an important prerequisite for linear correlation. However, this is not always evaluated; it is the variation of y from the estimated value of y for each value of x that must be normally distributed and rarely is the sample population large enough for this criterion to be satisfactorily tested. This means that the use of Pearson's method requires a careful study of the univariate distribution of each of the variables before determination of r. In addition, it is useful to routinely investigate a log-transformation of the data (Section 2.7) before calculating r.

Table 2.4 Correlation matrices for the Limpopo Belt analyses (for data from Table 2.2)

(a) Pearson product-moment coefficient of correlation

	SiO_2	TiO_2	Al_2O_3	Fe_2O_3	MnO	MgO	CaO	Na_2O	K_2O	P_2O_5
SiO_2	1.0000									
TiO_2	−0.8394	1.0000								
Al_2O_3	−0.7468	0.4438	1.0000							
Fe_2O_3	−0.7840	0.8593	0.2267	1.0000						
MnO	−0.6233	0.6410	0.0915	0.8798	1.0000					
MgO	−0.8837	0.7838	0.4543	0.9041	0.8021	1.0000				
CaO	−0.8862	0.8437	0.5680	0.8225	0.6415	0.8617	1.0000			
Na_2O	−0.0690	−0.1688	0.4938	−0.2563	−0.3027	−0.2165	−0.1805	1.0000		
K_2O	0.4580	−0.5244	−0.1708	−0.6742	−0.5094	−0.5140	−0.6727	0.0173	1.0000	
P_2O_5	−0.7919	0.8639	0.5049	0.7858	0.6756	0.7790	0.7309	−0.0588	−0.4404	1.0000

(b) Spearman rank coefficient of correlation

	SiO_2	TiO_2	Al_2O_3	Fe_2O_3	MnO	MgO	CaO	Na_2O	K_2O	P_2O_5
SiO_2	1.0000									
TiO_2	−0.8405	1.0000								
Al_2O_3	−0.7801	0.5131	1.0000							
Fe_2O_3	−0.7964	0.8750	0.3700	1.0000						
MnO	−0.6082	0.6609	0.1170	0.8586	1.0000					
MgO	−0.9074	0.8731	0.5818	0.8810	0.7221	1.0000				
CaO	−0.8558	0.8592	0.5336	0.8768	0.7228	0.9326	1.0000			
Na_2O	−0.0958	−0.1798	0.4866	−0.2289	−0.3114	−0.1697	−0.2297	1.0000		
K_2O	0.4704	−0.4789	−0.1977	−0.6624	−0.5273	−0.5205	−0.6851	0.0889	1.0000	
P_2O_5	−0.8260	0.8746	0.6046	0.8048	0.6457	0.8333	0.7702	−0.0450	−0.3561	1.0000

A *robust* linear correlation in which data points far from the main body of data are down-weighted can be used to account for outliers. Nevertheless, when testing for the significance of r, the data should be normally distributed. In rank systems (Section 2.4.2) the ranking mitigates against outliers so *data transformation* is not needed. Otherwise a *log-transformation* of the data (Section 2.7) may be warranted.

2.4.2 Rank Correlation Coefficients

Sometimes geochemical data cannot be used in product moment correlation of the type described above as they do not fulfil the requisite conditions of being normally distributed and excluding outliers. Under such circumstances, an alternative to the Pearson product-moment coefficient of linear correlation is the non-parametric *rank correlation coefficient*. Both the Spearman and Kendall rank correlation coefficients can be used to determine the strength of the relationship between two variables. In most situations, the interpretations of the Kendall's tau and Spearman's rank correlation coefficients are similar and lead to the same inferences, although the Spearman coefficient is more widely used. Both methods can be performed in Excel.

2.4.2.1 Spearman Rank Correlation

The Spearman rank coefficient of correlation is usually designated r_s. This type of correlation is applicable to major or trace element data measured on a ranking scale rather than the equidistant scale used in Pearson's product-moment correlation. The Spearman rank correlation coefficient is defined as:

$$r_s = 1 - \left[6\sum D^2/n\left(n^2 - 1\right)\right] \tag{2.3}$$

where D is the difference in ranking between the x-values and y-values and n is the number of pairs. In this case the only assumptions are that x and y are continuous random variables, which are at least ranked and are independent paired observations. If the rank orders are the same, then $D = 0$ and $r_s = +1.0$. If the rank orders are the reverse of each other, $r_s = -1.0$. The significance of r_s can be assessed using significance

tables for the Spearman rank coefficient of correlation (Table 2.3b) in a similar way to that described for product-moment correlation in Section 2.4.1. The Spearman rank coefficients of correlation for the major element data from the Limpopo Belt are shown in Table 2.3b. In this instance, the values do not differ greatly from the Pearson product moment coefficient of correlation. The particular advantages of the Spearman rank correlation coefficient are that they are applicable to ranked data and are superior to the product-moment correlation coefficient when applied to populations that are not normally distributed and/or include outliers. A further advantage is that the Spearman rank correlation coefficient (r_S) is quickly and easily calculated and can be used as an approximation for the product-moment correlation coefficient (r).

2.4.2.2 Kendall Rank Correlation

The Kendall rank correlation coefficient (Greek letter τ, tau) is another measure of rank correlation that is used to assess the similarity of the orderings of data when ranked by two respective variables. When +1, the agreement between the two rankings is perfect and the two rankings are the same; if 0, the rankings are completely independent; if −1, the disagreement between the two rankings is perfect and one ranking is the reverse of the other. The general formula for Kendall's correlation is:

$$\tau = \frac{n_c - n_d}{n(n-1)/2} \tag{2.4}$$

where n_c is the number of concordant pairs, n_d is the number of discordant pairs in a ranking of two variables, and n is the number of ranked variables. Kendall's correlation coefficient is generally smaller than Spearman's, is less sensitive to the size of the deviation between the rank ordered pairs than Spearman's, has better statistical properties (the sample estimate is close to the population variance so confidence levels are more reliable) and is better for small sample sizes (≲12). Significance levels associated with the Kendall rank coefficient of correlation for small datasets are calculated individually. Larger datasets tend to converge on a normal distribution and significance can be determined using the z-value:

$$z = \frac{3 * \tau \sqrt{n(n-1)}}{\sqrt{2(2n+5)}} \tag{2.5}$$

where n is the number of ranked variables. The critical significance table for Kendall's tau is given in Table 2.5.

2.4.3 The Strength of a Correlation

The correlation coefficient, r, estimates the strength and direction of a linear relationship between x and y. The reliability of the linear model, however, is also a function of the number of observed data points in the population such that the sample size (n) and r must be considered together. As shown in Section 2.4.1.1, when the calculated significance is greater than the critical value for the number of samples in the dataset (for bivariate data, $n - 2$), the correlation coefficient of the dataset *is statistically significant*. There is no single cut-off that defines a 'strong' linear correlation but values of $r \geq 0.7$ and $\tau \geq 0.5$ are generally taken to indicate good to strong correlations. In geochemistry the *significance* of a correlation is usually assigned at the 5% level (or *95% confidence* level). The coefficient of determination (R^2) is the square of r. The usefulness of R^2 is that there is no distinction between positive and negative values (as with r) and it ranges in value from 0 to 1.0. It is therefore important to specify the significance or confidence level and n for all values of r or R^2 reported.

2.4.4 Correlation and Non-homogeneous Data

Some statistical tests require or assume a homogeneous sample distribution and applying such a test to a non-homogeneous dataset can yield false correlations. For example, consider a dataset of nine basaltic andesites and nine andesites (Figure 2.2). When combined in a bivariate plot the two compositional groups are strongly correlated ($r = 0.922$), well above the 5% significance limit in Table 2.3a. However, when assessed independently the basaltic andesites are not significantly correlated with each other ($r = 0.458$, below the 5% significance limit in Table 2.3a). In this case, the apparent correlation between the basaltic andesites and the andesites may reflect the incorrect combination of two distinct sub-populations into a single non-homogeneous group. Understanding the geological field relationships is critical therefore to identifying the correct statistical treatment of data.

Another consideration concerns outliers (Section 2.2.2.4). For normally distributed data, outliers can be defined by the '3σ rule': the deviation from the mean by more than three times the standard deviation. This means that only one in 370 samples should deviate from the mean. Deletion of outlier data is controversial

Table 2.5 Significance, Kendall's rank correlation coefficients[a]

	Nominal significance							Nominal significance					
n	*0.10*	*0.05*	*0.025*	*0.01*	*0.005*	*0.001*	*n*	*0.10*	*0.05*	*0.025*	*0.01*	*0.005*	*0.001*
4	1.000	1.000	–	–	–	–	*30*	0.172	0.218	0.255	0.301	0.333	0.393
5	0.800	0.800	1.000	1.000	–	–	*31*	0.166	0.213	0.252	0.295	0.325	0.389
6	0.600	0.733	0.867	0.867	1.000	–	*32*	0.165	0.210	0.246	0.290	0.323	0.379
7	0.524	0.619	0.714	0.810	0.905	1.000	*33*	0.163	0.205	0.242	0.288	0.314	0.375
8	0.429	0.571	0.643	0.714	0.786	0.857	*34*	0.159	0.201	0.237	0.280	0.312	0.369
9	0.389	0.500	0.556	0.667	0.722	0.833	*35*	0.156	0.197	0.234	0.277	0.304	0.361
10	0.378	0.467	0.511	0.600	0.644	0.778	*36*	0.152	0.194	0.232	0.273	0.302	0.359
11	0.345	0.418	0.491	0.564	0.600	0.709	*37*	0.150	0.192	0.228	0.267	0.297	0.351
12	0.303	0.394	0.455	0.545	0.576	0.667	*38*	0.149	0.189	0.223	0.263	0.292	0.346
13	0.308	0.359	0.436	0.513	0.564	0.641	*39*	0.147	0.188	0.220	0.260	0.287	0.341
14	0.275	0.363	0.407	0.473	0.516	0.604	*40*	0.141	0.185	0.218	0.256	0.285	0.338
15	0.276	0.333	0.390	0.467	0.505	0.581	*41*	0.141	0.180	0.215	0.254	0.280	0.334
16	0.250	0.317	0.383	0.433	0.483	0.567	*42*	0.138	0.178	0.213	0.250	0.275	0.329
17	0.250	0.309	0.368	0.426	0.471	0.544	*43*	0.138	0.176	0.209	0.247	0.274	0.324
18	0.242	0.294	0.346	0.412	0.451	0.529	*44*	0.137	0.173	0.207	0.243	0.268	0.321
19	0.228	0.287	0.333	0.392	0.439	0.509	*45*	0.135	0.172	0.204	0.240	0.267	0.317
20	0.221	0.274	0.326	0.379	0.421	0.495	*46*	0.132	0.169	0.202	0.239	0.264	0.314
21	0.210	0.267	0.314	0.371	0.410	0.486	*47*	0.132	0.167	0.199	0.236	0.260	0.310
22	0.203	0.264	0.307	0.359	0.394	0.472	*48*	0.129	0.167	0.197	0.232	0.257	0.307
23	0.202	0.257	0.296	0.352	0.391	0.455	*49*	0.129	0.163	0.196	0.230	0.253	0.303
24	0.196	0.246	0.290	0.341	0.377	0.449	*50*	0.127	0.162	0.192	0.228	0.251	0.300
25	0.193	0.240	0.287	0.333	0.367	0.440	*51*	0.126	0.161	0.191	0.225	0.249	0.297
26	0.188	0.237	0.280	0.329	0.360	0.428	*52*	0.124	0.158	0.189	0.223	0.246	0.294
27	0.179	0.231	0.271	0.322	0.356	0.419	*53*	0.123	0.157	0.187	0.221	0.244	0.290
28	0.180	0.228	0.265	0.312	0.344	0.413	*54*	0.122	0.156	0.185	0.219	0.241	0.287
29	0.172	0.222	0.261	0.310	0.340	0.404	*55*	0.121	0.154	0.182	0.216	0.239	0.285

[a] Significance levels at critical value as close as possible but not exceeding the nominal significance. Modified from P. Lee, University of York, www.york.ac.uk/depts/maths/tables/kendall.pdf.

especially in small datasets or those in which a normal distribution cannot be assumed. Rejection of outliers is more acceptable when associated with instrument measurements and the distribution of measurement error is known. In the case of measurement error, outliers should either be discarded or a form of statistics used that is robust to outliers such as the ranked coefficient of correlation. In any case the exclusion of any data point(s) should be explicitly reported. Where a distribution is skewed, a non-Gaussian distribution is implied, and statistical tests suited for non-normal distributions should be applied.

2.4.5 Correlation Matrices

Frequently, a geochemical dataset will have as many as 30 variables. This means that there are 435 possible bivariate diagrams (Section 3.3.2) for a single dataset. While simple bivariate plots provide information about the data, its structure and interrelationships, making more than 400 plots is not an efficient way to proceed. As an initial step, the creation of a correlation matrix allows significant correlations to be quickly and easily identified. This may be a prelude to making selected bivariate plots or to applying more sophisticated statistical analyses. A correlation matrix requires determining a correlation coefficient between variable pairs and presenting the results as a matrix as in Table 2.4. Rahimi et al. (2016) used a correlation matrix to identify correlated rare earth elements in their investigation of the Lakehsiya ore deposit and from the observed correlations were able to identify those accessory minerals which were the host to the REE identified. It should be noted, however, that (1) extreme outliers can perturb a correlation matrix; therefore, decisions regarding the handling of outliers are required before creating the matrix, and that (2) although the correlation matrix is useful and

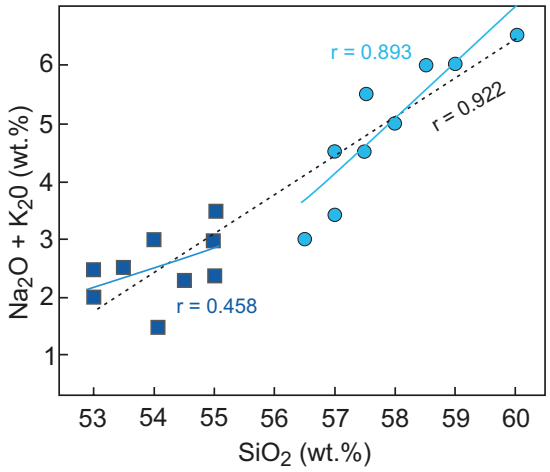

Figure 2.2 False correlations in non-homogeneous data. Nine basaltic andesites (squares) and nine andesites (circles) yield a strong linear correlation (r = 0.922 at >5% significance), whereas the basaltic andesites in the subgroup (r = 0.458) are not correlated at the 5% significance level.

correlation coefficients are convenient statistical descriptors, caution is needed in their application to geochemical data because of their unusual 'closed' nature (see Section 2.2).

2.5 Regression Analysis

Often in geochemistry the strength of an association, as defined by the correlation coefficient, is sufficient information from which petrological conclusions may be drawn. Sometimes, however, it is useful to quantify that association. This is traditionally done using regression analysis. For example, regarding the association between CaO and Al_2O_3 in the tonalites and trondhjemites of Table 2.2 the question 'If the CaO concentration were 3.5 wt.%, what would be the concentration of Al_2O_3?' can be answered with a linear regression of the two variables CaO and Al_2O_3. The quantification of this association is carried out by fitting a straight line through the data and finding the equation of its line. The equation for a straight line relating variables x and y is:

$$y = a + bx \tag{2.6}$$

The constant a is the value of y given by the straight line at $x = 0$. The constant b is the slope of the line and shows the number of units in y (increase or decrease) that accompanies an increase in one unit of x. The constants a and b are determined by fitting the straight line to the data. The relation above is ideal and does not allow for any deviation from the line. In reality this is not the case, for most observations have associated error(s) and the data may form a cloud of points to which a straight line must be fitted. This introduces some uncertainty into line-fitting procedures resulting in a number of alternative approaches. Regression analysis is the subject of a number of statistical texts; see, for example, Bingham and Fry (2010) and Montgomery et al. (2012). Below some of the more common forms of regression are described.

2.5.1 Ordinary Least Squares (OLS) Regression

Ordinary least squares (OLS) regression (also known as simple regression) is one of the most commonly used line-fitting techniques in geochemistry because it is simple to use and included in most spreadsheet software. It requires that the units for both variables are the same and are normally distributed. However, it is often inappropriate for geochemical data because there is the further assumption that one variable is independent and error-free. The least squares best-fit line is constructed so that the sum of the squares of the vertical deviations about the line is a minimum. In this case the variable x is the independent (non-random) variable and is assumed to be without error; y, on the other hand, is the dependent (random) variable with associated errors. In this case we say that y is regressed on x (Figure 2.3a). It is possible to regress x on y and in this case the best fit line minimises the sum of the squares of the horizontal deviations about the line (Figure 2.3b). Thus, there are two possible regression lines for the same data, a rather unsatisfactory situation for physical scientists who prefer a unique solution. The two lines intersect at the mean of the sample (Figure 2.3c) and approach each other as the value of the correlation coefficient (r) increases until they coincide at $r = 1$. In the case of ordinary least squares regression (y is regressed on x), the value of the intercept, a, may be computed from:

$$a = y - bx \tag{2.7}$$

where x and y are the mean values for variables x and y, and b is the slope of the line computed from

$$b = r(S_y/S_x) \tag{2.8}$$

where r is the Pearson product-moment correlation coefficient and S_x and S_y are the standard deviations

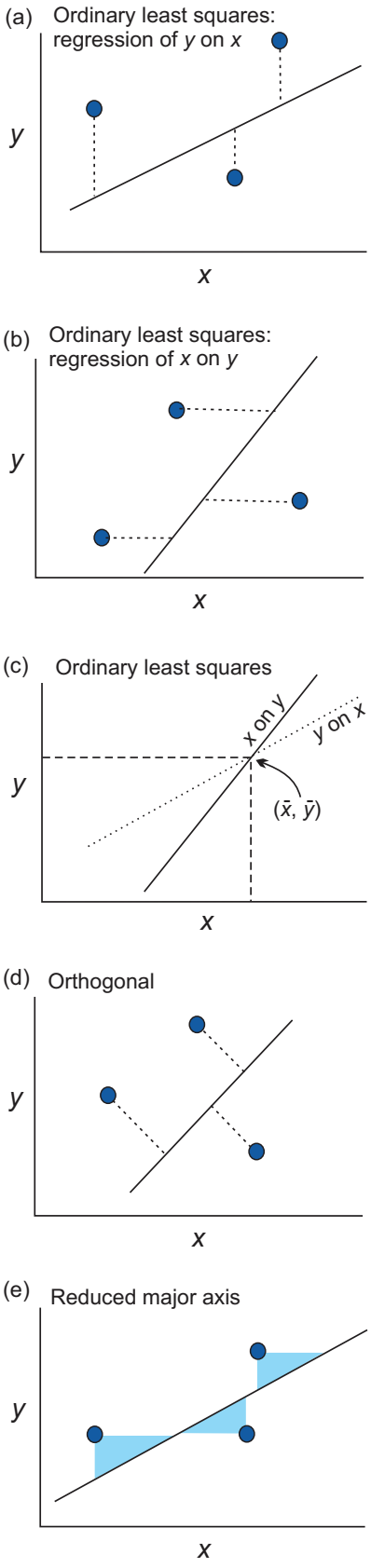

Figure 2.3 Types of linear regression. (a) Ordinary least squares regression of y on x; in this case the vertical distance between the point and the line is minimised. (b) Ordinary least squares regression of x on y; the horizontal distance between the point and the line is minimised. (c) Both ordinary least squares lines pass through the means $(\bar{x}, \bar{y})$, the centroid of the data. (d) Orthogonal regression which minimises the orthogonal distance from the observed data points to the regression line. (e) Reduced major axis regression; the line is fitted to minimise the area of the shaded triangles.

of the samples of x and y values. Linear confidence intervals can be expressed in terms of standard deviations (Montgomery et al., 2012). Thus, confidence intervals on values of y for a number of values of x may be used to draw a confidence band on the regression line. The confidence band will be wider at the ends of the fitted line because there are more points near the mean values.

Despite its wide use, OLS regression of geochemical data has some disadvantages. First, OLS regression is normally used in a predictive sense in which variable y is estimated from variable x. In geochemistry, however, regression is more commonly used to confirm the strength of association between variables and to calculate the slope and intercept of the linear correlation. Second, the OLS method yields two different lines, neither of which necessarily represents the actual relation between the variables. Finally, and most importantly, OLS regression assumes that error is restricted to the dependent variable. In geochemistry it is meaningless to define one variable as the dependent variable and the other as the independent variable since both variables have associated errors.

2.5.2 Orthogonal Regression

Orthogonal (also known as bivariate, two-dimensional Euclidean, or Deming) regression uses an alternate approach and is useful if both variables have the same units and their errors are similar. It assumes that the errors for the two variables are independent and are normally distributed. Instead of minimizing the vertical or horizontal distance, it minimises the orthogonal distance from the observed data points to the regression line (Figure 2.3d).

2.5.3 Reduced Major Axis Regression

Reduced major axis (RMA) (variously known as standardised principal component, standardised

major axis, geometric mean, ordinary least products, diagonal, least areas line) regression is more appropriate for geochemical data because it is designed to deal with errors in both x and y as well as different units (*scale variance*). It also assumes that the data have a bivariate normal distribution, although it is more robust than other forms of regression to non-normal data distribution and non-random errors. Following the method of Kermack and Haldane (1950) the sum of the products of the vertical and horizontal distances of the x, y values from the line is minimized; that is, the areas of the triangles between points and the best fit line are minimised (Figure 2.3e). The slope b of the reduced major axis line is given by:

$$b = \pm(S_y/S_x) \tag{2.9}$$

where S_x and S_y are the standard deviations of sample values x and y and the sign is taken from the correlation coefficient. Unlike OLS and least normal squares regression, the slope of the RMA line is independent of the correlation coefficient r. The intercept a is taken from Eq. 2.7. Standard errors can be calculated for the slope and intercept, and from these the confidence intervals on the slope and intercept can be calculated using $n - 2$ degrees of freedom (see Ludbrook, 1997). An example of the different forms of regression line is given in Figure 2.4 for the variables Fe_2O_3 and CaO from Table 2.2. This diagram shows how both types of OLS regression (x on y and y on x) and RMA regression are used to fit straight lines to the data. The equations for each of the lines are also given. As in Figure 2.4 the RMA regression line usually lies between the two OLS lines. Tofallis (2015) has recently extended RMA regression to handle multiple variables.

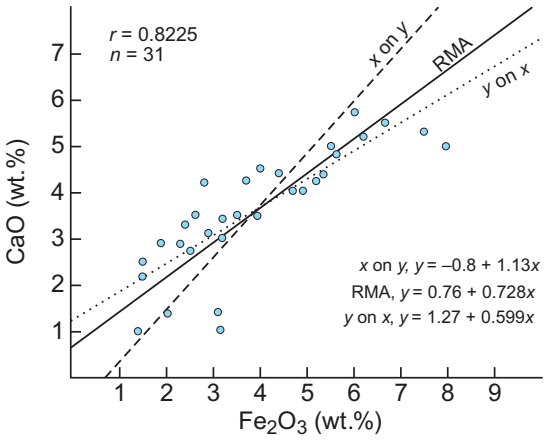

Figure 2.4 Different linear regressions for the same dataset (data from Table 2.2). The regression lines are: ordinary least squares regression of x on y (x *on* y), slope and intercept calculated from Eqs. 2.7 and 2.8; reduced major axis (RMA), slope and intercept calculated from Eqs. (2.9) and (2.7); ordinary least squares regression of y on x (y *on* x), slope and intercept calculated from Eqs. 2.7 and 2.8.

2.5.4 Weighted Least Squares Regression

Weighted least squares (WLS) or weighted linear regression is an appropriate line-fitting method for those types of geochemical data in which some data points are more reliable than others. WLS regression assumes that the errors between the variables are uncorrelated and that the variance between the two variables differs. This is known as *heteroscedasticity*; see Section 2.2.2.2.

In such cases each data point is weighted before line fitting following the method of York (1966) and York et al. (2004). Observations are inversely weighted proportional to the *error variance* or *the standard deviation(s)*, this means that an observation with small standard deviation has a large weight (more influence) and an observation with large standard deviation has a small weight (less influence). The weighting often takes the form of $1/s^2$ and is given relative to the weights of the other observations. If the error variance or standard deviation is not known, an OLS regression can be performed and the square of the residual can be used to estimate s^2.

The biggest limitations to WLS regression include (1) estimated weighting and (2) outliers. Where the weighting is estimated from a small number of replicated observations this can have an adverse effect on the result. Outliers (Section 2.2) need to be recognized and dealt with appropriately, otherwise they may also negatively impact WLS analysis.

An example of the WLS method is its application in geochronology for the construction of isochrons (York, 1967, 1969). In detail the different isotopic methods require slightly different approaches. For example, Brooks et al. (1972) showed that in Rb/Sr geochronology the errors in the isotope ratios are normally distributed and for $^{86}Sr/^{87}Sr$ ratios are less than 1.0 (the usual situation in whole rock analysis) and that the errors are not correlated. In Pb isotope geochronology, however, the errors between the lead isotope ratios are highly correlated and require a slightly different approach (see York, 1969).

2.5.5 Robust Regression

Robust linear regression is another weighted least-squares line-fitting technique which minimises the effect of a single data point such as an outlier from exerting a disproportionate influence on the computed value of the slope and intercept (Reimann et al., 2008). This is important because conventional OLS regression can be highly distorted by one or two outlying values. Consequently, before carrying out regression analysis the data should be inspected for outliers. Although no data point should be discarded simply because it is an outlier, outlying observations should be examined to see if they are in error (see Sections 2.3 and 2.4). Inspection for outliers may be carried out visually using a bivariate plot or a data analysis computer program. Zhou (1987) gives an example of the use of this technique in geochemical exploration where outliers (often anomalies and in this particular case the object of such an exercise) may hamper their own identification by distorting the results of statistical analysis.

2.5.6 Some Problems with Traditional Approaches to Correlation and Regression

In the introduction to this section we enquired about the association between pairs of elements in a geochemical dataset and asked the question: To what degree are the oxides CaO and Al_2O_3 associated in the dataset represented in Table 2.2? A more disturbing question and one that is not usually asked is: To what extent is the association between CaO and Al_2O_3 is controlled by other associations in the dataset? For example, does the fact that CaO correlates well with SiO_2 affect in any way its correlation with Al_2O_3? Traditionally, geochemists have looked at the relationships between pairs of elements in isolation from the other members of the dataset by plotting a large number of bivariate diagrams or by constructing a correlation matrix of the types described above. Yet the nature of geochemical data is that they are multivariate, with many variables measured in multiple samples. In other words, geochemists have tended to use a bivariate approach to solve a multivariate problem. This is not to say that bivariate analysis of geochemical data is useless and that parameters such as the correlation coefficient should not be used as sample descriptors. Nevertheless our purpose here is to argue that there are more appropriate methodologies for multivariate analysis, many of which are described in some detail for the petrologist by Le Maitre (1982). Even so, the more fundamental problem of geochemical data – the constant sum problem – is not resolved directly by the application of multivariate techniques, and the statistical difficulties resulting from this aspect of geochemical data are formidable, as discussed in Section 2.2.2.1.

2.6 Ratio Correlation

One specialised application of correlation and regression is in ratio correlation. The correlation of ratios can lead the user into a great deal of trouble and should normally be avoided. The exception is in geochronology, as discussed in Section 2.6.3. The dangers of ratio correlation in geochemistry have been documented by Butler (1981, 1986) and Rollinson and Roberts (1986) and are the subject of a text by Chayes (1971). A summary of the arguments is presented below.

Given a set of variables X_1, X_2, X_3, ... which show no correlation, ratios formed from these pairs which have parts in common such as X_1/X_2 versus X_3/X_2, X_1/X_2 versus X_1/X_3, or X_1 versus X_1/X_2 will be highly correlated. This was first recognised by Pearson (1896) in the context of simple anatomical measurements and brought to the attention of geologists by Chayes (1949). For the case where the X_1/X_2 is plotted against X_3/X_2, Pearson (1896) showed that a first-order approximation for the correlation coefficient r is given by the expression:

$$r = r_{13}C_1C_3 - r_{12}C_1C_2 - r_{23}C_2C_3 + {C_2}^2/\sqrt{\left({C_1}^2 + {C_2}^2 - 2r_{12}C_1C_2\right)} * \left({C_3}^2 + {C_2}^2 - 2r_{23}C_3C_2\right) \quad (2.10)$$

where r_{12} is the correlation coefficient between variables X_1 and X_2 and C_3 is the *coefficient of variation* (the standard deviation divided by the mean) of variable X_3, etc. This expression holds for small values of C (< 0.3), when the relative variance of X_2 is not large, and when the absolute measurements are normally distributed. The more general form of this equation for X_1/X_2 versus X_3/X_4 is given by Chayes (1971, p. 11).

If the variables X_1, X_2, X_3 are uncorrelated (i.e., $r_{12} = r_{23} = r_{13} = 0$) and the coefficients of variation are all the same (i.e., $C_1 = C_2 = C_3$), then

the expression reduces to 0.5. Thus, even though the variables X_1, X_2, X_3 are uncorrelated, the correlation coefficient between the ratios X_1/X_2 and X_3/X_2 is 0.5. In the case where X_1, X_2 and X_3 are uncorrelated, and C_1 and C_3 are equal and C_2 is three times their value, then the expression reduces to 0.9. These correlation coefficients are spurious correlations for they appear to indicate a correlation between the original variables where none exists. An example of the effects of ratio correlation is given in Figure 2.5, which uses data from a suite of meta-komatiites and meta-basalts from an Archaean greenstone belt (Rollinson, 1999). A plot of oxide wt.% data for CaO versus Fe as Fe_2O_3 shows scattered uncorrelated data ($R^2 = 0.0014$, Figure 2.5a) whereas a molar ratio plot of the same data using TiO_2 as the ratioing or 'conserved' element shows a highly correlated 'trend' ($R^2 = 0.9661$, Figure 2.5b).

Given these observations, Butler (1986) argued that in the case of ratio correlation the assessment of the strength of a linear association cannot be tested in the usual way, against a probabiity of zero. Rather, the null value must be the value computed for the spurious correlation (i.e., r in Eq. 2.8) and will therefore vary for every diagram plotted. An even more complex null hypothesis proposed by Nicholls (1988) is that the correlation coefficient of the dataset is compared with that of a set of random numbers with a similar range of values, means and variances as the data under investigation. This is not, however, a fruitful approach (see Aitchison, 2005).

2.6.1 The Improper Use of Ratio Correlation: Pearce Element Ratio Diagrams

An example of the misuse of ratio correlation can be seen in the molecular proportion diagrams of T.H. Pearce, also known as 'Pearce element ratio' (PER) diagrams. These diagrams require the plotting of ratios of oxides recast as molar quantities (the wt.% oxide divided by the formula weight) on an x–y graph. The ratios have an element in common, which is termed the conserved element, and which is usually a common denominator (Pearce, 1968, 1970). Pearce diagrams were originally developed to solve two particular problems: (1) to avoid the effects of closure inherent in plotting percentages, discussed in Section 2.2.2.1, and the conventional method of displaying major element geochemical data and (2) to use the slope and intercept of a best-fit line between the data points on a bivariate oxide plot to provide a better way of discriminating between rival petrological hypotheses and in particular to discriminate between different models of crystal fractionation (Pearce, 1968, 1970).

Pearce element ratios have enjoyed limited use in petrology. There was some activity in the late 1980s and early 1990s (e.g., Russell and Nicholls, 1988; Stanley and Russell, 1989; Pearce and Stanley, 1991) and a recent resurgence in interest some 20-plus years later (see the review by Nicholls and Russell, 2016). The most popular applications have been in identifying the fractionating phase(s) in igneous suites and in

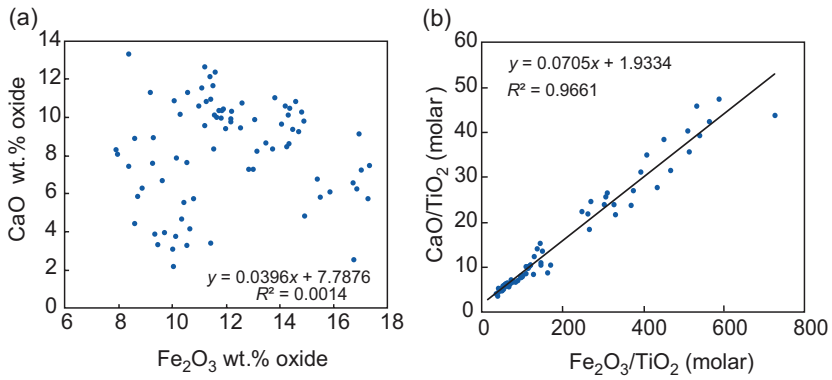

Figure 2.5 Ratio correlation. (a) CaO wt.% versus Fe_2O_3 wt.% for meta-basalts and meta-komatiites from the Sula Mountains greenstone belt, Sierra Leone (data from Rollinson, 1999). The data are uncorrelated as indicated by the equation for a 'best fit' line through the data and the R^2 value. (b) CaO/TiO_2 versus Fe_2O_3/TiO_2 as molar values using the same data as in (a). In this case the molar ratios are highly correlated as indicated by the best fit line and the R^2 value. This is an example of a spurious correlation resulting from the use of a common denominator.

identifying mobile elements in altered volcanic rocks, particularly in altered basalts and komatiites. They have also been used in petrogenetic studies to aid in the identification of mantle phases influencing the chemistry of partial melts, in identifying participating phases in crystal fractionation and in investigating mixing between crystals and melt. Pearce element ratio diagrams have also been used in mineralogy to identify atomic substitutions in mineral lattices.

Pearce element ratio diagrams should not be used for the following three reasons:

1. Pearce element ratio diagrams are based upon the correlation of ratios with a common denominator, which as discussed above leads to statistically spurious correlations. In other words, the diagrams generate apparent correlations where none exist and therefore the conclusions drawn from these diagrams are at least doubtful and at worst incorrect. This flaw in the application of Pearce element ratio diagrams was pointed out by Butler (1982, 1986) and Rollinson and Roberts (1986) following the earlier work of Chayes (1971). The problems arising out of spurious correlations have been acknowledged (see, e.g., Pearce and Stanley, 1991) and a number of mitigating solutions have been proposed. These include using two different conserved elements in the ratio process. While this circumvents the common denominator problem, in practice it is complex to apply (Pearce and Stanley, 1991). The calculation of 'non-intuitive' numerators and/or denominators as advocated by Nicholls and Russell (2016) is both cumbersome and does not avoid the problem of ratio correlation.
2. A particular claim for Pearce element ratio diagrams is that the slope of a trend on a ratio plot is of significance in discriminating between rival hypotheses. For example, it is claimed that it is possible to discriminate between olivine and orthopyroxene fractionation in a basaltic magma from the slope of the regression line on a ratio plot. In other words, the slope is a function of the stoichiometry of the mass transfer process and different slopes identify different mass transfer processes. However, this argument too is flawed, for regression lines drawn through the data will have incorrect slopes because in the case of ordinary least squares regression, the slope of the line is directly related to the correlation coefficient (Eq. 2.8), which in this case is spurious. Some authors have sought to circumvent the problems of ratio correlation by transforming their data into logarithmic form. Unfortunately, this approach does not provide a solution, for the problems are preserved even as log-ratios (see Kenney, 1982; Rollinson and Roberts, 1986).
3. Pearce element diagrams require the identification of a conserved element, essential in the construction of the molar ratio plots. The conserved element is defined as one which is excluded from the differentiation process and remains sequestered in the melt (Nicholls and Russell, 2016), and is otherwise known as an incompatible element. In the case of olivine fractionation in a basaltic melt, the conserved element might be the oxide of Al since Al is not structurally accommodated by olivine. Although acceptable in principle, the identification of a conserved element is applicable only to modelling the simplest of geological processes such as olivine fractionation in mafic and ultramafic rocks as in the example of magnesian basalts from Hawai'i cited in Pearce and Stanley (1991). Even then, olivine is usually joined on the liquidus by a spinel phase which will contain Al. More advanced fractionation of such rocks frequently involves the addition of a pyroxene and or plagioclase by which stage there are few conserved elements left to select, maybe P or K. In felsic rocks it is even harder to identify a conserved element given the fractionation of ferromagnesian phases and one or more feldspars. Furthermore, the conserved elements identified even in mafic rocks are almost always elements whose concentration in the rock is low. Thus, there is concern about the accuracy of the analysis, possible element mobility, and the amplifying effect of small numbers in the denominator (see Stanley, 1993).

In summary, there are several problems with the statistical validity of major element oxide ratio plots. In contrast to the ongoing advocacy that 'Pearce element ratios and diagrams faithfully depict the chemical variations in geochemical datasets' (Nicholls and Russell, 2016), we note their limited use in the wider the geochemical community since the early 1990s and recommend that they no longer be used.

2.6.2 Application to Trace Element Diagrams

A number of elemental plots of trace elements are presented as ratio plots of the form X_1/X_2 versus

X_3/X_2, X_1 versus X_1/X_2 or X_1 versus X_2/X_1 and all are subject to the constraints of ratio correlation discussed in Section 2.6.1. In some cases, the trace element diagrams are designed only for classification purposes, but where linear trends are important for petrogenetic interpretation, then the problem of spurious correlation applies. In this case the trace element ratio plots should be considered carefully and ideas tested on alternative plots which are not based on ratios before any petrological conclusions are drawn from the data.

2.6.3 Ratio Correlation in Isotope Geology

Ratios with a common denominator are the staple diet of much of geochronology and isotope geology, and the statistical validity of Rb-Sr isochron diagrams was questioned by Chayes (1977) and was discussed more fully by Butler (1982) and Dodson (1982). Butler (1982) pointed out that in the case of Rb-Sr isochron diagrams where the isotope ratio $^{87}Sr/^{86}Sr$ is plotted against $^{87}Rb/^{86}Sr$ the presence of a common denominator (^{86}Sr) 'should raise the suspicion that some or all of the observed variation on a scatter diagram may be due to the effects of having formed ratios with a common denominator'. Dodson (1982) responded to this argument by showing that, unlike ratios formed from major element oxide pairs, isotopic ratios such as $^{87}Sr/^{86}Sr$ are never calculated from independent measurements. Rather, they are a directly measured property of the element under consideration, are unrelated to the amount sampled, and can only be altered in a limited number of ways, the most important of which is radioactive decay. Dodson proposed the null hypothesis for isotope geochemistry that 'variations in the measured isotopic composition of an element are unrelated to its concentration or to any other petrochemical property of the materials sampled'. He showed that if the null hypothesis is true, then the expected value of the ratio correlation coefficient is zero and that isochron diagrams are not subject to the common denominator effect.

2.7 Compositional Data Analysis

As previously noted, a severe problem with major element geochemical data is the problem of closure (Section 2.2.2.1). Over the past four decades this problem has been addressed at length by the geostatistical community under the more general theme of compositional data analysis and data transformation. A very particular aspect of compositional data analysis is in the use of bivariate plots, and this is discussed separately in Chapter 3 in Sections 3.3.2.1 and 3.3.2.2.

2.7.1 Aitchison's Approach to Constrained Compositional Data

The first major step forward in finding a solution to the closure problem and its implications in geochemistry was in the work of John Aitchison, who addressed the constant sum effect in a series of detailed papers (Aitchison 1981, 1982, 1984, 1986, 2003). Subsequent developments led by research groups in Girona and Florence are outlined in the works of Pawlowsky-Glahn and Olea (2004) and Buccianti et al. (2006). This field of statistical research is still evolving, as summarised in recent reviews (Buccianti and Grunsky, 2014; Pawlowsky-Glahn and Egozcue, 2016; Buccianti et al., 2018).

Aitchison's fundamental premise was that 'the study of compositions is essentially concerned with the relative magnitudes of the ingredients rather than their absolute values' (Aitchison, 1986, p. 65). This frees percentage data from its restricted region (the 'simplex' in the terminology of Aitchison) to spread more freely though sample space and transforms 'constrained' data to 'unconstrained' data. Consequently, when formulating questions about associations between variables in a geochemical dataset, our thinking should be based on ratios rather than percentages. Aitchison's method involves the construction of a log-ratio covariance matrix which expresses compositional data as the covariance of (natural) log-ratios of the compositional variables (Aitchison, 1986, 2003). The calculation of log-ratios has the advantage of freeing compositional data from their restricted range and allowing them to vary between +/− infinity.

In his 1986 and 2003 texts Aitchison proves (for the mathematically literate) that the covariance structure of log-ratios is superior to the covariance structure of a percentage array. The covariance structure of log-ratios is free from the problems of negative bias and of data sub-compositions which bedevil percentage data. Aitchison (1986, 2003) proposed that three types of matrix might be usefully constructed:

1. A *variation matrix* in which the log-ratio variance is plotted for every variable ratioed to every other variable. This matrix provides a measure of the relative variation of every pair of variables and

can be used in a descriptive sense to identify relationships within the data array and in a comparative mode between data arrays.
2. An *additive log-ratio covariance matrix* in which every variable is ratioed against a common denominator. The choice of variable as the denominator is immaterial because it is the structure of the matrix that is important.
3. A *centred log-ratio covariance matrix* in which the single denominator of the log-ratio covariance matrix is replaced by the geometric mean of all the components. This has the conceptual advantage for the geochemist over the log-ratio covariance form that no one element is singled out as the denominator.

The additive log-ratio (ALR) and centred log-ratio (CLR) data transformations are fairly common in sedimentology, soil science and ore geology (see Delbari et al., 2011; Ward et al., 2012; Sun et al., 2014). Egozcue et al. (2003) presented cogent arguments in favour of the isometric log-ratio (ILR) transformation which has good mathematical and geometric properties. ALR-transformed data allow correlation coefficients to be calculated and other multivariate statistical analyses to be performed for all elements excluding the selected divisor element. CLR-transformed data are singular so multivariate statistics cannot be applied; on the other hand, no variables are excluded in a CLR transformation and so if a direct relationship between all of the variables is needed, CLR may be preferred. ILR overcomes the singularity issue of the CLR transformation so covariance can be determined for all variables, and by inverting the ILR-transformation, the data can be transformed back to the original data space.

The early formulations of Aitchison's work were to transform compositional data from its restrictive sample space (the 'simplex') into a more workable ('unconstrained') sample space in which standard statistical methods could be applied. More recently, Aitchison and Egozcue (2005) have proposed that an alternative approach is to work with compositional data within the simplex and to investigate problems within this space with its specific algebraic–geometric structure. This staying-in-the-simplex approach 'proposes to represent compositions by their coordinates, as they live in a Euclidean space, and to interpret them and their relationships from their representation in the simplex'. This requires the internal simplicial operation of perturbation and the external operation of powering. Perturbation is a differential scaling operator and is computed by multiplying compositions component to component, and afterwards dividing each component by the sum of all of them to attain a unit sum. Powering, the analogue of scalar multiplication in real space, consists of raising each component to a constant and then applying closure to the result (see Aitchison and Egozcue, 2005). In current practice many workers adopt a bilateral approach and attempt to interpret compositional data from both the log-ratio and the staying-in-the-simplex approach. It should always be explicitly stated if parameters are determined from a transformed dataset and which transformation has been used.

2.7.2 The Biplot

In the context of compositional data analysis, a biplot is a means of displaying a data matrix graphically (Gabriel, 1971). In geochemistry it is a means of displaying a matrix of major element oxide data in which the samples comprise the rows and the oxide variables the columns. The purpose of the biplot is to show the entire compositional variation of the dataset within a single figure rather than the alternative, which is multiple plots of oxide pairs. An excellent text on the use of biplots is Greenacre (2010).

In most applications the raw data matrix is transformed to obtain a new matrix and this transformed matrix is shown in the biplot. The most common transformation is that of 'centring of the data' with respect to column means (oxide variables) using the centred log-ratio transformation. The matrix is then transformed again using singular value decomposition (Aitchison and Greenacre, 2002; Daunis-I-Estadella et al., 2006).

The key components of a biplot applied to geochemical data include:

- an origin, which is the centre of the compositional dataset
- the rays, which represent the relative variability of the different oxide compositions
- data points, which are the individual sample compositions.

This means that both the row points (samples) and column points (oxide variables) are centred at the

origin of the biplot. Rays provide information about relative variability in a compositional dataset. Both their length and direction are important. A join between two rays is known as a link. Cosines of the angles between links estimate the correlation between log-ratios such that links at right angles to each other signify zero correlation and links that are co-linear have a high degree of correlation.

There are few examples in the literature of the application of the biplot approach to the exploration of major element oxide data. Daunis-I-Estadella et al. (2006) describe the major element chemistry of soil samples collected from serpentinites, gabbros and basalts in ophiolitic terrains in Tuscany. Their biplot (Figure 2.6) shows rays meeting at the origin for eight major element oxides. The authors note that 'the serpentinitic soil samples show high dispersion when compared with the others but that the three groups of soils maintain good separation'. They also note that the grouping of the basalt and gabbro samples offers the prospect of good sample discrimination. The opposition of the co-linear Al_2O_3 and Fe_2O_3 + MnO rays may indicate processes related to clay mineral formation, although the co-linear opposition of TiO_2 and MgO + SiO_2 is not discussed.

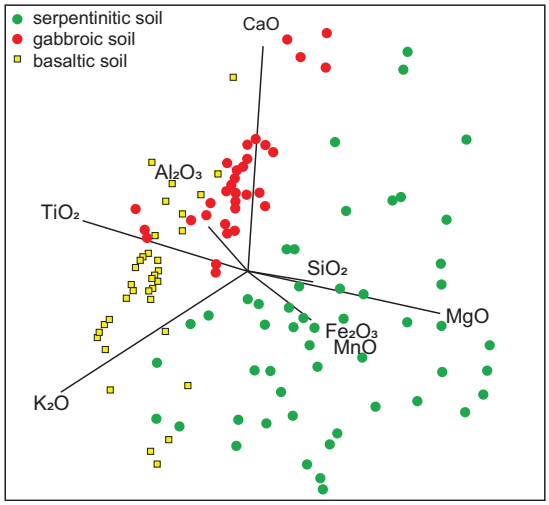

Figure 2.6 A biplot of major element oxides showing the composition of serpentinitic, gabbroic and basaltic soils from ophiolites in Tuscany. The biplot shows rays for each of the major element oxides and points for the three main soil groups. (From Daunis-I-Estadella et al., 2006; with permission from the Geological Society of London)

2.7.3 Some Geochemical Applications of the Log-Ratio Approach

One area in which geochemists agree with statisticians, probably without realising it, is in the use of log-normalised trace element diagrams in which rare earth elements (REE) are referenced to the composition of chondritic meteorites. In such plots a selected suite of incompatible elements is referenced to the composition of the Earth's primitive mantle, and these are effectively log-ratio plots. However, since Aitchison's initial work in the 1980s, and apart from the application to the REE, the impact of the log-ratio approach in geochemistry and petrology has been small and there are only a few examples of the application of this approach in the literature.

One application of an early formulation of Aitchison's method was that of Rollinson (1992), who tested the log-ratio approach on a suite of basalts from Kīlauea Iki lava lake, Hawai'i, whose compositional variability was well understood and thought to be related to olivine fractionation (Richter and Moore, 1966). The data are presented in Table 3.6 and a bivariate diagram displaying these data is given Figure 3.12. The percentage data matrix was recalculated in three ways: as a variation matrix, a covariance matrix, and a centred covariance matrix. The results of this analysis indicated that in all three variation matrices, the greatest relative variation was between those elements *included* in the fractionating phase olivine (Mg, Fe, Mn) and those elements which were *excluded* (K, Ti, P, Na, Ca and Al) and concentrated in the melt. Hence the log-ratio approach supports the model initially proposed on the basis of field observations.

A similar study of a suite of over 3000 samples of Cenozoic volcanic rocks from the Carpatho-Pannonian region of Hungary (Kovacs et al., 2006) showed three discrete groups of samples on a biplot. One group was identified as alkaline basalts and is separated along the TiO_2 and P_2O_5 rays from a group identified as calc-alkaline basaltic-andesites (andesites and dacites aligned along the CaO and Fe_2O_{3T} rays), and a third more dispersed group which is rhyolitic in composition. The rhyolites scatter around the co-linear rays for Al_2O_3, SiO_2, Na_2O and K_2O, implying some alkali feldspar control. What is novel about this study is that the results of the log-ratio analysis are directly compared with the results of a traditional bivariate oxide diagram in which the same three

groups are evident. The authors concluded that the 'compositional geometry shows ... good agreement with geological models based on scientific methods which do not include a strict statistical approach'.

Log-ratio analysis has also been used to discriminate between limestone types as an aid to lithostratigraphy and correlation in the Scottish Dalradian (Thomas and Aitchison, 2006). Using a log-ratio plot of Fe_2O_3/CaO versus MgO/CaO the authors created a discrimination diagram which allows the different limestone groups to be differentiated and similar limestone types to then be correlated in what is otherwise a structurally complex region.

Perhaps the most helpful example of analysing compositional data is the work of Daunis-I-Estadella et al. (2006). These authors describe in some detail the process of exploratory compositional data analysis as applied to major and trace elements, and the concepts are accompanied with a worked example. They identify three essential processes which are important in this analysis: (1) fundamental descriptive statistics which are required for compositional data analysis, (2) the graphical biplot approach (Section 2.7.2) and (3) the importance of data sub-composition analysis. They propose that a compositional data matrix can be described by the calculation of the centre (the geometric mean), the variation matrix and the total variance. They graphically display their results in a biplot. A key test of compositional data analysis is that any selected sub-composition should have the same statistical properties as the larger data matrix from which it has been taken (Section 2.9).

2.8 Multivariate Data Analysis

After data transformation, additional statistical methods can be applied. These are intended to reduce multivariate data to two dimensions for easy visualisation. In addition to the biplot (Section 2.7.2) these include principal component and factor analysis, discriminant analysis and multidimensional scaling; these are discussed in the sections below.

2.8.1 Principal Component and Factor Analysis

Given that a typical geochemical analysis may include up to 30 different elements, principal component analysis (PCA) is a useful technique to reduce a large number of variables (elements or oxides) to a smaller number of uncorrelated variables and is often the first step in any multivariate analysis. Although PCA will generate as many components as there are variables, the bulk of the information is usually contained within the first few components, thus allowing a single variation diagram to contain information about a large number of variables (see Section 3.3). On the other hand, there are two obvious disadvantages to this approach: (1) the complex plotting parameters on variation diagrams are difficult to comprehend and (2) the art of geochemical detective work is to identify the role that each element plays in elucidating a geochemical process. This cannot be done when a number of variables are combined into a single component.

The method is well described in most statistical textbooks; see, for example, Reimann et al. (2008). Data presented in different units, such as major element oxides in wt.% and trace elements in ppm, should not be treated together, since the most abundant variable will control the absolute magnitude of variance. Compositional data should be transformed (ALR, CLR, ILR) and the original, transformed, set of variables converted into a new set of variably scaled principal component coordinates called *eigenvectors* (or latent vectors). The first eigenvector is the direction of maximum spread of the data in terms of *n*-dimensional space. It is a 'best fit' line in *n*-dimensional space and the original data can be projected onto this vector using the first set of principal component coordinates. The variance of these coordinates is the first *eigenvalue* (or latent root) and is a measure of the spread in the direction of the first eigenvector. Thus eigenvector 1 may be expressed as:

$$\text{Eigenvector } 1 = x_1SiO_2 + x_2TiO_2 + x_3Al_2O_3$$

where x_1, x_2, x_3, etc., define the principal component coordinates. The method then defines a second eigenvector which has maximum spread at right angles to the first eigenvector, and so on. The eigenvalues are used to measure the proportion of data used in each eigenvector. By definition the first eigenvector will contain the most information and succeeding eigenvectors will contain progressively less information. Therefore, it is often the case that the majority of information is *contained in the first two or three eigenvectors*. Eigenvectors and eigenvalues may be calculated from a covariance matrix if the variables

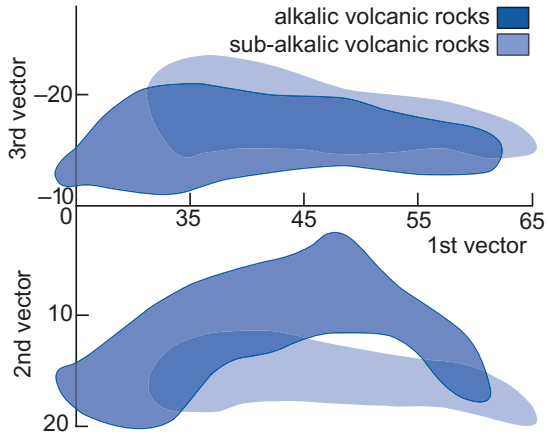

Figure 2.7 Principal component analysis. The second and third eigenvectors are plotted in two dimensions relative to the first eigenvector to illustrate the chemical differences between the alkalic and sub-alkalic rock series. (Data from Le Maitre, 1968)

are measures in the same units, or a correlation matrix if the variables are expressed in different units. The three eigenvectors are plotted as a two-dimensional graph in Figure 2.7. Aitchison (1984, 1986, 2003) describes how log-ratio transformed data may be used in principal component analysis in preference to percentage data.

The new variables represent a convenient way of expressing variations in multivariate data. The first two components express the main variability in the dataset and additional components are identified as needed until the majority of the variability is accounted for. Typically, these principal components will account for >70% of the variance in the data.

The application of PCA is widespread in the geosciences. Demšar et al. (2013) present an overview on the application of PCA to spatial data. Soesoo (1997) used PCA to distinguish between pressure and temperature environments of basaltic magmas on the basis of clinopyroxene compositions. The PCA of geochemical data by Thy and Esbensen (1993) allowed them to clearly distinguish between the sheeted dike complex and the upper lava suite of the Troodos ophiolite complex.

Factor analysis (FA), an approach which is closely related to PCA, also seeks to minimize the variation in multivariate data to as few 'factors' as possible. It differs from PCA in that the number of axes does not equal the number of variables (as in PCA). Instead, FA defines a small number of 'factors' which explain the greatest proportion of the data. FA is performed using the standardised correlation matrix, weighting all the variables equally, and converting principal component vectors into several 'factors'. It is widely used in sedimentology (Hofer et al., 2013), the environmental sciences (Rezaei et al., 2017) and economic geology (Zhao et al., 2017).

2.8.2 Discriminant Analysis

Discriminant analysis (discriminant function analysis) is similar to principal component analysis inasmuch as it is aimed at reducing dimensionality of multivariate datasets. In geochemistry linear discriminant analysis has been applied particularly fruitfully in the investigation of relationships between the major and trace element chemistry of igneous and sedimentary rocks. This section, therefore, serves as a theoretical introduction to the discussion of petrological discrimination diagrams which is given in Chapter 5.

Samples are arranged into groups on the basis of multiple variables by maximising the ratio of between-group variance and within-group variance in order to achieve maximum separation. The method requires the initial calculation of means and standard deviation of the individual variables in order to provide some idea of differences and overlaps between the groups. If the separation of variables between groups is good, then the variance between groups is compared to that within the groups.

In discriminant analysis a set of samples is nominated as belonging to two or more groups. From the distributions of these groups it is possible to calculate one or more linear functions of the variables measured which will achieve the greatest possible discrimination between the groups. The functions have the form:

$$F_i = a_i x_1 + b_i x_2 + c_i x_3 + \ldots + p_i x_p \qquad (2.11)$$

where $x_1, x_2, \ldots, x_p$ are the discriminating variables (major elements or trace elements), $a_i, b_i, \ldots, p_i$ are the discriminating function coefficients and F_i is the discriminant score. The magnitudes of the discriminating function coefficients associated with the variables show the relative importance of the variables in separating the groups along the discriminant function. The data are then plotted on a diagram in which the

axes are defined by the discriminant functions, and in linear discriminant analysis linear boundaries between groups are fitted by eye.

A classic example of the application of discriminant analysis in igneous petrology is found in the papers of J.A. Pearce (1976) and Pearce and Cann (1971, 1973), who employed discriminant analysis in an attempt to classify basalts on the basis of their major and trace element chemistry (see also Chapter 5). The Pearce (1976) study was based upon a collection of geologically recent basalts taken from six different tectonic environments: ocean-floor basalts, island arc tholeiites, calc-alkaline basalts, shoshonites, ocean-island basalts and continental basalts. The objective of the study was to see if there is a relationship between major element chemistry and tectonic setting.

The initial part of the investigation was an analysis of the within-group and between-group variation. In this way the parameters which are most likely to contribute to the separation of groups were identified, and those likely to be the least effective were discarded. This was then followed by the quantitative step: the discriminant analysis, which determined the characteristics of the dataset which contribute most to the separation of the groups. These characteristics are expressed as the following parameters (see Table 2.6; data from Pearce, 1976):

- eigenvectors: These are the coefficients (a_i, b_i, . . . , p_i) of the discriminant function equations (see Eq. 2.11).
- eigenvalues (for each discriminant function): These show the contribution made by the function to the total discriminating power. In the case of *F1* it can be seen from Table 2.6 that it contributes to 49.7% of the discrimination and that *F1* and *F2* together contribute to 76.1% of the total discrimination.
- scaled eigenvectors: These show the relative contributions of each variable to the discriminant function. In the case of *F1* the variables TiO_2 (−0.85) and SiO_2 (+0.34) show the largest scores and will dominate this particular discriminant function.

A convenient way of visually examining the group separation may be obtained by plotting the discriminating functions *F1* and *F2* as the axes of an *x*–*y*

Table 2.6 Results of discriminant analysis for basaltic rocks[a]

	F1	*F2*	*F3*	*F4*	*F5*
			Eigenvectors		
SiO_2	0.0088	−0.013	−0.0221	0.0036	0.0212
TiO_2	−0.0774	−0.0185	−0.0532	−0.0326	0.0042
Al_2O_3	0.0102	−0.0129	−0.0361	−0.0096	−0.0071
FeO	0.0066	−0.0134	−0.0016	0.0088	0.0141
MgO	−0.0017	−0.0300	−0.0310	0.0277	−0.0017
CaO	−0.0143	−0.0204	−0.0237	0.0321	0.0153
Na_2O	−0.0155	−0.0481	−0.0614	0.0140	0.0701
K_2O	−0.0007	0.0715	−0.0289	0.0899	0.0075
Eigenvalues	2.58	1.37	0.65	0.5	0.09
% of trace	49.7	26.4	12.4	9.7	1.7
Cumulative %	49.7	76.1	88.5	98.2	99.9
			Scaled eigenvectors		
SiO_2	0.34	−0.51	−0.86	0.14	0.83
TiO_2	−0.85	−0.20	−0.59	−0.36	0.05
Al_2O_3	0.32	−0.40	−1.12	−0.30	−0.22
FeO	0.18	−0.37	−0.04	0.24	0.24
MgO	−0.04	−0.74	−0.76	0.68	−0.04
CaO	−0.29	−0.41	−0.48	0.65	0.31
Na_2O	−0.17	−0.54	−0.69	0.16	0.79
K_2O	−0.01	0.70	−0.28	0.88	0.07

[a]From Pearce (1976).

graph as illustrated in Figure 5.5 (*DF1* and *DF2*). Individual analyses are plotted as their *F1* and *F2* discriminant function scores. The only disadvantage of this plot is that the discriminating functions are less easy to visualise than the original oxide variables. The value of a discriminant function diagram is measured by its success rate in correctly classifying the data as expressed as the percentage of correct classifications. This may use part of the data as a 'training set' for which the discriminating functions are derived; the remainder of the data is then used as a 'testing set' with which the calculated functions may be optimised so as to minimise the number of misclassifications.

2.8.2.1 Limitations of Discriminant Analysis

One of the criticisms of discriminant analysis is its relatively low accuracy, which in part is due to the dependence upon boundaries drawn by eye and the relatively small number of variables incorporated into the discriminant functions. An alternative approach based upon Bayesian probability theory was discussed by Pearce (1976, 1987) and developed more recently by Agrawal et al. (2004) and Shragge and Snow (2006).

Shragge and Snow (2006) proposed a multidimensional geochemical discrimination technique based upon probability density functions that quantify the likelihood of a sample formed in a specified tectonic setting given a particular chemical composition. The compositions of samples of unknown origin are then used to assess the probability of their being formed in a particular tectonic setting. The results of this methodology are plotted as probability functions, that is, the probability that a given sample formed at a mid-ocean ridge, an island arc, or an ocean-island hotspot, on a ternary diagram. The probability functions are based upon seven relatively immobile trace elements – Ni, Sr, Zr, Nb, Ti, Pb and Ta – and of 471 samples more than 90% of each of the three categories were correctly classified. However, despite the increased accuracy of the method, the use of probability functions is not intuitive. Further, Shragge and Snow (2006) caution against a purely geochemical approach to discrimination and emphasise the importance of additional petrological inference. For example, they argue that samples with 70% SiO_2 may be correctly geochemically classified by their methodology whereas a petrological understanding would strongly suggest that an island arc origin is more likely than a MORB origin.

Chapter 5 includes a detailed discussion of the application of discrimination diagrams in geochemistry. However, it is important to note that the methodology of discriminant analysis as applied to the separation of rocks from different tectonic settings has been subject to some criticism. The early work of Pearce and Cann (1971, 1973) was criticised by Butler and Woronow (1986) for their use of a ternary diagram. This is because the formation of ternary percentages induces closure into the dataset resulting in an unknown amount of the depicted variability being an artefact of closure (see Section 2.2.2.1). Instead, they propose a diagram based upon principal component analysis (Section 2.8.1) in which the first two principal components are used as the axes of a 'discrimination' diagram.

More recently, Vermeesch (2006a) proposed that the additive log-ratio approach could be adopted in the use of discrimination diagrams to circumvent the problems of closure inherent in ternary plots. In addition, he argued that the traditional approach in which the arithmetic mean is used to identify the discrete populations in the early stages of discriminant analysis is not the best measure of the average value (as discussed in Section 2.3.2). Vermeesch (2006a), Sheth (2008) and Verma et al. (2013) have proposed a number of new discrimination diagrams using a wide range of trace or major elements, all of which successfully use the log-ratio approach. These diagrams are discussed more fully in Chapter 5. An alternative to conventional discriminant analysis is the use of classification trees (Vermeesch, 2006b), although this laborious and non-intuitive approach has not been widely adopted.

2.8.3 Multidimensional Scaling (MDS)

Multidimensional scaling (MDS), or proximity analysis, is a visual representation of *dissimilarity* between sets of variables in which those variables that are more similar plot closer together and those variables that are less similar plot farther apart. MDS can also be used to reduce high-dimensional data to a lower dimensionality, making the data more amenable to interpretation. MDS generally uses a matrix of relational data and follows these steps:

1. Assigns data points to coordinates in *n*-dimensional space.
2. Calculates the Euclidean distances for all pairs of points.

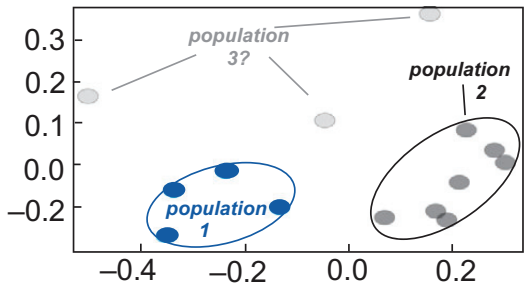

Figure 2.8 Multidimensional scaling plot of detrital zircon U-Pb ages. The axes are unitless and show the K-S measure of dissimilarity (Vermeesch, 2013). Similar populations plot close together (populations 1 and 2) and dissimilar populations plot far apart (population 3). (After Robinson et al., 2019; with permission from the Geological Society of America)

3. Compares the similarity matrix with the original input matrix.
4. Adjusts the coordinates to improve the 'goodness-of-fit'.

Although there can be errors associated with *small* datasets, MDS analysis is useful when dealing with large amounts of multivariate data. The method requires computer code in languages such as Matlab or R. However, given the increased amount of geochemical data being generated, such methods are likely to be increasingly used. Robinson et al. (2019) applied MDS analysis to a provenance study in the Brooks Range fold and thrust belt of Alaska (Figure 2.8) in which they identified two similar detrital zircon U-Pb age populations. Studies utilising small sample sets do not usually require MDS and, as the Robinson et al. (2019) study showed, similar results were obtained from the same dataset using cumulative distribution functions analysis. Nonetheless, when sediment provenance studies using detrital zircon U-Pb geochronology have large numbers of samples and there is a large volume of data per sample (hundreds to thousands of analyses) they lend themselves to MDS analysis.

2.9 Statistics and Ternary Plots

The use of ternary diagrams is a common way of presenting geochemical data in geochemistry (see also Section 3.3.3). Geochemical compositional data plotted onto triangular diagrams are frequently used in rock classification, for comparing measured rock compositions with those determined experimentally or empirically, for demonstrating compositional variation in geochemical data (see Chapter 3), and for discriminating between superficially similar rocks formed in different tectonic environments (see Chapter 5). Here we consider the statistical particularities of ternary diagrams.

Compositional data used in ternary diagrams are an example of a 'sub-composition'. That is to say they represent a subset of the larger parent dataset recast in proportions of 100%. For example, the A-F-M diagram (Section 3.3.3) is a ternary plot of the oxides $(Na_2O + K_2O)$–FeO_T–MgO in which the oxide values are re-normalised to 100% and their relative proportions plotted on a triangular graph (Figure 3.18). This procedure is of particular concern to the geostatistical community for two reasons. First, sub-compositions should represent the statistical variation of the parent dataset from which they are drawn, although the process described above does not allow this to be assessed. Aitchison (1986, Table 3.1) and Butler (1979, tables 1 and 2) showed that sub-compositions may have different rank orderings from the parent dataset. For example, in the AFM data subset the variance may be A > F > M, but in the parent dataset the variance may be F > A > M. Hence Butler (1979) comments that 'given the fact that major reversals of variance can occur simply as the result of ternary percentage formation it should be reasonable to expect that at least part of any trend is artificial'. Second, the effect of *re-normalising* a sub-composition of the main dataset which is already summed to 100% further magnifies the effects of closure – although in the case where trace elements such as Ti-Zr-Y are plotted on a ternary diagram, the fact that they make up only a small proportion of the whole means the impact of the constant sum is greatly reduced (Vermeesch, 2006a).

There are multiple examples in the geostatistical literature where the interpretation of triangular diagrams is heavily criticised, for example, Aitchison and Egozcue (2005). In order to minimise this problem, Vermeesch (2006a) applied the Aitchison log-ratio technique in which the ternary compositional data are first transformed into log-ratios, then a 'standard' statistical procedure is applied, and then finally the data are back-transformed and plotted on the ternary diagram. With this approach Vermeesch (2006a) showed that a smaller percentage of data are misclassified. Although this type of discriminant analysis is more robust, the fact that it is not more widely applied suggests that it is not readily implemented.

On the basis of the concerns mentioned here, we suggest that only those ternary diagrams tested for statistical rigour should be used. Ternary diagrams should be treated with caution, and if tested for statistical 'robustness' can be used in the following ways:

- as a descriptive tool for the identification of distinct clusters of data or trends in data
- to compare rock compositional data with mineral chemical data and/or the results of experimental and/or empirical studies
- in discriminating between rock types
- to formulate petrological hypotheses.

2.10 Geochemical Data and Statistical Analysis

Much of the discussion in this chapter has been about the correct use of statistics given the rather unusual nature of geochemical data. We have sought to steer a path between the 'pure' approach of geo-statisticians and those using geochemical data to obtain petrological or geological 'meaning'. In this context it is helpful to stand back from the detail and survey the full breadth of geochemistry in all its different expressions, for over the past few decades there has been an explosion in the amount of data generated. This has been captured in the creation of some very large databases, such as GEOROCK and PetDB. Clearly, the era of scientific 'big data' has come to geochemistry; see, for example, Vermeesch and Garzanti (2015) and Zhang and Liu (2019). This rapid increase in the volume of data coupled with advances in computer software lends itself to increasingly sophisticated ways of manipulating such data. Nonetheless, it is important to return to one of the basic premises of this book, that geochemical data are most meaningfully interpreted within a geological context, not in the abstract.

Currently, there are two contrasting approaches being applied to the analysis of geochemical datasets. The first approach extracts large datasets from databases through 'data mining' and these are manipulated by means of statistical analysis to produce useful results, as illustrated by the work of Grunsky and de Caritat (2019) in exploration geochemistry. Even here, however, geological intelligence based upon the context of the samples must be applied to the interpretation of the data. The second and, in our view, better approach is to test geological hypotheses using carefully selected data. That is to say, large datasets are screened so that only the highest quality data and the best constrained samples are used for data analysis. An example is found in the work of Herzberg et al. (2010) in their study of mantle potential temperatures through geological time. This work was based upon the geochemistry of komatiites and magnesian basalts, thought to be primary magmas, and from which their compositions were used to calculate mantle potential temperatures. In this study the initial data base contained 1500 samples of magnesian basalt, but after careful screening only 33 samples were regarded as suitable candidates for primary magmas from which the mantle potential temperatures could be calculated. A further example comes from the study of mantle trondhjemites in the Oman ophiolite (Rollinson, 2014). In this case a small suite of 12 samples was carefully selected in the field for geochemical analysis to examine whether or not felsic melts interact with the shallow mantle during their ascent. Despite their small number, geochemical data from these deliberately selected samples displayed patterns that clarified the hypothesis in a way that randomly collected material could not have done. This was possible only because of a knowledge of the geological context coupled with careful sampling.

3 Using Major Element Data

3.1 Introduction

This chapter examines the ways in which major element data are used to understand the genesis and evolution of the major rock types. Here we discuss the role of the elements Si, Ti, Al, Fe, Mn, Mg, Ca, Na, K and P – the 10 elements that are traditionally given as oxides in a major element chemical analysis – but do not consider in any depth the volatile elements H, CO_2, S or N. Although we recognise that the volatile elements play an important role in understanding the evolution of our planet in terms of chemical mass-balance through volcanic degassing and hydrothermal alteration, a full discussion of these themes is beyond the scope of this text and the reader is referred to other sources (e.g., Luft, 2014). For a detailed discussion of the major element chemistry of the oceans, again we refer the reader elsewhere (e.g., Millero, 2014).

This chapter is concerned with the three principal ways in which geochemists make use of major element data:

- in rock classification,
- in the construction of variation diagrams
- in comparison with experimentally determined rock compositions whose conditions of formation are known.

The combination of major and trace elements can often be used to identify the original tectonic setting of igneous and some sedimentary rocks, and this topic is addressed in Chapter 5.

The application of major element chemistry to rock classification and nomenclature is widely used in igneous petrology and can also be useful for some sedimentary rocks. Variation diagrams display major element data on bivariate or trivariate plots. These diagrams are used to show the interrelationships between elements in a dataset and from these relationships geochemical processes may be inferred. Variation diagrams based upon trace element concentrations are discussed in Chapters 4 and 5. The third use of major element data, plotting the chemical composition of an igneous rock onto a phase diagram, assumes that the chemistry of the rock is the same as that of the original igneous melt. In this case the comparison of a rock composition with experimentally determined phase boundaries for melts of similar composition under a range of physical conditions may allow inferences to be made about the conditions of melting and/or the subsequent crystallisation history of the melt.

However, before major element data are used in any of these ways it is important that the data are evaluated for quality and are processed in a uniform and consistent manner. In particular, it is important that the oxidation state of Fe is treated uniformly, that analysis totals are normalised to exclude the presence of volatiles and that a decision is made about whether the data should are presented as weight percent oxide or as cations. Here we propose a standardised method of data processing to allow a better comparison between data generated using different methods and/or in different laboratories.

3.1.1 Processing Major Element Data

The first step of any geochemical investigation is to assess the quality of the data to be used. A petrographic evaluation of sample thin sections is helpful for this and allows any alteration products to be identified. Data quality can then be evaluated with respect to the relative proportions of primary and hydrous secondary phases, the value of the loss on ignition (LOI) and the analysis total. 'Dry' samples which contain no hydrous minerals or alteration products should have an analysis total between 99% and 101%, whereas 'wet' samples containing primary hydrous minerals or alteration products may have lower totals due to the loss of volatiles recorded as LOI. For example, island arc andesites are often water-saturated and commonly have primary amphibole, and may therefore have LOIs of 3–6% (Ruscitto et al., 2012; Plank et al., 2013). In such circumstances, and given the absence of petrographic alteration, low totals because of high LOI may be acceptable. In this case it is good practice to normalise the data on a volatile-free (anhydrous or dry) basis.

The next step is to assess the oxidation state of Fe. This is usually governed by the method of sample preparation. Historically, when major elements were determined using solution chemistry, all the Fe was reduced to FeO and reported as such in the chemical analysis. Today major element analyses are generated by XRF and ICP in which samples are converted into a fused, homogeneous glass prior to analysis. If a graphite crucible is used during sample fusion, then all the Fe in the sample is reduced to FeO and the analytical result is presented as FeO. If a platinum crucible is used, all the Fe in the sample is oxidised to Fe_2O_3 and the analytical result is presented as Fe_2O_3. It is important to report Fe as it was analysed to allow others to fully assess data quality. This is normally done using the terms FeO_T or Fe_2O_{3T}, or sometimes as FeO(tot) and Fe_2O_3(tot), to indicate that all the iron is reported in a single oxidation state. Note, however, that reporting all the Fe in a single oxidation state does not reflect the true chemical evolution of magmatic systems, which tend to become more oxidising as they evolve. This topic is discussed further in Section 3.2.2.3.

Finally, a decision has to be made about the format of the data and whether or not oxide data should be converted to moles or cations. This usually depends on how the data are going to be used. Current practice is to present major element chemistry for rocks as weight (wt.) % and to convert as needed to cations, cation % or parts per million (see Section 3.2.3), although the chemical composition of water is typically presented in molar concentrations.

3.1.2 Major Element Mobility

Before beginning to classify and investigate the petrogenesis of a suite of samples it is important to consider whether or not they preserve their original chemistry and whether they have been altered in any way. This typically involves chemical changes which take place *after* rock formation, usually through interaction with a fluid. These changes may sometimes be described as *metasomatic*. Major element mobility typically occurs during diagenesis and metamorphism or through interaction with a hydrothermal fluid. In metamorphic rocks element mobility may take place as a result of solid-state diffusion or melt generation and migration.

The mobility of major elements is controlled by three main factors: the stability and composition of the minerals in the unaltered rock, the stability and composition of the minerals in the alteration product and the composition, temperature and volume of the migrating fluid or melt phase. Element mobility may be detected from mineralogical phase and compositional changes that have taken place in a rock as a result of metamorphism or hydrothermal activity and from the mineral assemblages present in associated veins. Thus, careful petrography is an important tool in identifying chemically altered rocks. Scattered trends on variation diagrams are also a useful indicator, although chemical alteration can sometimes produce systematic changes which may mimic other mixing processes such as crystal fractionation. These apparent trends may result from volume changes arising from the removal or addition of a single component of the rock.

An example of major element mobility is given in the dataset presented in Table 3.1 in which a suite of Permian basalts from Sumatra has been analysed for the major elements. There are two unusual features about these basalt data. First, the samples have very high LOI, indicating significant hydration. This parameter alone can be taken as an indicator of possible major element mobility (e.g., Smith and Humphries, 1998). The Sumatran samples also appear to have very high Na_2O contents relative to fresh MORB and MORB glass (Table 3.2b). When recalculated as anhydrous and plotted on a TAS diagram (see Section 3.2) the samples plot between basalts and trachybasalts (inset, Figure 3.1a), suggesting that they are alkaline basalts. However, given their very high water content, an alternative explanation is that they have been altered by interaction with seawater and have thus become more sodic or spilitised. Further evidence for basalt alteration comes from the study of fluid-mobile trace elements, and this will be discussed in more detail in Chapter 4.

3.1.3 The Compositions of Some Major Earth Reservoirs

It is sometimes useful for comparison or normalisation to have representative values of some of the major Earth reservoirs. These are summarised in Table 3.2 for the major elements and in Table 4.9 for trace elements. Table 3.2a shows major element compositional data for the whole Earth (or the bulk Earth), the silicate Earth (or the bulk silicate Earth, or BSE, a term interchangeable with primitive upper mantle, or PM) and the Earth's core. The data are expressed in wt.% elemental concentrations and

Table 3.1 Permian basalts from Sumatra[a]

	1	*2*	*3*	*4*	*5*	*6*	*7*	*8*	*9*
Measured compositions									
	MR136	MR137	MR139	IG5	IG4	MR150	MR152	MR153	95SM11
SiO_2	45.13	44.82	46.31	37.60	46.01	42.70	43.64	40.76	48.03
Al_2O_3	14.11	13.79	14.25	14.21	12.91	13.42	14.87	13.28	14.46
Fe_2O_{3T}	8.93	9.16	9.05	10.54	11.58	9.30	8.74	9.06	12.78
MnO	0.11	0.12	0.10	0.15	0.11	0.11	0.11	0.12	0.19
MgO	7.34	8.75	7.34	6.54	7.08	6.32	6.34	8.37	7.74
CaO	10.88	8.95	7.36	9.89	6.16	10.04	8.32	10.90	7.92
Na_2O	4.00	4.09	5.04	3.83	3.70	4.54	4.24	3.58	3.46
K_2O	0.72	0.67	0.28	0.15	0.10	0.10	0.19	0.18	1.10
TiO_2	1.29	1.42	1.32	1.31	1.70	1.57	1.33	1.19	1.35
P_2O_5	0.68	0.87	0.81	0.75	1.29	1.22	0.85	0.61	0.23
LOI	6.77	7.07	7.39	12.02	7.83	9.88	10.41	10.60	2.65
Recalculated dry to 100%									
SiO_2	48.43	48.38	50.41	44.25	50.76	47.81	49.24	46.29	49.38
Al_2O_3	15.14	14.89	15.51	16.72	14.24	15.02	16.78	15.08	14.87
Fe_2O_{3T}	9.58	9.89	9.85	12.40	12.78	10.41	9.86	10.29	13.14
MnO	0.12	0.13	0.11	0.18	0.12	0.13	0.13	0.14	0.20
MgO	7.88	9.45	7.99	7.70	7.81	7.08	7.15	9.51	7.96
CaO	11.67	9.66	8.01	11.64	6.80	11.24	9.39	12.38	8.14
Na_2O	4.29	4.42	5.49	4.51	4.08	5.08	4.78	4.07	3.56
K_2O	0.77	0.72	0.30	0.18	0.11	0.11	0.21	0.20	1.13
TiO_2	1.38	1.53	1.44	1.55	1.88	1.75	1.50	1.35	1.39
P_2O_5	0.73	0.94	0.88	0.88	1.42	1.37	0.96	0.69	0.24
	100.00	100.00	100.00	100.00	100.00	100.00	100.00	100.00	100.00

[a]Data from Crow et al. (2019) and M. Crow, pers. comm.

oxygen is shown separately. This is because the core contains no oxygen and so expressing the data as elemental concentrations allows comparisons to be made between the silicate Earth and the core. In addition to the 10 major elements present in most silicate rocks, the metals Ni and Cr and the light elements H, C and S are also included as they constitute a measurable fraction of the composition of the whole Earth. These data are from McDonough (2014a) and assume that the original undifferentiated Earth was similar in composition to carbonaceous chondritic meteorites. It is known that the Earth's core contains a few wt.% of a light element in addition to Fe and Ni, and the McDonough (2014a) model presented here argues that the principal light element is Si, but that there is also some S present.

Table 3.2b provides the major element compositions of the major silicate reservoirs. The magnesium number (*Mg#*), its meaning and calculation are discussed in Section 3.3.2.1. As shown above, the primitive mantle is the same as the bulk silicate Earth – the Earth after the separation of the core but before the development of continental crust. Using the Earth reservoir data from Table 3.2a converted to oxide wt.%, the models of McDonough (2014a) and Palme and O'Neill (2014) are provided. The composition of the depleted mantle (DM) calculated by Workman and Hart (2005) is given for comparison and represents mantle from which some basaltic melt has been extracted. The DM, relative to PM, is more magnesian and slightly depleted in elements such as Ca, Al and Si which are preferentially incorporated into basaltic melt. A mean composition of over 2000 mid-ocean ridge basalt (MORB) samples from the floor of the major oceans is given and is very slightly different from the mean value of over 3000 MORB glass samples (data from White and Klein, 2014). Note, however, that these compositions simply represent what is found on the floor of the oceans and does not necessarily represent a primitive or primary MORB composition. The mean composition of the continental crust calculated by Rudnick and Gao (2014) is a weighted composite of the compositions of the upper, middle and more mafic lower continental crust.

Table 3.2 Major element compositions of Earth reservoirs

(a) Earth reservoirs (element wt.%)

	Bulk Earth	*BSE/ primitive mantle*	*Earth's core*
Ref	*1*	*1*	*1*
Si	16.100	21.000	6.000
Ti	0.081	0.120	0.000
Al	1.590	2.350	0.000
Fe	32.000	6.260	85.500
Mn	0.080	0.105	0.030
Mg	15.400	22.800	0.000
Ca	1.710	2.530	0.000
Na	0.180	0.270	0.000
K	0.016	0.024	0.000
P	0.072	0.009	0.200
Ni	1.820	0.196	5.200
Cr	0.470	0.263	0.900
O	29.700	44.000	0.000
H	0.026	0.010	0.060
C	0.073	0.012	0.200
S	0.635	0.025	1.900
Total	99.953	99.973	99.990

Reference: 1, McDonough (2014a).

(b) Earth reservoirs (oxides wt.%)

	BSE/ primitive mantle	*BSE/ primitive mantle*	*Depleted mantle*	*Mean MORB (whole rock)*	*Mean MORB (glass)*	*Mean continental crust*	*Mean upper continental crust*	*Mean middle continental crust*	*Mean lower continental crust*
Ref	*1*	*2*	*3*	*4*	*4*	*5*	*5*	*5*	*5*
SiO_2	44.91	45.40	>44.71	50.06	50.60	60.60	66.60	63.50	53.40
TiO_2	0.16	0.21	0.13	1.52	1.67	0.72	0.64	0.69	0.82
Al_2O_3	4.44	4.49	3.98	15.00	14.79	15.90	15.40	15.00	16.90
FeO_T	8.05	8.10	8.18	10.36	10.46	6.71	5.04	6.02	8.57
MnO	0.13	0.14	0.13	0.19	0.19	0.10	0.10	0.10	0.10
MgO	37.81	36.77	38.73	7.71	7.42	4.66	2.48	3.59	7.24
CaO	3.54	3.65	3.17	11.46	11.38	6.41	3.59	5.25	9.59
Na_2O	0.36	0.35	0.13	2.52	2.77	3.07	3.27	3.39	2.65
K_2O	0.03	0.031	0.006	0.190	0.190	1.810	2.800	2.300	0.610
P_2O^5	0.02	0.020	0.019	0.160	0.180	0.130	0.150	0.150	0.100
Total	99.46	99.16	99.19	99.17	99.65	100.11	100.07	99.99	99.98
Mg#	89.3	89.0	89.4	59.0	58.0	55.3	46.7	51.5	60.1

References: 1, McDonough (2014a); 2, Palme and O'Neill (2014); 3, Workman and Hart (2005); 4, White and Klein (2014); 5, Rudnick and Gao (2014).

Table 3.2 (*cont.*)

(c) Continental lithospheric mantle (oxide wt.%)

Ref	*Xenolith Average 1*	*PUM 2*	*PUM 3*	*PUM 4*	*PUM 5*
SiO_2	44	45.96	45.14	46.2	44.92
Al_2O_3	2.27	4.06	3.97	4.75	4.44
FeO	8.43	7.54	7.82	7.7	8.05
MgO	41.4	37.78	38.3	35.5	37.8
CaO	2.15	3.21	3.5	4.36	3.54
Na_2O	0.24	0.33	0.33	0.4	0.36
K_2O	0.05	0.03	0.03	*nd*	0.29
Cr_2O_3	0.39	0.47	0.46	0.43	0.38
MnO	0.14	0.13	0.14	0.13	0.14
TiO_2	0.09	0.181	0.217	0.23	0.201
NiO	0.012	0.28	0.27	0.23	0.25
CoO	0.014	0.013	0.013	0.012	*nd*
P_2O_5	0.06	0.02	*nd*	*nd*	0.02

Notes: *nd*, no data.
References: 1, McDonough (1990); 2, Zindler and Hart (1986); 3, Jagoutz et al. (1979); 4, Palme and Nickel (1985); 5, McDonough and Sun (1995).

Another important major Earth reservoir is the continental lithospheric mantle (CLM), often referred to in the literature as the sub-continental lithospheric mantle (SCLM) (see Table 3.2c). Fragments of the mantle provide our only direct samples of the CLM and include orogenic peridotites, ophiolites, and xenoliths transported via volcanism. Mantle xenoliths broadly define two compositional types: spinel- and garnet-facies peridotites associated with kimberlites, and spinel-facies peridotites associated with predominantly alkalic rocks. The former are generally found in cratonic settings and the latter in non-cratonic (rift) settings. Table 3.2c shows a compilation of xenolith and primitive upper mantle (PUM) model compositions from Pearson et al. (2014).

3.2 Rock Classification

With the advent of automated XRF and rapid ICP analytical methods most geochemical investigations produce a large volume of elemental data that allows for the classification of rocks on the basis of their chemical composition. This section reviews the classification schemes in current use and outlines the rock types for which they may be specifically suited. A summary of the classification schemes discussed is given in Box 3.1. We adhere to the guidelines of the International Union of Geological Sciences Subcommission on the Systematics of Igneous Rocks (Le Maitre et al., 2002) for the naming and classification of rocks. We concur that a classification scheme should be easy to use, widely applicable, have a readily understood logical basis and reflect as accurately as possible the existing nomenclature based upon mineralogical criteria.

3.2.1 Classifying Igneous Rocks Using Oxide-Oxide Plots

Bivariate oxide-oxide major element plots are the most straightforward way in which to classify igneous rocks, especially volcanic rocks, and the principal diagrams are summarised below.

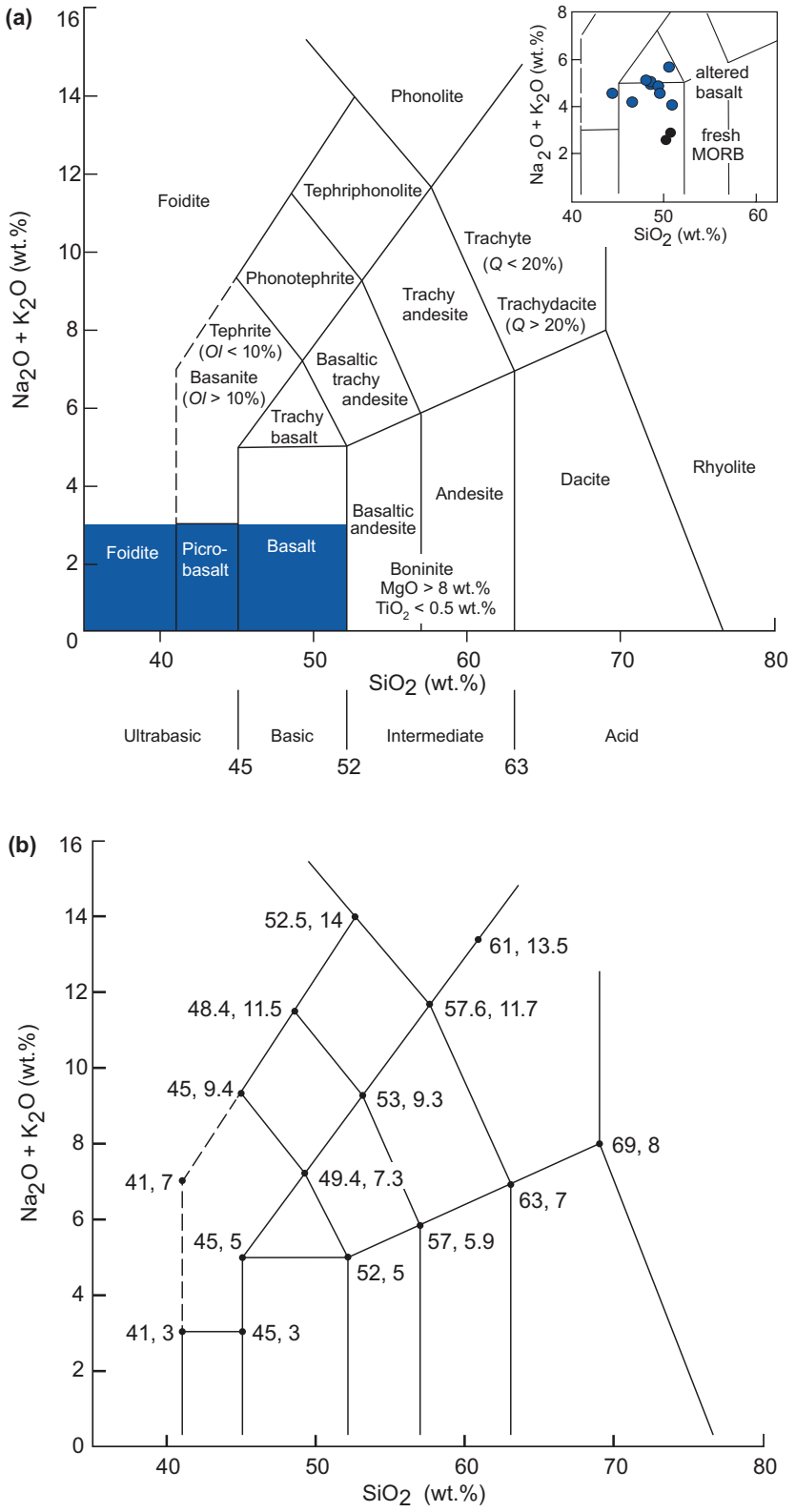

Figure 3.1 The total alkalis versus silica (TAS) diagram for volcanic rocks. (a) The chemical classification and nomenclature of Le Maitre et al. (2002) after Le Bas et al. (1986). *Q* = normative quartz, *Ol* = normative olivine. Ol- and Px-rich rocks occur in the shaded region, which is expanded in Figure 3.8. The inset shows the possible Na-enrichment of Permian basalts from Sumatra relative to fresh MORB. (b) Plotting coordinates for the field boundaries expressed as 'SiO_2 and (Na_2O + K_2O)' after Le Bas et al. (1986).

Box 3.1 Summary of chemical classification schemes described in Section 3.2

Igneous rocks

3.2.1 Oxide-oxide plots
The total alkalis-silica diagram (TAS)
- for volcanic rocks
- for plutonic rocks
- for discriminating between the alkaline and sub-alkaline rock series

Subdivision of sub-alkalic volcanic rocks using K_2O versus SiO_2

3.2.2 NORM-based classifications
Basalt classification using the *Ne–Di–Ol–Hy–Q* diagram
Granite classification using the *Ab–An–Or* diagram

3.2.3 Cation classifications
Komatiitic, tholeiitic and calc-alkaline volcanic rocks using the Jensen plot
High-Mg rocks using the Hanski plot

3.2.4 Combined major element oxide and cation classification for granitoids
The Frost diagrams

Sedimentary rocks

3.2.5 The chemical classification of sedimentary rocks
Sandstones
Mudrocks
Limestones

3.2.1.1 The Total Alkalis-Silica Diagram (TAS) for Volcanic Rocks

The total alkalis-silica diagram is one of the most useful classification schemes available for volcanic rocks. Using wt.% oxide chemical data from a rock analysis that has been recalculated to 100% on an anhydrous (volatile-free) basis, the sum of $Na_2O + K_2O$ (total alkalis, TA) and SiO_2 (S) are plotted onto the classification diagram. The original version of the diagram (Le Bas et al., 1986) was expanded by Le Maitre et al. (1989) using 24,000 analyses of fresh volcanic rocks (Figure 3.1a). Le Maitre et al. (2002) further expanded the classification to include olivine- and pyroxene-rich rocks (Section 3.2.3.3).

The field boundaries were defined by minimizing the overlap between adjoining fields, and the boundary coordinates are given in Figure 3.1b. The TAS diagram divides rocks into ultrabasic, basic, intermediate and acid on the basis of their silica content following the usage of Peccerillo and Taylor (1976). The nomenclature is based upon a system of root names with additional qualifiers to be used as necessary. For example, the root name 'basalt' may be qualified to 'alkali basalt' or 'sub-alkali basalt'. Some rock names cannot be allocated until the normative mineralogy has been determined. For example, a tephrite contains less than 10% normative olivine, whereas a basanite contains more than 10% normative olivine (see Section 3.2.2 on the norm calculation).

The TAS classification scheme is intended for common volcanic rocks and should not be used with weathered, altered or metamorphosed volcanic rocks because the alkali elements can be mobilised. Potash-rich rocks (nephelinites, mela-nephelinites) should not be plotted on the TAS diagram, and ultramafic or high-Mg rocks (boninite, komatiite, meimechite, picrite) should be checked for their TiO_2 contents before assigning a name from the TAS diagram (see Section 3.2.3.3). Rocks showing obvious signs of crystal accumulation should also be avoided.

3.2.1.2 A TAS Diagram for Plutonic Rocks

Of the various schemes for the naming of plutonic rocks, the two most popular ones based on major element chemistry are the TAS diagram for plutonic igneous rocks (after Wilson, 1989) and the normative *Q–Or–Ab* triangular plot for granitoids (Section 3.3.2). The TAS diagram for plutonic rocks (Figure 3.2) is useful inasmuch as it is simple and convenient to use. It is important to note, however, that its boundaries are *not the same* as the boundaries of the TAS diagram for volcanic rocks. There are other classification schemes for plutonic rocks which are based on modal mineralogy, but these are not discussed here.

3.2.1.3 Discrimination between the Alkalic and Sub-alkalic Rock Series Using TAS

Igneous rocks can be subdivided into an alkalic or sub-alkalic magma series on the TAS diagram. Using data from Hawaiian basalts, MacDonald and Katsura (1964) were the first to define a boundary separating the alkalic and sub-alkalic (tholeiitic) magma series on a TAS

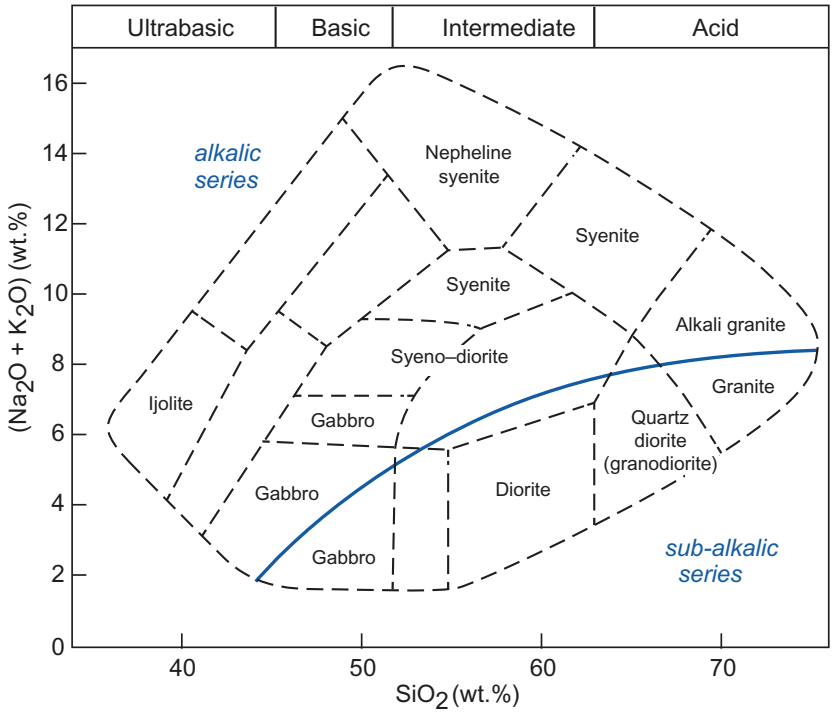

Figure 3.2 The chemical classification and nomenclature of plutonic rocks using the total alkalis versus silica diagram (adapted by Wilson, 1989, from Cox et al., 1979). The curved solid line subdivides the alkalic from the sub-alkalic rock series.

diagram. A later study by MacDonald (1968) expanded the boundary to cover a wider range of SiO_2. Similar diagrams by Kuno (1966) and Irvine and Baragar (1971) place the boundary in slightly different positions on the TAS plot (Figure 3.3). Currently, the boundary curve of Irvine and Baragar (1971) is the most widely used, although the recent reassessment by El-Hinnawi (2016a) indicates that the coordinates of MacDonald and Katsura (1964) provide the best distinction between the alkalic and sub-alkalic series for *basaltic compositions* ($SiO_2 \leq 52$ wt.%). There is less clarity for compositions with a higher SiO_2 content. The boundary coordinates are given in the caption to Figure 3.3.

Alkaline plutonic rocks enriched in magnesium are known as sanukitoids. They were originally defined by Stern et al. (1989) as plutonic rocks containing 55–60 wt.% SiO_2 and with $Mg\# > 0.6$ (see Section 3.3.2). However, it is now known that there are sanukitoid suites which range in composition from pyroxenite to quartz monzonite with SiO_2 between 38 wt.% and 68 wt.% and $Mg\# = 0.49$–0.89. This is illustrated in the study by Lobach-Zhuchenko et al. (2008, figure 4).

3.2.1.4 The K_2O versus SiO_2 Diagram for the Sub-division of the Sub-alkalic Series

Volcanic rocks of the sub-alkalic series may be further subdivided into the calc-alkalic or tholeiitic series on the basis of their K_2O and SiO_2 concentrations (Peccerillo and Taylor, 1976). Le Maitre et al. (1989) proposed a subdivision of sub-alkalic rocks into low-, medium- and high-K types and suggested that these terms be used to qualify the names 'basalt', 'basaltic andesite', 'andesite', 'dacite' and 'rhyolite'. This nomenclature broadly coincides with the low-K (tholeiitic) series, medium-K (calc-alkalic) series and high-K (calc-alkaline) series of Rickwood (1989). A compilation of curves from Rickwood (1989) and Le Maitre et al. (1989) is given in Figure 3.4.

3.2.2 Classifying Igneous Rocks Using Normative Mineralogy

The norm represents a theoretical mineral assemblage which is calculated from a whole rock chemical analysis. In the context of rock classification it provides the basis for a number of mineralogical classification schemes. The calculated normative mineralogy is based entirely upon the chemistry of the rock and its strength lies in the fact that it permits the classification of rocks, such as glassy rocks, for which the determination of the mode is not possible, and allows a direct comparison to be made between such rocks and their crystalline or metamorphosed counterparts. Hence rocks with the

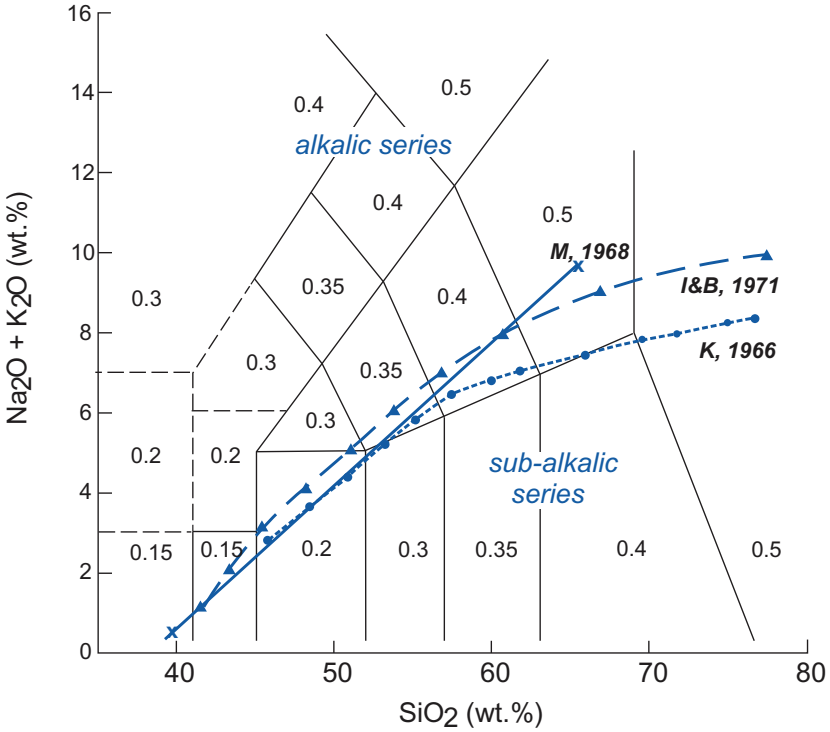

Figure 3.3 The TAS diagram for volcanic rocks showing (i) subdivisions between the alkalic and sub-alkalic magma series and (ii) the Fe_2O_3/FeO ratios for volcanic rock compositions recommended by Middlemost (1989). Note: Boundaries and plotting coordinates (SiO_2, total alkalis) are, respectively, from Kuno (1966 – K, 1966 – filled circles [dotted line 45.85, 2.75; 46.85, 3.0; 50.0, 3.9; 50.3, 4.0; 53.1, 5.0; 55.0, 5.8; 55.6, 6.0; 60.0, 6.8; 61.5, 7.0; 65.0, 7.35; 70.0, 7,85; 71.6, 8.0; 75.0, 8.3; 76.4, 8.4]); MacDonald (1968 – M, 1968 – crosses [solid line 39.8, 0.35 to 65.5, 9.7]) and Irvine and Baragar (1971 – I&B, 1971 – filled triangles [dashed line 39.2, 0.0; 40.0, 0.4; 43.2, 2.0; 45.0, 2.8; 48.0, 4.0; 50.0, 4.75; 53.7, 6.0; 55.0, 6.4; 60.0, 8.0; 65.0, 9.6; 66.4, 10.0]). The data are from the compilation of Rickwood (1989). Note the greater divergence between the boundaries at higher SiO_2.

same chemical composition should result in the same normative mineral assemblage, although it is important to note that the norm calculation is sensitive to the oxidation state of iron (see Section 3.2.2.3).

3.2.2.1 CIPW Norm

There are a number of different approaches to calculating the norm but the CIPW norm, named after its originators – Cross, Iddings, Pirrson and Washington (Cross et al., 1902) – is the most commonly used. The CIPW norm calculation makes a number of simplifying assumptions and follows a prescribed set of rules. A simplified version of the calculation scheme is given in Appendix 3.1. An example of the conversion steps needed to calculate molar proportions necessary to determine the norm is given in Table 3.3. Weight percent oxide values (column 1) are divided by their molecular weights (column 2) to calculate molecular proportions (column 3). The molecular proportions are the basis of the norm calculation given in Appendix 3.1. At the end of the calculation the resulting normative minerals are multiplied by their molecular weight to recast them into wt.% (column 9). The CIPW norm calculation can be carried out in Excel using the programme norm 4 (https://minerva.union.edu/hollochk/c_petrology/other_files/norm_calculation.pdf) or in a variety of open-source computer programs such as NORRRAM (González-Guzmán, 2016, in R) or CIPWFULL (Al-Mishwat, 2015, in FORTRAN). However, it is important to understand the principles which lie behind the norm calculation, and so before using these programs we recommend the manual calculation of a simple CIPW norm.

The CIPW norm is widely used in the classification of basalts (Section 3.2.2.4) and in the classification of granitoids (Section 3.2.2.5). Errors can arise in CIPW norm calculations if volatiles in the rock composition are not correctly allocated and if the

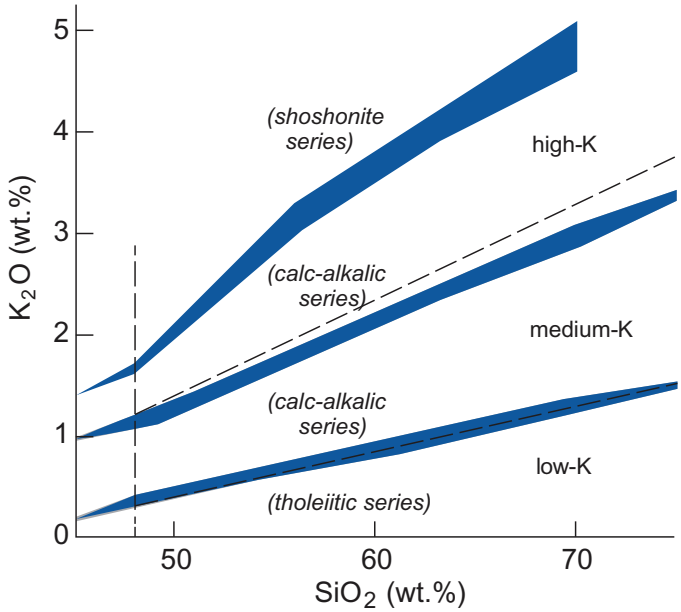

Figure 3.4 The subdivision of alkalic and sub-alkalic rocks using the K_2O versus silica diagram. The diagram shows the subdivisions of Le Maitre et al. (1989) (dashed lines and upper case text) and of Rickwood (1989) (text in parentheses). The shaded regions include the boundaries of Peccerillo and Taylor (1976), Ewart (1982), Innocenti et al. (1982), Carr (1985) and Middlemost (1985) as summarised by Rickwood (1989). The plotting parameters are as follows (SiO_2, K_2O): Le Maitre et al. (1989): (dashed lines) high-K/medium-K boundary 48.0, 1.2; 68.0, 3.1; medium-K/low-K boundary 48.0, 0.3; 68.0, 1.2; vertical boundary at 48 wt.% SiO_2. Rickwood (1989): the band between the shoshonitic series and the high-K series 45.0, 1.38; 48.0, 1.7; 56.0, 3.3; 63.0, 4.2; 70.0, 5.1; and 45.0, 1.37; 48.0, 1.6; 56.0, 2.98; 63.0, 3.87; 70.0, 4.61; the band between the high-K and the calc-alkalic series 45.0, 0.98; 49.0, 1.28; 52.0, 1.5; 63.0, 2.48; 70.0, 3.1; 75.0, 3.43; and 45.0, 0.92; 49.0, 1.1; 52.0, 1.35; 63.0, 2.32; 70.0, 2.86; 75.0, 3.25; the band between the calc-alkalic and the low-K series 45.0, 0.2; 48.0, 0.41; 61.0, 0.97; 70.0, 1.38; 75.0, 1.51; and 45.0, 0.15; 48.0, 0.3; 61.0, 0.8; 70.0, 1.23; 75.0, 1.44.

oxidation state of the iron is incorrectly stated. In addition, some rock types, in particular, cumulate rocks and alkaline rocks with a high CO_2 content, may result in the calculation of an improbable range of accessory mineral phases.

3.2.2.2 The Cation Norm

The *Barth-Niggli* norm, also known as the cation norm or the molecular norm, is an older norm calculation that is no longer widely used. The norm is calculated using the equivalent weights of the oxides, that is, the molecular weight when one cation is present (Barth, 1952). In the case of oxides such as CaO or TiO_2 the equivalent weight is the same as the molecular weight, but for Al_2O_3 or Na_2O the equivalent weight is half the molecular weight. The calculation of a cation norm is illustrated in Table 3.3. In this case the wt.% oxide values (column 1) are divided by their *equivalent* weights (divide by column 2 and multiply by column 4), converted into cation proportions (column 5) and then converted into cation percent (column 7). Molecules are then constructed according to the standard CIPW rules (Appendix 3.1), although the proportions of the components in which cations are allocated are different from the CIPW norm. The cation norm is not recalculated on a wt.% basis, but is expressed in molecular % (column 10). One advantage of the cation norm is that the proportions of opaque minerals are closer to their volume percentages as seen in thin section.

3.2.2.3 Normative Mineralogy and the Oxidation State of Iron

The norm calculation is particularly sensitive to the oxidation state of iron. This is problematic for mafic rocks where the Fe content is typically much higher

Table 3.3 Comparison of CIPW and cation norms for an average tonalite[a]

	1	*2*	*3*	*4*	*5*	*6*	*7*	*8*		*9*	*10*
	Wt.% oxide of rock	*Mol. wt.*	*Mol. proportions*	*Number of cations*	*Cation proportions*	*Millications*	*Cation %*	*Mole %*	*Normative minerals*	*CIPW norm*	*Cation norm*
SiO_2	61.52	60.09	1.0238	1	1.0238	1023.80	58.03	67.86	*Q*	15.94	15.12
TiO^2	0.73	79.9	0.0091	1	0.0091	9.14	0.52	0.61	*Or*	12.23	12.45
Al_2O_3	16.48	101.96	0.1616	2	0.3233	323.26	18.32	10.71	*Ab*	30.71	33.2
Fe_2O_3	1.83	159.69	0.0115	2	0.0229	22.92	1.30	0.76	*An*	22.52	22.98
FeO	3.82	71.85	0.0532	1	0.0532	53.17	3.01	3.52	*Di*	2.17	2.18
MnO	0.08	70.94	0.0011	1	0.0011	1.13	0.06	0.07	*Hy*	10.32	10.47
MgO	2.8	40.3	0.0695	1	0.0695	69.48	3.94	4.61	*Mt*	2.64	1.95
CaO	5.42	56.08	0.0966	1	0.0966	96.65	5.48	6.41	*Il*	1.38	1.04
Na_2O	3.63	61.98	0.0586	2	0.1171	117.13	6.64	3.88	*Ap*	0.56	0.53
K_2O	2.07	94.2	0.0220	2	0.0439	43.95	2.49	1.46			
P_2O_5	0.25	141.95	0.0018	2	0.0035	3.52	0.20	0.12	**TOTAL**	98.47	99.92
TOTAL	98.63				1.7641		100.00	100	*An*	34%	33%
									Ab	47%	48%
									Or	19%	18%

[a] Analysis from Le Maitre (1976).

than in felsic rocks, and can be an issue for felsic rocks since magmatic systems generally become more oxidising as they evolve. Given that Fe is usually reported as either FeO or as Fe_2O_3 it is necessary to estimate the Fe_2O_3/FeO ratio in a given rock. Two approaches have been taken. In volcanic rocks, Middlemost (1989) assigned specific values of Fe_2O_3/FeO to particular rock types in TA-S space (Figure 3.3). El-Hinnawi (2016b), on the other hand, used a database of >12,000 analyses for which Fe was measured as Fe^{2+} and Fe^{3+} to directly calculate the Fe_2O_3/FeO ratio. This study showed that there is a linear relationship between total alkalis (Na_2O + K_2O) and the degree of iron oxidation (Ox_{Fe} = $Fe_2O_3/(Fe_2O_3$ + FeO) in wt.%) in the alkalic and sub-alkalic volcanic rock series (Figure 3.5). The equations are:

For *alkalic* samples,

$$OX_{Fe} = 0.033(Na_2O + K_2O) + 0.163 \quad (3.1)$$

For *sub - alkalic* samples,

$$OX_{Fe} = 0.072(Na_2O + K_2O) + 0.03 \quad (3.2)$$

These results are applicable to the majority of volcanic rock types, although 'transitional' basalts with compositions between the two fields are more difficult to constrain.

Given the widespread use of normative mineralogy in classifying basaltic and granitic rocks and the impact the oxidation state of Fe can have on the normative mineralogy, it is necessary to specify how Fe has been allocated between its two oxidation states when reporting the results of norm calculations.

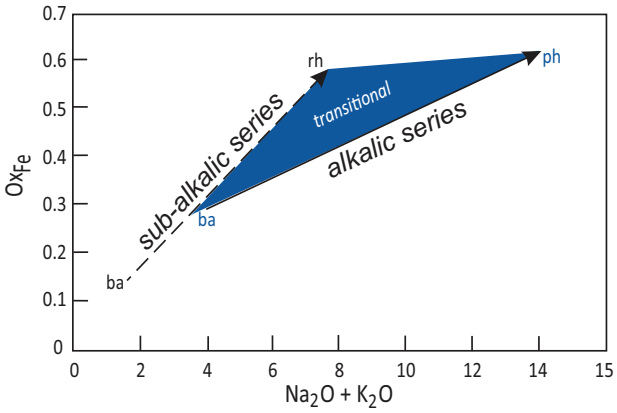

Figure 3.5 Average degree of iron oxidation (Ox_{Fe} = $Fe_2O_3/(Fe_2O_3$ + FeO)) associated with total alkalis of the alkalic and sub-alkalic volcanic rock series (after El-Hinnawi, 2016b). As a magma evolves towards more sialic differentiates, the increase in oxygen fugacity leads to an increase in iron oxidation, resulting in the strong positive correlation for both the alkalic (solid arrow) and sub-alkalic (dashed arrow) series. The arrows indicate direction of evolution from basaltic (ba) to rhyolitic (rh)/phonolitic (ph) compositions. The shaded area indicates region of 'transitional' basalts, which will have intermediate Ox_{Fe}.

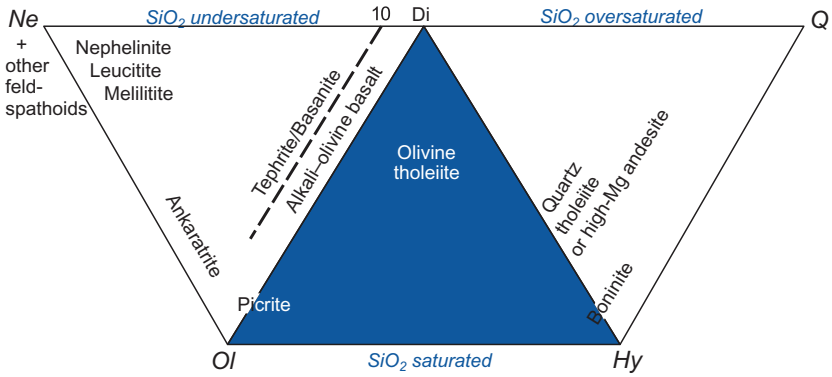

Figure 3.6 The classification of basalts and related rocks based upon their CIPW normative compositions expressed as *Ne–Ol–Di*, *Ol–Di–Hy* or *Di–Hy–Q*. (After Thompson, 1984)

3.2.2.4 Normative Mineralogy and Basalt Classification

Thompson (1984) proposed a classification scheme for basaltic rocks based upon the CIPW normative proportions of *Ne* (and other feldspathoids), *Ol*, *Di*, *Hy* and *Q* (see Appendix 3.1 for abbreviations). This classification diagram (Figure 3.6) is an expanded version of the Yoder-Tilley (1962) low-pressure basalt tetrahedron (Figure 3.22a). The three equilateral triangles of the diagram *Ne–Ol–Di*, *Ol–Di–Hy* and *Di–Hy–Q* represent basaltic and related rocks which are, respectively, undersaturated, saturated and oversaturated with silica (Figure 3.6). Thus silica undersaturated basalts (alkali basalts) are characterised by normative *Ol* and *Ne*, silica saturated basalts (olivine tholeiites) are characterised by normative *Hy* and *Ol*, and silica oversaturated basalts (quartz tholeiites) are characterised by normative *Q* and *Hy*.

Silica saturation is particularly important in basaltic magmas, because in dry magmas this single parameter determines the crystallisation sequence of minerals and evolution of the melt during fractional crystallisation. Weight % normative compositions (calculated assuming $FeO/(FeO + Fe_2O_3) = 0.85$, or $Fe_2O_3/FeO = 0.18$) are projected onto one of the three triangles by summing the three relevant normative parameters and calculating the value of each as a percentage of their sum. The calculation and plotting procedure for triangular diagrams is given in Section 3.3.3. This diagram is intended to be used with basalts which have $MgO > 6$ wt.% and should not be used for highly evolved magmas. Disadvantages of this classification are that it uses only about half of the calculated norm and so is not fully representative of the rock chemistry. It is also sensitive to small errors in Na_2O and so is inappropriate for altered rocks.

3.2.2.5 Normative Mineralogy and Granite Classification

The *Ab–An–Or* normative classification diagram of Barker (1979) modified from O'Connor (1965) provides a convenient way of classifying felsic plutonic rocks on the basis of their major element chemistry (Figure 3.7). The normative calculation provides a more accurate estimate of feldspar compositions than a modal classification, for it reflects solid solution in the feldspars. The *An–Ab–Or* diagram represents a projection from quartz onto the feldspar face of the normative 'granite' tetrahedron *Q–Ab–An–Or*. The diagram can be applied to felsic rocks with more than 10% normative quartz and is based entirely upon the normative feldspar composition recast to 100%. The feldspar compositions in this classification were originally calculated using the Barth-Niggli molecular norm, although it is not clear whether this procedure has been followed by all users. That said, the plotting parameters in the *Ab–An–Or* projection are within 2% of each other from either norm calculation scheme; this is illustrated in Table 3.3 where the *Ab–An–Or* plotting parameters for a tonalite are calculated using both the CIPW and the molecular norm. Field boundaries of the original O'Connor (1965) diagram were empirically defined from a dataset of 125 plutonic rocks for which there was both normative and modal data. Barker's (1979) revised classification has the advantage of field boundaries which are clear and easy to reproduce, and which effectively separate tonalites, trondhjemites, granites and granodiorites from each other. The diagram can

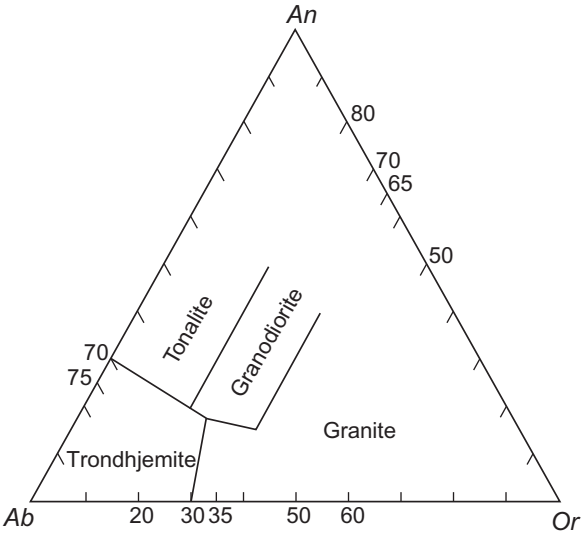

Figure 3.7 The classification of 'granitic' rocks according to their molecular normative *An–Ab–Or* composition after Barker (1979).

also be used (with caution) for deformed and metamorphosed granitic rocks, permitting an estimate of their original magma type.

3.2.3 Classifying Igneous Rocks Using Cations

The conversion of wt.% oxides to cations is calculated in the same way as in the initial stages of the cation norm calculation. The wt.% of the oxide is divided by the equivalent weight of the oxide set to one cation. It is sometimes alternatively expressed as the wt.% oxide divided by the molecular weight of the oxide and multiplied by the number of cations in the formula unit. Thus the wt.% SiO_2 is divided by 60.09. However, the wt.% Al_2O_3 is divided by 101.96 and then multiplied by 2. If millications are needed, then multiply the cationic proportions by 1000. Worked examples are given in columns 5 and 6 of Table 3.3.

3.2.3.1 The Jensen Plot

Jensen (1976) proposed a cation-based classification scheme for sub-alkalic volcanic rocks. It is based upon the cation proportions of $\Sigma(Fe^{2+} + Fe^{3+} + Ti)$, Al and Mg recalculated to 100% and plotted on a triangular diagram (Figure 3.8b). The elements were selected on the basis of their variability in sub-alkalic rocks, for the way in which they vary in inverse proportion to each other and for their stability under low grades of metamorphism. Thus, this classification scheme can be used successfully with metamorphosed volcanic rocks that have experienced mild metasomatic loss of alkalis – an advantage over other classification schemes for volcanic rocks. However, this diagram is important because it shows komatiites and komatiitic basalts as separate fields from those of basalts and calc-alkaline rocks and so is useful for Archean metavolcanic rocks. The original diagram of Jensen (1976) was slightly modified by Jensen and Pyke (1982), who moved the komatiitic basalt/komatiite field boundary to a lower value of Mg, and this is the version presented in Figure 3.8b. The plotting parameters of the field boundaries are taken from Rickwood (1989).

3.2.3.2 The Hanski Plot

The Hanski plot is also useful for distinguishing between high-Mg rocks (Figure 3.8c). The diagram is based upon the molecular proportions of Al_2O_3 and TiO_2 (normalised to unity) and projected from olivine. All the iron is assumed to be ferrous (Hanski et al., 2001). The plotting parameters are as follows:

$$[Al_2O_3] = Al_2O_3/(2/3 - MgO - FeO) \quad (3.3)$$

$$[TiO_2] = TiO_2/(2/3 - MgO - FeO) \quad (3.4)$$

Figure 3.8c distinguishes between komatiites and picrites and between Al- and Ti-enriched/depleted komatiites. It has the advantage that rock or liquid compositions with an olivine-controlled liquid-line-of-descent will have constant $[Al_2O_3]$ and $[TiO_2]$ values, thus a fixed position on the plot. However, the diagram does not distinguish between komatiites and komatiitic basalts.

3.2.3.3 Classification of High-Mg Rocks on the TAS Diagram

Although not a cation plot, it is relevant here to consider the classification of high-Mg rocks within the framework of the TAS diagram. Le Maitre et al. (2002) sought to differentiate between picrites and komatiites and other highly magnesian rocks on the basis of their MgO and TiO_2 content (see the shaded region in Figures 3.1 and 3.8a).

3.2.4 A Combined Major Element Oxide and Cation Classification for Granitoids

We recommend a major element scheme for distinguishing between groups of granitoids. We suggest

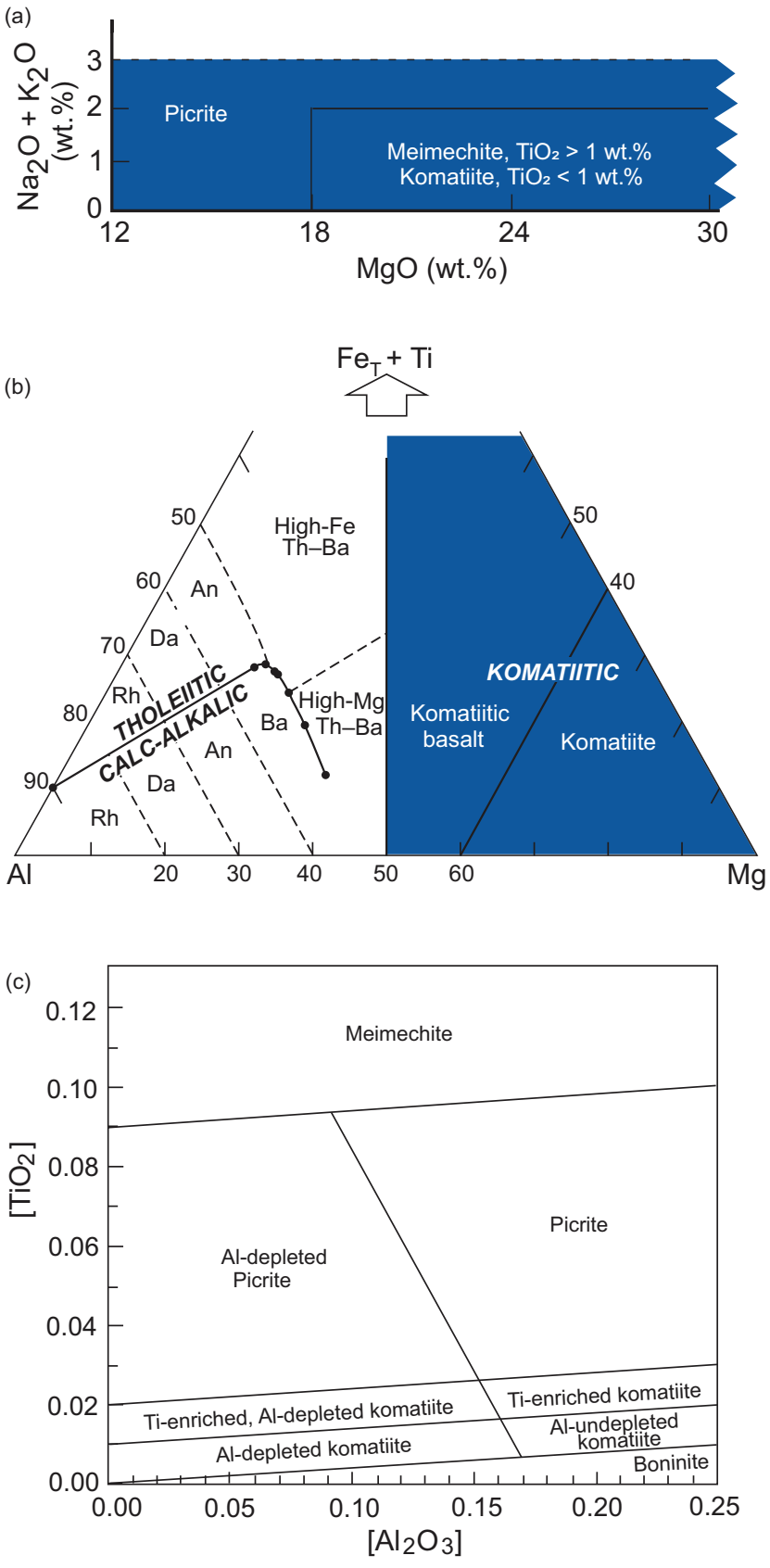

Figure 3.8 The classification of high-Mg volcanic rocks. (a) High-Mg rocks (shaded region in lower left of the TAS diagram in Figure 3.1) are further divided on the basis of their wt.% MgO and TiO_2 (Le Maitre et al., 2002). (b) High-Mg basalts and komatiitic rocks are classified using cation percentages of Al, (Fe[total] + Ti) and Mg. The field boundaries are after Jensen (1976) and Jensen and Pyke (1982) (heavy lines). An, andesite; Ba, basalt; Da, dacite, Rh, rhyolite; Th, tholeiite. The boundary between the tholeiitic and calc-alkalic fields is defined by the coordinates (Al, Fe + Ti, Mg) 90, 10, 0; 53.5, 28.5, 18; 52.5, 29, 18.5; 51.5, 29, 19.5; 50.5, 27.5, 22; 50.3, 25, 24.7; 50.8, 20, 29.2; 51.5, 12.5, 36 (Rickwood, 1989; corrected). (c) High-Mg rocks classified using molecular proportions of Al_2O_3 and TiO_2 normalised to unity using the equation $[Al_2O_3] = Al_2O_3/(2/3 - MgO - FeO)$ and $[TiO_2] = (TiO_2/(2/3 - MgO - FeO)$. (Hanski et al., 2001)

that this is superior to trace element classifications since these can be distorted by the accumulation of accessory mineral phases (Bea, 1996). The scheme proposed here is non-genetic and so lacks any assumption about the origin of the granitoid, thereby avoiding some of the pitfalls of the SIAM-type granite classification of Chappell and White (1974). Further it avoids the less-intuitive approach of the R1-R2 classification proposed by de la Roche et al. (1980).

Instead, we follow the classification scheme of Frost et al. (2001), modified by Frost and Frost (2008). The 'Frost' classification subdivides granitoids on the basis of five indices:

1. an iron index
2. a modified alkali-lime index (after Peacock, 1934)
3. the aluminium saturation index
4. an alkalinity index
5. a feldspathoid saturation index.

These parameters are summarised in Table 3.4, plotted in Figure 3.9 and discussed in more detail below.

The Fe-index separates those rocks enriched in Fe from those that are not and identifies them as ferroan or magnesian (Figure 3.9a). The index is calculated as $FeO^* = [FeO + 0.9\ Fe_2O_3/(FeO + 0.9\ Fe_2O_3 + MgO)]$ (wt.%) and the boundary between ferroan and magnesian rocks fits the equation $[FeO^* = 0.46 + 0.005\ SiO_2]$ (Frost and Frost, 2008).

The modified alkali-lime index (MALI) reflects the wt.% abundance of sodium and potassium relative to calcium using the equation $Na_2O + K_2O - CaO$. When the MALI index is plotted against SiO_2 it distinguishes between alkalic, alkali-calcic, calc-alkalic and calcic compositions (Figure 3.9b). Rocks with more than ~ 60% SiO_2 are controlled by the abundance and composition of feldspars and quartz; at lower SiO_2, the removal of augite during fractionation exerts a dominant control on increasing MALI in the residual magma.

The aluminium saturation index (ASI) is based on molecular Al/(Ca − 1.67P + Na + K) and identifies rocks as metaluminous or peraluminous (after Shand, 1947; Zen, 1988) (Figure 3.9c). Peraluminous varieties (ASI > 1) have more Al than is needed to make feldspars (molecular Na + K < AI), whereas metaluminous varieties (ASI < 1) lack the necessary Al needed to make feldspars (molecular Na + K > AI). Alkaline rocks are deficient in either alumina or silica or both, and contain higher alkalis than can be accommodated in feldspar alone.

The alkalinity index (AI) and the feldspathoid silica-saturation index (FSSI) combine to discriminate between alkaline rocks on the basis of alumina relative to alkalis [AI = molecular Al − (K + Na)] as well as between silica-saturated and undersaturated compositions (Figure 3.9d). The FSSI is based on the molecular norm using the equation $Q - [Lc + 2(Ne + Kp)]/100$.

On the basis of these five indices, it is possible to classify the majority of granitoids.

3.2.5 The Chemical Classification of Sedimentary Rocks

Most sedimentary rock classification schemes use those features that can be observed in hand specimen or thin section. In clastic rocks these are grain size and the mineralogy of the grains and matrix (Milliken, 2014; Garzanti, 2019) and in limestones they are depositional textures (Dunham, 1962) or grain compositions (Folk, 1959).

The chemical composition of clastic rocks is a complex function of the composition of the protolith, mediated by the processes of weathering, transport, diagenesis and depositional environment. For this reason the bulk-rock chemistry of a clastic sediment is more useful in investigating processes such as hydraulic sorting, chemical weathering and the detrital mineralogy of the source than in rock

Table 3.4 Granite classification[a]

Index	*Formula*	*Units*
1. Fe-index	FeO/(FeO+MgO)	Wt.% oxide
2. Modified alkali-lime index (MALI)	$Na_2O + K_2O - CaO$	Wt.% oxide
3. Aluminum-saturation Index (ASI)	Al/(Ca − 1.67P + Na + K)	Molecular
4. Alkalinity index (AI)	Al − (K + Na)	Molecular
5. Feldspathoid silica-saturation Index (FSSI)	$Q - [Lc - 2(Ne + Kp)]/100$	Molecular norm

[a] After Frost et al. (2001) and Frost and Frost (2008).

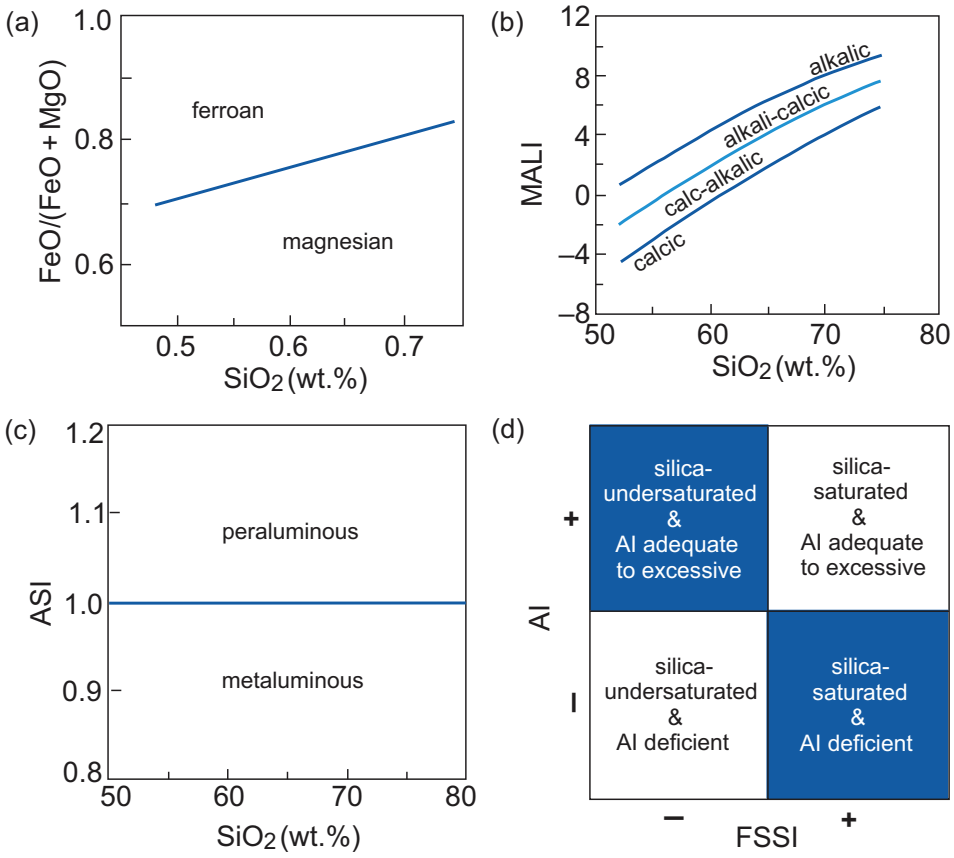

Figure 3.9 Granite classification using major elements (after Frost et al., 2001 and Frost and Frost, 2008). (a) The Fe-index distinguishes magnesian versus ferroan rocks on the basis of total iron in the rock calculated as wt.% Fe-index = FeO + $0.9Fe_2O_3$/(FeO + $0.9Fe_2O_3$ + MgO). This is similar to the 'calc-alkalic' and 'tholeiitic' trends of Miyashiro (1974). The boundary fits the equation FeO* = 0.46 + $0.005SiO_2$. (b) The modified alkali-lime index (MALI) reflects the wt.% relationship of $Na_2O + K_2O - CaO$ relative to SiO_2 and is a function of the crystallising assemblage. This index separates the alkalic, alkali-calcic, calc-alkalic and calcic rocks from one another. (c) The alumina saturation index (ASI) is based on molecular Al/(Ca – 1.67P + Na + K) and defines rocks as metaluminous (ASI < 1) or peraluminous (ASI > 1). (d) The combination of the molecular alkalinity index (AI) and the normative feldspathoid silica-saturation index (FSSI) identifies alkalic rocks, and SiO_2-saturated or under-saturated rocks, respectively. AI = molecular Al/(Ca – 1.67P + Na + K) (after Shand, 1947); FSSI = normative $Q - [Lc + 2(Ne + Kp)]/100$.

classification (Johnsson, 1993; Mangold et al., 2011; Fedo et al., 2015). Nevertheless, there are now abundant, precise elemental data for both coarse- and fine-grained sedimentary rocks, and so, with the above caveats in mind, some applications associated with major element chemistry are presented below.

3.2.5.1 Sandstones

Sandstone geochemistry can be used to distinguish between mature and immature varieties using the relative abundances of quartz, feldspar + clay, and ferromagnesian minerals. Prolonged weathering breaks down ferromagnesian minerals and so depletes the sediment in Ti + Mg + Fe. In a similar way through the breakdown of feldspars and micas the sediment is depleted in K + Na. This gives rise to an increase in residual quartz (SiO_2) and a high level of compositional maturity as illustrated in Figure 3.10a (Roser et al. 1996). Using these same principles for the classification of sandstones and shales, Herron (1988) plotted the parameters log (SiO_2/Al_2O_3) against log (Fe_2O_{3T}/K_2O) (Figure 3.10b). The ratio Fe_2O_{3T}/K_2O is a measure of the stability of ferromagnesian minerals and permits sandstones to be more successfully classified than simply using the K-Na scheme of Pettijohn et al. (1972). Shales are identified on the

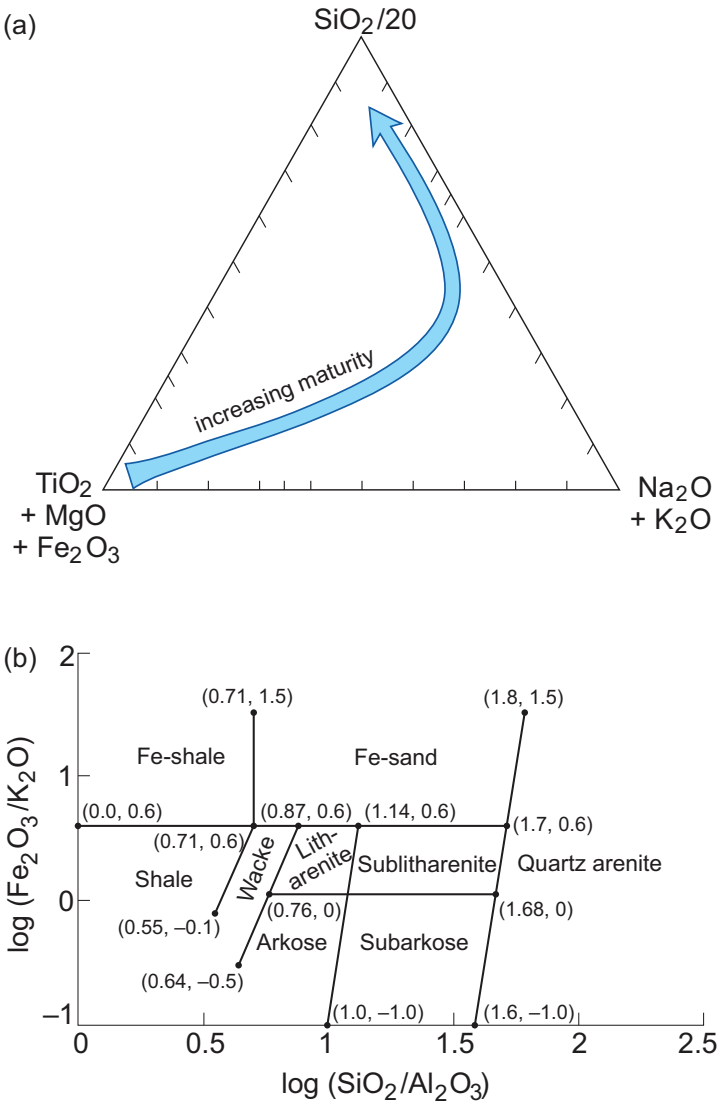

Figure 3.10 Major element classification of sediments. (a) Sandstone maturity as a function of wt.% $SiO_2/20$, $K_2O + Na_2O$, and $TiO_2 + MgO + Fe_2O_3$ (after Kroonenberg, 1990). The mature sandstones are nearest the SiO_2 apex. (b) Terrigenous sandstones and shales in a log (Fe_2O_3/K_2O) versus log (SiO_2/Al_2O_3) plot (after Herron, 1988). The numbers shown in parentheses are the plotting coordinates for the field boundaries expressed as [log (SiO_2/Al_2O_3), log (Fe_2O_3/K_2O)].

basis of their low SiO_2/Al_2O_3. A further advantage of the Herron classification is that it can be used to identify shales, sandstones, arkoses and carbonate rocks in situ from geochemical well logs using neutron activation and gamma-ray tools (Herron and Herron, 1990). However, sediment classification diagrams based on major elements must be applied with caution as Na and K can be easily mobilised during diagenesis and metamorphism. The degree of chemical alteration can be evaluated using the alteration parameters listed in Table 3.5 and is discussed further in Section 3.3.

3.2.5.2 Mudrocks

There is no widely recognised major element chemical classification of mudrocks. This is surprising given that they have a more variable chemistry than sandstones. Whole-rock major element data are typically presented normalized to a reference composition such as the Post-Archean Australian Shale (PAAS) of Taylor and McLennan (1985). The index of compositional variability (ICV) ($[Fe_2O_3 + K_2O + Na_2O + CaO + MgO + MnO + TiO_2]/Al_2O_3$) has also been used to indicate increasing or decreasing proportions of clay minerals on the basis that clay minerals have greater amounts of alumina (Cox et al., 1995). More recently Fazio et al. (2019) used Na_2O versus SiO_2 and Na_2O versus Al_2O_3 (wt.%) to distinguish between varieties of mudrock.

3.2.5.3 Limestones

Most carbonate rocks are dominated by calcite, dolomite and their ferroan equivalents and contain only a

Table 3.5 Common major element indices associated with alteration of sedimentary rocks

Index	*Units*	*Reference*
Index of compositional variability (ICV) $[Fe_2O_3 + K_2O + Na_2O + CaO + MgO + MnO + TiO_2]/Al_2O_3$	Wt.% oxide	Cox et al. (1995)
Plagioclase index of alteration (PIA) $[(Al_2O_3 - K_2O)/(Al_2O_3 + CaO + Na_2O - K_2O)] \times 100$	Wt.% oxide	Fedo et al. (1995)
Chemical index of weathering (CIW) $[Al_2O_3/(Al_2O_3 + CaO + Na_2O)] \times 100$	Wt.% oxide	Harnois (1988)
Chemical index of weathering without CaO (CIW′) $Al_2O_3/(Al_2O_3 + Na_2O)$	Wt.% oxide	Cullers (2000)
Chemical index of alteration (CIA) $[Al_2O_3/(Al_2O_3 + CaO^* + Na_2O + K_2O)] \times 100$	Molar	Nesbitt and Young (1982)
Chemical proxy of alteration (CPA) $100 \times [Al_2O_3/(Al_2O_3 + Na_2O)]$	Molecular norm	Buggle et al. (2011)

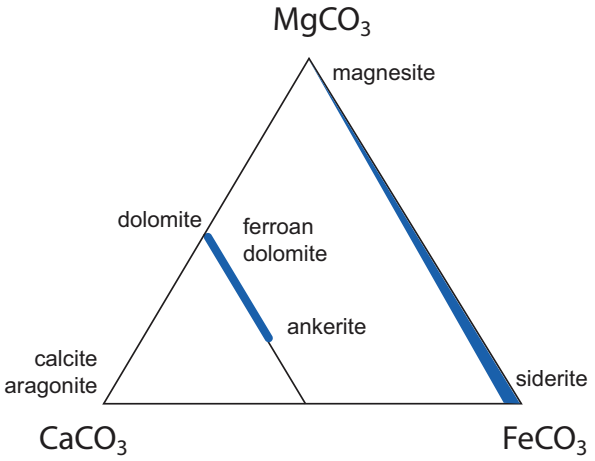

Figure 3.11 Carbonate rock classification. Carbonate minerals stable at sub-greenschist (<250°C) conditions (data from Anovitz and Essene, 1987). Ca, Mg and Fe provide the dominant major element components. Shaded areas signify solid-solution.

limited amount of other constituents. Consequently, their major element chemistry is dominated by Ca, Mg and Fe (Figure 3.11). Limestones and marbles can be classified on the basis of their relative $CaCO_3$ and $MgCO_3$ content and divided into two main categories: magnesite (≥50% $MgCO_3$) and calcite-dolomite [$CaCO_3$–(Ca, Mg)CO_3]. The calcite-dolomite group can be further subdivided into six categories on the basis of their purity (Carr and Rooney, 1983).

Future developments in this field include the use of chemostratigraphy on carbonate cores using a hand-held XRF. Yarbrough et al. (2019) used major element analyses to better characterise the Upper Jurassic reservoir facies of the carbonate Smackover Formation, Alabama, and found that the elements Al, Si, Ca, Ti and Fe were significant (>95% confidence level) predictors of porosity.

3.2.6 Discussion

It can be seen from the above that there is no simple major element chemical classification scheme for all igneous rocks or for all sediments. The most effective classification is for fresh volcanic igneous rocks using the TAS diagram. Plutonic rocks are more complicated, although for granitic rocks the normative An-Or-Ab diagram is a good place to start, followed by the use of major element oxide diagrams (Section 3.2.4) to recognize distinct chemical groups of granitoids. There is no simple, uniformly applicable classification scheme for sedimentary rocks based on their major element compositions, although in the future a more complex statistical evaluation of major element compositions using multivariate analysis is likely to provide better insight to sediment genesis (Mongelli et al., 2006; Hofer et al., 2013).

3.3 Variation Diagrams

A table of geochemical data from a particular igneous province, metamorphic terrain or sedimentary succession may at first sight show an almost incomprehensible

variation in the concentration of individual elements. Given that the samples are likely to be geologically related, a major task for the geochemist is to devise a way in which the variation between individual rocks may be simplified and condensed so that relationships between the individual samples may be identified. The device which is most commonly used and has proved invaluable in the examination of geochemical data is the variation diagram. This is a bivariate graph on which two selected variables are plotted. Diagrams of this type were popularised as long ago as 1909 by Alfred Harker in his *Natural History of Igneous Rocks*, and one particular type of variation diagram, in which SiO_2 is plotted along the *x*-axis, is known as the Harker diagram.

An illustration of the usefulness of variation diagrams can be seen from a comparison of the data in Table 3.6 and the variation diagrams plotted for the same data (Figure 3.12). It is clear that the variation diagrams have condensed and rationalised a large amount of numerical information and show qualitatively that there is an excellent correlation (either positive or negative) between each of the major elements displayed and SiO_2. Traditionally, this strong geochemical coherence between the major elements in a related suite of rock, in this case basalts from a single volcano, has been used to suggest that there is an underlying process which can explain the relationships between the major elements. Nonetheless, from the discussion in Chapter 2 on closure and the problems associated with applying univariate statistics to multivariate data, caution is needed, and such correlations should always be rigorously tested.

3.3.1 Recognising Geochemical Processes on a Major Element Variation Diagram

Most trends on variation diagrams are the result of *mixing*. In igneous rocks the mixing may be between two magmas, because of the addition and/or subtraction of solid phases during contamination or fractional crystallisation, or due to the addition of melt increments during partial melting. In sedimentary rocks trends on a variation diagram will also result from mixing, but in this case it is the mixing of chemically distinct components that defines the composition of the sediment. In metamorphic rocks trends on a variation diagram will usually reflect the processes in the igneous or sedimentary protolith, masked to some degree by specific metamorphic processes such as *metasomatism*, the chemical alteration of a rock by non-deuteric fluids. In some instances, however, deformation can mechanically mix more than one rock type, giving rise to a mixing line of metamorphic origin. Below we consider some of the more important mixing processes.

3.3.1.1 Fractional Crystallisation

Fractional crystallisation is a major process in the evolution of many igneous rocks and is frequently the cause of trends seen on their variation diagrams. The fractionating mineral assemblage is normally indicated by the phenocrysts present. A test of crystal fractionation may be made by accurately determining the composition of the phenocrysts using an electron microprobe and then plotting the compositions on the same graph as the rock analyses. If trends on a variation diagram are controlled by phenocryst compositions, it may be possible to infer that the rock chemistry is controlled by crystal fractionation. It should be noted, however, that (1) fractional crystallisation may take place at depth in which case the fractionating phases may not be represented in the lower pressure and temperature phenocryst assemblage and, as discussed below, that (2) mineralogical control can also be exercised by partial melting processes.

The importance of fractional crystallisation was expounded at length by Bowen (1928) in his book *The Evolution of the Igneous Rocks* and who argued that geochemical trends for volcanic rocks represent a '*liquid line of descent*'. This is the path taken by residual liquids as they evolve through the differential withdrawal of minerals from the magma. The ideas of Bowen now need to be qualified in the context of modern findings in the following ways:

1. Trends identical to those produced by crystal fractionation can also be produced by partial melting.
2. Only phenocryst-poor or aphyric volcanic rocks will give a true indication of the liquid path.
3. Rarely does a suite of volcanic rocks showing a progressive chemical change erupt in a time sequence. Even a highly correlated trend on a variation diagram of phenocryst-free volcanic rocks from a single volcano is unlikely to represent a liquid line of descent. Rather, it represents an approximation of the liquid line of descent of similar, overlapping, sub-parallel lines of descent.

Table 3.6 Chemical analyses of rocks from Kīlauea Iki lava lake, Hawai'i[a]

	1	2	3	4	5	6	7	8	9	10	11	12	13	14	15	16	17
SiO_2	48.29	48.83	45.61	45.50	49.27	46.53	48.12	47.93	46.96	49.16	48.41	47.90	48.45	48.98	48.74	49.61	49.20
TiO_2	2.33	2.47	1.70	1.54	3.30	1.99	2.34	2.32	2.01	2.73	2.47	2.24	2.35	2.48	2.44	3.03	2.50
Al_2O_3	11.48	12.38	8.33	8.17	12.10	9.49	11.43	11.18	9.90	12.54	11.80	11.17	11.64	12.05	11.60	12.91	12.32
Fe_2O_3	1.59	2.15	2.12	1.60	1.77	2.16	2.26	2.46	2.13	1.83	2.81	2.41	1.04	1.39	1.38	1.60	1.26
FeO	10.03	9.41	10.02	10.44	9.89	9.79	9.46	9.36	9.72	10.02	8.91	9.36	10.37	10.17	10.18	9.68	10.13
MnO	0.18	0.17	0.17	0.17	0.17	0.18	0.18	0.18	0.18	0.18	0.18	0.18	0.18	0.18	0.18	0.17	0.18
MgO	13.58	11.08	23.06	23.87	10.46	19.28	13.65	14.33	18.31	10.05	12.52	14.64	13.23	11.18	12.35	8.84	10.51
CaO	9.85	10.64	6.98	6.79	9.65	8.18	9.87	9.64	8.58	10.55	10.18	9.58	10.13	10.83	10.45	10.96	11.05
Na_2O	1.90	2.02	1.33	1.28	2.25	1.54	1.89	1.86	1.58	2.09	1.93	1.82	1.89	1.73	1.67	2.24	2.02
K_2O	0.44	0.47	0.32	0.31	0.65	0.38	0.46	0.45	0.37	0.56	0.48	0.41	0.45	0.80	0.79	0.55	0.48
P_2O_5	0.23	0.24	0.16	0.15	0.30	0.18	0.22	0.21	0.19	0.26	0.23	0.21	0.23	0.24	0.23	0.27	0.23
H_2O+	0.05	0.00	0.00	0.00	0.00	0.08	0.03	0.01	0.00	0.06	0.08	0.00	0.09	0.02	0.04	0.02	0.04
H_2O-	0.05	0.03	0.04	0.04	0.03	0.04	0.05	0.04	0.00	0.02	0.02	0.02	0.00	0.00	0.01	0.01	0.02
CO_2	0.01	0.00	0.00	0.00	0.00	0.11	0.04	0.02	0.00	0.00	0.00	0.01	0.00	0.01	0.01	0.01	0.01
TOTAL	100.01	99.89	99.84	99.86	99.84	99.93	100.00	99.99	99.93	100.05	100.02	99.95	100.05	100.06	100.07	99.90	99.95

[a] Data from Richter and Moore (1966), courtesy of the U.S. Geological Survey.

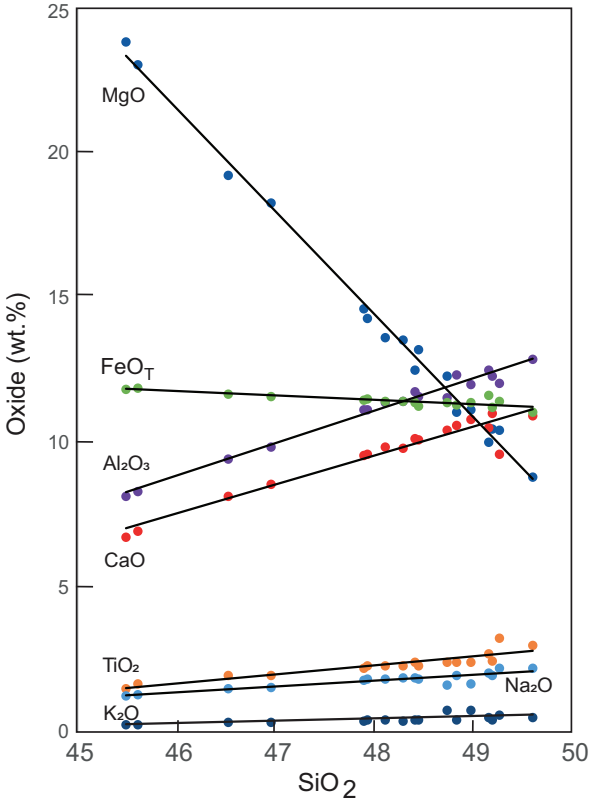

Figure 3.12 Bivariate plots of major element oxides versus SiO_2. The data represent basaltic lavas from the lava lake Kīlauea Iki associated with the 1959–1960 volcanic eruption of Kīlauea, Hawai'i (from Richter and Moore, 1966). A linear trend is fitted for each of the oxides. The data are given in Table 3.6.

As an example, the variation in composition of olivine-rich basalts from the lava lake Kīlauea Iki, Hawai'i (Table 3.6), are presented as bivariate plots (Figure 3.12). This variation is thought to be the product of fractional crystallisation which was 'controlled principally by the physical addition or removal of olivine phenocrysts' (Richter and Moore, 1966). A detailed comparison with olivine compositions indicates that other phases were also involved in crystal fractionation but that olivine was the major control.

3.3.1.2 Assimilation and Fractional Crystallisation

If phenocryst compositions cannot explain trends in a rock series and a fractional crystallisation model does not appear to work, it is instructive to consider the possibility of simultaneous processes such as assimilation of the country rock combined with fractional crystallisation. Assimilation plus fractional crystallisation, often abbreviated AFC, was first proposed by Bowen (1928), who argued that the latent heat of crystallisation during fractional crystallisation can provide sufficient thermal energy to consume the wall rock. Consequently, hot magmas undergoing fractional crystallisation assimilate cool crust as a consequence of heat transfer from the magma to the crust.

Kuritani et al. (2005) illustrate this process for an alkali basalt-dacite suite from the magma chamber of the Rishiri volcano in northern Japan. They show that major element variations in the lava suite can be explained by mixing of a magma in the main magma body with a melt transported from a mushy boundary layer in the partially fused floor of the magma chamber. A slightly different example comes from mantle petrology where very high temperature melts have the capacity to react with the rock through which they are transiting, in particular, when the two are out of equilibrium. A well-studied example is the reaction between MORB melts and highly depleted harzburgitic mantle. This reaction consumes orthopyroxene and precipitates olivine, leading to dunite channels in the harzburgite which indicate the route followed by the migrating melt (e.g., Kelemen, 1990 and Kelemen et al., 1995).

It has been proposed that AFC processes can result in the 'decoupling' of the major element chemistry from that of the trace elements and/or isotopes and so may not always be evident in the major element data. For example, the contamination of a basalt precipitating olivine, clinopyroxene and plagioclase will result in increased precipitation of the fractionating minerals but may cause only a minor change in the silica content of the liquid. Trace element levels and isotope ratios, however, might be changed and provide a better means of recognising assimilation.

3.3.1.3 Partial Melting

Progressive fractional melting will show a trend on a variation diagram which is controlled by the chemistry of the solid phases being added to the melt. However, this can be very difficult to distinguish from a fractional crystallisation trend on a major element variation diagram, for both processes represent crystal–liquid equilibria involving almost identical liquids and identical minerals. One way in which progressive partial melting and fractional crystallisation

may be distinguished using major elements is if the two processes take place under different physical conditions. For example, if partial melting takes place at great depth in the mantle and fractional crystallisation is a crustal phenomenon, then some of the phases involved in partial melting will be different from those involved in fractional crystallisation. Trace elements (discussed in Chapter 4) provide additional means of discriminating between these two processes.

3.3.1.4 Mixing Lines in Sedimentary Rocks

Trends on variation diagrams for sedimentary rocks may result from the mixing of the different components which constitute the sediment. There are a number of examples of this effect in the literature. Bhatia (1983) in a study of turbidite sandstones from eastern Australia presented bivariate plots (Figure 3.13) in which there is a change in the mineralogical maturity, as evidenced by an increase in quartz (SiO_2) coupled with a decrease in the proportions of lithic fragments and feldspar represented by the other oxides.

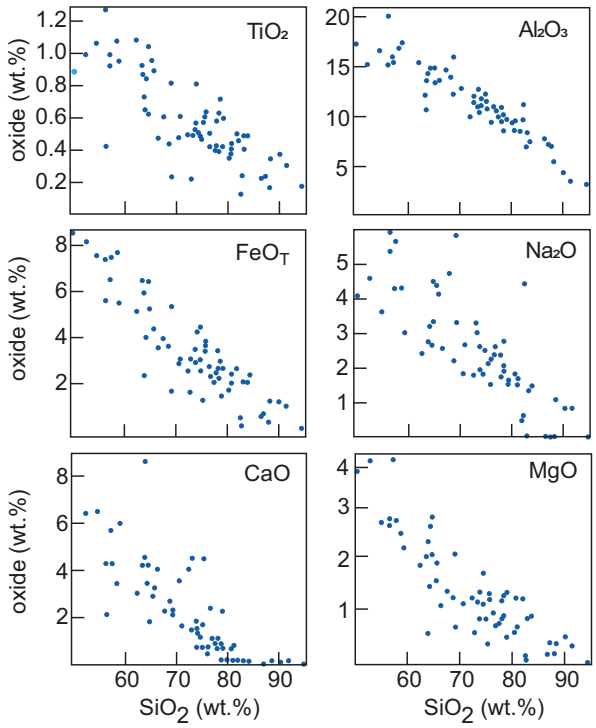

Figure 3.13 Bivariate plots for quartz-rich sandstone suites from eastern Australia (after Bhatia, 1983). The increase in SiO_2 reflects an increased mineralogical maturity, that is, a greater quartz content and a smaller proportion of other detrital minerals.

3.3.1.5 The Identification of Former Weathering Conditions in Sedimentary Rocks

A good measure of the degree of chemical weathering can be obtained from the chemical index of alteration (CIA; Nesbitt and Young, 1982):

$$CIA = Al_2O_3/(Al_2O_3 + CaO^* + Na_2O + K_2O) \quad (3.5)$$

Concentrations are expressed as molar values and CaO* is CaO in silicate phases only. The index was originally devised to reconstruct palaeoclimatic conditions from early Proterozoic sediments in northern Canada but has subsequently been used as a proxy to quantify the intensity of chemical weathering in drainage basins (Shao et al., 2012).

An extension of the CIA index is the $(CaO^* + Na_2O)$–Al_2O_3–K_2O triangular plot (Nesbitt and Young (1984, 1989). On a diagram of this type the initial stages of weathering form a trend parallel to the tie between $(CaO^* + Na_2O)$ and Al_2O_3 of the diagram, whereas advanced weathering shows a marked loss in K_2O as compositions move towards the Al_2O_3 apex (Figure 3.14a). The trends follow mixing lines representing the removal of alkalis and in solution the breakdown of first plagioclase and then potassium feldspar and finally the ferromagnesian silicates. Deviations from such trends can be used to infer chemical changes resulting from diagenesis or metasomatism (Nesbitt and Young, 1984, 1989). This approach has also been applied to mudstones, and the major and trace element chemistry of ancient and modern muds can be used to determine the degree of weathering in their source (Nesbitt et al., 1990).

Nesbitt and Young (1996) also proposed an A–CNK–FM diagram which uses the molar proportions of Al_2O_3–$(CaO + Na_2O + K_2O)$–$(FeO_T + MgO)$ to show those chemical changes in sediments which are a function of grain size. It also demonstrates an increase in the ferromagnesian component with decreasing grain size (Figure 3.14b).

3.3.1.6 Artificial Trends

Sometimes trends on variation diagrams are artificially produced by the numerical processes used in plotting the data rather than reflecting geochemical relationships. This is well documented by Chayes (1960) and Aitchison (1986), who have shown that correlations in compositional data can be forced as a result of the unit sum constraint (see Section 2.2).

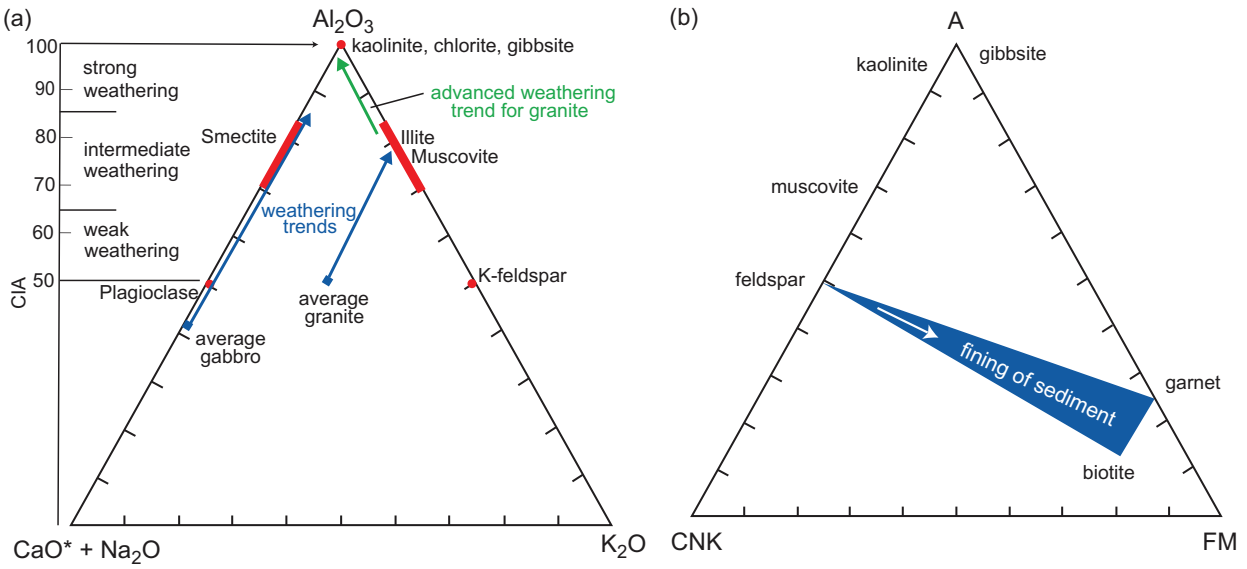

Figure 3.14 Weathering effects. (a) The $(CaO + Na_2O)$–Al_2O_3–K_2O diagram showing weathering intensity and the weathering trends for an average granite and an average gabbro (after Nesbitt and Young, 1984, 1989; Shao et al., 2012). The advanced weathering trend for granite is also shown. Compositions are plotted as molar proportions. CaO* represents the CaO associated with the silicate fraction of the sample. (b) The A (Al_2O_3), CNK ($CaO + Na_2O + K_2O$), FM ($FeO_T + MgO$) molar proportions diagram showing chemical change with sediment grain size. (Nesbitt and Young, 1996)

The most helpful way to circumvent this problem is to examine trends on variation diagrams in the light of a *specific hypothesis to be tested*. The closeness of fit between the model and the data can then be used to evaluate the hypothesis.

3.3.2 Selecting a Variation Diagram

Two main types of variation diagrams – bivariate plots and ternary diagrams – are widely used by geochemists and are considered here.

3.3.2.1 Bivariate Plots

The principal aim of a bivariate plot, such as that illustrated in Figure 3.12, is to show variation between samples and to identify trends. Hence the element plotted along the *x*-axis of the diagram should be selected either to show the maximum variability between samples or to illustrate a particular geochemical process. Normally, the oxide which shows the greatest range in the dataset would be selected – in many cases this would be SiO_2, but with basic igneous rocks it could be MgO and in clay-bearing sediments Al_2O_3. The initial stage of a geochemical investigation often requires the preparation of a large number of diagrams in order to delimit the possible geological processes operating. In such cases the initial screening of the data is best done using a correlation matrix (see Section 2.4.5) to explore for strong correlations. However, it is important to remember that meaningless correlations can arise through a cluster of data points and a single outlier. Similarly, poor correlations can arise if the dataset contains multiple populations, each with a different trend. More normally, and more fruitfully, most geochemical investigations are designed to solve a specific problem and to test a particular hypothesis – usually formulated from geological or other geochemical data. In this case the plotting parameter for a variation diagram should be selected with the process to be tested in mind. For example, in the case of an igneous rock suite for which a crystal fractionation mechanism is envisaged, then an element should be selected which is contained in the fractionating phase and that will be enriched or depleted in the melt.

(a) *Bivariate plots using SiO_2 as the x-axis.* These are the oldest form of variation diagram and are one of the most frequently used means of displaying major element data (see Figures 3.12 and 3.13). SiO_2 is commonly chosen as the plotting parameter for many igneous rock series and for suites of sedimentary rocks with a variable quartz content

because it is the major constituent of the rock and shows greater variability than any of the other oxides. However, the very fact that SiO_2 is the most abundant oxide can sometimes lead to spurious correlations, as discussed in Section 3.3.2.2.

(b) *Bivariate plots which use MgO as the x-axis.* Another common bivariate diagram uses MgO on the *x*-axis instead of SiO_2. This is most appropriate for mafic and ultramafic suites in which the range of SiO_2 concentration may be small. MgO, on the other hand, is an important component of the solid phases in equilibrium with mafic melts, such as olivine and the pyroxenes, and shows a great deal of variation due either to the breakdown of magnesian phases during partial melting or to their removal during fractional crystallisation. Figure 3.15 shows an olivine-controlled fractionation trend in komatiites from the Belingwe greenstone belt in Zimbabwe (data from Bickle et al., 1993). *Mg#* (for definition, see subsection (e) below) is sometimes substituted for MgO, but the underlying principle is the same – to use the component with the greatest spread.

(c) *Bivariate plots using cations.* It is sometimes simpler to display mineral compositions on a variation diagram if major element chemical data are plotted as cation %, that is, the wt.% oxide value divided by the molecular weight and multiplied by the number of cations in the oxide formula and then recast to 100% (see Section 3.2.2 and Table 3.3). Alternatively, the results may be expressed as mol %, that is, the wt.% oxide values divided by the molecular weight and recast to 100% (see Section 3.2.2 and Table 3.3).

(d) *Elemental weight ratio plots.* The Al/Si versus Mg/Si diagram is used to show differences in the composition of meteoritic materials and identify the processes operating during the differentiation of the Earth's mantle. These elements are chosen because they represent the more refractory elements formed during the condensation of the solar nebula, and the ratio plot represents the relative fractionation of the different planetary materials. The plotting parameters are calculated by reducing the oxide wt.% of each of the components to their elemental wt.% concentrations; that is, multiply Al_2O_3 by 0.529, SiO_2 by 0.467, and MgO by 0.603. In Figure 3.16 trends for mantle peridotites and meteorites are plotted together with the field for the likely chondritic material parental to the Earth and the primitive mantle compositions from Table 3.2.

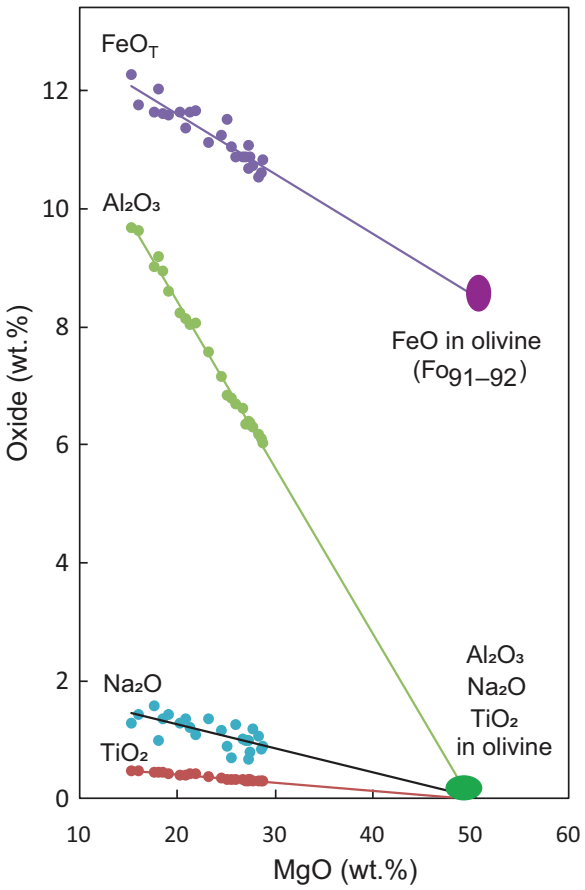

Figure 3.15 Oxides versus MgO variation for komatiites from the Archaean Belingwe greenstone belt in Zimbabwe (data from Bickle et al., 1993). The extended lines show that the fractionation trend is principally controlled by olivine with the composition $Fo_{91–92}$. The slight scatter in the Na_2O trend probably indicates a small amount of element mobility.

(e) *Bivariate plots using the magnesium number (Mg#).* The older geochemical literature carries a large number of examples of complex, multi-element plotting parameters which were used as a measure of fractionation during the evolution of an igneous sequence. These are rather complicated to use and difficult to interpret, and have fallen into disuse. One which is usefuland so survives, however, is based on the magnesium–iron ratio, the so-called magnesium number. The magnesium–iron ratio is particularly useful as an index of crystal fractionation in basaltic liquids for here the Mg-Fe ratio changes markedly in the early stages

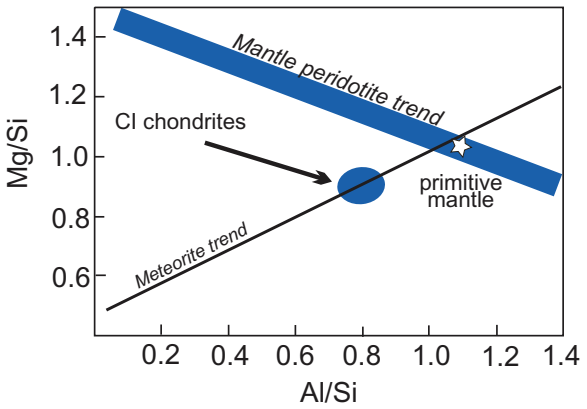

Figure 3.16 Differentiation of planetary materials. Elemental Al/Si versus Mg/Si plot showing the meteorite and peridotitic mantle trends relative to CI chondrites and the composition of the Earth's primitive mantle. (Adapted from Rollinson, 2007; with permission from John Wiley & Sons)

of crystallisation as a result of the higher Mg-Fe ratio of the liquidus ferromagnesian minerals than that of their host melts. The *Mg#* has been variously defined as follows: MgO/(MgO + FeO + Fe_2O_3), 100 Mg/(Mg + Fe^{2+}), (Mg/Mg + Fe_{tot}), and presented either by weight or atomic proportions. We define the *Mg#* as 100 × Mg^{2+}/(Mg^{2+} + $Fe^{2+}{}_{tot}$) calculated in atomic proportions. To calculate the *Mg#* divide the wt.% oxide values for MgO and FeO_T (recalculated as Fe^{2+}) by their respective molecular weights of 40.3 and 71.8. Whenever the term *Mg#* is used, the formula used should be specified.

3.3.2.2 Compositional Data and Bivariate Diagrams

Statisticians have been warning geochemists about their inappropriate treatment of compositional data for several decades (Section 2.2.2.1). This criticism is typified in the comment on bivariate diagrams by Aitchison and Egozcue (2005), who state that Harker diagrams are 'best condemned as misleading and best left out of any attempts to interpret compositional variability'. A similar sentiment is put more mildly by Buccianti and Grunsky (2014): 'Compositional data analysis in geochemistry: Are we sure to see what really occurs during natural processes?' This ongoing challenge to the time-honoured treatment of compositional data, and in particular, its representation on bivariate plots, presents the geochemical community with a dilemma, but experience seems to suggest that the challenge from the statistical community is misplaced for several reasons:

1. Bivariate diagrams seem to work and yield geologically meaningful results.
2. There is little evidence from the application of the log-ratio approach, the recommended alternative (Section 2.7.1), that this methodology provides a deeper or superior understanding of geochemical and petrological processes as displayed in bivariate plots. This may in part reflect its dominant application to the compositional analysis of soils, volcanic gases and water chemistry (see Buccianti et al., 2006), rather than the geochemical data associated with geochemistry and petrology.
3. Making geological sense of log-ratios is not practicable. In 1989, Rock pointed out in response to Aitchison that 'abstract log ratio variables (as proposed by the Aitchison log-ratio technique) ... cannot easily be related to physical measurements'.

3.3.2.3 So Why Do Bivariate Plots Appear to Work?

An essential element missing from the debate between statisticians and geochemists over the use and misuse of bivariate diagrams is an appreciation of the geological context. When a suite of samples is collected to test a particular hypothesis or to investigate a particular process, the data are set in a particular context which in turn places constraints on the interpretation of the data. In other words – and this is a theme which will recur throughout this text – geological field control is essential for the meaningful interpretation of geochemical data.

Cortés (2009) takes issue with the criticism of bivariate diagrams by Aitchison and Egozcue (2005) and argues that bivariate diagrams 'are not a correlation tool but [rather] a graphical representation of the mass actions and mass balances in the context of a geological system'. They serve as a simple display of evolutionary trends which are thought to represent a process or set of processes; the trends observed, 'spurious or not, are given by the law of mass action'. Hence the expectation is not to discover the covariance structure associated with these trends, but rather to interpret them within a

geological context, and where trends are observed these may be used as robust evidence of the link between samples. He further argues that trends on bivariate diagrams can be used quantitatively to calculate the proportion of species involved in a particular geological process. For example, he suggests that a suite of basalts from a particular lava flow might be collected because they are expected to be chemically related. If, in addition, there is field evidence to suggest that these basalts have experienced a common process such as olivine fractionation, then there is a testable hypothesis as to the nature of their relationship. Thus, Cortés (2009), following Rollinson (1992), cites the major element oxide data for samples from the Kīlauea Iki lava lake (Table 3.6, Figure 3.12) which show near perfect, but allegedly spurious, correlations. In line with the geological context, however, the trends confirm a common magmatic origin – the working hypothesis behind the data collection. Further, in the context of mass balance, the variation between samples can be shown to be consistent with olivine addition and removal, again the working hypothesis set by the geological context.

We support the logic of Cortés (2009) and argue that given a geological context, bivariate plots can be an important exploratory tool for the visualisation of geochemical data, a point which is also acknowledged by Egozcue (2009) in his response to Cortés's (2009) critique. Thus, a suite of bivariate plots for a single dataset remains a powerful tool for understanding geological processes. This conclusion is entirely consistent with the view of log-ratios expressed by Rock (1989). Geochemists work with rock compositions in which, for the most part, variation is controlled by minerals with fixed stoichiometries and together these data must be interpreted within the geological context in which the samples were found.

The preceding discussion argues that compositional data analysis may tell us that the correlation coefficient computed for a particular trend is not meaningful and that the correlation is spurious; nevertheless, the trend may be real and have geological meaning. In the case of bivariate major element plots, it is not the value of the correlation coefficient that is important; rather, it is the presence and shape (linear, curvilinear or kinked) of the trends that are significant. These are the properties that need to be interpreted.

3.3.3 Ternary Diagrams

Ternary diagrams, also known as triangular or trivariate diagrams or plots, are used when it is necessary to show simultaneous change between three variables. There are statistical problems associated with the plotting of data on ternary diagrams (Section 2.9) and they must be used with care. The plotting procedure for ternary diagrams is described in Figure 3.17. This can be carried out using an Excel macro that projects orthogonal coordinates onto triangular geometry. These include the free online 'Triangular Graph Constructor', 'Ternary Plot Generator', or TRIPLOT (Graham and Midgley, 2000).

3.3.3.1 The AFM Diagram

The igneous AFM diagram (not to be confused with the metamorphic diagram of the same name) is used to distinguish between the tholeiitic and calc-alkaline

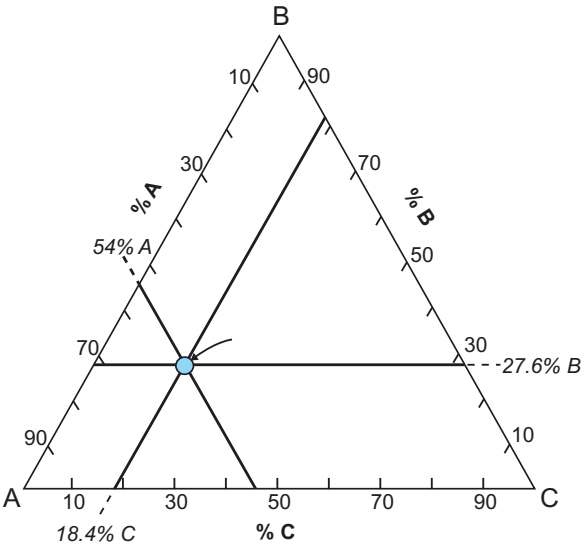

Figure 3.17 The plotting procedure for triangular diagrams. To plot a single point for the variables A = 54%, B = 27.6% and C = 18.4% on a triangular diagram, follow this procedure. Variable B is 100% at the top of the plotting triangle and 0% along the base of the triangle. Counting upwards from the base (the concentrations are given on the right-hand side of the triangle), draw the horizontal line representing 27.6%. In a similar way draw the line representing A = 54% parallel to the right side of the triangle. The point at which the two lines intersect is the plotting position. To check that it has been accurately located, the line for variable C at 18.4% should pass through the intersection of the two other lines.

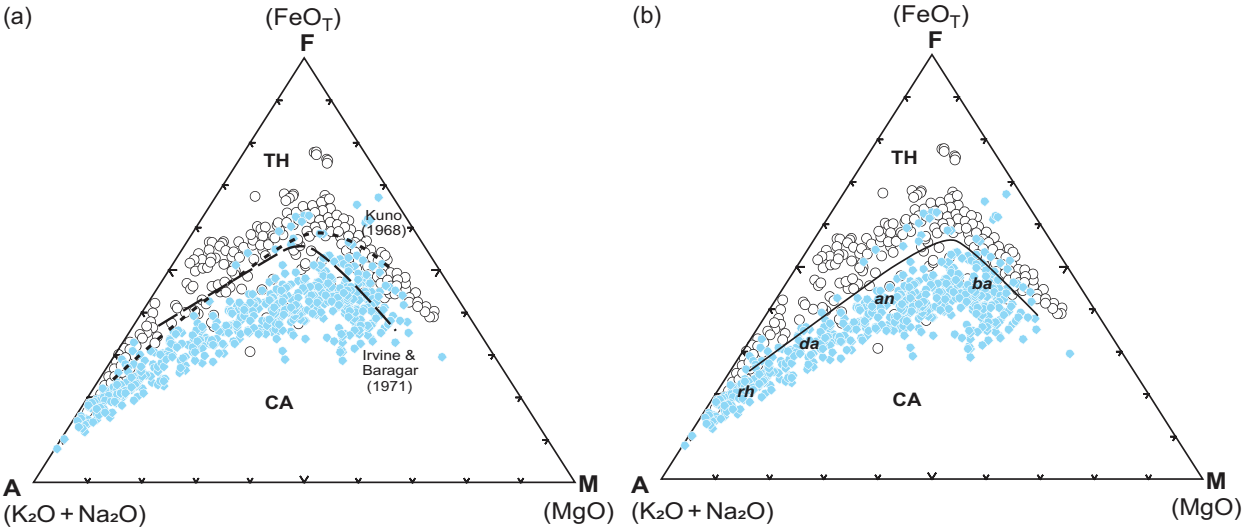

Figure 3.18 The AFM diagram. This diagram distinguishes between the calc-alkaline (CA) and tholeiitic (TH) rock series. The data points shown represent ~ 1100 analyses (~500 tholeiitic Icelandic lavas = filled symbols; ~ 600 calc-alkaline Cascade lavas from the western United States = open symbols) taken from www.earthchem.org/portal (NAVDAT and USGS databases). All Fe was converted to FeO_T. Only complete analyses with reported locations, low LOIs (< 3 wt.%), and appropriate $Na_2O + K_2O$ (to exclude alkaline rocks) were used. The data shown here were randomly selected from the filtered dataset and plotted using Tri-plot (Graham and Midgley, 2000). (a) The boundaries of Irvine and Baragar (1971) and Kuno (1968). (b) The new boundary curve recommended here. The coordinates for the curve are A, F, M: 11, 39, 50; 14, 50, 36; 18, 56, 26; 28, 52, 20; 40, 45, 15; 70, 26, 4). *ba*, basalt; *an*, andesite; *da*, dacite; *rh,* rhyolite.

differentiation trends of the sub-alkaline magma series (Figure 3.18). The diagram takes its name from the oxides plotted at its apices: **A**lkalis ($Na_2O + K_2O$), **F**eO_T and **M**gO. The plotting parameters are calculated by summing the oxides ($Na_2O + K_2O$), (FeO + Fe_2O_3) recalculated as FeO, and MgO; each component is then recalculated as a percentage of the total. Historically, ambiguity exists over the treatment of Fe, but the standard today is that **F** should reflect all Fe as FeO_T to accommodate most modern analytical data for which the separate oxidation states of iron have not been determined.

Most authors use oxide wt.% data when plotting an AFM diagram, but in some cases atomic proportions are used. Since data points plot in different positions depending upon the calculation method (Barker, 1978), it essential to specify which method has been adopted.

The boundary between the calc-alkaline and the tholeiite series on the AFM diagram has previously been defined by Kuno (1968) and Irvine and Baragar (1971) (Figure 3.18a). Both authors use wt.% oxide and represent **F** as FeO_T. Kuno's boundary defines a smaller field for the tholeiitic suite than that of Irvine and Baragar (Figure 3.18a). Here we define a new boundary curve which better discriminates between the two magma series. We have used representative data for tholeiitic and calc-alkaline lavas from Icelandic lavas and lavas from the Cascades of the western United States, respectively. Our result is shown in Figure 3.18b, and the coordinates for the new curve and details of the analyses used are described in the figure caption.

It is important to note that the AFM diagram is limited in the extent to which quantitative petrogenetic information may be extracted. This is a function of the way in which ternary plots are constructed, for they use percentage data, not absolute values, and use only a part of the rock chemistry. In most rocks the A–F–M components make up less than 50% of the total oxide weight percentage and they are therefore a subcomposition of the rock chemistry. In addition, when a compositionally varied rock series is plotted, different proportions of each sample are normalised to 100%, and so the relationship between the plotted values is distorted. For example, in a series of volcanic rocks in the compositional range

basalt to dacite about 40% of the basalt major element chemistry is used when plotting onto an AFM diagram, whereas only about 15% of the dacite major element chemistry is used. For these reasons, the main use of AFM diagrams is to subdivide the sub-alkaline rock series into tholeiitic and calc-alkaline magma types as discussed above.

3.3.4 Interpreting Trends on Variation Diagrams

From the discussion above of bivariate and trivariate plots, it is clear that there are a variety of processes which can produce similar looking trends on major element variation diagrams. It is important therefore to discover the extent to which these various processes might be distinguished from one another and identified.

3.3.4.1 Extract Calculations

One approach is to try to calculate the composition of the materials added to or subtracted from a magma and to quantify the amount of material involved. This may be done using an extract calculation, a method described in some detail by Cox et al. (1979). The method is illustrated in Figure 3.19a in which the chemical compositions (expressed in terms of variables A and B) of both minerals and rocks are plotted on the same variation diagram. Mineral X crystallises from liquid L_1 and the residual liquid follows the path to L_2. The distance from L_1 to L_2 will depend upon the amount of crystallisation of mineral X. This may be quantified as follows:

the amount of liquid L_2 is proportional to the distance $X-L_1$

the amount of mineral X is proportional to the distance L_1–L_2

Therefore,

the percentage of $L_2 = 100 \times XL_1/XL_2$

the percentage of $X = 100 \times L_1L_2/XL_2$

This relationship is known as the *lever rule*.

If there are two or more minerals crystallising simultaneously from liquid L_1 in such proportions that their average composition is C (Figure 3.19b, c), then the liquid path will move from C towards L_2. The proportion of solid to liquid will be given by the ratio L_1L_2:CL_1. The proportions of the minerals X and Y in Figure 3.19b is given by YC:XC. In these variation diagrams the predicted trends form straight lines. However, minerals whose compositions vary because of solid solution will produce curved trends during fractionation (Figure 3.19d).

It is also possible to use extract diagrams to seek to understand partial melting processes. However, in practice extract calculations are inexact for often the minerals involved have complex solid solutions. In addition there may be statistical uncertainties in fitting a straight line through the trend on a variation diagram (Cox et al., 1979). For these reasons the differences between mineral melt equilibria in melting reactions and during fractional crystallisation may be difficult to resolve.

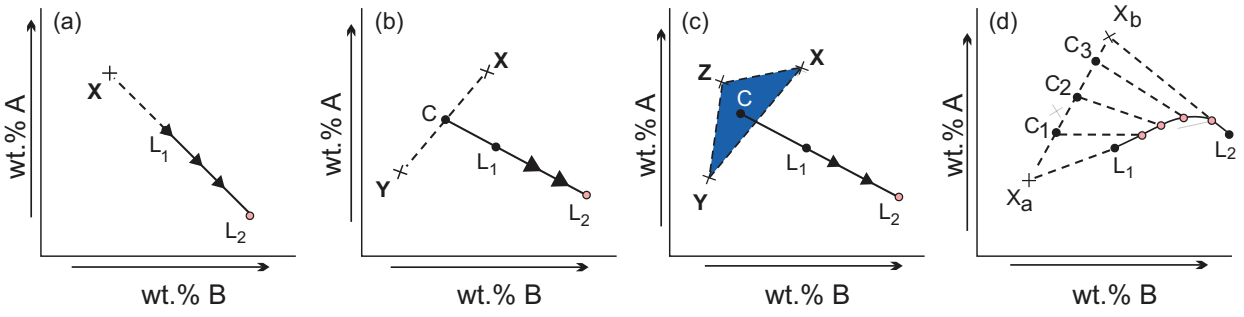

Figure 3.19 Mineral extract calculations. (a) Mineral X is removed from liquid L_1 and the liquid composition moves from L_1 to L_2; (b) mineral extract C (made up of minerals X and Y) is removed from liquid L_1 and drives the liquid composition to L_2; (c) mineral extract C (made up of the minerals X, Y and Z) is removed from liquid L_1 and drives the resultant liquid composition to L_2; (d) mineral X is a solid solution made up of components X_a and X_b. As the mineral composition changes from X_a to X_b via the intermediate compositions C_1 to C_3 the mineral extracts incrementally change the composition of the liquid from L_1 to L_2 along a curved path.

3.3.4.2 Addition–Subtraction Diagrams

An alternative approach to identifying the composition of the solid phase during magmatic fractionation is to use an addition–subtraction diagram to calculate the composition of the fractionating phase or phases. In this case the entire major element chemistry of two or more rocks is used and plotted on a bivariate diagram as is shown in Figure 3.20. Back projection of the data shows that five of the elements reduce to zero at 41.5% SiO_2, consistent with olivine control. The composition of the olivine can be estimated from the diagram, and a simple calculation shows that composition A can be converted to composition B by the removal of 15% olivine. This result would be confirmed from the presence of olivine phenocrysts in the lava.

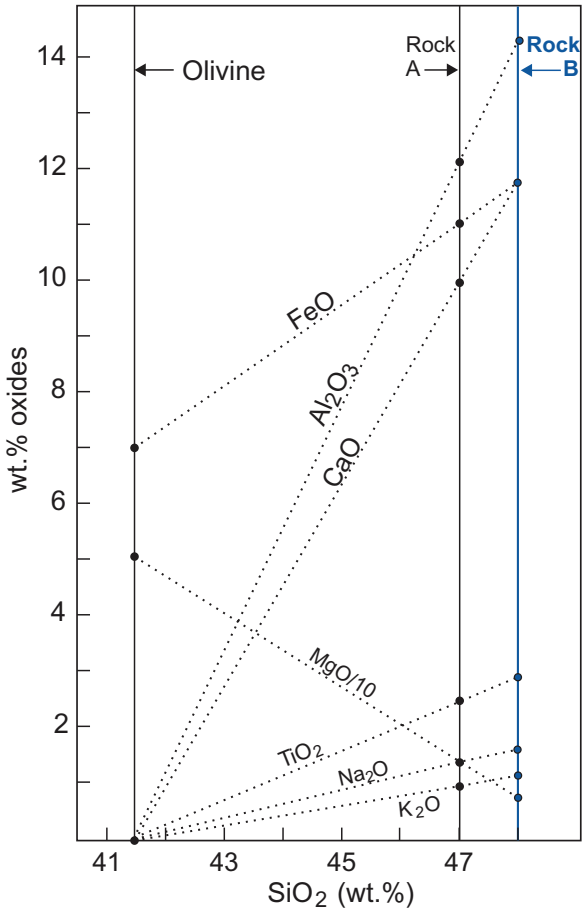

Figure 3.20 The addition–subtraction diagram for the calculation of the composition of the fractionating phase in magmatic rocks. Using samples A and B it can be shown that rock composition B is generated by the extraction of olivine from the composition of rock A. This is done using the back projection of trends for Al_2O_3, CaO, TiO_2, Na_2O and K_2O. These converge on zero at SiO_2 = 41.5 wt.%, indicating an olivine extract. MgO and FeO values at 41.5 wt.% SiO_2 indicate the composition of the olivine removed from rock A to produce composition B.

3.3.4.3 Limitations to the Application of Extract Calculations

In some volcanic rocks it may be difficult to perform an extract calculation because of the large number of phenocryst phases involved. For example, some evolved calc-alkaline lavas may have undergone fractionation of the total assemblage olivine-clinopyroxene-biotite-plagioclase-potassium feldspar-sphene-apatite-magnetite in a series of magma chambers prior to eruption. A further complication is that the close chemical equivalence of mineral assemblages such as plagioclase + olivine, orthopyroxene + augite + magnetite and hornblende can give rise to some ambiguity of interpretation (Gill, 1981).

Other limitations to extract calculations are when the observed liquid line of descent is in reality a mix of several lines, when the compositions of the crystallising phases change during the process of fractionation with the changing composition of the magma and when the phenocrysts present in lava are not representative of the fractionating phases.

3.3.4.4 Trends Showing an Inflection

Some variation diagrams are segmented and show an inflection point. The inflection generally indicates either the entry of a new phase during crystal fractionation or the loss of a phase during partial melting. This is illustrated with the data of Garcia et al. (2018) for basaltic glasses from the Keanakāko'i Tephra from Kīlauea, Hawai'i (Figure 3.21). Data plotted on MgO variation diagrams for the oxides CaO, FeO_T, Al_2O_3, and K_2O show that at ≥7 wt.% MgO, CaO and Al_2O_3 increase as MgO decreases, whereas below 7 wt.% MgO the oxide concentrations of CaO and Al_2O_3 decrease and FeO_T and K_2O increase. These trends suggest that at MgO concentrations ≥7 wt.% the changing melt compositions are controlled by olivine fractionation during which MgO is removed from the melt and the relative proportions of residual CaO and Al_2O_3 increase. At MgO concentrations <7 wt.% the co-precipitation of plagioclase and clinopyroxene reduce the absolute amount of CaO and Al_2O_3 in the melt and the relative

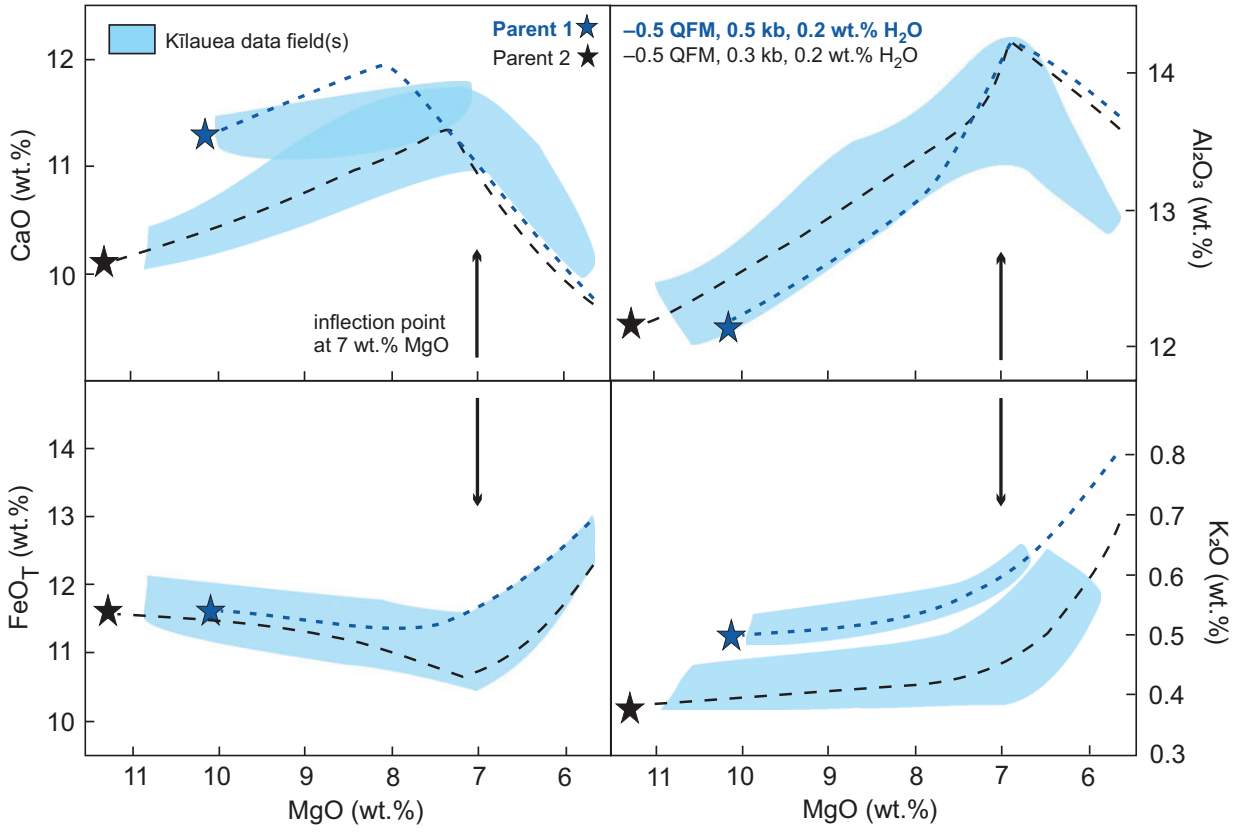

Figure 3.21 Select bivariate plots for the Keanakāko'i Tephra from Kīlauea, Hawai'i (after Garcia et al., 2018). Shaded regions represent the data fields. The change in slope at about MgO = 7 wt.% in CaO, Al_2O_3, FeO_T and K_2O is consistent with a change in the fractionating phases at this point. The two dashed lines represent the best-fit forward modelling compositional trends using AlphaMELTS (Smith and Asimow, 2005) which indicate that the range in tephra composition is consistent with crystal fractionation at low pressure (0.3–0.5 kb), low water content (0.2 wt.% H_2O) and an oxygen fugacity of QFM = −0.5.

proportions of FeO_T and K_2O increase due to the constant sum effect (Section 2.2.2.1).

Inflections will be apparent on variation diagrams of a rock series only if the chemistry of the extracted phase is reflected in the plotting parameters. However, when inflections are present they should be located at the same point in the rock series as is the case for the Hawaiian data shown in Figure 3.21. Inflections are most obvious when the number of fractionating minerals is small as in basaltic melts. In calc-alkaline volcanic rocks, where the number of fractionating phases is large, the entry or exit of a single phase may not sufficiently affect the bulk chemistry of the melt to be seen on a variation diagram.

3.3.4.5 Scattered Trends

Observation shows that some variation diagrams define well-constrained trends whereas others do not. For example, the data for Kīlauea Iki illustrated in Figure 3.12 show very clear trends which are indicative of one main geological process. In contrast the data for the Australian sandstones illustrated in Figure 3.13 shows more scattered trends, as do some of the trends in the data for the Limpopo Belt tonalitic and trondhjemitic gneisses listed in Table 2.2.

In general terms, scattered trends on variation diagrams may arise through the following:

- Sampling error: For example, samples may have been collected over a wide area but they are not all genetically related. Alternatively, an unintended bias may be present in the sampling process.
- Analytical error: Scatter on variation diagrams can arise through uncertainties in the analytical measurements or when measurements on subsets of the data have been made in different laboratories.

- The operation of multiple geological processes: In the case of the data for the Belingwe Greenstone Belt (Figure 3.15) the greater scatter associated with Na_2O versus MgO might indicate a primary control by olivine fractionation combined with secondary scatter due to Na mobility related to late fluid movement through the rock.
- In sedimentary rocks scatter may be a function of the mixing processes leading to the formation of the sediment.
- In metamorphic rocks scattered trends may reflect the geochemical imprint of a metamorphic process on earlier igneous or sedimentary processes.
- In igneous rocks a scattered trend can arise for a number of reasons: these include the mixing of melt and cumulus minerals due to either the accumulation of phenocrysts in a lava or the formation of a cumulate rock in a magma chamber, the sampling of multiple magma compositions in a lava pile, and/or a change in the fractionating assemblage during fractional crystallisation.

3.3.5 Modelling Major Element Processes in Igneous Rocks

Computer-based modelling offers a quantitative alternative to the deductive use of variation diagrams for investigating petrological processes. There are two approaches. *Forward modelling* begins with a known starting composition and determines how this composition will evolve to a derivative or daughter composition given specific physical conditions. *Inverse modelling* begins with a derived composition and works 'backwards' to determine the composition of the parent. If both starting and end compositions are known, as for example in a volcanic series, it is possible to explore the processes that might link the two. These might include the addition or removal of mineral phases, changes in pressure and temperature during the evolution of the magma, and/or the amount of H_2O present in the melt. Models of this type are designed to use real analytical data in order to test specific hypotheses regarding magma genesis and they provide feasible but not necessarily unique pathways of magma evolution. If a rock has a complex history, the modelling may be better formulated as a series of steps.

The success of any model is estimated from the residuals of the calculation, that is, the difference between the actual and calculated compositions (Table 3.7). In addition all model results should be evaluated petrologically and the relative proportions and composition of the calculated fractionating phases should be compared with the phenocryst assemblage present in the sample suite. A computer model will normally produce a 'best-fit' solution, although it is important to stress that the result may be non-unique and that the 'solution' is not always correct. For this reason, many workers test models based on major element chemistry with further calculations based upon trace element and/or isotopic data.

Table 3.7 Petrological mixing calculation for differentiated of Kīlauea lavas, Hawai'i[a]

	Parent	*Differentiate*	*Minerals removed from parent*				*Residuals*	
			Olivine	*Augite*	*Plagioclase*	*Ilmenite*	*Max.*	*Min.*
1955 components	1921	1955E, MgO = 5.39	3.00	22.42	21.84	1.66		
Composition (wt.%)	100	51.08	Fo_{70}		An_{61}		0.005	0.00
1977 components	1961	1977, MgO = 5.34	3.85	17.31	15.29	0.58		
Composition (wt.%)	100	62.97	$Fo_{77.1}$		$An_{68.4}$		0.006	0.001
1977 components	1961	1977, MgO = 5.89	3.20	12.80	10.31	0.29		
Composition (wt.%)	100	73.39	$Fo_{77.1}$		$An_{69.38}$		0.01	0.001

[a]Data from Wright and Marsh (2016).

3.3.5.1 Modelling Fractional Crystallisation

In their simplest forms, fractional crystallisation models take the general form

rock A (starting point) − (mineral X + mineral Y + mineral Z) = rock B (end point).

This generalised equation can be rearranged to solve for any of the parameters involved such as the parent melt, the derived melt or the crystallising assemblage. For a given silicate liquid, the aim of the modelling is to determine the nature of crystallising phase, the composition of the melt at the different stages during its evolution, the temperature of crystallisation, and the crystallisation sequence of the phases. Three different approaches are used:

1. The calculation of the distribution of major elements between mineral phases and a coexisting silicate melt from experimental phase equilibria using regression techniques.
2. The determination of mineral–melt equilibria from measured distribution coefficients.
3. The application of equilibrium thermodynamic models for magmatic systems. These require valid mixing models for the liquid and an internally consistent set of solid–liquid thermochemical data.

Wright and Marsh (2016) performed fractional crystallisation calculations (Table 3.7) for Kīlauea volcano, Hawai'i, using a least squares regression technique. The purpose of the study was to test whether or not the more differentiated lavas erupted from Kīlauea's East Rift Zone were derived from the more primitive compositions from the Kīlauea caldera summit more than 30 km to the west. Using the oxide compositions of phenocrysts combined with whole rock compositions and the temperature of the presumed parents, they were able to determine the percentages of olivine, augite, plagioclase and ilmenite necessary to generate the differentiated lavas from the assumed parent composition. The very low values calculated for the maximum and minimum residuals in Table 3.7 confirm the reasonableness of the results.

The thermodynamic modelling of phase equilibria offers a powerful approach for investigating processes in magmatic systems. Of the software packages available, the MELTS (http://melts.ofm-research.org) suite of programs is widely used. These programs permit the calculation of equilibrium phase relations for mafic magmatic systems (Ghiorso and Sack, 1995; Asimow and Ghiorso, 1998) and felsic systems (Gualda et al., 2012; Ghiorso and Gualda, 2015) over a broad range of temperatures and pressures (500–2000°C, 0–2 GPa). They are used to explore magmatic processes such as adiabatic decompression melting, energy-constrained assimilation and, post-entrapment crystallization in melt inclusions. They also permit the evaluation of oxygen fugacity in magmatic systems and monitor magmatic evolution along specified oxygen buffers. In addition, it is possible quantify the amount of water present in a magmatic system and model this as a function of temperature, pressure and liquid composition.

Garcia et al. (2018) used AlphaMELTS, the menu-driven interface to subroutines of MELTS (Smith and Asimow, 2005), to constrain the petrogenesis of the Keanakāko'i Tephra from Kīlauea in Hawai'i (Figure 3.21). They showed through the forward modelling from inferred parent compositions that the tephra must have formed under conditions of low pressure, low water content and low oxygen fugacity (Figure 3.21). Although the model did not constrain all subsets of the data, it provides a theoretical constraint on the petrogenesis of a significant part of the Keanakāko'i Tephra.

3.3.5.2 Modelling Fractional Crystallisation and Assimilation

The MELTS software is also incorporated into a comprehensive modelling program known as the Magma Chamber Simulator (MCS) of Bohrson et al. (2014) (https://mcs.geol.ucsb.edu/). The MCS integrates major element, trace element and isotopic data into an energy- and mass-constrained open-system thermodynamic computational tool. It uses energy-constrained assimilation-fractional crystallization equations that account for heating and partial melting of crustal wall rock. Heinonen et al. (2016, 2019) used the MCS to constrain the petrogenesis of Karoo flood basalts from Vestfjella in western Dronning Maud Land, Antarctica. They were able to show that the Vestfjella continental flood basalts could be produced by minor (1–15 wt.%) contamination of asthenospheric parental magmas with lithospheric melts. Their work implies that estimates for the degree of contamination of

continental flood basalts by the continental lithosphere are likely to be overestimated (Heinonen et al., 2016).

3.4 Diagrams on Which Rock Chemistry and Experimentally and Thermodynamically Determined Phase Boundaries Are Plotted Together

A number of igneous systems have been sufficiently well determined in the laboratory to allow the geochemist to interpret natural rock compositions in the light of experimentally determined phase boundaries. Increasingly, laboratory data for a system such as mantle peridotite are synthesised from a variety of sources, parameterised, and the results extrapolated using thermodynamic modelling to be widely applicable across a range of melting conditions and source compositions. Diagrams of this type seek to simplify multivariate experimental data sets by projecting the results onto a two-dimensional plane and allowing natural rock data to be projected onto them in a similar manner for interpretive purposes.

Historically, the purpose of many experiments on basaltic and granitic systems was to determine the composition of primary magmas using simplified rock compositions. However, there are problems with this approach for its success depends upon the extent to which the system under investigation matches the natural rock composition; it is now known that presence of only a few percent of an additional component may dramatically change the position of the phase boundaries. Further it is also apparent that some (felsic) rock compositions do not always equate to melt compositions.

In the classical literature the results of multi-oxide experimental studies were projected from a tetrahedron into a planar representation. More recently, the results of experimental studies tend to be expressed in a series of bivariate plots which are simpler to interpret and do not require complex projection procedures. However, there remain a number of projections still in use, and since they are still sometimes referred to, they are described briefly below and summarized in Box 3.2. Each projection is slightly different and has distinct rules. A more general approach to transforming data from quaternary systems into ternary plots is given in the works of Maaloe and Abbott (2005) and Shimura and Kemp (2015).

Box 3.2 Summary of diagrams in which rock chemistry can be plotted with experimental data discussed in Section 3.4

Melting the mantle
The Yoder–Tilley CIPW normative tetrahedron
  The normative *Ne-Di-Ol-Hy-Q* diagram
  Projections in *Ol-Pl-Di-Q*
  The low-pressure tholeiitic phase diagram of Cox et al. (1979)
CMAS diagrams
  Diagrams of O'Hara (1968)
  Expanded CMAS (Herzberg and O'Hara, 2002)
FeO-MgO plots
Melting mafic crust
Melting felsic (continental) crust
  The granite system
  Partial melting of crustal rocks

3.4.1 Melting the Mantle

The mineralogy of the upper mantle can be simplified to the phases olivine + orthopyroxene together with minor amounts of clinopyroxene and an aluminous phase (either plagioclase, spinel or garnet depending on pressure). Chemically, the rocks of the mantle simplify to the oxides $CaO–MgO–Al_2O_3–SiO_2$, often abbreviated to *CMAS*. Together with Na_2O (*CMASN*) this simplified system also represents the compositional range of most basaltic melts. These mineralogical and chemical systems are the basis for many common projection schemes used to represent mantle melting processes and the evolution of basaltic melts. The most commonly used include the following:

1. The Yoder and Tilley (1962) scheme based upon the main normative minerals observed in basalts (diopside–olivine–anorthite–quartz–nepheline).
2. The CMAS system of O'Hara (1968) based on the oxides $CaO–MgO–Al_2O_3–SiO_2$ as indicated above.

The two schemes are broadly parallel inasmuch as diopside = C, olivine = M, anorthite = A, quartz = S, and nepheline = Na_2O.

3.4.1.1 The Yoder and Tilley CIPW Normative Tetrahedron

The normative nepheline–diopside–olivine–quartz tetrahedron was originally proposed by Yoder and Tilley (1962) for the classification of basalts as illustrated in Figure 3.22a and discussed in Section 3.2. The tetrahedron has also been extensively used for comparing the results of experimental studies on mantle peridotites with the chemical composition of basalts and is the focus of this discussion. A variety of projection procedures have been used and these are outlined below.

(a) *The normative Ne–Di–Ol–Hy–Q diagram.* This diagram in Figure 3.6 represents the full range of compositions considered in the Yoder and Tilley (1962) tetrahedron (Figure 3.22a) and as previously noted is a means of classifying basalts using their CIPW normative compositions (Thompson, 1984). It can also be used to display experimental and natural rock data for basalts which range from saturated to undersaturated compositions (Thompson, 1984; Gibson et al., 2000) and to show the changing composition of initial melts of different mantle compositions, produced at different pressures (Figure 3.22b).

The calculation procedure is as follows:

- CIPW normative compositions are calculated on a wt.% basis and plotted on one of the three triangles.
- Fe_2O_3 is calculated as 15% of the total iron content.

An example of how the diagram may be used is given in Figure 3.22b, which shows the fields of flood basalts and ferro-picrites from the Parana province (Gibson et al., 2000) together with the 1 atm and 9 kb cotectics for melts in equilibrium with olivine, plagioclase and clinopyroxene (data from Thompson, 1983). A variant of the diagram is used by Falloon et al. (2001) in which the *Ne*-apex is replaced by jadeite + Ca-Tschermak's + leucite (*Jd* + *CaTs* + *Lc*). In this case molecular norms are projected from olivine onto *Di–Qz–Jd* + *CaTs* + *Lc* and from diopside onto *Ol–Qz–Jd* + *CaTs* + *Lc*.

(b) *Projections in the tholeiitic basalt tetrahedron Ol–Pl–Di–Q.* A restricted portion of the Yoder and

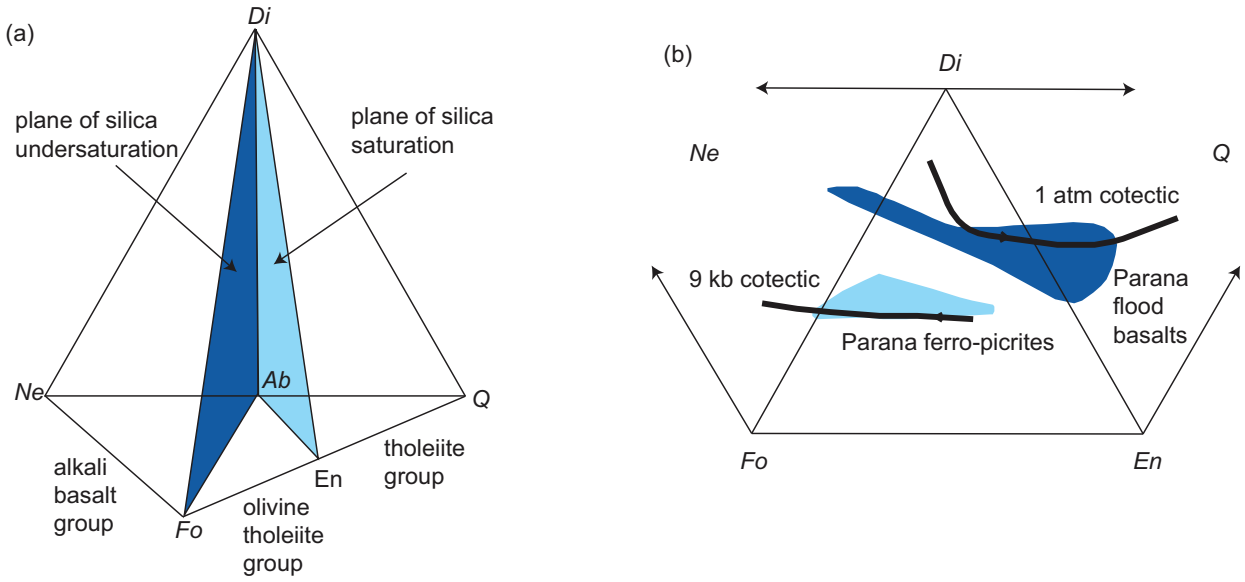

Figure 3.22 (a) The normative diopside (*Di*)–nepheline (*Ne*)–forsterite (*Fo*)–enstatite (*En*)–quartz (*Q*)–albite (*Ab*) tetrahedron after Yoder and Tilley (1962) showing the diopside–albite–forsterite plane of silica undersaturation, compositions to the left of which contain normative nepheline, and the diopside–albite–enstatite plane of silica saturation, compositions to the right of which contain normative quartz. (b) The planar projection of the Yoder and Tilley tetrahedron showing the expanded *Di–Fo–En* face and extensions into *Ne*-normative undersaturated compositions and *Q*-normative saturated compositions. Also shown are wt.% normative data for ferro-picrites and flood basalts from the Parana province together with low-pressure and high-pressure cotectics for liquids in equilibrium with Ol, Pl, and Cpx from Thompson et al. (1983). (After Gibson et al., 2000, with permission from Elsevier)

Tilley (1962) diagram – the silica-saturated, tholeiitic basalt segment of the tetrahedron – delimited by the phases olivine–plagioclase–diopside–quartz has also been used extensively for demonstrating relationships between melting experiments and mafic igneous rocks. In this case four different algorithms by Walker et al. (1979), Elthon (1983), Grove (1993) and Presnall et al. (2002) have been devised for plotting experimental and rock data (Figures 3.23 and 3.24). Because the plotting parameters are slightly different from each other, and the allocation of Fe between Fe^{2+} and Fe^{3+} also differs, it is important to note which plotting procedure is used in any given projection of the data. An example of each of the calculation schemes is presented in Table 3.8.

Presnall et al. (2002) recalculated rock compositions as CIPW norms, setting the $Fe^{2+}/(Fe^{2+} + Fe^{3+})$ ratio to 0.91. The mineral proportions are expressed as mole percent and the plotting parameters are defined as follows:

$$Pl = Al_2O_3 - K_2O$$

$$Di = CaO + K_2O + Na_2O - 3.33P_2O_5 - Al_2O_3$$

$$Ol = (MgO + FeO + MnO + 3.33P_2O_5 + Al_2O_3 - TiO_2 - Cr_2O_3 - Fe_2O_3 - CaO - K_2O - Na_2O)/2$$

$$Q = SiO_2 - 5.5(K_2O + Na_2O) - 0.5(Al_2O_3 + MgO + FeO + MnO - TiO_2 - Fe_2O_3) - 1.5CaO + 5P_2O_5$$

Hypersthene is calculated as equivalent olivine and quartz. The main projections in the tetrahedron *Di–Ol–Pl–Q* are from diopside onto the *Pl–Ol–Q* face, and from plagioclase onto the *Di–Ol–Q* face. In the case of the plagioclase projection, the proportions of *Di, Ol* and *Q* are normalised to their sum and plotted on a molecular basis. The diopside projection is calculated in a similar manner (see Table 3.8). An example of the use of this projection scheme is shown in Figure 3.23, the projection of MORB glass compositions from *Di* onto the *Pl–Ol–Q* face and from *Pl* onto the *Di–Ol–Q* face of the tholeiitic basalt tetrahedron *Ol–Pl–Di–Q* (data from Presnall et al., 2002).

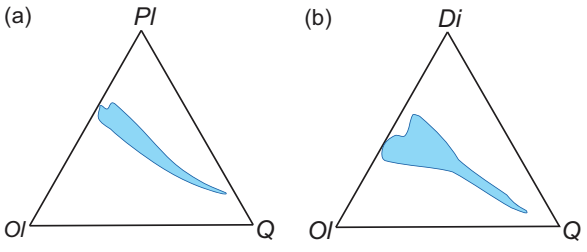

Figure 3.23 Projections of MORB glass compositions in the tholeiitic basalt tetrahedron *Ol–Pl–Di–Q* using the molar norm method of Presnall et al. (2002). (a) The diopside projection onto the *Pl–Ol–Q* plane. (b) The plagioclase projection onto the plane of *Di–Ol–Q*. (Data from Presnall et al., 2002, with permission from Elsevier)

Walker et al. (1979) developed a different algorithm for plotting data in the same projections, although the end result is similar to that of Presnall et al. (2002). Weight % oxides are divided by their molecular weight to obtain molecular proportions, all Fe is presented as FeO, and the plotting parameters are calculated from the molecular proportions as follows:

$$PLAG = Al_2O_3 + Na_2O + K_2O$$

$$DI = CaO - Al_2O_3 + Na_2O + K_2O$$

$$OL = (FeO + MgO + MnO + 2Fe_2O_3 + Al_2O_3 - CaO - Na_2O - K_2O)/2$$

$$SIL = SiO_2 - (Al_2O_3 + FeO + MgO + MnO + 3CaO + 11Na_2O + 11K_2O + 2Fe_2O_3)/2$$

Walker et al. (1979) use the notation DI–OL–SIL and OL–SIL–PLAG for projections from plagioclase onto the *Di–Ol–Q* face and from diopside onto the *Pl–Ol–Q* face. In the case of the plagioclase projection. the proportions of DI, OL and SIL are calculated and then normalised to their sum (Table 3.8) and plotted on a molecular basis.

Elthon (1983) proposed a third algorithm arguing that chemical trends in oceanic basalt suites projected in the olivine–clinopyroxene–silica plane are greatly improved if the plagioclase feldspars are separated along the anorthite–albite join and do not plot at a single point. In this 'isomolar' projection plagioclase compositions are spread along the silica–anorthite edge of the *Di–Ol–An–Q* tetrahedron. The normative mineralogy is projected onto the planes Cpx–Ol–Si and Ol–Si–Pl. The plotting parameters are calculated from the molecular proportions, using the nomenclature of Walker et al. (1979) as follows:

$$PLAG = Al_2O_3 + Fe_2O_3$$

$$DI = CaO + Na_2O + K_2O - Al_2O_3 - Fe_2O_3$$

$$OL = [(FeO + MgO + MnO - TiO_2) - (CaO + Na_2O + K_2O) + (Fe_2O_3 + Al_2O_3)]/2$$

Table 3.8 Projection procedures for basaltic compositions in the Yoder and Tilley tetrahedron (using mean MORB glass from Table 3.2)

	Wt.% oxide of rock	Mol wt	Mol prop	Mol %		Grove conversion	Grove mol %
SiO_2	50.60	60.09	0.8421	52.92		52.92	47.19
TiO_2	1.67	79.90	0.0209	1.31		1.31	1.17
Al_2O_3	14.79	101.96	0.1451	9.12	$AlO_{0.5}$	18.23	16.26
Fe_2O_3	0.00	159.69	0.0000	0.00	$Fe^{3+}\ O_{1.5}$	0.00	0.00
FeO	10.46	71.85	0.1456	9.15		9.15	8.16
MnO	0.19	70.94	0.0027	0.17		0.17	0.15
MgO	7.42	40.30	0.1841	11.57		11.57	10.32
CaO	11.38	56.08	0.2029	12.75		12.75	11.37
Na_2O	2.77	61.98	0.0447	2.81	$NaO_{0.5}$	5.62	5.01
K_2O	0.19	94.20	0.0020	0.13	$KO_{0.5}$	0.25	0.23
P_2O_5	0.18	141.95	0.0013	0.08	$PO_{2.5}$	0.16	0.14
TOTAL	99.65		1.5913	100.00		112.13	100.00
						FMO	18.48
						Alk	5.24

Plotting procedure of Presnall et al. (2002)

Pl = Al_2O_3–K_2O (molecular)	0.143
Di = CaO + K_2O + Na_2O–3.33P_2O_5–Al_2O_3	0.100
Ol = (MgO + FeO + MnO + 3.33P_2O_5 + Al_2O_3–TiO_2–Cr_2O_3–Fe_2O_3–CaO–K_2O–Na_2O)/2	0.106
Q = SiO_2–5.5(K_2O + Na_2O) –0.5(Al_2O_3 + MgO + FeO + MnO–TiO_2–Fe_2O_3)–1.5CaO + 5P_2O_5	0.059

Plagioclase projection		%
di =	0.100	37.90
ol =	0.106	39.87
q =	0.059	22.23
sum =	0.265	100.00

Plotting procedure of Walker et al. (1979)

PLAG = Al_2O_3 + Na_2O + K_2O(molecular)	0.192
DI = CaO–Al_2O_3 + Na_2O + K_2O	0.105
OL = (FeO + MgO + MnO + 2Fe_2O_3 + Al_2O_3–CaO–Na_2O–K_2O)/2	0.114
SIL = SiO_2–(Al_2O_3 + FeO + MgO + MnO + 3CaO + 11Na_2O + 11K_2O + 2Fe_2O_3)/2	0.042

Plagioclase projection		%
DI =	0.105	40.14
OL =	0.114	43.72
SIL =	0.042	16.15
sum =	0.261	100.00

Plotting procedure of Elthon (1983)

PLAG = Al_2O_3 + Fe_2O_3 (molecular)	0.145
DI = CaO + Na_2O + K_2O–Fe_2O_3–Al_2O_3	0.105
OL = ((FeO + MgO + MnO–TiO_2) + (Al_2O_3 + Fe_2O_3)–(CaO + Na_2O + K_2O))/2	0.103
SIL = SiO_2–((FeO + MgO + MnO–TiO_2) + (Al_2O_3 + Fe_2O_3) + 3(CaO + Na_2O + K_2O))/2	0.239

Plagioclase projection		%
Di =	0.105	23.38
Ol =	0.103	23.12
Si =	0.239	53.50
Sum =	0.447	100.00

Table 3.8 (*cont.*)

Plotting procedure of Grove et al (1993)		
Sum = SiO_2–CaO–2 × Alk + Cr_2O_3 + TiO_2 (molecular %)		26.52
Qtz = (SiO_2–0.5 × FeMO–1.5 × CaO–0.25 × $AlO_{1.5}$–2.75 × Alk + 0.5 × Cr_2O_3 + TiO_2)/sum		0.136
Plag = 0.5($AlO_{1.5}$ + $NaO_{0.5}$–$KO_{0.5}$)/(sum)		0.445
Oliv = (FMO + 0.5 × ($AlO_{1.5}$–Alk)–CaO–TiO_2–Cr_2O_3 + 1.667 × $PO_{2.5}$)/(2*sum)		0.194
Cpx = (CaO–0.5 × $AlO_{1.5}$ + 0.5 × Alk–1.667 × $PO_{2.5}$)/sum		0.221
Plagioclase projection		%
Cpx =	0.221	40.14
Ol =	0.194	35.18
Q =	0.136	24.68
Total =	0.551	100.00

$$SIL = SiO_2 - [(FeO + MgO + MnO - TiO_2) + (Al_2O_3 + Fe_2O_3) + 3(CaO + Na_2O + K_2O)]/2$$

Fe^{3+}/Fe^{2+} is assumed to be 0.10. This method of projection results in different plotting positions from the algorithms of Presnall et al. (2002) and Walker et al. (1979) and compositions are shifted towards the silica apex. A model calculation is given in Table 3.8.

In a fourth, rather different approach, Grove (1993; corrected from Grove et al. 1992, 1982) requires the conversion of the original analysis from wt.% oxides to mole % and the recalculation of Al to $AlO_{1.5}$, Fe^{3+} to $Fe^{3+}O_{1.5}$, K to $KO_{0.5}$, Na to $NaO_{0.5}$ and P to $PO_{2.5}$. The calculation of Grove (1993) treats all Fe as FeO. From these values molar % MgO and FeO are combined to become FMO and $K_{0.5}O$ + $Na_{0.5}O$ become Alk. These molar % values are then transformed to mineral components as follows:

$$Sum = SiO_2 - CaO - 2 \times Alk + Cr_2O_3 + TiO_2$$

$$Quartz = (SiO_2 - 0.5 \times FeMO - 1.5 \times CaO - 0.25 \times AlO_{1.5} - 2.75 \times Alk + 0.5 \times Cr_2O_3 + 0.5TiO_2 + 2.5 \times PO_{2.5})/sum$$

$$Plag = 0.5 \times (AlO_{1.5} + NaO_{0.5} - KO_{0.5})/sum$$

$$Oliv = 0.5 \times (FMO + 0.5 \times [AlO_{1.5} - Alk] - CaO - 2 \times TiO_2 - Cr_2O_3)/sum$$

$$Cpx = (CaO - 0.5 \times AlO_{1.5} + 0.5 \times Alk)/sum$$

An example of the use of the plagioclase projection to summarise the results of anhydrous mantle melting is given by Villiger et al. (2004).

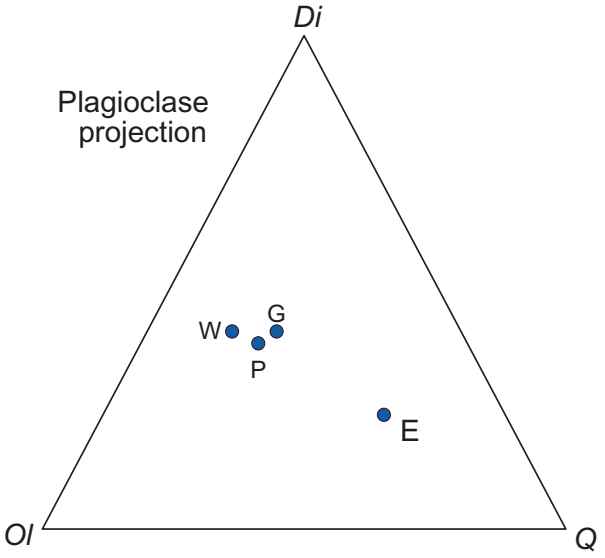

Figure 3.24 Projection of the composition of average MORB glass (Table 3.2) from plagioclase onto the plane *Di–Ol–Q* in the tholeiitic basalt tetrahedron. The data show the results of the four different projection schemes discussed in the text and in Table 3.8. P = Presnall et al. (2002), W = Walker et al. (1979), E = Elthon (1983), G = Grove et al. (1993).

Table 3.8 shows the projection calculations for the different methods for the composition of mean MORB glass, and the results are plotted in Figure 3.24. It is clear that the Grove, Presnall and Walker methods give similar results, whereas Elthon's is significantly shifted towards the quartz apex.

(c) *A low pressure tholeiitic basalt phase diagram.* Cox et al. (1979) proposed a low-pressure phase

diagram based upon the silica-poor part of the normative basalt system *Ol–Cpx–Pl–Q*. The diagram is based on the CIPW normative composition of a tholeiitic (hypersthene normative) basalt which is projected from SiO_2 onto the *Fo–Ab–Di* plane, that is, the plane of silica saturation, of the Yoder-Tilley (1962) tetrahedron shown in Figure 3.22. This diagram is useful for estimating the phases present in the initial stages of low-pressure crystallisation and for estimating the order in which the main phases crystallised of a given tholeiite. In constructing this diagram the *Fo–Ab–Di–Qz* tetrahedron becomes the *Ol–Plag–Cpx–Q* tetrahedron (Figure 3.25). The hypersthene content of the norm is recalculated as an equivalent amount of olivine and quartz, and the plotting parameters are then calculated from the norm as follows:

Plagioclase = normative anorthite + albite
Clinopyroxene = normative diopside
Olivine = normative olivine
+ that recalculated from hypersthene
Quartz = normative quartz
+ that recalculated from hypersthene

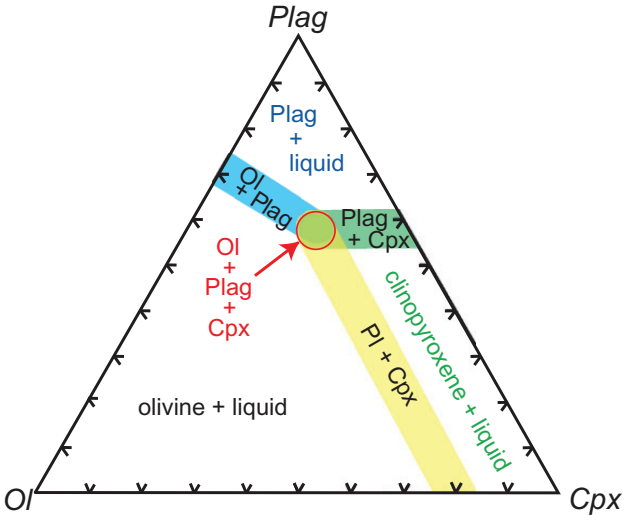

Figure 3.25 The low-pressure tholeiitic basalt phase diagram of Cox et al. (1979). The projection is from normative quartz onto the critical plane of silica undersaturation in the Yoder–Tilley basalt tetrahedron, modified to olivine–plagioclase–clinopyroxene. *Plag* = plagioclase, *Cpx* = clinopyroxene, *Ol* = olivine.

The four parameters are calculated as percentages of the total, although samples in which the normative plagioclase is $<An_{50}$, the ratio $(FeO + Fe_2O_3)/(MgO + FeO + Fe_2O_3) > 0.7$, $K_2O > 1.0$ % and quartz > 10 % should be screened out. For the remaining analyses the plotting parameters plagioclase, olivine and clinopyroxene are recalculated to 100% and plotted onto the triangular phase diagram.

3.4.1.2 CMAS Diagrams

The components of the CMAS system (CaO–MgO–$Al2O_3$–SiO_2) comprise about 70–85 wt.% of most basalts and more than 90 wt.% of most mantle peridotites. Consequently, the CMAS system is used by experimental petrologists as a simplified analogue of more complex basalt and mantle systems. The CMAS projection (Figure 3.26a) provides an excellent framework in which the possible melting behaviour of upper mantle materials may be discussed and is a powerful tool in constructing petrological models. It also may be used to compare the chemistry of particular rock suites with experimentally determined phase boundaries at low and high pressure. Partial melting trends may be identified from a linear array of rock compositions projecting through the plotted source composition and fractional crystallisation trends may be identified as linear arrays projecting through the composition of the fractionating phase(s). The CMAS tetrahedron has apices in a different orientation from those of the tholeiitic component of the Yoder–Tilley tetrahedron. Mineral phases plotted in CMAS space are abbreviated as follows:

- All Fe–Ni–Mg olivines as forsterite = M_2S
- Enstatite; = MS
- All feldspar is projected as equivalent anorthite = CAS_2
- All hercynite, ulvospinel, magnetite and chromite projected as spinel = MA
- All garnet plots along the grossular = C_3AS_3–pyrope M_3AS_3 join
- All clinopyroxenes along the diopside = CMS_2–Ca-Tschermak's molecule = CAS join

(a) *Projecting rock compositions into CMAS.* The CMAS system (Figure 3.26a) was first used for mantle and basaltic compositions by O'Hara (1968), who proposed a polybaric phase diagram for dry natural basalts and ultramafic rocks up to pressures of 30 kb. He devised a scheme whereby natural rock compositions could be presented in

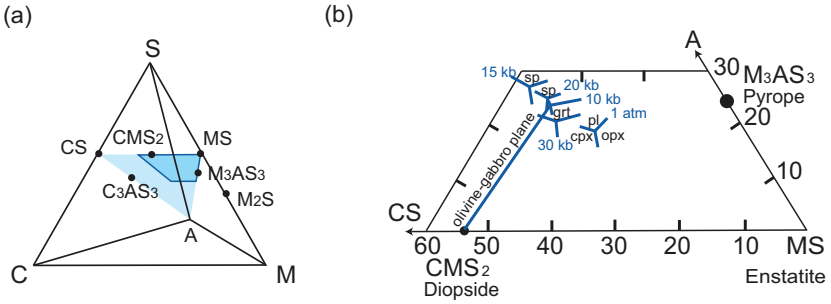

Figure 3.26 (a) The CMAS tetrahedron for the projection of basaltic and mantle compositions showing the relative positions of the main phases and planes of projection. (b) Projection from olivine (M_2S) onto the plane CS–MS–A in the CMAS system showing invariant peritectic points for 1 atm, and 10, 15, 20 and 30 kb. The olivine–gabbro plane divides the diagram into nepheline normative compositions (enstatite-poor) and tholeiitic compositions (enstatite-rich). The stability fields of the different phases are indicated (pl = plagioclase; opx = orthopyroxene; cpx = clinopyroxene; sp = spinel; grt = garnet); in addition, all fields include olivine.

such a way as to be directly comparable with experimental results in the CaO–MgO–Al_2O_3–SiO_2 (CMAS) system. Weight % oxides are converted to molecular proportions and the plotting parameters are calculated as follows:

$$C = (\text{mol. prop. } CaO - 3.33P_2O_5 + 2Na_2O + 2K_2O) \times 56.08$$

$$M = (\text{mol. prop. } FeO + MnO + NiO + MgO - TiO_2) \times 40.31$$

$$A = (\text{mol. prop. } Al_2O_3 + Cr_2O_3 + Fe_2O_3 + Na_2O + K_2O + TiO_2) \times 101.96$$

$$S = (\text{mol. prop. } SiO_2 - 2Na_2O - 2K_2O) \times 60.09$$

Cox et al. (1979) gives the equations for CMAS projections as follows:

1. For projection from the olivine projection onto the plane CS–MS–A:

$$C_cM_mA_aS_s + pM_{57.3}S_{42.7} = xC_{48.3}S_{51.7} + yM_{40.1}S_{59.9} + zA_{100}$$

2. For projection from orthopyroxene into M2S–C2S3–A2S3:

$$C_cM_mA_aS_s + pM_{40.1}S_{59.9} = xM_{57.3}S_{42.7} + yC_{38.4}S_{61.6} + zA_{53.1}S_{46.9}$$

3. For projection from diopside into C3A-M-S:

$$C_cM_mA_aS_s + pC_{25.9}M_{18.6}S_{55.5} = xC_{62.3}A_{37.7} + yM_{100} + zS_{100}$$

where p is the amount of olivine required to bring the rock into the required plane (this can be a positive or negative amount); c, m, a and s are the calculated values for C, M, A and S for the rock as calculated above; and x, y, z when recast as a percentage are the plotting parameters required for CS, MS and A, respectively.

Rock compositions are usually displayed in one of three projections, chosen to include the important mineral phases and to minimise any distortion from the projection. The most used projections are:

(a) from olivine into the plane CS–MS (enstatite) –A
(b) from enstatite into the plane M2S–A2S3–C2S3
(c) from diopside into either the plane C3A–M–S or CA–M–S.

The olivine projection plane contains the pyroxene and garnet solid solutions (Figure 3.26b). The olivine–plagioclase piercing point (not shown) is the point at which the olivine–plagioclase join cuts the CS–MS–A plane, and the line which joins this piercing point to diopside (the olivine–gabbro plane) is the plane of silica saturation (Figure 3.26b). This olivine–gabbro plane divides the diagram into *Ne*-normative compositions on the enstatite-poor side and tholeiitic compositions on the enstatite-rich side. An example of the calculation procedure for projecting a basaltic composition from olivine onto the CS–MS–A plane is given in Table 3.9. France et al. (2009) have created a software package which converts oxide proportions into CMAS coordinates and allows the visualisation of the results in 3D.

(b) *Interpreting CMAS diagrams.* For a projection to be useful in interpreting crystal–liquid equilibria it must be made from a phase which is present in

Table 3.9 Calculation scheme for the CMAS projection

	Wt.% oxide of rock	Molecular weight	Molecular proportions
SiO_2	46.95	60.09	0.7813
TiO_2	2.02	79.9	0.0253
Al_2O_3	13.1	101.96	0.1285
Fe_2O_3	1.02	159.69	0.0064
FeO	10.07	71.85	0.1402
MnO	0.15	70.94	0.0021
MgO	14.55	40.3	0.3610
CaO	10.16	56.08	0.1812
Na_2O	1.73	61.98	0.0279
K_2O	0.08	94.2	0.0008
P_2O_5	0.21	141.95	0.0015
TOTAL	100		

CMAS plotting parameters

C =	13.110
M =	19.265
A =	43.493
S=	43.493

Projection parameters for olivine projection into CS–MS–A using the equation of Cox et al. (1979)

Balance the equation $\text{rock} + p.\text{olivine} = x.CS + y.MS + z.A$

$C_cM_mA_aS_s + p.M_{57.3}S_{42.7} = x.C_{48.3}S_{51.7} + y.M_{40.1}S_{59.9} + z.A100$

Balancing C $48.3x = 13.11$

Balancing M $40.1y = 50.73p + 19.269$

Balancing A $100z = 19.261$

Balancing S $51.7x + 59.9y = 43.493 + 42.7p$

			%
CS	$x =$	0.271	27.95
MS	$y =$	0.507	52.21
A	$z =$	0.193	19.84
	sum =	0.971	

the melt; otherwise, the observed trends are meaningless. Second, the projection should not be made from a phase at an oblique angle to the projection plane, otherwise trends which are simply a function of the oblique projection can be misinterpreted and given geological significance where there is none. In addition, although the CMAS projection uses all of the chemical constituents of a rock analysis, the effects of individual components cannot be easily identified. It is important to note that small uncertainties in the chemical analysis may translate into large shifts in the projected compositions. This is particularly acute for uncertainty associated with Na_2O and SiO_2, where the direction of shift is parallel to an identified fractional crystallisation trend. Thus Presnall et al. (1979) and Presnall and Hoover (1984) make the point that some fractional crystallisation trends observed in ocean-floor tholeiitic glasses could be an artefact resulting from analytical uncertainties magnified by the projection procedure.

(c) *An expanded CMAS system.* More complex systems which are closer to natural samples include the addition of Na_2O and FeO and hence the CMASN and CMASF systems, respectively. Herzberg and O'Hara (2002) describe a more complete, expanded version of the CMAS plot which incorporates other elements and brings the projection more into line with the Yoder and Tilley type plots described above. They show that the addition of the components TiO_2, Cr_2O_3, FeO, MnO, Na_2O, K_2O and NiO can expand and contract liquidus crystallisation fields, although the replacement of MgO by FeO does not change crystallisation fields greatly.

In this expanded version of CMAS the diopside projection onto the plane olivine–anorthite–quartz requires all wt.% compositions be converted to mole % and any Fe_2O_3 combined with diopside so that the precise point of projection is diopside + Fe_2O_3 + $Na_2O.Si_3O_6$ + $K_2O.Si_3O_6$. The projection coordinates are calculated in the following way (Herzberg and O'Hara, 2002):

$$\begin{aligned}\text{olivine} = &-1.5TiO_2 + 0.5Al_2O_3 + 0.5Cr_2O_3 + 0.5FeO \\ &+ 0.5MnO + 0.5MgO - 0.5CaO - 0.5Na_2O \\ &+ 3.0K_2O + 0.5NiO\end{aligned}$$

$$\text{anorthite} = 1.0TiO_2 + 1.0Al_2O_3 + 1.0Cr_2O_3$$

$$\begin{aligned}\text{quartz} = &\ 1.0SiO_2 - 0.5Al_2O_3 - 0.5Cr_2O_3 - 0.5FeO \\ &- 0.5MnO - 0.5MgO - 1.5CaO \\ &- 3.0Na_2O - 3.0K_2O - 0.5NiO\end{aligned}$$

An example of the projection is given in Figure 3.27 (after Herzberg et al., 2007).

3.4.1.3 FeO–MgO Plots

Many mafic and ultramafic rocks have experienced olivine fractionation – both the removal or accumulation of olivine – and thus it can be difficult to establish the composition of the initial primary magma. In order to solve this problem Herzberg and O'Hara (2002) parameterised a large experimental database for mantle peridotites to explore the effects of

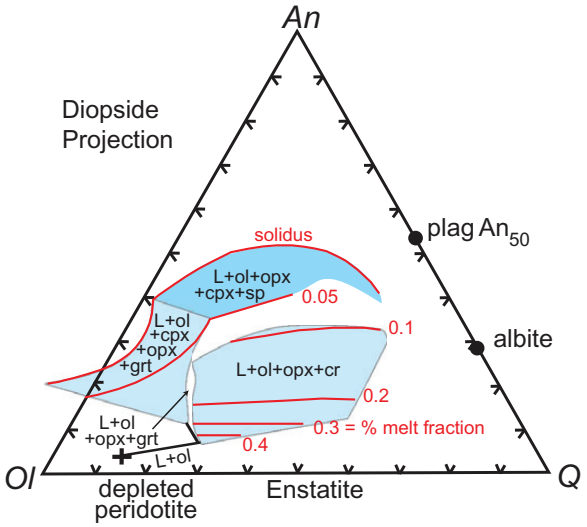

Figure 3.27 The diopside projection of the expanded CMAS system showing the projection of liquid compositions (mole percent) in equilibrium with depleted mantle peridotite from diopside + Fe_2O_3 + $Na_2O.Si_3O_6$ + $K_2O.Si_3O_6$ onto the plane olivine–anorthite–silica. Red lines show the contours of equal melt fractions (after Herzberg et al., 2007; with permission from John Wiley & Sons). L = liquid, ol = olivine, cpx = clinopyroxene, sp = spinel, grt = garnet, cr = chromite, plag = plagioclase.

equilibrium melting, fractional melting and peridotite source composition on the FeO and MgO content of potential primary mantle melts. This work has particular relevance to the study of magnesian basalts, MORB, picrites and komatiites and, when coupled with further experimental data, has the potential to provide information on the depth of melting and the mantle potential temperature of primary mantle melts (see Herzberg et al., 2007).

Herzberg and O'Hara (2002) showed that MgO and FeO in a mantle melt are both highly sensitive to differing source compositions, pressure of melting and degree of melting. For a range of different mantle compositions which include fertile and depleted mantle peridotite and Fe-rich and Fe-poor peridotite they calculated melt compositions which are in equilibrium with a harzburgitic residue (olivine + orthopyroxene) and with olivine, and show how they vary in MgO–FeO space with variations in the mode of melting (equilibrium melting and accumulated fractional melting), the degree of melting (the melt fraction) and the depth of equilibration (pressure in GPa). An example of their approach is shown in Figure 3.28a which is based on a fertile, low-Fe peridotite (KR-4003, Kettle River peridotite) with a composition very similar to that of the primitive mantle of McDonough (2014a) described in Table 3.2. In detail the approach employs the extrapolation of the results of melting experiments on a given peridotite composition using existing exchange coefficient data for olivine and orthopyroxene in mafic and ultramafic melts together with mass balance considerations.

In order to apply this parameterisation to a cogenetic suite of magnesian melts in equilibrium with olivine, Herzberg and O'Hara (2002) provide an 'inverse model'. This method consists of selecting a representative lava composition in which olivine has a composition in equilibrium with the melt. Olivine is then incrementally added or subtracted in 1 wt.% increments from the melt (see Herzberg and O'Hara, 2002, appendix 5). The suite of calculated compositions is transferred onto the FeO–MgO plot and compared with the range of liquid compositions computed (see Herzberg et al., 2007, appendix A). A unique solution is found when the liquid along the olivine addition–subtraction line displays a common melt fraction in FeO–MgO space and in either another two-dimensional plot such as MgO–SiO_2 or a projection in CMAS space (Figure 3.26). It is important to note that this method is sensitive to the accurate estimation of the Fe^{3+}/Fe^{2+} ratio of the melt.

Residual peridotite compositions are also a function of initial and final decompression pressures and Herzberg (2004) computed the fields of residual peridotites formed in equilibrium with basaltic melts using the experimental data of Walter (1998) for fertile peridotite KR-4003 and mass balance calculations. Model residue compositions from fractional melting are shown in Figure 3.28b for dunites (see the range of olivine compositions) and harzburgites (the field of olivine + orthopyroxene) and garnet and spinel lherzolites for initial melting pressures between 2 and 10 GPa and final melting pressures of between 0 and 5 GPa for a range of melt fractions.

3.4.2 Melting Mafic Crust

Experimental studies show that when mafic rocks melt, the composition of the melt tends to be felsic and this is particularly relevant when the melting takes place in the presence of water. However, since most mafic rocks are very low in potassium, the derived felsic melts tend to be more sodic than typical

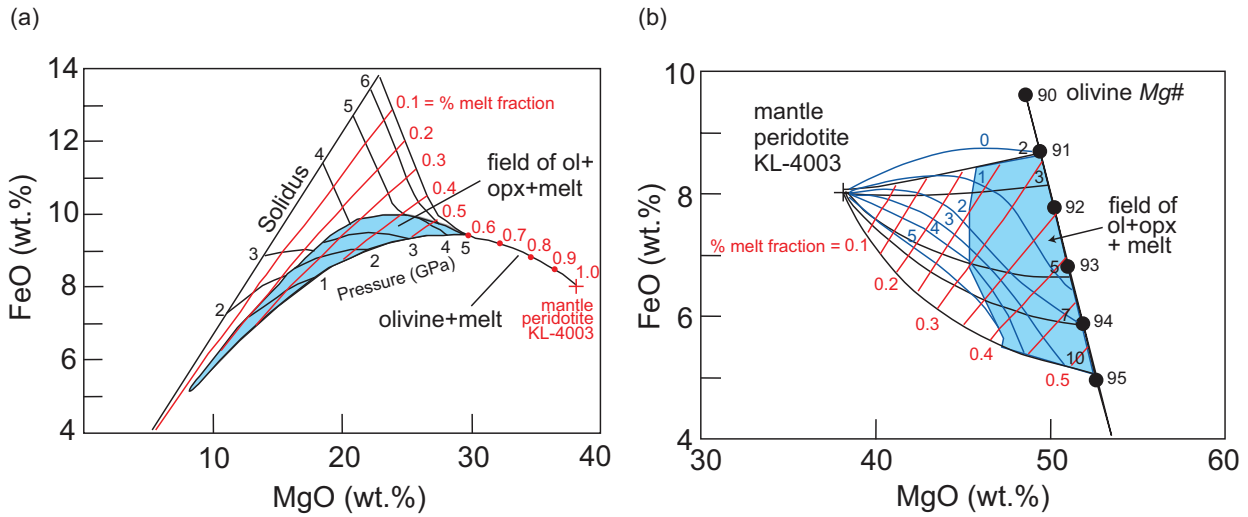

Figure 3.28 FeO–MgO plots for mantle melting showing how melt compositions vary according to the melt fraction, the pressure of initial melting and the final pressure of melting. (a) Partial melt compositions from the accumulated fractional melting of mantle peridotite KL-4003, a peridotite similar in composition to the primitive mantle. The shaded area shows the field of melts in equilibrium with a harzburgite residue (ol + opx + melt) and to the right are melts in equilibrium with olivine. Red lines show partial melt fractions and the black lines show the pressure of initial melting in GPa (after Herzberg and O'Hara, 2002; by permission of Oxford University Press). (b) The composition of model melt residues formed after the fractional melting of peridotite KL-4003. The olivine line shows the field for dunite residues, the shaded area shows the field of harzburgite residues (ol + opx + melt) and the area to the left is the field of spinel/garnet peridotite residues. The heavy black line shows the composition of olivine in dunite residues with the olivine *Mg#* values indicated. The black lines show the initial pressure of melting, the blue lines show the final pressure of melting, and the red lines show percent melt fraction (after Herzberg, 2004; by permission of Oxford University Press). ol = olivine, opx = orthopyroxene.

granites and fall in the compositional range of tonalites, trondhjemites and granodiorites. It is this observation which has led many geochemists to infer that the Earth's early continental crust which is predominantly tonalite–trondhjemite–granodiorite (TTG) in composition was primarily formed through the melting of mafic crust, either at the base of a thickened crust or in a subduction setting (Rollinson, 2007). Studies of oceanic plagiogranites also suggest that some may be the product of partial melting of mafic oceanic crust (see Rollinson, 2009).

The most common way to express the melting of mafic rocks is on the 'granite' normative *An–Ab–Or* diagram described in Section 3.2.2. Rock compositions are most often recalculated using the CIPW norm and the *An–Ab–Or* components recast as 100%, then plotted on the ternary diagram as outlined in Section 3.2.2. This is illustrated in Figure 3.29 which shows the locus of calculated compositions from the water-saturated melting of an enriched Archaean tholeiite. These compositions were calculated from the results of thermodynamic equilibrium modelling in the ten-component NCKFMASHTO system using the THERMOCALC software of Powell and Holland (1988). In detail the results of experimental studies vary quite widely, not just as a result of pressure and temperature of melting, but also as a consequence of the extent to which water is included in the melting process and the chemical composition of the basaltic starting material. A more extensive range of felsic melt compositions produced in basalt melting experiments is given in Johannes and Holz (1996).

3.4.3 Melting Felsic (Continental) Crust

Classical studies in the 1950s sought to understand the origin of granitic crust in terms of the melting behaviour of potassic granites. Experiments were constructed to understand the behaviour of granites and rhyolites during their initial melting or final stages of

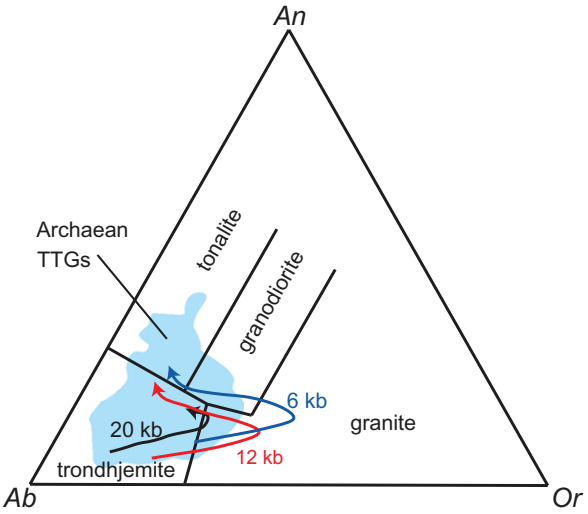

Figure 3.29 The normative *An–Ab–Or* plot with compositional fields of Barker (1979). Calculated compositions from water-saturated melting of an enriched Archaean tholeiite with increasing temperature (arrow) from the solidus at 600–700°C to 1000°C (head of arrow) for three different pressures (6, 12 and 20 kb). The results are compared with the compositional field of an Archaean tonalite–trondhjemite–granodiorite (TTG) suite. Diagram after Palin et al. (2016).

crystallisation in which the major part of the rock compositions could be reduced to the normative minerals quartz, albite and orthoclase. In recent decades the approach has become different, for we now assume that felsic rocks in general, and granites and rhyolites in particular, are for the most part the product of partial melting of pre-existing sialic crust such as metamorphosed sediments or pre-existing granites or 'granitic' gneisses. In addition, some felsic rocks are the product of the partial melting of mafic rocks, as discussed in Section 3.4.2, and in rare cases the product of crystal fractionation of mafic rocks. This has led to some new questions about the genesis of granitic rocks. First is the question of the protolith: What melted? Second, what were the melting reactions which controlled the composition of the melts that were produced (e.g., Weinberg and Hasalova, 2015)? Pertinent to this discussion is the extent to which water and other volatiles facilitated or inhibited the partial melting process. Was the melting process 'dry' or was it facilitated by the presence of water, supplied either from the breakdown of hydrous phases such as the micas and amphiboles in the protolith or from an external supply? Finally, to what extent is a given felsic rock composition representative of a melt? In the case of glassy rocks or melt inclusions the answer is straightforward, but it is possible that many granitic rocks contain restitic materials from their source which did not melt. Some granites therefore may contain 'parental' phenocrysts, or *xenocrysts*, which will distort the rock composition from that of a primary melt.

3.4.3.1 The Normative Albite–Orthoclase–Quartz Diagram: The 'Granite System'

In 1958 Tuttle and Bowen demonstrated a marked coincidence between the compositions of natural rhyolites and granites containing more than 80 wt.% normative albite, orthoclase and quartz and the normative compositions of experimentally determined minima and eutectics in the system albite–orthoclase–quartz–H_2O. This system is sometimes known as the *haplogranite* system. Their observations provided a way for igneous petrologists to attempt to correlate experimental information with analytical data projected into the system $Ab–Or–Q–H_2O$. Tuttle and Bowen (1958) and subsequent workers determined the compositions at which the phases quartz, orthoclase and albite coexist with a water-saturated melt at a variety of pressures (Table 3.10) and plotted their results as a projection onto the anhydrous base of the $Ab–Or–Q–H_2O$ tetrahedron. The plotting procedure requires three steps:

1. Calculation of the CIPW norm from the chemical analysis
2. Summation of the normative values of albite, orthoclase and quartz
3. Recasting of these values as a percentage of their sum.

These values are plotted on a ternary diagram. The results of these experiments show that the quartz–alkali feldspar boundary moves away from the quartz apex with increasing pressure from 1 to 10 kb (Figure 3.30a). Accompanying this expansion is the increased solubility of water in the melt (see Table 3.10). A lesser expansion is observed between 10 and 30 kb (Figure 3.23b). At approximately 3.5 kb and 660°C the quartz–alkali feldspar field boundary intersects the crest of the alkali feldspar solvus and the liquid at this point coexists with quartz, orthoclase and albite (Merrill et al., 1970). At 30 kb the assemblage is coesite, sanidine hydrate and jadeiite. Thus, a direct comparison can be made between

Table 3.10 Plotting coordinates of minima and eutectics in the granite system

Pressure (kb)	Temperature (°C)	Composition (wt.%)				H_2O (wt.%)	X H_2O		Reference
		Ab	*Or*	*Q*					
SYSTEM: ALBITE–ORTHOCLASE–QUARTZ–H_2O									
0.001	990	33	33	34		0.0	1.00	Minimum	Schairer and Bowen (1935)
0.500	770	30	30	40		3.0	1.00	Minimum	Tuttle and Bowen (1958)
1.000	720	33	29	38		4.4	1.00	Minimum	Tuttle and Bowen (1958)
2.000	685	39	26	35		6.5	1.00	Minimum	Tuttle and Bowen (1958)
2.000	685	39	25	36		6.5	1.00	Minimum	Holz et al. (1992)
2.000	775	36	29	35		3.6	0.70	Minimum	Holz et al. (1992)
2.000	830	34	31	35		2.5	0.50	Minimum	Holz et al. (1992)
3.000	665	42	25	33		8.3	1.00	Minimum	Tuttle and Bowen (1958)
4.000	1000	32	34	34		0.0	0.00	Minimum	Steiner et al. (1975)
3.923	665					9.7	1.00	Eutectic	Tuttle and Bowen (1958)
4.000	655	47	23	30		9.9	1.00	Eutectic	Steiner et al. (1975)
5.000	640	50	23	27		11.0	1.00	Eutectic	Luth et al. (1964)
5.000	645	47	22	31		11.0	1.00	Eutectic	Holz et al. (1992)
5.000	735	43	25	32		4.0	0.85	Minimum	Holz et al. (1992)
5.000	790	40	28	32		3.0	0.70	Minimum	Holz et al. (1992)
5.000	756	43	30	27		4.1	0.50	Minimum	Ebadi and Johannes (1991)
5.000	990	35	33	32		1.0	0.07	Minimum	Becker et al. (1998)
8.000	1050	37	34	29		1.0	~0.1	Minimum	Holz et al. (1992)
10.000	620	56	21	23		17.0	1.00	Eutectic	Luth et al. (1964)
10.000	1070	26	45	29		0.0	0.00	Minimum	Huang and Wyllie (1975)
20.000	630	63	19	18		21.0	1.00	Eutectic	Huang and Wyllie (1975)
30.000	680	67	18	15		24.5	1.00	Eutectic	Huang and Wyllie (1975)
SYSTEM: ALBITE–ORTHOCLASE–QUARTZ–ANORTHITE–H_2O									
1	730	32	29	39	An_3 plane	nd		Piercing point	James and Hamilton (1969)
1	745	22	36	42	An_5 plane	nd		Piercing point	James and Hamilton (1969)
1	780	11	42	47	$An_{7.5}$ plane	nd		Piercing point	James and Hamilton (1969)
SYSTEM: ALBITE–ORTHOCLASE–QUARTZ–H_2O–F									
1	690	45	26	29	1% F	ca 4.0		Minimum	Manning (1981)
1	670	50	25	25	2% F	ca 4.0		Minimum	Manning (1981)
1	630	58	27	15	4% F	ca 4.0		Eutectic	Manning (1981)

Note: nd = not determined.

experimentally determined phase boundaries and natural rock compositions. A synthesis of much of the relevant experimental work is given in the text by Johannes and Holz (1996) and a summary of the locus of the minima and eutectics for the water saturated system is given in Figure 3.30b.

Many experimental studies following the early work of Tuttle and Bowen (1958) focussed on the effect of water on melting conditions in the haplogranite system – in particular, melting under water-undersaturated conditions. The results summarised in Table 3.10 and Figure 3.30 show two main effects: (i) the position of the cotectic curve does not alter significantly, but the temperature of melting increases as melting approaches dry conditions and (ii) the minimum shifts towards the quartz–orthoclase boundary and the relative volume of albite expands at the expense of orthoclase as the volume of quartz remains constant (Figure 3.30b). More recent studies show a similar, although more extreme shift, accompanying the presence of NaCl–KCl brines during melting (Aranovich et al., 2013).

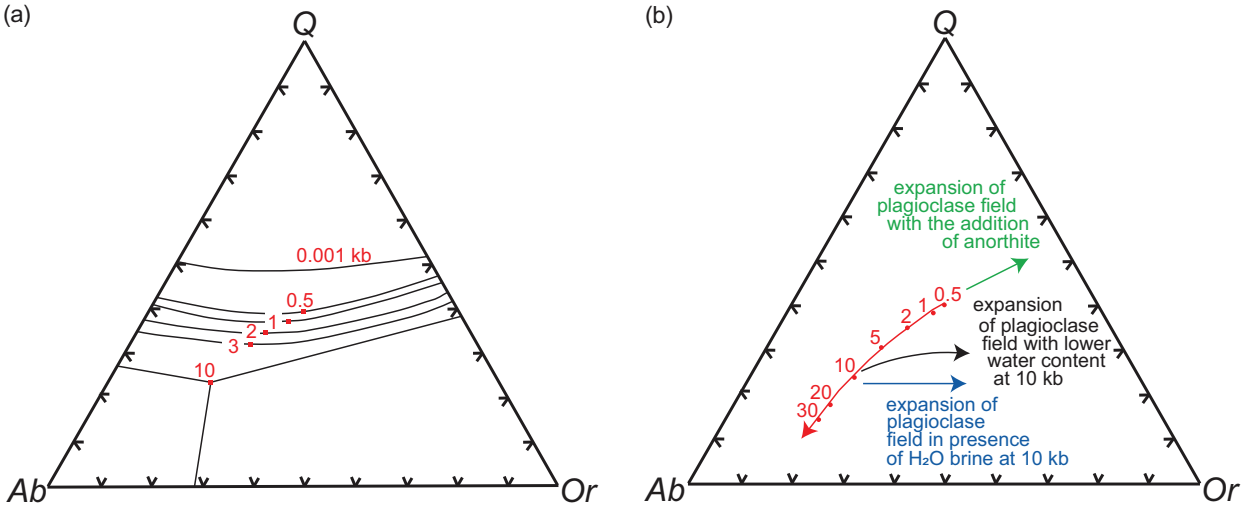

Figure 3.30 The haplogranite system. (a) Cotectics, minima and eutectics (red squares) for the water-saturated haplogranite system (*Q–Ab–Or–H₂O*, wt.%) at a range of pressures (after Blundy and Cashman, 2001; adapted by permission from Springer-Nature). (b) Minima and eutectics in the *Q–Ab–Or–H₂O* system projected from H_2O onto the plane *Ab–Q–Or* for 0.5–30 kb pressure (red circles). Also shown are the trajectories for undersaturated melts at 10 kb (black arrow), melts in equilibrium with H_2O-brines (blue arrow) and the expansion of plagioclase phase volume with the addition of anorthite to the system (green arrow), after Aranovich et al. (2013). Data for water-saturated system at 1 kb from James and Hamilton (1969). Data summarised in Table 3.10.

The addition of anorthite to the 'granite' system expands the phase volume of plagioclase and shifts compositions into the granodiorite and tonalite fields. This was investigated by James and Hamilton (1969) at 1 kb, who found that the position of the piercing point minimum shifts towards the quartz–orthoclase boundary of the projection with increasing anorthite, indicating an increase in the primary phase volume of plagioclase (Figure 3.30b).

Petrologists have used the haplogranite system to explore the processes of crustal differentiation during anataxis and the genesis of plutonic felsic rocks, as well as the ascent and crystallisation of felsic volcanic rocks. For example, Blundy and Cashman (2001) used glass compositions preserved in dacitic magmas from Mount St Helens to distinguish between ascent-driven and cooling-driven crystallisation. Their work supports a view of polybaric fractional crystallisation, indicating that there are limits to the use of isobaric experiments on their own. Cesare et al. (2015) and Acosta-Vigil et al. (2017) used melt inclusion data, combined with experimental diffusion studies of granitic melts plotted relative to experimentally determined phase boundaries in the haplogranite system, in order to explain the processes of partial melting in the middle and lower continental crust.

3.4.3.2 Partial Melting of Crustal Rocks

Experimental studies of crustal melting focus on the melting of meta-sediments (pelites and meta-greywackes) and pre-existing volcanic and plutonic felsic rocks and their gneissose equivalents. The results of these studies are typically plotted on the normative wt.% 'granite' *An–Ab–Or* diagram (Section 3.2). Typically, crustal melting is facilitated by the presence of water derived during the dehydration of the protolith (dehydration melting) or from water fluxing (fluid-present or water-present melting). Weinberg and Hasalova (2015) provide a helpful review of the physical and petrological processes which are involved and summarise a series of relevant experimental studies with melt compositions plotted on the normative *An–Ab–Or* diagram. They show that during water-undersaturated melting conditions (dehydration melting) melt compositions are more potassic and plot in the granite and granodiorite fields, whereas water-saturated melting produces more sodic compositions which plot in the trondhjemite field (see Figure 3.31 for a compilation of similar results).

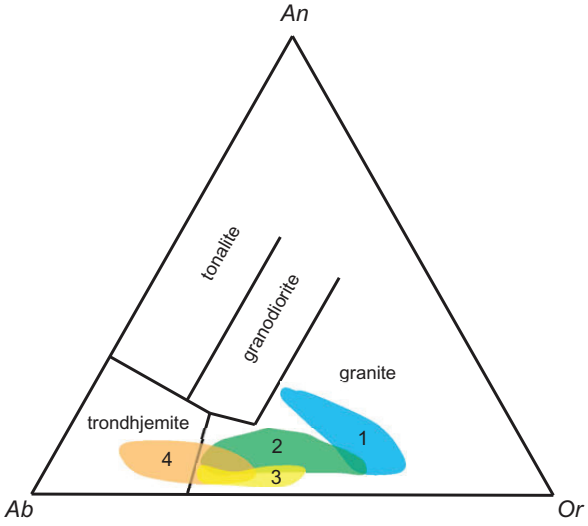

Figure 3.31 Normative anorthite–albite–orthoclase (wt.%) granite classification diagram of Barker (1979) showing melt fields for felsic igneous rocks and metasediments. 1: Dehydration melting of biotite gneiss (at 3–15 kb, 875–1000°C) (Patino Douce and Beard, 1995); 2: vapour-absent melting of tonalite at ultra-high pressures (at 15–32 kb, 900–1150°C) (Patino Douce, 2005); 3: dehydration melting of muscovite schist and muscovite biotite schist (at 6–10 kb, 750–900°C) (Patino Douce and Harris, 1998); 4: water-fluxed melting of muscovite schist (at 6–10 kb, 700–750°C) (Patino Douce and Harris, 1998).

3.4.4 What Melted?

Establishing the nature of the protolith of granite requires a full range of geochemical analyses including major and trace elements, radiogenic isotopes and sometimes stable isotopes. For this reason, major element data on their own can yield only a preliminary indication of the nature of a granitic source – nonetheless, these data can be useful. The two approaches outlined here include the aluminium-saturation index (Frost and Frost, 2008) and the Al–Fe–Mg–Ti–Ca diagrams of Patino Douce (1999).

3.4.4.1 The Aluminium Saturation Index (ASI)

The aluminium saturation index is defined in Section 3.2.4. As summarized there, peraluminous rocks contain more Al than is necessary to make feldspars and this excess Al may show itself as normative corundum (Zen, 1988), as phases in granites such as muscovite and biotite, or if the rock is strongly peraluminous, as one of the aluminosilicates, garnet or cordierite. Rocks with excess Al imply a clay-rich protolith and so might have had a metasedimentary source. Metaluminous rocks with ASI < 1.0, but molecular Na + K < molecular Al, are likely to have an excess of Ca and so may contain calcic phases such as hornblende or clinopyroxene. It is sometimes helpful to make a bivariate plot showing changing ASI versus SiO_2 (as illustrated in Figure 3.9).

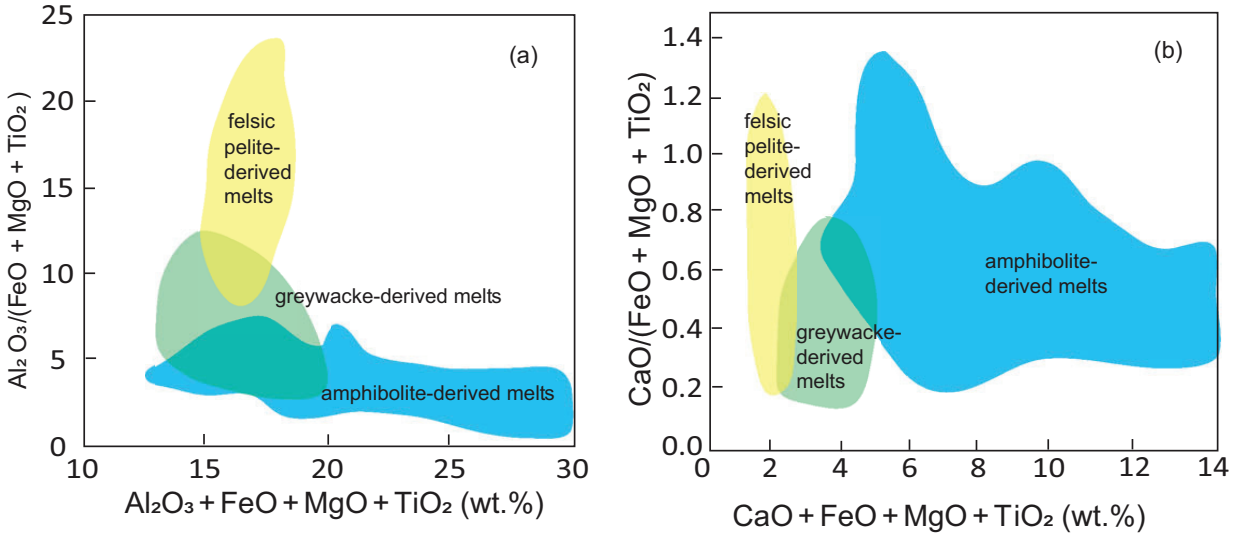

Figure 3.32 (a) $Al_2O_3/(FeO + MgO + TiO_2)$ versus $(Al_2O_3 + FeO + MgO + TiO_2)$ and (b) $CaO/(FeO + MgO + TiO_2)$ versus $(CaO + FeO + MgO + TiO_2)$ plots showing the fields of partial melts derived from felsic pelites, greywackes and amphibolites. All oxide values are wt.%. Experimental data from Patino Douce (1999).

3.4.4.2 Al–Fe–Mg–Ti–Ca Diagrams

Experimental studies by Patino Douce (1999) show that there are compositional differences between melts of pelites, greywackes and amphibolite in Al–Fe–Mg–Ti–Ca–oxide space. This work is the result of a series of dehydration melting experiments on fertile source rocks containing either biotite and or muscovite in the case of pelites and psammites, and hornblende in the case of amphibolites. Patino Douce's (1999) fields for partial melts of felsic pelites, psammites and amphibolites show how pelite-derived melts are more aluminous than psammite-derived melts, which in turn are more aluminous than melts from amphibolite (Figure 3.32a). Amphibolite-derived melts are also enriched in FeO, MgO and CaO, relative to pelitic and psammitic melts (Figure 3.32b).

4 Using Trace Element Data

4.1 Introduction

A trace element may be defined as an element which is present in a rock in concentrations of less than 0.1 wt.%, that is, less than 1000 parts per million (ppm). This means that it is not normally a stoichiometric constituent of the minerals which make up the rock; rather, it substitutes for one of the major elements in the structure of a host mineral. As a consequence of their low abundances, trace elements do not influence the chemical or physical properties of the system. There are, however, some limitations to this definition, for in igneous rocks the elements K and P behave as trace elements in mid-ocean ridge basalts, whereas in granites they form discrete minerals such as K-feldspar and, in the case of P, apatite or monazite. Unlike the major elements whose concentrations in the Earth's crust vary over a relatively narrow range, the range of trace element concentrations may be several orders of magnitude.

As analytical methods have improved in both the range of elements that can be analysed and in the precision that their concentrations can be measured, trace element studies have become a vital part of modern petrology. This is because of the following:

1. Trace elements are more sensitive to geochemical processes than major elements and are therefore better at discriminating between petrological processes.
2. Their great chemical diversity coupled with the fact that different elements behave in different ways permits a wide range of possible processes to be assessed.

Thus, one of their principal uses is in the identification of geochemical processes. Particularly important is the fact that there are mathematical models to describe trace element distributions which allow the quantitative testing of petrological hypotheses. These are most applicable to processes in magmatic systems which are controlled by crystal–melt or crystal–fluid equilibria, but are also relevant to the processes involved in the formation of meteorites, sediments and ore deposits.

In this chapter we first develop some of the theory behind the distribution of trace elements and explain the physical laws used in trace element modelling. Then various methods of displaying trace element data are examined as a prelude to showing how trace elements might be used in identifying geological processes and in testing hypotheses.

4.1.1 The Classification of Trace Elements According to Their Geochemical Behaviour

A frequently used classification of the elements based upon their geochemical behaviour was proposed by Goldschmidt (1937), often regarded as the 'father of geochemistry'. He proposed a fourfold classification, the nomenclature for which is still largely in current use:

Atmophile elements: those which typically form gases or liquids at the Earth's surface

Lithophile (the rock-loving elements): those which are found in silicate rocks and so are found in the silicate portion of the Earth

Chalcophile elements (copper-loving elements): those which have an affinity for a sulphide melt

Siderophile (the iron-loving elements): those which are concentrated in a metallic iron melt and so will be concentrated in the Earth's core.

To this quartet has been added (Lee, 2016):

Organophile elements: those which form or associate with organic compounds, in particular those which form organo-metallic complexes.

Apart from the term 'atmophile', which is almost never used, this nomenclature is still in use today albeit with slightly different meanings. It is important to note, however, that some elements will demonstrate more than one type of geochemical behaviour.

A further classification of elements which is widely discussed is the cosmochemical classification relating to processes of planetary accretion. In this case elements are classified according to their condensation temperature from gaseous to solid or liquid state during the cooling of a solar nebula. This classification is relevant

to the formation of meteorites and the earliest stages of Earth formation, and so is useful when discussing large-scale planetary features, although is less relevant when considering crust and mantle geochemistry. Elements are grouped as follows according to condensation temperature in kelvin (K):

- Highly refractory (>1700 K), to include Re, Os, W, Zr and Hf
- Refractory (1500–1700 K), to include Al, Sc, Ca and Ti
- Moderately refractory (1300–1500 K), to include Mg, Si, Cr, Fe, Co and Ni
- Moderately volatile (1100–1500 K), to include Cu, Ba and Mn
- Volatile (700–1100 K), to include Na, K, S and Rb
- Highly volatile (<700 K), to include Pb, O, C, N, H and noble gases

Trace elements are often studied in groups, and deviations from group behaviour or systematic changes in behaviour within the group are used as an indicator of petrological processes. The association of like trace elements also helps to simplify what can otherwise be a very unwieldy data set. Most geochemically important trace elements can be classified either on the basis of their position in the periodic table or according to their behaviour in magmatic systems, as discussed below.

4.1.1.1 Trace Element Groupings in the Periodic Table

Goldschmidt's geochemical classification of the elements presented above can be interpreted in terms of location within the periodic table. Here specific elemental groups are highlighted for their particular importance in trace element geochemistry (Figure 4.1). The most obvious in this respect are the lanthanides, elements with atomic numbers 57–71 (La to Lu), or the *rare earth elements* (REE) as they are usually called in geochemistry. Y also behaves in a manner similar to the REE. The *platinum group elements* (PGE, or platinum group metals, PGM) include elements with atomic numbers 44–46 – Ru, Rh, Pd – and 76–79 – Os, Ir, Pt. They are known as the *noble metals* if they also include Au. An expanded grouping of the PGE is known as the *highly siderophile elements* (HSE) and includes Os, Ir, Ru, Rh, Pt and Pd, together with Re and Au, which have some similar properties. This group can be used in understanding the large-scale processes associated with planetary accretion and differentiation, in particular, core formation, due to their affinity for metal relative

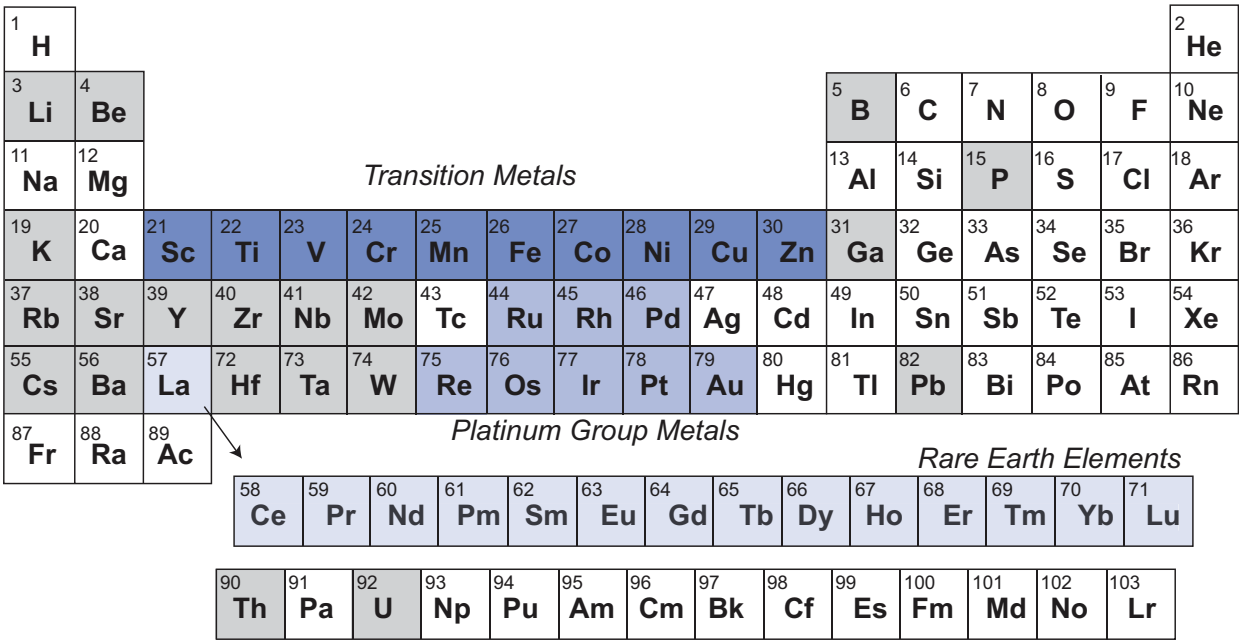

Figure 4.1 The periodic table of the elements. The three main groups of trace elements which are treated together in geochemistry because of their relative positions on the periodic table are highlighted. These are the elements of the first transition series (transition metals), the platinum group elements + Re and Au (platinum group metals) and the rare earth elements. Other trace elements important in geochemistry are shaded light grey.

to silicate minerals. The term *transition metals* (atomic numbers 21–30, Sc–Zn) is usually restricted to the first transition series and includes the two major elements Fe and Mn.

The elements in each of these respective groups have similar chemical properties and for this reason are expected to show similar geochemical behaviour. However, this may not always be the case, for geological processes can take advantage of subtle chemical differences within an elemental group and fractionate elements one from the other. Thus, one of the tasks of trace element geochemistry is to discover which geological processes may have this effect and to quantify the extent of particular processes.

4.1.1.2 Trace Element Behaviour in Magmatic Systems

When the Earth's mantle is melted, trace elements display a preference either for the melt phase or the solid (mineral) phase. Trace elements whose preference is the mineral phase are described as *compatible*, whereas elements whose preference is to remain in the melt are described as *incompatible*; in other words, they are incompatible in the mineral structure and will leave at the first available opportunity. In detail there are degrees of compatibility and incompatibility, and so trace elements may be described as moderately incompatible or highly incompatible. The degree of trace element incompatibility is quantified by the mineral-melt partition coefficient (see Section 4.2.1). Trace element incompatibility is also the basis for the ordering of elements in mantle normalised trace element diagrams (see Section 4.4). The degree of incompatibility will vary between melts of different compositions. For example, P is incompatible in mantle minerals and during partial melting will be concentrated in the melt. In granites, however, even though P is present as a trace element it is compatible because it is accommodated in the structure of the accessory mineral phases apatite and monazite.

It is sometimes helpful to subdivide the incompatible elements on the basis of their charge to size ratio. This property is often described as the field strength and may be thought of as the electrostatic charge per unit surface area of the cation. It is also described as the ionic potential of an element and is quantified as the ratio of the valence to the ionic radius, which is measured in picometres. Figure 4.2 shows a plot of ionic size versus charge for a range of trace elements. In addition, some major elements are shown to indicate where atomic substitutions most commonly occur. Small highly charged cations located in the lower right of the diagram are known as *high field strength* (HFS) cations (ionic potential > 0.02). The broadest definition of HFS elements (HFSE) includes the trivalent REE, Y, Sc, Th, U and the PGE, although more commonly the term is restricted to those elements that are tetravalent (Hf, Ti, Zr), pentavalent (Nb, Ta) and hexavalent (W, Mo). With the exception of Mo, the HFS elements are commonly *fluid immobile* and therefore their concentrations normally remain unchanged during weathering or metamorphism.

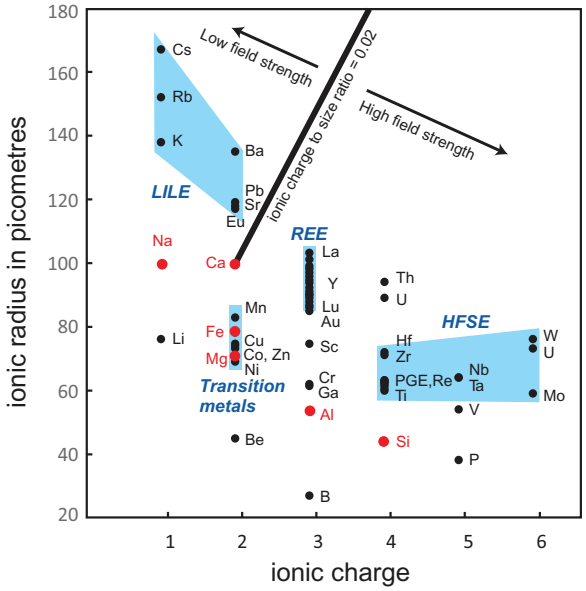

Figure 4.2 Plot of ionic radiius (measured in picometres, 10^{-12} m) versus ionic charge for incompatible trace elements of geological interest. Major elements (in red) indicate where trace element ionic substitutions will most readily occur. An ionic potential (charge to size ratio) of 0.02 subdivides the incompatible elements into low field strength (LFS) elements (also known as large ion lithophile elements, LILE) and high field strength elements (HFSE). The ionic radii are from Shannon (1976) and are quoted for six-fold coordination to allow a comparison between all elements.

Elements with ionic radii too large to fit into most silicate minerals and with a small charge are known as low field strength cations (ionic potential < 0.02). They are also known as the *large ion lithophile elements* (LILE) and are primarily the alkali and alkali earth elements (Figure 4.2). The term 'LILE' has been used in a number of different ways, but Chauvel and

Rudnick (2018) recommend that the term be restricted to lithophile trace elements having large radius to charge ratios and which have ionic radii greater than those of Ca^{2+} and Na^{1+} (100 and 102 picometers, respectively) – these are the largest cations commonly found in rock-forming minerals. By this definition, the list of LILE is restricted to K, Rb, Sr, Cs, Ba, Pb^{2+} and Eu^{2+}. LILE elements are commonly *fluid mobile elements*, and so their primary concentrations may change during post-solidus alteration.

Other important trace elements include the following:

- The small cations such as Li^{+}, Be^{2+}, B^{3+}, P^{5+} which are all moderately incompatible.
- Ga, which substitutes for Al and so is concentrated in Al-rich minerals in the crust; during partial melting of the mantle, Ga is incompatible in most phases, including garnet, but is compatible in spinel (Davis et al., 2013).
- Although not trace elements, volatiles with low solubility such as CO_2 in mafic melts may also behave as trace elements (Saal et al., 2002).

Some elements have very similar charge and size, and observing their geochemical behaviour can be particularly important. These include the following elements:

- Hf and Zr, and Nb and Ta; both element pairs are almost identical in size and charge and show very similar geochemical behaviour. Nevertheless, in some circumstances the element pairs are fractionated; thus, the ratios Hf/Zr and Nb/Ta are important geochemical parameters.
- U and Th have a similar charge and size and both are highly incompatible in magmatic systems but may be fractionated with Th being the more incompatible; U/Th may also be fractionated during fluid–rock interaction.
- Amongst the low field strength, large ion lithophile cations, Sr, divalent Eu and divalent Pb have almost identical ionic radii and charge.

A version of the ionic charge to size ratio diagram is given by Chauvel (2018) contoured for element incompatibility in the mineral clinopyroxene. The diagram shows that the most compatible elements are those with an ionic charge and size closest to the major cations in the host mineral (in this case, divalent Ca, Mg and Fe). Incompatibility increases with the difference in charge and size from that of the major cations, such that the monovalent LILE and the pentavalent HFSE are highly incompatible.

4.1.1.3 Trace Elements of Economic Significance

Some trace elements may have strategic importance in local economies and these have become known as the *critical metals*. These are metals that are economically important for industry but their supply may be limited because they can be obtained from only a few locations worldwide (Moss et al., 2011). They include elements such as the REE, the PGE, Ga, Sb, In, Be, Co, W, Nb and Ta. The critical metals are important in the electronics industry, and a subset of them, known as the *E-tech elements*, are important in the development of renewable energy technologies (Grandell et al., 2016). These elements include Co, Ga, In, Te, Li and the heavy REE (HREE). Some of these elements, such as indium (In, atomic number 49) and tellurium (Te, atomic number 52), are very rare and not well understood geochemically.

4.2 Physical Controls on Trace Element Distribution

Modern quantitative trace element geochemistry assumes that trace elements are present in a mineral in solid solution through substitution. The principal variables are the charge and size of the trace ion relative to the charge and size of the lattice site. These properties were recognised by Goldschmidt (1937), who through empirical observation proposed a series of qualitative rules to govern the priority which is given to ions with similar charge and size competing to enter a given crystal lattice. However, modern studies of trace element partitioning have shown that Goldschmidt's rules are not universally correct, for it is also necessary to also consider the energetics of the crystal lattice itself (Blundy and Wood, 2003; also see Section 4.2.1.2).

More recently, this approach has been quantified and trace element distributions are now described in terms of equilibrium thermodynamics. Trace elements may mix in their host mineral in either an ideal or a non-ideal way. Their very low concentrations, however, lead to relatively simple relationships between composition and activity. When mixing is ideal, the relationship between activity and composition is given by *Raoult's law*, that is,

$$a_i = X_i \tag{4.1}$$

where a_i is the activity of trace element i in the host mineral and X_i is its composition.

If the trace element interacts with the major components of the host mineral, the activity will depart from the ideal mixing relationship, and at low concentrations the activity composition relations obey *Henry's law*. This states that at equilibrium the activity of a trace element i in mineral j (a_i^j) is directly proportional to its composition:

$$a_i^j = k_i^j X_i^j \tag{4.2}$$

where k_i^j is the Henry's law constant – a proportionality constant (or activity coefficient) for trace element i in mineral j and where X_i^j is small. In fact, White (2013) suggests that adherence to Henry's law can be a helpful way of defining a trace element.

A detailed study by Drake and Holloway (1981) demonstrated that for elements that are homovalent (of identical charge) Henry's law seems to apply through a wide range of trace element concentrations. Similarly, Wood and Blundy (1997) showed that REE partitioning in clinopyroxene follows Henry's law behaviour even though the REE concentrations in clinopyroxene ranged from tens to thousands of ppm. However, where the substitutions are heterovalent and the mineral structure has to be electrostatically balanced either through a vacancy or an ion with a balancing charge, then Henry's law may not always apply. In this case, partitioning may depend upon the concentration of specific ions. For example, Grant and Wood (2010) showed this to be the case for Sc partitioning in olivine in which D_{Sc}^{ol} (the partition coefficient for Sc between olivine and melt) varied according to the concentration of Sc in the melt. Henry's law also ceases to apply at very high concentrations, although the point at which this takes place cannot be easily predicted and must be determined for each individual system. For example, Prowatke and Klemme (2006) demonstrated that Sm partitioning into titanite showed a dependence on the bulk composition of both the melt and the titanites themselves, and that Henry's law ceased to apply at bulk compositions containing several thousand ppm Sm. In the case where trace elements form the essential structural constituent of a minor phase, such as Zr in zircon, Henry's law behaviour does not strictly apply.

However, for the majority of trace elements in most rock-forming minerals, the relatively simple mixing relationships between trace elements and major elements in their host minerals means that the distribution of trace elements between minerals and melt can be quantified in a simple way, as outlined below.

4.2.1 Partition Coefficients

The distribution of trace elements between phases may be described by a partition coefficient or a distribution coefficient (McIntire, 1963). It is used extensively in trace element geochemistry and describes the equilibrium distribution of a trace element between a mineral and a melt. Where the partition coefficient is calculated as a weight fraction, typical for trace element geochemistry, it may also be known as the Nernst partition coefficient. The distribution coefficient is defined by

$$D_{\text{element}_i}^{\text{mineral-melt}} = C_{\text{element}_i}^{\text{mineral}} / C_{\text{element}_i}^{\text{melt}} \tag{4.3}$$

where $D_{\text{element}_i}^{\text{mineral-melt}}$ is the partition coefficient for element i between a mineral and a melt, and C is the concentration of the trace element i in ppm or wt.% in either the mineral or the melt. For example, if a plagioclase phenocryst in a glassy lava contains 500 ppm Sr and there is 125 ppm Sr in the glassy matrix of the lava, then $D_{Sr}^{\text{mineral-melt}} = 4.0$. The partition coefficient as defined above includes the Henry's law constants for trace element i in the mineral and the melt and is a function of temperature, pressure and composition of the melt, but is not controlled by the concentration of the trace element of interest nor by the concentration of other trace elements. Similar partition coefficients may be written for mineral–fluid or mineral–mineral distributions.

A mineral-melt partition coefficient of 1.0 indicates that the element is equally distributed between the mineral and the melt. A value of greater than 1.0 implies that the trace element has a 'preference' for the mineral (solid) phase and in the mineral–melt system under investigation is a *compatible element.* A value of less than 1.0 implies that the trace element has a 'preference' for the melt and is an *incompatible element.*

A *bulk partition coefficient* is a partition coefficient calculated for a rock for a specific element from the partition coefficients of the constituent minerals weighted according to their proportions. It is defined by the expression

$$D_i = x_1 D_1 + x_2 D_2 + x_3 D_3 + \ldots \tag{4.4}$$

where D_i is the bulk partition coefficient for element i, and x_1 and D_1, etc., are the percentage proportion and partition coefficient for element i in mineral 1, respectively. For example, in a rock containing 50% olivine, 30% orthopyroxene and 20% clinopyroxene,

the bulk partition coefficient (D) for the trace element i would be

$$D_i = 0.5\ D_i^{\mathrm{ol}} + 0.3\ D_i^{\mathrm{opx}} + 0.2\ D_i^{\mathrm{cpx}}$$

4.2.1.1 Measuring Partition Coefficients

Partition coefficients can be determined in natural systems from the analysis of minerals and their glassy matrix in rapidly cooled volcanic rocks. Many of the early mineral-melt partition coefficient measurements were obtained in this way by carefully analysing a clean mineral separate of unzoned minerals and their glassy matrix to obtain mineral-matrix or phenocryst-matrix partition coefficients (Philpotts and Schnetzler, 1970). More recently, this approach has been extended to the analysis of melt inclusions in phenocryst phases. However, there are a number of difficulties with the early approaches to trace element partition coefficient measurement using phenocryst–matrix pairs, not least the problem of ensuring equilibrium in natural samples. Other difficulties include the presence of mineral inclusions in samples where bulk minerals have been analysed.

An alternative to using natural systems is to use experimental data in which synthetic or natural starting materials are doped with the element of interest. This approach has the advantage that variations in temperature, pressure and oxygen fugacity can be more carefully monitored than in natural systems. However, in experimental studies of trace element partitioning it is important to attempt to establish Henry's law behaviour, for this then allows the results to be extrapolated to other compositions and used in petrogenetic modelling (Dunn, 1987). More recently, these approaches have been enhanced with the development of high-precision microbeam techniques which allow the precise measurement of low trace element concentrations to be made in situ in experimental charges. These methods include the field emission electron microprobe, laser ICPMS and ion-probe (SIMS) and are discussed in Section 1.4. A full discussion of potential sources of error in experimental partition coefficient determination is given by Neilson et al. (2017).

As the volume of experimental data has increased it has become clear that many different variables may influence the value of a partition coefficient, and these may be categorised into two groups. First, there are the effects of crystal chemistry. This is amenable to quantification using lattice strain theory as discussed in Section 4.2.1.2. A second major control on the value of trace element partition coefficients is the composition of the melt, based on the understanding that melt structure and degree of melt polymerisation will strongly influence the extent to which a melt might accommodate trace elements (see Section 4.2.1.3).

4.2.1.2 Calculating Partition Coefficients Using Lattice Strain Theory

To experimentally determine the partition coefficients for all trace elements in a range of melt compositions at different pressures and temperatures is an almost impossible task. In addition, it is often assumed that mineral-melt partition coefficients are constant during a given magmatic process, although thermodynamically this is most unlikely (Wood and Blundy, 2014). Thus, a number of workers (Beattie, 1994; Blundy and Wood, 1994, 2003; Wood and Blundy, 1997, 2014) have sought to develop predictive models of trace element partitioning based upon a thermodynamic extrapolation of experimental data. This approach has led to the development of 'lattice strain' models which are, in effect, the quantification of the qualitative ideas developed by Goldschmidt.

The lattice strain approach was developed by Nagasawa (1966) and Brice (1975) and is based upon the concept that trace ions in a crystal lattice can be treated as charged point defects in the structure. The disruption of the lattice around these point defects is minimised by relaxing the neighbouring ions and distributing the surplus elastic or electrostatic energy through the lattice. The basic equation, often known as the Brice equation, for a partition coefficient D for element i is

$$D_i = D_o\, exp\left(\frac{-4\pi E_s N_A\left(\frac{r_o}{2}(r_i - r_o)^2 + \frac{1}{3}(r_i - r_o)\right)^3}{RT}\right) \tag{4.5}$$

where

- D_i is the partition coefficient
- D_o is the strain-free partition coefficient, i.e., the partition coefficient for an ion the same size as that of the site and the same charge as i which enters the lattice without strain
- E_s is the effective Young's modulus of the site (the elastic response to lattice strain). Blundy and Wood (1994) showed that elasticity varies linearly with the charge of the cation.

N_A is Avogadro's number
r_o is the radius of the site
r_i is the radius of ion i
R is the gas constant
T is temperature in Kelvin

(Wood and Blundy, 2014)

Two tests of the lattice strain model demonstrate its utility. First, on a cation radius versus partition coefficient diagram of the type first pioneered by Onuma et al. (1968) and often known as an *Onuma diagram*, comparisons between measured partition coefficients and those calculated using the equation of Brice (1975) (Eq. 4.5) show very good agreement (Blundy and Wood, 1994) indicating that the model is appropriate for cations with a range of ionic charge in a number of different silicate phases (Figure 4.3). Second, the lattice strain model has a powerful predictive capability which allows partition coefficients to be calculated for elements where there are no

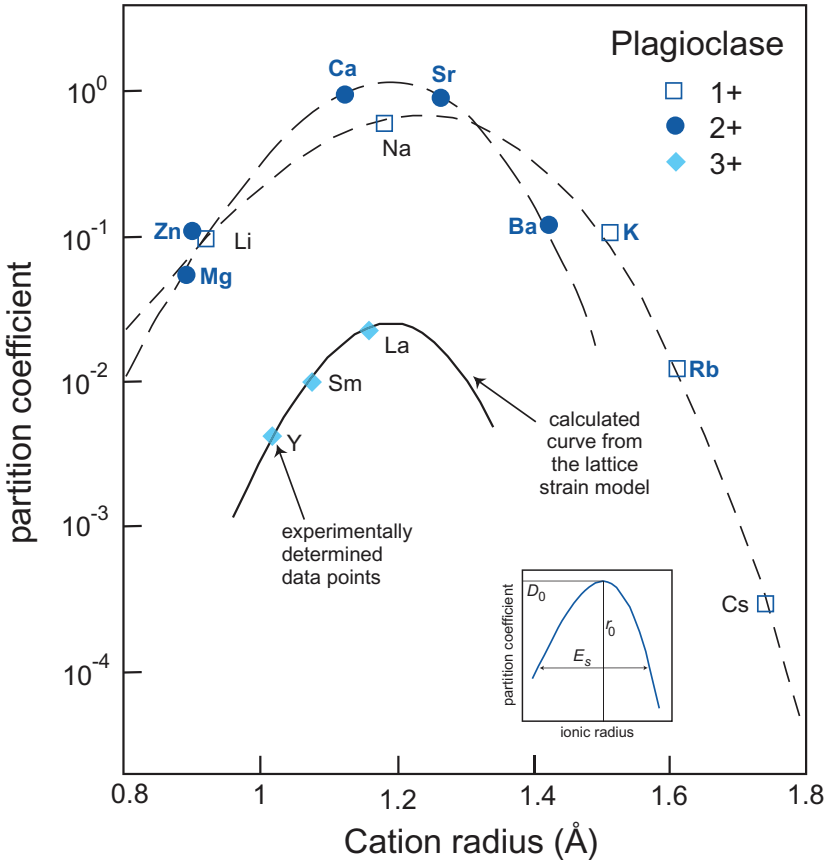

Figure 4.3 A plot of experimentally determined partition coefficients (expressed as log to the base 10) versus ionic radius (in angstroms: 10^{-10} m) for trace elements in plagioclase in equilibrium with silicate melt in the system diopside–albite–anorthite (after Wood and Blundy, 1997; adapted by permission of Springer-Nature). Diagrams of this type are known as Onuma diagrams. The curves drawn through the cations of equal valency are calculated from the lattice strain model (Eq. 4.5). The measured partition coefficients for mono-, di- and trivalent cations define separate parabolic curves which become tighter as the charge on the cation increases. This is due to the increase in the effect of Young's modulus on the site with increasing charge. The peak of the parabola corresponds to the 'best fit' ionic radius r_o and partition coefficient D_o which is the optimum size of the site in plagioclase (see inset). Partition coefficients decrease as the size of the site deviates either positively or negatively from r_o. Deviations from the anticipated parabolic pattern may reveal controls on trace element partitioning other than those of the size and charge of the cation. Onuma diagrams can also be used to estimate the size of a distribution coefficient when measurements have been made for a similar element. The inset diagram illustrates the three key parameters of the lattice strain model: r_o, the radius of the site; D_o, the strain-free partition coefficient; and E_s, the elastic response of that site to lattice strain as measured by Young's modulus. (After Wood and Blundy, 2014; with permission from Elsevier)

experimental data from those whose values are already known. Blundy and Wood (1994) calculated partition coefficients for Ra in plagioclase and clinopyroxene at a time when these were not experimentally determined. Subsequent experimental studies found excellent agreement between the measured and calculated values.

Thermodynamic theory indicates that the lattice strain parameters (D_o, r_o and E_s) are a function of key variables such as pressure, temperature and composition, and increasingly the trend is for the lattice strain parameters to be parameterised from a range of experimental studies. These equations can then be used to calculate partition coefficients for a specific set of conditions for a given group of trace elements. Wood and Blundy (1997) show how this methodology may be used to quantify partition coefficients for REE and Y in clinopyroxene and allows for the precise quantification of D_{REE} during the polybaric fractional melting of the mantle.

4.2.1.3 Physical Controls on the Value of Partition Coefficients in Mineral-Melt Systems

Thus far we have shown how ionic size and charge are important parameters in the partitioning of trace elements between minerals and melt and how these properties may be quantified from experimental data. We have also noted that consideration of mineral-melt equilibria from a thermodynamic standpoint indicates that partitioning is also governed by properties such as melt composition, temperature and pressure. In the section that follows we illustrate empirically the effects of these and other intensive variables on the size of mineral-melt partition coefficients.

(a) *Composition*. Two very significant studies from the 1970s demonstrate that trace elements show distinct preferences when partitioned between immiscible acid and basic melts (Watson, 1976; Ryerson and Hess, 1978), indicating that melt composition exerts a major control on trace element partitioning. Typically, the values of partition coefficients are higher in more siliceous melts, sometimes by as much as an order of magnitude, as illustrated with respect to the partitioning of the REE between hornblende and basaltic, intermediate and felsic melts (Figure 4.4a).

Much of this compositional dependence is related to structural changes in the melt phase and the increased polymerisation of the more silica-rich melts. There are two commonly used models for describing the degree of structural organisation in a melt. There is the NBO/T notation in which the ratio of non-bridging oxygen (NBO) ions is expressed relative to the proportion of tetrahedrally coordinated cations (T) ions (Si and Al). It has been shown that with increasing melt polymerisation there is a decrease in NBO ions which leads to fewer sites available in the melt to accommodate trace elements such as the REE. This gives rise to higher partition coefficients for the REE. In contrast, partition coefficients for cations with a low charge/size ratio decrease with increasing melt polymerisation due to their coupled substitution with Al (Bennett et al., 2004). The parameter NBO/T can be calculated using the method of Mysen (1988) and varies between 4.0 for an unpolymerised melt to less than 1.0 for a 3D network. This notation has been used as a measure of melt composition in trace element partitioning studies by Schmidt et al. (2006).

A slightly different notation is the X_{nf}/X parameter where X_{nf} is the sum of the molar fraction of the network-forming (nf) cations (Si and some Al) normalised to X, the sum of all the cations calculated on a molar basis. This has been used to assess changes in melt structure in amphibole trace element partitioning experiments by Tiepolo et al. (2001, 2007).

In addition to the importance of the silica content of melts on the magnitude of trace element partition coefficients, other elements may also play an important role. Bennett et al. (2004) show that the Na content of a melt in the Na_2O–CMAS system has an important effect on trace element partitioning between clinopyroxene and melt. In more sodic melts partition coefficients of the more highly charged (3^+ and 4^+) ions are higher by up to an order of magnitude relative to values in the 'pure' CMAS system. In addition, in some phases compositional controls on element partitioning may be exerted by 'local' crystal-chemical controls in specific mineral phases. Examples are given below in the mineral data for basalt partition coefficients (Section 4.2.1.5).

(b) *Temperature*. A good example of the control of temperature on partition coefficients comes from the compilation of experimental data by Bédard (2014) for calcic clinopyroxenes. These results show a strong negative correlation between D_{Ti}^{cpx} and temperature for both mafic and felsic melts, such that at higher temperatures Ti is incompatible in clinopyroxene, whereas at low temperatures it is compatible (Figure 4.4b). In a similar way, Sun et al. (2017) show that REE partitioning in plagioclase is positively correlated with temperature. Using the lattice

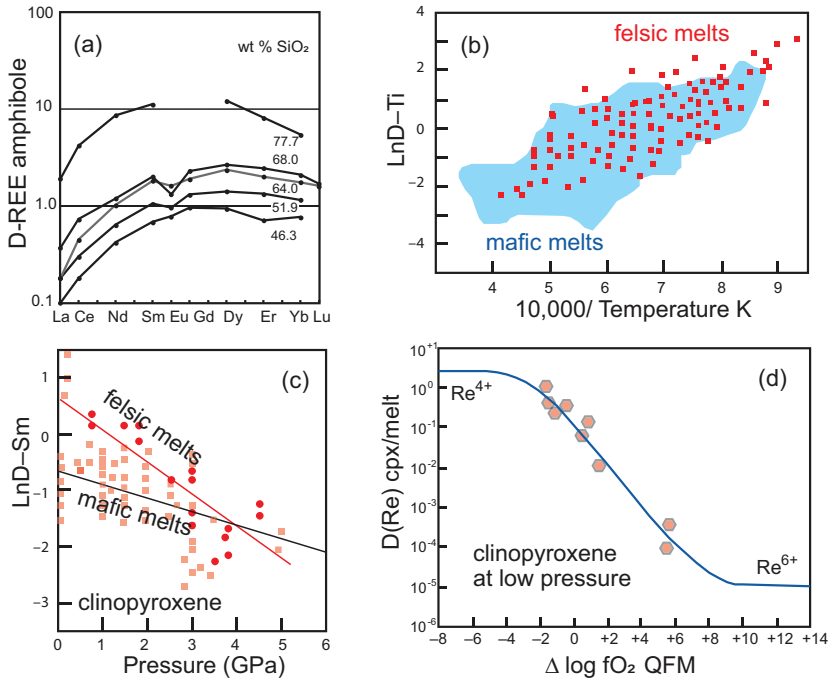

Figure 4.4 (a) Partition coefficients for REE between amphibole and silicate melt show an increase with increasing SiO_2 content of the melt (data from Tiepolo et al., 2007). In mafic melts (low silica content) light REE are incompatible and middle and heavy REE are compatible. In felsic melts (high silica content) all the REE are compatible. (b) Variation in partition coefficient for Ti in clinopyroxene with temperature. LnD–Ti increases with falling temperature (increasing 10,000/K). Mafic melts are represented by the shaded field and felsic melts by squares (after Bédard, 2014; with permission from John Wiley & Sons). (c) Variation in partition coefficient for Sm in clinopyroxene with pressure. LnD–Sm decreases with increasing pressure. The solid red line and circular data points are for felsic melts, the grey line and square data points are for mafic melts (after Bédard, 2014; with permission from John Wiley and Sons). (d) Variation in partition coefficients for Re in clinopyroxene with changing oxygen fugacity. At high oxygen fugacities the dominant ion is Re^{4+} which is compatible. At low oxygen fugacities the dominant ion is Re^{6+}, which is strongly incompatible. (After Mallman and O'Neill, 2007; with permission from Elsevier)

strain model and a large experimental database they parameterised the partition coefficients for mono-, di- and trivalent cations in the plagioclase M site. Their results show that the temperature term in their equations was highly significant for the trivalent ions (the REE and Y), whereas for the mono- and divalent cations it had a much smaller influence. They used their results to model plagioclase fractionation during the crystallisation of the Lunar magma ocean and show that during cooling from 1250 to 995°C there is an order of magnitude reduction in plagioclase–melt partition coefficients for the REE + Y (excluding Eu). D_{Ce}, for example, reduces from 0.0097 to 0.00066.

(c) *Pressure*. One of the more convincing demonstrations of the effect of pressure on partition coefficients is the work of Green and Pearson (1983, 1986) on the partitioning of REE between sphene and an intermediate silicic liquid. Within a small compositional range (56–61 wt.% SiO_2) at 1000°C they showed that there is a measurable increase in partition coefficient with increasing pressure from 7.5 to 30 kb. A more recent and petrologically important example is that of REE partitioning in clinopyroxene by Bédard (2014). He reviewed a voluminous amount of experimental data and showed that in both mafic and felsic melts D_{REE} decreases with increasing pressure (illustrated with D_{Sm} in Figure 4.4c). Given that clinopyroxene is the principal host of REE in mantle rocks this observation has important implications for melting at different depths in the mantle. Similarly, some HFSE

(notably Ti and Zr) show a similar property and in some amphiboles $D_{Ti,Zr}$ decreases with increasing pressure (Dalpe and Baker, 2000).

(d) *Oxygen fugacity and the importance of redox-sensitive trace elements*. In experimental studies oxygen fugacity (fO_2) is often buffered and this is normally reported relative to the quartz–fayalite–magnetite (QFM) oxygen buffer. fO_2 values are a function of temperature, and so reference is sometimes made to the QFM fO_2–T buffer curve. The QFM buffer tends to be used as a reference point since this is thought to approximate to the oxidation state of the upper mantle. However, in natural magmatic systems oxygen fugacity can vary by several orders of magnitude, and so the redox effect on trace element partitioning for heterovalent cations can be significant. Elements in this category include the first-row transition series elements, the PGE + Re and Eu, although experimental studies show that the most important redox-sensitive trace elements can be reduced to just V, Re, Eu and the major element Fe. As an example, the element Re may form the ions Re^{4+} and Re^{6+} in terrestrial magmas. As the Re ion becomes more oxidised there is a reduction in ionic size from 63 to 55 pm (10^{-12} m) (Shannon, 1976). This reduction in ionic size influences the partitioning of the element into specific sites in the mineral lattice. Mallmann and O'Neill (2007) showed that Re^{4+} is moderately compatible in garnet and clinopyroxene, slightly incompatible in orthopyroxene and spinel, and incompatible in olivine, but Re^{6+} is incompatible in all phases (Figure 4.4d). In a similar way the trace element V has the potential to form the ions V^{2+}, V^{3+}, V^{4+} and V^{5+} with the resultant reduction in ionic radius from 79 to 54 pm, for six-fold coordination, with increased oxidation (Shannon, 1976). Mallmann and O'Neill (2009) explored the change in the measured partition coefficients for D_V during mantle melting over a wide range of redox conditions (−13 to +11 fO_2 relative to the quartz–fayalite–magnetite oxygen buffer) – this covers the known redox conditions of the entire inner solar system. They showed that at low oxygen fugacity V is compatible in the phases olivine, pyroxene and spinel, whereas at high oxygen fugacity it is highly incompatible. The systematic change in partition coefficient with increasing oxygen fugacity for elements such V and Re means that their concentrations in basaltic melts will vary according to the redox conditions of mantle melting. These data have been inverted to calculate the redox state of the mantle in different tectonic settings (see Mallmann and O'Neill, 2007, 2009, 2013, 2014; Laubier et al., 2014).

The most redox-sensitive trace element in plagioclase is Eu. At low oxygen fugacities europium forms Eu^{2+} whereas at high fugacities it forms Eu^{3+} and the two species behave very differently in their partitioning between plagioclase and a basaltic melt, for the larger Eu^{2+} ion is more compatible than the smaller Eu^{3+} in plagioclase. Eu when divalent follows Sr, whereas the trivalent oxidised form follows the REE (Drake and Weill, 1975; Aigner-Torres et al., 2007). The net result of this is that the partitioning behaviour of Eu may depart from that of the other REE leading to an Eu anomaly in the REE pattern.

(e) *Water content of the melt*. The addition of water to a silicate melt has two opposing effects on partition coefficients. First, since the presence of water lowers the crystallisation temperature of a melt, this may cause partition coefficients to *increase*, but, second, the presence of water may the lower the activity and activity coefficients of the trace components in the melt such that partition coefficients may *decrease* (Wood and Blundy, 2014). Gaetani et al. (2003) found that during the partial melting of hydrous peridotite clinopyroxene REE partition coefficients were lower than predicted. They attributed this reduction in D_{REE} to a change in the degree of melt polymerisation caused by the addition of water to the melt. In plagioclase Bédard (2006) noted that D_{Ti} and D_{REE} increase as the water content of the melt increases.

4.2.1.4 Selecting an Appropriate Partition Coefficient

It is clear from the foregoing discussion that selecting an appropriate partition coefficient is not simple given the large number of variables to consider. A further complexity is the observation that mineral-melt partition coefficients are not constant during differentiation processes, for as a melt differentiates the composition of the melt, the pressure and the temperature will all change (Wood and Blundy, 2014). Sometimes the effects of the different variables can be inter-related, as, for example, when the liquidus temperature of a melt is a function of composition as in the case for olivine in a magnesian melt. At other times the effects of two different variables may cancel each other out. An example would be the contrasting effects of increased pressure, which serves to increase the partition coefficient, and increasing temperature, which reduces it.

Given the important control of melt composition on the size of partition coefficients, Nielsen and Drake (1979) and Neilsen and Dungan (1983) sought to minimise the impact of this variable by considering melt composition as a two-lattice melt model. In this model, the melt is assumed to be made up of two independent lattices comprising the network-forming and the network-modifying cations and anions. Partition coefficients are then parameterised against complex functions of melt chemistry. However, as Bédard (2005) pointed out there are some difficulties with this approach. First, some cations can fulfil multiple structural roles within the melt. In addition, the parameterisation of *D*-values requires that the melt composition be known exactly, and while this might work in laboratory experiments it cannot always be applied to natural rock samples.

Given that not all trace element data is adequately parameterised, a more empirical approach is taken here. Tables of partition coefficients (Tables 4.1–4.4) have been compiled from the literature to illustrate 'indicative' partition coefficients. It is recommended that these are used as a *guide* in petrological modelling and should not be taken as definitive. For a particular petrological model, partition coefficients should be taken from experimental studies that most closely match those of the conditions being modelled. The partition coefficients tabulated here are organised by melt composition and are drawn from the huge wealth of experimental work on trace element partitioning now published.

Much of the older partition coefficient (Kd) data is summarised in the GERM (Geochemical Earth Reference Model) database collated by R. Neilson at https://earthref.org/KDD/.https://earthref.org/GERM/tools/tep.htm. This database includes partition coefficients for a range of mineral species hosted in a wide range of rock types and has the advantage of being searchable, and the results can be downloaded into an Excel spreadsheet. In addition to individual experimental studies, there are some helpful syntheses such as the special volume of *Lithos* edited by Austreheim and Griffin (2000). In addition, compilations of partition coefficient data for specific minerals include olivine (Bédard, 2005), plagioclase (Bédard, 2006), orthopyroxene (Bédard, 2007), clinopyroxene (Bédard, 2014), and amphibole Tiepolo et al. (2007).

The longer-term aim of trace element partitioning studies is that all the relevant variables should be parameterised. This will include the composition of the mineral host, the composition of the melt, pressure and temperature. The extent to which this has already been accomplished is summarised in the review by Wood and Blundy (2014).

4.2.1.5 Partition Coefficients in Basalts

Some indicative partition coefficients for the geologically important trace elements in minerals in equilibrium with basaltic melts are listed in Table 4.1. The compilation is based upon a range of sources outlined below. Some REE values are interpolated, and those associated with some minerals common in mafic melts are shown in Figure 4.5. In the discussion that follows the relevant experimental conditions are included where possible. Averages are calculated as median values.

(a) *Olivine.* Most partition coefficients for trace elements in olivine vary with the MgO content of the melt and with temperature, for the two variables are strongly correlated. Many of these partition coefficients have been parameterised by Bédard (2005). For the highly siderophile elements partition coefficients tend to vary as a function of fO_2 with an increase in D_i as fO_2 decreases (Righter et al., 2004). For the REE, partition coefficients increase with increasing Al in olivine and decrease with increasing pressure and with Fo content of the olivine (Sun and Liang, 2013).

Olivine–melt partition coefficients for Ti, V, Mn, Co and Ni are taken from the experimental study of Laubier et al. (2014) for MORB melts (MgO = 8.56 wt.%) using median values for experimental runs between 1150 and 1190°C, at 0.1 MPa (atmospheric pressure) and fO_2= QFM. Values for K, Cs, Pb, Th, U, Zr, Nb, Hf and Ta are from the parameterisation of Bédard (2005) for melts with 11 wt.% MgO. Values for Li, Be, Cu, Mo and Ga are also from the compilation of Bédard (2005). Values for the REE, Y, Sc, Sr and Ba are from Beattie (1994) using the recommended results for a komatiitic melt (experiment C10) as most appropriate for partial melting calculations. This experiment was conducted at 1495°C, at atmospheric pressure and at $\log fO_2 = -4.7$. Partition coefficients for the HSE Ru, Pd, Re and Au are from the experimental study of Righter et al. (2004) on a Hawaiian ankaramite (MgO = 9.75 wt.%) at atmospheric pressure and 1300°C, adjusted for the oxygen fugacity of natural systems. Os, Ir and Pt are from the compilation of Bédard (2005). Zn and Cr are from the GERM database.

Table 4.1 Mineral-melt partition coefficients for trace elements in basaltic melts

Atomic number	*Symbol*	*Name*	*Olivine*	*Orthopyroxene*	*Clinopyroxene*	*Garnet*	*Plagioclase*	*Ca-Amphibole*
3	**Li**	Lithium	0.198	0.200	0.200	0.022	0.2940	0.104
4	**Be**	Beryllium	0.248	0.016	0.047	0.003	0.5675	0.170
5	**B**	Boron	0.0055	0.018	0.036	0.0045	0.1860	0.010
19	**K**	Potassium	0.006845	0.0003	0.007	0.00061	0.2030	0.400
21	**Sc**	Scandium	0.1200	1.290	1.750	2.620	0.0160	4.940
22	**Ti**	Titanium	0.0096	0.759	0.380	0.290	0.0380	2.665
23	**V**	Vanadium	0.0896	0.856	2.900	3.600	0.0100	6.080
24	**Cr**	Chromium	1.180	3.520	8.100	2.010	0.0450	6.030
25	**Mn**	Manganese	1.632	1.410	0.895	0.865	0.0290	*nd*
27	**Co**	Cobalt	5.294	2.480	1.350	0.950	0.1490	*nd*
28	**Ni**	Nickel	24.010	7.380	2.600	5.100	0.1620	*nd*
29	**Cu**	Copper	0.1100	*nd*	0.360	0.575	0.1400	*nd*
30	**Zn**	Zinc	0.8300	*nd*	0.490	1.148	0.1300	*nd*
31	**Ga**	Gallium	0.1026	0.206	0.740	1.010	1.7000	*nd*
37	**Rb**	Rubidium	0.0007	0.003	0.010	0.0007	0.1140	0.090
38	**Sr**	Strontium	0.000138	0.0012	0.088	0.0074	1.6290	0.660
39	**Y**	Yttrium	0.007190	0.0950	0.670	8.5000	0.0371	1.325
40	**Zr**	Zirconium	0.008	0.0320	0.1115	0.7300	0.0010	0.370
41	**Nb**	Niobium	0.004	0.0013	0.0037	0.0055	0.0970	0.390
42	**Mo**	Molybdenum	0.1034	0.0039	0.014	*nd*	*nd*	*nd*
44	**Ru**	Ruthenium	1.0000	*nd*	2.400	*nd*	*nd*	*nd*
45	**Rh**	Rhodium	2.6960	*nd*	0.240	*nd*	*nd*	*nd*
46	**Pd**	Palladium	0.1000	*nd*	< 0.3	*nd*	*nd*	*nd*
55	**Cs**	Caesium	0.0007	*nd*	*nd*	*nd*	0.5960	0.030
56	**Ba**	Barium	0.000023	0.000006	0.0002	0.00037	0.2470	0.385
57	**La**	Lanthanum	0.000022	0.0008	0.086	0.0047	0.1630	0.200
58	**Ce**	Cerium	0.000045	0.0016	0.175	0.0179	0.0960	0.350
59	**Pr**	Praseodymium	0.000085	0.0032	0.289	0.0593	0.1320	0.610
60	**Nd**	Neodymium	0.000200	0.0056	0.470	0.170	0.0908	0.730
62	**Sm**	Samarium	0.000636	0.0150	0.810	0.870	0.1060	1.075
63	**Eu**	Europium	0.001200	0.0300	1.000	1.630	0.1005	1.130
64	**Gd**	Gadolinium	0.001800	0.0340	1.040	2.550	0.0502	1.370
65	**Tb**	Terbium	0.002750	0.0540	1.220	4.200	0.0500	1.390
66	**Dy**	Dysprosium	0.004000	0.0770	1.400	6.200	0.0293	1.405
67	**Ho**	Holmium	0.006430	0.1000	1.350	8.200	0.0250	1.360
68	**Er**	Erbium	0.0110	0.1200	1.340	9.600	0.0181	1.275
69	**Tm**	Thulium	0.0140	0.17	1.380	11.100	0.0150	1.200
70	**Yb**	Ytterbium	0.0188	0.2200	1.420	12.600	0.0110	1.050
71	**Lu**	Lutetium	0.0280	0.2200	1.160	13.700	0.0093	0.850
72	**Hf**	Hafnium	0.0080	0.0600	0.383	0.480	0.0100	0.680
73	**Ta**	Tantallum	0.0300	0.0025	0.0239	0.0215	0.0750	0.335
75	**Re**	Rhenium	0.010	0.180	0.200	0.100	*nd*	*nd*
76	**Os**	Osmium	0.53437	*nd*	0.010	*nd*	*nd*	*nd*
77	**Ir**	Iridium	0.42619	*nd*	*nd*	*nd*	*nd*	*nd*
78	**Pt**	Platinum	0.05140	*nd*	*nd*	*nd*	*nd*	*nd*
79	**Au**	Gold	0.10000	*nd*	*nd*	*nd*	*nd*	*nd*
82	**Pb**	Lead	0.0013	0.0013	0.009	0.00034	1.5920	0.095
90	**Th**	Thorium	0.0018	0.00002	0.013	0.0015	0.3050	0.020
92	**U**	Uranium	0.0013	0.00004	0.006	0.0104	0.0107	0.010

Notes: *nd*, no data

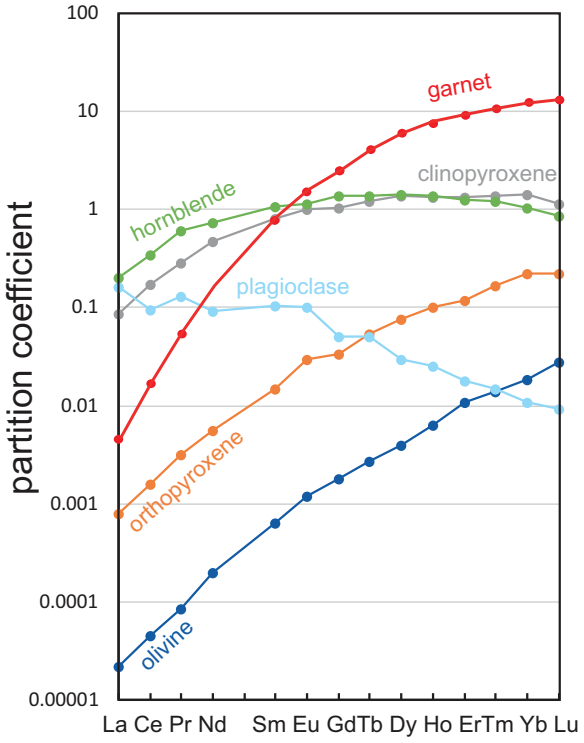

Figure 4.5 REE mineral-melt partition coefficients between the major silicate minerals and basaltic melts. (Data from Table 4.1)

(b) *Orthopyroxene.* Partition coefficient data for orthopyroxene in a basaltic melt for the REE, HFSE and Sr are from the experimental study of Green et al. (2000). This study shows that partition coefficients in orthopyroxene are strongly influenced by the Al content of the orthopyroxene. Average values were taken from experiments on a tholeiitic basalt ($Mg\# = 59$), conducted under hydrous conditions at 2.0–7.5 GPa and 1080–1200°C and a fO_2 between the Ni–NiO and magnetite–wustite buffers. Partition coefficients for Sc, Ti, V (at QFM) and Mn, Co, Ni, Ga are from the average experimental values of Laubier et al. (2014) in a MORB melt (MgO = 8.56 wt.%) at 1150–1190°C, 0.1MPa and fO_2 = QFM to NNO+2. Partition coefficients for B, Be and Li are from the experimental study of Brenan et al. (1998) on a basaltic andesite at 1000–1350°C at atmospheric pressure. Data for K, Rb and Ba are from the GERM database and Cr is for Cr^{3+} from Mallmann and O'Neill (2009), who show that chromium partition coefficients for orthopyroxene increase with increasing oxygen fugacity.

(c) *Clinopyroxene.* Bédard (2014) showed that there is significant crystal chemical control in trace element partitioning in clinopyroxene. For example, there is a positive correlation between D_{Ti} and the tetrahedral Al content of clinopyroxenes implying a coupled Ti–Al substitution. A similar pattern was observed for D_{Zr} and D_{Co} which also increase with increasing alkali content and silica content but decrease with increasing *Mg#* and CaO content (Bédard, 2014).

Here partition coefficient data for clinopyroxenes for the REE, HFSE and Sr are from the experimental study of Green et al. (2000) conducted on a tholeiitic basalt ($Mg\# = 59$), as described above for orthopyroxene. In these experiments both the water content and the temperature of the melt influence trace element partitioning, although the effect of water is greater than that of temperature such that partition coefficients are lower under hydrous conditions. Sr values are pressure-sensitive and D_{Sr} increases with increasing pressure. Partition coefficient values for the elements Mo, Ru, Rh and Pd are from the compilation of Bédard (2014) and Be, B, Sc, K, Ti, V, Cr, Mn, Ga, Rb, Re, Os, Pb, U and Th are from the GERM database; median values are used where there are multiple records.

(d) *Garnet.* Partition coefficient data for garnet for the REE, HFSE and Sr are from the experimental study of Green et al. (2000) on a tholeiitic basalt ($Mg\# = 59$), as described above for orthopyroxene. As noted, both the water content and the temperature of the melt influence trace element partitioning such that at lower temperatures partition coefficients increase whereas under higher water contents partition coefficients decrease. Thus, the two effects tend to cancel each other out. Partition coefficients for Li and K are from the experimental study of Gaetani et al. (2003) on the melting of hydrous peridotite at 1.2 GPa and 1185°C. Partition coefficients for B, Be, Sc, Ti, V, Ni, Rb, Ba, Cr, Mn, Co, Ni, Zn, Ga, Pb, Th and U are from the GERM database. Re is reported as Re^{4+} at the conditions of the QFM buffer after Mallmann and O'Neill (2007).

(e) *Plagioclase.* Trace element partitioning between plagioclase and a basaltic melt is strongly dependent on the An content of the plagioclase and most partition coefficients increase with decreasing An content (Blundy and Wood, 1991; Bindeman et al., 1998; Bédard, 2006; Tepley et al., 2010). In addition, the partition coefficients of a small number of elements (Zr, Fe, Eu and Cr) are sensitive

to fO_2 (Aigner-Torres et al., 2007). There is no significant temperature control (Bindeman et al., 1998).

Partition coefficient data for plagioclase for the LILE, HFSE and first transition series elements were selected from the experimental database of Aigner-Torres et al. (2007) for the partitioning between plagioclase ($An_{73–79}$) and MORB at 1200°C, atmospheric pressure and fO_2 = QFM. Additional data for B, Be, V, Co, Ni, U and the REE + Y were obtained from the experimental studies of Bindeman et al. (1998) and Bindeman and Davis (2000). These experiments are for a basaltic andesite at T = 1426–1572 K, in air, at atmospheric pressure with plagioclase compositions between An_{75} to $An_{77.2}$. Partition coefficients for Zn, Ga, Hf and Cu are from the GERM database.

(f) *Amphibole.* Trace element partitioning in amphibole is complex because of the number of different sites in the mineral lattice. There are three octahedral sites: M1, M2 and M3; an eight-fold M4 site occupied by Ca and Na; and a twelve-fold A-site occupied by Na and K or that may be vacant. The different sizes of these sites mean that they will exert different preferences for trace elements. Experimental studies show that partition coefficients in amphibole vary primarily as a function of the degree of melt polymerisation and are not strongly influenced by changes in P or T (Tiepolo et al., 2007). The effects of melt composition have been parameterised for the REE and Y as a function of X_{nf}/X (Tiepolo et al., 2007) (see Section 4.2.1.3). In addition, there are local crystal-chemical effects such as the Ca content (Wood and Blundy, 2014) and *Mg#* (Tiepolo et al., 2001), and for a few elements (Ti, Hf, Zr, Rb, Ba, La, Nd) oxygen fugacity also exerts a small effect (Dalpe and Baker, 2000).

The partition coefficient data listed here are for calcic-amphiboles and are from the review of Tiepolo et al. (2007). Experimental data were selected for melts in the range SiO_2 = 48.1–52.4 wt.% at temperatures and pressures between 950 and 1070°C and 0.2–1.4 GPa and at fO_2 = QFM − 2.

4.2.1.6 Partition Coefficients in Andesites

The partition coefficients for trace elements between rock-forming minerals and andesitic melts (57–63 wt.% SiO_2 as defined in the TAS classification) are shown in Table 4.2 and Figure 4.6. This compilation is based upon the range of sources outlined below. Some REE values are interpolated. Where possible the relevant experimental conditions are included. Averages are calculated as median values. Some data are from the GERM database. Early compilations for mineral–andesite partition coefficients are based upon phenocryst–matrix studies but are highly variable (Luhr and Carmichael, 1980; Gill, 1981). This is, in part, due to the range of melt compositions examined, the presence of mineral inclusions in the mineral separates analysed and the precision of the analytical methods used.

The olivine partition coefficients reported in Table 4.2 are from a single andesite (experimental melt compositions 56–60 wt.% SiO_2) in Dunn and Sen (1994); Be, B and Li are from Brenan et al. (1998); and other data are from the GERM database. Similarly, the *orthopyroxene* data represent three andesite samples (experimental melt compositions 56–61 wt.% SiO_2) from Dunn and Sen (1994) and the GERM database. The *clinopyroxene* REE and HFSE data are calculated from Klein et al. (2000) for a hydrous tonalitic melt (SiO_2 = 57.9 wt.%) at 900–1000°C and 1.5–3.0 GPa, Be, B and Li from Brenan et al. (1998) and the GERM database. As in the case of basaltic melts clinopyroxene REE partition coefficients are composition-dependant and vary according to the jadeite content of the pyroxene. Experimental studies show that *garnet* REE partition coefficients are strongly temperature-dependent with partition coefficients increasing with decreasing temperature Klein et al. (2000). For this reason, garnet REE and HFSE partition coefficients are taken from a single hydrous experiment in the study of Klein et al. (2000) in which the temperature is 950°C and pressure 1.5 GPa. The *hornblende* REE and HFS partition coefficients are from Klein et al. (1997) for a melt composition with 57.9 wt.% SiO_2; other data are from Brenan et al. (1995) and the GERM database. The partition coefficient data for *plagioclase* are averages from the four andesitic compositions studied by Dunn and Sen (1994) and from the GERM database, although, as already discussed, partition coefficients for plagioclase are in part a function of the An content of the plagioclase.

4.2.1.7 Partition Coefficients in Dacites and Rhyolites

Some indicative partition coefficients from published sources for the major rock-forming minerals in dacites, rhyodacites, rhyolites and high silica rhyolites are given in Table 4.3. These rocks have > 63 wt.%.

Table 4.2 Mineral-melt partition coefficients for trace elements in andesitic melts

Atomic number	*Symbol*	*Name*	*Olivine*	*Orthopyroxene*	*Clinopyroxene*	*Garnet*	*Plagioclase*	*Hornblende*
3	**Li**	Lithium	1.300	0.783	*nd*	*nd*	0.450	0.124
4	**Be**	Beryllium	*nd*	0.360	*nd*	*nd*	0.300	*nd*
19	**K**	Potassium	*nd*	0.014	0.011	0.010	*nd*	*nd*
21	**Sc**	Scandium	0.283	3.875	14.000	3.900	*nd*	10.550
22	**Ti**	Titanium	0.030	*nd*	*nd*	2.620	0.047	2.320
23	**V**	Vanadium	0.080	1.000	3.150	8.000	0.270	9.650
24	**Cr**	Chromium	5.3–34	21–143	30–245	22.000	(0.075)	1.59–60.5
25	**Mn**	Manganese	*nd*	7.300	4.500	*nd*	*nd*	0.680
27	**Co**	Cobalt	1.885	12.000	5.500	1.800	*nd*	1.77–6.1
28	**Ni**	Nickel	20.800	0.79–24	4.6–9	0.600	*nd*	10.000
29	**Cu**	Copper	2.200	0.190	0.660	*nd*	*nd*	11.600
30	**Zn**	Zinc	1.500	3.500	2.000	*nd*	*nd*	0.42–8.7
31	**Ga**	Gallium	0.250	0.320	0.470	*nd*	*nd*	nd
37	**Rb**	Rubidium	0.036	0.022	0.030	0.010	0.015	0.140
38	**Sr**	Strontium	0.020	0.005	0.280	*nd*	2.625	0.280
39	**Y**	Yttrium	0.045	0.343	2.000	11.000	0.024	2.500
40	**Zr**	Zirconium	0.010	0.031	0.290	0.530	0.001	0.260
41	**Nb**	Niobium	0.035	0.027	2.100	0.040	0.018	0.280
42	**Mo**	Molybdenum	0.111	1.323	*nd*	*nd*	*nd*	*nd*
55	**Cs**	Caesium	0.01–0.27	0.01–0.38	0.01–0.64	*nd*	0.038	0.01–0.5
56	**Ba**	Barium	0.020	0.115	0.068	*nd*	0.498	0.120
57	**La**	Lanthanum	0.008	0.002	0.099	0.028	0.119	0.120
58	**Ce**	Cerium	0.008	0.005	0.193	0.080	0.094	0.240
59	**Pr**	Praseodymium	0.010	0.005	0.290	0.130	0.072	0.420
60	**Nd**	Neodymium	0.011	0.019	0.420	0.222	0.065	0.630
62	**Sm**	Samarium	0.015	0.073	0.750	0.810	0.046	1.370
63	**Eu**	Europium	0.017	0.057	0.990	1.540	0.630	1.080
64	**Gd**	Gadolinium	0.016	0.140	0.910	4.590	0.040	1.490
65	**Tb**	Terbium	0.025	0.240	1.050	6.300	0.053	1.650
66	**Dy**	Dysprosium	0.031	0.260	1.200	9.000	0.025	1.770
67	**Ho**	Holmium	0.037	0.410	1.550	15.000	0.018	1.600
68	**Er**	Erbium	0.044	0.430	1.900	20.000	0.014	1.470
69	**Tm**	Thulium	0.071	0.645	1.400	22.000	0.012	1.300
70	**Yb**	Ytterbium	0.071	0.590	0.900	24.000	0.010	1.150
71	**Lu**	Lutetium	0.110	1.035	0.700	24.000	0.009	1.070
72	**Hf**	Hafnium	0.020	0.115	0.368	0.440	*nd*	0.430
73	**Ta**	Tantallum	0.065	0.049	0.430	0.080	0.069	0.270
82	**Pb**	Lead	0.014	*nd*	0.870	*nd*	$\gg$ 0.012	0.120
90	**Th**	Thorium	0.039	0.010	0.100	*nd*	$>$ 0.012	0.017
92	**U**	Uranium	0.057	0.012	*nd*	*nd*	0.012	0.008

Notes: *nd*, no data; values in parentheses are uncertain.

SiO_2 in the TAS classification. Compared with basaltic rocks, there are fewer modern experimental determinations of partition coefficient data for felsic rocks. Many published data sets are based upon phenocryst–matrix determinations and show some variability. In part this is because of the way partitioning behaviour is governed by melt structure and composition, but it also relates to other uncertainties with the matrix–phenocryst method discussed above. Data are drawn from a number of published sources supplemented with the compilations of Bacon and Druitt (1988) based upon rhyolites with 71 wt.% SiO_2 and that of Nash and Crecraft (1985) for high-silica rhyolites (71–76 wt.% SiO_2). The REE partition coefficients associated with some minerals common in felsic melts are shown in Figure 4.7.

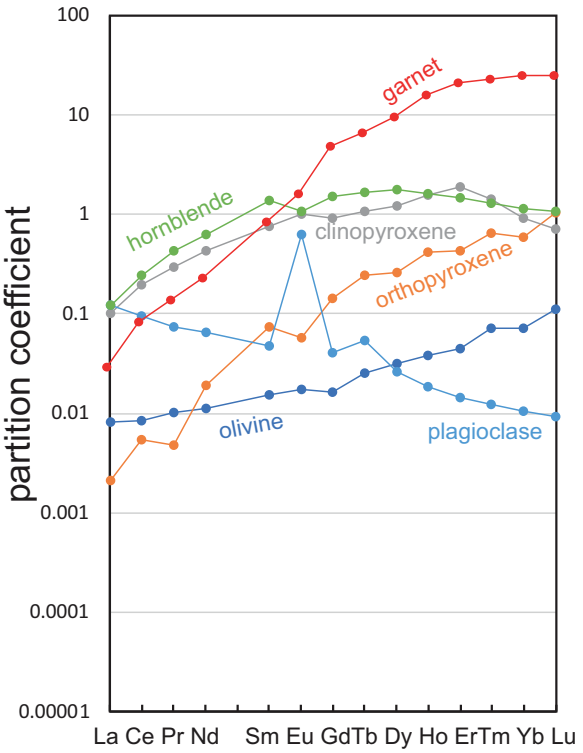

Figure 4.6 REE partition coefficients for the major silicate minerals in andesitic melts. (Data from Table 4.2)

Plagioclase partition coefficients for Li, Sr, Y, Zr, Nb, Ba, Hf and the REE are from Brophy et al. (2011). In this study phenocrysts in equilibrium with a rhyolitic partial melt in gabbro (SiO_2 = 72–73 wt.%) were analysed by ion microprobe. The partition coefficients reported are median values of multiple analyses. Data for the elements Ti, Mn, Zn, Cu and Pb are from the experimental study of Iveson et al. (2018) conducted at 810–860°C, 1.5–4.05 kb and oxygen fugacity NNO = −0.5 to +2 log units. Melt compositions have 73–75 wt.% SiO_2 (dry) and the plagioclase is $An_{39–59}$. Other values are from Bacon and Druitt (1988). It has already been noted that trace element partition coefficients for plagioclase are strongly dependent on the composition of the host mineral and on melt temperature (Sun et al., 2017). In particular, there is a strong relationship between the partition coefficients for Sr and Ba and the mole fraction of anorthite in plagioclase. Both elements are more compatible in albite than in anorthite (Blundy and Wood, 1991).

Partition coefficient data for *K-feldspar* are from the GERM database. REE values are based upon average values and the missing values estimated by interpolation. Partition coefficient data for more sodic alkali feldspars are given by Streck and Grunder (1997) for the trace elements Cr, Mn, Co, Rb, Sr, Cs, Ba, REE, Hf, Ta and Th and by Wolff and Ramos (2014) for Rb, Cs, Sr, Ba and Pb.

Trace element partition coefficients for *clinopyroxene* are taken from the experimental study of Huang et al. (2006) for Cs, La, Ce, Sm, Eu, Er and Yb, with the remaining REE interpolated. In this study the silica content of the melt was ca. 69 wt.%. Data for Li, Sc, V, Mn, Zn, Ga, Cu, Sr, Y, Zr, Nb, Ba, Hf and Pb are from the more siliceous melts in the experimental study of Iveson et al. (2018). K and Ti are from the Severs et al. (2009) phenocryst–melt inclusion data for dacitic melts (SiO_2 = 65 wt.%). The remaining elements are from Bacon and Druitt (1988) and from the GERM database.

Partition coefficient data for *orthopyroxene* for Li, Sr, Y, Zr, Nb, Ba, Hf and REE are from Brophy et al. (2011), with data for K, Ti and Pb from Severs et al. (2009) and for Ni from Stimac and Hickmott (1994). Other trace elements are from Bacon and Druitt (1988). It should be noted that there is considerable variation in some published trace element partition coefficients between orthopyroxene and felsic melts – compare, for example, the REE in the compilation of Bacon and Druitt with the study of Brophy et al. (2011), where the differences between these two studies may reflect the different silica content of the melts.

Trace element partition coefficients for *amphibole* for Li, Sr, Y, Zr, Nb, Ba, Hf and the REE are from Brophy et al. (2011), and for the elements Sc, V, Mn, Ni, Cu, Zn, Ga, Rb, Mo and Pb from Iveson et al. (2018). There are some differences between these and other published data, in particular for Rb, Sr, Zr, Ba, Mo and Pb, and again it appears that small differences in melt composition may induce significant variations in partition coefficient values. Other data are from Bacon and Druitt (1988).

Garnet partition coefficient data are from the GERM database where the REE data are based upon the phenocryst–matrix data of Irving and Frey (1978). *Biotite* partition coefficients also from the GERM database and are mostly phenocryst–matrix measurements taken from Nash and Crecraft (1985). Partition coefficient data for *magnetite* are from the compilation of Nash and Crecraft (1985) and Bacon and Druitt (1988). *Ilmenite* data are from the GERM

Table 4.3 Mineral-melt partition coefficients for trace elements in rhyolitic melts

Atomic number	*Symbol*	*Name*	*Orthopyroxene*	*Clinopyroxene*	*Garnet*	*Plagioclase*	*Amphibole*	*K-feldspar*	*Biotite*	*Ilmenite*	*Magnetite*
3	**Li**	Lithium	0.076	0.260	*nd*	0.152	0.700				
19	**K**	Potassium	0.004	0.002	*nd*	*nd*	*nd*	*nd*	*nd*	*nd*	*nd*
21	**Sc**	Scandium	7.100	15.900	20.200	0.010	11.790	0.027	4.9–20	5.9	5.000
22	**Ti**	Titanium	0.229	0.412	5.600	0.060	*nd*	*nd*	*nd*	150–235	*nd*
23	**V**	Vanadium	*nd*	7.440	7.000	*nd*	6.670	*nd*	*nd*	*nd*	*nd*
24	**Cr**	Chromium	10.000	30.000	3.850	0.100	40.000	*nd*	8.3–31	3.0000	30.000
25	**Mn**	Manganese	4.055	4.900	*nd*	0.060	3.890	*nd*	13.6–230	15–35	28–37
27	**Co**	Cobalt	38.000	17.000	3.000	0.150	37.000	*nd*	*nd*	*nd*	80.000
28	**Ni**	Nickel	11–25	*nd*	*nd*	*nd*	94.830	*nd*	*nd*	*nd*	*nd*
29	**Cu**	Copper	*nd*	0.110	*nd*	0.080	0.080	*nd*	*nd*	*nd*	*nd*
30	**Zn**	Zinc	6.000	1.960	*nd*	0.140	2.990	*nd*	*nd*	10.500	15.000
31	**Ga**	Gallium	*nd*	0.590	*nd*	*nd*	0.710	*nd*	*nd*	*nd*	*nd*
37	**Rb**	Rubidium	*nd*	0.030	*nd*	0.300	0.030	0.415	2.3–4.1	*nd*	0.010
38	**Sr**	Strontium	0.008	0.230	0.020	31.000	6.595	5.900	0.541	*nd*	0.010
39	**Y**	Yttrium	0.215	3.510	130.000	0.016	5.670	*nd*	1–1.4	0.2–1.6	*nd*
40	**Zr**	Zirconium	0.009	0.210	0.400	0.0002	0.450	0.195	1.3	*nd*	0.240
41	**Nb**	Niobium	0.002	0.210	*nd*	0.0025	1.400	*nd*	4–9.5	50.9–64.2	*nd*
42	**Mo**	Molybdenum	*nd*	*nd*	*nd*	*nd*	0.030	*nd*	1.7–5.7	3.000	6–16
55	**Cs**	Caesium	0.010	0.023	*nd*	0.030	0.100	0.123	1.2–4.4	*nd*	0.010
56	**Ba**	Barium	0.0007	0.010	*nd*	0.200	0.200	14.450	18	*nd*	0.100
57	**La**	Lanthanum	0.001	0.130	0.278–0.54	0.170	0.710	0.085	0.76–15.1	7.100	0.660
58	**Ce**	Cerium	0.002	0.410	0.79–0.93	0.130	1.350	0.042	0.86–11	7.800	0.710
59	**Pr**	Praseodymium	0.010	0.500	*nd*	0.110	2.300	0.039	*nd*	*nd*	*nd*
60	**Nd**	Neodymium	0.013	0.600	0.27–0.73	0.094	3.280	0.035	0.9–5.7	7.600	0.930
62	**Sm**	Samarium	0.045	0.760	0.84–1.04	0.100	4.950	0.023	1–4.3	6.900	1.200
63	**Eu**	Europium	0.018	0.190	0.167–0.31	0.200	0.750	4.900	0.59–4.7	2.500	0.910
64	**Gd**	Gadolinium	0.080	0.760	3.7–5.3	0.060	7.400	0.011	*nd*	*nd*	*nd*
65	**Tb**	Terbium	*nd*	0.900	7.2–11.9	*nd*	*nd*	0.030	0.87–3.9	6.500	1.300
66	**Dy**	Dysprosium	0.345	1.000	*nd*	0.045	12.165	0.065	0.76–3.4	4.900	1.6–4.4
67	**Ho**	Holmium	*nd*	1.070	28.2–34.5	*nd*	*nd*	0.050	*nd*	*nd*	*nd*
68	**Er**	Erbium	1.700	1.150	*nd*	0.060	20.000	0.040	*nd*	*nd*	*nd*
69	**Tm**	Thulium	*nd*	1.050	*nd*	*nd*	*nd*	0.030	*nd*	*nd*	*nd*
70	**Yb**	Ytterbium	3.150	0.960	54–67	0.025	29.465	0.023	0.6–3	4.100	0.440
71	**Lu**	Lutetium	4.400	0.900	47–64	0.060	30.000	0.030	0.6–3.4	3.600	0.300
72	**Hf**	Hafnium	0.054	1.410	*nd*	0.050	0.855	*nd*	0.44–0.84	3.100	0.240
73	**Ta**	Tantallum	0.110	0.500	*nd*	0.030	0.430	0.011	1.2–1.9	64–85	1.200
82	**Pb**	Lead	0.018	0.020	*nd*	0.180	*nd*	1.825	0.1–1.6	*nd*	*nd*
90	**Th**	Thorium	0.140	0.100	*nd*	0.010	0.160	0.220	0.27–2	7.500	0.010
92	**U**	Uranium	*nd*	*nd*	*nd*	*nd*	*nd*	0.048	0.46–1.2	3.200	0.21–0.83

Notes: *nd*, no data

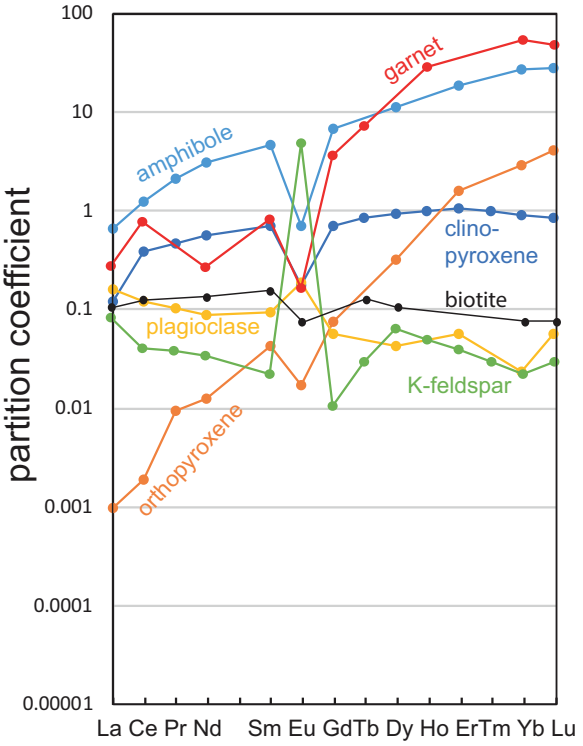

Figure 4.7 REE partition coefficients for the major silicate minerals in felsic melts. (Data from Table 4.3)

database with the REE from Nash and Crecraft (1985), and values for Ti, Mn, Y, Zr and Ta are from the study of Stimac and Hickmott (1994) in which the melt composition was ~75 wt.% SiO_2.

4.2.1.8 Partition Coefficients in Accessory Minerals

The minerals zircon, monazite, apatite, titanite and allanite occur primarily as accessory phases in felsic melts. These minerals occupy only a small volume of their parent rock but exercise a disproportionate effect on the distribution of some trace elements, in particular the REE. Further, they contain elements which are normally regarded as trace elements, but in these particular phases form a stoichiometric component of the host mineral. This means that they do not obey Henry's law (Section 4.2.1) and therefore do not behave in the same way as other trace elements (Prowatke and Klemme, 2006; Chapman et al., 2016).

The appearance of an accessory phase in a melt is governed by the solubility of the phase in the melt. For example, in the case of zircon ($ZrSiO_4$) the crystallisation of the mineral from a melt is governed by the solubility of Zr in the melt, such that when the melt is saturated in Zr, zircon will crystallise from the melt. In practice, therefore, zircon (and other accessory minerals) will appear in an igneous sequence towards the end of a differentiation process. Zr solubility is controlled by variables such as melt composition and temperature. Formulations of accessory mineral solubility have been given by Kelsey et al. (2008) for zircon and monazite, by Stepanov et al. (2012) for monazite, and by Harrison and Watson (1984) for apatite.

In this section the main focus is on the partition coefficients for the REE and for element pairs such as Nb–Ta and Th–U where either large partition coefficients or, in the case of element pairs, very different partition coefficients between the pair may have a major impact on the trace element composition of the melt. Partition coefficients for other elements derived from older mineral–matrix measurements are given in the GERM database. Relevant values are summarised in Table 4.4 and a plot of partition coefficients for the REE in accessory phases is given in Figure 4.8.

Zircon ($ZrSiO_4$) is one of the best studied accessory minerals because of its importance in geochronology and its use, when found as detrital grains in sediment, for recovering information about ancient continental crust. Hanchar and van Westrenen (2007) review the REE partition coefficient data for zircon and show that many of the published values in the older literature determined using phenocryst–matrix methods do not conform to the lattice strain model and are probably in error. This is particularly true for the incompatible light REE. They recommend the values of Sano et al. (2002) for zircon in equilibrium with a dacitic melt, and these are given in Table 4.4. A more recent study by Chapman et al. (2016) calculated trace element partition coefficients for a suite of bulk rock compositions from the Coast Mountains Batholith in British Columbia with SiO_2 = 51–76 wt.%. The median values calculated for this suite are given in Table 4.4. An accurate measure of REE partition coefficients in zircon is particularly important when the partition coefficient data are inverted to estimate the parental melt composition as in the case of detrital zircons whose origin is unknown. The Chapman et al. (2016) partition coefficients seem robust in this respect. Trace element data for Y and Nb are from Chapman et al. (2016) and for B, Ti, Rb, Sr and Ba from Thomas et al. (2002). Ti concentrations in zircon may be used as a geothermometer

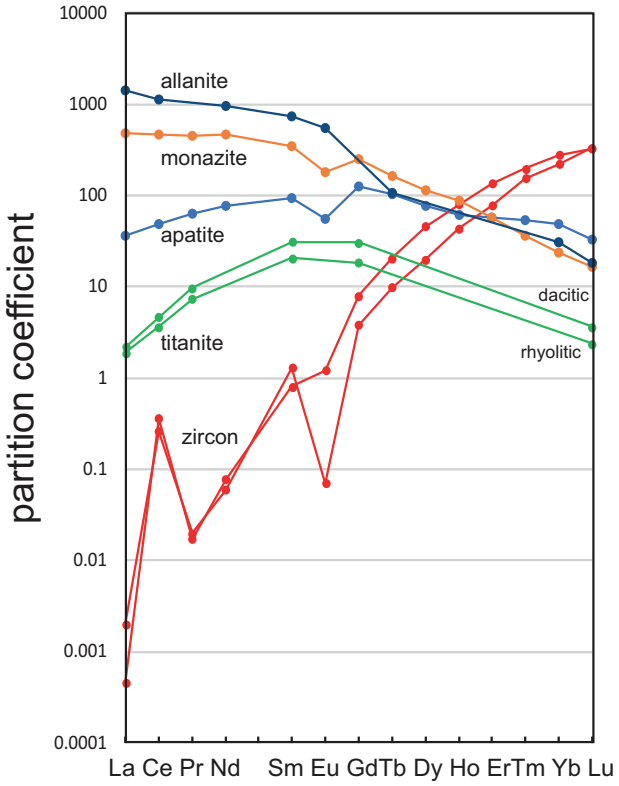

Figure 4.8 Partition coefficients for the REE in accessory minerals in felsic rocks (data from Table 4.4). Note the difference in scale from Figures 4.5–4.7.

(Watson et al., 2006) although Schiller and Finger (2019) give a more recent evaluation of the applicability of this methodology.

Partition coefficient data for the REE in apatite ($Ca_5(PO_4)_3(F, Cl, OH)$) given in Table 4.4 are from the ion microprobe study of Sano et al. (2002) for apatite in equilibrium with a dacitic melt and from Brophy et al. (2011) for apatite in contact with natural interstitial rhyolitic (71–76% SiO_2) glass. Median values are given for the Brophy et al. (2011) REE partition coefficients, for these show a wide range of measured values and are higher than the Sano et al. (2002) data for the heavy REE.

Monazite ((LREE)PO_4) is a light REE phosphate, xenotime mirror monazite ((Y,HREE)PO_4) is its rarer heavy REE counterpart, and these phases are important in controlling REE concentrations during the melting and fractionation of crustal rocks. Stepanov et al. (2012) present partition coefficient data for Y, REE, Th and U in monazite. These partition coefficients were experimentally determined over a temperature range of 750–1200°C and a pressure range of 1–5 GPa on a hydrous Fe-, Mg-free peraluminous granitic melt with 76–78 wt.% SiO_2. Partition coefficient values vary by over an order of magnitude, and the ratio of D-values for heavy to light REE increases with temperature and decreases with the water content of the melt. For this reason, the range of experimentally determined values and a median value are given in Table 4.4.

Selected trace element partition coefficients have been experimentally determined for titanite (sphene, $CaTiSiO_5$) by Prowatke and Klemme (2005), who show that partition coefficients are strongly dependent upon melt composition. For this reason, values for both dacite (SiO_2 = 64.3 wt.%) and rhyolite (SiO_2 = 69.8 wt.%) are given in Table 4.4.

Klimm et al. (2008) give partition coefficients for allanite, a REE-rich member of the epidote group (Ca, (REE)$Al_2Fe^{2+}(Si_2O_7)(SiO_4)O(OH)$), in felsic melts with between 71 and 74 wt.% SiO_2 produced during the water-saturated melting of basalt. Their results for La, Ce, Nd, Sm and Eu, given as a range in Table 4.4, show that the partition coefficients are strongly temperature-dependant and decrease from 900 to 800°C. Partition coefficients for Tb, Yb and Lu are from Chesner and Ettlinger (1989).

4.2.2 Geological Controls on the Distribution of Trace Elements

The geochemical study of trace elements is a powerful tool for understanding and recognising geological processes. Our knowledge of the partitioning of trace elements between minerals and their parental melt means that a range of geological processes in which minerals are in equilibrium with a melt can be modelled. Further, inverting the modelling means that processes operating in a particular magmatic system may be identified. In contrast to magmatic systems, however, our knowledge of the behaviour of trace elements in aqueous and sedimentary systems is less amenable to quantification, and the main focus of this discussion is therefore upon magmatic systems. In this section we consider a range of geological processes for which there are quantitative models to describe the behaviour of trace elements. The relevant equations are given and the terms used are defined (Table 4.5). The interested reader will find a full derivation of the relevant equations in the text by Shaw (2006).

Table 4.4 Mineral-melt partition coefficients for trace elements in accessory phases

Atomic number	Symbol	Name	Zircon		Apatite		Monazite		Titanite		Allanite	
		Ref	1	2, 3	1	4	5 range	5 median	6 Dacite	6 Rhyolite	7, 8 range	7, 8 median
3	**Li**	Lithium	*nd*	*nd*	*nd*	0.005	*nd*	*nd*	*nd*	*nd*	*nd*	*nd*
5	**B**	Boron	*nd*	0.017	*nd*	*nd*	*nd*	*nd*	*nd*	*nd*	*nd*	*nd*
22	**Ti**	Titanium	*nd*	3.150	*nd*	*nd*	*nd*	*nd*	*nd*	*nd*	1.94–4.03	2.675
37	**Rb**	Rubidium	*nd*	0.006	*nd*	*nd*	*nd*	*nd*	0.00026	0.00033	*nd*	*nd*
38	**Sr**	Strontium	*nd*	0.034	*nd*	24.000	*nd*	*nd*	0.62	0.44	*nd*	*nd*
39	**Y**	Yttrium	*nd*	47.000	*nd*	24.000	20–606	78.500	14.3	8.96	*nd*	*nd*
40	**Zr**	Zirconium	*nd*	*nd*	*nd*	0.012	*nd*	*nd*	3.78	3.48	*nd*	*nd*
41	**Nb**	Niobium	*nd*	0.150	*nd*	0.009	*nd*	*nd*	7.26	5.44	*nd*	*nd*
55	**Cs**	Caesium	*nd*	*nd*	*nd*	*nd*	*nd*	*nd*	0.0023	0.0022	*nd*	*nd*
56	**Ba**	Barium	*nd*	0.004	*nd*	0.010	*nd*	*nd*	0.0025	0.0029	*nd*	*nd*
57	**La**	Lanthanum	0.00046	0.002	36.0	24.0	74–3240	485.0	2.17	1.88	775–2819	1399
58	**Ce**	Cerium	0.360	0.260	48.0	47.0	66–3011	459.5	4.6	3.61	628–2245	1120
59	**Pr**	Praseodymium	0.017	0.020	64.0	34.0	71–3194	446.0	9.7	7.39	*nd*	*nd*
60	**Nd**	Neodymium	0.077	0.060	77.0	36.0	73–3125	463.0	*nd*	*nd*	538–1980	970
62	**Sm**	Samarium	0.800	1.300	93.0	42.0	56–2526	344.0	31.2	20.4	272–1254	728
63	**Eu**	Europium	1.220	0.070	55.0	8.0	12–1759	177.5	*nd*	*nd*	138–794	549
64	**Gd**	Gadolinium	8.000	3.800	127.0	45.0	49–1920	252.0	30.5	18.2	*nd*	*nd*
65	**Tb**	Terbium	20.700	9.900	102.0	*nd*	34–1400	163.5	*nd*	*nd*	107–139	108
66	**Dy**	Dysprosium	45.900	20.000	76.0	46.0	27–1015	115.5	*nd*	*nd*	*nd*	*nd*
67	**Ho**	Holmium	80.000	44.000	62.0	*nd*	20–709	86.5	*nd*	*nd*	*nd*	*nd*
68	**Er**	Erbium	136.000	77.000	57.0	88.0	16–534	57.5	*nd*	*nd*	*nd*	*nd*
69	**Tm**	Thulium	197.000	154.000	53.0	*nd*	12–324	36.0	*nd*	*nd*	*nd*	*nd*
70	**Yb**	Ytterbium	277.000	219.000	48.0	95.0	10–237	23.5	*nd*	*nd*	19–36	31
71	**Lu**	Lutetium	325.000	331.000	33.0	91.0	8–187	16.5	3.65	2.38	12–23	18
72	**Hf**	Hafnium	*nd*	*nd*	*nd*	*nd*	*nd*	*nd*	6.9	4.9	*nd*	*nd*
73	**Ta**	Tantallum	*nd*	*nd*	*nd*	*nd*	*nd*	*nd*	84	54.8	*nd*	*nd*
82	**Pb**	Lead	*nd*	*nd*	*nd*	*nd*	*nd*	*nd*	0.87	0.750000	*nd*	*nd*
90	**Th**	Thorium	*nd*	*nd*	*nd*	*nd*	86–3853	691.000	0.14	0.101000	416–1331	732
92	**U**	Uranium	*nd*	*nd*	*nd*	*nd*	9–377	60.000	0.07	0.090000	22–97	53

Notes: *nd*, no data

Ref = References: 1, Sano et al. (2002); 2, Chapman et al. (2016); 3, Thomas et al. (2002); 4, Brophy et al. (2011); 5, Stepanov et al. (2012); 6, Prowatke and Klemme (2005); 7, Klimm et al. (2008); 8, Chesner and Ettlinger (1989).

Table 4.5 Equations terms used to determine trace element partitioning between solid and melt (Section 4.2.2)

Term	*Definition*
C_A	Concentration of a trace element in the wall rock being assimilated during AFC processes
C_L	Weight concentration of a trace element in the liquid
$\bar{C}_L$	Average weight concentration of a trace element in a mixed melt
C_O	In partial melting the weight concentration of a trace element in the original unmelted solid; in fractional crystallisation the weight concentration in the parental liquid
C_k	Weight concentration of a trace element in the residual solid during crystal fractionation
C_S	Weight concentration of a trace element in the residual solid (after melt extraction)
$_{SS}C_B$	Weight concentration of a trace element in a steady state liquid after a large number of RTF cycles
D_O	Bulk distribution coefficient of the original solids
D_I	Mineral-melt partition coefficient, or the bulk distribution coefficient of the fractionating assemblage, during crystal fractionation
D_S	Strain-free partition coefficient in the lattice strain model
D_{RS}	Bulk distribution coefficient of the residual solids
F	Weight fraction of melt produced in partial melting; in fractional crystallisation the fraction of melt remaining
f	Fraction of melt allocated to the solidification zone in in situ crystallisation which is returned to the magma chamber
f'	A function of F, the fraction of melt remaining in AFC processes
M_L	Mass of the liquid remaining during in situ crystallisation
M_O	Total mass of the magma chamber in in situ crystallisation
n	Number of rock volumes processed during zone refining
P	Bulk distribution coefficient of minerals which contribute to a melt
r	Ratio of the assimilation rate to the fractionation rate in AFC processes
x	In an RTF magma chamber, the mass fraction of the liquid crystallised in each RTF cycle; during in situ crystallisation, the proportion of trapped melt in the magma chamber
y	Mass fraction of the liquid escaping in each RTF cycle

Notes: AFC, assimilation and fractional crystallisation; RTF, periodically replenished, periodically tapped, continuously fractionated.

4.2.2.1 Element Mobility

Any suite of rocks which has been affected by hydrothermal alteration or metamorphism is likely to have experienced some level of element mobility. It is essential, therefore, in any trace element study to first demonstrate that element concentrations are undisturbed and original before inferences can be made about the petrogenesis of the rock group. As was noted in Section 3.1.2, element mobility is controlled by the mineralogical changes which take place during alteration and the composition, temperature and relative volume of the migrating fluid or melt phase. Trace element mobility may be detected from mineralogical phase and compositional changes that have taken place in a rock as a result of metamorphism or hydrothermal activity, and careful petrography is an important tool in identifying chemically altered rocks. In addition, scattered trends on variation diagrams or divergent irregular patterns on multi-element plots (Section 4.4) are also useful indicators.

As a generalisation, incompatible elements which belong to the low field strength LILE group (Cs, Rb, K, Ba, Sr, ± Eu, and Pb) (Figure 4.2) are fluid-mobile, whereas the high field strength elements (the REE, Sc, Y, Th, Zr, Hf, Ti, Nb, Ta and P) are immobile (Pearce, 1983). Such generalisations are normally valid, but should not be assumed. For example, Humphries (1984) found that there is no simple relationship between the degree of mobility of the traditionally immobile REE and rock type, emphasising the importance of localised mineralogical and fluid controls. Humphries (1984) showed that the REE may be more easily released from a glassy basalt during alteration than from a rock with the same composition which is crystalline and that the REE may be mobilised by halogen-rich or carbonate-rich mineralising fluids in a rock in which they would otherwise be stable in the presence of an aqueous fluid.

4.2.2.2 Partial Melting

Melting in the Earth's mantle typically takes place through the upwelling of hot mantle material and melting through decompression. For example, at a mid-ocean ridge hot mantle rises adiabatically, that is, without loss of heat by conduction, and progressively melts as it rises to the surface. Melting takes

place at grain boundaries and is normally incomplete – hence the term 'partial' melting. For this reason, two important parameters must be considered in modelling partial melting processes. First is the nature of what is melting: the minerals involved in the melting process. The involvement of particular mineral phases at any stage in a particular partial melting event may be described with a *melting reaction* that is determined either experimentally or through petrographic observation. The phases included in the melting reaction are those which will govern the bulk partition coefficient of the melting process. The second key parameter is the extent of melting, or the *melt fraction*. This process is limited by the ability of the melt to 'escape' from its unmelted environment. This in turn is governed by the properties of both the melt and the host, in particular, the viscosity of the melt and the shape of the mineralogical network of the host.

Two types of partial melting process are commonly described in the geological literature and represent end-member models of natural processes. *Batch melting*, also known as equilibrium fusion and equilibrium partial melting, describes the formation of a partial melt in which the melt is continually reacting and re-equilibrating with the solid residue at the site of melting until mechanical conditions allow it to escape as a single 'batch' of magma. In *fractional melting*, also known as Rayleigh melting, only a small amount of liquid is produced before it is instantly isolated from the source. In this case, equilibrium is achieved only between the surface of the mineral grains in the source region.

Which partial melting process is appropriate in a particular situation depends upon the ability of a magma to segregate from its source region, which in turn depends upon the permeability threshold of the source. The problem is discussed in some detail by Wilson (1989). Fractional melting may be an appropriate model for some basaltic melts, as physical models of melt extraction from the mantle indicate that very small melt fractions can be removed from their source region (McKenzie, 1985; O'Nions and McKenzie, 1988). More viscous, felsic melts have a higher permeability threshold and probably behave according to the batch melting equation. It is important to note that physical models of melt extraction describe melt fractions in terms of their *volume*, whereas the chemical models used here more usefully describe melt fractions in terms of their *mass*.

(a) *Batch melting.* The concentration of a trace element in the melt C_L is related to its concentration in the unmelted source C_o by the expression

$$C_L/C_o = 1/[D_{RS} + F(1 - D_{RS})] \tag{4.6}$$

and the concentration of a trace element in the unmelted residue C_S relative to the unmelted source C_o is

$$C_S/C_o = D_{RS}/[D_{RS} + F(1 - D_{RS})] \tag{4.7}$$

where D_{RS} is the bulk partition coefficient of the residual solid (see Eq. 4.4) and F is the weight fraction of melt produced. It should be noted that the bulk partition coefficient is calculated for the residual solids present at the instant the liquid is removed, so that solid phases that were present but are consumed during melting do not influence the trace element concentration in the liquid (Hanson, 1978). This formulation of the batch melting equation is very straightforward to use.

Modelling trace element behaviour during partial melting depends upon whether or not the minerals in the source rock contribute to the melt in their modal proportions. In the case of *modal melting* (where the minerals contribute to the melt in proportion to their concentration in the rock), the ratio of a trace element in the melt and the unmelted residue relative to the source is given by Eqs. 4.6 and 4.7. If, however, the phases in the host rock do not contribute to the melt in their modal proportions, then the batch melting equation for *non-modal melting* is expressed in terms of the original mineralogy of the source and the relative contributions each phase makes to the melt as determined from the melting reaction. In this case the equation for the melt is

$$C_L/C_o = 1/[D_o + F(1 - P)] \tag{4.8}$$

where D_o is the bulk distribution coefficient at the onset of melting and P is the bulk distribution coefficient of the minerals which are contributing to the melt. P is calculated from

$$P = p_1D_1 + p_2D_2 + p_3D_3 + \ldots \tag{4.9}$$

where p_1 is the weight normative fraction of mineral 1 in the melt and D_1 is the mineral-melt distribution coefficient for a given trace element for mineral 1. Shaw (2006) illustrates the way in which the results of non-modal melting diverge from modal melting for elements with different compatibilities. His results indicate that for compatible elements at low degrees

of melting (up to 10%) the two models give very similar results, whereas for incompatible elements the two models diverge after about 6–7% melting. More complex formulations which allow a phase to be consumed during melting, melt proportions to vary during partial melting, and variations in partition coefficients are given by Hertogen and Gijbels (1976) and Apted and Roy (1981).

Taking the most simple case where D is calculated for the unmelted residue (D_{RS}, Eq. 4.6), the degree of enrichment or depletion relative to the original liquid (C_L/C_o) for different values of F can be determined for different values of D_{RS}, the bulk distribution coefficient (Figure 4.9a). When D_{RS} is small, Eq. 4.6 reduces to $1/F$ and marks the limit to trace element enrichment for any given degree of batch melting (effectively, the area to the right of $D = 0.01$ in Figure 4.9a). When F is small, Eq. 4.6 reduces to $1/D$ and marks the maximum possible enrichment of an incompatible element and the maximum depletion of a compatible element relative to the original source. It can be seen from this plot that at small degrees of melting the degree of enrichment or depletion varies hugely between compatible elements which are not enriched in the melt and incompatible elements which are strongly enriched in the melt. Thus, during batch melting incompatible/compatible element ratios are very sensitive at small degrees of melting. Enrichment and depletion in the solid residue in equilibrium with the melt (Eq. 4.7) for different values of F and D is shown in Figure 4.9b. Even small degrees of melting will deplete the residue significantly in incompatible elements, whereas compatible elements remain very close to their initial concentrations.

(b) *Fractional melting.* In fractional melting the melt is removed from the source as soon as it is created. There are two versions of the fractional melting equation: one considers the formation of only a single melt increment (C_L), whereas the other considers the composition of the aggregate liquid formed by the collection of a large number of small melt increments ($\overline{C}_L$). If it is assumed that during fractional melting the mineral phases enter the melt in the proportions in which they are present in the source (modal melting), then the concentration of a trace element in the liquid relative to the parent rock for a given melt increment is given by the Rayleigh fractionation law leading to the expression

$$C_L/C_o = 1/D_o * (1 - F)^{(1/Do-1)} \tag{4.10}$$

where F is the fraction of melt removed from the source and D_o is the bulk partition coefficient for the original solid phases prior to the onset of melting. The equation for the residual solid is

$$C_S/C_o = (1 - F)^{(1/Do-1)} \tag{4.11}$$

The general expressions for the more probable case where minerals do not enter the melt in their modal proportions are given by

$$C_L/C_o = 1/D_o * (1 - PF/D_o)^{(1/P-1)} \tag{4.12}$$

and

$$C_S/C_o = (1/[1 - F]) * (1 - PF/D_o)^{1/P} \tag{4.13}$$

where P is the bulk distribution coefficient of the minerals which make up the melt and is calculated from Eq. 4.9.

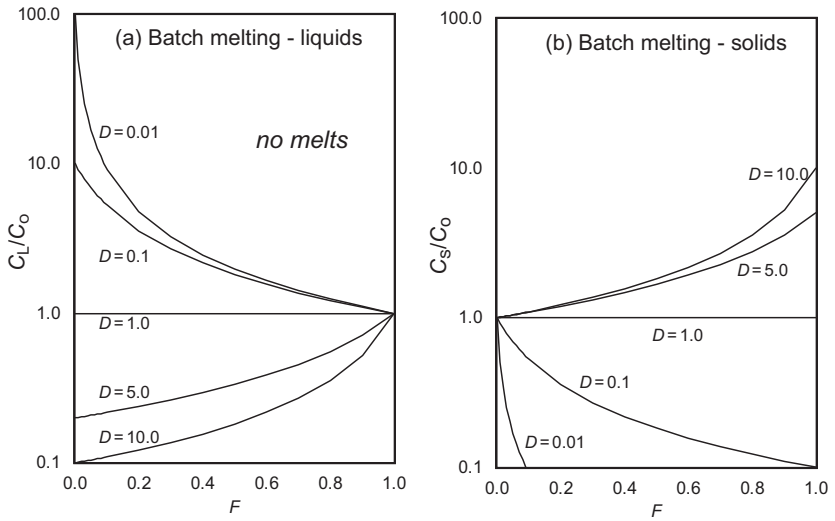

Figure 4.9 The enrichment of a trace element in a melt relative to its source (C_L/C_o) as a function of the fraction of melting (F), during modal batch melting for different values of bulk partition coefficient (D). (a) Relative concentrations in the melt fraction during modal batch melting. (b) Relative concentrations in the unmelted solid residue during modal batch melting.

The variation in trace element concentrations relative to the original liquid (C_L/C_o) during fractional melting for a single melt increment at different degrees of melting and for different values of D is shown for modal melting (Eq. 4.10) in Figure 4.10a. In the range 0–10% melting the changes in element concentrations relative to the original source are more extreme than in batch melting, although the limiting value of $1/D$ is the same. Trace element concentrations in the original solid, momentarily in equilibrium with the liquid (Eq. 4.11), are shown in Figure 4.10b. Incompatible elements are more strongly depleted than in batch melting, although compatible element concentrations are unchanged relative to the source until very high melt fractions are reached.

When several melt increments have collected together the general expression becomes

$$\overline{C}_L/C_o = 1/F * \left[1 - (1 - PF/C_o)^{1/P}\right] \quad (4.14)$$

where $\overline{C}_L$ is the *averaged concentration* of a trace element in a mixed melt. In the case of modal melting Eq. 4.14 simplifies to

$$\overline{C}_L/C_o = 1/F * \left[1 - (1 - F)^{1/Do}\right] \quad (4.15)$$

The relative enrichment of trace elements in the melt relative to the source during fractional melting in which the melt increments are collected together in a common reservoir is illustrated in Figure 4.10c. In this case fractional melting is indistinguishable from batch melting except for compatible elements at very large degrees of melting (Figure 4.9a).

A comparison between the degrees of relative enrichment during batch melting, fractional melting,

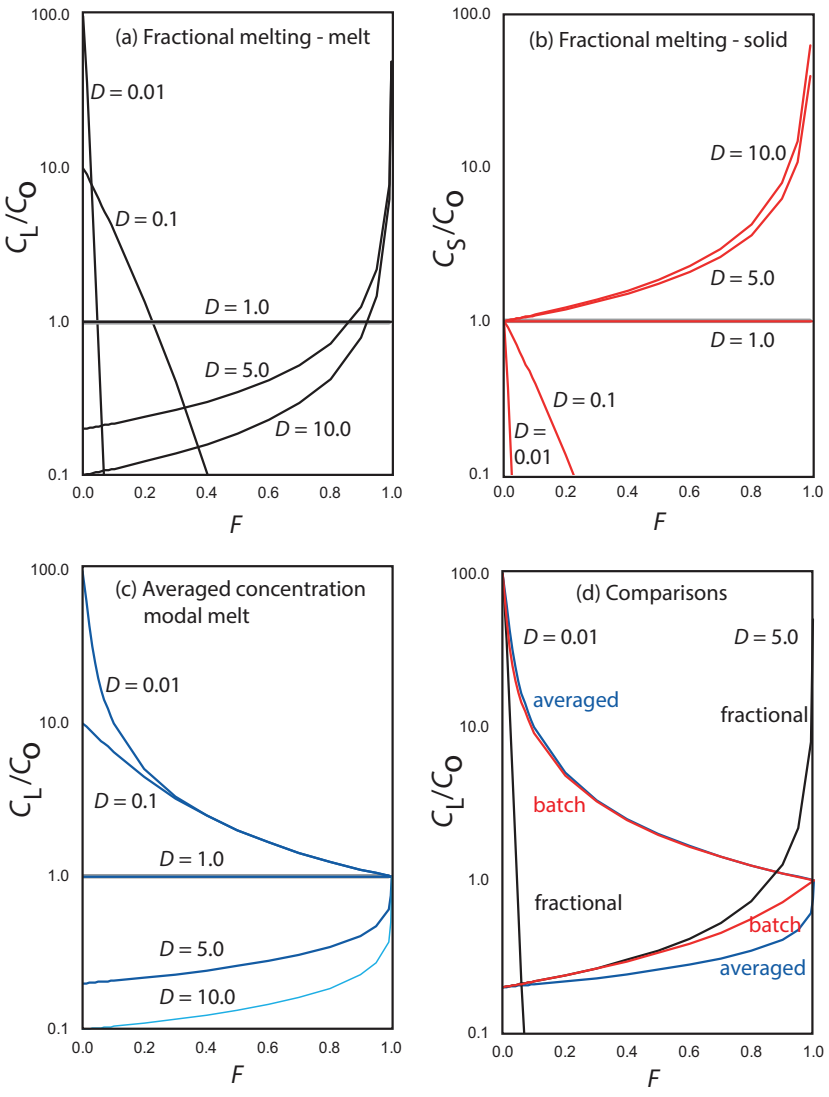

Figure 4.10 The enrichment of a trace element in a melt relative to its source (C_L/C_o) as a function of the fraction of melting (F), during modal fractional melting for different values of bulk partition coefficient (D). During fractional melting only a very small melt fraction is produced and it is instantly removed from the source. (a) Relative concentrations in the melt fraction during modal fractional melting. (b) Relative concentrations in the unmelted solid residue during modal fractional melting. (c) Relative concentrations in the melt fraction during modal fractional melting. In this case small melt fractions are removed instantly from the source but aggregate together and the composition averaged. This process produces very similar results to that of batch melting. (d) A comparison between the effects of batch melting (red curves), fractional melting (black curves), and averaged fractional melting (blue curves) for incompatible elements (D = 0.01) and compatible elements (D = 5).

and averaged fractional melting is shown in Figure 4.10d for highly incompatible elements ($D = 0.01$) and compatible elements ($D = 5$). For incompatible elements there is a large difference in concentration ratios between fractional melting and batch melting. Ratios for averaged fractional melting are very close to those for batch melting. For compatible elements there is little difference between the three models until high melt fractions of >20% are reached.

(c) *Dynamic melting.* Batch melting and fractional melting might be regarded as end-members of two different modes of melt extraction. However, studies of mid-ocean ridge basalts in the 1970s and 1980s suggested that mantle melting was a more complex and dynamic process than is implied by either batch or fractional melting (Langmuir et al., 1978; Wood, 1979; McKenzie, 1985). These processes have been reviewed by Shaw (2006) and discussed in detail by Shaw (2000) and Zhou and Reid (2001). These authors propose numerical models for *dynamic melting*, by which they mean *continuous melting* with retained or trapped melt. This process may take place in either a closed or open system. In a closed system a melt may leave the system but nothing is added, whereas in an open system matter is being added while solid material melts and melt is being released. During dynamic melting trace element concentrations in the melt will be influenced by variable melt/source-rock ratios, a variable contribution of solid phases to the melt (modal or non-modal melting), as well as varying partition coefficients. In part the process is also governed by the *permeability threshold*, that is, the critical degree of melting at which melt first leaves the system. The effects of dynamic melting and the importance of the interstitial melt fraction on the relative concentrations of an incompatible element during non-modal melting of mantle peridotite are illustrated as a function of total melt fraction in Figure 4.11. The limiting concentrations are given by the batch melting and fractional melting curves and the continuous melting curves have a shape similar to that of the fractional melting curves. However, the models discussed by Shaw (2000) are limited inasmuch as they do not account for variable partition coefficients; melting proportions are held constant; and kinetic diffusion effects are ignored.

(d) *Zone refining.* Zone refining or zone melting is a process used in metallurgy for the purification of metals. The principle is that a metal rod or some similar material is passed through a heat source which causes melting of a small section of the rod. During this melting, incompatible impurities in the metal accumulate in the melt. As the rod is passed through the heat source the melt migrates and scavenges impurities as it moves. The end products are a metal rod depleted in impurities and a final melt enriched in impurities.

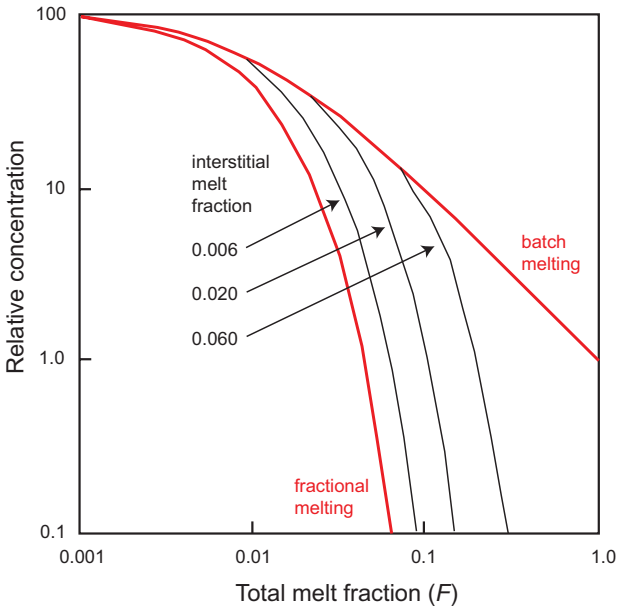

Figure 4.11 Behaviour of an incompatible element during the non-modal melting of peridotite. The limiting cases are batch melting and fractional melting. Dynamic melting defines relative concentration curves similar to that of fractional melting but shows a dependence on the value of the interstitial melt fraction. Three such curves are shown. (After Shaw 2000; with permission from the *Canadian Mineralogist*)

The equation for the enrichment of a trace element in the melt (C_L) relative to the original composition (C_o) by zone refining is

$$C_L/C_o = (1/D) - [(1/D) - 1]*e^{-n*D} \quad (4.16)$$

The depletion in the source (C_S) relative to the concentration in the original composition is

$$C_S/C_o = 1 - (1 - D)*e^{-n*D} \quad (4.17)$$

where n is the number of equivalent rock-volumes that have reacted with the liquid. Where n is very large the C_L/C_o reduces to $1/D$. The numerical effects of zone refining are illustrated in Figure 4.12, which shows the enrichment of a trace element relative to its original

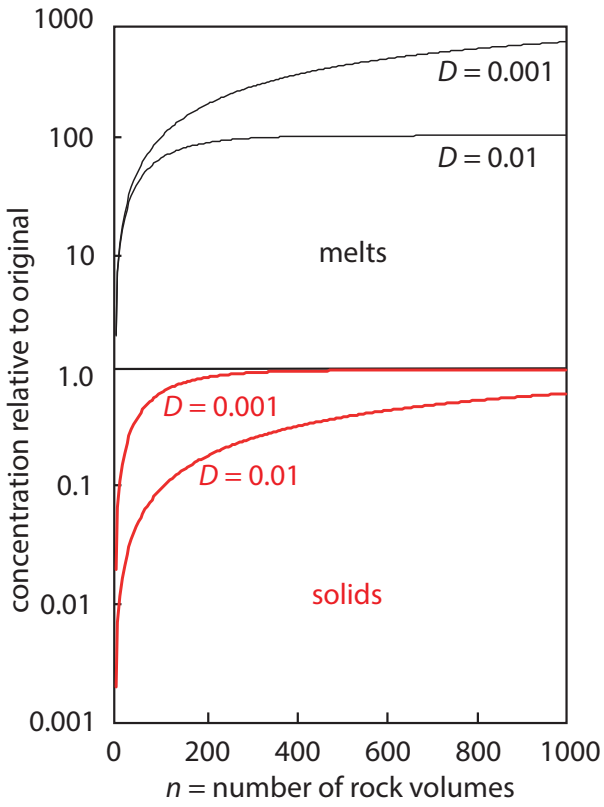

Figure 4.12 Plot of trace element enrichment during zone refining in both the melt and residual solid for incompatible elements with D = 0.01 and 0.001. The solid phase approaches the original composition and the melt phase the value of $1/D$ (the partition coefficient) after a large number of rock volumes.

concentration for the number of rock volumes consumed (n). For incompatible elements (0.001–0.01) the maximum enrichment in the melt is $1/D$ rock volumes. In the solid phase C_S/C_o rises to 1.0 after a large number of rock volumes (see also Shaw, 2006).

Originally, zone refining was thought to be applicable to mantle processes (Harris, 1974) and Neal and Davidson (1989) proposed a zone-refining process to model REE concentrations in a highly enriched potassic ultramafic rock parental to alnöite at Malaita in the Solomon Islands. However, it is now thought that most highly enriched mantle melts are the product of fractional melting in a dynamic melting environment (see above). Thus, most recent applications of zone refining involve the presence of a fluid phase and have been applied to the development of fluid inclusions (Lambrecht and Diamond, 2014), mineralisation in layered mafic intrusions (Brűgmann et al., 1989), the development of chimneys in hydrothermal vent systems (Yuan et al., 2018) and in the formation of granitoid magmas (Lundstrom, 2009).

4.2.2.3 Crystal Fractionation

This section examines the way in which trace elements behave during the crystallisation of a silicate melt and applies principally to magma chamber processes. Five types of crystallisation are considered: equilibrium crystallisation, Rayleigh fractionation, in situ crystallisation, assimilation and fractional crystallisation (AFC), and dynamic processes in a replenished magma chamber.

(a) *Equilibrium crystallisation*. The starting point of equilibrium crystallisation is a closed system in which a hot magma cools until one or more mineral phases begins to crystallise. The process describes complete equilibrium between all solid phases and the melt during crystallisation. This is not thought to be a common process, although the presence of unzoned crystals in some mafic rocks suggests that it may be applicable on a local scale in some mafic magmas. The distribution of trace elements during equilibrium crystallisation is the reverse of equilibrium or batch melting (Section 4.2.2), and the equation therefore is

$$C_L/C_o = 1/[D + F(1 - D)] \quad (4.18)$$

The equation for the crystallising solids is

$$C_R/C_o = D/[D + F(1 - D)] \quad (4.19)$$

In this case C_o is redefined as the initial concentration of a trace element in the initial melt, C_R the concentration of a trace element in the crystallising solid, F is the *fraction of melt remaining* and D is the bulk partition coefficient of the fractionating assemblage. The enrichment and depletion of trace elements relative to the original liquid for a range of partition coefficients is identical to that in the batch melting diagram (Figure 4.9a), but in this case the value of F (the fraction of melt remaining) is shown decreasing from left to right on the diagram (see Figure 4.13a).

(b) *Fractional crystallisation/Rayleigh fractionation*. More commonly, crystals are thought to be removed from the site of formation after crystallisation and the distribution of trace elements is not an equilibrium process. At best, surface equilibrium may be attained, and so fractional crystallisation is better described by the Rayleigh law. Rayleigh fractionation describes the extreme case where crystals are effectively removed

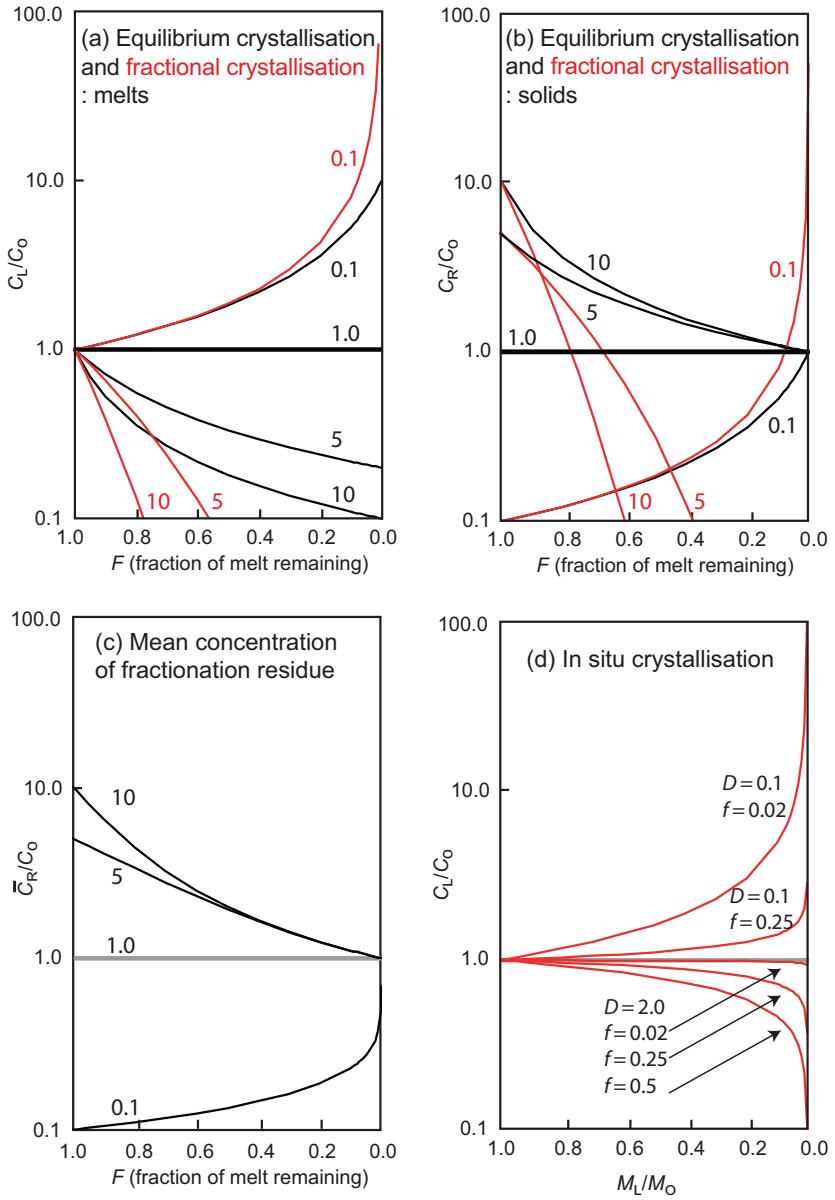

Figure 4.13 Relative concentrations versus fraction of melt remaining for trace elements in different crystallisation models for a range of partition coefficients (values shown adjacent to respective curves). (a) Relative concentrations in the melt during equilibrium crystallisation (black lines) and fractional crystallisation (red lines) for partition coefficient with values between 0.1 and 10; (b) relative concentrations in the solid residue during equilibrium crystallisation (black lines) and fractional crystallisation (red lines) for partition coefficient with values between 0.1 and 10; (c) average relative concentration in the accumulated solid residue during fractional crystallisation for partition coefficient with values between 0.1 and 10; (d) concentration in the melt during in situ crystallisation for D = 0.1 and f = 0.02 and 0.25 (f is the fraction of magma allocated to the solidification zone which is returned to the magma chamber) and for D = 2.0 and f = 0.02 and 0.5.

from the melt the instant they have formed. The equation for Rayleigh fractionation is

$$C_L/C_o = F^{(D-1)} \tag{4.20}$$

and the equation for the enrichment of a trace element relative to the original liquid in the crystals as they crystallise (the instantaneous solid) C_R is given by

$$C_R/C_o = D \times F^{(D-1)} \tag{4.21}$$

The equation for the mean enrichment of a trace element in the cumulate relative to the original liquid – the total residual solid $\overline{C}_R$ – is

$$\overline{C}_R/C_o = \left(1 - F^D\right)/(1 - F) \tag{4.22}$$

Rayleigh fractionation is illustrated in Figure 4.13a and shows the concentration of a trace element relative to its initial concentration in the liquid at differing values of F – the proportion of liquid remaining – for different values of D. For incompatible elements there is little difference between Rayleigh fractionation and equilibrium crystallisation until more than about 75% of the magma has crystallised at which point the efficient separation of crystals and liquid becomes physically difficult. The limiting case for incompatible elements is where $D = 0$ in which case $C_L/C_O = 1/F$,

the same as for equilibrium crystallisation. It is therefore impossible to enrich a liquid beyond this point by fractional crystallisation. Rayleigh fractionation is less effective than batch melting in changing the ratio of two incompatible elements for the Rayleigh fractionation curve, for $D = 0.01$ plots very close to the curve for $D = 0.1$. Compatible elements are removed from the melt more rapidly than in the case of equilibrium crystallisation (Figure 4.13a).

The concentration of trace elements in the instantaneous solid residue of Rayleigh fractionation is illustrated in Figure 4.13b. More relevant, however, is the mean concentration in the cumulate ($\overline{C}_R$) given by Eq. 4.22 (Figure 4.13c). At low degrees of fractionation, compatible elements are strongly enriched in the residue and incompatible elements strongly depleted relative to concentrations in the original liquid. In reality, crystallisation processes probably operate between the two extremes of equilibrium crystallisation and fractional crystallisation, and these should be seen as limiting cases.

(c) *In situ crystallisation.* It is also important to consider a more realistic view of fractional crystallisation in a magma chamber in which there is not a perfect separation of crystals and melt. Langmuir (1989) proposed that fractional crystallisation is an in situ process in which residual liquid is separated from a crystal mush – rather than vice versa – and that this takes place in a solidification zone at the magma chamber margin. The solidification zone is located between the cumulate pile and the magma, and it progressively moves through the magma chamber until crystallisation is complete. The equation which describes trace element concentrations in the melt during in situ crystallisation is presented for the simplified case where there is no trapped liquid in the solidification zone (Langmuir, 1989). This allows us to compare the results with the effects of fractional and equilibrium crystallisation. The relevant equation is

$$C_L/C_o = (M_L/M_o)^{(f(D-1)/[D(1-f)+f]} \quad (4.23)$$

where M_o is the initial mass of the magma chamber and M_L is the mass of liquid remaining so that the ratio (M_L/M_o) is equivalent to the term (F) – the fraction of melt remaining in equilibrium and fractional crystallisation models. The variable f is the fraction of magma allocated to the solidification zone which is returned to the magma chamber. Eq. 4.23 is similar in form to the Rayleigh fractionation equation but with a more complex exponent. The effects of in situ crystallisation on the ratio of a trace element relative to the parental magma (C_L/C_o) for different melt fractions returned to the magma chamber ($f =$ 0.02–0.5) is shown for two different bulk partition coefficients in Figure 4.13d. The chief differences between in situ crystallisation and Rayleigh fractionation may be observed by comparing Figures 4.13a and d. The limiting case is where $f =$ 1.0 which is Rayleigh fractionation. At low values of f, the enrichment of incompatible elements and the depletion of compatible elements are not as extreme during in situ fractional crystallisation as in Rayleigh fractionation.

Alternative approaches to modelling incomplete fractional crystallisation include the influence of a trapped melt. A range of models is summarised by Shaw (2006). For a simple model in which the composition of the trapped melt is identical to that in the magma chamber, then the relative enrichment of a trace element is given by

$$C_L/C_o = F^{[(1-x)\times(D-1)]} \quad (4.24)$$

where F is the degree of fractionation, x is the proportion of trapped melt, and D is the bulk partition coefficient. In general, the effect of in situ crystallisation on trace element concentrations, whether in a solidification zone or as the effects of a trapped melt, is to reduce the degree of fractionation.

(d) *Assimilation and fractional crystallisation.* It was Bowen (1928) who first proposed that the latent heat of crystallisation generated during fractional crystallisation may lead to wall-rock assimilation in the magma chamber (see Section 3.3.1). In practical terms this may be evidenced by the presence of xenoliths of country rock within magmatic rocks. Petrologically, the process of crustal assimilation is likely to be important in understanding the geochemistry of magmas erupted through the continental crust, for in this tectonic setting it is necessary to remove the effects of country rock assimilation before the composition of primary magmas can be established.

The first quantitative model in which assimilation and fractional crystallisation (AFC) were seen as coupled processes was given by DePaolo (1981b), who described the concentration of trace elements, and stable and radiogenic isotope ratios, in a melt relative to the composition of the original magma.

The general equation is given by DePaolo (1981b) and is

$$C_L/C_o = f' + [r/(r-1+D] \times [C_A/C_o \times (1-f')] \quad (4.25)$$

where r is the ratio of the assimilation rate to the fractional crystallisation rate and is kept constant, D is the bulk partition coefficient (also kept constant), C_L is the element concentration in the contaminated magma, C_A is the concentration of the trace element in the assimilated wall rock and f' is described by the relationship $f' = F^{-(r-1+D)/(r-1)}$ in which F is the fraction of magma remaining and D is the bulk distribution coefficient.

In subsequent studies Powell (1984) inverted the DePaolo (1981b) equations in order to characterise the chemistry of contaminants involved in magma evolution from observed isotope and trace element relationships, and Aitcheson and Forrest (1994) provided a graphical solution to calculate the proportion of crust assimilated relative to the mass of the magma. Cavazzini (1996) added the caveat that the time-averaged mass of assimilated crust can be significantly different from the instantaneous mass of material assimilated. More recently, Guzman et al. (2014) developed software to provide solutions to the equations of DePaolo (1981b) and Aitcheson and Forrest (1994). Other relevant studies include Cribb and Barton (1996), who extended the DePaolo (1981b) model to include the case where r is not constant and the mass of assimilated crust is decoupled from the mass crystallised, and Nishimura (2012, 2013), who provided a model and associated software for AFC processes which accommodate the effects of the imperfect separation of crystals from the melt. More advanced modelling based on the energy-constrained AFC (EC-AFC) models of Bohrson and Spera (2001, 2007) and Spera and Bohrson (2001), and the Magma Chamber Simulator of Bohrson et al. (2014), are used to model crystallization, magma recharge and assimilation processes by coupling thermodynamically based phase equilibria solutions to constraints based on trace elements and isotope geochemistry (Heinonen et al., 2019).

During AFC processes the concentration of a trace element in the final melt relative to the concentration in the initial parental magma is dependent on the fraction of melt remaining and the bulk distribution coefficient. This is illustrated in Figure 4.14 which shows two ratios for the rate of assimilation ($r = 0.2$ and 0.8), different ratios for the concentration of the trace element in the assimilant relative to the parent magma (C_A/C_o) = 0.1, 10 and 100) for different values of D (0.1 and 2). Where the rate of assimilation to fractional crystallization is small ($r = 0.2$) and the ratio of the concentration of the trace element in the assimilant relative to the parental magma (C_A/C_o) is small, incompatible elements behave in a manner similar to Rayleigh fractionation. However, as the value of (C_A/C_o) increases the concentration in the final melt rises rapidly even when there is a large fraction of melt remaining. Depletion in compatible

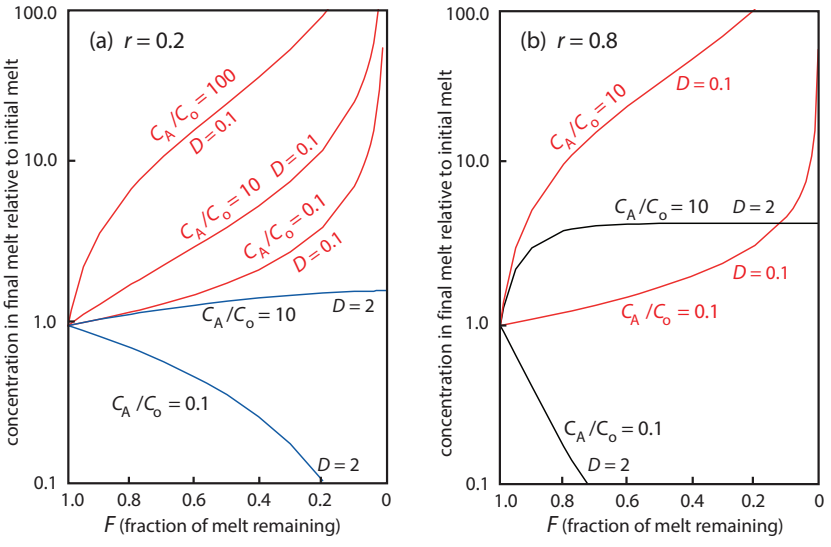

Figure 4.14 The concentration of trace elements in the final melt composition relative to the initial melt composition during AFC processes. The relative concentrations for incompatible element (D = 0.1) and a compatible element (D = 2) are plotted against the fraction of melt remaining in the magma chamber (F) during assimilation and fractional crystallisation for two different values of r (the ratio of the assimilation rate to the fractional crystallisation rate) and at a range of concentrations in the assimilant relative to the parental magma (C_A/C_o) (Eq. 4.25).

elements is less dramatic than in Rayleigh fractionation for low C_A/C_o values, and when the relative concentration of the trace element in the assimilant is higher than that in the primary magma, the final melt is enriched relative to the initial melt. For very compatible elements concentrations level off after a small degree of fractionation. Where the rate of assimilation is high ($r = 0.8$) and the concentration of the trace element in the assimilant relative to the parental magma (C_A/C_o) is small, incompatible elements are enriched and there is some separation between incompatible and strongly incompatible elements (Figure 4.14b). In contrast, compatible elements are strongly depleted. As the trace element concentration in the assimilant increases relative to the parental melt (C_A/C_o), compatible elements are enriched (Figure 4.14b).

AFC processes can be difficult to recognise on the basis of geochemistry alone for they require a strong contrast in trace element concentrations between magma and wall rock before they can be detected (Powell, 1984). For this reason, where field observations are available they should be included in formulating any hypothesis of AFC processes. The large number of variables in Eq. 4.25 means that the results plotted in Figure 4.14 will not provide a unique solution to the relative proportion of crustal assimilated into the magma. For this purpose, readers should follow the methods of Aitcheson and Forrest (1994) and Guzman et al. (2014).

(e) *Dynamic fractionation: the RTF magma chamber.* In an attempt to view magma chamber processes in a dynamic way, O'Hara (1977) and O'Hara and Matthews (1981) proposed a model to describe the behaviour of trace elements in a periodically replenished, periodically tapped, continuously fractionated magma chamber (abbreviated to RTF). In other words, this is an open magmatic system. Support for this approach comes from the petrology and geochemistry of layered mafic igneous intrusions and their associated lavas such as those from the Isle of Skye in Scotland (Fowler et al., 2004).

O'Hara (1977) and O'Hara and Matthews (1981) proposed that the life of a magma chamber comprises a series of cycles, each of which has four stages: fractional crystallisation, magma eruption, wall-rock contamination and replenishment. The simplest form of this model is where all parameters (melt fractions and partition coefficients) remain constant during the life of the magma chamber, there is no assimilation, the mass fractions of melt escaping and that being added to the system are small, and the melt is in a steady state. That is, the volume of melt leaving the system through crystallisation and eruption is the same as the volume melt added to system, so that the magma chamber maintains a constant volume of melt. In this case the concentration of a trace element in the steady state melt produced after a large number of cycles ($_{ss}C_B$) relative to the concentration in the parent magma (C_o) is given by the expression

$$_{ss}C_B/C_o = \left[(x+y)\times(1-x)^{D-1}\right] \Big/ \left[1-(1-x-y)\times(1-x)^{D-1}\right] \quad (4.26)$$

where x is the mass fraction of the liquid lost to crystallisation in each cycle, y is the mass fraction of the liquid escaping in each cycle, and D is the bulk distribution coefficient.

O'Hara and Matthews (1981) also provide a more general, iterating equation for the RTF magma chamber for the concentration of an element in a mixed magma after multiple cycles (see their Eq. 9). In the special case where $x + y = 1$, that is, the magma chamber is emptied, then

$$_{ss}C_B/C_o = (1-x)^{D-1} \quad (4.27)$$

which is the Rayleigh fractionation equation.

If x and y are very small, then

$$_{ss}C_B/C_o = (x+y)/(Dx+y) \quad (4.28)$$

When $D = 0$, that is, in the case of a totally incompatible trace element,

$$_{ss}C_B/C_o = 1 + x/y \quad (4.29)$$

and is a measure of the maximum enrichment attainable.

The degree of enrichment in the melt $_{ss}C_B/C_o$ (calculated using Eq. 4.26) is plotted against x, the mass fraction of liquid crystallised in each cycle (Figure 4.15). Assuming $y = 0.1$, the mass of melt crystallised for several different values of D shows that during dynamic fractionation the relative concentrations of compatible elements are similar to those produced during Rayleigh fractionation, but for the incompatible elements small changes in partition coefficient show measurable concentration differences at moderate x-values.

Since the early work of O'Hara (1977) and O'Hara and Matthews (1981) there have been a number of

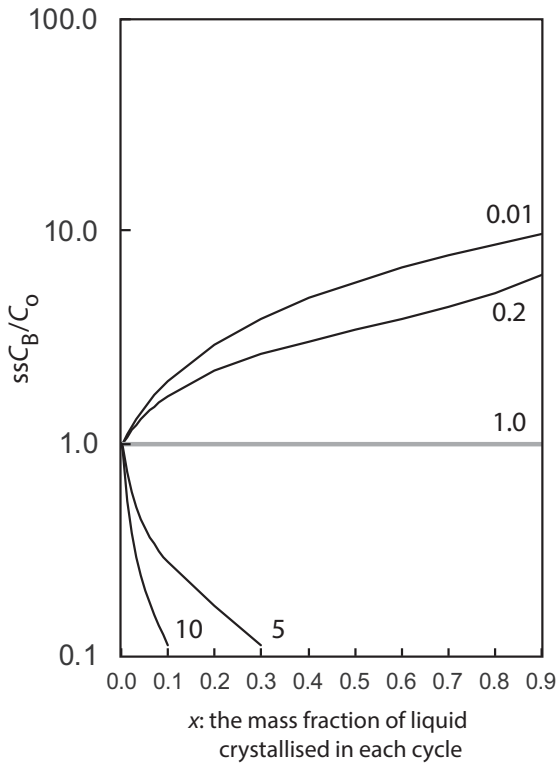

Figure 4.15 The degree of enrichment $_{ss}C_B/C_o$ versus x (the mass fraction of liquid crystallised in each RTF cycle) for a range of partition coefficients. y (the mass fraction of the liquid lost to crystallisation in each cycle) = 0.1. Note the difference in relative concentration between the incompatible and moderately incompatible element for low and intermediate values of x.

subsequent studies, which are summarised in Shaw (2006), Bohrson et al. (2014) and Nishimura (2019), and the consensus is that despite the dynamic nature of the processes involved in RTF magma chambers, trace element concentrations appear to show steady state behaviour. A particular and perhaps diagnostic feature of RFT processes is that 'significant changes can occur in the ratio of highly incompatible and moderately incompatible elements (D = 0.01–0.2)' (O'Hara and Matthews, 1981), although Langmuir (1989) points out that these properties are also very similar to those characterising in situ crystallisation processes discussed above and that care needs to be taken to discriminate between the two processes.

4.2.2.4 Sedimentary Processes

Trace element concentrations in sediment result from the competing influences of the provenance, weathering, diagenesis, sediment sorting and the aqueous geochemistry of the individual elements. For the most part, however, these processes have not been quantified in the same way as in igneous rocks. A notable exception is the field of low-temperature aqueous geochemistry in which advanced quantitative models developed by Bethke (2012) have been applied to chemical models of river water and seawater, to the formation of hydrothermal mineral deposits and to understanding the processes of weathering, sediment diagenesis and acid drainage.

Most trace elements have very low concentrations in river and seawater, and controls on their REE concentrations are discussed in Section 4.3.3.2. In sediments the highest concentrations of trace elements are found in clay-rich sediments, and most geochemical studies have concentrated on these. There is an extensive literature on the trace element geochemistry of shales. In particular, selected trace elements may be used to identify specific geochemical processes but also are important in identifying the provenance of sediments. The most important elements in this respect are the REE, Th, Sc and to a lesser extent Cr and Co. These elements have very low concentrations in seawater and river waters, low residence times in the ocean, and element ratios which are unaffected by diagenesis and metamorphism. Thus, they represent the terrigenous component of sediment and reflect the chemistry of their source (see Sections 4.3.3.3 and 4.6.2). Other immobile elements such as Zr, Hf and Sn may be mechanically distributed according to grain size and be controlled by the concentration of the so-called accessory heavy minerals.

The more soluble trace elements include Fe, Mn, Pb and sometimes Cr, and these can be mobile during diagenesis. During weathering the elements Cs, Rb and Ba are fixed but Sr can be leached. In chemical sediments trace element concentrations are most likely to reflect the composition of the water from which they were precipitated: seawater, pore water, or hydrothermal fluids (see Section 4.3.3.3).

4.3 The Rare Earth Elements (REE)

The rare earth elements (REE) are amongst the most useful of all trace elements in evaluating a wide range of processes in igneous, sedimentary and metamorphic petrology, and also make an important contribution to cosmochemistry. In geochemistry the REE, more accurately known as the lanthanide

REE, comprise the series of metals with atomic numbers 57–71 (the elements La to Lu, Table 4.6). In addition, the element Y has an ionic radius similar to that of the REE and is sometimes included with them. Typically, elements with low atomic numbers in the series are termed the light rare earth elements (LREE), those with the higher atomic numbers the heavy rare earth elements (HREE), and less commonly the middle members of the group (Sm to Ho) are known as the middle rare earth elements (MREE).

4.3.1 The Chemistry of the REE

The REE all have very similar chemical and physical properties. This arises from the fact that they all form stable 3+ ions of similar size. Typically, they substitute for large major element cations such as Ca^{2+} which has a similar ionic radius of 1.12 Å in eight-fold coordination. Such differences as there are in chemical behaviour are a consequence of the small but systematic decrease in ionic size with increasing atomic number, known in chemistry as the lanthanide contraction. This is illustrated for ions in eight-fold coordination state in Table 4.6. These small differences in size and behaviour are exploited by a number of petrological processes causing the REE series to become fractionated relative to each other. It is this phenomenon which is used in geochemistry to probe into the genesis of rock suites and unravel petrological processes. A small number of the REE also exist in oxidation states other than 3+ but the only ions of geological importance are Ce^{4+} and Eu^{2+}. These form a smaller and a larger ion, respectively, relative to the 3+ oxidation state and may be a useful monitor of redox conditions. A detailed review of the geochemistry of the REE is given by McLennan and Taylor (2012) and discussion of REE mineralisation and its importance in modern technology by Chakhmouradian and Wall (2012).

Table 4.6 The rare earth elements

Atomic number	*Name*	*Symbol*	*Ionic radius for eight-fold coordination*[a]	
57	Lanthanum	La	La^{3+}	1.160
58	Cerium	Ce	Ce^{3+}	1.143
			Ce^{4+}	0.970
59	Praesodymium	Pr	Pr^{3+}	1.126
60	Neodymium	Nd	Nd^{3+}	1.109
61	Promethium	Pm	*not naturally occurring*	
62	Samarium	Sm	Sm^{3+}	1.079
63	Europium	Eu	Eu^{3+}	1.066
			Eu^{2+}	1.250
64	Gadolinium	Gd	Gd^{3+}	1.053
65	Terbium	Tb	Tb^{3+}	1.040
66	Dysprosium	Dy	Dy^{3+}	1.027
67	Holmium	Ho	Ho^{3+}	1.015
68	Erbium	Er	Er^{3+}	1.004
69	Thulium	Tm	Tm^{3+}	0.994
70	Ytterbium	Yb	Yb^{3+}	0.985
71	Lutetium	Lu	Lu^{3+}	0.977
39	Yttrium	Y	Y^{3+}	1.019

[a] From Shannon (1976), in angstroms (10^{-10} m; 1 angstrom = 100 picometres).

4.3.2 Presenting REE Data

Rare earth element concentrations in rocks are usually normalised to a reference standard or particular rock type (Section 4.3.2.5). Chondritic meteorites are a common reference standard chosen because they are thought to be the most primitive, least fractionated samples of the solar system dating from the time of nucleosynthesis. However, the concentrations of the REE in the solar system are highly variable because of the different stabilities of the atomic nuclei. REE with even atomic numbers are more stable, and therefore more abundant, than REE with odd atomic numbers, thus producing a zig-zag pattern on a composition–abundance diagram (Figure 4.16a) known as the Oddo–Harkins effect. This pattern of abundance is also found in natural samples, and so chondritic normalisation has two important functions. First, it eliminates the abundance variation between odd and even atomic number elements, producing a smooth curve, and, second, it allows any fractionation of the REE group relative to chondritic meteorites to be easily identified. Normalised values and ratios of normalised values are denoted with the subscript N – hence, Ce_N, $(La/Ce)_N$, and so on. The REE are normally presented on a normalised concentration versus atomic number diagram, although O'Neill (2016) has recommended using the 3+ ionic radius as the x-axis rather than the atomic number. The advantage of using ionic radii is that the resulting pattern is generally smoother and highlights any anomalies; it is also amenable to the fitting of a polynomial which may be used in petrogenetic interpretation (O'Neill, 2016). Concentrations are plotted on the y-axis, normalised to the chondritic

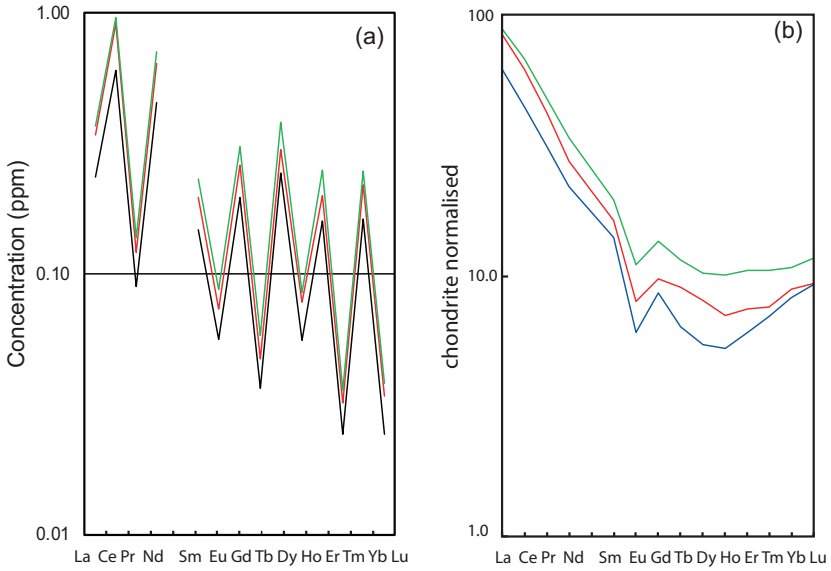

Figure 4.16 Plots of REE concentration. (a) REE concentrations in ppm for selected CI chondrites plotted against atomic number. REE with even atomic numbers have higher concentrations than those with odd atomic numbers. These values are used to normalise rock REE concentrations. The green line represents the data of Taylor and McLennan (1985) (column 12 in Table 4.7), the red line the data of Wakita et al. (1971) (column 9 in Table 4.7), and the black line the data of Anders and Grevesse (1989) (column 3 in Table 4.7). (b) An example of a chondrite normalised plot showing the REE plotted by atomic number on the *x*-axis and CI chondrite normalised concentrations plotted on a log scale *y*-axis. The data are for plagiogranites from the mantle section of the Oman ophiolite and are samples 13–18, 13–19 and 13–21 from Rollinson (2015). They are normalised using the values of Barrat et al. (2012) (Table 4.7, column 7). The samples show negative Eu anomalies with Eu/Eu* = 0.55–0.68.

reference value, and expressed as the logarithm to the base 10 of the value. Concentrations at individual points on the graph are joined by straight lines (Figure 4.16b). It is normal to plot the full range of atomic numbers (57–71) on the *x*-axis, even if not all the REE have been measured (e.g., Pm). This type of REE diagram is sometimes referred to as the Masuda–Coryell diagram after the original proponents of the diagram (Masuda, 1962; Coryell et al., 1963). Trends on REE diagrams are usually referred to as *REE patterns* and the shape of a REE pattern is of considerable petrological interest.

The plotted position of Eu may lie off the general trend defined by the other elements on a REE diagram (Figure 4.16b) and this defines a *europium anomaly*. If the plotted composition lies above the general trend, then the anomaly is described as positive; and if it lies below the trend, then the anomaly is said to be negative. Europium anomalies may be quantified by comparing the measured concentration (Eu) with an expected concentration obtained by interpolating between the normalised values of Sm and Gd to calculate Eu*. Thus the ratio Eu/Eu* is a measure of the europium anomaly; a value of greater than 1.0 indicates a positive anomaly, and a value of less than 1.0 is a negative anomaly.

Taylor and McLennan (1985) recommend using the geometric mean to calculate the Eu anomaly:

$$Eu/Eu^* = Eu_N/\sqrt{[(Sm_N)*(Gd_N)]}.$$

In a similar manner, Ce anomalies can be quantified:

$$Ce/Ce^* = Ce_N/\sqrt{[(La_N)*(Pr_N)]}$$

Normally anomalies should be less than 0.95 or greater than 1.05 to be considered significant.

4.3.2.1 Difficulties with Chondrite Normalisation

There are a large number of different values determined for the composition of chondritic meteorites, and so it is important to explore how this range of values has arisen and the implications this has for appropriate normalisation values. The logic behind

chondrite normalisation is that chondrites represent the undifferentiated material of the solar system, and so any divergence from these values is indicative of a process or set of processes that has operated on the Earth. It is important therefore to identify the most primitive of the chondrites as the reference point for the least differentiated materials of the solar system. Older chondrite analyses of the REE were based upon data for ordinary chondrites (Haskin et al., 1968), whereas CI (letters 'C' and 'I') carbonaceous chondrites do not contain chondrules (early solar system melts) and represent the least thermally altered samples of the early solar system. However, there are some difficulties with this approach:

- CI chondrites are extremely rare. There only five known and the largest is the Orgueil meteorite, a 14-kg meteorite which fell in France in 1868.
- Measurements are normally made using very small quantities of meteorite material. It is unclear how heterogeneous chondritic meteorites are (Barrat et al., 2012).
- Carbonaceous chondrites are rich in volatiles. Comparative studies must take account of possible differences in volatile content.
- Difference analytical approaches have been used to measure REE in chondrites. Early studies used neutron activation (INAA), although this method can analyse only for a subset of the REE, whereas more recent measurements are made by isotope dilution (IDMS) and ICP-MS.

4.3.2.2 Choosing a Set of Normalising Values

There are currently two different approaches to selecting an appropriate set of chondritic reference values for normalising the REE. Some authors normalise to the average composition of ordinary chondrites, whereas others use an average of CI chondrites. The ordinary chondrite values are higher than the CI chondrite values. Some typical normalising values currently in use are given in Table 4.7.

(a) *Normalisation to CI chondrites.* A carefully evaluated data set is given by Anders and Grevesse (1989), who calculated a mean value for CI chondrites from all published data at the time and found good agreement between their average chondrite data and solar element abundances determined independently from spectroscopy. (This similarity strongly supports the view that CI carbonaceous chondrites are representative of primitive solar system materials). They report two sets of values: an average of all CI meteorite data and an average for the Orgueil meteorite (Anders and Grevesse, 1989). The values of Sun and McDonough (1989) and McDonough and Sun (1995) are almost identical and are also based on average values from previous studies.

More recent determinations include those of Lodders et al. (2009), who provided a new CI average based upon data for the Orgueil meteorite, and Pourmand et al. (2012), who provide a new average based upon new multi-collector ICP-MS measurements of eight CI chondrites (five Orgeuil, two Ivuna and one Alais). Barrat et al. (2012) made new analyses of the Orgueil meteorite and of two other CI meteorites (Ivuna and Alais) by ICP-sector field mass spectrometry. They present a new average analysis for the Orgueil meteorite and show that it compares well with that of previous workers, although they note that the value for Tm in Anders and Grevesse (1989) may be too low.

(b) *Normalisation to ordinary chondrites (CI chondrite, calculated volatile-free).* Normalisation to ordinary chondrites is a means of taking into account the volatile content of CI chondrites. These values typically use the better-determined CI concentrations and introduce a factor to make the concentrations similar in absolute magnitude to those found in ordinary chondrites. For example, Korotev (1996) uses the compilation of Anders and Grevesse (1989) for CI chondrites multiplied by a factor of 1.36. A similar approach was adopted by Taylor and McLennan (1985, 2009), who used the values of Evensen et al. (1978) multiplied by 1.5, and Boynton (1984), who also used the values of Evensen et al. (1978) multiplied by 1.267 in order to be consistent with the average values of Haskin et al. (1968) and Wakita et al. (1971).

The normalising values currently in use are given in Table 4.7. It can be seen that the CI chondrite values calculated volatile-free are as much as 50% larger than the averaged CI values. It is important, therefore, that authors cite the source of the normalising values that they choose to use. Figure 4.16a shows the normalising concentrations plotted on a log-concentration versus REE atomic number plot. This diagram shows the higher concentrations of REE with even atomic numbers (the Oddo–Harkins effect) and shows that the normalising values based upon CI chondrites are all very similar. An example of a typical REE plot is given in Figure 4.16b.

Table 4.7 Chondrite values used in normalising REE (concentrations in ppm)

	Averaged CI chondrite								*'Older' ordinary chondrite*		*CI chondrite (recalculated volatile free)*			
	1	*2*	*3*	*4*	*5*	*6*	*7*	*8*	*9*	*10*	*11*	*12*	*13*	*14*
La	0.2370	0.2370	0.2347	0.2360	0.2420	0.2469	0.2350	0.24460	0.340	0.330	0.3670	0.3670	0.3191	0.3100
Ce	0.6120	0.6130	0.6032	0.6190	0.6220	0.6321	0.6000	0.63790	0.910	0.880	0.9570	0.9570	0.8201	0.8080
Pr	0.0950	0.0928	0.0891	0.0900	0.0946	0.0959	0.0910	0.09637	0.121	0.112	0.1370	0.1370	0.1211	0.1220
Nd	0.4670	0.4570	0.4524	0.4630	0.4710	0.4864	0.4640	0.47380	0.640	0.600	0.7110	0.7110	0.6151	0.6000
Sm	0.1530	0.1480	0.1471	0.1440	0.1520	0.1556	0.1530	0.15400	0.195	0.181	0.2310	0.2310	0.2000	0.1950
Eu	0.0580	0.0563	0.0560	0.0547	0.0578	0.0599	0.0586	0.05802	0.073	0.069	0.0870	0.0870	0.0761	0.0735
Gd	0.2055	0.1990	0.1966	0.1990	0.2050	0.2003	0.2060	0.20430	0.260	0.249	0.3060	0.3060	0.2673	0.2590
Tb	0.0374	0.0361	0.0363	0.0353	0.0384	0.0378	0.0375	0.03745	0.047	0.047	0.0580	0.0580	0.0494	0.0474
Dy	0.2540	0.2460	0.2427	0.2560	0.2550	0.2577	0.2540	0.25410	0.300	*nd*	0.3810	0.3810	0.3300	0.3220
Ho	0.0566	0.0546	0.0556	0.0552	0.0572	0.0554	0.0566	0.05670	0.078	0.070	0.0851	0.0851	0.0756	0.0718
Er	0.1655	0.1600	0.1589	0.1620	0.1630	0.1667	0.1660	0.16600	0.200	0.200	0.2490	0.2490	0.2160	0.2100
Tm	0.0255	0.0247	0.0242	0.0220	0.0261	0.0261	0.0262	0.02561	0.032	0.030	0.0356	0.0356	0.0329	0.0324
Yb	0.1700	0.1610	0.1625	0.1660	0.1690	0.1694	0.1680	0.16510	0.220	0.200	0.2480	0.2480	0.2209	0.2090
Lu	0.0254	0.0246	0.0243	0.0245	0.0253	0.0256	0.0246	0.02539	0.034	0.034	0.0381	0.0381	0.0330	0.0322
Y	1.5700	1.5700	1.5600	1.5300	1.5300	1.3950	1.5600	*nd*	*nd*	*nd*	2.2500	2.1000	2.1210	*nd*

Notes: *nd*, no data.

References: 1, Sun and McDonough (1989); 2, McDonough and Sun (1995); 3, Anders and Grevesse (1989) average; 4, Anders and Grevesse (1989) Orgueil; 5, Lodders et al. (2009); 6, Pourmand et al. (2012); 7, Barrat et al. (2012); 8, Evensen et al. (1978); 9, Wakita et al. (1971); 10, Haskin et al. (1968); 11, Taylor and McLennan (2009); 12, Taylor and McLennan (1985); 13, Korotev (1996); 14, Boynton (1984).

4.3.2.3 REE Ratio Diagrams

The degree of fractionation of a REE pattern can be expressed by the ratio of the normalised concentration of a light REE (La or Ce) divided by the normalised concentration of a heavy REE such as Yb or the trace element Y. Hence the ratio $(La/Yb)_N$ is often plotted against either Ce_N or Yb_N on a bivariate graph and is a measure of the degree of REE fractionation, that is, the steepness of the REE pattern, with changing REE content. This is particularly helpful for large REE data sets, for a single diagram can summarise the results of otherwise very crowded REE plots. Similar diagrams may be constructed to measure the degree of fractionation of subgroups within the REE. In this way the ratio $(La/Sm)_N$ might be indicative of the degree of light REE fractionation and a ratio such as $(Gd/Yb)_N$ indicative of heavy REE fractionation. These two variables might be combined in bivariate plots such as $(La/Sm)_N$ versus La_N or $(Gd/Yb)_N$ versus Yb_N to show the relative fractionation of the light or heavy REE, respectively. When a data set shows variable REE patterns, it can be helpful to screen them and group them on a $(La/Sm)_N$ versus $(Gd/Yb)_N$ diagram (Figure 4.17).

4.3.2.4 Shale Normalisation for Sediments

It has been observed that the concentration of many elements in fine-grained sedimentary rocks from continental platforms around the world is similar. This is a consequence of mixing through repeated cycles of erosion and the resultant 'average sediment' might be seen as an average composition of the Earth's upper continental crust. Average shale compositions therefore are often used as the normalising value for REE concentrations in sedimentary rocks. Whether shale normalisation should be used rather than chondrite normalisation is governed by the nature of the problem to be solved. If the composition of a suite of sediments is to be compared to the average 'background' composition of the Earth's upper crust – the likely source of the sediments – then shale normalisation is suitable. In this case any divergence from the shale value indicates the specific processes through which the sediment was produced. If chondrite normalisation is used, then the sediments are being compared with the primitive material of the solar system and divergence from the chondrite values will reflect the sum of all the processes that have taken place between the formation of the Earth and the formation of the sediment.

A range of commonly used shale averages is given in Table 4.8. Frequently, the reference sample chosen is continent-specific and includes the following:

- The North American shale composite (NASC; McLennan, 1989)
- Mud from Queensland denoting modern alluvial sediment (MUQ; Kamber et al., 2005)
- Post-Archaean Australian shale (PAAS; Pourmand et al., 2012)
- European shale (ES; Bau et al., 2018).

In addition, a world shale average (WSA) has been proposed by Bau et al. (2018). The average value of the upper continental crust determined by Rudnick and Gao (2014) is based upon an average of surface derived samples, sediments and loess (Figure 4.18a). It has an identically shaped REE pattern to that of the shale samples, although the absolute REE concentrations in the average upper crust are slightly lower due to the dilution effect of REE-poor clastic and carbonate sediments. Relative to chondritic meteorites, shale averages have > 100 times light REE and show steep light REE patterns $(La/Sm)_N = 3.1–4.3$. They have a small negative Eu anomaly and a relatively flat heavy REE pattern $(Gd/Yb)_N = 1.4–1.6$, with about 20–30 times chondrite concentrations (Figure 4.18a).

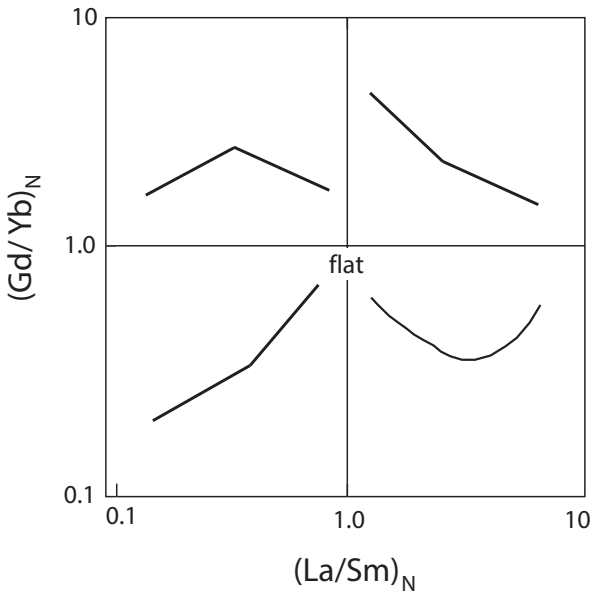

Figure 4.17 Log-log $(La/Sm)_N$ versus $(Gd/Yb)_N$ plot showing typical shapes of REE patterns indicated by the different quadrants of the diagram.

Table 4.8 Reference compositions used for normalising the REE concentrations in sedimentary rocks and typical REE concentrations in ocean and river waters

	Sediment						Water				
	NASC ppm	MUQ ppm	PAAS ppm	ES ppm	WSA ppm	UCC ppm	Pacific 49-m depth ppm	Pacific 2576-m depth ppm	North Sea ppm	Rhine River ppm	MORT years
	1	2	3	4	5	6	7	8	9	10	11
La	32.00	32.51	44.56	44.300	40.30	31.00	1.25E-06	6.2E-06	2.89E-06	7.87E-05	1630
Ce	73.00	71.09	88.25	88.500	83.30	63.00	9.64E-07	2.17E-06	4.90E-06	2.90E-05	130
Pr	7.90	8.46	10.15	10.600	9.54	7.10	2.07E-07	9.44E-07	1.05E-06	5.35E-06	800
Nd	33.00	32.91	37.32	39.500	36.60	27.00	1.04E-06	4.38E-06	4.60E-06	2.31E-05	950
Sm	5.70	6.88	6.884	7.300	6.63	4.70	2.38E-07	8.78E-07	1.23E-06	1.27E-05	970
Eu	1.24	1.57	1.215	1.480	1.31	1.00	6.53E-08	2.34E-07	3.71E-07	1.46E-06	820
Gd	5.20	6.36	6.043	6.340	5.86	4.00	3.4E-07	1.33E-06	2.47E-06	1.10E-05	1100
Tb	0.85	0.99	0.8914	0.944	0.90	0.70	6.99E-08	2.13E-07	3.38E-07	9.98E-07	1130
Dy	5.80	5.89	5.325	5.860	5.66	3.90	4.49E-07	1.56E-06	2.40E-06	6.08E-06	1510
Ho	1.04	1.22	1.053	1.170	1.09	0.83	1.19E-07	4.26E-07	6.10E-07	1.32E-06	6800
Er	3.40	3.37	3.075	3.430	3.30	2.30	3.63E-07	1.44E-06	1.97E-06	3.92E-06	6800
Tm	0.50	0.51	0.451	0.492	0.48	0.30	5.07E-08	2.21E-07	*nd*	*nd*	*nd*
Yb	3.10	3.25	3.012	3.260	3.12	2.00	3.29E-07	1.51E-06	1.96E-06	3.78E-06	*nd*
Lu	0.48	0.49	0.4386	0.485	0.47	0.31	4.72E-08	2.68E-07	3.50E-07	6.57E-07	*nd*
Y	27.00	31.85	27.31	31.900	28.70	21.00	6.69E-06	2.24E-05	2.60E-05	3.75E-05	5100

Notes: *nd*, no data.

References: 1, North American shale composite (McLennan, 1989); 2, Queensland mud (Kamber et al., 2005); 3, post-Archaean average Australian sedimentary rock (Pourmand et al., 2012); 4, average European shale (Bau et al., 2018); 5, world shale average (Bau et al., 2018); 6, average upper continental crust (Rudnick and Gao, 2014); 7, northwest Pacific (49-m depth) (Alibo and Nozaki, 1999); 8, northwest Pacific (2576-m depth) (Alibo and Nozaki, 1999); 9, seawater, North Sea (Bau et al., 2018); 10, river water, Rhine (Bau et al., 2018); 11, mean oceanic residence time in years (Alibo and Nozaki, 1999).

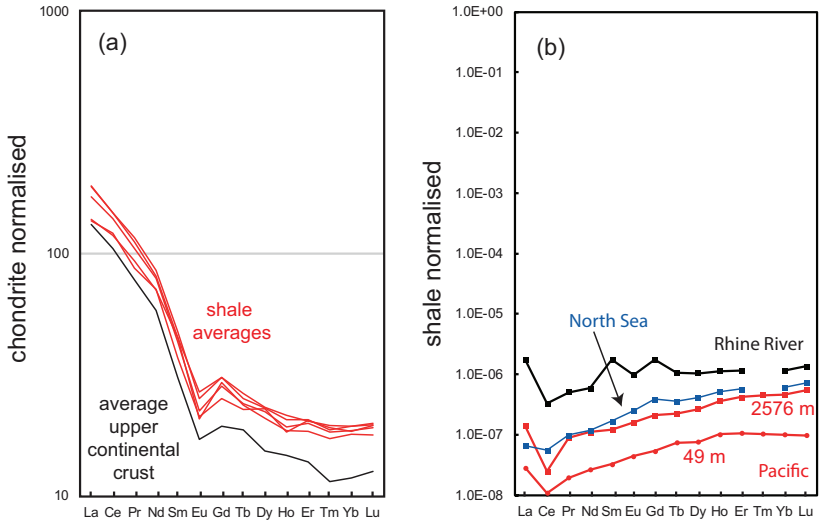

Figure 4.18 Sediment normalization. (a) Five average shale compositions (red) and the average composition of the upper continental crust (black) (from Table 4.8), plotted relative to their concentration in chondritic meteorites using the normalising values of Barrat et al. (2012). (b) The composition of ocean water and river water (Table 4.8) normalised to the composition of European shale (Table 4.8, column 4). The composition of filtered North Sea water and Rhine River water are from Bau et al. (2018) and the total dissolved concentrations of REE from two different depths in the northwest Pacific Ocean are from Alibo and Nozaki (1999). Note the different scales in (a) and (b).

4.3.2.5 Rock Normalisation

Some authors normalise REE concentrations to a particular sample in a rock suite as a measure of relative change. This is also useful when the REE concentrations of the individual minerals in the rock have also been determined, for then they can be expressed relative to the concentration in the whole rock as a means of showing where the REE are concentrated in the sample. A similar form of normalisation is used to express REE concentration in a mineral relative to the composition of the groundmass and this can also be used to display mineral-melt partition coefficients (Section 4.2.1).

4.3.3 Interpreting REE Patterns

The REE are regarded as amongst the least soluble trace elements and are relatively immobile during low-grade metamorphism, weathering and hydrothermal alteration. This is evident from the very low concentrations found in modern river waters and seawater (see Section 4.3.3.2 and Figure 4.18b). However, the REE are not totally immobile and the reader should be cautious when interpreting the REE patterns of heavily altered or highly metamorphosed rocks. Nevertheless, in some rocks which have experienced moderate grades of metamorphism the REE can faithfully represent the original composition of the unaltered parent and a fair degree of confidence can be placed in the significance of peaks, troughs and the slope of the REE pattern.

4.3.3.1 REE Patterns in Igneous Rocks

An igneous rock may be may be interrogated to determine which process was involved in generating its REE pattern. The analysis of any igneous geochemical data set should systematically screen for the following processes, in this order:

- Identify and eliminate samples which show the effects of chemical weathering, although given the relatively immobile nature of the REE this is unlikely to have any major effect.
- Identify (and eliminate) the effects of magma chamber processes such as crystal fractionation or assimilation.
- Identify the composition of parental melt(s), and from these compositions attempt to determine the nature of the source.

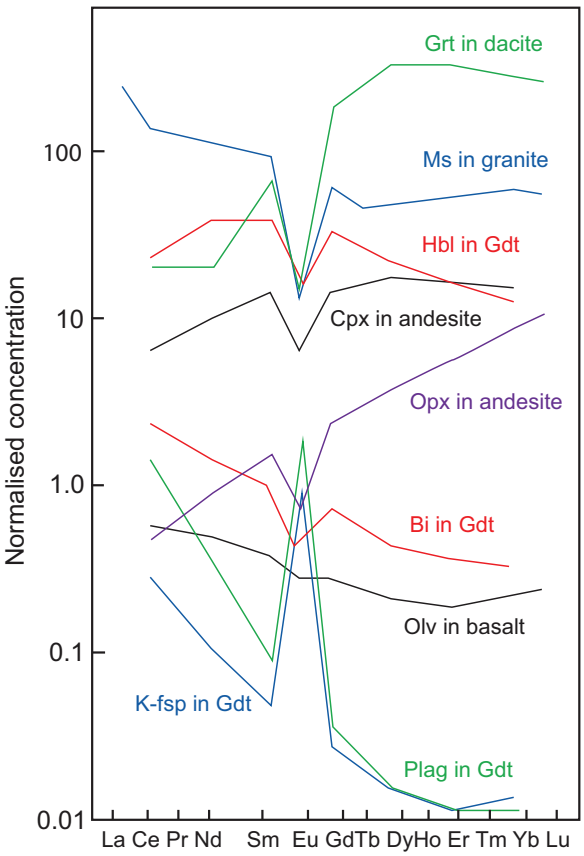

Figure 4.19 Chondrite-normalised REE patterns in common rock-forming minerals in a range of host lithologies (after McLennan, 2018; adapted by permission of Springer-Nature). Grt, garnet; Ms, muscovite; Hbl, hornblende; Cpx, clinopyroxene; Opx, orthopyroxene; Bi, biotite; Olv, olivine; Plag, plagioclase; K-fsp, alkali feldspar; Gdt, granodiorite.

Figure 4.19 shows the chondrite-normalised REE patterns for common rock-forming minerals to indicate the role different mineral phases play during magmatic evolution, either during partial melting of the source or in subsequent crystal fractionation. A greater level of detail may be obtained from the plots of partition coefficient data (Figures 4.5–4.8), although these are the inverse of the concentrations shown in this figure.

Feldspars have very low concentrations of REE, but when present in felsic rocks have a prominent positive Eu anomaly which may strongly influence the shape of a REE pattern. Similarly, in mafic rocks olivine has very low concentrations of REE and is unlikely to fractionate REE during partial melting or crystal fractionation. Of the pyroxenes, orthopyroxene has

lower REE concentrations than clinopyroxene, and in mafic rocks clinopyroxene may be the major site of the REE in the rock. Both may have small negative Eu anomalies but may be large enough in clinopyroxene to be inherited by a melt. Both tend to be richer in the heavy REE than the light REE. Hornblende is typically enriched in the REE and is often distinctive in being enriched in the middle REE. It also has higher concentrations of heavy REE than light and together these features can lead to the development of a slightly U-shaped REE pattern in a melt. Garnet is always richer in the heavy REE than the light, to the extent that the heavy REE are compatible in garnet whereas the light REE are not, leading to extreme REE fractionation. Muscovite is enriched in REE and may be a significant host to REE in felsic rocks, whereas biotite is not. Both have negative Eu anomalies.

In felsic melts accessory phases such as sphene, zircon, allanite, apatite and monazite may strongly influence a REE pattern, for although they may be present in only small quantities (often much less than 1% of the rock) their very high partition coefficients for the REE mean that they have a disproportionate influence on the REE pattern (see Figure 4.8). Zircon will have an effect similar to that of garnet and will deplete a melt in the heavy REE; titanite and apatite partition the middle REE relative to the light and heavy; and monazite and allanite cause depletion in the light REE.

4.3.3.2 REE Patterns in Seawater and River Water

The REE contents of seawater and river water are extremely low (Table 4.8) and because of this many analytical protocols utilise a *pre-concentration* method. Concentrations are reported as ppb, or as pmol/kg. The conversion from moles to grams is to multiply by the atomic weight of the element. Values are usually normalised to a shale reference standard. REE concentrations in seawater are between 6 and 7 orders of magnitude smaller that the shale value, and river waters are about an order of magnitude higher (Figure 4.18b). On a shale-normalised plot, seawater tends to show a gradual enrichment in REE concentrations from the light to heavy REE and often shows a prominent negative Ce anomaly which is expressed as Ce/Ce* (see Section 4.3.2). When Y is included with the REE, it is plotted between Dy and Ho and may also show a positive Y anomaly (Bau et al., 2014). Concentrations in water from the river Rhine also show a small negative Ce anomaly and an increase in REE concentrations from the light to heavy REE, similar to that observed in seawater (Figure 4.18b).

The geochemical processes operating in the aqueous environment are different from those operating in igneous or sedimentary rocks. For example, REE in seawater may be present in solution or adsorbed onto particulate matter contained in the seawater, and for this reason many authors distinguish between *filtered* and *unfiltered* results. In seawater the fraction of adsorbed REE is usually small, except for the element Ce, which may be significant (Alibo and Nozaki, 1999), although in river water the REE content of the suspended load is greater. Further, REE concentrations in seawater increase with depth (Figure 4.18b) and show what is known as nutrient-like behaviour in their concentration versus depth distribution. In the case of the heavy REE and Y this increase may be as much as a factor of four. This variability with depth is related to the observation that the REE are ultimately removed from seawater by the *scavenging effect* and settling of particulate matter (Schijf et al., 2015); thus, they have a finite life in seawater. Consequently, it is possible to estimate the length of their life in ocean water; this is known as the *residence time*. Mean oceanic residence times (MORT) for most of the REE are given in Table 4.8, column 11, although it should be noted that these estimates are approximate and may vary by a factor of two to three (Alibo and Nozaki, 1999). The greater residence time of the heavy REE relative to that of the light REE is in part related to their greater concentration in the particulate component (Alibo and Nozaki, 1999). A further consideration is the effect of oxidation, which can be seen in the Ce anomaly reflecting the oxidation of Ce^{3+} to Ce^{4+} and the precipitation of Ce^{4+} from solution as CeO_2.

REE concentrations in ocean waters provide information about oceanic input from rivers, hydrothermal vents and aeolian sources (Elderfield, 1988). Eu anomalies reflect either aeolian or hydrothermal input. In the case of the Rhine River water the anomalous concentrations of La, Sm and Gd reflect an anthropogenic component (Kulaksiz and Bau, 2013).

4.3.3.3 REE Patterns in Sediment

REE concentrations of sedimentary rock are usually normalised to one of the shale reference standards listed in Table 4.7, although this practice is not universal and some authors use chondritic normalisation.

Many studies also include Y. There are two main contributions to the REE chemistry of sediment: the terrigenous component, as typified by clastic sediment, and the marine component, as typified by chemical sediment. Most sediment exhibits both components in varying proportions and here we consider the end members.

(a) *Clastic sediment.* The single most important factor contributing to the REE content of clastic sediment is its provenance (McLennan, 1989). This is because the REE are present in very low concentrations in seawater and river water, and therefore the REE present in a sediment are chiefly transported as particulate matter and reflect the chemistry of their source. In comparison, the effects of weathering and diagenesis are minor. Studies such as those by Nesbitt (1979) show that while the REE are mobilised during weathering they are reprecipitated at the site of weathering, and in the case of extreme weathering the source can still be recognised in the REE chemistry of the derivative material (Nesbitt et al., 1990). Diagenesis has little influence on the redistribution of the REE and very large water–rock ratios are required to effect any change in sediment chemistry.

(b) *Clay-bearing sediment*. Clay-bearing sediments/rocks have a much higher concentration of total REE than other types of sediment. It is for this reason that many authors have used the REE content of the clay portion of a sediment or clay-rich sediment to identify sedimentary processes and sediment provenance. The presence of quartz has a diluting effect on REE concentrations, as does carbonate. The presence of heavy minerals, particularly zircon, monazite and allanite, may have a significant (and possibly erratic) effect on the REE pattern of an individual sample (Totten et al., 2007).

(c) *Chemical sediment*. Chemical sediment is most likely to reflect the composition of the water from which it precipitated. In detail this may be seawater, pore water or hydrothermal fluids. Nodules and crusts precipitated from seawater are termed 'hydrogenetic' and approach the inverse of the seawater pattern with positive Ce and negative Y anomalies; precipitates from pore fluids and diagenetic crusts show similar patterns but with lower concentrations and negative Ce anomalies. Hydrothermal deposits have REE patterns similar to that of seawater but are characterised by a positive Eu anomaly (Bau et al., 2014). On this basis it is possible to use REE concentrations to discriminate between different types of ferromanganese crusts and nodules.

A similar approach may be taken in the study of Archaean banded iron formations and carbonates, and these may be used to obtain information about the composition and redox conditions of Archaean seawater. Kamber and Webb (2001) measured REE in Archaean microbial carbonates. Their samples showed no negative Ce anomaly but did have a positive Eu anomaly, suggesting anoxic ocean waters to explain the lack of Ce oxidation and a hydrothermal component to account for the Eu anomaly. Oonk et al. (2018) similarly reported a lack of negative Ce anomaly in the carbonate content of banded iron formations, supporting the view that conditions were less oxidising in the Archaean ocean than in the modern oceans.

4.4 Normalised Multi-element Diagrams or Incompatible Element Diagrams

Normalised multi-element plots are useful for visualising a large amount of geochemical data and showing geochemical similarities or differences between rocks in a sample suite. They are based upon a set of incompatible elements arranged in order of their incompatibility during mantle melting. They are similar to the more familiar chondrite-normalised rare-earth element diagrams inasmuch as they represent a normalisation scheme which uses an agreed-upon set of reference values of geochemical significance.

In recent decades as the portfolio of readily analysed trace elements has increased, the suite of elements used in multi-element diagrams also increased. There are about 30 elements which are commonly used in various normalisation schemes today (see Table 4.9, where concentrations are given in ppm). It should be noted that this list of trace elements includes some elements listed as major elements (K, P and Ti) and so the concentrations of these elements must be converted from wt.% oxide to ppm. The precise order in which the elements are presented in multi-element diagrams varies according to the application of each diagram and the author. It is therefore necessary that internal consistency is applied in any study and that where particular anomalies are found, the elements flanking that anomaly are clearly identified. A number of different multi-element normalisation schemes emphasising slightly different functions are outlined below.

Table 4.9 Normalising values used in multi-element diagrams (all values in ppm)

					MORB				Continental crust			
	CI chondrite		*Primitive mantle*		*Global mean*	*Global LN-mean*	*N-MORB mean*	*N-MORB mean*	*NASC*	*Upper crust*	*Average crust*	*GLOSS II*
Ref	*1*	*2*	*3*	*4*	*5*	*6*	*7*	*8*	*9*	*10*	*11*	*12*
Cs	0.1900	0.1880	0.0210	0.0180	0.053	0.019	0.019	0.007	5.16	4.90	2.00	4.9
Rb	2.3000	2.3200	0.6000	0.6050	4.050	1.500	1.360	0.560	125.00	84.00	49.00	83.7
Ba	2.4100	2.4200	6.6000	6.8500	43.400	16.600	14.700	6.300	636.00	628.00	456.00	786
Th	0.0290	0.0300	0.0795	0.0849	0.491	0.219	0.186	0.120	12.30	10.50	5.60	8.1
U	0.0074	0.0081	0.0203	0.0229	0.157	0.080	0.068	0.047	2.66	2.70	1.30	1.73
K	550	546	240	260	1237	1620	857	600	31545	23244	15026	18345
Nb	0.2400	0.2830	0.6580	0.5950	6.440	3.440	2.330	2.330	*nd*	12.00	8.00	9.42
Ta	0.0136	0.0150	0.0370	0.0430	0.417	0.224	0.191	0.132	1.12	0.90	0.70	0.698
La	0.2370	0.2414	0.6480	0.6832	4.870	3.770	3.390	2.500	31.10	31.00	20.00	29.1
Ce	0.6130	0.6194	1.6750	1.7529	13.100	11.500	10.200	7.500	66.70	63.00	43.00	57.6
Pb	2.4700	2.6200	0.1500	0.1850	0.657	0.570	0.460	0.300	*nd*	17.00	11.00	21.2
Pr	0.0928	0.0939	0.2540	0.2657	2.080	1.910	1.740	1.320	*nd*	7.10	4.90	7.15
Sr	7.2500	7.7900	19.9000	22.0000	138.000	130.000	110.000	90.000	142.00	320.00	320.00	302
Nd	0.4570	0.4737	1.2500	1.3410	10.400	9.800	9.220	7.300	27.40	27.00	20.00	27.6
Be	0.0250	0.0219	0.0680	0.0620	0.640	0.490	0.500	*nd*	*nd*	2.10	1.90	1.99
Zr	3.8200	3.6300	10.5000	10.3000	103.000	90.100	88.800	74.000	200.00	193.00	132.00	129
Hf	0.1030	0.1065	0.2830	0.3014	2.620	2.400	2.360	2.050	6.30	5.30	3.70	3.42
Sm	0.1480	0.1536	0.4060	0.4347	3.370	3.250	3.190	2.630	5.59	4.70	3.90	6
Eu	0.0563	0.0588	0.1540	0.1665	1.200	1.220	1.150	1.020	1.18	1.00	1.10	1.37
Ti	440	447	1205	1265	9110	8500	*nd*	7600	4705	3836	4315	3836
Gd	0.1990	0.2069	0.5440	0.5855	4.420	4.400	4.290	3.680	*nd*	4.00	3.70	5.81
Tb	0.0361	0.0380	0.0990	0.1075	0.810	0.780	0.810	0.670	0.85	0.70	0.60	0.92
Dy	0.2460	0.2558	0.6740	0.7239	5.280	5.110	5.270	4.550	*nd*	3.90	3.60	5.43
Ho	0.0546	0.0564	0.1490	0.1597	1.140	1.110	1.140	1.010	*nd*	0.83	0.77	1.1
Y	1.5700	1.4600	4.3000	4.1300	32.400	30.000	32.200	28.000	*nd*	21.00	19.00	33.3
Er	0.1600	0.1655	0.4380	0.4684	3.300	3.150	3.310	2.970	*nd*	2.30	2.10	3.09
Tm	0.0247	0.0261	0.0680	0.0738	0.490	0.480	0.490	0.456	*nd*	0.30	0.28	*nd*
Yb	0.1610	0.1687	0.4410	0.4774	3.170	3.000	3.200	3.050	3.06	2.00	1.90	3.01
Lu	0.0246	0.0250	0.0675	0.0708	0.480	0.450	0.490	0.455	0.456	0.31	0.30	0.495
Li	1.5000	1.9700	1.6000	1.4500	6.630	5.100	6.640	4.300	*nd*	24.00	16.00	44.8

Notes: *nd*, not determined.

References: 1, McDonough and Sun (1995); 2, Palme and O'Neill (2014); 3, McDonough and Sun (1995); 4, Palme and O'Neill (2014); 5, White and Klein (2014); 6, Arevalo and McDonough (2010); 7, White and Klein (2014); 8, Sun and McDonough (1989); 9, Gromet et al. (1984); 10, Rudnick and Gao (2014); 11, Rudnick and Gao (2014); 12, Plank (2014).

4.4.1 Multi-element Diagrams for Igneous Rocks

There are three popular ways of normalising trace element data from igneous rocks. These include using the compositions of (i) the Earth's primitive mantle, (ii) chondritic meteorites and (iii) primitive mid-ocean ridge basalt (MORB). Each approach has its own logic and areas of application, and it is important that the suite of elements, the order in which they are presented and the normalisation scheme chosen are appropriate to the geological problem being investigated.

4.4.1.1 Chondrite-Normalised Multi-element Diagrams

Chondrite normalised multi-element plots are an extension of REE plots but use a larger suite of trace elements. These are ordered from left to right across the diagram in the sequence of increasing mantle compatibility to maintain consistency with the REE patterns and chondritic values of McDonough and Sun (1995) and Palme and O'Neill (2014) (Table 4.9). Element concentrations are plotted on a logarithmic scale. The logic of chondrite normalisation is that sample compositions are being compared with the primitive materials of the solar system. The advantage of using chondrite normalisation is that the chondrite values have been directly measured rather than calculated as in the case of the primitive mantle with all the attendant assumptions that such models bring. However, for more evolved igneous rocks and sediment, chondrite normalisation is unlikely to be an appropriate approach, for many processes have been operating between the formation of the solar system and the formation of the rocks being examined.

4.4.1.2 Primordial (Primitive) Mantle Normalised Multi-element Diagrams

The primitive or primordial mantle is the composition of the Earth's mantle before the continental crust was extracted. It is the same composition as that of the bulk silicate Earth (BSE) – the composition of the Earth after it had differentiated to form the core but before it had differentiated to form any continental crust. The assumptions used in calculating the composition of primitive mantle are that the bulk Earth is chondritic, that there is a constant ratio of refractory lithophile elements in the Earth relative to CI chondrites, and that many other trace element concentrations can be determined by extrapolation from natural mantle samples. Palme and O'Neill (2014) use a ratio of 2.83 for the enrichment of the primitive mantle relative to CI chondrites, reflecting the increase in the concentration of lithophile elements in the BSE after core formation. The concentrations of the more volatile elements are based upon their abundances in mantle rocks (Li, Cs), mantle isotope ratios (Rb, Pb) and mantle incompatibility relative to other refractory lithophile elements (K). The primitive mantle values of Palme and O'Neill (2014) and McDonough and Sun (1995) used for normalisation are given in Table 4.9. Element concentrations are plotted on a logarithmic scale and ordered from left to right across the diagram with increasing compatibility in the mantle.

The main function of a primitive mantle normalised plot is to show how different the sample is from the composition of the Earth's primitive mantle. This may represent changes in the mantle source and so reflect the processes of mantle differentiation, the different types of melting process and/or degree of melting, or those processes which have taken place in a magma chamber. This normalisation scheme works particularly well for basalts. The main features to be identified and explained relate to (i) the shape of smooth patterns of overall enrichment or depletion as element compatibility changes relative to the primitive mantle and (ii) the recognition of elements with anomalous behaviour in the form of positive or negative anomalies relative to the overall trend. In this context the element pairs Nb–Ta, Hf–Zr and the element Pb are often of interest (see Figure 4.20a). Sometimes the effects of crystal fractionation may give rise to very confused multi-element plots in which individual sample patterns cut across each other. For this reason Thompson et al. (1983) proposed the recalculation of normalised data to make $(Yb)_N = 10.0$ (or one of the other elements located on the right-hand side of the diagram). This additional normalisation of the data can result in a clearer set of patterns.

4.4.1.3 MORB-Normalised Multi-element Diagrams

MORB normalised multi-element diagrams are most appropriate for evolved basalts, arc basalts, andesites, and the felsic rocks of the continental crust. The logic is that MORB normalisation is used to understand those rocks for which MORB might be the parental material. For the most part these are the rocks of the continental crust.

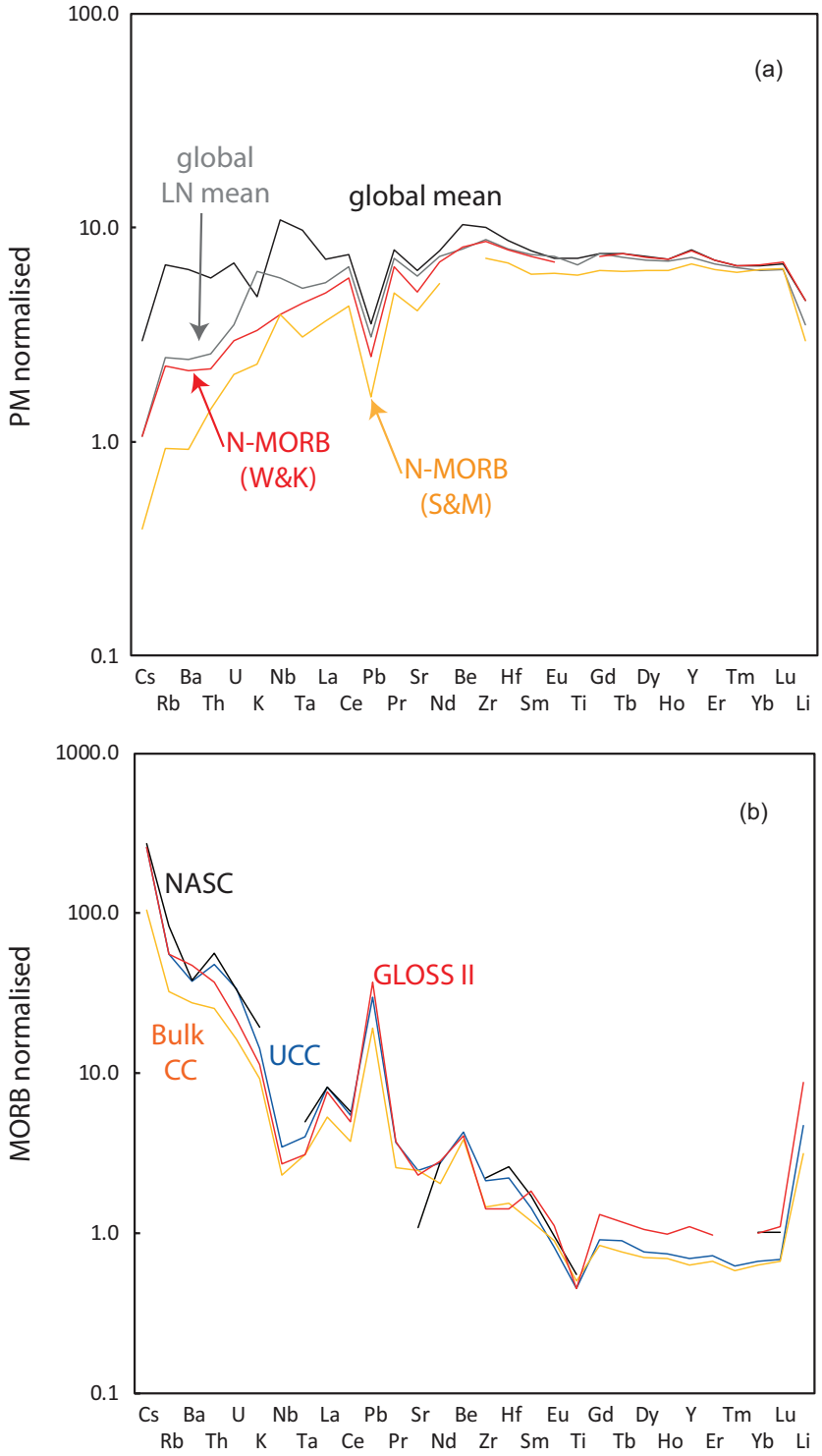

Figure 4.20 (a) Primitive mantle normalised plots for MORB (global mean, black line; White and Klein, 2014); MORB (global LN mean, grey line; Arevalo and McDonough, 2010); N-MORB (global mean, red line; White and Klein, 2014); and N-MORB (global mean, orange line; Sun and McDonough, 1989). The data are given in Table 4.9, columns 5–8. The normalising values are from the PM composition of Palme and O'Neill (2014) and given in Table 4.9, column 4. (b) MORB normalised plots of NASC (Gromet et al., 1984), upper continental crust (UCC) and bulk continental crust (bulk CC) (Rudnick and Gao, 2014) and GLOSS II (Plank, 2014). The data are given in Table 4.9, columns 9–12. The normalising values are from the global LN-MORB of Arevalo and McDonough (2010) given in Table 4.9, column 6.

Four sets of normalising values are given in Table 4.9. The global MORB average of White and Klein (2014) represents the mean of 1975 MORB samples from all the major ocean basins, filtered for data quality. However, not all samples report values for all trace elements and their distribution is not Gaussian; therefore, it is recommended to use the log-normal mean values of Arevalo and McDonough (2010) (Table 4.9, column 6). N ('normal')-MORB is MORB which is depleted in highly incompatible

elements and has a $(La/Sm)_N$ ratio of <1.0. N-MORB represents MORB which has not been influenced by mantle plumes (and thereby enriched). Two sets of N-MORB values are given in Table 4.9, that of White and Klein (2014) and the much-used values of Sun and McDonough (1989). The newer values of White and Klein (2014) are preferred since they are based upon more and better quality data.

4.4.1.4 Interpreting Multi-element Diagrams for Igneous Rocks

As an example of how to interpret multi-element diagrams, consider the primitive mantle normalised plot for N-MORB (Figure 4.20a). In this diagram trace element concentrations in N-MORB are characterised by a strong depletion of the most incompatible elements at the left side of the diagram, increasing to higher concentrations and a flatter trend for the more compatible elements on the right side of the diagram. Normalised values progressively increase from ~ 1× PM to about 8× PM with increasing compatibility; the more compatible high field strength (HFS) elements show a flat trend with values about 8× PM. In this particular order of the elements there are negative anomalies for Pb, Sr and Li. Concentrations in the global LN-MORB are similar, but values for the highly incompatible elements are higher and there is a small positive K anomaly. In contrast the trend for highly incompatible elements in the global mean is more erratic than for N-MORB and the global LN mean (Figure 4.20a). Despite the difference between these models of MORB, all averages show a strong pattern of incompatible element depletion, indicating that the MORB source has experienced previous melt extraction. The small anomalies for individual elements are thought to be a particular feature of the source.

A second example shows a MORB-normalised plot for the average composition of the bulk continental crust (Figure 4.20b). Here there is a pronounced decrease in element concentrations associated with increasing element compatibility during MORB melting. The most incompatible elements are present at more than 100× MORB, whereas the HFS element concentrations are generally similar to MORB, indicating the way in which incompatible elements tend to be fractionated into the continental crust. Significant deviations from this trend are the negative anomalies in the concentrations of Nb, Ta and Ti, which may represent the presence of a Ti-bearing phase in the source, and positive anomalies for Pb, Be and Li, which may reflect fluid-related processes. In more evolved felsic rocks, anomalies for specific elements may be controlled by individual minerals; for example, Zr concentrations may be controlled by zircon, P by apatite, the LREE and Th by allanite, HREE by garnet, Sr by plagioclase, and Ti, Nb and Ta by ilmenite, rutile or titanite (see Section 4.2.1.8).

4.4.2 Multi-element Diagrams for Clastic Sediments

The processes controlling the trace element composition of sedimentary rock may also be investigated using multi-element normalised diagrams, although they are not as widely used as their equivalents in igneous petrology. The most commonly used normalising values have been those for the North American shale composite (NASC) of Gromet et al. (1984) taken to represent 'average crustal material'. However, the range of trace elements reported is small (see Table 4.9, column 9) and there are now better-quality data for more elements. For this reason, the average values for the upper continental crust or the bulk crust of Rudnick and Gao (2014) are preferred. An alternative is to use the average global subducting sediment (GLOSS) recently recalculated as GLOSS II by Plank (2014; Table 4.9, column 12) which is based on the average geochemical composition of subducting sediments. GLOSS II represents the average of 27 averages from each of the different subduction zone trenches. Trace element concentrations in GLOSS II are very similar to those for the upper continental crust (Figure 4.20b).

Multi-element diagrams for clastic sediments record information about the source of the sediment, continental weathering processes (seen in the concentrations of K, Rb, Cs, Li) and contributions from both biological (REE) and hydrothermal (Pb and REE) marine processes. This may be seen in GLOSS II where, although the shape of the pattern is similar to that of the bulk continental crust, some values are higher, indicating input from sources in addition to the crustal source, and others are lower, due to the dilution effect of a biological component (Plank 2014). The composition of GLOSS is also important for understanding large-scale subduction processes and may be used for tracing elements added to a subduction system through their input as sediments.

4.5 Diagrams Displaying Highly Siderophile Elements (HSE) and Platinum Group Elements (PGE)

The *highly siderophile elements* (HSE) include the elements Re, Os, Ir, Ru, Pt, Rh, Pd and Au. The *platinum group elements* (PGE), also known as the platinum group metals (PGM), are a subset of the HSE and include the elements Ru, Rh, Pd, Os, Ir and Pt. The PGE are known as the *noble metals* when they include Au. The PGE are divided on the basis of their geochemical behaviour into two subgroups:

- the Ir group of PGE (*IPGE*): Os, Ir, Ru and Rh
- the Pd group of PGE (*PPGE*): Pt and Pd.

Gold is often associated with the latter group. The concentrations of HSE in planetary materials and in rocks are extremely low. For example, in MORB, where concentrations are particularly low, they are reported in either parts per billion (ppb) or parts per trillion (ppt).

The HSE are particularly important in both cosmochemistry and mantle geochemistry. As the name indicates, they are siderophile and they show a strong affinity for the metallic iron phase. Thus, their concentrations in planetary bodies relate to the formation of an iron-rich metallic core. In the absence of metallic iron, they are strongly chalcophile and have a strong affinity for a sulphide phase. The basic data for the HSE, the melting temperature of the metals, the 50% equilibrium condensation temperatures (a function of processes), the metal–silicate partition coefficients, and concentrations in CI chondrites and the primitive mantle are given in Table 4.10.

4.5.1 The Application of the HSE in Cosmochemistry

In cosmochemistry the HSE can aid our understanding of the large-scale processes associated with planetary differentiation, in particular, the process of core formation. This is because of their strong affinity for metal relative to silicate. With the exception of Au all have higher melting temperatures than that of iron (1665 K) (Table 4.10). The Ir-group PGE are characterised by higher melting temperatures than the Pt-group PGE. When presented on element versus concentration diagrams the HSE are ordered according to their melting temperature with Re having the highest melting temperature to the left of the plot, through to Au with the lowest melting temperature on the right, and arranged in the order given in Table 4.10 (Figure 4.21a). The elements are separated with equal spacing, although not every study reports the full range of elements and Rh is frequently omitted. Concentrations are normalised using the measured values for CI chondrites (Table 4.10) and presented on a log scale (Figure 4.21a).

The distribution of the HSE in planetary materials can also be understood in terms of their temperature of condensation during the cooling of a solar nebula. This data is normally reported as the temperature at which 50% of the metal is condensed. The elements Re, Os, Ir, Ru, Pt and Rh are regarded as ultra-refractory because they have a very high condensation temperature and condense to refractory metal alloy grains. The elements Au and Pd are classified as moderately volatile with lower condensation temperatures. A further means of understanding the partitioning of

Table 4.10 The highly siderophile elements (HSE)

Element	Symbol	Atomic number	Melting temperature, K	50% equilibrium condensation temperature, K	Metal–silicate D at 1 bar	CI chondrite Orgueil (ppm)	CI chondrite (ppm)	Primitive mantle (ppm)	Primitive mantle (ppm)
Reference			1	1	1	1	2	1	2
Rhenium	Re	75	3453	1821	1.1×10^5–2.8×10^6	0.0381	0.040	0.00035	0.00035
Osmium	Os	76	3327	1812	1.5×10^4–1.0×10^6	0.4605	0.495	0.00390	0.00390
Iridium	Ir	77	2683	1603	2.1×10^5–3.5×10^7	0.4306	0.469	0.00350	0.00350
Ruthenium	Ru	44	2583	1551	1.3×10^5–7.4×10^6	0.6374	0.690	0.00700	0.00740
Platinum	Pt	78	2045	1408	3.7×10^4–8.6×10^5	0.8735	0.925	0.00760	0.00760
Rhodium	Rh	45	1826	1392	4.5×10^4–1.6×10^6	0.1310	0.132	0.00120	0.00120
Palladium	Pd	46	1825	1324	2.2×10^3–2.0×10^4	0.5705	0.560	0.00710	0.00710
Gold	Au	79	1337	1060	1.0×10^3–5.0×10^3	0.1750	0.148	0.00170	0.00170

References: 1, Day et al. (2016); 2, Palme and O'Neill (2014).

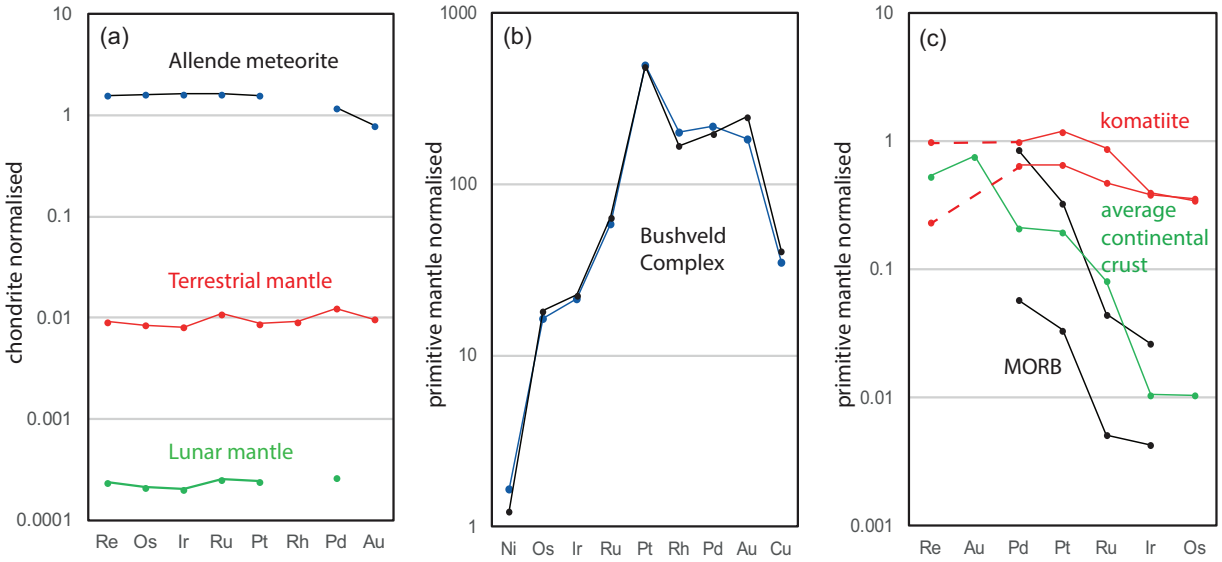

Figure 4.21 (a) CI-chondrite normalised plot for the HSE in the Allende meteorite, the lunar mantle and the Earth's primitive mantle (Terrestrial mantle). CI normalising values from Day et al. (2016). Allende data, lunar mantle data and primitive terrestrial mantle data also from Day et al. (2016). Elements organized in order of decreasing melting temperature, left to right. (b) HSE data with Ni and Cu normalised to values for the primitive mantle for two PGE-rich samples from the Merensky Reef of the Bushveld Igneous Complex, South Africa. PM normalising values from Palme and O'Neill (2014), rock data from Barnes and Maier (2002). Elements organized in order of decreasing mantle compatibility, left to right. (c) HSE data for MORB (black lines, range from Rehkamper et al., 1999), komatiites in the Barberton greenstone belt, South Africa (red lines, from Puchtel et al., 2014) and the average bulk continental crust of Rudnick and Gao (2014) (green line). PM data from Palme and O'Neill (2014). Elements organized in order of increasing mantle compatibility, left to right. Note the different scales.

elements during planetary formation and differentiation is through their metal–silicate partition coefficient, given in Table 4.10 for 1 bar of pressure.

4.5.2 The Application of the HSE in Mantle Geochemistry

In mantle geochemistry the HSE are treated slightly differently from in cosmochemistry, and in trace element variation diagrams the elements tend to be arranged according to their incompatibility in the silicate mantle. The sequence of *increasing compatibility*, from the most incompatible to those elements which are more compatible, is:

$$(\textit{most incompatible})\ \mathrm{Re} \leq \mathrm{Au} < \mathrm{Pd} < \mathrm{Pt} \leq \mathrm{Rh} < \mathrm{Ru} \leq \mathrm{Ir} \leq \mathrm{Os}\ (\textit{more compatible})$$

This is the order in which the elements will be concentrated during the partial melting of a purely silicate mantle. One measure of the degree of fractionation during partial melting is the ratio $(\mathrm{Pd/Ir})_N$. This records the fractionation between one of the least compatible elements (Pd) relative to one of the more compatible elements (Ir).

Estimates of the composition of the primitive mantle are given in Table 4.10, and these can be used as an alternative to chondritic values for normalising mantle-derived melts. Compositional estimates of the primitive mantle are based upon the observation that Ir has a near uniform distribution in mantle peridotites. HSE ratios relative to Ir are then determined in fertile mantle peridotites (samples with high Al_2O_3), and calculated using the constancy of Ir concentrations. As noted above, HSE concentrations in the mantle are very low – about 100× less than chondrite – but are broadly chondritic (Figure 4.21a). Nevertheless, despite their very low concentrations their abundances are higher than those predicted from the process of core formation alone and imply the additional input of HSE into the Earth after core formation. This process is referred to as the addition

of a *late veneer* of chondritic material to the Earth after core formation.

There are three important controls on HSE concentrations in melts during mantle melting. The first is the degree of partial melting. Day et al. (2016) showed that for the highly incompatible element Pd, concentrations increase in melts in parallel with the degree of melting, so that high-degree melts such as komatiites have higher concentrations of Pd than low-degree melts such as alkali basalts. A second control is the sulphur content of the source. In the absence of grains of metallic iron and PGE alloys, the HSE will be strongly partitioned into sulphides in the source. This effect will continue to be seen until the sulphide minerals in the source are completely melted out. A further control is mineralogical. The presence of PGE alloys and also chrome spinel in the source are both thought to exercise some control on HSE abundances in mantle melts and may govern the concentrations of Ir and Ru. However, the role of chrome spinel is complex, for a detailed examination shows that often the PGE are not present in solid solution but are present as inclusions of PGE alloys and oxides.

In MORB, HSE concentrations may be so low that some elements are below the limits of detection. In this case analyses may be limited to the elements Ir, Ru, Pt and Pd (e.g., Rehkamper et al., 1999; Bézos et al., 2005; Figure 4.21c). In MORB immiscible sulphide melts can be important in scavenging the PGE. In gabbros, particularly where they are associated with sulphides, concentrations of HSE are higher and may be present at the ppm level. In this case a wider range of HSE are reported along with Ni and Cu concentrations. For example, Barnes and Maier (2002) in their study of the Merensky Reef in the Bushveld Igneous Complex, South Africa, report the elements Ni, Os, Ir, Ru, Rh, Pt, Pd, Au and Cu (Figure 4.21b). The relevant normalising values for Ni are CI = 10,910 ppm and PM = 1860 ppm, and for Cu are CI = 133 ppm and PM = 20 ppm (data from Palme and O'Neill, 2014).

HSE data for komatiites, MORB and the continental crust are plotted according to their incompatibility in Figure 4.21c. In all cases the concentrations of the least compatible elements are the highest and decrease in the direction of the more compatible elements. This is clear in the MORB samples and indicates a strong control by partial melting. The affinity with the crustal pattern may suggest a relationship between MORB and the continental crust. In komatiites, the higher concentration of the more compatible elements may reflect higher degrees of melting of the HSE hosts.

4.6 Bivariate Trace Element and Trace Element Ratio Plots

Thus far in this chapter we have concentrated on the display of trace element data using different types of multi-element plot. This approach has the advantage of utilising a large number of elements and allowing broad conclusions to be drawn from their geochemical behaviour. However, multi-element plots have the disadvantage that only a few samples can be shown on a single diagram before it becomes cluttered and hard to read. In this case a bivariate plot showing elements or element ratios is preferred, in particular, when geochemical trends are sought. The principles behind variation diagrams have already been discussed in Section 3.3 with respect to major element geochemistry, and many of these principles also apply to trace elements plots.

4.6.1 The Selection of Trace Elements to Plot on Bivariate Graphs for Igneous Rocks

Many igneous rocks have had a complex history of solid–liquid equilibria in their journey from the source region to their site of emplacement. In addition, they may have interacted with fluids during or after their solidification. The task for the igneous geochemist, therefore, is to work out which trace elements are indicative of which processes in this complex history. The clues come from a knowledge of mineral-melt (and the lesser known mineral-fluid) partition coefficients and the physical laws which govern the concentrations of trace elements in igneous rocks. Most fruitful are trace elements which show extreme behaviour, such as the highly incompatible and the highly compatible elements. This is illustrated in general terms in Figure 4.22, in which the fractionation of selected trace and major elements between the continental crust, MORB and residual mantle is plotted against their partition coefficients (Hofmann, 2014).

Further clues may come from the inspection of multi-element plots, in particular, where trace element concentrations depart from otherwise smooth trends, for these elements may form the basis for identifying particular processes and in some instances even source

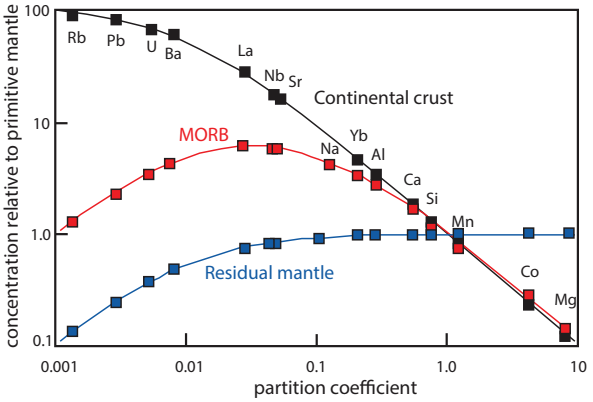

Figure 4.22 The abundances of selected trace and major elements in average continental crust, average MORB and residual mantle normalised to primitive mantle plotted relative to their partition coefficient. (After Hofmann, 2014; with permission of Elsevier)

characteristics. In this case it is instructive to plot the ratio of the anomalous element to an adjacent element which defines part of the overall smooth trend. However, care must be exercised in this process because some 'anomalous' trace element concentrations may be a function of the order in which the elements are plotted on the multi-element diagram. These trace elements or element ratios may then be used to determine variables such as the mechanism or style of melting, the degree of partial melting, the degree of fractional crystallisation and the composition and mineralogy of the source composition which has been melted. A similar approach is discussed by Pearce (2008) in which the logic used in selecting different trace elements to identify different magmatic process is carefully argued.

4.6.1.1 The Behaviour of the Highly Incompatible Elements

Highly incompatible element concentrations are particularly sensitive to partial melting processes when the degree of partial melting is low, as is illustrated in Figures 4.9a and 4.10a. The more incompatible an element is, the more sensitive it is to the degree of partial melting. This is true for both batch melting and fractional melting, but the effect is more extreme during fractional melting. This is illustrated with reference to the batch melting equation (Section 4.2.2.2, Eq. 4.6): when D is very small ($D < 0.001$), C_L/C_o reduces to $1/F$. In other words, the concentration of a highly incompatible element in a melt relative to the source is inversely proportional to F, the degree of melting. Thus, when the melt fraction is small, all of the highly incompatible trace elements partition into the melt. A similar effect is seen during fractional crystallisation when the bulk partition coefficient of the fractionating phases is very small: at small fractions of melt remaining, C_L/C_o reduces to $1/F$ (Figure 4.13a). This effect is even more strongly marked in AFC processes (Figure 4.14).

It has also been shown that when D is very small, the ratio of two highly incompatible elements in a basaltic melt will mirror that of the source. For example, during batch melting, when $D < 0.01$, then $C_L^{elt\text{-}1}/C_L^{elt\text{-}2} = C_o^{elt\text{-}1}/C_o^{elt\text{-}2}$ (see Hofmann et al., 1986; Arevalo and McDonough, 2010). This relationship is very powerful because it means that the ratio of a pair of highly incompatible elements whose bulk partition coefficients are very similar will not vary in the course of fractional crystallisation and will vary little during batch partial melting, and so allows us to 'see through' the effects of fractional crystallisation and through different degree of partial melting to identify the character of the source materials.

4.6.1.2 Estimation of Partition Coefficients from Trace Element Concentration Plots

Minster and Allegre (1978) showed that, from a rearrangement of the batch melting equation, a bivariate plot of the reciprocals of incompatible elements can be used to obtain information about partition coefficients during melting. Provided the mass fractions of the minerals in the melt remain constant, a linear trend on such a diagram characterises the batch melting process. Further, the slope and intercept of the trend can provide information about the difference in bulk partition coefficient between the two elements. If the samples are first normalised to the most enriched sample, elements with the same bulk partition coefficient will have a slope of 1 and an intercept of 0. If the bulk partition coefficients for the two elements change at different rates during melting, then a curvilinear trend will be produced (Bender et al., 1984). This approach was extended by Sims and DePaolo (1997) to show that log–log element plots are a useful way of assessing differences in D values between two incompatible elements. Elements with similar incompatibilities will plot as a straight line on a log–log plot (Figure 4.23), and where the incompatibility is identical the slope of the line will be

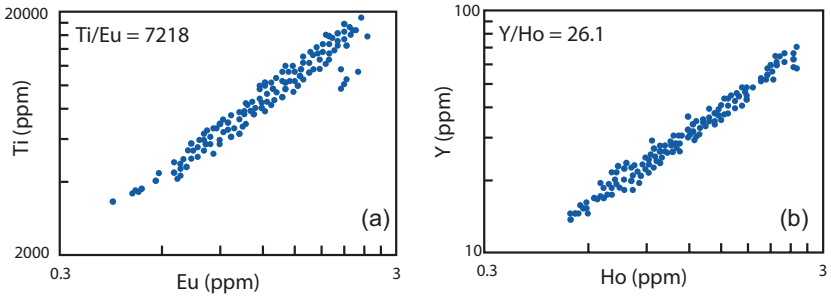

Figure 4.23 Log–log trace element plots for highly incompatible elements. (a) Ti versus Eu, and (b) Y versus Ho show the constancy of the respective trace element ratios (Ti/Eu = 7218 and Y/Ho = 26.1). These trace element ratios have been termed *canonical* trace element ratios and are thought to reflect the elemental ratios of the depleted mantle source. (Data from Jenner and O'Neill, 2012; with permission from John Wiley & Sons)

unity. When the incompatible elements have differing *D*-values the slope will diverge from unity.

4.6.1.3 Identification of Igneous Source Characteristics from Incompatible Element Ratio Plots

Authors working on oceanic basalts noted that some highly incompatible trace element ratios were constant regardless of the absolute concentrations of the elements present or the geographic location of the samples (e.g., Hofmann et al., 1986). Given their identical incompatibilities these 'constant' trace element ratios were termed *canonical* trace element ratios (Arevalo and McDonough, 2010; Hofmann, 2014) for they were thought to define the elemental ratios of the bulk silicate Earth (BSE). However, recent high-precision measurements on basalts from a range of MORB and ocean island basalt sources show the ratios vary between mantle sources and they are not indicative of the BSE. Instead, these trace element ratios are thought to reflect the trace element ratios of the individual sources of the different types of oceanic basalt (Arevalo and McDonough, 2010).

Early studies sought to demonstrate the constancy of trace element ratios using a plot in which a trace element ratio is plotted on the *y*-axis and the numerator of the ratio is plotted on the *x*-axis over a range of abundance. However, as discussed in Section 2.6, this type of plot can give rise to spurious self-correlation (see also Sims and DePaolo, 1997). A better alternative, therefore, is a plot of the trace element ratio versus MgO, in which MgO is a proxy for the fractionation index (Arevalo and McDonough, 2010), for this has the capacity to show the constancy of the ratio over a range of melt compositions. The most robust approach, however, as discussed in Section 4.6.1.2, is to use elemental log–log plots (Figure 4.23), for where these plots have a slope of 1, the elements have identical incompatibilities (Hofmann, 2014), and where the slope of the correlation line is not unity, the relative incompatibilities can be estimated.

In a detailed high-precision analytical study of 792 samples of MORB, Arevalo and McDonough (2010) showed that the ratios Ti/Eu, Y/Ho and Ce/Pb remain constant during MORB genesis and that these ratios reflect the composition of the MORB (depleted mantle) source (Figure 4.23). They showed that different ocean basins have sources with slightly different trace element ratios, raising the interesting question as to why this should be so. Conversely, the trace element ratios Ba/Th, Nb/U, Zr/Hf, Nb/Ta, Sr/Nd and Th/U, previously also thought to be indicative of the MORB source, are now known to fractionate during MORB genesis and do not faithfully record the composition of the depleted mantle.

4.6.1.4 Some Important Trace Element Ratios

There is a very large number of possible trace element ratios that can be plotted to summarise relationships in large geochemical data sets. A number of workers have sought to characterise the proposed mantle end-member compositions in terms of their trace element concentrations (Salters and Stracke, 2004; Willbold and Stracke, 2010; White and Klein, 2014). In addition, Rudnick and Gao (2014) provide a comprehensive review of the trace element composition associated with continental crust. Some values currently in use for highly incompatible trace element

ratios which are immobile during metamorphism are given in Table 4.11. A selection of incompatible element ratios is described below with a particular emphasis on basaltic samples.

The trace element ratio of the light REE elements $(La/Sm)_N$ is particularly useful in classifying MORB samples, for while these are typically depleted in the light REE, some are enriched. The ratio $(La/Sm)_N$ is a useful measure of light REE depletion, and samples with $(La/Sm)_N > 1.0$ are classified as E-MORB (enriched MORB), whereas those with $(La/Sm)_N < 1.0$ are classified as N-MORB (normal MORB). These differences may be shown on REE plots, but they can be helpfully summarised on a $(La/Sm)_N$ versus La trace element plot. A similar distinction is useful in examining some mantle peridotites to show the extent to which they may have been depleted and/or re-fertilised (Figure 4.24).

Trace elements with identical charge and ionic size are expected to behave in an identical manner and the ratios of the trace element pairs *Nb/Ta and Zr/Hf* in all terrestrial rocks should be similar to that in chondritic meteorites (Nb/Ta = 18.9; Zr/Hf = 34.1; Palme and O'Neill, 2014). However, this is not always the case, demonstrating that these trace element ratios have the power to identify petrological processes. For example, Niu and Batiza (1997) showed that the two ratios vary significantly in seafloor basaltic lavas from seamounts near the axis of the East Pacific Rise, and Foley et al. (2002), in a study on the origin of felsic continental crust, exploited the differences in the Nb/Ta ratio between oceanic basalt and Archaean continental crust to argue for an amphibolite melting model for early continental crust.

The *K/U ratio* is important in constraining the Earth's heat budget and noble gas abundances in the

Table 4.11 Incompatible trace element ratios in mantle and crustal reservoirs

	Zr/Nb	La/Nb	Ba/Nb	Ba/Th	Rb/Nb	Th/Nb	Th/La	Ba/La
Mantle								
DM[a]	48.1	1.21	6.13	114	0.61	0.05	0.04	5.07
HIMU[b]	4.02	0.66	4.97	75.8	0.35	0.07	0.10	7.51
EMI[b]	6.36	1.3	14.9	173	0.97	0.09	0.07	11.8
EMII[b]	4.53	0.98	10.7	79.5	0.83	0.13	0.14	10.9
Continental crust[c]								
Upper	16.1	2.6	52.0	59.4	7.0	0.88	0.34	20.1
Middle	14.9	2.4	53.2	81.8	6.5	0.65	0.27	22.2
Lower	13.6	1.6	51.8	216	2.2	0.24	0.15	32.4

[a]Average values from Excel table A1 of Salters and Stracke (2004).
[b]Values from compilation of Willbold and Stracke (2010).
[c]Values from Rudnick and Gao (2014).

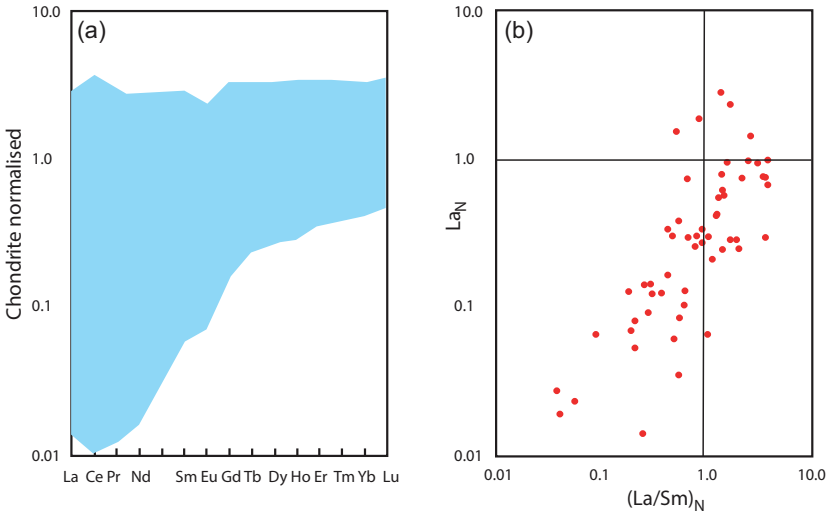

Figure 4.24 REE data for ocean floor mantle peridotites. (a) REE patterns show a wide range of patterns, some of which show extreme depletion in the light REE; (b) the same data presented as $(La/Sm)_N$ versus La_N. (Data selected from the dataset of Niu, 2004)

primitive Earth. One approach to resolving these first-order issues is to measure the K/U of MORBs, for, given that K and U behave similarly during partial melting and crystal fractionation, these provide a window into the K/U of the upper mantle. Arevalo et al. (2009) reported a K/U ratio for MORB of 19,000, but found that this differed from the ratio in ocean island basalts. However, given the potential for the mobility of these elements, the measurements need to be determined on fresh basaltic glass.

It can be helpful to compare the trace element ratios between major crustal reservoirs. For example *Nb/Th* is ~1.4 in average continental crust, ~15.7 in MORB, and 7–8 in the primitive mantle, indicating that there has been significant fractionation during the formation of MORB and the continental crust. These differences were exploited by Pearce (2008) in an attempt to identify mantle–continental crust interaction in basaltic magmas. In this study, Pearce normalised the Nb/Th ratio using Yb, to minimise the effects of fractional crystallisation and on the resulting Th/Yb–Nb/Yb plot identified a mantle array which encompasses the full range of MORB and ocean island basalt compositions (Figure 4.25). In a similar way, Fitton et al. (1997) used the incompatible element ratios Nb/Y and Zr/Y to show the differences between plume and N-MORB mantle sources, and Condie (2005) proposed that incompatible element ratios Zr/Nb, Nb/Th, Zr/Y and Nb/Y can be used to characterise the mantle source of tholeiitic basalts.

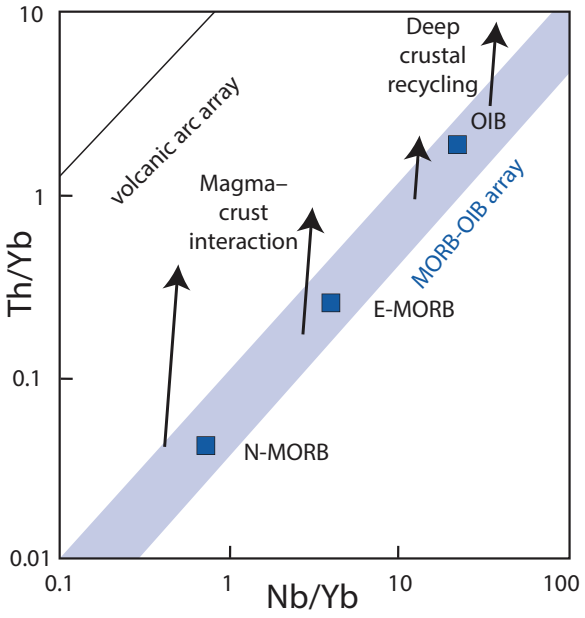

Figure 4.25 Nb/Yb versus Th/Yb diagram showing the MORB-OIB (ocean island basalt) mantle array (shaded area) and the compositions of average normal MORB (N-MORB), average enriched MORB (E-MORB) and average ocean island basalt (OIB). Volcanic arc basalts plot above the mantle array. The effects of magma–crust interaction and deep crust recycling are indicated by the arrows. (After Pearce, 2008; with permission of Elsevier)

4.6.1.5 Applications to Felsic Rocks

Identifying similar 'canonical' trace element ratios in felsic rocks (and thus their source characteristics) is much more difficult than in mafic rocks. This is because felsic melts are often highly fractionated and/or modified by fluid mobility. Further, the fractionation of minor phases such as apatite, zircon, monazite, titanite and ilmenite modifies many of the critical trace element ratios to the extent that it is impossible to determine the nature of the source using this method.

However, some trace element ratios can be used to evaluate large-scale mass balance models involving felsic crust. This is because some highly incompatible element ratios are very different in the continental crust from the mantle. For example, Arevalo and McDonough (2010) use the ratios Y/Ho and Th/U to demonstrate the complementarity of the continental crust and depleted mantle relative to a chondritic source (although this is not consistent with the result from Ti/Eu and Nb/Ta ratios). Similarly, Collerson and Kamber (1999) used the changing ratio of Nb/Th in mantle rocks over time to evaluate the extraction of the continental crust from the Earth's mantle.

4.6.1.6 Compatible Element Plots

Compatible trace element concentrations change dramatically in an igneous liquid during fractional crystallisation (Figure 4.13a). Thus, bivariate plots of compatible elements, plotted against an index of fractionation (e.g., MgO) can be used as a test for fractional crystallisation. The effect is less marked during in situ crystallisation except for the case when a large melt fraction is returned to the magma chamber (Figure 4.13d). Compatible elements are also strongly depleted during AFC processes when the rate of assimilation is high and the trace element concentration in the wall rock is less than in the melt (Figure 4.14).

During low and moderate degrees of partial melting the concentrations of highly compatible elements in the source are buffered by the solid phases present. This means that even if the source has undergone prior partial melting, trace element concentrations will remain largely unchanged during both batch (Figure 4.9b) and fractional (Figure 4.10b) melting.

4.6.2 Bivariate Plots in Sedimentary Rocks

Bivariate trace element plots in sedimentary rocks are mostly used to detect mixing processes in sediments. Norman and De Deckker (1990) suggest that linear correlations amongst a diverse group of elements over a broad range of concentrations may indicate mixing of two sedimentary components, although major element plots can also be used to discern this process (Figure 3.13). A more complete discussion of bivariate trace element plots in sediments is given in Section 5.5.3.

4.7 Enrichment–Depletion Diagrams

Enrichment–depletion diagrams are a convenient way of showing relative enrichment and depletion in trace (or major) elements as a 'positive–negative' histogram. Diagrams of this type can be useful for demonstrating the extent of elemental enrichment or depletion in an igneous suite by comparing the chemistries of early and late members of a series. Hildreth (1981) compared the relative concentrations of the early and late members of Bishop Tuff (Figure 4.26). The *x*-axis of the graph shows the elements arranged by atomic number and the *y*-axis the concentration of an element in the latest erupted ejecta divided by concentrations for the earliest erupted ejecta. The values on the *y*-axis may also be presented on a logarithmic scale.

Enrichment–depletion diagrams are also useful as a way of displaying element mobility. This has been used particularly in alteration zones associated with hydrothermal mineralisation. For example, Taylor and Fryer (1980) show the relative mobility of trace and major elements in the zones of potassic and propylitic alteration associated with a porphyry copper deposit. In this case the enrichment/depletion is measured relative to the composition of the unaltered country rock. In a similar way, enrichment–depletion diagrams may be used in the study of compositional change during rock weathering such that the composition of the weathered product can be shown relative to the composition of the original rock.

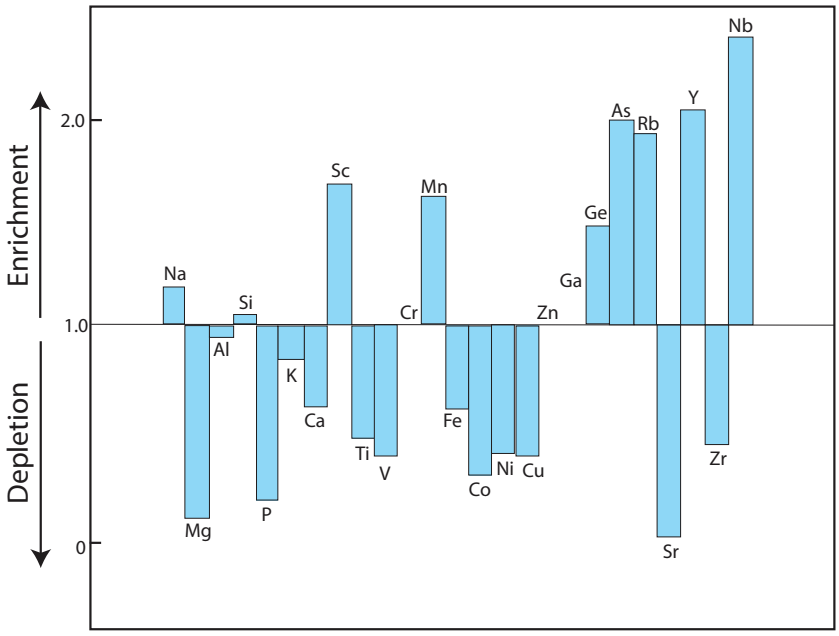

Figure 4.26 Enrichment–depletion histogram. The enrichment factors for selected major and trace elements from Bishop Tuff are arranged in order of increasing atomic number. The diagram compares the concentrations of the late members relative to the early members of Bishop Tuff and is thought to be a measure of the zonation of the magma chamber. (Data from Hildreth, 1981)

4.8 Modelling Trace Element Processes in Igneous Rocks

One of the most important uses of trace elements in modern igneous petrology is in the testing of hypotheses through the modelling of geochemical processes. This frequently involves constructing a geochemical model which is thought to represent the processes which have taken place and then comparing the model results with those of the actual measurements (Allègre and Minster, 1978; Shaw, 2006). Trace element modelling depends upon the mathematical expressions which describe the equilibrium partitioning of trace elements between minerals and melt during igneous processes (Section 4.2.2) and a precise knowledge of trace element partition coefficients (Section 4.2.1 and Tables 4.1–4.4). For successful geochemical modelling, three conditions should be fulfilled. First, trace element concentrations must be determined with great accuracy; otherwise, it is impossible to discriminate between competing hypotheses (Arth, 1976). Second, partition coefficients for the conditions under which the process is being modelled must be known accurately. Third, the starting composition must be known. This last condition is not always fulfilled and sometimes a reasonable assumption of the starting composition must be made which is later refined as the model is developed.

The ultimate aim of geochemical modelling is to determine the processes operating within a given suite of rocks. Often this is at a local scale, such as in an individual magma chamber, or at a regional scale, such as a volcanic province; but such is the power of geochemistry that in some instances it can be about large-scale reservoirs, such as the whole of the continental crust or the entire depleted upper mantle.

As previously discussed, many igneous rocks have evolved through a range of processes and each of these may need to be determined separately and if necessary 'stripped away' in order to reveal underlying processes. An extreme example would be a suite of rocks in which first the effects of element mobility have to identified and the relevant samples removed from the data set. Then the effects of crystal fractionation identified and the least fractionated samples isolated. The remaining samples can then be used to identify the conditions of partial melting and ultimately the nature of the source.

It is important to note that geochemical models do not necessarily provide a unique solution to a geological problem. Uncertainty about the precise initial composition of the source or the melt, the correct partition coefficients and the precise physical processes of melting and/or fractionation may mean that multiple solutions can fit the observed data. For this reason trace element modelling often has to be constrained by other data. These may be geochemical – major element or isotopic data, the results of experimental petrology, or field and petrographic observations. Often when these additional external constraints are introduced, reasonable assumptions can be made about the nature of the process being investigated. Allegre and Minster (1978) use the example of a suite of alkali basalts, for which they made the assumptions that they were formed by a small degree of partial melting of typical mantle material. These two assumptions, limiting the composition of the source and the range of F, simplified subsequent trace element modelling.

The results of trace element modelling calculations are plotted on a bivariate or multivariate graph and compared with an observed trend of measured rock compositions. This process is often carried out using a computer package such as t-IgPet (Carr and Gazel, 2017), Petrograph (Petrelli et al., 2005), or WinRock (Kanen, 2004). There is also the substantial work by Janousek et al. (2016) whose software is written using the R language. Here we illustrate modelling using the results of calculations in a spreadsheet so that the methodology is transparent. Initially, in Section 4.8.1 we discuss forward modelling in which model calculations are compared with the observed data, and then we consider inverse modelling where the data themselves can be used to constrain the model (Section 4.8.3).

4.8.1 Vector Diagrams

Changes in trace element concentrations may be modelled on a bivariate plot using vectors to show the amount and direction of change which will take place as a consequence of a particular process. Diagrams of this type are useful for quantifying the extent either of fractional crystallisation or of partial melting. For example, mineral vectors can be calculated to show the evolving composition of a melt in response to the removal of a *fractionating* mineral phase or mineral assemblage (Figure 4.27). The effects of fractionation calculated using the Rayleigh equation (Eq. 4.20) for plagioclase, clinopyroxene, orthopyroxene, hornblende,

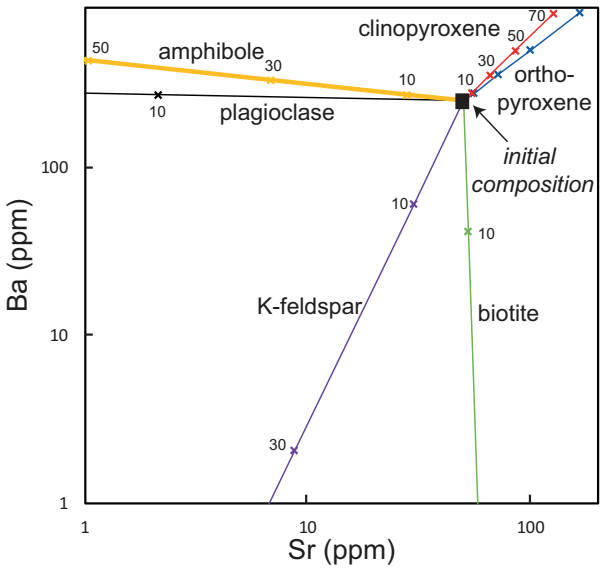

Figure 4.27 Vector diagram for Ba versus Sr (ppm). The figure shows the effects of Rayleigh fractionation of a felsic melt with an initial composition of 250 ppm Ba and 50 ppm Sr. Fractionation trends are shown for the phases orthopyroxene, clinopyroxene, plagioclase, amphibole, K-feldspar and biotite. The tick marks on the fractionation curves show the effects of 10, 30, 50 and 70% fractionation. The partition coefficient values for Sr and Ba are from Table 4.3. Note the logarithmic scale.

biotite and orthoclase from a granitic melt are shown in Figure 4.27. *Partial melting* vectors may be calculated in a similar way using the appropriate equations, to show changing melt or source compositions during the partial melting of a given source composition and mineralogy. The effects of different melting models, source compositions and mineralogy may be all explored in this way.

Thus, vector diagrams can be used to identify a fractionating phase on a bivariate plot. If, for example, on a plot of Ba versus Sr, the rock compositions define a liquid trend which could have been produced by crystal fractionation, then the slope of the trend can be compared with a mineral vector diagram (Figure 4.27) and the phase responsible for the fractional crystallisation trend can be identified. In addition, it is possible from the compositional range of the two elements to make an estimate of the amount of fractional crystallisation that has taken place. When there is more than one fractionating phase present, a composite vector can be calculated, although when this is the case it is not always possible to find a unique composition for the fractionating mineral assemblage. Although vector diagrams select only two out of a vast array of possible elements, they have the advantage of being able to display data from a large number of samples. This means that it is possible to view trends in the data. Consequently, both mineral and partial melting vectors can be plotted alongside observed trends on bivariate plots in order to identify possible magmatic processes.

4.8.2 Modelling on Multivariate Diagrams

In this section we illustrate the way in which trace element modelling has been used to identify different petrogenetic processes in igneous rocks. Multivariate diagrams such as REE plots and multi-element diagrams can be used for petrogenetic modelling, although these are unable to clearly show more than a few samples on a single diagram. In this case the same operation is performed on each element in the plot and the resultant data array is compared with a measured rock composition. The process is illustrated in Figure 4.28 to show the effects of partial melting of a primitive mantle source (Figure 4.28a, b) and of olivine fractionation on a basaltic liquid (Figure 4.28c).

4.8.2.1 Partial Melting

An example of the behaviour of the REE during the partial melting of a mantle source to produce a basaltic melt is given in Table 4.12 and the results shown graphically (Figure 4.28). In this model all the results are chondrite normalised using the values of Barrat et al. (2012) (Table 4.7). The starting composition is the primitive mantle composition of Palme and O'Neill (2014) and this melting model is therefore more directly applicable to basaltic compositions in the Archaean. Two sets of partition coefficients are chosen to illustrate the way in which even the choice of partition coefficient may influence the outcome of geochemical modelling. On the left side of Table 4.12 the partition coefficients from Table 4.1 are used and on the right side of Table 4.12 the values of Bédard (2005, 2014) are used. It should be noted that the values for clinopyroxene are different in the two data sets, and since these values are much higher than those for olivine or orthopyroxene, they strongly influence the value of the calculated bulk partition coefficient D.

The melting model is based upon a primitive mantle mineralogy with 50% olivine, 40% orthopyroxene, 8% clinopyroxene and 2% spinel. Two different models are illustrated: (i) modal batch melting is shown for 5%, 10%, 15%, 20% and 25% melting (Figure 4.28a),

Table 4.12 A summary of partition coefficients

Partition coefficients from Table 4.1						Partition coefficients from Bédard (2005, 2014)					
	Olivine	*Ortho pyroxene*	*Clino pyroxene*	*Spinel*			*Olivine*	*Ortho pyroxene*	*Clino pyroxene*	*Spinel*	
	50%	*40%*	*8%*	*2%*	*D*		*50%*	*40%*	*8%*	*2%*	*D*
La	0.0000	0.0008	0.0860	0.0000	0.0072	La	0.0002	0.0012	0.0900	0.0000	0.0078
Ce	0.0000	0.0016	0.1750	0.0000	0.0147	Ce	0.0004	0.0020	0.1600	0.0000	0.0138
Pr	0.0001	0.0032	0.2890	0.0000	0.0244	Pr	0.0008	0.0034	0.2000	0.0000	0.0178
Nd	0.0002	0.0056	0.4700	0.0000	0.0399	Nd	0.0012	0.0054	0.2800	0.0000	0.0252
Sm	0.0006	0.0150	0.8100	0.0000	0.0711	Sm	0.0026	0.0118	0.4000	0.0000	0.0380
Eu	0.0012	0.0300	1.0000	0.0000	0.0926	Eu	0.0051	0.0163	0.3300	0.0000	0.0355
Gd	0.0018	0.0340	1.0400	0.0000	0.0977	Gd	0.0050	0.0215	0.5000	0.0000	0.0511
Tb	0.0028	0.0540	1.2200	0.0000	0.1206	Tb	0.0067	0.0285	0.6000	0.0000	0.0628
Dy	0.0040	0.0770	1.4000	0.0000	0.1448	Dy	0.0089	0.0371	0.7000	0.0000	0.0753
Ho	0.0064	0.1000	1.3500	0.0000	0.1512	Ho	0.0115	0.0468	0.6700	0.0000	0.0781
Er	0.0110	0.1200	1.3400	0.0000	0.1607	Er	0.0143	0.0573	0.6500	0.0000	0.0821
Tm	0.0140	0.1700	1.3800	0.0000	0.1854	Tm	0.0172	0.0683	0.6600	0.0000	0.0887
Yb	0.0188	0.2200	1.4200	0.0000	0.2110	Yb	0.0203	0.0794	0.6800	0.0000	0.0963
Lu	0.0280	0.2200	1.1600	0.0000	0.1948	Lu	0.0233	0.0903	0.6800	0.0000	0.1022

Batch modal partial melting													
		F	*0.05*	*0.10*	*0.15*	*0.20*	*0.25*			*F*	*0.05*	*0.10*	*0.15*	*0.20*	*0.25*
		PM-normalised								*PM-normalised*					
57	La	2.907	51.138	27.301	18.621	14.129	11.383	57	La	2.907	50.657	27.170	18.563	14.097	11.364
58	Ce	2.922	45.699	25.809	17.983	13.798	11.194	58	Ce	2.922	46.292	25.987	18.064	13.843	11.221
59	Pr	2.920	39.877	23.933	17.097	13.299	10.881	59	Pr	2.920	43.662	25.174	17.685	13.631	11.088
60	Nd	2.890	32.863	21.259	15.711	12.460	10.323	60	Nd	2.890	39.107	23.565	16.863	13.129	10.749
62	Sm	2.841	24.167	17.324	13.500	11.060	9.366	62	Sm	2.841	32.991	21.168	15.584	12.331	10.201
63	Eu	2.841	20.594	15.497	12.423	10.367	8.894	63	Eu	2.841	33.948	21.538	15.772	12.441	10.272
64	Gd	2.842	19.902	15.124	12.196	10.218	8.792	64	Gd	2.842	28.842	19.469	14.693	11.799	9.858
65	Tb	2.867	17.422	13.748	11.354	9.670	8.421	65	Tb	2.867	26.153	18.320	14.098	11.458	9.650
66	Dy	2.850	15.195	12.374	10.437	9.024	7.948	66	Dy	2.850	23.452	16.988	13.318	10.952	9.300
67	Ho	2.822	14.570	11.951	10.130	8.791	7.764	67	Ho	2.822	22.724	16.572	13.041	10.751	9.144
68	Er	2.822	13.923	11.535	9.846	8.588	7.615	68	Er	2.822	22.050	16.229	12.840	10.622	9.057
69	Tm	2.818	12.462	10.560	9.161	8.090	7.243	69	Tm	2.818	20.985	15.668	12.501	10.399	8.902
70	Yb	2.842	11.346	9.802	8.628	7.705	6.961	70	Yb	2.842	20.083	15.222	12.256	10.257	8.819
71	Lu	2.879	12.249	10.458	9.124	8.091	7.269	71	Lu	2.879	19.579	15.000	12.157	10.220	8.815

Accumulated fractional melt

		F *PM-normalised*	*0.01*	*0.02*	*0.05*	*0.10*	*0.15*			*F* *PM-normalised*	*0.01*	*0.02*	*0.05*	*0.10*	*0.15*
57	La	2.907	218.584	136.537	58.097	29.072	19.382	57	La	2.907	210.841	134.530	58.065	29.072	19.382
58	Ce	2.922	144.945	109.246	56.662	29.193	19.476	58	Ce	2.922	151.119	112.285	57.010	29.201	19.477
59	Pr	2.920	98.437	82.111	51.234	28.806	19.440	59	Pr	2.920	126.178	99.184	55.144	29.120	19.463
60	Nd	2.890	64.296	57.367	41.799	26.834	18.938	60	Nd	2.890	95.175	79.767	50.276	28.462	19.237
62	Sm	2.841	37.443	35.129	29.199	21.954	17.014	62	Sm	2.841	65.998	58.557	42.080	26.634	18.678
63	Eu	2.841	29.223	27.847	24.169	19.306	15.667	63	Eu	2.841	70.107	61.689	43.444	26.956	18.748
64	Gd	2.842	27.784	26.547	23.218	18.755	15.358	64	Gd	2.842	50.747	46.408	36.012	24.806	18.161
65	Tb	2.867	22.926	22.112	19.866	16.702	14.146	65	Tb	2.867	42.426	39.455	32.017	23.319	17.677
66	Dy	2.850	19.111	18.557	17.003	14.733	12.815	66	Dy	2.850	35.614	33.537	28.160	21.468	16.806
67	Ho	2.822	18.144	17.643	16.233	14.159	12.389	67	Ho	2.822	34.082	32.166	27.177	20.898	16.464
68	Er	2.822	17.107	16.667	15.421	13.569	11.969	68	Er	2.822	32.523	30.785	26.227	20.401	16.215
69	Tm	2.818	14.869	14.546	13.621	12.216	10.967	69	Tm	2.818	30.180	28.693	24.745	19.586	15.778
70	Yb	2.842	13.218	12.973	12.265	11.170	10.175	70	Yb	2.842	28.159	26.886	23.467	18.900	15.440
71	Lu	2.879	14.478	14.182	13.331	12.028	10.861	71	Lu	2.879	26.975	25.829	22.729	18.526	15.283

Fractional crystallisation of olivine

		F *15% batch modal melt*	*0.90*	*0.80*	*0.70*	*0.60*	*0.50*
57	La	18.621	20.690	23.276	26.601	31.034	37.241
58	Ce	17.983	19.981	22.478	25.689	29.970	35.964
59	Pr	17.097	18.997	21.371	24.424	28.494	34.192
60	Nd	15.711	17.457	19.638	22.443	26.183	31.418
62	Sm	13.500	15.000	16.873	19.282	22.493	26.989
63	Eu	12.423	13.802	15.525	17.740	20.693	24.826
64	Gd	12.196	13.549	15.239	17.412	20.308	24.362
65	Tb	11.354	12.612	14.183	16.204	18.896	22.664
66	Dy	10.437	11.591	13.034	14.888	17.359	20.815
67	Ho	10.130	11.248	12.644	14.438	16.828	20.170
68	Er	9.846	10.927	12.277	14.010	16.317	19.542
69	Tm	9.161	10.164	11.416	13.022	15.160	18.146
70	Yb	8.628	9.568	10.740	12.243	14.243	17.033
71	Lu	9.124	10.108	11.334	12.904	14.990	17.897

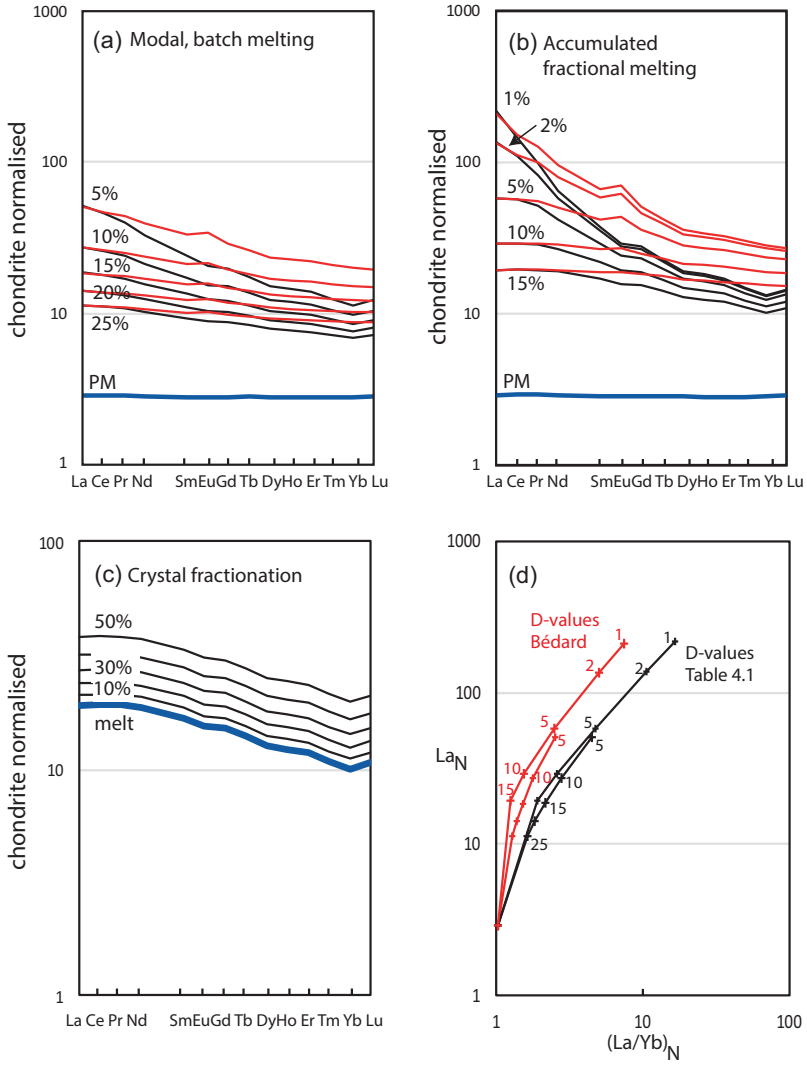

Figure 4.28 Geochemical modelling using REE. (a) REE plot showing the results of 5–25% modal batch melting of a primitive mantle composition. (b) REE plot showing the results of 1–15% accumulated fractional melting of a primitive mantle composition. (c) REE plot showing the results of 10–50% olivine fractionation in a basaltic melt produced by 15% modal batch melting of primitive mantle using partition coefficient data from Table 4.1. (d) $(La/Yb)_N$ versus La_N summarising the change in REE composition for the models presented in panels (a) and (b). The longer curves show the results of accumulated fractional melting and the shorter curves the result of modal batch melting. The numbers by the curves show the fraction of melting. In all panels the compositions shown as black lines use the partition coefficient data from Table 4.1, and those shown as red lines use the partition coefficient data of Bédard (2005, 2014). Further details are given in Table 4.12 and in the text.

and (ii) accumulated fractional melting for 1%, 2%, 5%, 10% and 15% melting (Figure 4.28b). The results using the partition coefficients from Table 4.1 are shown in black (the steeper REE trends), while results using the partition coefficients from Bédard (2005, 2014) are shown in red (the flatter REE trends) for both melting models (Figure 4.28a, b).

These results are summarised using $(La/Yb)_N$ versus La_N to show the degree of REE fractionation (Figure 4.28d). It is clear that the degree of fractionation of the REE (the $(La/Yb)_N$ ratio) is dependent on both the mechanism of melting and on the choice of partition coefficient.

4.8.2.2 Crystal Fractionation

A worked example of the behaviour of the REE during fractional crystallisation is given in Table 4.12 and illustrated in Figure 4.28c. In this example the starting composition is the 15% melt of primitive mantle formed during batch modal melting, calculated in Table 4.12. The effect on REE concentrations by the removal of 10%, 20%, 30%, 40% and 50% olivine ($F = 0.9$ to 0.5) using the olivine partition coefficients from Table 4.1 is shown (Figure 4.28c). It is clear that in this model, because of the highly incompatible nature of the REE in olivine, the REE concentrations in the melt increase, but the overall shape of the REE pattern does not change from that of the parental melt. Hence the $(La/Yb)_N$ ratio of the melt does not change even though the La content of the melt does.

4.8.2.3 Crustal Contamination and AFC Processes

Komatiitic magmas are thought to have had exceptionally high liquidus temperatures and often to have

been contaminated with continental crust leading to the formation of basaltic komatiites. Geochemical support for this hypothesis comes from the enhanced ratios of trace elements such as Nb/La and La/Sm which correlate with Nd–isotopic compositions (Arndt et al., 2008). Arndt and Jenner (1986) calculated the compositional change in a komatiite from the Kambalda greenstone belt contaminated with a mixture of sediment and basalt using AFC modelling for major and trace elements.

One of the difficulties in recognising crustal contamination is that it is not always clear whether the 'contamination' has taken place in the crust or is a property of the mantle source, perhaps reflecting some very ancient modification of a mantle source with either subducted basalt or subducted sediment. Thus, Hughes et al. (2014) modelled AFC processes on a multi-element diagram for the contamination of primary mantle melts with Archaean continental crust. In this case the study suggests that crustal contamination was *not* a major contributor to the magmatic processes under consideration and that the trace element variability was a function of the mantle source compositions involved.

4.8.2.4 Open System Processes

Open system behaviour in magma chambers has been described in some detail in Section 4.2.2.3. However, the early work of O'Hara and Matthews (1981) and later studies such as that of Wooden et al. (1993), Fowler et al. (2004), and Heinonen et al. (2019) make it clear that fractional crystallisation in an open system is often accompanied by AFC processes as the magma reacts with the walls of the magma chamber in either the deep crust or the shallow continental crust. O'Hara and Matthews (1981) explored in some detail the behaviour of trace elements in an RTF magma chamber. They show the contrasting behaviour of incompatible and highly incompatible elements and show that potentially open system fractional crystallization is far more efficient in changing the ratio of incompatible and highly incompatible elements than is closed system fractional crystallization. Using chondrite normalised values of Ce/Yb to represent the slope of the REE diagram and Sm values as a measure of REE concentrations, they show on a bivariate plot of normalised Ce/Yb versus Sm the effects of the RTF process on partial melts of a variety of mantle sources coupled with crystal fractionation.

Recognising RTF processes in a lava sequence requires a very detailed and complete geochemical section. In a study of Oligocene andesites and basalts from southwest Idaho, USA, Norman and Leeman (1990) recognised a cyclicity in the trace and major element chemistry going up the stratigraphic section. On bivariate Ba–Sc and Th–Sc plots they showed that the scatter in the data cannot be accommodated by calculated fractional crystallisation and AFC trends alone, and required the addition of more mafic magmas during evolution of the magma chamber.

4.8.2.5 Magma and Source Mixing

A set of general mixing equations given by Langmuir et al. (1978) can be used to identify magma mixing and mixing in an igneous source region. These equations predict that mixing between two elements produces a straight line, whereas mixing between an element and an element ratio or between two ratios produces an asymptotic curve.

These two types of mixing (magma mixing and source mixing) can be differentiated by using differences in behaviour between compatible and incompatible elements. For example, since highly incompatible element ratios do not change during partial melting or fractional crystallisation, a mixing curve based upon incompatible element ratios is ambiguous, indicating either magma mixing or source mixing. Compatible elements ratios, on the other hand, are strongly fractionated during partial melting but will not reflect the ratios of the source region. Thus, if mixing is in the source region a compatible element plot will show a scattered trend, whereas the mixing of two melts will produce a simple mixing line.

4.8.3 Inversion Techniques Using Trace Elements

Trace element inversion techniques make use of the trace element composition of a mineral or melt to calculate the composition of the parental material – in the case of a mineral this is the melt from which it has crystallised, or in the case of a melt, it is the mineralogy and composition of the source from which it was derived. Inversion techniques require both the precise measurement of trace element concentrations in the mineral or melt to be investigated and a good knowledge of mineral-melt partition coefficients. In their most simple form, inversion methods use the mineral-melt partition coefficient equation (Eq. 4.3)

and solve for either the melt composition if the composition of the solid phase is known or the solid phase if the melt composition is known. More detailed approaches utilise the trace element partitioning equations discussed in Section 4.2.2, although if not all the unknowns are determined some assumptions have to be made during the modelling.

The original methodology of trace element inversion was developed in a series of papers by Allegre et al. (1977), Minster et al. (1977), Allegre and Minster (1978), and Minster and Allegre (1978). These authors made use of the variability in elemental concentrations in a suite of cogenetic igneous rocks to determine unknowns such as the composition and mineralogy of the source, the physical process causing these variations (crystal fractionation, partial melting or other process), and the degree of partial melting or crystal fractionation. More recent mathematical inversion formulations for fractionation and partial melting processes have been given in Janousek et al. (2016), although are unhelpfully termed 'reverse' methods.

Inverse methods can in principle be applied to all petrological processes, although only fractional crystallisation and melting models are illustrated here. A first step in using the inverse approach for the study of trace elements is to attempt to identify the likely physical process which accounts for the variation in the data. This may be done by plotting selected trace elements on bivariate plots. For example, elements which are compatible will vary drastically in concentration during fractional crystallisation, while highly incompatible elements will vary most in abundance during partial melting. In addition, it is important to apply any other available constraints on the petrological process in addition to those governed by the trace element data; these may include the geology of the rock units under consideration and their major element and isotopic geochemistry (Minster and Allegre, 1978).

It is important to emphasise yet again that in this style of trace element modelling assumptions have to made which may or may not be correct, and there is no certainty that a unique solution can be obtained. However, since the time of Allegre and Minster (1978) we have a much more accurate knowledge of trace element partition coefficients, and so these need no longer be treated as unknowns. In addition, with microbeam technology we also have much more precise methods of measuring trace element concentrations in minerals, and so these can be known with much greater certainty.

4.8.3.1 Inverting Mineral Compositions to Estimate the Composition of a Melt

The trace element composition of an early formed mineral phase, that is, one that formed on or close to the liquidus, should in principle reflect the composition of the parental melt. In mafic melts this might be the mineral olivine or spinel. In practice, however, both these phases have very low concentrations of the lithophile trace elements. For this reason, the mineral clinopyroxene is often used since it tends to have much higher concentrations of lithophile trace elements. This approach can be used with early-formed phenocryst phases or with cumulates, in which case the composition of the evolving melt might be monitored through the changing trace element content of the cumulus phases. In felsic rocks early formed mafic phases such as hornblende might provide a useful monitor of the trace element composition of the original melt. In some instances, it is possible to validate calculations of this type by comparison with the measured composition of associated melt inclusions trapped in early-formed phenocryst phases.

An example of the simple inversion of clinopyroxene compositions using known partition coefficients is given by Koga et al. (2001), who investigated the REE chemistry of secondary clinopyroxene in mantle transition-zone dunites from the Oman ophiolite. In order to calculate the REE composition of the melt with which clinopyroxene was originally in equilibrium, they measured the clinopyroxene compositions using an ion microprobe and inverted the compositions using clinopyroxene–mafic melt partition coefficients. The calculated melt compositions had REE patterns which closely mirrored those of the basaltic lavas of the Oman ophiolite, suggesting that clinopyroxene crystallised from a basaltic melt with a MORB-like chemistry (Figure 4.29). This observation led to the inference that the mantle transition-zone dunites of the Oman ophiolite had been re-fertilised, that is, clinopyroxene had been added through the percolation of a basaltic melt which had partially crystallised in the harzburgite host.

An advance on the linear inversion methods of Allegre and Minster (1978) was the non-linear, numerical inversion technique for quantifying MORB trace element compositions proposed by Coogan and Dosso (2016). Their approach takes

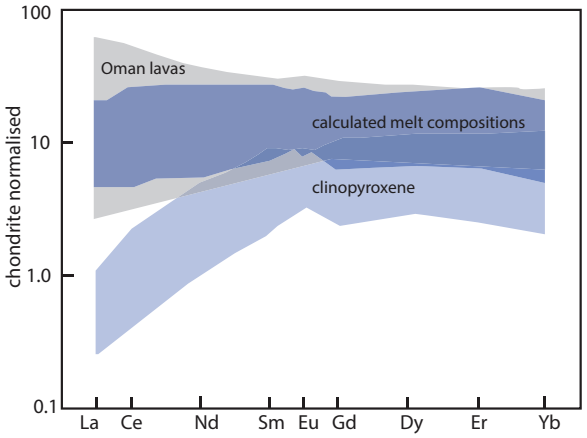

Figure 4.29 REE concentrations in clinopyroxene (pale blue shading) and calculated melt compositions in equilibrium with clinopyroxene (blue shading) in dunites from the upper part of the mantle section of the Oman ophiolite. The range of calculated melt compositions reflects the different degrees of melt fractionation recorded by the clinopyroxene grains. The grey region shows the range of REE abundances in volcanic rocks of the Oman ophiolite. (After Koga et al., 2001; with permission from John Wiley & Sons)

account of the more complex and more realistic nature of fractionation in an open-system magma chamber by including the effects of assimilation and in situ crystallisation. Using this approach, Coogan and Dosso (2016) concluded that parental MORB magmas from the East Pacific Rise are more trace element–depleted than had been previously supposed.

4.8.3.2 Inverting Melt Compositions to Estimate the Melting Process and the Nature of the Source

Many of the applications of the inverse method to igneous melts have been directed towards a better understanding of mantle melting. In this case the unknowns are (i) the chemistry of the source (its composition and mineralogy), (ii) the bulk partition coefficient for each element considered, (iii) the degree of partial melting for each sample and (iv) the mechanism of melting. There are often too many unknowns for a direct solution, and so a number of initial assumptions have to be made. Early studies followed the methods of Minster and Allegre (1978) and used the batch melting model and incompatible trace element ratios and abundances. Melting parameters were extracted from measured trace element data through least squares analysis. A different approach was taken by McKenzie and O'Nions (1991), who sought to investigate the process of mantle melting particularly where small melt fractions were implied. In this case they used a more complex form of inverse theory and assumed a fractional melting model. The mineralogy of the peridotite source was calculated from the composition of the bulk Earth; the average basaltic REE concentrations were from a range of different basalt types; and they used measured REE partition coefficients. With these assumptions, equations were solved for the melt fraction at different mantle depths to demonstrate that MORB melting took place in the shallow mantle and that melt fraction increased with decreasing depth.

In contrast to models based on melt composition, some authors have used melting residue as their starting point for inversion modelling. For example, Zou (1997) presented a methodology which can be applied to a suite of cogenetic melting residues (residual peridotites or clinopyroxenes) that permit the calculation of both the degree of partial melting and the source composition. This approach uses variations in the residue concentration ratios of incompatible trace elements that have different bulk distribution coefficients to obtain the degree of partial melting. Source concentrations can be calculated after obtaining the percentage of partial melting. Liu and Liang (2017) developed this method with a more advanced statistical approach using Markov chain Monte Carlo simulation. They applied their methodology to calculate the extent of melting, the fraction of melt present during melting and the extent of disequilibrium between melt and source from measured clinopyroxene compositions in mid-ocean ridge peridotites.

4.8.4 A Final Comment on Geochemical Modelling

Trace element modelling in petrology is an important technique widely used as a geochemical means of hypothesis testing, and in recent decades the mathematical approaches have become increasingly sophisticated. However, it is important to remember a number of key points:

- Trace element modelling does not always produce a unique solution. Often petrological problems of this type may contain too many unknowns, but nevertheless the approach may set constraints on possible processes.

- Trace element modelling must be regarded as a means of hypothesis testing and should be used to verify an already constrained model. Wherever possible trace element studies should be part of a broader approach to understanding a geochemical problem that integrates constraints from field relationships together with major element and isotopic chemistry.
- Partition coefficient values can depend upon a large number of variables, and it is important to select partition coefficients which represent as closely as possible the physical conditions to be modelled.
- The ultimate aim of geochemical modelling is to constrain the geochemical processes operating. Where possible this is normally best approached using inverse methods.

5 Using Geochemical Data to Identify Tectonic Environments

5.1 Introduction

The idea of using rock chemistry to 'fingerprint' different tectonic settings is probably best attributed to the work of Pearce and Cann (1971, 1973). In these two important papers the authors showed that it was possible to use the geochemistry of basaltic rocks to distinguish between those produced in known and distinct tectonic settings. Their relatively simple approach and the wide applicability of 'tectono-magmatic discrimination diagrams' – geochemical variation diagrams which segregate rock types according to their various tectonic settings – meant that the environment of eruption of both ancient and modern basalts could be defined from the chemical analysis of a rock using a few readily determined elements. Such diagrams were later applied to both sedimentary (Bhatia, 1983) and plutonic (granitic) (Pearce et al., 1984) rocks.

The pioneering work of Pearce and Cann (1971, 1973) was based upon trace elements generally considered to be immobile under hydrothermal conditions and they were used to identify distinct tectonic environments. However, much of this early work was impaired by an inadequate statistical treatment of the data due to low sample numbers, the problems associated with closed data sets and non-uniform errors – heteroscedasticity (see the discussion in Chapter 2). Today, such diagrams are being reconsidered in light of proper statistical treatment and larger trial and test datasets. This ongoing work is resulting in more robust tectonic discrimination diagrams (Section 5.2).

An unfortunate consequence of the advent of tectono-magmatic discrimination diagrams is the plethora of simplistic tectonic interpretations of suites of igneous rocks found in the geological literature. This is not helpful, and our purpose here is to encourage the reader to seek to understand *how and why* particular geochemical signatures are associated with different tectonic environments and to consider 'tectono-magmatic discrimination diagrams' as a means to an end, rather than an end in themselves. In other words, to move beyond mere geochemical taxonomy and sample classification in order to develop discrimination diagrams that can be used to investigate geochemical *processes*. Ultimately, it is the understanding of geochemical processes that will lead to the proper identification of the former tectonic setting of igneous and sedimentary rocks.

In this chapter we critically evaluate the current status of tectonic discrimination diagrams and their use in geochemistry. We briefly explore the principles and assumptions behind their derivation, highlight those diagrams which are useful and identify others which may now be redundant, in order to develop future good practice in their use. We restrict ourselves to tectonic discrimination diagrams which were determined using major and trace element whole-rock chemistry. There are many other discrimination diagrams which are based upon the chemistry of mineral phases such as clinopyroxene and chromite, which are not considered here.

5.1.1 Tectonic Environments

Our knowledge of tectonic environments is much refined since the plate tectonic paradigm was established in the 1960s. This reflects the advances made in our understanding of both earth processes and the chemistry of igneous rocks. Pearce and Cann (1971, 1973) originally worked with volcanic rocks and were able to distinguish between volcanic arc, ocean floor and within-plate environments. Today volcanic, plutonic and sedimentary rocks are all being investigated and we recognize a multitude of environments including island arcs, island back arcs, island back-arc basins, continental arcs, continental back arcs, continental arcs with thick crust (Andean type), continental back arcs with thick crust (Andean type), continental extension, continental rifts, ocean islands, oceanic plateaus, ocean islands at oceanic plateaus, mid-ocean ridges, incipient mid-ocean ridges, and mid-ocean ridges close to ocean islands, as well as extensional

environments associated with syn- and post-collisional regimes. A summary of the tectonic environments that may be recognized on the basis of geochemical data is given in Box 5.1.

5.1.2 The Current Approach to Discrimination Diagrams

Given the statistical advances that now allow us to deal with the unique aspects of geochemical data (Chapter 2), discriminant analysis is a preferred method for developing both binary and ternary tectonic discrimination diagrams. Discriminant analysis of geochemical data reduces a large number of variables (typically oxides or elements) to a smaller number of parameters known as the *discriminants* (Section 2.8.2). The discriminants are typically a few distinct combinations of the oxides/elements which simultaneously encompass most of the data, but at the same time effectively subdivide samples into separate compositional groups (Section 2.8.2). The most powerful discriminants, plotted as elemental concentrations or as calculated discriminant functions based upon the elemental concentrations, are then used to define the axes of binary plots or the apices of ternary diagrams.

The creation of a successful discrimination diagram properly involves a 'large' data set of analyses from known settings which is split into 'training' and 'test' data. The training data are used for the empirical derivation of boundaries between different groups of samples. These boundaries are selected to maximize the successful classification of the data from known environments and allow 'unknown' samples to be classified with greater confidence. The success of the diagram is evaluated using the 'test' data, which is quantified using either the percentage of successfully classified data or the percentage of misclassified data. The method of 'back-projection' to triangular space not only allows for the correct statistical treatment of the data, but is likely to be more widely used as triangular plots are a familiar tool in geology and geochemistry (see, e.g., Section 5.2.5). Helpful reviews of this approach include those of Vermeesch (2006a) and Verma (2020).

Unfortunately, the application of discriminant analysis to geochemical data is not entirely straightforward and requires a number of steps to ensure the uniformity of the data, followed by the application of statistical software. This process usually includes the following:

1. Initial data quality assessment
2. Standardizing the Fe-oxidation adjustment (see Chapter 3)
3. Normalizing the major elements to 100% anhydrous (see Chapter 3)
4. Performing the natural logarithm (ln or log e) transformation of element ratios using a common divisor (see Chapter 2)
5. Filtering the log-transformed data for outliers (see Chapter 2)
6. Performing discriminant analysis (linear or quadratic) on the outlier-free log-ratio data
7. Plotting the data on binary discriminant function diagrams or performing the inverse log-ratio transformation for ternary plots.

There are two other matters of concern. One is the tension between the number of elements used to create a discriminant function and understanding its geological significance. Although increasing the number of elements in discriminant analysis generally results in a more robust function, it also becomes more

Box 5.1 Tectonic environments recognizable using geochemical criteria

Ocean ridge (igneous)
- Normal ocean ridge (characterised by N-type MORB)
- Anomalous ocean ridge (characterised by E-type MORB)
- Incipient spreading centre
- Back-arc basin ridge
- Fore-arc basin ridge (located above a subduction zone)

Volcanic arc (igneous)
- Oceanic arc dominated by tholeiitic basalts
- Oceanic arc dominated by calc-alkali basalts
- Active continental margin

Collisional setting (igneous)
- Continent–continent collision
- Continent–arc collision

Intraplate setting (igneous)
- Intra-continental, normal crust
- Intra-continental, attenuated crust
- Ocean island

Active continental margin (sedimentary)

Passive continental margin (sedimentary)

difficult to ascertain the geochemical significance of multi-element axes with respect to petrogenetic processes. Therefore, while such diagrams are useful for classification, they should be combined with other forms of assessment to verify testable hypotheses related to petrogenesis. Second, we note that even though discriminant function binary plots have been in use for several decades (e.g., Pearce and Cann 1971, 1973; Roser and Korsch, 1986), they have not been widely adopted by the geochemical community; we surmise this is because of the complexity involved in performing discriminant analysis combined with the uncertain petrogenetic significance of the multi-element axes.

5.1.3 Immobile Trace Elements

A major step forward in the development of discrimination diagrams was the rapid and accurate analysis of trace elements in silicate materials. This work was initially carried out by X-ray fluorescence analysis and is now also the purview of mass spectrometry (ICP-MS), which allows the measurement of trace elements at ppm to sub-ppm levels. Of particular importance are the trace elements thought to be immobile under most forms of hydrothermal activity (Section 4.2.2.1), for these can also be used with altered and metamorphosed rocks. High field strength elements such as Ti, Zr, Y, Nb, V and P are relatively immobile in aqueous fluids (unless there are high activities of F^-) and are stable during hydrothermal alteration, sea-floor weathering and up to medium metamorphic grades (mid-amphibolite facies). However, elements generally considered to be more mobile in a fluid can also be used provided the samples are *fresh*. For example, Sr is often among the top-ranked elements for discriminating tectonic environments (Vermeesch, 2006a).

5.1.4 Using Discrimination Diagrams

Discrimination diagrams should be used to suggest a possible tectonic affiliation which forms a basis for further hypothesis testing. They do not constitute *proof* of a tectonic setting. In particular, it is important to remember that discrimination diagrams are:

1. A statistical representation
2. Intended to be used with a *suite* of samples (rather than just a few analyses)
3. Constructed with analyses from modern tectonic settings; this means that the further back in time we go, the less likely the discriminant will reflect reality. For example, using a discrimination diagram constructed from modern volcanic rocks to postulate an Archaean tectonic setting after >2.5 Ga years of crustal recycling is likely to produce equivocal results.

We now review discrimination diagrams relevant to igneous and sedimentary rocks. In the case of diagrams that use immobile elements, these may also be applied to their metamorphosed equivalents. These diagrams are grouped into three types: binary, ternary and discriminant function (DF) binary. All DF binary diagrams are the product of *linear discriminant analysis* unless otherwise stated. In Table 5.1 each diagram is ranked within its geochemical compositional group (basic, intermediate, acid, sedimentary) and evaluated according to the percentage of data misclassified as listed in the error column of Table 5.1.

Factors to be considered when evaluating the efficacy of a discrimination diagram include the following:

1. The number of trial data and test data used
2. The degree of overlap between the proposed fields
3. The effects of element mobility
4. The range of tectonic environments represented.

The diagrams presented here have been generated and tested using hundreds to thousands of analyses from known tectonic settings. The success of the classification scheme and the degree of overlap between fields are directly correlated. Some of the older diagrams have been assessed for their statistical performance in relation to the issues raised in Section 5.1.2, and some are now known to *significantly (60–100%) misclassify* samples (Vermeesch, 2006a; Verma, 2010). Many diagrams have yet to be evaluated statistically, but given that of those evaluated up to 30% do not perform well (Table 5.1), we may expect a similar performance for those diagrams not yet evaluated (marked as 'unevaluated' in Table 5.1). Those diagrams which significantly misclassify or have not yet been statistically assessed are not considered further here. Our discussion is restricted to only those diagrams with better than 30% misclassification (or ≥70% successful classification) and these diagrams are shaded in Table 5.1. The 30% cut-off is somewhat arbitrary and others

Table 5.1 A summary of tectonic discrimination diagrams

Classification	*Plot type*[a]	*Error (%)*[b]	*Reference(s)*	*Comments*[c]
Basic volcanic rocks				
Nb_N–Th_N	Binary	<6%	Saccani (2015)	Good for MORB-OIB array and arc array
Ti/Y–Zr/Y	Binary	<11[d]	Pearce and Gale (1977)	Good for plate margin and within-plate, excluding E-MORB
Ti/1000–V	Binary	18[e]	Shervais (1982)	Good for OI, okay for MOR, marginal for IA
Zr–Ti	Binary	19[e]	Pearce and Cann (1973)	Good for OIB, IAB
Nb/Y–Ti/Y	Binary	<29[d]	Pearce (1982)	Only good for within-plate
Zr–Zr/Y	Binary	>34[d]	Pearce and Norry (1979)	
Y–Cr	Binary	*unevaluated*	Pearce (1982)	
Ce/Sr–Cr	Binary	*unevaluated*	Pearce (1982)	
Y/Nb–TiO_2	Binary	*unevaluated*	Floyd and Winchester (1975)	
Zr–P_2O_5	Binary	*unevaluated*	Winchester and Floyd (1976)	
Zr/(P_2O_5 × 10,000)–Nb/Y	Binary	*unevaluated*	Winchester and Floyd (1976)	
Zr/(P_2O_5 × 10,000)–TiO_2	Binary	*unevaluated*	Winchester and Floyd (1976)	
Ta/Yb–(K_2O/Yb × 0.001)	Binary	*unevaluated*	Pearce (1982)	
H_2O–K_2O	Binary	*unevaluated*	Muenow et al. (1990)	
Sc/Ni–La/Yb	Binary	*unevaluated*	Bailey (1981)	
Na/100–25Nb–Sr	Ternary	<5[e] (QDA)	Vermeesch (2006a)	Good for OI, IAB, but not good for MORB
Si/1000–Ti/40–Sr	Ternary	6[e]	Vermeesch (2006a)	Good for OI, MOR, IA
100Eu–500Lu–Sr	Ternary	7[e]	Vermeesch (2006a)	Good for OI, MOR, IA
V–Ti/50–5Sc	Ternary	10[e]	Vermeesch (2006a)	Good for OIB, IAB
50Sm–Ti/50–V	Ternary	10[e] (QDA)	Vermeesch (2006a)	Immobile elements, good for altered rocks
Th–Hf/3–Ta	Ternary	20[e]	Wood (1980)	Poor for IA (large spread in composition)
La/10–Y/15–Nb/8	Ternary	≤29[d]	Cabanis and Lecolle (1989)	Only good for arc (island and back arc) and N-MORB
Zr/4–2Nb–Y	Ternary	38[e]	Meschede (1986)	
Zr–Ti/100–3Y	Ternary	36[e]	Pearce and Cann (1973)	
Zr–Ti/100–Sr/2	Ternary	*unevaluated*	Pearce and Cann (1973)	
MgO–FeO–Al_2O_3	Ternary	*unevaluated*	Pearce et al. (1977)	
10MnO–TiO_2–10P_2O_5	Ternary	*unevaluated*	Mullen (1983)	
Major elements (-Fe)	DF	7[e]	Pearce (1976); Vermeesch (2006a)	Good for oceanic basalts
TiO_2–Zr–Y–Sr	DF	8[e]	Butler and Woronow (1986); Vermeesch (2006a)	Good for oceanic basalts
TiO_2, Nb, V, Y, Zr	DF	<10	Verma and Agrawal (2011)	Good for CR, IA, MOR, OI
All (except Si)	DF	<24	Verma et al. (2016)	Good for high Mg rocks
Intermediate volcanic rocks				
Y–Sr/Y	Binary	*unevaluated*	Defant and Drummond (1990)	Arc, adakites
Yb–La/Yb	Binary	*unevaluated*	Defant and Drummond (1990)	Arc, adakites
Major elements	DF	≤29	Verma and Verma (2013)	
TiO_2, MgO, P_2O_5, Nb, Ni, V, Y, Zr	DF	<30	Verma and Verma (2013)	
Trace elements	DF	<44	Verma and Verma (2013)	Immobiles, good for altered rocks

Table 5.1 (*cont.*)

Classification	*Plot type*[a]	*Error (%)*[b]	*Reference(s)*	*Comments*[c]
Acid plutonic rocks				
Yb–Ta	Binary	22–25[f]	Pearce at al. (1984)	~22% VAG, ~26% WPG, ~72% syn-Col
Y– Nb	Binary	26–31[f]	Pearce at al. (1984)	~31% VAG + syn-Col, ~26% VAG + syn-Col, ~29% CR
(Yb + Ta)–Rb	Binary	*unevaluated*	Pearce at al. (1984)	
(Y + Nb)–Rb	Binary	*unevaluated*	Pearce at al. (1984)	
Hf–Rb/10–3Ta	Ternary	*unevaluated*	Harris et al. (1986)	
Hf–Rb/30–3Ta	Ternary	*unevaluated*	Harris et al. (1987)	
Major elements	DF	≤15[f]	Verma et al. (2012)	Good for IA, CA, CR, COL
Sedimentary rocks				
SiO_2–log (K_2O/Na_2O)	Binary	31[g]	Roser and Korsch (1986)	Good for IA, lacks CA
Th–La	Binary	≥70[g]	Bhatia and Crook (1986)	Cannot distinguish between ACM and PM
($Fe_2O_3^T$ + MgO)–K_2O/Na_2O	Binary	>70[g]	Bhatia (1984)	Cannot distinguish between ACM and PM
($Fe_2O_3^T$ + MgO)–TiO_2	Binary	>75[g]	Bhatia (1983)	Cannot distinguish between ACM and PM
($Fe_2O_3^T$ + MgO)–Al_2O_3/SiO_2	Binary	>65[g]	Bhatia (1983)	Cannot distinguish between ACM and PM
($Fe_2O_3^T$ + MgO)–Al_2O_3/($CaO + Na_2O$)	Binary	>70[g]	Bhatia (1983)	Cannot distinguish between ACM and PM
Sc/Cr–La/Y	Binary	*unevaluated*	Bhatia and Crook (1986)	Cannot distinguish between ACM and PM
La/Sc–Ti/Zr	Binary	*unevaluated*	Bhatia and Crook (1986)	Cannot distinguish between ACM and PM
Th–La–Sc	Ternary	>95[g]	Bhatia and Crook (1986)	Cannot distinguish between ACM and PM
Co–Zr/10–Th	Ternary	*unevaluated*	Bhatia and Crook (1986)	Cannot distinguish between ACM and PM
Sc–Th–Zr/10	Ternary	*unevaluated*	Bhatia and Crook (1986)	Cannot distinguish between ACM and PM
Major elements	DF	≤25%	Verma and Armstrong-Altrin (2013)	For arc, rift and collisional settings
Major elements	DF	>90[g]	Bhatia (1983)	Cannot distinguish between ACM and PM

[a] DF = discriminant function binary plot.
[b] Re-substitution error (%) of trial dataset using linear discriminant analysis unless otherwise indicated (QDA, quadratic discriminant analysis;PCA, principal component analysis).
[c] ACM, active continental margin; CA, continental arc; Col, collisional; CR, continental rift; IA, island arc; MOR, mid-ocean ridge; OI, ocean island; OIA, oceanic island arc; ORG, ocean ridge granite; PM, passive margin; syn-Col, syn-collisional granite; VAG, volcanic arc granite; WPG, within-plate granite.
[d] Verma (2010).
[e] Vermeesch (2006a).
[f] Verma et al. (2012).
[g] Verma and Armstrong-Altrin (2013).

might set a more restrictive limit, but we regard diagrams with >30% misclassification as unreliable. Discriminant function diagrams (marked DF in Table 5.1) can be employed by using the DF axis equations, which are given in Appendix 5.1. *Note, however, that for all diagrams the input data must be processed in the same way as the trial/test data used to generate the original figure in order for the results to be meaningful.*

Overall, immobile trace elements provide greater classification success than major elements when using the same number of elements, and binary or discriminant function binary diagrams generally yield greater classification success than ternary diagrams. An issue for all diagrams is the difficulty in discriminating between samples from island arcs and from continental arcs. This is in part due to the large compositional variation which results from the effects of crystal fractionation in arc-related rocks. A further difficulty is distinguishing between the different 'within plate' settings, for there are compositional similarities between volcanic rocks found in continental rift and ocean island environments, particularly in the more evolved compositions.

A final point to note is that some discrimination diagrams are designed to be used in a particular sequence. This is particularly true for those associated with DF analysis. Typically, in order to show all environments, the first diagram presents some combined fields. Once analyses in the combined field are categorised, subsequent diagrams can then be used to refine their tectonic settings. This allows the user to discriminate between sample sets which show some overlap in the first diagram and to separate them in subsequent diagrams into discrete tectonic settings, as is the case for volcanic rocks formed within arcs and those erupted in within-plate settings. Examples of the sequential approach to discrimination diagrams are given in Sections 5.2.14 and 5.3.

5.2 Elemental Discrimination Diagrams for Ultramafic and Mafic Volcanic Rocks

Robust statistical discrimination diagrams for mafic volcanic rocks use major or trace elements and include all three diagram types: binary, ternary and discriminant function (Section 5.1.4). These diagrams are presented in rank order for each of the diagram types in Table 5.1 and ranked according to the smallest percentage of data misclassified. The strength(s) and weakness(es) of each diagram are highlighted in the comments column of Table 5.1.

It is important to note that before using a discrimination diagram the geochemistry of the individual samples must be carefully evaluated and samples with anomalous compositions identified. For example, samples with a high cumulus plagioclase content will have reduced absolute concentrations of Ti and Zr because of the dilution effect of abundant plagioclase. Similarly, rocks containing large amounts of cumulus Ti-bearing phases such as titanomagnetite or clinopyroxene will also give biased results.

5.2.1 Nb/Y–Ti/Y, Nb_N–Th_N, and Ce, Dy, Yb Diagrams

Pearce (1982) used a log–log version of the Nb/Y–Ti/Y binary diagram to distinguish between within plate basalts (Ti/Y > 400) and plate margin basalts (Ti/Y < 400). He suggested that the higher Ti/Y ratios in within-plate basalts reflect an enriched mantle source relative to the sources of MORB and volcanic-arc basalts. However, subsequent studies have shown that there are some limitations to the use of this plot as a discrimination diagram. Verma (2010) demonstrated that although the diagram is statistically robust for identifying within-plate basalts (71% success), there is significant overlap between basalts from arc and MORB environments and so it is of limited use for samples from these environments. A further problem is that of the potential spurious correlations which can result from the use of a common denominator in binary diagrams (Section 2.6), a feature that was confirmed for the Th/Yb versus Nb/Yb diagram of Pearce (2008) by Saccani (2015). Using a trial dataset of >2000 analyses from known tectonic settings, Saccani (2015) documented up to 31% misclassification for this diagram, particularly for samples of E-MORB, P-MORB and alkali basalt.

Pearce (2008) demonstrated the utility of the Th-Nb proxy for identifying a crustal component in basalts, most probably introduced via subduction fluids, and thereby discriminating between subduction-related and non-subduction oceanic settings. In this case Saccani (2015) avoided the problem of spurious self-correlation by normalizing Nb and Th to the N-

MORB values of Sun and McDonough (1989). Using a test dataset of 565 analyses, he was able to verify a high level of distinction (>94%) between the MORB–OIB and the volcanic arc arrays (Figure 5.1a) and interpreted these within a plate tectonic framework (Figure 5.1b). To better distinguish basalts within the MORB–OIB array, Saccani (2015) was also able to successfully (>99%) discriminate between island arc tholeiites and boninites using a Dy_N–Yb_N diagram (Figure 5.1c) and between normal (N-) MORB (99%) and garnet influenced (G-) MORB (96%) on the binary diagram Ce_N/Yb_N versus Dy_N/Yb_N (Figure 5.1d). In the latter two diagrams samples are normalized to the chondrite values of Sun and McDonough (1989).

5.2.2 Ti/Y–Zr/Y

The Ti/Y–Zr/Y binary diagram of Pearce and Gale (1977) discriminates between basalts from within-plate settings (continental rift and ocean island settings) and those from plate margins (island arc, continental arc and N-MORB settings) (Figure 5.2a). It utilises the enrichment in Ti (ppm) and Zr (ppm) in the source of within-plate basalts to distinguish them from plate margin basalts. Verma (2010) validated the continued use of this diagram with a data set of almost 4000 analyses (including some from E-MORB settings), which were processed using the statistical methods described in Section 5.1.4. He demonstrated that, when the E-MORB data are excluded, <11% of the data are misclassified. We conclude that this diagram is robust apart from its application to E-MORB samples which can be misclassified as within-plate basalts >40% of the time.

5.2.3 Ti/1000–V

A Ti–V discrimination diagram was first proposed by Shervais (1982). Major element (Ti) wt.% data is converted to ppm. The logic behind the diagram is that although Ti and V are adjacent members of the first transition series of the periodic table, they behave in different ways in silicate systems. The principal reason for this is that in silicate magmas V can exist in more than one oxidation state (V^{3+}, V^{4+} or V^{5+}) and yet Ti exists only as Ti^{4+}. The redox-sensitive nature of V means that mineral–melt partition coefficients in minerals such as orthopyroxene, clinopyroxene and magnetite may vary over several orders of magnitude as a function of oxygen activity (see Section 4.2.1.3). For this reason, variations in the concentration of V relative to Ti in mafic melts reflect the oxygen activity of the magma and also any crystal fractionation processes which have taken place. These parameters can be linked to the environment of eruption and form the basis of this discrimination diagram. An added feature of the diagram is it that can be used with altered mafic compositions, for Ti and V are immobile during hydrothermal alteration and also at intermediate to high grades of metamorphism.

Vermeesch (2006a) used a training data set of 756 analyses, with SiO_2 contents between 45 and 53 wt.%, from known tectonic settings and processed the data using the statistical method outlined in Section 5.1.4 to create a new Ti/1000 (ppm) versus V diagram. The new diagram is a modification of the original diagram of Shervais (1982), and the boundaries between the fields of island arc, ocean island and mid-ocean ridge basalts have been adjusted in the light of the new data set. The resulting diagram (Figure 5.2b) successfully classified 100% of the ocean island analyses, 74% of the mid-ocean ridge analyses and 70% of the island arc basalts in the test data set ($n = 182$). The marginal performance of island arc samples likely reflects their wide compositional variation.

5.2.4 Zr–Ti

The original Zr–Ti binary discrimination diagram of Pearce and Cann (1973) was used for basalts with a limited compositional range (20 wt.% > CaO + MgO > 12 wt.%). It also excluded alkali basalts, which were identified on the basis of their low Y/Nb ratios. The statistical reassessment of this diagram by Vermeesch (2006a) resulted in significant modifications. The original boundaries are no longer viable as there was no separation between tholeiitic and calc-alkaline basalts on the basis of their zirconium content. For this reason, the new diagram distinguishes only between island arc, ocean island, and mid-ocean ridge environments (Figure 5.2c) and correctly classifies most ocean island (94%) and island arc (77%) basalts of the test data. However, the classification of mid-ocean ridge basalts is poor (only 64% correctly classified), probably reflecting their natural variation from 'normal' to 'enriched' compositions along mid-ocean ridges.

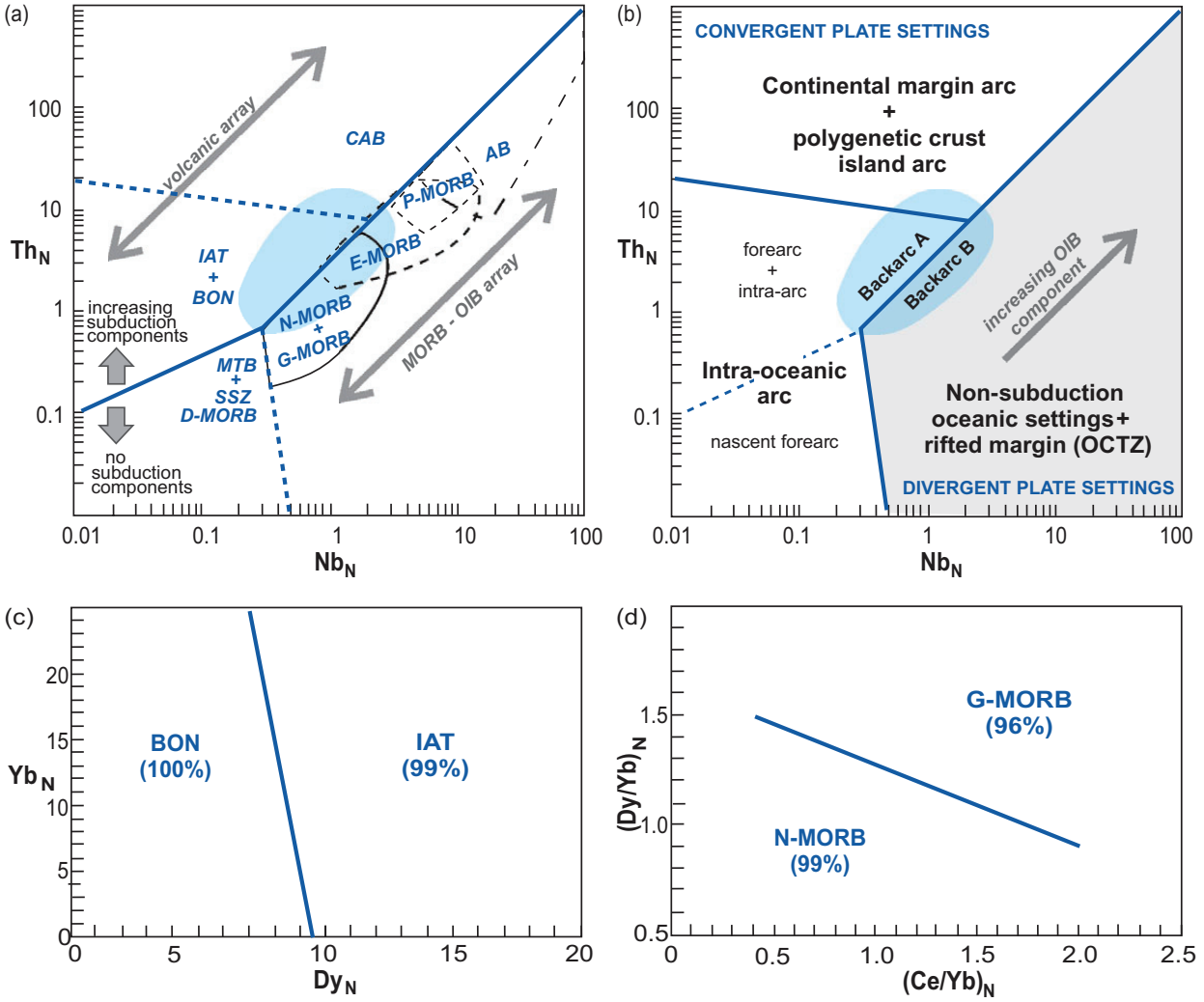

Figure 5.1 Binary classification of ophiolite-related basalts (after Saccani, 2015; with permission of Elsevier). In panels (a) and (b) the elements are normalized to the N-MORB compositions of Sun and McDonough (1989). (a) Solid line separates basalts influenced by subduction components. Central shaded area = BABB field with overlaps to IAT + BON, CAB, and the MORB–OIB array. Note progressive overlap in the MORB–OIB array from N-+ G-MORB to AB. (b) Segregation of convergent (white) and divergent (grey) tectonic settings. Within the grey field, the direction of increasing OIB component is shown by the arrow. Solid line in convergent settings separates intra-oceanic from other arc-related settings. Dashed line separates forearc and intra-arc environments from nascent forearcs. Note two types of BABB: one with subduction or crustal components (Back arc A, immature intra-oceanic or ensialic back arcs) and one lacking subduction or crustal components (Back arc B, mature intra-oceanic back arcs). Boundary coordinates in panels (a) and (b) are (0.01, 0.1), (0.01, 20), (0.5, 0.01), (0.306, 0.708), (2.2, 8.0), (100, 1000). In panels (c) and (d) the elements are normalized to the chondrite values of Sun and McDonough (1989). (c) IAT and BON may be distinguished using Dy_N and Yb_N. Boundary coordinates (9.5, 0; 7, 25). (d) N-MORB and G-MORB may be separated with Ce_N/Yb_N versus Dy_N/Yb_N. Boundary coordinates (0.4, 1.5; 2.0, 0.9). AB, Alkaline basalt; BABB, back arc basin basalt; BON, boninite; CAB, continental arc basalt; D-MORB, depleted MORB; E-MORB, enriched MORB; G-MORB, garnet MORB; IAT, island arc tholeiite; MORB, mid-ocean ridge basalt; MTB, medium-Ti basalt; N-MORB, normal MORB; OCTZ, ocean–continent transition zone; OIB, ocean island basalt; P-MORB, plume MORB; SSZ, supra-subduction zone.

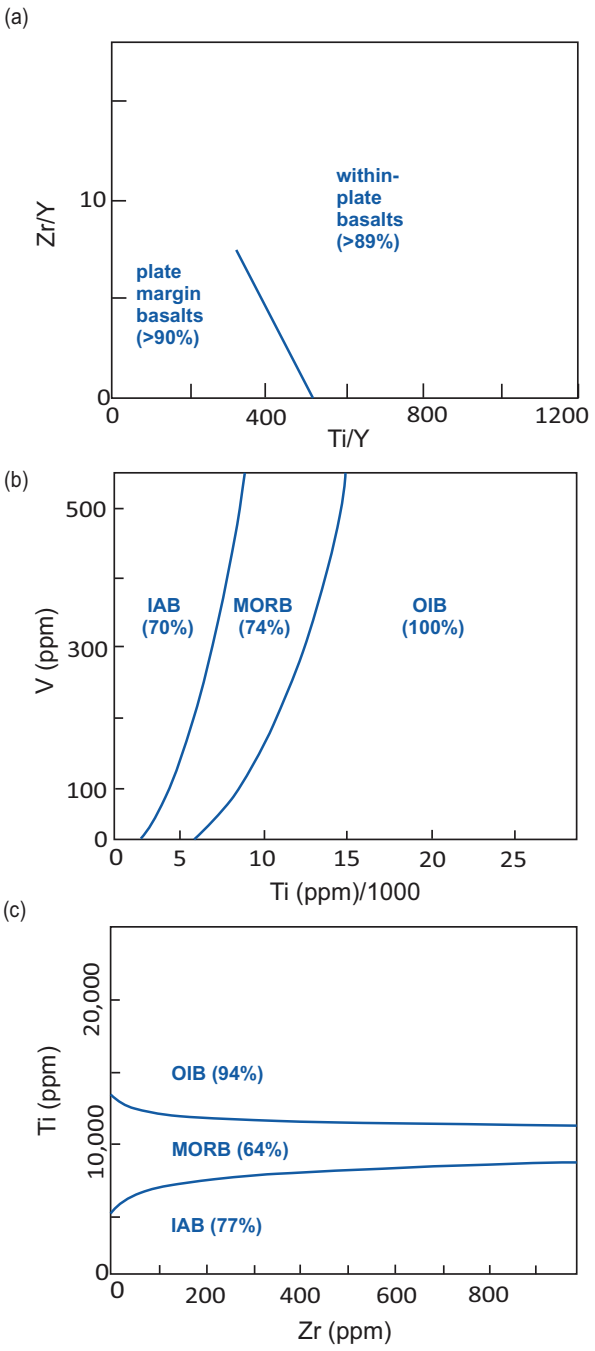

Figure 5.2 Binary classification diagrams for mafic volcanic rocks. Numbers in parentheses represent the percentage of the empirical test data set successfully classified. (a) Ti/Y versus Zr/Y (Pearce and Gale, 1977). This diagram only provides a robust statistical distinction between within-plate (rift and ocean island) and plate margin (island arc and back-arc) basalts and excludes enriched mid-ocean ridge (E-MORB) compositions (Verma, 2010). Boundary coordinates: (513, 0) and (313, 7.5). (b) Ti/1000 versus V (Shervais, 1982) with the redefined boundaries of Vermeesch (2006a; with permission from John Wiley & Sons). This diagram provides a robust statistical recognition of island arc, mid-ocean ridge and ocean island basalts. The curved boundaries of this diagram should be accurately traced or scanned. (c) Zr versus Ti (Pearce and Cann, 1973) with the redefined boundaries of Vermeesch (2006a; with permission from John Wiley & Sons). This diagram provides the robust statistical recognition of island arc and ocean island basalts, but is less reliable for MORB. The curved boundaries should be accurately traced or scanned. IAB, island arc basalt; MORB, mid-ocean ridge basalt; OIB, ocean island basalt.

5.2.5 Na/100–25Nb–Sr

The Na/100–25Nb–Sr triangular diagram shown in Figure 5.3a was created using robust statistical methods based on quadratic discriminant function analysis and the back-projection of the results onto triangular space (Vermeesch, 2006a). Major element (Na) wt.% data is converted to ppm. It successfully classifies all the IAB and OIB samples in the test dataset ($n = 182$), but is less able to correctly define MORB samples (only 58% successfully classified). The poor performance of MORB samples is probably due to Na mobility associated with seawater alteration, emphasizing the need for fresh samples.

5.2.6 Si/1000–Ti/40–Sr

The Si/1000–Ti/40–Sr triangular diagram (Figure 5.3b) was also generated through linear discriminant function analysis (Vermeesch, 2006a) and is a very successful discrimination diagram for basalts from oceanic environments (MORB, OIB and IAB). Major element (Si, Ti) wt.% data are converted to ppm. Using a test data set of 182 samples, Vermeesch (2006a) found that the diagram successfully classified 74% of the IAB samples, 98% of MORBs and all of the OIB samples.

5.2.7 100Eu–500Lu–Sr

The 100Eu–500Lu–Sr triangular diagram is based upon the differences in the REE concentrations of enriched and depleted mantle sources and can be applied to MORB, OIB and IAB. Using a test dataset of 182, Vermeesch (2006a) found that this diagram misclassifies only 24% of island arc basalt analyses (IAB) and that it correctly classifies all mid-ocean

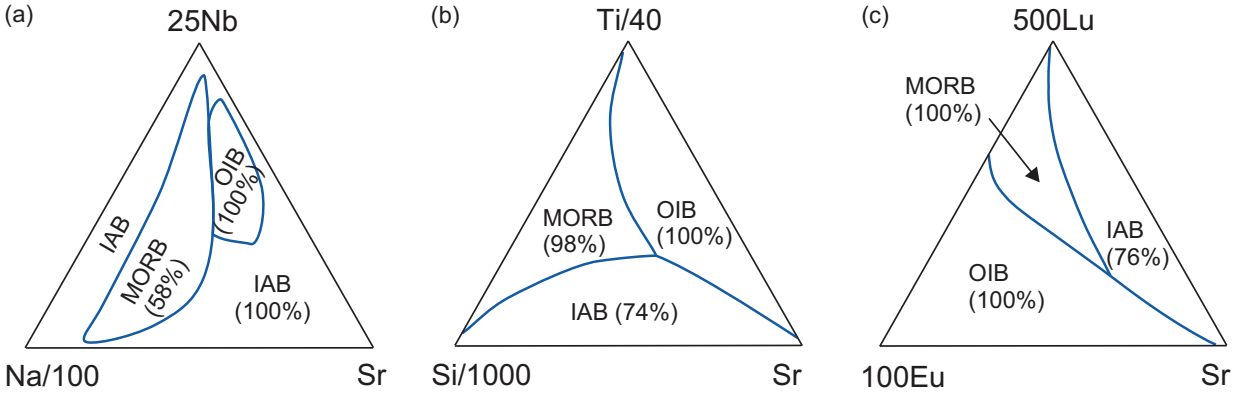

Figure 5.3 Ternary classification diagrams for mafic volcanic rocks. Numbers in parentheses represent the percentage of the empirical test data set successfully classified. Curved boundaries should be scanned. (a) Na/100–25Nb–Sr provides robust statistical classification of IAB and OIB. (b) Si/1000–Ti/40–Sr provides robust statistical classification of IAB, OIB and MORB. (c) 100Eu–500Lu–Sr provides robust statistical classification of IAB, OIB and MORB from oceanic environments. (All three panels are from Vermeesch, 2006a; with permission from John Wiley & Sons)

ridge basalts (MORB) and ocean island basalts (OIB) (Figure 5.3c). Given that Sr is mobile during alteration and metamorphic processes, the diagram is most applicable to pristine, unaltered basalts.

5.2.8 V–Ti/50–5Sc

Vermeesch (2006a) found that the immobile, incompatible elements V, Ti and Sc (all as ppm) are effective in distinguishing between oceanic environments when back-projected into triangular space and plotted on a V–Ti/50–5Sc diagram (Figure 5.4a). Using a test data set of 182 samples the diagram was found to work well for OIB and IAB settings (100% success), but is less effective for MORB environments, in which only 67% were classified correctly.

5.2.9 50Sm–Ti/50–V

The 50Sm–Ti/50–V triangular diagram (Figure 5.4b) is based on the quadratic discriminant function analysis of immobile elements in basalts (Vermeesch, 2006a). Major element (Ti) wt.% data is converted to ppm. The classification is robust and the diagram misclassifies only 10% of the trial data. It is also successful with a test data set of 182 samples and correctly classifies OIB (100%), MORB (88%) and IAB (92%) and so is recommended for oceanic compositions.

5.2.10 Th–Hf/3–Ta

The Th–Hf/3–Ta triangular diagram (Figure 5.4c) was originally proposed by Wood (1980) and subsequently recalculated by Vermeesch (2006a). New non-linear boundaries were determined by Vermeesch (2006a) on the basis of a robust statistical analysis and the back-conversion of the data to triangular space. The new version of the diagram successfully classifies IAB (>74%) and OIB (100%) samples. There were no MORB analyses with the elements Th, Hf, Ta in the test data set, although the field was well defined by the trial data.

5.2.11 La/10–Y/15–Nb/8

The La/10–Y/15–Nb/8 triangular diagram (Figure 5.4d) for the classification of basalts was devised by Cabanis and Lecolle (1989) and more recently recalculated by Verma (2010) using a more robust statistical approach. This diagram is only reliable for island arc and back-arc (IAB) samples (<24% misclassification) and for N-MORB samples (<29% misclassification). Samples from the other tectonic environments shown in this diagram have high percentages of misclassification. Continental rift basalts (CRB) are 42% misclassified, OIB 58% and E-MORB 55%, and so this diagram should not be used for samples from these environments.

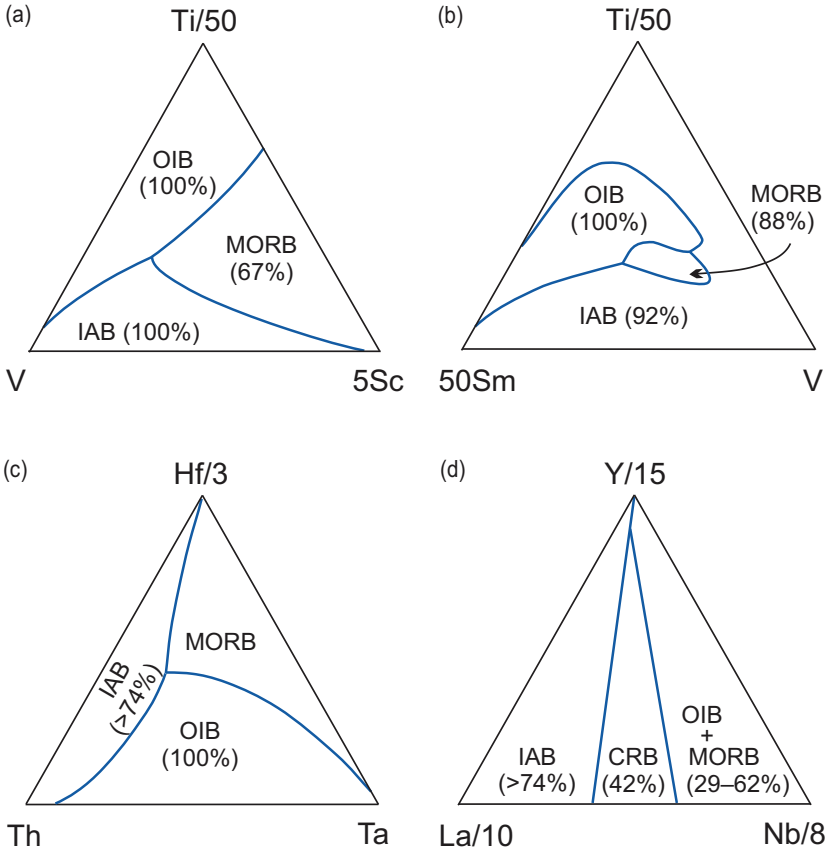

Figure 5.4 Ternary classification diagrams for mafic volcanic rocks. Numbers in parentheses represent the percentage of the empirical test data set successfully classified. The curved boundaries of this diagram need to be accurately traced or scanned. (a) V–Ti/50–5Sc (Vermeesch, 2006a; with permission from John Wiley & Sons) provides a robust statistical classification of IAB and OIB. (b) 50Sm–Ti/50–V (Vermeesch, 2006a; with permission from John Wiley & Sons) provides a robust statistical classification of IAB, OIB and MORB tectonic settings. (c) Th–Hf/3–Ta (Wood, 1980 with refined boundaries of Vermeesch, 2006a) provides a robust statistical classification of IAB and OIB; there were no MORB analyses with these elements in the test data set, but the field is well defined by the trial data. (d) La/10–Y/15–Nb/8 (Cabanis and Lecolle, 1989) provides a robust statistical classification for only IAB (island arc and back arc) tectonic settings (Verma, 2010). CRB (continental rift basalts), OIB + MORB (ocean island basalts and mid-ocean ridge basalts) are significantly misclassified.

5.2.12 Major Elements

The first attempt to classify basalts from different oceanic environments using the discriminant function (DF) analysis of major element compositions was carried out by Pearce (1976). However, this work pre-dated our ability to overcome the statistical 'closure' problem of major element data (Section 2.2.2.1). For this reason, Vermeesch (2006a) reassessed the major element compositions of basalts using robust statistical techniques and DF analysis, and showed that it is possible to distinguish between arc, ocean-island and ocean ridge basalts. The resulting diagram is highly successful with only 7% misclassification (Figure 5.5a). The discriminant functions are based upon the oxides SiO_2, Al_2O_3, TiO_2, CaO, MgO, MnO, K_2O and Na_2O (note that FeO is excluded) and the definition of the DF axes is given in Appendix 5.1. Again, however, we note that while multi-element DF axes may be excellent for taxonomy and classification, they say little to illuminate petrogenetic processes.

Verma et al. (2016) proposed a DF binary diagram based upon their major element compositions to classify high-Mg rocks following the IUGS nomenclature of Le Bas (2000). The diagram was developed with a

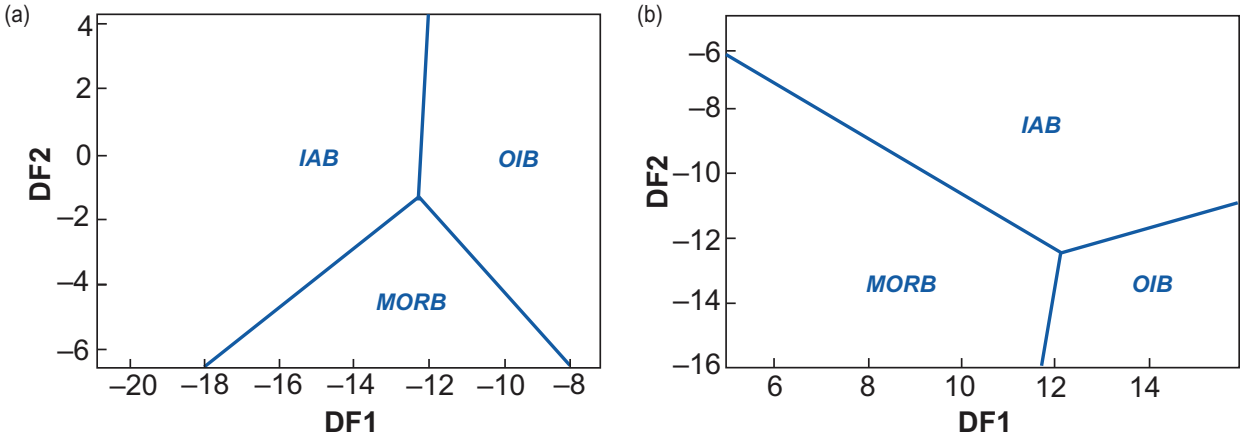

Figure 5.5 Discriminant function binary diagrams for oceanic basalts. (a) Major element oxides (without FeO) (after Pearce, 1976, and reassessed by Vermeesch, 2006a). The overall misclassification of trial data is only 7%. Boundary coordinates: central point (−12.23, −1.37), IAB–OIB (−12, 4), OIB–MORB (−8, −6.45), MORB–IAB (−18, −6.6). (b) TiO_2–Zr–Y–Sr (after Butler and Woronow, 1986, and reassessed by Vermeesch, 2006a). The overall misclassification of trial data is only 8%. Boundary coordinates: central point (12.17, −12.23), IAB–OIB (15.9, −10.93), OIB–MORB (11.85, −16), MORB–IAB (5.02, −6.28). IAB, island arc basalt; MORB, mid-ocean ridge basalt; OIB, ocean island basalt. See Appendix 5.1 for discriminant function equations.

trial data set of over 900 high-Mg samples analyses, is statistically robust (<24% misclassification) and successfully classifies komatiites, meimechites, picrites and boninites.

5.2.13 TiO_2, Zr, Y, Sr

The TiO_2–Zr–Y–Sr DF binary diagram (Figure 5.5b) was originally generated by Butler and Woronow (1986) using principal component analysis. More recently, it was statistically reassessed by Vermeesch (2006a) using the log-ratio transformation approach. This new diagram successfully classifies basalts from MORB, IAB and OIB oceanic settings with <8% misclassification, although the reader should be aware that Sr has the potential to be mobile and so the diagram is best applied to unaltered volcanic rocks. See Appendix 5.1 for the definition of the DF axes.

5.2.14 TiO_2, Nb, V, Y, Zr

The TiO_2–Nb–V–Y–Zr DF binary diagrams (Figure 5.6) exploit the variation between incompatible elements in ophiolitic ultramafic and mafic rocks from different tectonic settings. TiO_2 is as wt.% while the other elements are in ppm. Refining the work of Pearce and Norry (1979), Verma and Agrawal (2011) statistically evaluated the chemistry of ophiolitic ultramafic and mafic rocks from four distinct settings (continental rift, ocean island, island arc and mid-ocean ridges) with a high degree of success (<10% misclassification). These diagrams are intended to be used in sequence, with the first identifying those analyses likely to be associated with the combined continental rift and ocean island field (Figure 5.6a). Once identified, these analyses are plotted on the remaining DF diagrams (Figure 5.6b–d) to minimize misclassification and better to define their most likely tectonic association. See Appendix 5.1 for the definition of the DF axes.

5.3 Elemental Discrimination Diagrams for Intermediate Volcanic Rocks

There are only a few discrimination diagrams which may be used with volcanic rocks of intermediate composition. Verma and Verma (2013) present three suites of statistically rigorous DF binary diagrams which use the following:

1. Eleven major elements (including Fe as Fe_2O_3 and FeO)
2. The immobile trace elements La, Ce, Sm, Nb, Th, Y, Yb, Zr
3. A combination of immobile major and trace elements (TiO_2, MgO, P_2O_5, Nb, Ni, V, Y, Zr).

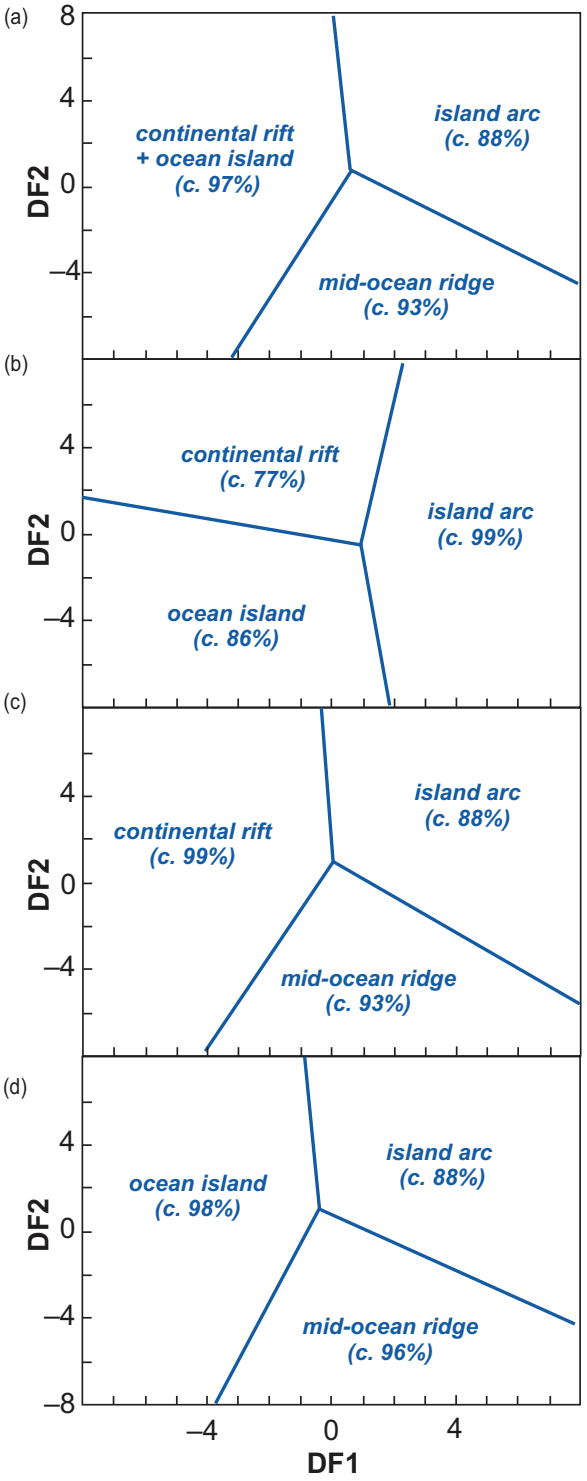

Figure 5.6 Discriminant function binary diagrams using Nb, V, Zr and TiO_2 for ophiolitic ultramafic and mafic rocks (after Verma and Agrawal, 2011). Numbers in parentheses are the classification success rates of the empirical test data set. (a) Combines all four settings into three fields, then the other diagrams are used to improve/refine the classification. (b) Most useful for identifying island arc samples.

These diagrams may be used to distinguish those intermediate volcanic rocks which formed in island arc (IA), continental arc (CA), collisional (COL), and within-plate (combining continental rift [CR] and oceanic island [OI]) settings (Figure 5.7) and may be applied to the following rock compositions: basaltic andesite, andesite, basaltic trachyandesite, trachyandesite, tephriphonolite, phonolite and boninite. The DF analysis was based on >3600 analyses for the major element diagrams, on >1500 analyses for the immobile trace element diagrams and on >1800 analyses for the combined major and trace element diagrams. All of the analyses used outlier-free data sets from known tectonic settings.

The 'success rate' of each diagram is summarised in Table 5.2, and it can be seen that each of the element groups have particular strengths for identifying particular tectonic settings. The major elements provide a satisfactory indication of tectonic setting for intermediate rock compositions (Figure 5.7). However, if trace element chemistry is also available, the most confident indication for collisional settings is achieved by combining immobile major and immobile trace elements (91% success). Arc settings are best indicated by the immobile trace elements (island arc, 90% success; continental arc, 96%).

These discrimination diagrams (Figure 5.7) are intended to be used sequentially. In each case the first panel (a) successfully segregates within plate (CR +

Figure 5.6 (*cont.*) (c) Most useful for identifying continental rift samples. (d) Most useful for identifying ocean island and mid-ocean ridge settings. Boundary coordinates in: (a) central point (0.63849, 0.87812) connects with CR+OI–IA (0.02820, 8.0), IA–MOR (8.0, −4.5532) and MOR–CR+OI (−3.2318, −8.0); (b) central point (0.883172, −0.667465) connects with IA–CR (2.27820, 8.0), CR–IA (−8.0, 1.66740) and OI–IA (1.87600, −8.0); in (c) central point (−0.016496, 0.972583) connects with IA–CR (−0.43580, 8.0), IA–MOR (8.0,-5.79920) and CR–MOR (−4.19440, −8.0); (d) central point (−0.322489, 1.040295) connects with IA–OI (−0.81840, 8.0), IA–MOR (8.0, −4.365) and OI–MOR (−3.721, −8.0). CR, continental rift;, IA, island arc; MOR, mid-ocean ridge; OI, ocean island. See Appendix 5.1 for discriminant function equations.

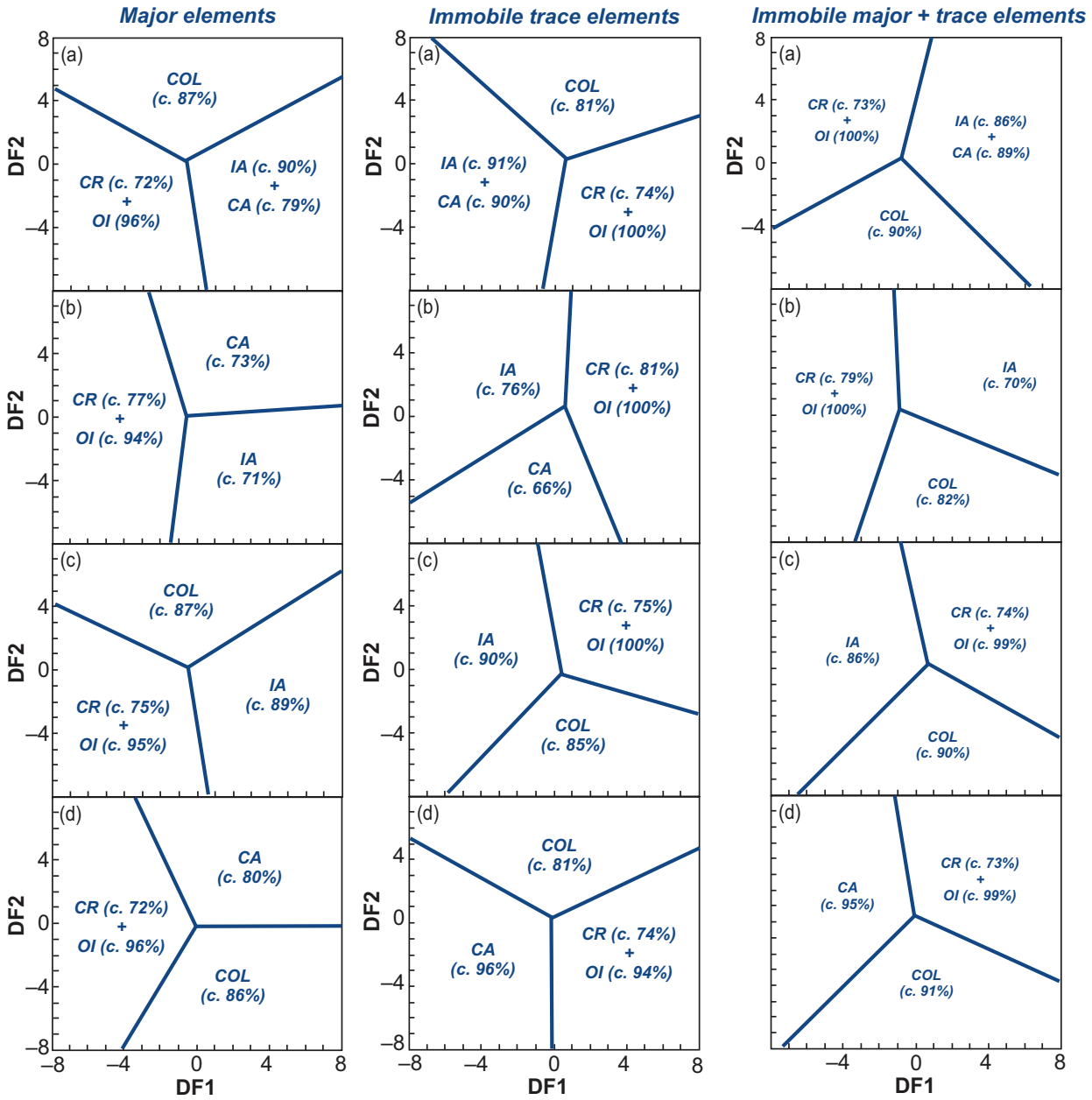

Figure 5.7 Major element discriminant function binary diagrams for intermediate rocks (after Verma and Verma, 2013). Numbers in parentheses represent the percentages of successfully classified test data. All diagrams combine five tectonic settings into three fields (a panels) and use subsequent diagrams (b–d) to separate the two arc environments. *Major elements*: (a) Initial groupings. Central point (−0.67554, 0.27663), CR + OI–COL (−8.0, 4.73569), COL–IA + CA (8.0, 5.53331), IA + CA–CR + OI (0.42744, −8.0). (b) Shows the separation of CA from IA. Central point (−0.63205, 0.08764), CR + OI–CA (−2.73408, 8.0), CA–IA (8.0, 0.76690), IA–CR + OI (−1.50230, −8.0). (c) Most useful for identifying continental arc rocks. Central point (−0.44102, 0.17933), CR + OI–COL (−8.0, 4.24657), COL–IA (8.0, 6.27226), IA–CR + OI (0.66776, −8.0). (d) Most useful for identifying continental rift, island arc and collisional settings. Central point (−0.033967, −0.10997), CR + OI–CA (−3.42497, 8.0), CA–COL (8.0, −0.16286), COL–CR + OI (−4.17272, −8.0). *Immobile trace elements*: (a) Initial groupings. Central point (0.64148, 0.34301), IA + CA–COL (−6.91145, 8.0), COL–CR + OI (8.0, 3.04640), CR + OI–IA + CA (−0.69292, −8.0). (b) Shows the separation of CA and IA. Central point (0.58959, 0.68699), CA–IA (−8.0, −5.45793), IA–CR + OI (0.87619, 8.0), CR + OI–CA (3.67939, −8.0). (c) Most useful for identifying IA and COL. Central point (0.37157, −0.26385), IA–CR + OI (−0.87235, 8.0), CR + OI–COL (8.0, −2.82217), COL–IA (−6.10890, −8.0). (d) Most useful for identifying CA. Central point (−0.15459, 0.29462),

OI) and collisional (COL) settings from arc (IA + CA) settings. The remaining panels (b–d) are used to better differentiate between the different arc settings and minimize misclassification. In Figure 5.7 we present only four of the five original diagrams by Verma and Verma (2013) (shown shaded in Table 5.2) because these have the highest probability of successful classification. See Appendix 5.1 for the DF axes equations.

5.4 Elemental Discrimination Diagrams for Acid Plutonic Rocks

The first systematic study in which granite geochemistry was related to tectonic setting was by Pearce et al. (1984). In this study the term 'granite' was defined very loosely as 'any plutonic rock containing more than 5 per cent of modal quartz'. Using suite of 600 selected granites, the authors determined that the elements Y, Yb, Rb, Ba, K, Nb, Ta, Ce, Sm, Zr and Hf most effectively discriminated between ocean ridge (ORG), volcanic-arc (VAG), within-plate (WPG) and syn-collisional (S-COLG) granite types. Verma et al. (2012) reassessed these data using modern statistical methods and concluded that ORGs cannot be classified using this approach (although the number of ORG samples in the original data set was very low, $n = 5$).

5.4.1 The Yb–Ta and Y–Nb Discrimination Diagrams

In their reassessment of trace element-based discrimination diagrams for granites, Verma et al. (2012) argued that the Yb–Ta and Y–Nb binary diagrams originally proposed by Pearce et al. (1984) have limited functionality. However, if ORG samples can be excluded from the data set on the basis of their field setting, then these diagrams can be used to distinguish between WPG, VAG and S-COLG. For example, the Yb–Ta diagram successfully differentiates between WPG (no misclassification), VAG (11% misclassification), and S-COLG (~25% misclassification) (Figure 5.8a), and the Y–Nb diagram successfully separates WPG (~18% misclassification) from the combined field of VAG + S-COLG (~4% misclassification) (Figure 5.8b).

5.4.2 Major Element Diagrams

A series of DF binary diagrams (Figure 5.9) based upon granite major element chemistry was proposed by Verma et al. (2012). The DF diagrams were generated using robust statistical methods (see Section 5.1.2) and based upon a trial data set of >1000 outlier-free analyses, all with $SiO_2 > 63$ wt.% and from known tectonic settings. The test data set contained 100 analyses. This suite of diagrams distinguishes between granitoids from island arc (IA), continental arc (CA), continental rift (CR), and continental collisional (COL) settings. As usual for DF analysis, the first diagram presents all the data, in this case by combining the two arc settings (IA + CA). The subsequent diagrams are then used to better segregate the two arc settings and minimize misclassification (generally better than 16%). Here we have selected the three most successful diagrams of the original five diagrams presented by Verma et al. (2012). The DF equations include all the major element oxides and are given in Appendix 5.1.

5.4.3 Some Words of Caution

There are a number of pitfalls that may be encountered when using discrimination diagrams with granitic lithologies. These are identified below.

Figure 5.7 (*cont.*) CA–COL (−8.0, 5.41425), COL–CR + OI (8.0, 4.74335), CR + OI–CA (−0.10284, −8.0). *Immobile majors + trace elements*: (a) Initial groupings. Central point (−0.82858, 0.29965), CR + OI–IA + CA (0.92190, 8.0), IA + CA–COL (6.39297, −8.0), COL–CR + OI (−8.0, −4.20284). (b) Provides an initial separation of IA and CA. Central point (−0.95018, 0.45941), CR + OI–IA (−1.24490, 8.0), IA–CA (8.0, −3.76290), CA–CR + OI (−3.41007, −8.0). (c) Most useful for identifying IA. Central point (0.62149, 0.34939), IA–CR + OI (−0.87616, 8.0), CR + OI–COL (8.0, −4.51524), COL–IA (−6.61289, −8.0). (d) Most useful for identifying CA and COL. Central point (−0.028516, 0.35743), CA–CR + OI (−1.16430, 8.0), CR + OI–COL (8.0, −3.84452, COL–CA (−7.33632, −8.0). CA, continental arc; CR, continental rift; COL, collisional; IA, island arc; OI, oceanic island. See Appendix 5.1 for discriminant function equations.

Table 5.2 Summary of discriminant function success for intermediate volcanic rock compositions shown in Figure 5.7[a]

Tectonic setting	*A* [b]	*B* [b]	*C* [b]	*D* [b]	*E* [b]
Major elements					
IA, island arc	90% + 79%	71%	69%	**89%**	–
CA, continental arc		73%	69%	–	**80%**
COL, collisional	87%	–	86%	**87%**	86%
CR, continental rift	72% + 96%	77% + 94%	–	75% + 95%	72% + 96%
OI, oceanic island					
Immobile trace elements					
IA, island arc	91% + 90%	76%	73%	**90%**	–
CA, continental arc		66%	65%	–	**96%**
COL, collisional	81%	–	84%	**85%**	81%
CR, continental rift	74% + 100%	81% + 100%	–	75% + 100%	74% + 94%
OI, oceanic island					
Immobile majors + traces					
IA, island arc	86% + 89%	70%	63%	**86%**	–
CA, continental arc		82%	76%	–	**95%**
COL, collisional	90%	–	93%	90%	**91%**
CR, continental rift	73% + 100%	79% + 100%	–	74% + 99%	73% + 99%
OI, oceanic island					

[a]Percentage successful classification for each tectonic setting (after Verma and Verma, 2013). Arc environments (IA + CA) are combined in 'a'; in all diagrams 'rift' settings (CR + OI) are indistinguishable and combined. Highest percentages in **bold**.
[b]Refers to original five figure panels of Verma and Verma (2013).

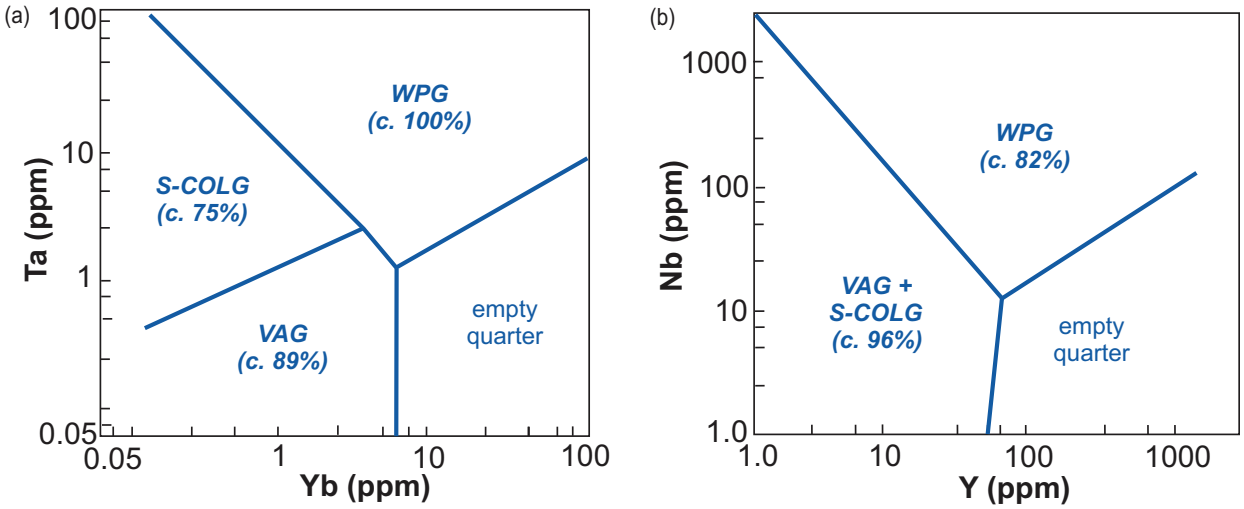

Figure 5.8 Trace element binary diagrams for granites (modified from Pearce et al., 1984). Numbers in parentheses represent the percentages of successfully classified test data (Verma et al., 2013). (a) Yb/Ta successfully distinguishes between VAG, S-COLG and WPG. Boundary coordinates: VAG–S-COLG (0.1, 0.35; 3, 2); S-COLG–WPG (0.1, 100; 3, 2), VAG–WPG (3, 2; 5, 1); WPG–empty (5, 1; 100, 7), empty–VAG (5, 0.05; 5, 1). (b) Y/Nb successfully separates VAG + S-COLG from WPG. Central point (50, 10), VAG + S-COLG–WPG (1, 2000), WPG–empty (1000, 100), empty–VAG + S-COLG (40, 1). S-COLG, syn-collisional; VAG, volcanic-arc; WPG, within-plate.

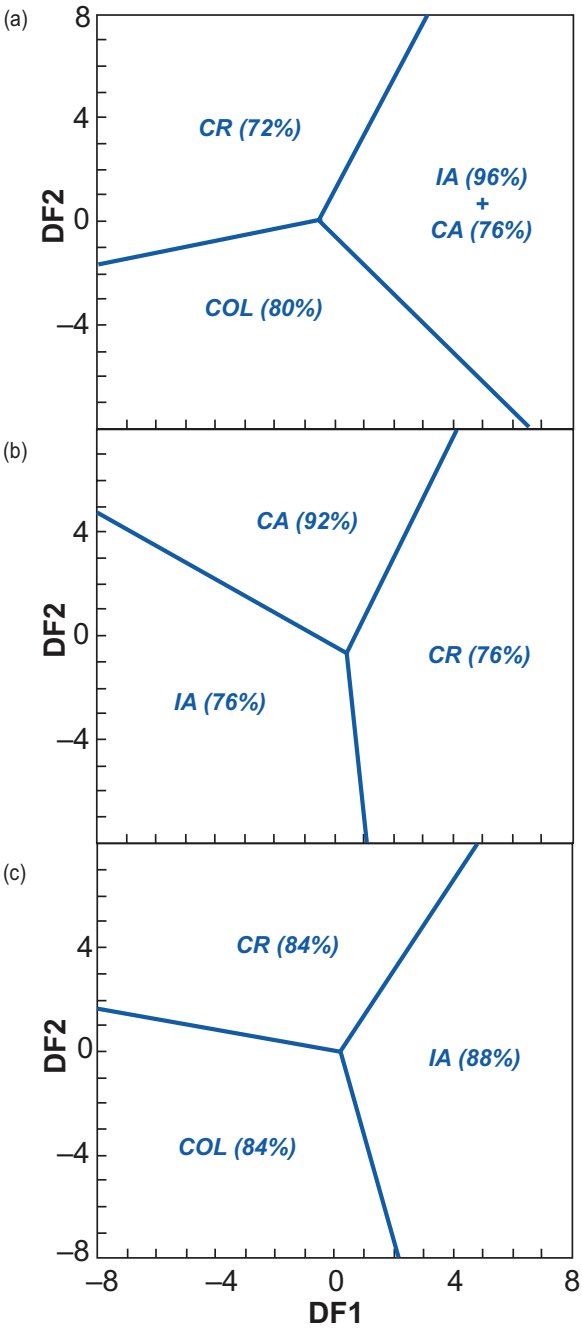

Figure 5.9 Major element discriminant function binary diagrams for acid rocks from island arc, continental arc, continental rift and syn-collisional tectonic settings (after Verma et al., 2012). 'Acid rocks' are those with >63 wt.% SiO_2 (anhydrous, Fe oxidation state of Middlemost, 1989). Numbers in parentheses represent the classification success rates of the empirical training data. (a) The initial groupings. Central point (−0.52237, 0.105108), CR–IA + CA (3.0914, 8.00), IA + CA–COL (6.5177, −8.00), COL–CR (−8.00, −1.6511). (b) This figure effectively identifies CA. Central point (0.41929, −0.66705), CA–CR (4.1608, 8.00),

1. Increasingly, it is becoming clear that the chemical composition of granitic rocks does not always represent the composition of a simple melt but is instead a mix of crystals and melt (Collins et al., 2020). For this reason, discrimination diagrams for granitic rocks should be used with great care.
2. Granitic melt compositions are often modified by the effects of crystal fractionation and, late in their crystallisation, by their interaction with hydrothermal fluids. This will influence those discrimination diagrams which are based upon major element chemistry such as the DF diagrams of Verma et al. (2012).
3. Finally, it is necessary to repeat the words of caution given earlier about the general use of discriminant function diagrams. DF diagrams can work quite well if their principal purpose is to classify rocks and assign rock suites to their former tectonic setting. Nevertheless, the discriminant functions themselves are petrologically opaque and are unable to help us evaluate geochemical processes.

5.5 Discrimination Diagrams for Clastic Sediments

Sedimentary basins form through the extensional, compressional or transcurrent motion of the Earth's tectonic plates. A large number of different types of basin are associated with each of these settings and are summarised in Box 5.2. Sediment may inherit a geochemical signature from its tectonic environment in two separate ways. First, different tectonic environments may have distinctive provenance characteristics which can be transposed into the sedimentary record. Second, some tectonic environments may be characterised by distinctive sedimentary processes. In both cases the geochemical signature is most likely to be seen in immature sediments which contain lithic fragments and so directly reflect the composition of their source. From this information the provenance may be identified and from the provenance the tectonic setting may often be inferred.

Figure 5.9 (*cont.*) CR–IA (1.0939, −8.00), IA–CA (−8.00, 4.7147). (c) This panel effectively separates CR, AI and COL. Central point (0.20518, −0.01689), CR–IA (4.7956, 8.00), IA–COL (2.1584, −8.00), COL–CR (−8.00, 1.61186). See Appendix 5.1 for discriminant function equations.

Box 5.2 Sedimentary basins (after Ingersoll, 2011)

Divergent plate motion
- Continental rift
- Oceanic rift on a ridge
- Proto-oceanic rift
- Cratonic (intracontinental) basins
- Rift-sag (failed rift) basins
- Passive margin basins
- Active oceanic (abyssal) basins

Convergent plate motion
- Oceanic islands, aseismic ridges, plateaus
- Oceanic trench
- Fore-arc basins
- Back-arc basins
- Intramontaine/intra-arc basins
- Pro-(peripheral) foreland basins
- Retro-foreland basins
- Thrust sheet-top (piggyback) basins

Transcurrent plate motion
- Transtensional (pull-apart) basins
- Transpressive basins
- Transrotational basins

Since the 1980s, when many of the discrimination diagrams for clastic sediments were first developed, it has become apparent that there are a number of factors which can distort the geochemical signature of sediments such that it will not reflect the true tectonic setting of deposition. These factors include the heterogeneities which are associated with the initial source region, the weathering of the source rocks, the differences in mineral size/shape/density created through physical sorting and the mineralogical alteration that takes place during hydrological transport and diagenesis.

Some early studies claimed to successfully define the tectonic setting of a sedimentary basin using geochemical data from clastic sediments (e.g., Bhatia, 1983; Roser and Korsch, 1986), although the more recent reassessment of these diagrams using robust statistical techniques has found that the majority (>70%) are now known to be *unable* to discriminate between active and passive margin settings (Table 5.1). Consequently, the sediment which most faithfully records its original tectonic setting via its geochemistry must be locally derived, proximal to its source and juvenile in character, and even then the results must be critically evaluated. Sediment that has been recycled or derived from mixed sources is not easily interpreted, although Totten et al. (2000) outline some approaches that may be used to extract information about provenance and tectonic setting from more mature sediments. There are also some instances when DF analysis may successfully distinguish between clastic sediments formed in arc, rift and collisional tectonic settings (Section 5.5.1).

5.5.1 A Discrimination Diagram for Sand-Sized Clastic Sediment

The DF binary diagram of Verma and Armstrong-Altrin (2013) (Figure 5.10) discriminates between arc, rift and collisional settings in sand-sized clastic sediment (Table 5.1). The diagram is based on ten major element oxides (SiO_2, Al_2O_3, CaO, Na_2O, K_2O, P_2O_5, TiO_2, MnO, MgO, FeO_T) and its effectiveness is optimised when clastic sediments are divided into high-silica (SiO_2 = 63–95 wt.%) and low-silica (SiO_2 = 35–63 wt.%) groups. The field boundaries were determined using a trial dataset of >2200 analyses; the DFs are given in Appendix 5.1. Both diagrams successfully differentiate between arc settings in which there is active volcanism, extensional rift settings and sediments formed in a collisional, compressional setting (<25% misclassification). These authors also demonstrate that the chemical changes caused by weathering, recycling and diagenesis are unlikely to significantly affect the results of major element DF analysis.

5.5.2 Discrimination Diagrams for Fine-Grained Clastic Sediment

The use of shale or mudstone chemistry to determine tectonic setting is based on the assumption that fine-grained rocks efficiently homogenise source materials and therefore can be used to determine the tectonic setting in which the rock was deposited (Condie et al., 1991). Fine-grained sediment chemistry is often normalized to the composition of the upper continental crust (UCC; Rudnick and Gao, 2014) or to various shale composites such as the North American shale composite (NASC; McLennan, 1989) or the post-Archaean Australian shale (PAAS; Pourmand et al., 2012) (see Section 4.3.2.4 and Table 4.8) in order to illustrate the degree to which the composition of the

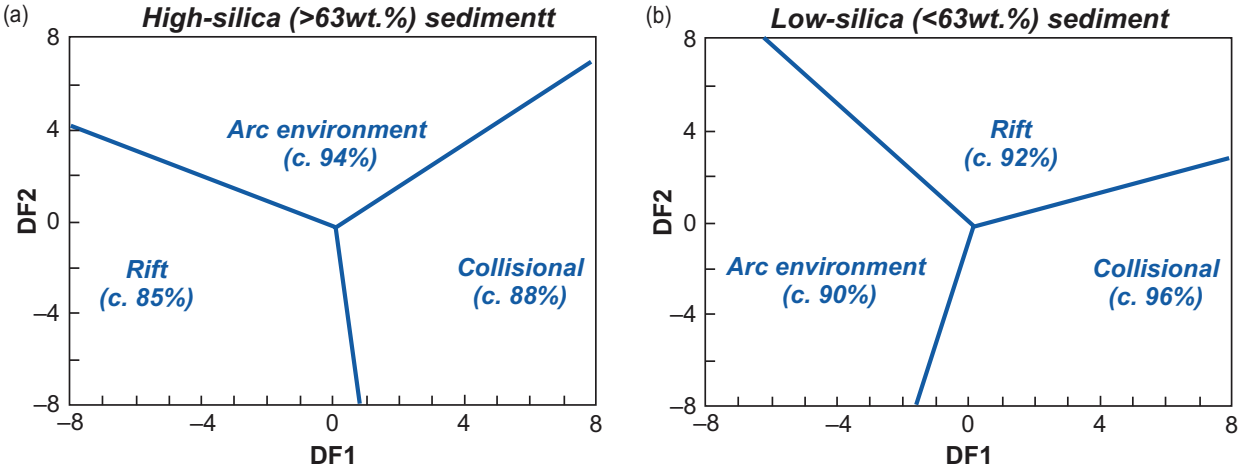

Figure 5.10 Major element discriminant function binary diagrams for classification of siliciclastic sediment from arc, rift and syn-collisional tectonic settings (after Verma and Armstrong-Altrin, 2013). Numbers in parentheses represent the classification success rates of the empirical test dataset. (a) High-silica sediment. Central point (0.051, −0.220), Arc–Col (8, 7.090), Col– Rift (0.794, −8), Rift–Arc (−8, 4.153). (b) Low-silica sediment. Central point (0.180, −0.178), Arc–Rift (−6.226, 8), Rift–Col (8, 2.822), Col–Arc (−1.629, −8). See Appendix 5.1 for discriminant function equations.

sediment is different from the average composition of the continental crust.

A useful application of a NASC-normalised multi-element diagram is given by Totten et al. (2000). These workers compare normalized average compositions for the Stanley shale from the Ouachita Mountains to the normalized average values of passive and combined active and continental arc margins of Floyd et al. (1991). They concluded that the Stanley shale was derived from a mixed provenance which included felsic and mafic sources. The values for the normalized average values of passive and combined active and continental arc margins are shown in Figure 5.11. Average passive margin sediments are characterised by negative anomalies for the elements Sr, Ta and Nb and positive anomalies for the elements U, Cs, Ti, Hf and Zr, whereas the average arc margin sediments are characterised by negative Ta and Nb anomalies and positive Ba, Cr, Ni, Ti and Sc.

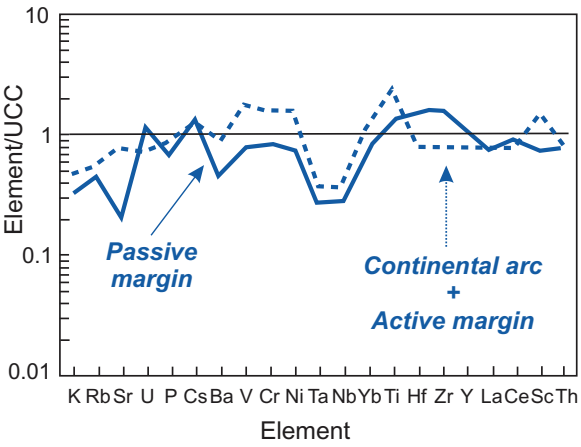

Figure 5.11 Multi-element discrimination diagram for shale (after Floyd et al., 1991) showing the normalized average values for passive margins (solid line) and the normalized combined average for continental arc and active margins (dashed line). The sedimentary compositions are normalized to the upper continental crust values of Taylor and McLennan (1985).

5.5.3 Provenance Studies

The use of trace elements as indicators of provenance in fine-grained sediments has been discussed by Cullers et al. (1988), Condie and Wronkiewicz (1990), McLennan and Taylor (1991) and Totten et al. (2000). These authors have exploited the geochemical differences between elements in fine-grained sediments such as Th and La (indicative of a felsic igneous source) and Sc and Cr (indicative of a mafic source), and have used plots such as Th/Sc versus Sc and Cr/Th versus Sc/Th as indicators of contrasting felsic and mafic provenance in shales. Floyd et al. (1989) quantified such mixing processes using the general mixing equation of Langmuir et al. (1978)

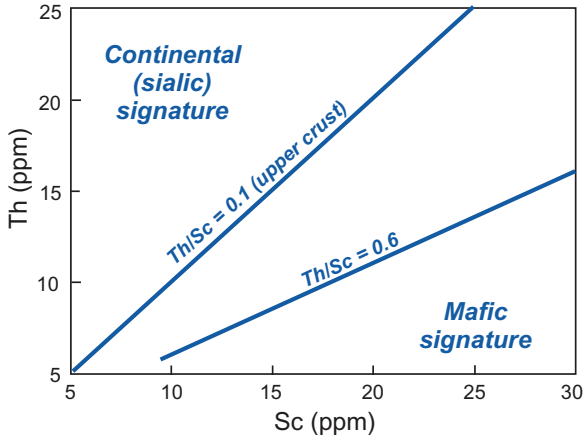

Figure 5.12 Immobile element discrimination diagram for shales. The incompatible element Th is enriched in silicic rocks, whereas the compatible element Sc is enriched in mafic rocks. Thus Th/Sc near unity suggests upper continental crustal derivation, whereas Th/Sc near 0.6 suggests a dominant mafic component. (After Totten et al. (2000); with permission from the Geological Society of America)

discussed in Section 4.8.2.5, and Tang et al. (2016) sought to identify the proportion of mafic components in sediments using Ni/Co and Cr/Zn ratios. This work was based upon the argument that Ni and Cr are more compatible in early fractionating phases in mafic rocks than are Co and Zn and that these elements are normally insoluble during chemical weathering, hence the ratios Ni/Co and Cr/Zn are a useful indicator of the mafic contribution to fine-grained sediments. Their study also suggested that over Earth history the mafic component in fine-grained sediments has decreased with time. Totten et al. (2000) used Th/Sc ratios to characterise mafic and felsic sources, as illustrated in Figure 5.12. However, we recommend that diagrams using common denominator ratio pairs such as Th/Sc versus La/Sc should be used with care because of the possible effects of spurious self-correlation.

5.6 Tectonic Controls on Magmatic and Sedimentary Geochemistry

The underlying tectonic controls on the chemistry of magmatic and sedimentary rocks is an issue which is much wider than that of discrimination diagrams (see Condie, 2015; Li et al., 2015, for discussion), and is a major focus of much of modern geochemistry. In recent decades, our understanding of tectonic processes and their influence on trace element and isotope geochemistry has grown exponentially. Alongside this we have also learned something of the inherent complexity of both tectonic systems and of geochemical processes. For this reason, a naive 'cookbook' approach to the identification of former tectonic environments by means of geochemical fingerprinting is unproductive, and likely to bypass the fundamental processes which are operating in those environments. Consider a few examples:

1. A basaltic melt which assimilates continental crust. During transit through the crust, the basaltic melt assimilates continental crustal material. In this case, the geochemical signature of the basalt may be predominantly *inherited* from the crustal source and not reflect its tectonic setting.
2. Secular variation in Earth history. The composition of the mantle has likely changed with time given the secular variation of the Earth's temperature, the chemical differentiation of its mantle composition and the recycling of tectonic plates over 4.6 Ga. Clearly, this variation imposes limits on the projection of modern geochemical signatures through time.
3. The derivation of tectonic information from fine-grained sediment. Fine-grained clastic sediments are often far removed from their source(s) and compositionally altered to clay, making it difficult to extract meaningful information from them regarding the tectonic setting from which they were derived.

Given such complexities, it is important to progress beyond simplistic classification in order to understand the petrological processes involved in, and thereby the petrogenetic links between, geochemistry and tectonic setting. There are two other important factors that we have sought to emphasise in this chapter. First, it is necessary to perform a rigorous statistical evaluation of any ternary, bivariate or multivariate diagram. Only after trial testing with large data sets from known settings and after dealing with the problems of closure and spurious self-correlation should a tectonic discrimination diagram be used by the geochemical community. Even then, discrimination diagrams should not be regarded as a proof; rather, they are a

guide to a testable hypothesis which may be validated through a more comprehensive geological and geochemical evaluation. Second, in our view the primary function of geochemical data is to reveal geochemical, and thereby geological, processes. These in turn can make apparent petrological processes which can (sometimes) help to identify the tectonic environment in which those processes have taken place. It is in this spirit that we must approach the use of tectonic discrimination diagrams.

6 Using Radiogenic Isotope Data

6.1 Introduction

Radiogenic isotopes are used in geochemistry in two principal ways: (i) to determine the age of rocks and minerals and (ii) to identify geological processes and sources. The former application is geochronology, while the latter is known as isotope geology or isotope geochemistry. There are some excellent texts which deal with these disciplines (e.g., Rink and Thompson, 2015; White, 2015; Reiners et al., 2018) and the reader is referred to these for more detailed treatments of the topics introduced here.

In the first part of this chapter the main principles of geochronology are briefly described and the interpretation of geochronological results reviewed. The second half of the chapter describes the use of radiogenic isotopes in petrogenesis, an exciting and rapidly evolving field. The use of radiogenic isotopes as tracers of petrogenetic processes has allowed geochemists to sample the deep interior of the Earth, previously the sole domain of geophysicists. The results of such studies have led to important geochemical constraints on the nature of the continental crust and the Earth's mantle, which can be combined with our physical knowledge of these domains to help provide a unified chemical-physical model of the deep Earth.

6.2 Radiogenic Isotopes in Geochronology

The foundations of modern geochronology were laid at the turn of the century in the work of Rutherford and Soddy (1903) on natural radioactivity. They showed that the process of radioactive decay is exponential and independent of chemical or physical conditions. Thus, rates of radioactive decay may be used for measuring geological time. The isotopic systems used in age calculations are listed in Table 6.1 and Box 6.1. In this section we discuss two of the most common techniques used in geochronological calculations: isochron diagrams and model age calculations. This is followed by a discussion of the significance of the calculated ages.

6.2.1 Isochron Calculations

An isochron diagram is a bivariate plot of measured parent–daughter isotope ratios for a suite of cogenetic samples or for a mineral suite from a single sample. When the sample suite defines a linear array, this is said to be an isochron, and the slope of the line is proportional to the age of the sample suite. Consider, for example, the Rb–Sr system where the total number of ^{87}Sr atoms in a rock which has been a closed system for t years is given by the equation:

$$^{87}Sr_m = 87Sr_i + {}^{87}Rb_m\left(e^{\lambda t} - 1\right) \quad (6.1)$$

$^{87}Sr_m$ is the total number of atoms of ^{87}Sr present today, $^{87}Sr_i$ is the number of atoms of ^{87}Sr initially present when the sample first formed, $^{87}Rb_m$ is the number of atoms of ^{87}Rb present (measured) today, and λ (lambda) is the radioactive decay constant (Table 6.1). The precise measurement of absolute isotope concentrations is difficult, so instead isotope ratios are normally determined. An isotope not involved in the radioactive decay scheme is used as the denominator. In the case of the Rb–Sr isotope system this isotope is ^{86}Sr and Eq. 6.1 is rewritten as:

$$\left(\frac{^{87}Sr}{^{86}Sr}\right)_m = \left(\frac{^{87}Sr}{^{86}Sr}\right)_i + \left(\frac{^{87}Rb}{^{86}Sr}\right)_m \left(e^{\lambda t} - 1\right) \quad (6.2)$$

The ratios $(^{87}Sr/^{86}Sr)_m$ and $(^{87}Rb/^{86}Sr)_m$ are measured by mass spectrometry, leaving the initial ratio $(^{87}Sr/^{86}Sr)_i$ and the age of the rock (t) as unknowns. Since Eq. 6.2 is the equation of a straight line, the age and intercept can be calculated from a plot of measured $(^{87}Sr/^{86}Sr)_m$ and $(^{87}Rb/^{86}Sr)_m$ for a suite of cogenetic samples. This methodology is illustrated in Figure 6.1. The age is calculated from the slope of the line using the equation

$$t = 1/\lambda \ln(\text{slope} + 1) \quad (6.3)$$

where t is the age and λ is the decay constant. Time is measured from the present and is expressed as either Ma (10^6 years) or Ga (10^9 years). The intercept on the $(^{87}Sr/^{86}Sr)$ axis is equal to the initial ratio $(^{87}Sr/^{86}Sr)_i$,

Table 6.1 Isotopic systems used in age calculations

Technique	Decay scheme	Decay constant λ (yr^{-1})	Reference	Isochron plot	
				x-axis	y-axis
Rb–Sr	$^{87}Rb \rightarrow {}^{87}Sr + \beta$	1.42×10^{-11}	1[a]	$^{87}Rb/^{86}Sr$	$^{87}Sr/^{86}Sr$
Sm–Nd	$^{147}Sm \rightarrow {}^{143}Nd + He$	6.54×10^{-12}	2	$^{147}Sm/^{143}Nd$	$^{143}Nd/^{143}Nd$
Lu–Hf	$^{176}Lu \rightarrow {}^{176}Hf + \beta$	1.867×10^{-11}	3[b]	$^{176}Lu/^{177}Hf$	$^{176}Hf/^{177}Hf$
Re–Os[c]	$^{187}Re \rightarrow {}^{187}Os + \beta$	1.666×10^{-11}	4	$^{187}Re/^{188}Os$	$^{187}Os/^{188}Os$
				^{187}Re (ppb)	^{187}Os (ppb)
K–Ar	$^{40}K \rightarrow {}^{40}Ar - \beta$	0.581×10^{-10}	1[d]	$^{40}K/^{36}Ar$	$^{40}Ar/^{36}Ar$
				$^{39}Ar/^{36}Ar$	$^{40}Ar/^{36}Ar$
K–Ca[c]	$^{40}K \rightarrow {}^{40}Ca + \beta$	4.962×10^{-10}	1, 5	$^{40}K/^{42}Ca$	$^{40}Ca/^{42}Ca$
	K total	5.543×10^{-10}	1		
La–Ce[c]	$^{138}La \rightarrow {}^{138}Ce + \beta$	2.37×10^{-12}	6	$^{138}La/^{136}Ce$	$^{138}Ce/^{136}Ce$
La–Ba[c]	$^{138}La \rightarrow {}^{138}Ba - \beta$	4.44×10^{-12}	7	$^{138}La/^{137}Ba$	$^{138}Ba/^{137}Ba$

[a] Officially accepted value today, but other values exist and may be in use (1.393×10^{-11}; Nebel et al., 2011). Older data use $\lambda^{87}Rb = 1.39 \times 10^{-11}$ and can be recalculated for the modern decay constant using a correction factor (e.g., 1.39/1.42).
[b] Older data use $\lambda^{176}Lu = 1.94 \times 10^{-12}$ (DePaolo, 1988) or 1.96×10^{-12} (Patchett and Tatsumoto, 1980).
[c] Specialist techniques carried out in only a few laboratories.
[d] Revised by Renne et al. (2010) to 0.5755×10^{-10} and is also in use.
References: 1, Steiger and Jager (1977); 2, Lugmair and Marti (1978); 3, Söderlund et al. (2004); 4, Smoliar et al. (1996); 5, Marshall and DePaolo (1982); 6, Tanimizu (2000); 7, Sato and Hirose (1981).

a parameter of considerable petrogenetic importance and discussed more fully later in this chapter.

Thus, an isochron calculation requires a suite of cogenetic samples formed from the same parental material – this may be a suite of whole rock samples from a single pluton or a suite of different minerals from a single sample. The isochron calculation assumes that there has been no exchange of parent–daughter isotopes other than through radioactive decay. An example of a Sm–Nd isochron derived from a suite of related volcanic rocks using the data in Table 6.2 is shown in Figure 6.2.

6.2.1.1 Pb Isotope Isochrons

A Pb–Pb whole rock isochron is constructed by plotting the isotope ratios $^{206}Pb/^{204}Pb$ on the x-axis and $^{207}Pb/^{204}Pb$ on the y-axis. However, the interpretation of a linear array on this diagram is more complicated than for the Rb–Sr system because ^{206}Pb and ^{207}Pb are the products of separate radioactive decay schemes with different rates of decay (Box 6.1). In this case the isochron equation and must be solved iteratively (see Harmer and Eglington, 1987); see Section 6.2.5.3.

6.2.1.2 Fitting an Isochron

A simple but approximate method to fit an isochron is to draw a best-fit straight line by eye through the plotted points. Provided a suitable scale is chosen, both the slope of the line and the intercept can be determined with reasonable accuracy and these may be used to make *preliminary* estimates of the age and initial ratio. Precise results are obtained from statistical line-fitting procedures which estimate the slope and intercept of the isochron. These normally use a version of weighted least squares regression (see Section 2.5) and standard equations can be found in Excel, IsoplotR (Vermeesch, 2018b), and other statistical packages.

An important aspect of isochron regression is the realistic estimate of the uncertainty associated with the age and initial ratios. A measure of the 'goodness of fit' of an isochron is the mean squares of weighted deviates (MSWD). This is a measure of the fit of the line to the data within the limits of analytical error. Ideally, an isochron should have a MSWD of ≤ 1; anything greater than this implies that the scatter in the data points cannot be explained solely by

Box 6.1 Constants used in U-Th-Pb isotope geochronology

(a) Decay constants (Steiger and Jager, 1977)
$^{238}U \rightarrow {}^{206}Pb$ 1.55125×10^{-10} yr^{-1} (λ_1)
$^{235}U \rightarrow {}^{207}Pb$ 9.8485×10^{-10} yr^{-1} (λ_2)
$^{232}Th \rightarrow {}^{208}Pb$ 4.9475×10^{-11} yr^{-1} (λ_3)

(b) Isotope ratios of primeval lead (represented by Canyon Diablo troilite of Tatsumoto et al., 1973)
$(^{206}Pb/^{204}Pb) = 9.307$
$(^{207}Pb/^{204}Pb) = 10.294$
$(^{208}Pb/^{204}Pb) = 29.476$

(c) Age of the Earth derived from the meteoritic isochron (Tatsumoto et al., 1973; Tilton, 1973)
$^{207}Pb/^{204}Pb$ versus $^{206}Pb/^{204}Pb$ yields an isochron with a slope = 0.626208 and an age for the Earth of 4.57 Ga.

(d) Present day ratio $^{238}U/^{235}U = 137.88$

(e) Symbols used in U–Th–Pb isotope geochemistry
$\mu = {}^{238}U/^{204}Pb$, $\kappa = {}^{232}Th/^{238}U$

(f) Ratios used for plotting the U–Pb concordia curve

Age (Ga)	$^{206}Pb/^{238}U$	$^{207}Pb/^{235}U$
0.0	0.00000	0.00000
0.4	0.06402	0.48281
1.0	0.16780	1.67741
1.4	0.24256	2.97009
1.8	0.32210	4.88690
2.2	0.40674	7.72917
2.6	0.49679	11.94371
3.0	0.59261	18.19308
3.4	0.69456	27.45973
3.6	0.74796	33.65562
3.8	0.80304	41.20041
4.0	0.85986	50.38776
4.2	0.91846	61.57526
4.4	0.97892	75.19836
4.6	1.04128	91.78732

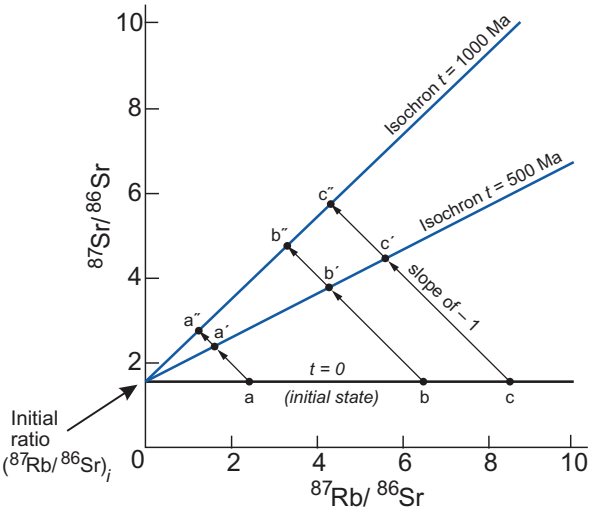

Figure 6.1 Schematic isochron diagram. A suite of igneous rocks (a–c) form at $t = 0$ from the same batch of magma which subsequently differentiated. They evolve over 500 Ma and 1000 Ma. At $t = 0$ each member of the rock suite has the same initial ratio $(^{87}Sr/^{86}Sr)_i$ but because the magma suite is chemically differentiated, each rock has a different concentration of Rb and Sr, and therefore a different $^{87}Rb/^{86}Sr$ ratio. Each sample plots as a separate point on the $^{87}Rb/^{86}Sr$ versus $^{87}Sr/^{86}Sr$ isochron diagram. From $t = 0$ to $t = 500$ Ma or $t = 1000$ Ma, individual samples evolve along a straight line with a slope of −1 (e.g., a–a′–a″) reflecting the decay of a single atom of ^{87}Rb to a single atom of ^{87}Sr. In practise the resulting change in $^{87}Sr/^{86}Sr$ is small and the vertical scale is normally exaggerated so the path taken by these points will be closer to a vertical line. The amount of ^{87}Sr produced in a given sample is proportional to the amount of ^{87}Rb present. The slope of each isochron ($t = 500$ Ma, $t = 1000$ Ma) is proportional to the age of the sample suite. The intercept on $^{87}Sr/^{86}Sr$ is the initial ratio.

experimental error. However, Brooks et al. (1972) suggest that this value be restricted to isochrons involving infinitely large numbers of samples, whereas for more typical datasets higher values up to ~2.5 may be acceptable.

6.2.1.3 Errorchrons

The origin of the scatter on an isochron is one of the most important interpretive aspects of geochronology. If the scatter results in a MSWD of ≤2.5, it is deemed analytical. If the MSWD is >2.5, it is geological. Brooks et al. (1972) proposed the term 'errorchron' for the situation where a straight line cannot be fit to a suite of samples within the limits of analytical error. An errorchron by definition implies that the scatter of the data is a consequence of geological error and indicates that one or more of the initial assumptions of the

Table 6.2 Samarium–neodymium isotopic ratios, lower ultramafic unit of the Onverwacht volcanics, South Africa[a]

Sample	Rock type	$^{147}Sm/^{144}Nd$[b]	$^{143}Nd/^{144}Nd$ ($\pm 2\sigma$ error)
HSS-74	Sodic porphyry	0.1030	0.510487 ± 36
HSS-161	Acid tuff	0.1054	0.510570 ± 32
HSS-52B	Felsic pillow lava	0.1653	0.511950 ± 22
HSS-56	Basaltic lava	0.2040	0.512875 ± 32
R-14	Basaltic komatiite	0.1888	0.512504 ± 34
HSS-32	Basaltic komatiite	0.1649	0.511957 ± 22
HSS-88A	Peridotitic komatiite	0.1792	0.512292 ± 34
HSS-92	Peridotitic komatiite	0.1858	0.512439 ± 34
HSS-95	Peridotitic komatiite	0.1902	0.512541 ± 28
HSS-523	Peridotitic komatiite	0.1701	0.512084 ± 20

[a]Hamilton et al. (1979b); data used to construct Figure 6.2.
[b]$^{147}Sm/^{144}Nd$ determined to a precision of 0.2% at the 2σ level.

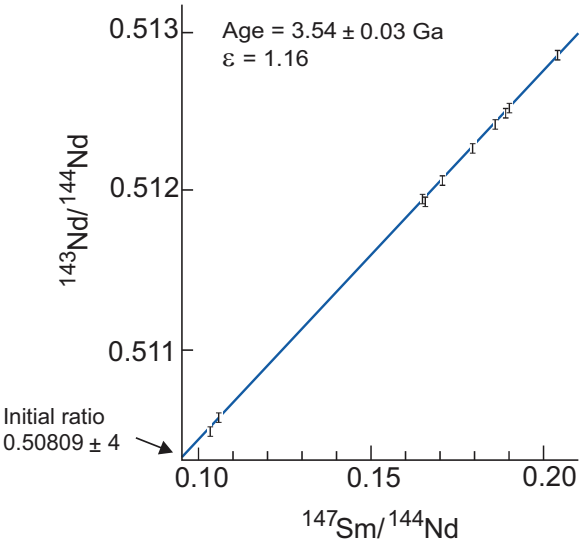

Figure 6.2 A Sm–Nd isochron. An isochron plot of $^{147}Sm/^{144}Nd$ and $^{143}Nd/^{144}Nd$ for volcanic rocks from the Onverwacht group, South Africa (after Hamilton et al. (1979b)). The data are given in Table 6.2. Error bars for $^{143}Nd/^{144}Nd$ are 2σ (errors on $^{147}Sm/^{144}Nd$ are too small to show). The slope of the best fit line is proportional to the age or the suite (3.54 ± 0.03 G(a); the intercept of this line on the $^{143}Nd/^{144}Nd$ axis where $^{147}Sm/^{144}Nd = 0$ is the initial $^{143}Nd/^{144}Nd$ ratio (0.50809 ± 0.00004). The ε_{Nd} value (+1.16) is a measure of the difference between the initial ratio and a chondritic model for the Earth's mantle at 3.54 Ga expressed in parts per 10,000 (see Section 6.3.4 and Box 6.2). The positive value for ε_{Nd} indicates that the volcanic rocks were derived from a (slightly) depleted mantle source at 3.54 Ga, although there are large errors on this estimate.

isochron has not been fulfilled, that is, that the samples are not cogenetic or that there has been subsequent parent–daughter isotopic exchange.

6.2.1.4 The Geochron

The geochron represents an isochron drawn at $t = 0$ and uses the composition of the appropriate isotope ratio at the time the Earth formed, that is, the Earth's primordial isotopic composition. In principle, a geochron can be defined for any isotopic system, although in practice it is most commonly used in the interpretation of lead isotopes and is used as a reference line in some lead isotope studies. The lead isotope geochron (constructed as in Section 6.2.1.1) is calculated using the initial values for the Earth given in Box 6.1(b) for ages between 4.4 and 4.6 Ga. Its precise position is a function of the presumed age of the Earth, and so although a geochron represents a zero age isochron, the age of the Earth used in its computation (say, 4.57 Ga) must also be specified.

6.2.2 Model Ages

A model age is a measure of the length of time a sample has been separated from the mantle from which it was originally derived. Model ages are most commonly quoted for the Sm–Nd and Lu–Hf systems and can be calculated for an individual rock from a single pair of parent–daughter isotopic ratios. They must, however, be interpreted with care as the basis of all model age calculations requires an assumption about the isotopic composition of the mantle source region from which the samples were originally derived which may or may not be correct. There are two frequently quoted models for such mantle reservoirs, CHUR (the chondritic uniform reservoir) and depleted mantle (DM).

6.2.2.1 CHUR Model Ages

The CHUR model (sometimes referred to as T-CHUR) assumes that when the Earth was formed at 4.6 Ga, the Earth's primitive mantle had the same isotopic composition as the average chondritic meteorite. For neodymium isotopes CHUR is synonymous with the composition of the bulk Earth. A model age calculated relative to CHUR, therefore, is the time in the past at which the sample suite separated from the CHUR mantle reservoir and acquired a different Sm/Nd ratio. It is also the time

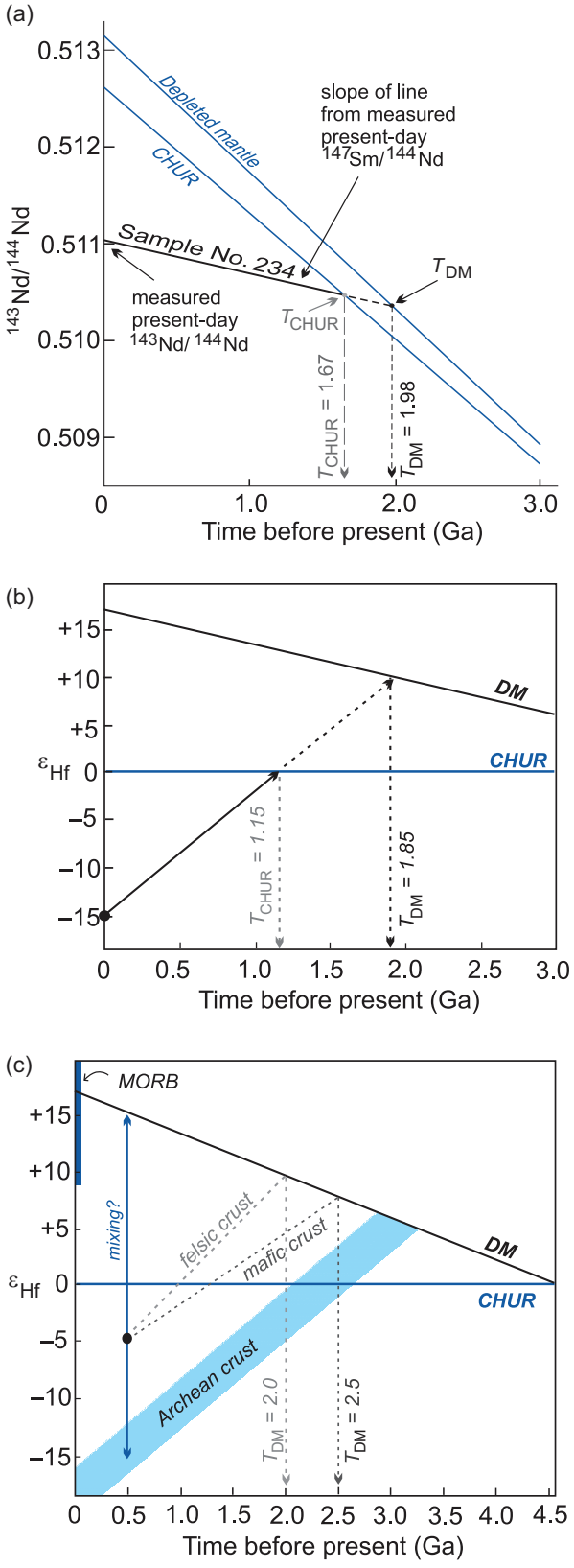

Figure 6.3 The calculation of Nd and Hf model ages. (a) The evolution of ^{143}Nd/^{144}Nd over time for sample 234 (Table 6.4) compared with two models of the mantle: CHUR (the chondritic uniform reservoir) and DM (the depleted mantle). A Nd model age is the time at which the sample had the same ^{143}Nd/^{144}Nd ratio as its mantle source. In this case there are two possible solutions depending upon the preferred mantle model. The T_{CHUR} model age is approximately 1.67 Ga and the T_{DM} model age is approximately 1.98 Ga. A similar diagram can be constructed using the epsilon notation (Section 6.3.4) in place of ^{143}Nd/^{144}Nd. (b) The evolution of ^{176}Hf/^{177}Hf expressed in ε_{Hf} units (see Section 6.3.4) versus time. The Hf model age is the time at which the sample had the same ^{176}Hf/^{177}Hf ratio as its depleted mantle source. In this example the whole-rock ^{176}Hf/^{177}Hf measured today ($\varepsilon_{Hf} = -15$) is extrapolated back through time until it intersects the model mantle composition of interest, providing the model age ($T^{Hf}_{CHUR} = 1.15$ Ga; $T^{Hf}_{DM} = 1.85$ Ga). (c) The evolution of ε_{Hf} versus time and Hf-in-zircon model ages (modified from Kemp and Hawkesworth, 2014; with permission from Elsevier). Three different scenarios are shown for a zircon crystallised from a melt at 500 Ma with an $\varepsilon_{Hf} = -5$. (i) The zircon crystallised from a melt that was derived from older mafic crust producing $T^{Hf}_{DM} = 2.5$ Ga; (ii) the melt was derived from an older felsic continental crust producing $T^{Hf}_{DM} = 2.0$ Ga; (iii) the melt was derived from a mixture of juvenile mantle melt and melt extracted from a heterogeneous Archean crust (dashed arrow) – in this case the model age has no significance. Also note the variation in depleted mantle composition as recorded by MORB ($\varepsilon_{Hf} = +8$ to $+22$) compared with the assumed DM model composition. In the absence of other constraints, all scenarios can generate significantly different model ages.

at which the sample had the same isotopic composition as CHUR. This is illustrated in Figure 6.3a in which the present-day $^{143}Nd/^{144}Nd$ composition of the sample is extrapolated back in time until it intersects the CHUR evolution line and gives the CHUR model age. The evolution curve for the sample is constructed from the present-day values for $^{147}Sm/^{144}Nd$ and $^{143}Nd/^{144}Nd$ for that sample and at some time (t) in the past ($^{143}Nd/^{144}Nd)_t$ is calculated from the equation

$$\left(\frac{^{143}Nd}{^{144}Nd}\right)_{sample} = \left(\frac{^{143}Nd}{^{144}Nd}\right)_{t} + \left(\frac{^{147}Sm}{^{144}Nd}\right)_{sample} \left(e^{\lambda t} - 1\right) \quad (6.4)$$

where λ is the decay constant, t is an arbitrarily selected time in the past to construct the evolution curve, and $^{147}Sm/^{144}Nd$ is the present-day ratio in the sample. Alternatively, a CHUR model age is calculated from the present-day $^{147}Sm/^{144}Nd$ and $^{143}Nd/^{144}Nd$ of a single sample using the equation

$$T^{Nd}_{CHUR} = \frac{1}{\lambda} \ln \left[\frac{\left(^{143}Nd/^{144}Nd\right)_{sample\ today} - \left(^{143}Nd/^{144}Nd\right)_{CHUR\ today}}{\left(^{147}Sm/^{144}Nd\right)_{sample\ today} - \left(^{147}Sm/^{144}Nd\right)_{CHUR\ today}} + 1 \right] \quad (6.5)$$

where λ is the decay constant for ^{147}Sm to ^{143}Nd (Table 6.1). Both the preferred and historical values used to calculate CHUR are given in Table 6.3b. Care must be taken in selecting which CHUR value to use because different values have been reported in the past and if data are to be compared, they need to be normalized to the *same* CHUR values. Model ages are also sensitive to the difference in Sm/Nd between the sample and CHUR, and only fractionated samples with Sm/Nd ratios which are sufficiently different from the chondritic value will yield precise model ages.

Currently, there is some debate over whether the Earth's mantle had a chondritic or a supra-chondritic (S-CHUR) composition. Caro and Bourdon (2010) provide an overview of the arguments in favour of S-CHUR and from studies of the short-lived Nd isotope ^{142}Nd argue that the non-chondritic $^{142}Nd/^{144}Nd$ of the Earth implies a non-chondritic Sm/Nd for the Earth. Their S-CHUR values are given in Table 6.3a, and S-CHUR model ages can be determined in the same way as T_{CHUR} by simple substitution of S-CHUR values for CHUR values. It should also be noted, however, that the Earth's mantle could have had a chondritic Sm/Nd but that this compositional component was sequestered at the base of mantle early in Earth's history – in which case the CHUR model remains applicable.

The calculation of model ages for the Lu–Hf isotopic system uses the same principles as the Sm–Nd system. The Lu–Hf system also involves relatively insoluble, immobile and refractory elements (Lu, Hf), and therefore the Lu/Hf of Earth is also expected to be similar to chondrite. The evolution curve for a sample is constructed from the present-day (measured) values of $^{176}Lu/^{177}Hf$ and $^{176}Hf/^{177}Hf$ for the sample, calculated at some time (t) using the equation:

$$\left(\frac{^{176}Hf}{^{177}Hf}\right)_{sample} = \left(\frac{^{176}Hf}{^{177}Hf}\right)_{t} + \left(\frac{^{176}Lu}{^{177}Hf}\right)_{sample} \left(e^{\lambda t} - 1\right) \quad (6.6)$$

where λ is the decay constant for ^{176}Lu to ^{176}Hf, t is an arbitrarily selected time in the past to construct the evolution curve, and the subscript 'sample' denotes the measured, present-day ratio of the sample. The CHUR model age is calculated from the present-day $^{176}Lu/^{177}Hf$ and $^{176}Hf/^{177}Hf$ of a sample using the equation:

Table 6.3a Mantle sources and preferred isotope values[a]

	DM[b]	BSE[b]	CHUR[c]	S-CHUR[d]
$^{87}Rb/^{86}Sr$			0.085	0.061
$^{87}Sr/^{86}Sr$	0.7026	0.7045	0.7047	0.7030
Rb (ppm)			600	430
$^{147}Sm/^{144}Nd$			0.1960	0.2082
$^{143}Nd/^{144}Nd$	0.51311	0.512634	0.512630	0.512990
$^{176}Lu/^{177}Hf$			0.0336	0.0375
$^{176}Hf/^{177}Hf$	0.28330	0.282843	0.282785	0.28313
$^{187}Re/^{188}Os$			0.40186	
$^{187}Os/^{188}Os$			0.1276[e]	

[a] Time = today (0 Ga).
[b] Average values of Salters and Stracke, 2004.
[c] Bouvier et al. (2008).
[d] Caro and Bourdon (2010).
[e] Walker et al. (2002).

Table 6.3b Other parameters used to calculate model ages and epsilon values[a]

Nd isotopes	*DePaolo; Wasserburg*[b]	*O'Nions; Allegre; Hawkesworth*[b]
Normalising factors		
$\frac{^{146}Nd}{^{142}Nd}$	= 0.636151 [1], = 0.63613 [2]	$\frac{^{146}Nd}{^{142}Nd}$ = 0.63223 [3]
$\frac{^{150}Nd}{^{142}Nd}$	= 0.2096 [1], = 0.209627 [4]	$\frac{^{146}Nd}{^{144}Nd}$ = 0.7219 [3]
Chondritic Uniform Reservoir		
$\frac{^{143}Nd}{^{144}Nd_{CHUR\ 4.6\ Ga}}$	= 0.505829 [1]	Sm/Nd = 0.31 [5] = 0.50677 ± 10 [6]
$\frac{^{143}Nd}{^{144}Nd_{CHUR\ \ today}}$	= 0.511847 [4], = 0.511836 [7]	= 0.51262 [8]
$\frac{^{147}Sm}{^{144}Nd_{CHUR,\ today}}$	= 0.1967 [1]	= 0.1966 [9], = 0.1967 [10], = 0.19637-0.1968 [11]
Depleted mantle		
$\frac{^{143}Nd}{^{144}Nd_{DM,\ today}}$	= 0.51235 [7], = 0.512245 [12]	= 0.51315 [10], = 0.51316 [9] = 0.513114 [13], = 0.51317-0.51330 [11]
$\frac{^{147}Sm}{^{144}Nd_{DM,\ today}}$	= 0.214 [7], = 0.217 [14] = 0.225 [15], = 0.23 [12]	= 0.2137 [10], = 0.222 [13], = 0.233-0.251 [11]
International rock standard BCR-1		
$\frac{^{143}Nd}{^{144}Nd_{BCR-1}}$	= 0.51184 [16]	= 0.512669 ± 8 [17]
Basaltic achondrite best initial (BABI)		
$^{87}Sr/^{86}Sr_{(4.6\ Ga)}$	= 0.6998 [18]	

[a] Assuming $\lambda = 6.54 \times 10^{-12}\ yr^{-1}$.
[b] References: [1] Jacobsen and Wasserburg (1980); [2] DePaolo (1981a); [3] O'Nions et al. (1977); [4]Wasserburg et al. (1981); [5] O'Nions et al. (1979); [6] Lugmair et al. (1975); [7] McCulloch and Black (1984); [8] Hawkesworth and van Calsteren (1984); [9] Goldstein et al. (1984); [10] Peucat et al. (1988); [11] Allegre et al. (1983); [12] McCulloch and Chappell (1982); [13] Michard et al. (1985); [14] Taylor and McLennan (1985); [15] McCulloch et al. (1983); [16] DePaolo and Wasserburg (1976); [17] Hooker et al. (1981); [18] Hans et al. (2013).

$$T^{Hf}_{CHUR} = \frac{1}{\lambda}\ \ln\left[\frac{\left(^{176}Hf/^{177}Hf\right)_{sample\ today} - \left(^{176}Hf/^{177}Hf\right)_{CHUR\ today}}{\left(^{176}Lu/^{177}Hf\right)_{sample\ today} - \left(^{176}Lu/^{177}Hf\right)_{CHUR\ today}} + 1\right] \tag{6.7}$$

where λ is the decay constant for ^{176}Lu to ^{176}Hf (Table 6.1). This is illustrated in Figure 6.3b in which the present-day $^{176}Hf/^{177}Hf$ composition of the sample is extrapolated back in time until it intersects the CHUR evolution line, providing the CHUR model age. The values for CHUR are given in Table 6.1. In Figure 6.3b the Hf isotope values are expressed in ε_{Hf} units – this is an alternative way of expressing an isotope ratio relative to CHUR. The ε notation is frequently applied to both Hf and Nd isotopes and is discussed more fully in Section 6.3.4. As in the case of Nd isotope model ages, when compiling data it is necessary to check that all the data are normalized to the *same* CHUR value.

6.2.2.2 Depleted Mantle Model Ages (T_{DM})

Studies of *initial* $^{143}Nd/^{144}Nd$ (often denoted with the subscript *i*) from Precambrian terrains suggest that the mantle which generated the continental crust has evolved since earliest times with a Sm/Nd ratio greater than that of CHUR. Consequently, model ages for the continental crust are usually calculated with reference to the depleted mantle (DM) reservoir rather than CHUR. Depleted mantle model ages are calculated by substituting the values for $(^{143}Nd/^{144}Nd)_{CHUR\ today}$ with $(^{143}Nd/^{144}Nd)_{DM\ today}$

and $(^{147}Sm/^{144}Nd)_{CHUR\,today}$ with $(^{147}Sm/^{144}Nd)_{DM\,today}$ into Eq. 6.5. Similarly, Hf depleted mantle model ages are calculated by substituting the appropriate DM values into Eq. 6.7 such that $(^{176}Hf/^{177}Hf)_{CHUR\,today}$ and $(^{176}Lu/^{177}Hf)_{CHUR\,today}$ become $(^{176}Hf/^{177}Hf)_{DM\,today}$ and $(^{176}Lu/^{177}Hf)_{DM\,today}$. The appropriate values are given in Table 6.3 and a graphical solution of a T_{DM} model age calculation for both the Nd and Hf systems (using the epsilon notation – see Section 6.3.4) is illustrated Figure 6.3a, b.

6.2.2.3 Hf Depleted Mantle Model Ages Calculated for Zircon

Hf model ages (or crustal residence ages; see Section 6.2.3.2) can also be calculated for the mineral zircon and are used to trace crustal evolution – see, for example, Kemp and Hawkesworth (2014) for an excellent overview. Zircon has a very low Lu/Hf (<0.002) and therefore a low in-growth of radiogenic ^{176}Hf and so preserves the near-initial $^{176}Hf/^{177}Hf$ inherited from its source at the time it crystallised. For the simplest scenario, that of an igneous zircon with a U–Pb crystallisation age the same as its Hf model age, the U–Pb age directly dates the time at which the host melt was extracted from its (depleted) mantle reservoir. These ages therefore reflect the timing of the formation of new crust, although it is important to note that there is some uncertainty over the $^{176}Hf/^{177}Hf$ of the depleted mantle (Chauvel and Blichert-Toft, 2001).

However, in contrast to the simple scenario outlined above, many zircon U–Pb ages are significantly younger than their T^{Hf}_{DM} ages and may differ by several hundred million years (Figure 6.3c). In this case, the interpretation of Hf model ages can be much more ambiguous. This uncertainty arises because zircon sequesters Hf more strongly than Lu, and so the Lu/Hf in zircon is not easily converted into Lu/Hf of the parent magma. Further, as shown in the ε_{Hf} versus time plot in Figure 6.3c, the mixing between a magma and a melt derived from source rocks containing zircons of different ages will provide a calculated model age without geological significance. There is also a range of possible DM growth curves which will affect both Nd and Hf model ages. These are discussed more fully in Section 6.3.3.

6.2.2.4 Assumptions in the Calculation of Model Ages

When calculating a model age it is important to ensure that the assumptions on which the calculation is based are fulfilled. The first major assumption is that of the composition of the isotopic reservoir which is being sampled, for this could be S-CHUR, CHUR or DM. This is important because there can be as much as 300 Ma difference between T_{CHUR} and T_{DM} Nd model ages as illustrated in Figure 6.3a. A further concern is that there are several different models for the depleted mantle source. Three of these are illustrated in Figure 6.14b below using the ε_{Nd} notation (the deviation of the isotopic composition from CHUR) and it is important therefore that the model being used for the depleted mantle is specified. There are also a number of different normalisation schemes in use for the Nd isotope system. These are listed in Table 6.3b. It is important therefore that when calculating model ages or plotting data from different sources the same set of normalising values is used consistently.

A second major assumption used in model age calculations is that the parent/daughter element ratio of the sample has not been modified by fractionation after its separation from the mantle source. A third assumption is that all material is extracted from the mantle was derived in a single event. Examples of Nd–model age calculations using Eq. 6.5 for T^{Nd}_{CHUR} and T^{Nd}_{DM} for a suite of metamorphic rocks from central Australia are given in Table 6.4.

Table 6.4 Nd model ages calculated using CHUR and DM for rocks from the Strangeways range, Central Australia[a]

Sample no.	$^{147}Sm/^{144}Nd$	$^{143}Nd/^{144}Nd$	T^{Nd}_{CHUR} (Ga)	T^{Nd}_{DM} (Ga)
Mafic granulites				
226	0.1853	0.511772 ± 36	0.856	2.203
234	0.1251	0.511049 ± 30	1.672	1.975
551	0.2134	0.512122 ± 36	2.596	2.950
868	0.2046	0.512013 ± 24	3.388	2.491
Quartzofeldspathic and calc-silicate rocks				
501A	0.1248	0.511006 ± 28	1.755	2.034
507	0.1310	0.511039 ± 24	1.844	2.115
503	0.1248	0.510967 ± 32	1.837	2.093
512	0.1150	0.510794 ± 32	1.938	2.145

[a]Data from Windrim and McCulloch (1986) using a whole-rock isochron age = 2.07 ± 0.125 Ga. Nd isotopes normalized to $^{146}Nd/^{142}Nd = 0.636151$. NdDM values are $(^{143}Nd/^{144}Nd)_{today} = 0.51235$, $(^{147}Sm/^{144}Nd)_{today} = 0.225$. Calculations made using Eq. 6.5.

6.2.3 Important Concepts in Geochronology

6.2.3.1 Closure Temperature (T_c)

One of the principal controls on the retention of a radiogenic daughter product in a mineral is temperature, and so it is important to know the point at which a rock or mineral becomes a closed system with respect to retention of a particular daughter isotope. This temperature is known as the *closure or blocking temperature* (T_c) (Figure 6.4). The concept of closure temperature was defined by Dodson (1973, 1979) as 'the temperature of a system at the time of its apparent age'. A more recent discussion of this topic in the context of a wider discussion of thermochronology is given by Reiners et al. (2018).

The T_c of a mineral depends on the thermally activated diffusion or annealing of radioisotopic daughter products, which in turn is a complex function of composition, grain size, grain shape, activation energy, cooling rate and whether or not a fluid is present to facilitate diffusion. For this reason, different minerals close at different temperatures and a single mineral will have a different T_c for each isotopic system (Table 6.5). It is unlikely, therefore, given the number variables that control the T_c, that there is a specific T_c for a given mineral associated with a particular isotopic system (Reiners, 2009; Cassata et al., 2011; Cassata and Renne, 2013). Even so, the cooling rate seems to exert the strongest influence on T_c, with a higher cooling rate generally producing a higher T_c (Figure 6.5). With this caveat in mind, T_c is most commonly used to describe minerals, and the T_c measured in several different minerals from a single rock may help to define the cooling history of that rock (Figure 6.6).

A distinction must be made between closure temperature and the resetting of an isotopic system. The latter will take place in samples which have been thermally overprinted and/or subject to fluid flow, and normally it is the process of fluid interaction that is more influential in resetting an isotopic system than temperature alone. Choosing between closure temperature (mainly controlled by volume diffusion) and the resetting of an isochron (most commonly a function of fluid flow) to explain discordant isotopic ages requires a consideration of the scale of isotopic homogenisation. For example, rocks which have been isotopically reset may yield a range of ages that vary from the time of crust formation to the most recent metamorphic event, and this may depend upon the scale of sampling such that large samples may escape isotopic re-homogenisation and preserve old ages, whereas individual minerals may have recrystallised

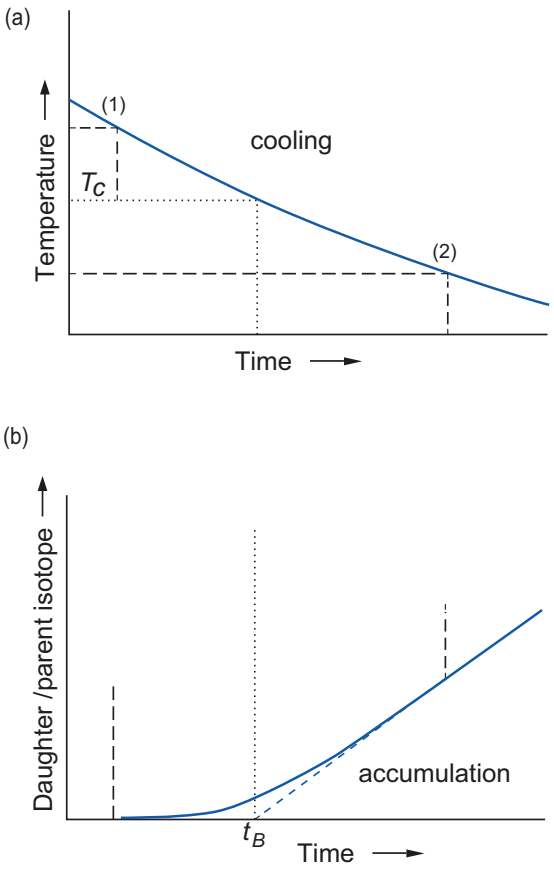

Figure 6.4 Closure (or blocking) temperature (after Dodson, 1979). (a) The cooling curve as a function of time. When a mineral is near its temperature of crystallisation (1) the daughter isotope will diffuse out of the mineral as fast as it is produced and cannot accumulate. As cooling continues, the mineral enters a transitional stage (between (1) and (2)) in which some of the daughter isotope is lost and some is retained, until finally at low temperatures the rate of escape is negligible and the daughter isotope is retained (2). (b) The accumulation curve of the concentration of the daughter to parent isotope as a function of time. The 'age' of the system (t_B) is an extrapolation of the accumulation curve to the time axis (blue dashed line). The closure temperature (T_c) is the projection of this point onto the cooling curve in (a) (dotted line). T_c depends partly upon the cooling rate of the system but is independent of the starting temperature if the latter is sufficiently high. In a specific isotopic system, fast cooling rates have a higher T_c, while lower cooling rates have a lower T_c.

Table 6.5 Minerals, isotopic systems, and closure temperatures[a]

Mineral	Reference	T_c (°C)
U–Th–Pb isotopic system		
Monazite	Cherniak et al. (2004)	1018
Zircon	Cherniak and Watson (2001)	974
Rutile	Cherniak (2000)	624
Titanite	Cherniak (1993)	645
Apatite	Cherniak et al. (1991)	473
Lu–Hf isotopic system		
Zircon	Cherniak et al. (1997)[b]	>900
Garnet	Scherer et al. (2000)	$\geq Gt_{Nd}$
Sm–Nd isotopic system		
Diopside	Cherniak et al. (1997)	>750
Titanite	Cherniak et al. (1997)	>700
Garnet	Ganguly et al. (1998)	690
Apatite	Cherniak et al. (1997)	400–1000
Rb–Sr isotopic system		
Biotite	Hammouda and Cherniak (2000)	581
Muscovite	Jenkin (1997)	521
Plagioclase	Jenkin et al. (1995)	521
K-feldspar	Cherniak and Watson (1992)	396
$^{40}Ar/^{39}Ar$ isotopic system		
Hornblende (magnesian)	Harrison (1981)	569
Phlogopite	Giletti (1974)	459
Muscovite	Robbins (1972)	393
Biotite	Grove and Harrison (1996)	358
K-feldspar (low sanidine)	Wartho et al. (1999)	357
K-feldspar (orthoclase)	Foland (1994)	222
Maskelynite	Weiss et al. (2002)	6
(U–Th)/He isotopic system		
Magnetite	Blackburn et al. (2007)	247
Titanite	Reiners and Farley (1999)	212
Monazite	Farley (2007)	200
Olivine	Shuster and Farley (2005)	187
Zircon	Reiners et al. (2004)	184
Xenotime	Farley (2007)	176
Epidote	Nicolescu and Reiners (2005)	86
Apatite	Farley (2000)	69
Goethite	Shuster et al. (2005)	51
Quartz	Shuster and Farley (2005)	48
Basaltic glass	Kurz and Jenkins (1981)	24
Fission track		
Zircon	Rahn et al. (2004)	342
Apatite	Ketcham et al. (1999)	115
Fission track, He		
Apatite, ^4He 10^3 nmol/g	Shuster et al. (2006)	109
Apatite, ^4He 10^2 nmol/g	Shuster et al. (2006)	87
Apatite, ^4He 10 nmol/g	Shuster et al. (2006)	69
Apatite, ^4He 1 nmol/g	Shuster et al. (2006)	58
Apatite, ^4He 10^{-1} nmol/g	Shuster et al. (2006)	53

[a] After Reiners (2009) with additions.
[b] Differential diffusion between Lu and Hf in zircon.

and yield younger ages. In the following section we shall look more closely at the meaning of the term 'age' in the light of the T_c concept and discuss the different ways it has been used in both mineral and whole-rock systems.

6.2.3.2 What Is an 'Age'?

In geochronology we distinguish between a 'date' and an 'age'. The former is used to describe an analytical result that has not yet been interpreted or given any geochronological significance. The term 'age' is used when applied to the results of an isochron calculation or a model 'age' calculation on a whole rock or a mineral sample once the geological significance of the result has been evaluated. The meaning of the term 'age' is always a matter of *interpretation*, for there are a number of different processes that can impart geological significance to a calculated 'age'. For this reason, the term 'age' is best used with an additional qualifying term. These are discussed below.

(a) *Crystallisation age*. The crystallisation age of a mineral or a rock records the time at which it crystallised. In an igneous rock the crystallisation age of a mineral records the magmatic age of the rock. In the case of a metamorphic mineral, if the temperature of crystallisation is lower than the closure temperature, the instant the mineral forms it records its age of crystallisation.

(b) *Metamorphic age*. A metamorphic age is the time of peak metamorphism. This is different from the *cooling age*, which is discussed below. A metamorphic age depends upon the metamorphic grade. In low-grade metamorphic systems the metamorphic maximum may be determined from the blocking temperature of a specific mineral. In the case of high-grade metamorphism, the time of the peak of metamorphism can be inferred from the resetting of a

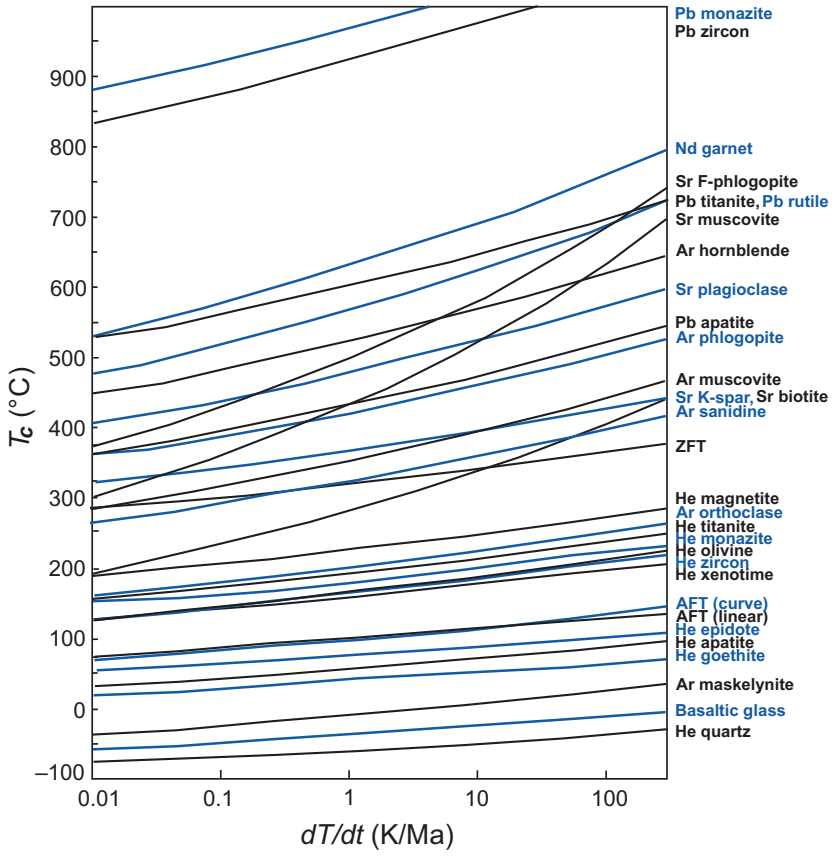

Figure 6.5 The closure temperature (T_c) of some common minerals as a function of cooling rate (after Reiners et al., 2018; with permission from John Wiley & Sons). Note that fast cooling rates have higher T_c. The isotopic system and mineral are specified on the right-hand axis. ZFT, zircon fission track; AFT, apatite fission track.

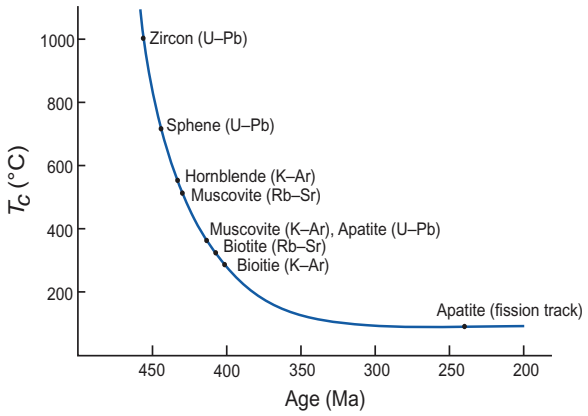

Figure 6.6 The cooling history of the Glen Dessary syenite, Scotland (after Van Breemen et al., 1979, and Cliff, 1985). Mineral age is plotted against approximate T_c (with mineral and method indicated). The combination of different minerals and isotopic systems define a range of T_c and produce 'cooling' ages; these define the cooling history for the pluton which can be expressed as °C/Ma.

whole-rock system such as Rb–Sr or Pb–Pb or the timing of new zircon growth (Figure 6.8).

(c) *Cooling age.* In a metamorphic rock the term 'cooling age' describes the time, after the main peak of metamorphism, when for a given isotopic system a mineral passes through its closure temperature. In an igneous rock the cooling age is the time after solidification of the melt that a mineral passes through its closure temperature. A cooling age therefore must be specified in terms of both the isotopic system and the mineral (Figure 6.5).

(d) *Crust formation age.* A crust formation age represents the time at which new continental crust is extracted from the mantle (O'Nions et al., 1983). Normally, the genesis of new continental crust is followed by deformation, metamorphism and melting, and so it is not always possible to easily determine the age of crust formation, only the timing of the later metamorphism and/or partial melting.

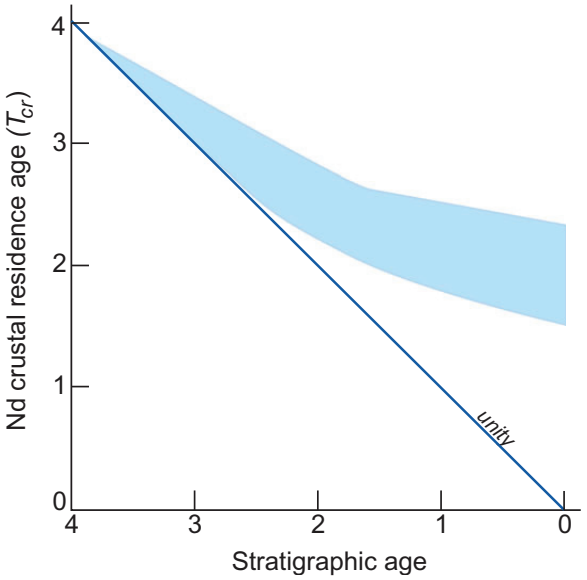

Figure 6.7 Crustal residence age (T_{cr}) diagram. Stratigraphic age is plotted against neodymium T_{cr} for fine-grained clastic sediments from 4.0 Ga to the present day (shaded region). The departure from the 1:1 line at about 2.5 Ga shows that Archaean sediments contain a mainly juvenile component, whereas Phanerozoic sediments contain an old crustal component. (After Miller and O'Nions, 1985)

(e) *Crustal residence age.* The term 'crustal residence age' applies to sediment derived from an area of continental crust and reflects the age of that crust (Figure 6.7). A Nd crustal residence age (T_{cr}) is calculated from Eq. 6.5 by substituting appropriate values for the depleted mantle DM (the original source of the continental crust) in place of the values for CHUR. Some authors use the term 'provenance age' instead of crustal residence age, although this should not be taken to signify a specific event such as stratigraphic age, but rather is the average crustal residence time of all the components of the rock. Typically, the crustal residence age of a sedimentary rock is older than its stratigraphic age (Figure 6.7).

6.2.4 Whole-Rock versus Mineral Age?

Choosing between a whole-rock or mineral age determination depends on the nature of the investigation. Useful age information may be extracted from whole rock systems as follows:

- In rapidly cooled volcanic rocks, it is possible to measure the time of crystallisation.
- In metamorphic rocks, whole-rock data can be used to measure the time of peak metamorphism.
- In some instances, whole-rock model ages can be used to determine the time of crust formation.

Isotopic measurements of minerals can be used in mineral isochron calculations to determine individual mineral ages or the cooling history of a rock (see Section 6.2.3.1). Highly refractory minerals such as zircon with a high T_c can provide magmatic crystallization ages and sometimes even after multiple metamorphic events may preserve the time of crust formation. Minerals preserved as inclusions within refractory phases such as zircon, garnet or diamond can be protected from later overprinting events and may record the very early history or even the prehistory of the parent rock (e.g., Delavault et al., 2016).

The advent of analytical tools which permit the in situ, high spatial resolution measurement of isotope ratios in individual mineral grains has revolutionised geochronology (Compston, 1984; Košler et al., 2002). Not only can multiple analyses be made on a single crystal, helping to unravel the geological history of complex mineral grains, but the low-sampling volume associated with SIMS analysis permits multiple methods to be applied to the same analytical domain. For example, it is common to determine both the U–Pb age and the Hf isotope model age from within a single growth zone of a zircon crystal (Robinson et al., 2019) or both the U–Pb age and the REE chemical composition at the same analytical position in a single grain of zircon or garnet (Whitehouse and Platt, 2003).

6.2.5 Isotopic Systems Used in Geochronology

The reader should refer to Table 6.1 for the details of the radioactive decay schemes discussed in the sections below.

6.2.5.1 The K–Ar and Ar–Ar Systems

Within the family of the longer-lived radiogenic isotope systems used for dating geological events, ^{40}K has one of the shortest half-lives. In addition, potassium is abundant in crustal rocks, whereas the concentration of the volatile noble gas Ar in the Earth is low, and so the Earth has a high $^{40}K/^{40}Ar$ ratio. For these reasons, the K–Ar system is the preferred method for accurately dating young events in fresh

igneous rocks and, because of the volatility of Ar, measuring the time of reheating in igneous and metamorphic rocks. K–Ar ages are precise to about 30,000 years.

The $^{40}Ar/^{39}Ar$ method was developed from the K–Ar method. ^{39}Ar does not occur naturally but is produced by irradiating a K-bearing sample with fast neutrons to produce ^{39}K (half-life of 269 years). The amount of ^{39}Ar produced is therefore a function of the amount of ^{39}K present in the sample. Since at any point in the Earth's history the $^{40}K/^{39}K$ ratio is constant, the amount of ^{40}K present in the sample can also be calculated from the ^{39}Ar measured. This forms the basis of $^{40}Ar/^{39}Ar$ dating.

Argon isotopes are most commonly measured in K-bearing minerals such as biotite, muscovite, K-feldspar and hornblende. The T_c associated with these minerals is in the 'mid-temperature' range (T_c = 200–550°C, Figure 6.5). At these temperatures, the closure temperature is highly dependent on the length scale of diffusion and the grain size and shape (Cassata et al., 2011; Cassata and Renne, 2013). This means that, depending on cooling rate, closure temperatures can vary by as much as ~200°C (Figure 6.5). Nonetheless, useful age data can be obtained from both K–Ar and $^{40}Ar/^{39}Ar$ methods and provide crystallization ages for rapidly cooled rocks, cooling ages in slowly cooled rocks (Rose and Koppers, 2019) and the time of diagenesis in sediments (Schomberg et al., 2019). Frequently, geochronological data are collected using a step heating method in which the cumulative ^{39}Ar released is used to produce an age spectrum. Modern laser ablation systems allow micron-level spatial resolution of argon isotope measurements, and the in situ measurement of volcanic glass and minerals has been successfully applied using ~100-μm analytical spots (Warren et al., 2012).

6.2.5.2 The Rb–Sr System

The elements Rb and Sr are sufficiently abundant in most crustal rocks (10–1000 ppm) for the Rb–Sr method of geochronology to be useful in a wide range of rock types and minerals. However, Rb and Sr are also relatively mobile and the Rb–Sr isotopic system is frequently disturbed by the influx of fluids or by later thermal events. Consequently, Rb–Sr dating requires pristine samples and is rarely useful for constraining crust formation ages. Nevertheless, a Rb–Sr isochron has meaning and can usually be attributed to an event such as the time of metamorphism or recystallisation in an igneous rock or the time of diagenesis in a sedimentary rock.

The Rb–Sr method is often applied to the minerals biotite, muscovite, plagioclase K-feldspar and apatite. Ages can be calculated from a two-point isochron method in which a mineral with a low concentration of Rb such as plagioclase feldspar is used as a control on the initial ratio of the rock. Alternatively, mineral ages can be determined from single crystals or even parts of single crystals associated with specific metamorphic fabrics (Cliff et al., 2017).

6.2.5.3 The U–Th–Pb/He System

The utility of the U–Th–Pb system lies in its independent and branching decay schemes and in the contrasting geochemical properties of the elements involved. U and Th are actinides, incompatible and refractory. Under oxidizing conditions U exists as U^{6+} and can be highly mobile. Pb is slightly less incompatible, is chalcophile and exists in several oxidation states.

The focus here is on the Pb–Pb, ^{235}U–^{207}Pb and ^{238}U–^{206}Pb systems. U-series dating, which involves the numerous intermediate to short-lived daughter products within the U–Th–Pb system, is useful for dating very young geological processes but is not addressed here. Nor are the methods of the He fission track system that is used to determine the timing of low-temperature process associated with erosion. For a thorough discussion of these systems, we refer the interested reader to White (2015) and Reiners et al. (2018).

Pb–Pb whole-rock and mineral isochrons can be plotted for a wide range of rock types from granites to basalts, and can also be used to determine the depositional age of some sediments. The method yields reliable ages in rocks with simple crystallisation histories. However, the differences in U and Pb mobility and geochemical behaviour may complicate the interpretation if the isotopes have been reset. Thus, the Pb–Pb isochron method rarely provides crust formation ages and is better used to determine the age of metamorphism.

The combined use of the $^{206}Pb/^{238}U$ and $^{207}Pb/^{235}U$ systems allows an assessment of whether the assumptions associated with T_c have been met. This approach is commonly applied to mineral samples such as zircon. When samples which have had an undisturbed thermal history are plotted on a $^{206}Pb/^{238}U$ versus $^{207}Pb/^{235}U$ plot, they should lie on

the 'concordia' curve (Figure 6.8). The concordia curve is the theoretical curve along which a series of ^{238}U and ^{235}U ages over time are the same (Figure 6.8, Box 6.1) and is calculated from the decay constants of the two systems. Hence a U-, Th-, Pb-bearing mineral population may define a linear array on a concordia diagram with an upper and lower time intercept on the concordia curve (Figure 6.8). The normal interpretation of the linear array, known as the discordia, is one of lead loss (or uranium gain) in which its upper and lower intercepts with the concordia curve may have petrological significance.

U and Th typically occur in zircon, monazite, rutile, titanite, epidote and apatite and so are often used in U–Th–Pb isotopic studies. Zircon in particular is a highly refractory mineral and so is especially useful since it can retain primary (crystallization) age information despite being affected by secondary processes (e.g., Reimink et al., 2016, and references therein). Thus, magmatic zircons in felsic rocks may be used to date the time of crystallisation from the upper intercept of the discordia curve. In contrast, granitic rocks which are melts of older crust may contain inherited (xenocrystic) zircons and in this case the lower intercept may represent the age of crystallisation, while the upper intercept may reflect the age of the crustal source (Amelin et al., 2000). In sediments, detrital zircons can reflect the age and composition of the sediment source (Zhang et al., 2015), and in metamorphic rocks zircons are used to date the age of the protolith and also the time of metamorphism (Hoiland et al., 2018). The application of high spatial resolution methods allows the dating of mineral growth zones within a single zircon grain and identification of the magmatic and, if applicable, the metamorphic chronology of the rock (Figure 6.8).

6.2.5.4 The Sm–Nd System

The REE elements Sm and Nd are incompatible and therefore are more abundant in the crust than in the mantle. They are less mobile than Rb, Sr, Th, U and Pb and so may preserve 'original' isotopic signatures

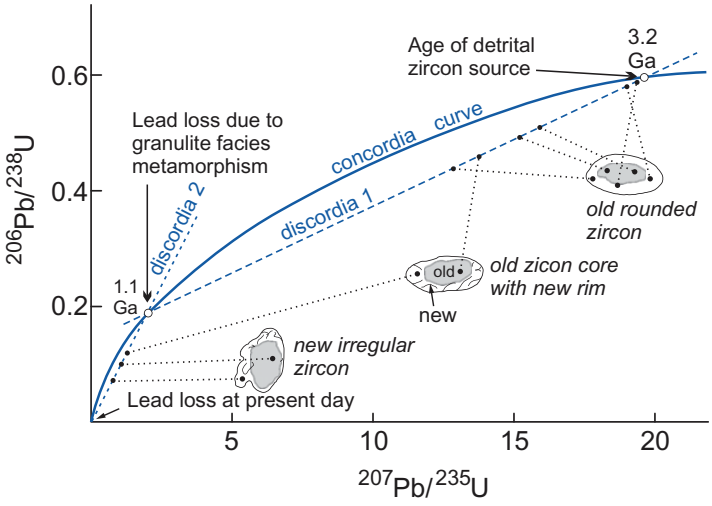

Figure 6.8 U–Pb concordia diagram. $^{207}Pb/^{235}U$ and $^{206}Pb/^{238}U$ data from zircon grains from a granulite facies metasediment from Sri Lanka (after Kroner et al., 1987). The concordia curve defines the theoretical evolution through time of $^{206}Pb/^{238}U$ and $^{207}Pb/^{235}U$ ages that are equivalent (Box 6.1). It is curved because ^{235}U and ^{238}U have different half-lives. A discordia is a line fitted to data points that are not concordant (do not coincide with the concordia curve). A discordia may intersect the concordia curve at two points. The sketches show morphologies of individual zircon grains and the locations analysed using a secondary ion mass spectrometer (SIMS). Old zircon grains and the cores of composite grains define a linear array (discordia 1) with an upper intercept at 3.2 Ga and a lower intercept at 1.1 Ga. The upper intercept is interpreted as the age of the source of detrital zircon and the lower intercept as the time of granulite facies metamorphism. New zircon grains (recognised on the basis of their irregular morphology) and new zircon overgrowth on composite grains define a second linear array (discordia 2) with an upper intercept at 1.1 Ga (the time of granulite facies metamorphism) and a lower intercept at the present day. The new zircon growth was interpreted to have occurred during the granulite facies event.

in rocks whose Rb–Sr and Pb isotopic chemistry has been disturbed. The Sm–Nd isotope system is important in dating mafic rocks and meteorites where there is sufficient Sm/Nd fractionation to allow the accurate determination of an age and is one of the best methods for obtaining crust formation ages from a whole-rock analysis.

The chief limitations of the Sm–Nd method are associated with its long half-life, which restricts its application to older rocks, and the relatively small variations in Sm/Nd found in most cogenetic rock suites. For this reason, some workers have combined different lithologies on an isochron diagram to obtain a wider spread of Sm/Nd ratios, although this strategy requires a clear demonstration of their cogeneticity; otherwise, samples extracted from different sources and with very different histories will generate a questionable isochron.

Some accessory minerals such as apatite, monazite, sphene or garnet fractionate the REE and are useful in Sm–Nd mineral geochronology. Garnet is particularly important in this regard, for it has a high T_c (~500–700°C, Figure 6.5) and can be used to date the peak of metamorphism. Garnet-bearing mineral assemblages also offer the potential for precise Sm–Nd mineral isochron ages because garnet has a high Sm/Nd ratio which allows the slope of a mineral isochron to be accurately determined with errors of only 5–10 Ma for Mesozoic ages (Zheng et al., 2002; Lotout et al., 2020). Garnet ages are determined on two-point isochrons between garnet and whole-rock or one or more of the minerals plagioclase, pyroxene and hornblende with less fractionated Sm/Nd. Mineral isochrons which do not involve garnet are also possible but generally define a smaller range in Sm/Nd, although they may still yield ages with errors of ~20 Ma.

6.2.5.5 The Lu–Hf System

The Lu–Hf system is similar to the Sm–Nd isotopic system inasmuch as Lu is also a REE, but the half-life of ^{176}Lu is shorter than ^{147}Sm (37 Ga versus 106 Ga). This means that Lu/Hf and therefore ^{176}Hf/^{177}Hf in rocks and minerals should have a greater range than is seen by ^{143}Nd/^{144}Nd in the Sm–Nd system. Theoretically, the Lu–Hf method should permit precise isochron age determinations for older rocks. In practice, however, the lack of significant Lu/Hf fractionation in most crustal rocks and in common rock-forming minerals prevents this method from being used to determine isochron ages. Instead, the main applications are limited to those few specific minerals which fractionate Lu/Hf, as will be discussed in Section 6.3.1.2.

Lu is the heaviest of the REEs and it is especially accommodated in those phases that prefer the HREE. Garnet is an excellent example and most garnet species strongly partition Lu relative to the lighter REEs and Hf. In addition, Hf is chemically similar to Zr and is therefore concentrated in the mineral zircon. Although this is an advantage in simple igneous systems and allows the application of Lu–Hf and U–Pb dating methods to the same zircon grains, the different diffusion rates of trivalent Lu and tetravalent Hf cations means that interpreting the results for metamorphic rocks is not always straightforward (Bloch et al., 2020, and references therein).

An important application of the Lu–Hf method is in the study of clastic sediments. These tend to concentrate the heavy minerals such as garnet and zircon in which it is possible to apply multiple isotopic techniques including U–Pb, O, and Lu–Hf isotopes, as well as to analyse for trace elements and the REE. This means that in both modern and ancient sedimentary systems individual detrital mineral grains can be used to obtain information about both their source and the processes operating in the source region (Hoiland et al., 2017). When sufficient grains are analysed it is also possible to constrain their likely tectonic setting (Cawood et al., 2012).

6.2.5.6 The Re–Os System

In contrast to the highly lithophile elements of the Rb–Sr, Sm–Nd or Lu–Hf systems, the elements Re and Os are highly siderophile elements (HSE) and so are depleted in the silicate Earth and are present only at the ppb to sub-ppb levels. Both Re and Os are HSE elements, but Os is also a PGE and therefore is associated with ultramafic rocks, sulphides and arsenides. In mantle phases Re is moderately incompatible, whereas Os is highly compatible. This results in crustal rocks having elevated Re/Os ratios relative to the mantle. As noted above, the overall concentrations of Re and Os in the crust are low, but it is the strong fractionation of Re/Os and their enrichment in specific minerals that forms the basis of Re–Os geochronology.

Because crustal materials have very low concentrations of Re and Os, the application of the Re–Os system is restricted to samples enriched in Re and with

high Re/Os. Re is particularly concentrated in molybdenite, to a lesser extent in Cu sulphides, and in black shales. This makes the Re–Os system useful in the study of iron meteorites, ore deposits, ultramafic rocks and hydrocarbons. Re–Os dating is based on the isochron method and combines related samples or minerals on an isochron (Kendall et al., 2006; Day, 2016). The method has also been used to date shales as young as 150 Ma (Cohen et al., 1999), and model ages in excess of 2 Ga have been calculated for Phanerozoic ophiolitic rocks (Meibom et al., 2002).

The Re–Os system has also been used to date mantle melt extraction events (Carlson, 2005). Os is compatible during mantle melting, whereas Re is moderately incompatible. Consequently, a melt residue will have lower Re and higher Os than either the fertile mantle or a mantle melt. This means that in residual peridotites the Re–Os system is less sensitive to contamination by migrating melts, thereby allowing whole rock mantle xenoliths to return useful chronological information on the timing of melt extraction.

6.2.5.7 Data Reduction Software Used in Geochronology

There are two free software packages commonly used for the reduction of geochronological data, Isoplot (Ludwig, 2009) and IsoplotR (Vermeesch, 2018b). Isoplot 4.15 (www.bgc.org/isoplot_etc/isoplot.html) is a PC-based add-on for Excel, and will work with some Mac Windows-enabling programs. Versions for older operating systems are also available. IsoplotR (www.ucl.ac.uk/~ucfbpve/isoplotr/) is a similar program written in R and can be used on-line or off-line with a computer that has R installed on it.

6.2.6 The Interpretation of Model Ages

A model age is an estimate of the time at which a sample separated from its mantle source region, and for igneous rocks and meta-igneous rocks this is a good estimate of the time of crust formation. However, as noted above in Section 6.2.2.4 a number of assumptions have to be made when calculating a model age.

In the case of Sr isotopes, none of these criteria is usually fulfilled with any certainty for either igneous rocks or sediments (Goldstein, 1988) and consequently model ages are not usually calculated for the Rb–Sr system. On the other hand, useful and meaningful model ages can be calculated for Nd, Hf and Os isotopes, although in each case the reference reservoir (CHUR or DM) must be specified and in the case of DM model ages the precise DM model evolution curve must also be defined.

Model ages for granitoids may be used to estimate the age of their source. In the case of mantle-derived granites, the model age gives the time that the basaltic precursor to the granite was extracted from the mantle. This is often close in time to the crystallisation age of the granite. Granitoids which are derived by the melting of older continental crust give model ages which are indicative of the age of their crustal source, although this is realistic only when the parent/daughter element ratio has not been disturbed by fractionation. Often granites are a mixture of crustal and mantle sources. When this is the case calculated model ages provide only a minimum age (Arndt and Goldstein, 1987; Figure 6.9).

Model ages for clastic sedimentary rocks provide an estimate of their crustal residence age (Section 6.2.3.2; O'Nions et al., 1983), again assuming minimal fractionation of the parent/daughter elements relative to the source. However, most continental sediment is a mixture of material from different sources. Consequently, model ages are likely to represent an average of the detrital input and provide only a minimum estimate of the crustal residence age or an average crustal residence age.

6.3 Using Radiogenic Isotopes in Petrogenesis

The mass difference between any pair of radiogenic isotopes is so small that the isotope pair cannot be fractionated by crystal–liquid processes. This means that during partial melting a magma retains the isotopic character of its source region and that isotope ratios remain unchanged during subsequent fractionation events.

These simple observations have led to two important developments in isotope geochemistry. First, source regions may have unique isotopic characteristics that can be defined, and, second, there may be mixing between isotopically distinct sources. Thus isotope geochemistry seeks to do the following:

- Identify and map the different isotopic reservoirs in the crust and mantle
- Characterise these reservoirs for different isotopic systems
- Evaluate and quantify the extent to which partial melting, recycling and mixing processes are involved in their genesis.

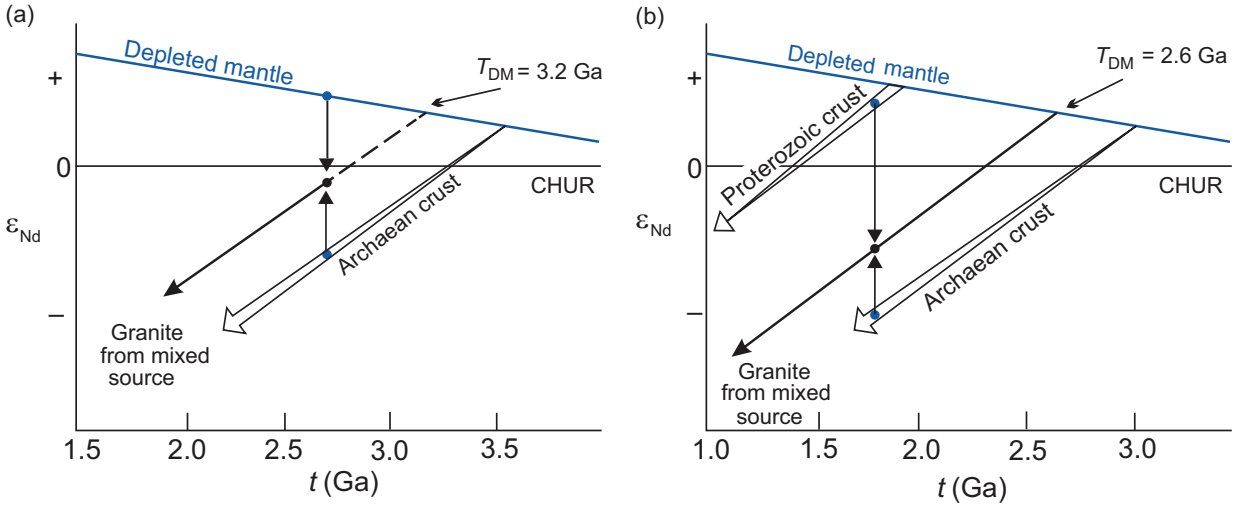

Figure 6.9 $^{143}Nd/^{144}Nd$ evolution of the depleted mantle reservoir with time (in epsilon units; see Section 6.3.4). Relative to CHUR the depleted mantle shows increasing $^{143}Nd/^{144}Nd$ (increasingly positive ε_{Nd} values) with time, whereas the continental crust shows retarded $^{143}Nd/^{144}Nd$ evolution (increasingly negative ε_{Nd} values). (a) The depleted mantle model age for a granite formed at 2.7 Ga (black dot) from a mixture of a juvenile component derived from the depleted mantle and Archaean crust formed at 3.5 Ga will be 3.2 Ga. (b) The depleted mantle model age of a granite formed by the mixture of 1.9 Ga Proterozoic and 3.0 Ga Archaean crustal sources at 1.8 Ga will be 2.6 Ga. These diagrams show that model ages calculated for rocks with mixed sources provide only minimum ages of the crustal source. (Arndt and Goldstein, 1987)

A range of crust and mantle reservoirs is listed in Table 6.6 to demonstrate their isotopic variability. The larger and more difficult question of how the different crust and mantle reservoirs have acquired their isotopic signatures leads into the subject of crust and mantle geodynamics, a topic which treated briefly at the end of this chapter in Section 6.3.6.

The isotopic variability between mantle sources may be thought of in terms of two separate processes. These are the process of mixing in which a number of different components contribute to the source, and the process of isotopic ingrowth in which the composition of the source evolves over geological time. Thus, radiogenic isotope ratios may be used to identify the separate components which have mixed to contribute to a particular magmatic suite such as in the case of the contamination of continental flood basalt with old continental crust. This mixing takes place over a relatively short time scale. In contrast, the isotopic evolution of a mantle source region as a function of the parent–daughter isotope ratio may take place over very long time scales – billions (Ga) rather than millions (Ma) of years.

Knowing how and when the different mantle sources acquired their separate identities is important for understanding the evolution of the Earth's mantle, and it is this subject to which we now turn.

6.3.1 The Role of the Different Isotope Systems in Identifying Reservoirs and Processes

The elements used in geological radiogenic isotope studies vary greatly in their chemical and physical properties, so much so that different isotope systems vary in their sensitivity to particular petrological processes. This variability may show itself in three ways. First, the parent and daughter elements may under certain circumstances behave geochemically in different ways, such that the two become fractionated. For example, during mantle melting an element such as Rb is more readily concentrated in the crust than is the element Sr. The order of incompatibility for the elements of interest can be obtained from Figure 4.22 where the relative enrichments in MORB relative to the residual mantle and in the continental crust relative to MORB are shown.

A second possibility is that a parent–daughter element pair may behave coherently and so will not be

Table 6.6 Isotopic character (present-day) of mantle and crustal reservoirs[a]

	^{87}Rb–^{86}Sr	^{147}Sm–^{143}Nd	^{238}U–^{206}Pb	^{235}U–^{207}Pb	^{232}Th–^{208}Pb	$^{176}Hf/^{177}Hf$	$^{187}Os/^{188}Os$
Oceanic basaltic sources							
DMM[b]	Low Rb/Sr Low $^{87}Sr/^{86}Sr$	High Sm/Nd High $^{143}Nd/^{144}Nd$ (positive ε_{Nd})	Low U/Pb Low $^{206}Pb/^{204}Pb$ (~17.2–17.7)	Low U/Pb Low $^{207}Pb/^{204}Pb$ (~15.4)	Th/U = 2.4 ± 0.4 Low $^{208}Pb/^{204}Pb$ (~37.2–37.4)	0.28330	0.1314–0.2316
HIMU	Low Rb/Sr low $^{87}Sr/^{86}Sr$ = 0.7029	Moderate Sm/Nd $^{143}Nd/^{144}Nd$ = <0.51282[c]	High U/Pb $^{206}Pb/^{204}Pb$ > 20.8	High U/Pb high $^{207}Pb/^{204}Pb$	High Th/Pb	0.28289 (Mangaia)	0.1305–0.1663
EM-1	Low Rb/Sr $^{87}Sr/^{86}Sr$ (~0.705)	Low Sm/Nd $^{143}Nd/^{144}Nd$ = <0.5112[c]	Low U/Pb $^{206}Pb/^{204}Pb$ = 17.6–17.7	Low U/Pb $^{207}Pb/^{204}Pb$ = 15.46–15.49	Low Th/Pb $^{208}Pb/^{204}Pb$ = 38.0–38.2	0.28274 (Gough)	0.1342–0.1432
EM-2	High Rb/Sr $^{87}Sr/^{86}Sr$ > 0.722	Low Sm/Nd $^{143}Nd/^{144}Nd$ = 0.511-0.5121[c]	High $^{207}Pb/^{204}Pb$ and $^{208}Pb/^{204}Pb$ at a given $^{206}Pb/^{204}Pb$			0.282816 (Samoa)	0.1173–0.1284
Bulk Earth	$^{87}Sr/^{86}Sr$ = 0.7045	$^{143}Nd/^{144}Nd$ = 0.512634	$^{206}Pb/^{204}Pb$ = 15.58 ± 0.08	$^{207}Pb/^{204}Pb$ = 18.4 ± 0.3	$^{208}Pb/^{204}Pb$ = 38.9 ± 0.3	0.282843	0.1272–0.1303
Continental crustal sources							
Upper crust (sialic)	High Rb/Sr high $^{87}Sr/^{86}Sr$	Low Sm/Nd low $^{143}Nd/^{144}Nd$ (negative ε_{Nd})	High U/Pb high $^{206}Pb/^{204}Pb$	High U/Pb high $^{207}Pb/^{204}Pb$	High Th/Pb high $^{208}Pb/^{204}Pb$		1.926
Mid crust	Semi-high Rb/Sr = 0.2–0.4 $^{87}Sr/^{86}Sr$ = 0.72–0.74	Crust shows retarded Nd evolution relative to chondritic source	U-depleted Low $^{206}Pb/^{204}Pb$	U-depleted Low $^{207}Pb/^{204}Pb$	Semi-high Th Semi-high $^{208}Pb/^{204}Pb$		
Lower crust (mafic)	Rb-depleted Rb/Sr < ~0.4 Low $^{87}Sr/^{86}Sr$ = 0.702–0.705	Very U-depleted Very low $^{206}Pb/^{204}Pb$ (~14.0)	Very U-depleted Very low $^{207}Pb/^{204}Pb$ (~14.7)	Very Th-depleted Very low $^{208}Pb/^{204}Pb$		0.8040	

[a]Disputed reservoirs are omitted (e.g., PREMA, FOZO, PHEM, C).
[b]Depleted MORB mantle.
[c]Normalized to $^{146}Nd/^{144}Nd = 0.7219$.
Additional notes: $^{176}Hf/^{177}Hf$ from Salters and Stracke (2004) and Salters et al. (2011); $^{187}Os/^{188}Os$ MORB (Escrig et al., 2005), HIMU (Lassiter et al., 2003), EM-1 (Garapić et al., 2015), EM-2 (Jackson et al., 2016), BE (Van Acken et al., 2011, and references therein).

fractionated, and yet behave in a very different manner from the parent–daughter pair of another isotopic system. For example, in the Sm–Nd and Lu–Hf systems the parent–daughter pairs share similar chemical and physical characteristics, whereas in the Re–Os, U–Th–Pb and Rb–Sr systems the parent–daughter pairs may be strongly fractionated relative to one another.

Finally, because of the geochemical similarity between the Sm–Nd and Lu–Hf isotope systems, it is reasonable to expect both systems to behave in a similar way and to display coupled geochemical behaviour. This is often evident on ε_{Nd} versus ε_{Hf} diagrams (Section 6.3.4). On occasion, the isotope systems display *decoupled* behaviour and this may also be of petrological significance.

We now briefly review some key geochemical properties of the Sr, Nd, Hf, Pb and Os systems. These are summarised in Table 6.6.

6.3.1.1 Sm–Nd Isotopes

In discussing the isotopes of Nd we differentiate between the long-lived Nd isotope system $^{147}Sm \rightarrow ^{143}Nd$ which is important in geochronology and the short-lived isotope system $^{146}Sm \rightarrow ^{142}Nd$ (half-life 103 Ma) which is relevant to our

understanding of processes in the very early history of the Earth. The significance of the $^{146}Sm \rightarrow ^{142}Nd$ system is discussed more fully in Section 6.3.4.

The Sm/Nd ratio in the continental crust is lower than that of the depleted mantle and so over time generates lower $^{143}Nd/^{144}Nd$ ratios than are found in the depleted mantle. In this respect the Sm–Nd isotopic system is similar to Lu–Hf, but differs markedly from the U–Th–Pb, Rb–Sr and Re–Os systems. Since the elements Sm and Nd are not significantly fractionated after crust formation by subsequent metamorphic or sedimentary processes, Nd isotope ratios tend to preserve a memory of the parent–daughter isotope ratios of their source. In addition, Sm and Nd are immobile under hydrothermal conditions, and so Nd isotopes reflect the actual proportions of rock or magma involved in specific petrological processes, although this isotope system is insensitive to small amounts of recycled crust in the mantle.

6.3.1.2 Lu–Hf Isotopes

The Lu–Hf isotope system behaves in a similar way to the Sm–Nd isotope system. The Lu/Hf ratio in continental crust is lower than that in the mantle, and so with time the $^{176}Hf/^{177}Hf$ of the crust evolves to lower values relative to the Earth's primitive mantle and the complementary depleted mantle evolves to higher values. A widespread and powerful application of Lu–Hf isotopes in petrology is the integration of Hf model ages with U–Pb crystallization ages for the mineral zircon. Recent studies have shown that in old continental crust, Hf model ages frequently exceed U–Pb zircon ages. This suggests that, if the U–Pb age represents the time of crystallisation of the crust, the Hf model age indicates an earlier event which is taken to be the time at which the precursor to the continental crust separated from the mantle (Kemp and Hawkesworth, 2014).

6.3.1.3 U–Th–Pb Isotopes

The U–Th–Pb system is more complex than other isotope systems used in geochemistry because it incorporates three independent decay schemes (Box 6.1) and because Pb isotopes do not define linear trends on lead isotope evolution diagrams. In terms of their geochemical behaviour U and Pb are incompatible in silicate minerals, although U enters a melt more readily than Pb, and U and Pb are relatively mobile in hydrothermal fluids, whereas Th is highly insoluble.

In detail the two isotopes of Pb produced from U decay (^{206}Pb and ^{207}Pb) show contrasting behaviour as a consequence of their differing radioactive decay rates (Box 6.1). Early in the history of the Earth ^{235}U decayed rapidly relative to ^{238}U, so that ^{207}Pb evolved rapidly with time. Thus, ^{207}Pb abundances are a sensitive indicator of an old source. Today, however, ^{235}U is largely extinct so that in recent Earth history ^{238}U decay is more prominent than that of ^{235}U, and consequently the abundance of ^{206}Pb shows a greater spread than ^{207}Pb. This difference in behaviour between the Pb isotopes allows the identification of several isotopic reservoirs (Table 6.6). Crustal reservoirs are best sampled by studying the isotopic composition of a mineral with a low U/Pb or Th/Pb ratio such as feldspar for they preserve the 'initial' Pb isotopic composition of the source. This approach was developed by Doe and Zartman (1979), is now applied to single crystals using in situ analytical methods (Geng et al., 2020) and is discussed further in Section 6.3.6.1.

6.3.1.4 Rb–Sr Isotopes

During crustal melting the Rb–Sr isotope system has the greatest difference in compatibility between the parent and daughter elements. Rb and Sr are therefore easily separated and are strongly fractionated between crust and mantle. This results in the accelerated evolution of strontium isotopes in the continental crust relative to the mantle and with time has produced higher $^{87}Sr/^{86}Sr$ ratios than in the primitive mantle. Within the continental crust, Rb and Sr are further separated during re-melting, metamorphism and sedimentation because Sr is partitioned into plagioclase, whereas Rb is preferentially partitioned into the melt, and Sr is relatively immobile under hydrothermal conditions, whereas Rb is more mobile.

6.3.1.5 Re–Os Isotopes

Re is moderately incompatible and Os highly compatible in the mantle. This results in crustal rocks having elevated Re/Os ratios relative to the mantle. In contrast, melt extraction from the mantle significantly lowers the Re/Os ratio of mantle peridotites and retards the in-growth of ^{187}Os from the decay of ^{187}Re. This allows the timing of melt extraction events

to be estimated solely from their $^{187}Os/^{188}Os$ ratio (Walker et al., 1989), although melt percolation through the mantle may obscure this signal. Re–Os methods have been applied to the study of mantle xenoliths in order to date melt extraction events and identify a range of fertile, depleted and re-fertilised mantle sources.

6.3.2 Recognising Isotopic Reservoirs

Relative to the composition of the Earth's primitive, undifferentiated mantle there are now a range of isotopically distinct reservoirs which can be recognised in both the mantle and the continental crust. Our purpose here is to show how these different reservoirs might be recognised on the basis of their present-day Sr, Nd, Hf, Pb and Os isotope chemistry (Tables 6.6 and 6.7).

Zindler and Hart (1986) first delineated four mantle end-member domains to explain the isotopic variation observed in mid-ocean ridge and ocean island basalts. In a simpler manner the continental crust can be divided into upper, middle and lower parts (Rundnick and Gao, 2014), each with distinctive geochemical and isotopic characteristics. In general, the upper and middle crust is more chemically evolved than the heterogeneous lower crust.

Ultimately, it is important to understand how the different reservoirs in the crust and mantle have gained their isotopic character. Major processes include chemical depletion through melt extraction, re-fertilisation by melt addition and by the recycling of continental crust or oceanic crust into the mantle via subduction. Over geological time these processes can produce compositional and isotopic heterogeneities from the mineral grain scale to a global scale (Salters et al., 2011; Farmer, 2014; Hofmann, 2014; Stracke, 2016).

6.3.2.1 Oceanic Mantle Sources

Young magmatic rocks record the isotopic composition of their source directly, as insufficient time has passed in a newly formed magma for the parent isotope to produce a daughter isotope via radioactive decay in addition to that inherited from the source. Thus the present-day isotopic compositions of recent oceanic basalts were used by Zindler and Hart (1986) to identify four possible end-member mantle reservoirs. These reservoirs are well characterised for Sr, Nd, Hf and Pb isotopes, as summarized by Hofmann (2014) and Stracke (2016). The commonly accepted reservoirs are shown in Figures 6.10 and 6.11, are summarised in Tables 6.6 and 6.7 and are discussed briefly below.

(a) *The Primary Uniform Mantle (PUM) reservoir*. Geochemical models of the Earth assume an initial primary uniform mantle (PUM) reservoir. This is the composition of a homogeneous primitive or primordial mantle that would have formed during the early degassing of the planet after core formation but prior to the formation of the continents. The PUM is also known as the bulk Earth (BE) or the bulk silicate Earth (BSE). While some oceanic basalts have isotopic compositions similar to the PUM (McCoy-West et al., 2018), there are no geochemical data that require such a mantle domain exists today, although the PUM is a useful geochemical 'frame of reference' and is shown in most of the following diagrams.

(b) *The depleted mantle (DM) reservoir.* The Earth's depleted mantle is characterised by high Sm/Nd and low Rb/Sr element ratios. This leads to high $^{143}Nd/^{144}Nd$ and low $^{87}Sr/^{86}Sr$ isotope ratios. In addition, the DM has high $^{176}Hf/^{177}Hf$ and low $^{206}Pb/^{204}Pb$. It is the primary source of most mid-ocean ridge basalts.

(c) *The HIMU mantle reservoir*. In lead isotope geochemistry the μ value is the ratio $^{238}U/^{204}Pb$. The high $^{206}Pb/^{204}Pb$, $^{207}Pb/^{204}Pb$ and $^{208}Pb/^{204}Pb$ observed in some ocean islands coupled with low $^{87}Sr/^{86}Sr$ (<0.7030) and intermediate $^{143}Nd/^{144}Nd$ and $^{176}Hf/^{177}Hf$ suggest a mantle source that is enriched in U and Th relative to Pb without an associated increase in Rb/Sr. This enrichment is thought to have taken place between 0.7 and 2.1 Ga (Hauri and Hart, 1993). A number of models have been proposed to explain the origin of this mantle reservoir. These include the mixing of altered oceanic crust (possibly contaminated with seawater) into the mantle via subduction, the loss of lead from this part of the mantle into the Earth's core, and the removal of lead (and Rb) by metasomatic fluids in the mantle.

(d) *Enriched mantle (EM) reservoirs*. The enriched mantle has variable $^{87}Sr/^{86}Sr$, low $^{143}Nd/^{144}Nd$, low $^{176}Hf/^{177}Hf$ and high $^{207}Pb/^{204}Pb$ and $^{208}Pb/^{204}Pb$ for a given value of $^{206}Pb/^{204}Pb$. Enriched mantle type 1 (EM1) has low $^{87}Sr/^{86}Sr$, whereas enriched mantle type 2 (EM2) has high $^{87}Sr/^{86}Sr$. Jackson et al. (2007) proposed an even higher $^{87}Sr/^{86}Sr$ (>0.702) for the EM2 component (as shown in Figure 6.10).

Table 6.7 Sr, Nd and Pb isotope ratios of some common rock types[a]

Rock type	$^{87}Sr/^{86}Sr$	$^{143}Nd/^{144}Nd$	$^{206}Pb/^{204}Pb$	$^{207}Pb/^{204}Pb$	$^{208}Pb/^{204}Pb$	$^{176}Hf/^{177}Hf$	$^{187}Os/^{188}Os$	Ref.
Depleted mantle MORB (DMM)								
Atlantic	0.702300–0.702920	0.512992–0.513175	18.084–19.437	15.440–15.568	37.51–38.77	0.283015–0.283354	0.137–0.2316	1, 2
Pacific	0.702150–0.702713	0.513098–0.513296	17.721–18.470	15.309–15.501	37.03–38.99	0.283165–0.283294	0.1315	1, 3
Indian	0.702690–0.704870	0.512437–0.513189	17.325–18.400	15.429–15.564	37.25–38.68	0.282768–0.283366	0.1295–0.3023	1, 4
Ocean island basalts (OIB)								
Pitcairn Is. (EM1)	0.703603–0.705296	0.512333–0.512692	17.72–18.10	15.47–15.50	38.61–39.03	0.282622–0.282834	0.1307–0.2539	5
Samoa (EM2)	0.705193–0.705853	0.512705–0.512900	18.78–19.41	15.55–15.65	38.77–39.86	0.282843–0.283099	0.1268–0.1394*	5–9
Continental flood basalts								
Parana/Etendeka	0.70397–0.71420	0.511860–0.512799	17.1–19.7	15.5–15.7	37.5–38.9	0.282440–0.282440	0.1295	10–13
Columbia River	0.702985–0703964	0.512834–0.513031	18.71–18.92	15.55–15.59	38.10–38.53	0.282985–0.283114	0.134–0.404	14, 15
Mantle xenoliths								
Continental lithosphere								
Siberia	0.70253–0.702235#	0.512590–0.513144#	18.6–19.0	15.5	38.2–40.6	0.282837–0.283793#	0.1156–0.1289#	16, 17
Oceanic lithosphere								
Hawai'i	0.703219–0.723422	0.513019–0.513180	18.06–18.45	15.45–15.49	37.80–38.04	0.283118–0.284630	0.1138–0.1269	18, 19
Kimberlites/Lamproites								
Southern India	0.700961–0.706647	$\varepsilon_{Ndt} = -6.0$ to -11.5	10.78–26.52	15.11–16.66	27.60–59.47	$\varepsilon_{Hft} = +4.4$ to -14.3	0.0967–0.5449	20, 21
Ocean island arcs								
Marianas	0.703440	0.512997	18.73	15.57	38.39	0.283235	0.1193–0.1274	22, 23
Izu	0.703352	0.513063	18.25	15.53	38.20	0.283248	0.1205–0.1272	22, 23
Modern pelagic sediment								
Pacific	0.70690–0.72253	0.512343–0.512392	16.72–19.17	15.57–15.75	38.43–39.19	0.283850–0.282901	1.044	24–26
Atlantic	0.709288–0.723619	0.511942–0.512553	18.61–19.01	15.68–15.74	38.93–39.19	0.282538–0.282960	1.044	25–27
Modern trench sediment								
Global range	0.70493–0.73631	0.51195–0.51291	18.55–19.49	15.52–15.81	38.17–39.76			28
Terrigenous sediment								
Ganga River	0.76913–0.78151	0.511736–0.511767	19.78–20.09	15.87–15.94	40.00–40.30	0.282133–0.282268	2.91–2.96	29, 30†, 31
Turbidites		0.51132–0.51306	16.91–19.91	15.50–15.90	36.44–40.02	0.281471–0.283153		25, 26
Archean chemical sediments								
Stromatolite	0.712396–0.726249	$\varepsilon_{Ndt} = -3.6$ to -7.4	14.1–20.9	14.9–16.2	33.3–35.4			32–34
BIF		$\varepsilon_{Ndt} = +1$						

[a]Initial values; *, melt inclusions in ol or cpx; #, mineral + whole rock; †, suspended load.

References: 1, Chauvel and Blichert-Toft (2001) and references therein; 2, Escrig et al. (2005); 3, Bennett et al. (1996); 4, Yang et al. (2013); 5, Eisele et al. (2002) and references therein; 6, Reinhard et al. (2018); 7, Workman et al. (2004); 8, Jackson and Shirey (2011); 9, Sobolev et al. (2011); 10, Beccaluva et al. (2017); 11, Owen-Smith et al. (2017); 12, Rocha-Júnior et al. (2012, 2013); 13, Zhou et al. (2020); 14, Mullen and Weiss (2013); 15, Wolff et al. (2008); 16, Ionov et al. (2006); 17, Maas et al. (2005); 18, Bizimis et al. (2004, 2007); 19, Blichert-Toft et al. (2003); 20, Chakrabarti et al. (2007); 21, Rao et al. (2013); 22, Pearce et al. (1999) and references therein; 23, Parkinson et al. (1998); 24, McDermott and Hawkesworth (1991); 25, Vervoort et al. (1999); 26, Hemming and McLennan (2001); 27, Hoernle et al. (1991); 28, Plank (2014); 29, Galy and France-Lanord (2001); 30, Garcon and Chauvel (2014); 31, Levasseur et al. (1999); 32, Bolhar et al. (2002); 33, Kamber et al. (2004); 34, Alibert and McCulloch (1993).

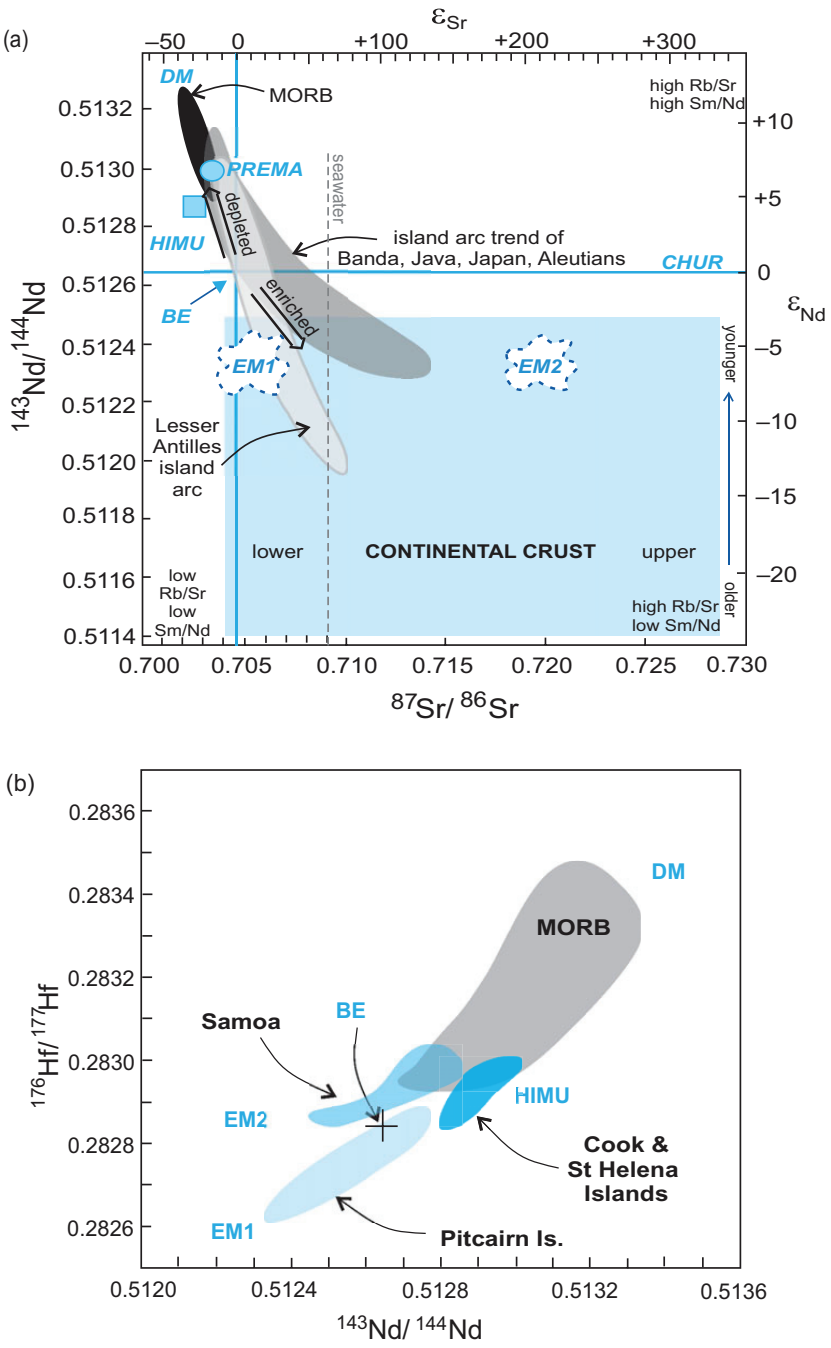

Figure 6.10 Mantle sources. (a) The $^{87}Sr/^{86}Sr$ versus $^{143}Nd/^{144}Nd$ diagram showing oceanic reservoirs for $t = 0$). These include the depleted mantle (DM), bulk silicate Earth (BE), enriched mantle (EM1, EM2), high-μ (U/Pb) (HIMU), and the 'prevalent mantle' (PREMA) compositions. The 'depleted' mantle reservoir in the upper left quadrant reflects residual mantle from which incompatible elements have been removed (it has been 'depleted'). Most crustal rocks plot in the lower-right 'enriched' quadrant which includes old and young upper and lower crust. Mixing arrays between depleted mantle and enriched mantle sources are suggested by the island arc trends. Note the negative correlation between these two systems. Data compiled from Zindler and Hart (1986), Jackson et al. (2007) and White (2015). (b) The $^{143}Nd/^{144}Nd$ versus $^{176}Hf/^{177}Hf$ diagram of oceanic reservoirs with DM represented by global MORB, EM1 by volcanic rocks from the Pitcairn Islands, EM2 by volcanic rocks from the island of Samoa and HIMU by the Cook and St Helena Island volcanic rocks (after Stracke, 2016). The positive covariation on this diagram reflects the similar chemical behaviour of the parent/daughter elements in the two systems.

A large-scale example of EM2 occurs in the Southern Hemisphere (Dupre and Allegre, 1983) and is known as the DUPAL anomaly (Hart, 1984). This component is identified with respect to a Northern Hemisphere Reference Line (NHRL) defined on plots of $^{206}Pb/^{204}Pb$ versus $^{207}Pb/^{204}Pb$ and $^{206}Pb/^{204}Pb$ versus $^{208}Pb/^{204}Pb$ by a linear array of mid-ocean ridge and ocean island basalts (Figure 6.11).

The equations for the NHRL in each of the plots is:

$$^{207}Pb/^{204}Pb = 0.1084\left(^{206}Pb/^{204}Pb\right) + 13.491 \quad (6.8)$$

$$^{208}Pb/^{204}Pb = 1.209\left(^{206}Pb/^{204}Pb\right) + 15.627 \quad (6.9)$$

The isotopic anomaly was expressed by Hart (1984) in terms of Δ7/4 and Δ8/4, defined as the vertical

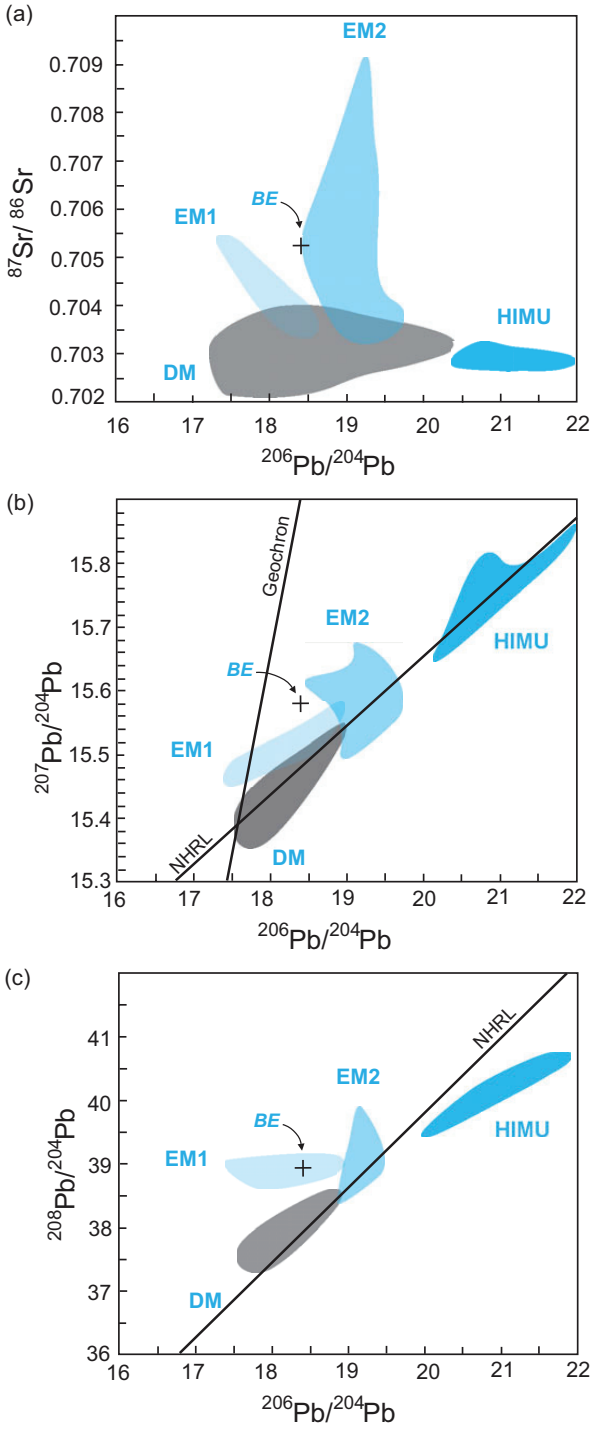

Figure 6.11 Mantle sources as defined by lead isotopes (data from Hofmann, 2014). (a) $^{206}Pb/^{204}Pb$ versus $^{87}Sr/^{86}Sr$; (b) $^{206}Pb/^{204}Pb$ versus $^{207}Pb/^{204}Pb$; (c) $^{206}Pb/^{204}Pb$ versus $^{208}Pb/^{204}Pb$. Bulk silicate Earth (BE) is shown for reference (see Table 6.6 for values). The geochron assumes single-stage Pb-evolution from 4.55 Ga. NHRL is the Northern Hemisphere Reference Line (after Hart, 1984). Volcanic rocks which plot above the NHRL are said to have an

deviation from the reference line, such that for a given data set (DS)

$$\Delta 7/4 = \left[\left(^{207}Pb/^{204}Pb\right)_{DS} - \left(^{207}Pb/^{204}Pb\right)_{NHRL}\right] \times 100 \quad (6.10)$$

$$\Delta 8/4 = \left[\left(^{208}Pb/^{204}Pb\right)_{DS} - \left(^{208}Pb/^{204}Pb\right)_{NHRL}\right] \times 100 \quad (6.11)$$

A similar notation was used for $^{87}Sr/^{86}Sr$:

$$\Delta Sr = \left[\left(^{87}Sr/^{86}Sr\right)_{DS} - 0.7\right] \times 10000 \quad (6.12)$$

There are three models which are used to explain the origin of the enriched mantle. The first model is subduction-driven recycling, in which compositionally distinct components such as marine sediment, crustal sediment and upper and lower crust are recycled into the mantle via subduction. The second model is that of mantle metasomatism, that is, enriched by melts and fluids within the mantle (see Willbold and Stracke, 2010, for an overview). The third model is based upon the similarity between enriched mantle and the sub-continental lithosphere and suggests that the enrichment is due to the mixing of sub-continental lithosphere into the mantle. EM1 has some compositional similarity with the lower continental crust and may represent the mixing of recycled lower crust. Alternatively, it may be enriched via mantle metasomatism. EM2 has affinities with the upper continental crust and may represent the recycling of continentally derived sediment, continental crust, altered oceanic crust, or ocean island crust.

(e) *Other reservoirs.* In the 1980s and 1990s, as the field of mantle isotope geochemistry expanded, every 'reservoir' that was identified seemed unique. However, the mantle geochemical database has increased exponentially since that time and coupled

Figure 6.11 (*cont.*) enriched (*DUPAL*) signature. The non-controversial mantle reservoirs include the depleted mantle (DM) represented by global MORB, enriched mantle (EM1 by the Pitcairn Islands and EM2 by the island of Samoa), and high-μ mantle (HIMU) by the Cook and St Helena Islands. It is significant that the enriched mantle sources have some overlap with continental crustal sources (see Figure 6.10).

with our improved understanding of melt extraction and mixing processes in the mantle we now define the number of compositional 'end members' or reservoirs as the minimum needed to explain the observed isotopic diversity. These are the DM, EM1, EM2 and HIMU end members. Other 'components', such as *PREMA*, *PHEM*, *C* and *FOZO*, represent compositional domains that may not be required, although this is the subject of ongoing discussion (see Hofmann, 2014, for an overview). Nonetheless, the reader may come across these terms in the literature and it is therefore useful to define them here.

PREMA (prevalent mantle) was defined by Zindler and Hart (1986) using basalts from ocean islands, intra-oceanic island arcs and continental basalt suites. It is characterised by $^{143}Nd/^{144}Nd = 0.5130$, $^{87}Sr/^{86}Sr = 0.7033$ and $^{206}Pb/^{204}Pb = 18.2–18.5$.

PHEM (primitive helium mantle) was defined by Farley et al. (1992) using basalts mostly from the Samoan islands to account for their high $^{3}He/^{4}He$, along with near-BE Sr and Nd compositions ($^{87}Sr/^{86}Sr = 0.7042–0.7052$, $^{143}Nd/^{144}Nd = 0.51265–0.51280$) and moderately radiogenic Pb isotopes ($^{206}Pb/^{204}Pb = 18.5–19.0$).

FOZO (focal zone) was originally defined by Hart et al. (1992) as the region or zone in which MORB and OIB isotopic signatures seemed to converge (or focus, hence the term 'focal zone'). Compositionally, it is similar to PREMA and C, although the term was later modified by Stracke et al. (2005) to extend the MORB array in $^{206}Pb/^{204}Pb$ (or $^{208}Pb/^{206}Pb$) versus $^{87}Sr/^{86}Sr$ space. According to this later definition, the FOZO field identified in lavas from the Cook–Austral islands is adjacent to but distinct from HIMU in Pb isotope space.

C (common component). This component was defined by Hanan and Graham (1996), using the convergence of MORB Pb isotope arrays. It is very similar to FOZO, with $^{87}Sr/^{86}Sr = 0.703–0.704$, $^{143}Nd/^{144}Nd = 0.51285–0.51295$, $^{206}Pb/^{204}Pb = 19.2–19.8$, $^{207}Pb/^{204}Pb = 15.55–15.65$ and $^{208}Pb/^{204}Pb = 38.8–39.6$.

(f) *The origin of oceanic basalts*. The recognition of a range of isotopic signatures in oceanic basalts associated with distinct mantle reservoirs has led to an appreciation of the complexity of mantle processes. This can be seen at the local scale, where, for example, detailed and high-precision isotopic studies of the Hawaiian–Emperor plume have identified multiple depleted and re-fertilised mantle components within a single plume (Béguelin et al., 2019; Harrison et al., 2020). At the global scale our perception of the mantle has changed from a simple two-layer mantle to one that is chemically and isotopically heterogeneous and contains at least four reservoirs. Sampling this heterogeneity is not trivial, for the process of partial melting homogenises those diverse compositions which have resulted from melt extraction, hybridization and mixing within the mantle.

6.3.2.2 Continental Crustal Sources

The isotopic composition of rocks from the continental crust is extremely variable, and isotope ratios are strictly comparable only if the samples are all of the same age. For this reason, compositional differences are best considered relative to a normalising parameter which takes into account the age of the sample. One such parameter is the composition of CHUR and its evolution through time; this is discussed in Section 6.3.3 below. Crustal samples may be plotted on a graph of isotopic composition versus time relative to reference reservoir (Figure 6.3). For Sr, Nd and Hf isotopes this can be quantified in terms of the epsilon notation, whereas Os isotopes use the gamma notation (these notations are discussed in Section 6.3.4). The general isotopic characteristics of crustal reservoirs are given in Table 6.6, and the isotopic compositions of some typical crustal rocks are presented in Table 6.7.

(a) *Upper continental crust.* The upper (sialic) continental crust is characterised by high Rb/Sr and consequently has high $^{87}Sr/^{86}Sr$ ratios. Neodymium and Hf isotope ratios, on the other hand, are low relative to mantle values as a consequence of the low Sm/Nd and Lu/Hf ratios which characterise the continental crust. U and Th are enriched in the upper continental crust and give rise to high ^{206}Pb, ^{207}Pb and ^{208}Pb isotope ratios.

(b) *Middle continental crust.* The mid-continental crust represents extensive areas of exhumed amphibolite facies gneisses found in granite–gneiss terrains. These rocks have retarded $^{143}Nd/^{144}Nd$ and $^{176}Hf/^{177}Hf$, and $^{87}Sr/^{86}Sr$ is generally lower than in the upper crust. Uranium, however, is depleted, and Th is lower than in the upper crust but not as depleted as U. $^{206}Pb/^{204}Pb$ and $^{207}Pb/^{204}Pb$ may be lower than in the mantle.

(c) *Lower continental crust.* The lower continental crust is characterised by mafic rocks and granulite facies metamorphosed rocks and is often strongly Rb-depleted. Thus, it has low $^{87}Sr/^{86}Sr$ ratios which are not greatly different from modern mantle values. This means that a modern granite derived from the lower crust will have an initial $^{87}Sr/^{86}Sr$ ratio very similar to one derived from the mantle. U/Pb and Th/Pb ratios in the lower crust are lower than modern mantle values so that ^{206}Pb, ^{207}Pb and ^{208}Pb isotope ratios are all very low and are therefore sensitive indicators of lower crust and mantle reservoirs.

(d) *Continental lithosphere.* The continental lithosphere is the region of mantle that lies beneath and is attached to continental crust. In areas of ancient crust it is extremely thick. It is known as the continental lithospheric mantle (CLM) or the sub-continental lithospheric mantle (SCLM) and is extremely variable in isotopic composition. Isotope data from CLM-derived mantle xenoliths show that the CLM typically has higher $^{87}Sr/^{86}Sr$ (>0.7045), lower ε_{Nd} (<0) and higher $^{207}Pb/^{204}Pb$ (at a given $^{206}Pb/^{204}Pb$) when compared with asthenospheric mantle sources (Pearson, 1999). Nd and Hf isotopes are decoupled during the fractionation of the lithospheric mantle with the result that Nd isotopes are more readily reset than Hf isotopes during mantle metasomatism. Only very young (0.35 Ga) and small (<5%) depletion events can fractionate Lu from Hf, which results in $^{176}Hf/^{177}Hf$ compositions in the CLM similar to those in the present-day convecting mantle ($\varepsilon_{Hf\ today} \sim +11$). Older and more extensive melting generally results in $^{176}Hf/^{177}Hf$ ratios that are more radiogenic than is seen in the convecting mantle and typically exceeds compositions recorded by mantle xenoliths. Os isotopic ratios in the CLM are in the range $^{187}Os/^{188}Os = 0.1100–0.1205$ and are statistically distinct from peridotites from the convecting mantle ($^{187}Os/^{188}Os = 0.1225–0.1265$; Pearson and Wittig, 2014). This is illustrated in Figure 6.12.

Most cratons are underlain by old CLM and the Re–Os isotope system is the preferred method for dating this ancient lithospheric mantle (Rudnick and Walker, 2009; Farmer, 2014). One of the best examples of the application of this method is from the Kaapvaal craton where the Mesoarchean craton was shown to be underlain by older, Eoarchean and Hadean lithospheric mantle which in turn is surrounded by lithospheric mantle reworked between 3.0 Ga and 2.0 Ga (Pearson and Wittig, 2014).

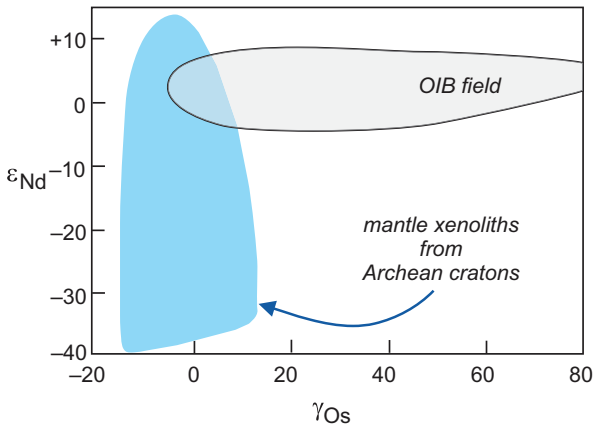

Figure 6.12 The isotopic composition of the continental lithospheric mantle (CLM) (after White, 2010; with permission from Elsevier). A γ_{Os} versus ε_{Nd} diagram (see Section 6.3.4) showing the difference in composition between xenoliths from the CLM (mantle xenoliths from Archaean cratons in Siberia, Wyoming, and South Africa) and that of ocean island basalts (Cook–Austral islands, Hawai'I and Samoa) representing the convecting mantle.

6.3.2.3 Seawater

A knowledge of the isotopic composition of seawater is important in studies of magmatic rocks which may have interacted with seawater such as the sea-floor alteration of oceanic basalts or the genesis of magmas in an arc environment, and in sediments such as the alteration rinds on sea-floor nodules. Its composition is related to the residence time of an element in seawater. This is the average time an element remains in seawater and is defined by the expression:

$$t_A = A/(dA/dt) \tag{6.13}$$

where t_A is the residence time, A is the total amount of the element dissolved in the oceans, and dA/dt is the amount of the element introduced into or removed from the ocean per unit time assuming a steady state. It is estimated that the oceans mix over ~1000 years so that an element with a residence time longer than this will be homogeneously distributed in the ocean, whereas an element which has a shorter residence time will reflect regional variations in isotopic composition (see Frank, 2002, for an overview).

The residence time of Sr in seawater is a few million years and the oceans are regarded as a well-mixed reservoir with uniform $^{87}Sr/^{86}Sr = 0.70918$ (Frank, 2002). This signature is the result of the solubility of

Sr and the complex interplay between continental run-off, mid-ocean ridge hydrothermal activity, input from old sediments and the extraction of Sr into carbonate shells and their subsequent burial in marine sediments. Osmium has a shorter residence time, 10,000–20,000 years. Veizer et al. (1999) and Peucker-Ehrenbrink and Ravizza (2000) demonstrate how Sr and Os isotope compositions have changed in seawater over the past 60 million years (Figure 6.13). They showed that isotope ratios of both elements were relatively low in the late Cretaceous and have gradually increased with time, probably as a result of increased continental weathering related to the uplift of major mountain ranges. The seawater curves for Sr in the Phanerozoic, and particularly the high precision curve for the last 70 Ma, has been used to date sediments and to determine the time of diagenetic processes.

In contrast, Nd, Hf and Pb have shorter residence times: Nd 600–2000 years, Hf about 200 years, and Pb 50–400 years (Frank, 2002). These shorter residence times indicate that the oceans are not well mixed with respect to isotopes of Nd, Hf and Pb. In fact, it has been long known that the Nd isotopic composition of seawater (using the ε notation) ranges from ε_{Nd} −27 to +1. This variability in $^{143}Nd/^{144}Nd$ between different ocean basins reflects the local Nd input from surrounding continents. The most radiogenic Nd isotopic compositions are found in the Arctic ($\varepsilon_{Nd} = -10.1$), the least radiogenic in the Pacific ($\varepsilon_{Nd} = -3.9$), and the Atlantic ($\varepsilon_{Nd} = -11.4$) and Indian Oceans ($\varepsilon_{Nd} = -6.6$) have intermediate compositions (Lacan et al., 2012). This pattern is also mirrored in the Hf and Pb compositions. $^{177}Hf/^{176}Hf$ in the Atlantic and Pacific Oceans ranges from ε_{Hf} −5.7 to +8.6 (Rickli et al., 2014, and references therein). Manganese nodules concentrate Pb from seawater and have $^{206}Pb/^{204}Pb$ in the range 18.5–19.3 (von Blanckenburg et al., 1996).

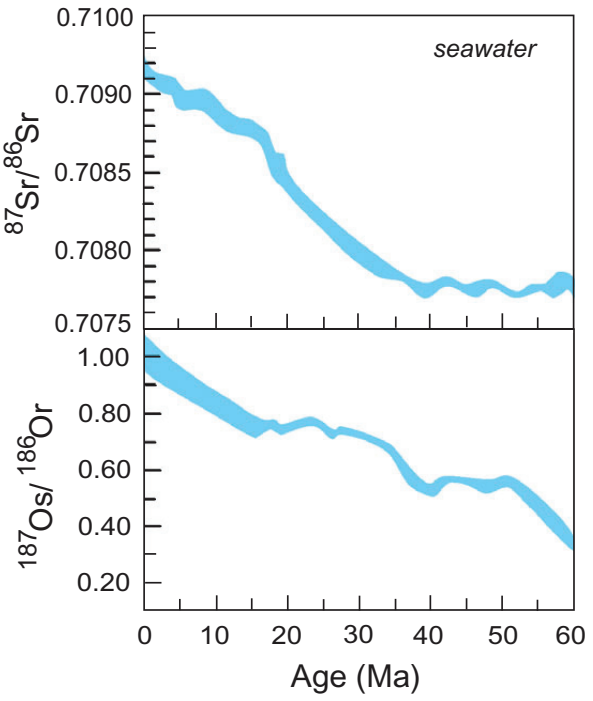

Figure 6.13 The isotopic variation in the composition of seawater over the last 60 Ma. The data for $^{87}Sr/^{86}Sr$ are from Veizer et al. (1999) and for $^{187}Os/^{188}Os$ from Peucker-Ehrenbrink and Ravizza (2000). The variation is thought to be associated with an increase in continental weathering during this time interval.

6.3.3 Mantle Evolution Diagrams and the Isotopic Evolution of the Mantle with Time

The isotopic compositions of mantle source regions change with time as a function of their parent/daughter element ratios. These may be plotted on isotope evolution diagrams to show the change in isotopic composition of the reservoir with time. They are calculated by measuring the isotopic composition of the mantle at the present day using modern lavas and by determining initial ratios from isochron diagrams using samples of ancient mantle melts. Diagrams of this type are also useful for depicting the isotopic evolution of crustal rocks of different ages and with different parent–daughter isotope ratios. All evolution diagrams require a starting isotopic composition for the Earth at ~4.57 Ga, and as previously stated this is usually linked to the composition of meteorites (see Table 6.3).

The isotopic evolution of the mantle over geological time can be represented graphically in two different ways. One type of diagram shows the change in the isotope ratio from the beginning of the Earth to the present. This is illustrated for Nd isotopes in Figure 6.14a, which shows a linear increase in the $^{143}Nd/^{144}Nd$ ratio in the depleted mantle and in the chondrite reservoir with time. A second type of diagram uses the ε (epsilon) notation to display the isotopic composition relative to CHUR, the chondrite standard (Figure 6.14b). In this case CHUR has a value of zero and the ε value for the depleted mantle increases with time. A full discussion of the ε notation for Nd and Hf isotopes

and its equivalent for Os isotopes – the γ notation – is given in Section 6.3.4.

6.3.3.1 The Evolution of Nd Isotopes with Time

The $^{143}Nd/^{144}Nd$ isotopic composition of the bulk Earth is thought to be approximated by the composition of chondritic meteorites (CHUR). The linear evolution of CHUR with time is shown in Figure 6.14a. However, studies of modern oceanic basalts, as well as ancient and modern granitic rocks, indicate that many igneous rocks are derived from a mantle composition which has a higher Sm/Nd than CHUR and has a higher $^{143}Nd/^{144}Nd$ ratio relative to CHUR – this is the depleted mantle (DM) reservoir. In Figure 6.14b three common models for the evolution of the depleted mantle reservoir are shown relative to CHUR using epsilon notation (see Section 6.3.4 and Box 6.2). The main differences between these models is the time at which the DM differentiated from the bulk Earth, and whether or not the depletion varied with time. Goldstein (1984) used a single-stage, linear evolution between the present day and the formation of the Earth at 4.6 Ga (Figure 6.14b, line 1), whereas DePaolo (1981a) used a non-linear model (Figure 6.14b, line 2).

Nägler and Kramers (1998) developed a $^{143}Nd/^{144}Nd$ evolution curve using mantle melts of known age free from crustal contamination and metamorphism (Figure 6.14b, line 3). They show that the average ε_{Nd} for the early Archaean is fairly constant, whereas from about 3.0 Ga to the present, ε_{Nd} steadily increases to a present-day value of +10. They conclude that the average ε_{Nd} value for the early Archaean has no geological significance, being partly an analytical artefact and partly is the product of uncertainty in the measurement of Nd in chondrites. In contrast, the steady increase in ε_{Nd} from 3 Ga to the present implies the progressive extraction of the LREE from the Earth's mantle through the formation of the continental crust. The Sm/Nd of the continental crust is highly fractionated (<1.0) relative to CHUR

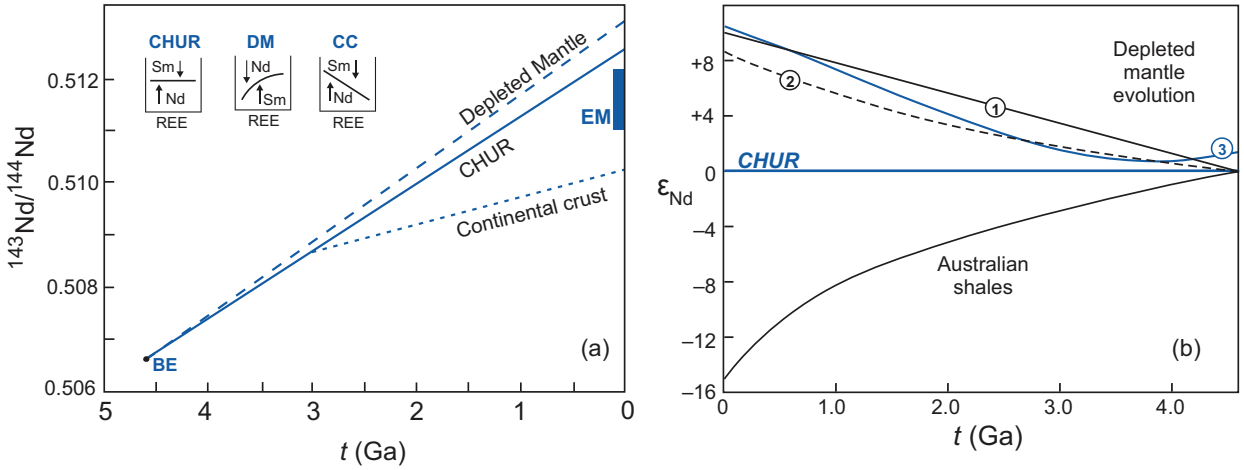

Figure 6.14 Evolution of Nd isotopes with time. (a) The evolution of $^{143}Nd/^{144}Nd$ for CHUR (solid line), DM (dashed line), and the continental crust (CC, dotted line) from the initial composition of the bulk Earth (BE). The fractionation of Sm/Nd from BE is normalised to unity for CHUR; DM has high Sm/Nd resulting in higher $^{143}Nd/^{144}Nd$; and CC has lower Sm/Nd which retards $^{143}Nd/^{144}Nd$ evolution with time. The enriched mantle (EM) component (blue box) shows some affinity with the continental crust inasmuch as it also has retarded $^{143}Nd/^{144}Nd$. Note that in the Sm–Nd system, the crust shows retarded isotopic evolution, whereas in the Rb–Sr system it shows accelerated evolution relative to BE and the mantle. (b) The contrasting evolution of the continental crust and mantle using ε_{Nd} notation (Section 6.3.4). CHUR = 0 and plots as a horizontal line. Three curves are shown for the evolution of the depleted mantle. Line 1 assumes a single-stage, linear evolution for the depleted mantle between 4.5 Ga ($\varepsilon_{Nd} = 0$) and the present day ($\varepsilon_{Nd} = +10$) (Goldstein et al., 1984). Curve 2 assumes an exponential evolution that is derived from the equation $0.25t^2 - 3t + 8.5$, where t is the time before present in Ga (DePaolo, 1981a). Curve 3 is a multi-stage model that shows an inflection at ~3 Ga thought to reflect the initiation of the growth of the continental crust (Nägler and Kramers, 1998). The curve in the bottom half of the diagram is for Australian shales and approximates to the evolution of average continental crust through time (Allegre and Rousseau, 1984). Note the time axes in (a) and (b) are reversed.

Box 6.2 Worked example of ε_{Nd} calculation

(1) *ε_{Nd} values for an isochron*

Using the data from Hamilton et al. (1979a) in Table 6.2, presented in Figure 6.2:
initial ratio = 0.50809
isochron age = 3.54 Ga
decay constant $\lambda = 6.54 \times 10^{-12}$ yr^{-1}

$$\varepsilon_{\mathrm{Nd}}^{isochron,t} = \left[\frac{\left(^{143}\mathrm{Nd}/^{144}\mathrm{Nd}\right)_{initial}}{\left(^{143}\mathrm{Nd}/^{144}\mathrm{Nd}\right)_{CHUR,t}} - 1 \right] \times 10^4 \tag{6.14}$$

First calculate the value of CHUR at time t using the CHUR values from Table 6.4 (normalised to ^{146}Nd/^{144}Nd = 0.7219, Sm/Nd = 0.325):

$$\left(^{143}\mathrm{Nd}/^{144}\mathrm{Nd}\right)_{CHUR,t} = \left(^{143}\mathrm{Nd}/^{144}\mathrm{Nd}\right)_{CHUR\ today} - \left(^{147}\mathrm{Sm}/^{144}\mathrm{Nd}\right)_{CHUR\ today} \times \left(e^{\lambda t} - 1\right) \tag{6.15}$$

$$\begin{aligned}\mathrm{CHUR},\ t &= 0.512638 - (0.1967 \times [e^{(6.54\times10^{-12})\times(3.54\times10^{+9})} - 1]) \\ &= 0.512638 - 0.004607 \\ &= 0.508031\end{aligned}$$

Then using Eq. 6.12:

$$\begin{aligned}\varepsilon_{\mathrm{Nd}}^{isochron,\ t} &= [(0.50809/0.508031) - 1] \times 10^4 \\ &= 1.16\end{aligned}$$

(2) *ε_{Nd} value for a rock at its time of formation*

Using a single rock from Table 6.2 (sample HSS-74, sodic porphyry, ^{147}Sm/^{144}Nd = 0.1030,

$$\varepsilon_{\mathrm{Nd}}^{t} = \left[\frac{\left(^{143}\mathrm{Nd}/^{144}\mathrm{Nd}\right)_{rock,t}}{\left(^{143}\mathrm{Nd}/^{144}\mathrm{Nd}\right)_{CHUR,t}} - 1 \right] \times 10^4 \tag{6.18}$$

First, calculate ^{143}Nd/^{144}Nd rock at 3.54 Ga:

$$\left(^{143}\mathrm{Nd}/^{144}\mathrm{Nd}\right)_{rock,t} = \left(^{143}\mathrm{Nd}/^{144}\mathrm{Nd}\right)_{rock\ today} - \left(^{147}\mathrm{Sm}/^{144}\mathrm{Nd}\right)_{rock\ today} \times \left(e^{\lambda t} - 1\right) \tag{6.19}$$

$$\begin{aligned}\varepsilon_{\mathrm{Nd}}^{t} &= 0.510487 - (0.1030 \times [e^{(6.54\times10^{-12})\times(3.54\times10^{+9})} - 1]) \\ &= 0.510487 - 0.002412 \\ &= 0.508075\end{aligned}$$

Then from Eq. 6.14:

$$\begin{aligned}\varepsilon_{\mathrm{Nd}}^{t} &= [(0.50807/0.512638) - 1] \times 10^4 \\ &= 0.87\end{aligned}$$

Continued

Box 6.2 (cont.)

(3) *ε_{Nd} value for a rock at the present day*

The present-day deviation from CHUR may be easily calculated from:

$$\varepsilon_{\mathrm{Nd}}^{\mathrm{today}} = \left[\frac{\left(^{143}\mathrm{Nd}/^{144}\mathrm{Nd}\right)_{rock,today}}{\left(^{143}\mathrm{Nd}/^{144}\mathrm{Nd}\right)_{CHUR,today}} - 1\right] \times 10^4 = [(0.510487/0.512638) - 1] \times 10^4 = -41.96 \quad (6.20)$$

Summary

$\varepsilon_{\mathrm{Nd}_{3.54\mathrm{Ga}}}^{\mathrm{isochron}} = 1.16$

$\varepsilon_{\mathrm{Nd}_{3.54\mathrm{Ga}}}^{\mathrm{sample\ HSS\text{-}74}} = 0.87$

$\varepsilon_{\mathrm{Nd}_{3.54\mathrm{Ga}}}^{\mathrm{sample\ HSS\text{-}74}} = -41.96$

and shows retarded $^{143}Nd/^{144}Nd$ evolution with time (Figure 6.14a).

6.3.3.2 The Evolution of Hf Isotopes

During mantle melting the fractionation of Lu relative to Hf is more extreme than for Sm and Nd. This generates a more strongly supra-chondritic ε_{Hf} signature than seen in ε_{Nd} for the same melting event. This is documented in modern oceanic basalts where ε_{Hf} is up to 1.5 times greater than ε_{Nd} (Vervoort and Blichert-Toft, 1999). Söderlund et al. (2004) proposed a single-stage evolution line for $^{176}Hf/^{177}Hf$ in the mantle (expressed as ε_{Hf} in Figure 6.15a) from ~4.6 Ga. This model is consistent with the work of Kemp et al. (2010), who showed from Hf isotopes in zircon that there was a depleted mantle in the Hadean. However, some authors have argued for a supra-chondritic mantle in the early Earth (Caro and Bourdon, 2010; Kemp and Hawkesworth, 2014).

6.3.3.3 The Evolution of Os Isotopes

Re is a moderately incompatible element during partial melting and so enters the melt phase, whereas Os is strongly compatible and remains in the unmelted residue. This leads to high Re/Os ratios in oceanic crust and relatively low Re/Os ratios in the depleted mantle. In felsic melts, however, Re and Os are both incompatible, and their concentrations are very low in the continental crust. This is very different from the Nd, Hf and Pb isotopic systems. These geochemical properties mean that the Os isotopic evolution of the upper mantle reflects the extraction of basaltic melts and is unlikely to reflect any interaction with the continental crust. Mantle melts which have supra-chondritic Os isotopic ratios are thought to be derived by the melting of ancient, high Re/Os, basaltic crust which has been recycled back into the mantle, making Os isotopes important 'tracers' of recycled ancient oceanic crust.

Figure 6.15b shows that OIB defines a wide range of $^{187}Os/^{188}Os$ ratios. This can be due to seawater contamination and/or the rapid in-growth of radiogenic ^{187}Os in melts which have a high initial Re contents. This 'Os enrichment' trend is seen in mantle plume–related samples, whereas some ophiolitic chromites have near-chondritic Os signatures (Figure 6.15b). Both the chondritic and the enriched 'reservoirs' must be long-lived features of the mantle since the parent isotopes require a long period of time to evolve into the isotope ratios measured today.

6.3.3.4 The Evolution of Pb Isotopes

The isotopic evolution of lead isotopes over geological time is illustrated in Figures 6.16 and 6.17. Given that

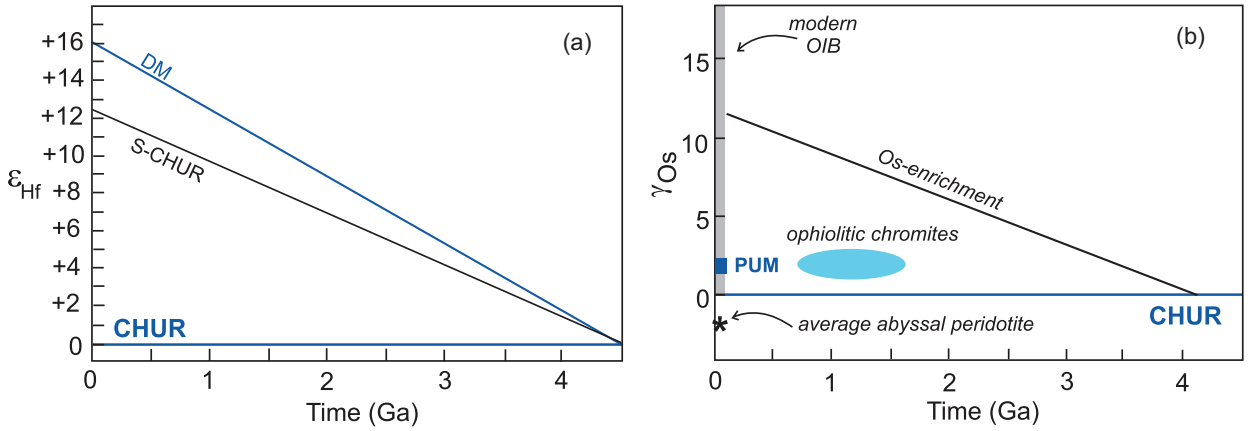

Figure 6.15 Mantle evolution with time for Hf and Os isotopes. (a) Hafnium isotopes (using ε_{Hf} notation) showing two linear models for mantle evolution for ε_{Hf} in the depleted mantle (DM) (after Söderlund et al., 2004) and for S-CHUR (after Caro and Bourdon, 2010). (b) Osmium isotopes (using γ notation) showing Os enrichment of the mantle as a function of time. Note the wide range of modern OIB compositions and the near-chondritic nature of some ophiolitic chromites; the primitive upper mantle (PUM), CHUR and average abyssal peridotite are shown for reference. (Data sources from Rollinson 2007)

there are three independent decay schemes in the lead isotopic system, Pb data is not displayed on the same type of time versus isotope ratio diagram as is used for Sr, Nd, Hf and Os isotopes; rather, a concordia diagram is used. On this diagram 'families' of concordia (growth) curves can be drawn for different $^{238}U/^{204}Pb$ (μ values) (Figure 6.16a, b). Each curve can be calibrated for time, and equal time points can be used to generate isochrons (Figure 6.16b, c). Bolhar et al. (2020) used this approach to calculate a Pb isochron age of 2054 ± 99 Ma for phoscorites and carbonatites from the Phalaborwa Complex, South Africa. These authors then used the isochron age to evaluate the relative crust and mantle contributions to the sulphide genesis.

The evolution of Pb isotopes in the mantle through time is shown in Figure 6.17 on a plot of $^{206}Pb/^{204}Pb$ versus $^{207}Pb/^{204}Pb$ (after Kramers and Tolstikhin, 1997). This figure illustrates the evolution of Pb isotopes over time from a chondritic starting composition of the early Earth. It is clear that there is a wider range of $^{207}Pb/^{204}Pb$ than $^{206}Pb/^{204}Pb$ in early Earth history and wider range of $^{206}Pb/^{204}Pb$ relative to $^{207}Pb/^{204}Pb$ during the more recent evolution of the Earth. This diagram also shows that a HIMU mantle evolves with a lower $^{207}Pb/^{204}Pb$ than that of the depleted mantle (Kamber, 2015).

6.3.4 Epsilon, Gamma and Mu Notations

Isotope ratios are only strictly comparable if the samples are of the same age. It is therefore useful to have an alternative way of expressing isotope ratios which allows greater flexibility in the way in which they are represented and is independent of their age. This is the basis of the ε notation used in the Nd, Hf and Sr systems (DePaolo and Wasserburg, 1976) and the γ notation used for Os isotopes (Walker et al., 1989).

6.3.4.1 Calculating Epsilon Values

The epsilon parameter is a measure of the difference between an isotope ratio from a sample or a suite of samples such as $^{143}Nd/^{144}Nd$ or $^{176}Hf/^{177}Hf$, and a reference value, typically CHUR. It is expressed in parts per 10^4 (see worked example in Box 6.2). Epsilon values are used in three slightly different ways, as described below.

(a) *Epsilon values calculated for an isochron.* The epsilon value for an isochron is calculated using the expression:

$$\varepsilon_{Nd}^{isochron,t} = \left[\frac{\left(^{143}Nd/_{144}Nd\right)_{initial}}{\left(^{143}Nd/_{144}Nd\right)_{CHUR,t}} - 1 \right] \times 10^4 \qquad (6.14)$$

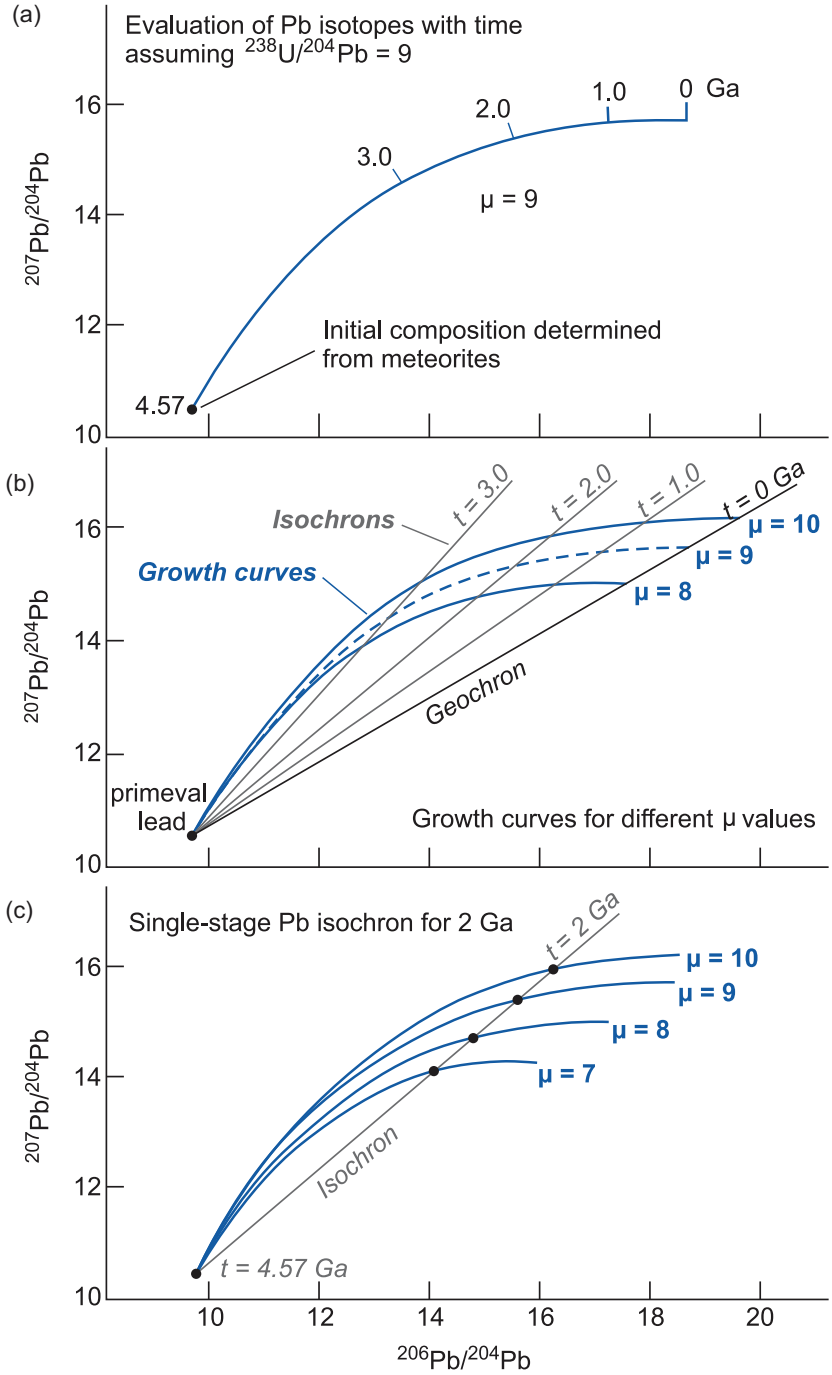

Figure 6.16 Lead isotope evolution curves. All panels show the growth curve(s) for $^{207}Pb/^{204}Pb$ and $^{206}Pb/^{204}Pb$ through time. (a) The isotopic evolution of $^{207}Pb/^{204}Pb$ and $^{206}Pb/^{204}Pb$ defines a curve because the two isotope ratios are produced at different rates. The starting composition at 4.57 Ga is taken from the isotopic composition of troilite in the Canyon Diablo meteorite (Box 6.1). This growth curve assumes a $^{238}U/^{204}Pb$ ratio (μ value) = 9.0. (b) A family of growth curves showing lead isotope growth associated with different $^{238}U/^{204}Pb$ ratios (μ = 8, 9 and 10), from primeval Pb at 4.57 Ga to the present. Isochrons for 0, 1.0, 2.0 and 3.0 Ga are created by joining similar age points on each growth curve. The zero Ga isochron is known as the geochron (see Section 6.2.1.4). (c) A single-stage lead isochron for 2.0 Ga. The isochron joins the 2.0 Ga points on the growth curves for four different μ values and passes through the primeval lead composition at 4.57 Ga; it represents a suite of samples which evolved from 4.57 Ga until 2.0 Ga. These values have remained 'frozen' in the samples since 2.0 Ga. The growth curves in these diagrams are based upon the assumption that the lead isotopes have evolved uninterrupted since the formation of the Earth. This is a simplification; normally a more complex model of lead isotope evolution is adopted, such as that of Stacey and Kramers (1975) or Kramers and Tolstikhin (1997).

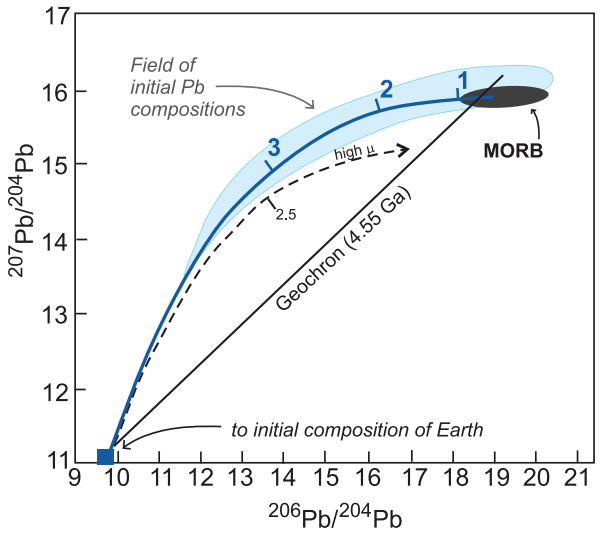

Figure 6.17 The evolution of lead isotopes with time. A $^{206}Pb/^{204}Pb$ versus $^{207}Pb/^{204}Pb$ plot showing the evolution of the depleted mantle (blue curve; after Kramers and Tolstikhin, 1997) and a HIMU mantle source (dashed curve; after Kamber, 2015). Note that the HIMU source has lower $^{207}Pb/^{204}Pb$ than DM for young samples. The MORB field and the field of initial Pb composition for crustal and mantle rocks are indicated. The numbers on the isotope evolution curves represent the time before the present in Ga.

where $(^{143}Nd/^{144}Nd)_{initial}$ is the measured initial ratio of the sample suite at the time of its formation (t) and is calculated from the isochron. $(^{143}Nd/^{144}Nd)_{CHUR,t}$ is the isotope ratio of CHUR at time (t) given by the expression:

$$\left(^{143}Nd/^{144}Nd\right)_{CHUR,t} = \left(^{143}Nd/^{144}Nd\right)_{CHUR\ today} - \left(^{147}Sm/^{144}Nd\right)_{CHUR\ today} \times \left[e^{\lambda t} - 1\right] \quad (6.15)$$

where λ is the decay constant of ^{147}Sm to ^{143}Nd and t is the time of interest. Values for CHUR are given in Table 6.3. It should be noted that different laboratories use different normalising values for $^{143}Nd/^{144}Nd$ and a consistent value of CHUR must be selected. However, if this is done, then any variation in $^{143}Nd/^{144}Nd$ due to interlaboratory differences virtually disappears, making the epsilon notation a very useful way of displaying data generated in different laboratories.

The equations for the Hf system are similar:

$$\varepsilon_{Hf}^{isochron,t} = \left[\frac{\left(^{176}Hf/_{177}Hf\right)_{initial}}{\left(^{176}Hf/_{177}Hf\right)_{CHUR,t}} - 1\right] \times 10^4 \quad (6.16)$$

where $(^{176}Hf/^{177}Hf)_{initial}$ is the measured initial ratio of the sample suite at the time of its formation (t) and is calculated from the isochron. $(^{176}Hf/^{177}Hf)_{CHUR,t}$ is the isotope ratio of CHUR at time (t) and is given by the expression:

$$\left(^{176}Hf/^{177}Hf\right)_{CHUR,t} = \left(^{176}Hf/^{177}Hf\right))_{CHUR\ today} - \left(^{176}Lu/^{177}Hf\right)_{CHUR\ today} \times \left[e^{\lambda t} - 1\right] \quad (6.17)$$

where λ is the decay constant of ^{176}Lu to ^{177}Hf and t is time in the past for the part of the evolution curve of interest. Values for CHUR are given in Table 6.3.

(b) *Epsilon values for individual samples at their time of formation.* The epsilon value for an individual rock sample calculated for time t, the time of formation, is usually tabulated along with Sm–Nd and Lu–Hf isotopic data. It is calculated using the expressions:

$$\varepsilon_{Nd}^{t} = \left[\frac{\left(^{143}Nd/_{144}Nd\right)_{rock,t}}{\left(^{143}Nd/_{144}Nd\right)_{CHUR,t}} - 1\right] \times 10^4 \quad (6.18)$$

$$\varepsilon_{Hf}^{t} = \left[\frac{\left(^{176}Hf/_{177}Hf\right)_{rock,t}}{\left(^{176}Hf/_{177}Hf\right)_{CHUR,t}} - 1\right] \times 10^4 \quad (6.19)$$

where the composition of CHUR at time t is calculated from Eq. 6.15 or Eq. 6.17. When calculating $\varepsilon_{Nd}{}^{t}$ for individual samples the value for t may be taken either from the isochron to which the samples belong or from an independent estimate of the age using some other geochronological technique such as a U–Pb zircon age.

(c) *Epsilon values for individual samples at the present day.* An epsilon value may also be calculated for an individual sample at the present day using the expression:

$$\varepsilon_{Nd}^{today} = \left[\frac{\left(^{143}Nd/_{144}Nd\right)_{sample\ today}}{\left(^{143}Nd/_{144}Nd\right)_{CHUR\ today}} - 1\right] \times 10^4 \quad (6.20)$$

The magnitude of the present-day ε_{Nd} value reflects the degree of time-integrated depletion in Nd relative to CHUR, as expressed by the Sm/Nd ratio (see $f_{Sm/Nd}$, Section 6.3.4.6). Again, such calculations are equally relevant to the Lu–Hf system and may occasionally be applied to the Rb–Sr system.

6.3.4.2 Epsilon Values for Sr Isotopes

Epsilon values may be calculated from $^{87}Sr/^{86}Sr$ ratios in exactly the same way as for Nd isotopes. Original estimates for the $^{87}Sr/^{86}Sr$ composition of the bulk Earth as a reference value vary significantly, but Salters and Stracke (2004) define a well-constrained BE composition of 0.7045 (Table 6.3). Using a realistic trace element ratio (Rb/Sr = 0.29–0.30) and assuming an initial $^{87}Sr/^{86}Sr$ of 0.69898, their BE composition yields $^{87}Sr/^{86}Sr$ values which are in agreement with values for modern MORB.

6.3.4.3 Calculating Gamma Values for Os Isotopes

The bulk Earth has near-chondritic $^{187}Os/^{188}Os$ and any deviations are relatively small, so a percentage variation from CHUR is easily expressed using the expression:

$$\gamma_{Os} = \left[\frac{\left(^{187}Os/_{188}Os\right)_{sample} - \left(^{187}Os/_{188}Os\right)_{CHUR}}{\left(^{187}Os/_{188}Os\right)_{CHUR}} - 1 \right] \times 100 \tag{6.21}$$

The 'gamma' parameter is directly analogous to the epsilon notation, but uses percentage of deviation instead of parts per 10^4. Here we term the reference material as CHUR; other workers use the term 'CHON'. The two are interchangeable and reference values are given in Table 6.3a.

6.3.4.4 Reducing Epsilon Uncertainties on Isochron Diagrams

Points on a Sm–Nd isochron typically plot far from the origin. In order to obtain a greater degree of accuracy in determining the initial ratio, it is possible to plot felsic rocks (with small Sm/Nd ratios) on the same isochron as basic igneous rocks with larger Sm/Nd ratios *if they are cogenetic*. As cogenicity is not always established, an alternative method for reducing the error associated with calculating initial ratios, and hence epsilon values, is to translate the origin of the $^{147}Sm/^{144}Nd$ axis from zero to the present-day composition of CHUR (0.1960; Table 6.3) before performing the line-fitting operation (Fletcher and Rosman, 1982). With this translation the $^{147}Sm/^{144}Nd$ origin usually falls within the compositional range of the data set and results in a more precise determination of the intercept. This intercept value is the present-day composition of $^{143}Nd/^{144}Nd$ in a hypothetical sample which has the same $^{147}Sm/^{144}Nd$ as CHUR. This value may then be compared with CHUR to calculate the epsilon value using the equation:

$$\varepsilon^{i}_{Nd} = \left[\frac{\left(^{143}Nd/_{144}Nd\right)_{sample\ at\ 0.1960,\ today}}{\left(^{143}Nd/_{144}Nd\right)_{CHUR,\ today}} - 1 \right] \times 10^4 \tag{6.22}$$

The definition of ε^{i}_{Nd} differs from $\varepsilon^{isochron,t}_{Nd}$ (Eq. 6.14), but the difference between the two calculated values in terrestrial rocks is less than 1%, or less than 0.1 epsilon unit.

6.3.4.5 The Significance of Epsilon Values

ε^{t}_{Nd} is the 'initial' value of ε_{Nd} in a sample at the time of its crystallisation and is useful because it provides information about the magma source. For example, if an isochron calculation yields $\varepsilon^{t}_{Nd} = 0$, the epsilon value indicates that the magma was derived from a mantle reservoir which had a chondritic Sm/Nd from the origin of the Earth until time t. A positive epsilon value for igneous rocks implies a magma derived from a source with a greater Sm/Nd than CHUR, that is, a depleted mantle reservoir. A negative epsilon value implies a source with a lower Sm/Nd than CHUR, that is, an enriched mantle or crustal source. Epsilon values for individual samples may be calculated as a test of cogenicity of samples used in an isochron plot.

Epsilon values (*today*) for individual samples are a measure of the extent to which the samples are fractionated relative to CHUR, as defined by the fractionation factor $f_{Sm/Nd}$ (Section 6.3.4.6). Epsilon values vary with time and the following approximation may be used to calculate epsilon for some time (t) in the past from epsilon measured (*today*):

$$\varepsilon^{t}_{Nd} = \varepsilon_{Nd}{}^{today} - Q_{Nd} f_{Sm/Nd} \times t \tag{6.23}$$

where $f_{Sm/Nd}$ is given by Eq. 6.24 and $Q = 25.13\ Ga^{-1}$ when $^{146}Nd/^{142}Nd$ is normalised to 0.63151 (DePaolo,

1988) or Q = 25.09 Ga^{-1} when $^{146}Nd/^{144}Nd$ is normalised to 0.7219.

6.3.4.6 The Fractionation Factor $f_{Sm/Nd}$

The fractionation factor (f) is the $^{147}Sm/^{144}Nd$ analogue of epsilon and it is a measure of Sm/Nd enrichment in a given reservoir relative to CHUR. It is often written as $f_{Sm/Nd}$ and is calculated from the expression:

$$f = \left[\left(^{147}Sm/^{144}Nd_{today}/^{147}Sm/^{144}Nd_{CHUR}\right) - 1\right] \quad (6.24)$$

Thus, an $f_{Sm/Nd}$ value of +0.09, as is adopted for one model of the DM, has a time-averaged Sm/Nd which is 9% higher than CHUR. Over time this leads to positive ε_{Nd} values for the depleted mantle. 3.8 Ga metakomatiites from Labrador have ε_{Nd} values between +0.16 and +0.59, indicating a depleted mantle source with a substantially higher Sm/Nd than CHUR (Collerson et al., 1991). This is illustrated in Figure 6.18 and shows how samples with high positive $f_{Sm/Nd}$ values evolve to very high present-day ε_{Nd} values.

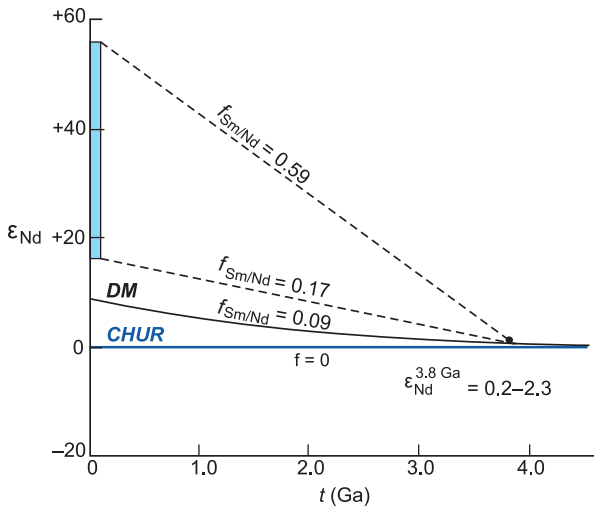

Figure 6.18 The variation of $f_{Sm/Nd}$ with time. Epsilon evolution diagram using variable Sm/Nd ratios ($f_{Sm/Nd}$). This example is for 3.8 Ga meta-komatiites from Labrador (after Collerson et al., 1991). The komatiites were produced from depleted mantle at 3.8 Ga with individual ε_{Nd} for the samples ranging from = +0.2 to +2.3, and with $f_{Sm/Nd}$ varying from 0.17 to 0.59. Individual samples have evolved to present-day epsilon values of +16 to +56. The metakomatiites show extreme depletion relative to the depleted mantle (DM, $f_{Sm/Nd}$ = 0.09) of DePaolo (1981a).

6.3.4.7 Epsilon Nd Time Plots

A convenient way of plotting calculated ε_{Nd} values and eliminating inter-laboratory differences associated with generating $^{143}Nd/^{144}Nd$ is an epsilon–time evolution diagram. This is analogous to the mantle evolution diagram described in Section 6.3.3 and shown in Figure 6.14. Many workers plot ε_{Nd} relative to CHUR and a model DM as a means of determining the likely mantle source of the sample (Figure 6.9). ε_{Nd} calculated for individual samples may also be plotted, provided the age of the sample is known. In addition, individual sample evolution curves may be drawn for different values of $f_{Sm/Nd}$ (Figure 6.18).

In contrast to DM, the continental crust shows retarded $^{143}Nd/^{144}Nd$ evolution with time relative to CHUR and generally has negative ε_{Nd} values (Figure 6.14). The curve for Australian shales (Figure 6.14b) is thought to approximate the evolution of average continental crust through time (Allegre and Rousseau, 1984).

6.3.4.8 Short-Lived Isotopes and the μ Notation

(a) *The ^{146}Sm-^{142}Nd system.* ^{142}Nd is a short-lived isotope produced by the decay of ^{146}Sm with a half-life of 103 Ma. This means that ^{142}Nd was produced only during the first few hundred million years of Earth history. Today ^{146}Sm is extinct and ^{142}Nd is no longer produced. Evidence of $^{146}Sm \rightarrow {}^{142}Nd$ decay is recorded as a ^{142}Nd anomaly and these are found only in ancient rocks where they are an indicator of processes which took place during the Hadean – a time interval that is opaque to many other isotopic methods. Modern mantle rocks do not have ^{142}Nd 'anomalies', indicating that the anomalies have been erased over geological time.

A ^{142}Nd anomaly represents the deviation of the measured isotopic composition from that of a standard and is expressed in ppm. The standard currently in use is the synthetic standard JNdi-1 which represents the average $^{142}Nd/^{144}Nd$ ratio in the Earth today. Deviations from the standard are represented by the symbol μ (mu), which is defined in a manner analogous to that of ε_{Nd}:

$$\mu^{142}Nd = \left(^{142}Nd/^{144}Nd_{sample}\right)/\left(^{142}Nd/^{144}Nd_{standard} - 1\right) \times 10^6 \quad (6.25)$$

$\mu^{142}Nd$ values may be recorded as excesses or deficits (positive or negative anomalies) indicating an

incompatible element–depleted mantle reservoir or an enriched crustal reservoir, respectively.

^{142}Nd anomalies tell us that the rock sample was originally extracted from a mantle domain in which ^{146}Sm was 'live', and so within the first 300 Ma of Earth history. Rizo et al. (2011) report lavas from the 3.7–3.8 Ga Isua Greenstone Belt in west Greenland which record ^{142}Nd excesses relative to the terrestrial standard (Figure 6.19), indicating that they were derived from a mantle source which was depleted in incompatible elements within the first 300 Ma of Earth history. Mafic rocks formed at 3.3 Ga from the same area of Greenland do not show ^{142}Nd anomalies, indicating that by 3.3 Ga the mantle in this region had been homogenised (Rizo et al., 2013; Figure 6.19). Rizo et al. (2011) also found that once the ^{142}Nd signature is preserved in ancient magmatic rocks, it is not modified by post-magmatic processes, leading them to conclude that 'after ^{147}Sm became extinct (at ca 4.2 Ga) no geological process is capable of generating ^{142}Nd variations'.

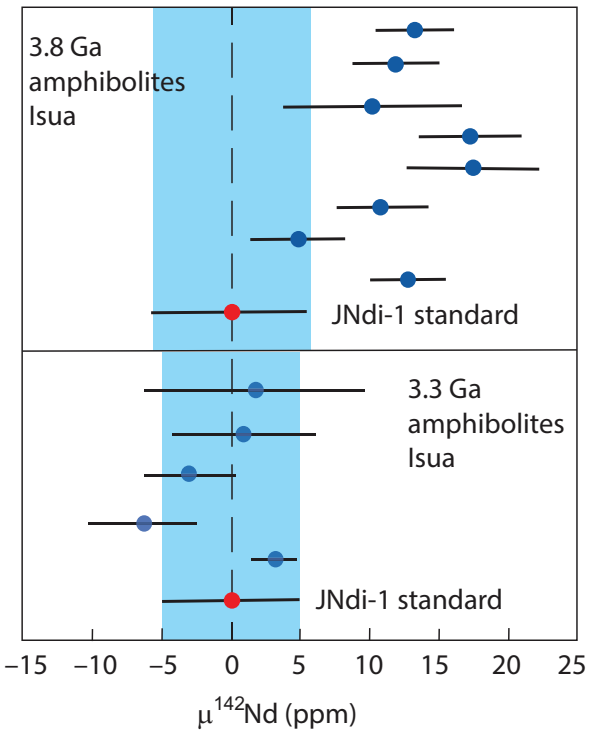

Figure 6.19 Variations in μ^{142}Nd. Variations in μ^{142}Nd in rocks from Isua in west Greenland. Sample compositions are plotted relative to the terrestrial JNdi-1 standard shown as the blue shaded area. 3.8 Ga amphibolites show positive deviations in μ^{142}Nd, indicating their derivation from a depleted mantle source in the Hadean; 3.3 Ga amphibolites show no deviation from the terrestrial standard, indicating that by this time all ^{142}Nd was homogenised in the mantle. (After Rizo et al., 2013; with permission from Elsevier)

(b) *The ^{182}Hf–^{182}W system.* The ^{182}Hf → ^{182}W system has a half-life of 8.9 Ma and so is valuable for measuring events in the first 50 Ma in the solar system. This isotope system is important in understanding metal-silicate differentiation processes since W is moderately siderophile and Hf is strongly lithophile; it has been used to estimate the time of core formation (Schoenberg et al., 2002). In silicate systems W is more incompatible than Hf, and so variations in Hf/W can also result from the processes of crystal–liquid fractionation. Tungsten isotopes are measured as the ^{182}W/^{184}W isotope ratio and deviations from the Alfa Aesar standard are represented as μ values analogous to μ^{142}Nd; μ^{182}W is expressed in ppm (Rizo et al., 2016).

6.3.5 Isotope Correlation Diagrams

Given the contrasting behaviour of the different isotopic systems outlined in Section 6.3.1, it is instructive to investigate more than one isotope system in given a suite of rocks. This allows us to identify correlations between pairs of isotope ratios, which in turn lead to a better understanding of their petrogenesis. The simplest way to investigate relationships of this type is on an isotope correlation diagram: an *x*–*y* graph on which a pair of isotope ratios is plotted. Diagrams of this type are used to display the contrasting compositions of crust and mantle reservoirs (Figures 6.10 and 6.11) and are a means of investigating mixing processes between sources of contrasting composition.

It is, however, unlikely that petrogenetic processes can always be satisfactorily reduced to two dimensions, and Hart et al. (1992) proposed a three-dimensional projection of Sr–Nd–Pb isotopes for oceanic basalts. This plot (Figure 6.20) better illustrates the controls on the Sr–Nd–Pb systematics of oceanic basalts by showing the influence of specific components. For example, the relative contributions of EM1 in samples from the Pitcairn Islands and EM2 in samples from Samoa is notable.

6.3.5.1 Using Isotope Correlation Diagrams and Epsilon Plots to Recognise Processes

Trends on isotope correlation diagrams are most commonly interpreted as mixing lines or mixing arrays.

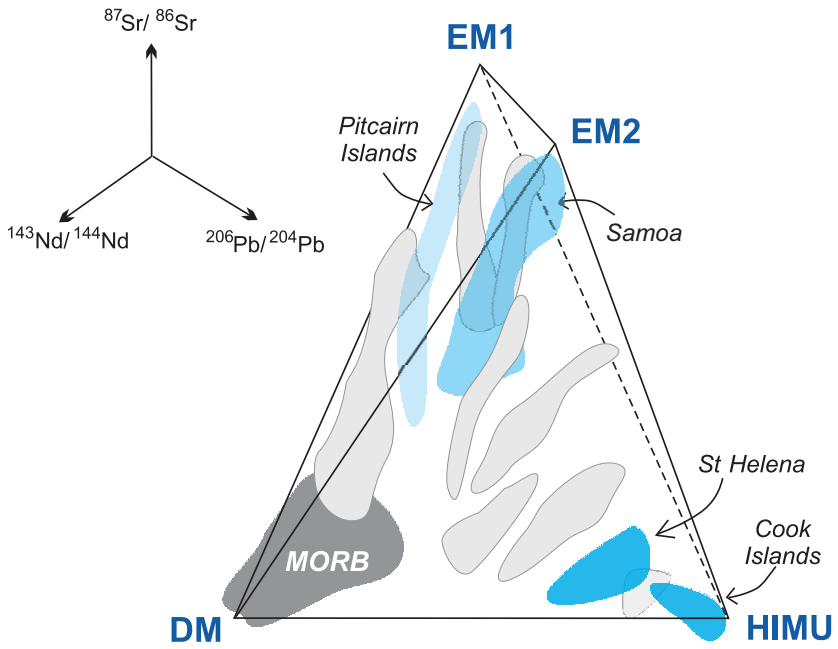

Figure 6.20 Three-dimensional projection of Sr, Nd and Pb isotopes for oceanic basalts. The interrelationship of the four principal mantle reservoirs is shown in this three-dimensional projection of Sr, Nd and Pb isotopes for oceanic basalts (data from Hart et al., 1992). Coherent trends between reservoirs indicate relative contributions of specific sources to particular OIB systems. For example, the compositional field of the Pitcairn Islands samples extends towards the EM1 component, whereas samples from Samoa trend towards EM2.

The 'mixing' may occur in the source region, during melt migration or in a magma chamber. Mixing in the source region may involve melts from different mantle reservoirs or melts produced by different degrees of partial melting. Mixing during melt migration may reflect melt–rock reaction in either the mantle or the continental crust, and, similarly, mixing in a magma chamber may be the result of reaction between the magma and the wall rock of the magma chamber or through the influx of compositionally distinct melts. There is software to model petrological mixing processes (see Chapter 4, Section 4.2.2), although a simple mixing equation such as that described by Langmuir et al. (1978) can easily be applied to isotope ratios. Compositions that result from mixing normally lie on a hyperbolic curve (see also Section 4.8.2), although if the ratios have a common denominator, as in the case of $^{87}Rb/^{86}Sr$ versus $^{87}Sr/^{86}Sr$ or $^{206}Pb/^{204}Pb$ versus $^{207}Pb/^{204}Pb$, then mixing will produce a linear trend. This straightforward approach can determine whether or not a hypothesis is viable and may place constraints on end-member compositions, distinguish between the mixing of sources and the mixing of magmas, and even determine whether mixing is recent or ancient.

(a) *Mixing between sources.* For a number of years students of basalt chemistry have regarded the isotopic compositions of oceanic basalts as the result of mixing of different mantle sources. This is suggested by the linear and curvilinear arrays on isotope correlation diagrams such as the Sr–Nd mantle array (Figure 6.10) and the Pb–Pb isotope NHRL (Figure 6.11). Similar principles apply to mixing between crust and mantle sources, and we illustrate this process in Figure 6.21 with a Nd–Sr isotope correlation diagram (after DePaolo and Wasserburg, 1979) for rear-arc basalts from the Southern Volcanic Zone (SVZ) of the Chilean Andes (data from Turner et al., 2017). The authors show that there is a mismatch between the isotopic composition of the volcanic rocks and a DM–SVZ sediment mixing line; instead, the data define a mixing line between DM and EM1, suggesting their derivation from mixing between the DM and the continental lithospheric mantle.

Mixing within the mantle and between the crust and mantle inevitably leads to deeper questions about mechanisms and scales of mixing and how these relate to plate tectonic processes. This takes us into the field of geodynamics, which we return to in Section 6.3.6.

(b) *Mixing in a magma chamber.* Layered mafic intrusions provide an opportunity to examine magma chamber processes and the process of crustal contamination. Wilson et al. (2017) analysed more than 130 samples from 2000 metres of drill core from

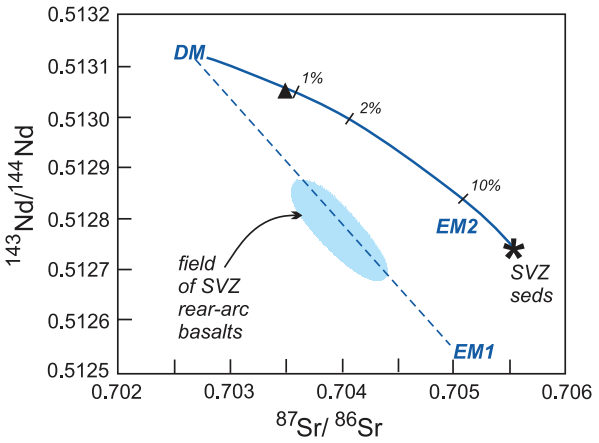

Figure 6.21 Sr–Nd isotope mixing diagram. $^{87}Sr/^{86}Sr$ versus $^{143}Nd/^{144}Nd$ (data from Turner et al., 2017) showing the theoretical (hyperbolic) mixing trend between DM and sediment of the Southern Volcanic Zone (SVZ), Chile (asterisk). The percentages indicate the amount of sediment mixed. EM2 and altered oceanic crust (triangle) are shown for reference. SVZ rear-arc basalts do not lie on this mixing trend but instead lie on a line between DM and EM1. Turner et al. (2017) use these relationships to argue that mixing between DM and SVZ sediment (or EM2) cannot explain the data trend, and therefore an EM1-like component is needed. Combining this with trace element data, the authors suggest that this component represents a metasomatised continental lithospheric mantle.

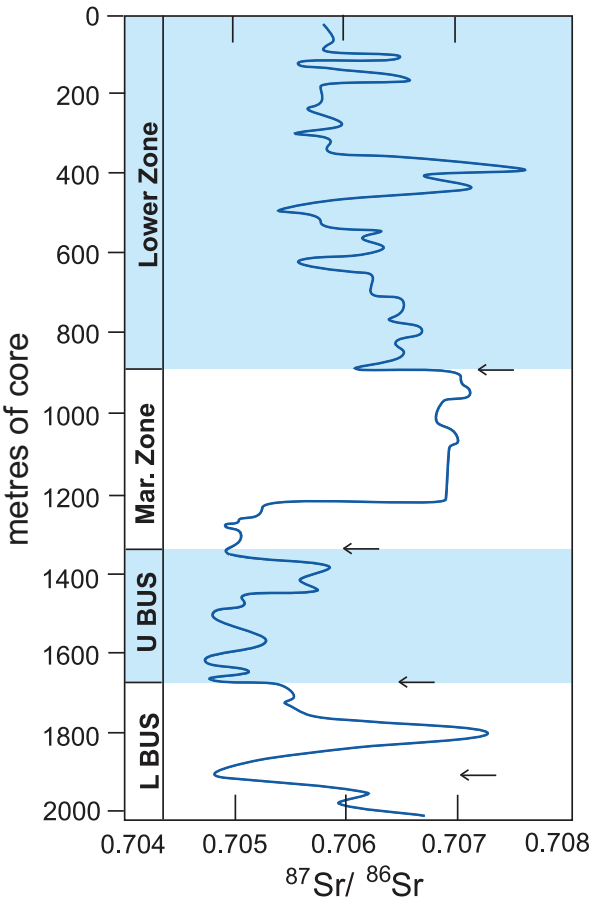

Figure 6.22 Mixing in a magma chamber. Variable $^{87}Sr/^{86}Sr_{i(2055\ Ma)}$ within the lower series of the Bushveld intrusion, South Africa (data from Wilson et al., 2017). Compare the small-scale variations within the upper basal ultramafic sequence (U BUS) or the higher part of the marginal (Mar.) zone, with the large-scale variations between them. Arrows denote sharp decreases in $^{87}Sr/^{86}Sr_i$ ratios interpreted to reflect influx of more primitive melt.

the lower Bushveld series in South Africa. They used in situ LA-MC-ICPMS microanalysis of plagioclase crystals from the Lower Zone, the Marginal Zone, and the Basal Ultramafic Sequence (upper and lower) to document variations in the $^{87}Sr/^{86}Sr_{i(2055\ Ma)}$ ratio between 0.7045 and 0.7073 (Figure 6.22). In detail, this profile shows small-scale, cyclic variations superimposed on larger-scale variations, which they attribute to sharp decreases in $^{87}Sr/^{86}Sr_i$ reflecting mixing between the resident magma and the influx of a more primitive magma.

6.3.5.2 Crustal Contamination

The phrase 'crustal contamination' is normally used to describe mantle melts which have interacted with continental crust. However, it is also used to describe a mantle source region into which crustal material has been introduced at some time in the past by a process such as sediment subduction. It is important to try to distinguish between these two possibilities.

(a) *Magmatic contamination by continental crust.* Pb is the most sensitive of the radiogenic isotopes to crustal contamination; Sr is moderately sensitive; and Nd is the least sensitive, although the combined application of radiogenic isotopes, stable isotopes (Section 7.3.1.3) and trace element ratios (Section 4.6) provides the best means of understanding the process of crustal contamination.

One helpful approach to quantifying crustal contamination is to study continental flood basalts on the basis that mantle-derived melts are sensitive to contamination from the continental crust and that the rapid emplacement of large volumes of basalt over short periods of time limits the interaction between

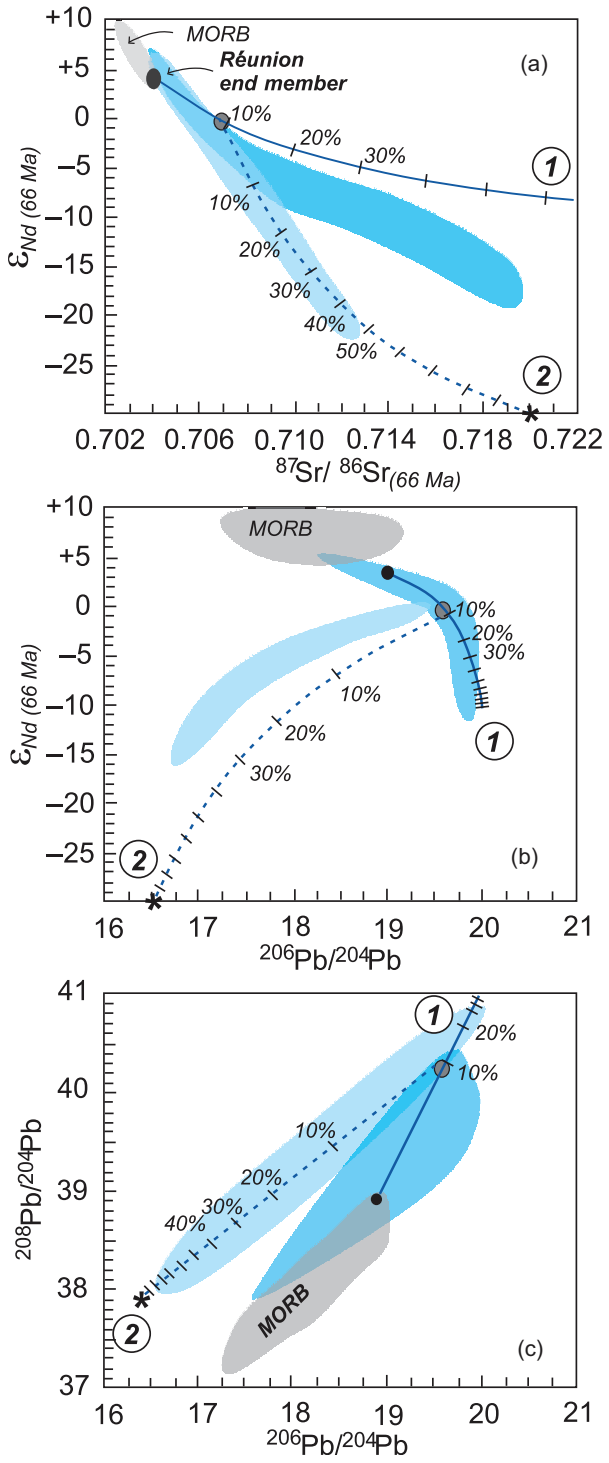

Figure 6.23 Crustal contamination of Deccan basalts. (a) $^{87}Sr/^{86}Sr_{i\ (66\ Ma)}$ versus ε_{Nd}; (b) $^{206}Pb/^{204}Pb$ versus ε_{Nd}; and (c) $^{206}Pb/^{204}Pb$ versus $^{208}Pb/^{204}Pb$. Deccan flood basalts have Sr, Nd and Pb isotopic compositions that define two compositional trends, implying a three-component mixing scenario (after Haase et al., 2019). The end-member compositions include a parental Réunion basalt (black dot), crustal component 1 (high $^{206}Pb/^{204}Pb$, high $^{87}Sr/^{86}Sr_i$ and low ε_{Nd}), and crustal component 2 indicated by the asterisk (low $^{206}Pb/^{204}Pb$, moderate $^{87}Sr/^{86}Sr_i$ and highly negative ε_{Nd}). Stage 1 involves the Réunion parent melt assimilating ~10% of crustal contaminant 1 and producing a hybrid melt (grey dot); this leads to stage 2, when the hybrid melt assimilates up to 50% of a plagioclase-rich crustal component.

them such that both components can be recognised. Haase et al. (2019) applied this approach to the Deccan flood basalts in India (Figure 6.23). They assumed that the parental magma was similar to a Réunion basalt but identified two additional components involved in the genesis of the Deccan magmatism. These were a crustal component with high $^{206}Pb/^{204}Pb$, high $^{87}Sr/^{86}Sr_i$ and low ε_{Nd}, which they interpreted as Archaean felsic lower crust, and a crustal component with low $^{206}Pb/^{204}Pb$, intermediate $^{87}Sr/^{86}Sr_i$, and highly negative ε_{Nd} representing a feldspar-rich contaminant. By combining this information with incompatible trace element ratios they proposed a two-stage evolution for the Deccan magmatism in which a parental magma first stagnates in the Archean lower crust and subsequently mixes with a plagioclase-rich crustal component.

(b) *Crustal contamination and AFC processes.* DePaolo (1981b) has shown that assimilation and fractional crystallisation (AFC) may shift compositions on an isotope correlation diagram far from what might be expected on the basis of simple mixing. On an Nd–Sr isotope correlation diagram simple mixtures will define a straight-line trend between the magma and contaminant, whereas in AFC processes when the bulk solid/liquid distribution coefficients for Nd and Sr differ markedly, then there is a significant departure from the simple mixing curve. A full discussion of AFC process is given in Section 4.2.2.3.

(c) *Contamination with seawater.* The isotopic composition of seawater is highly variable (Figure 6.3). Modern seawater has a high $^{87}Sr/^{86}Sr$ ratio (>0.709) relative to the mantle values of MORB (Farrell et al., 1995) and a moderate concentration of Sr, so the exchange of Sr between seawater and oceanic crust will produce relatively radiogenic $^{87}Sr/^{86}Sr$ ratios in young MORB. The $^{187}Os/^{188}Os$ ratio of modern seawater is ~1.1 (Woodhouse et al., 1999), which is 10 times higher than the mantle

value, and the precipitation of Fe- and Mn-oxyhydroxides on submarine lavas concentrates seawater Os on the surfaces of sea-floor rocks and increases the $^{187}Os/^{188}Os$ ratio. In contrast, the elements Nd and Hf are relatively insoluble in seawater, and so isotope ratios tend to be insensitive to seawater contamination: $^{143}Nd/^{143}Nd$ in seawater is low ($\varepsilon_{Nd} = -1$ to -18), whereas $^{177}Hf/^{176}Hf$ is intermediate ($\varepsilon_{Nd} = +8$ to -4) (Rickli et al., 2009; Stichel et al., 2012). Consequently, on a $^{87}Sr/^{86}Sr$ versus $^{143}Nd/^{144}Nd$ diagram the effect of contamination by seawater will show enhanced $^{87}Sr/^{86}Sr$ at relatively constant $^{143}Nd/^{144}Nd$. Pb isotopes in seawater vary widely ($^{206}Pb/^{204}Pb = 17.25 - 19.75$, $^{207}Pb/^{204}Pb = 15.3 - 15.65$, $^{208}Pb/^{204}Pb = 37 - 39.8$) and are susceptible to anthropogenic contamination.

6.3.5.3 Isotope versus Element Plots

Since an isotope ratio cannot be fractionated by crystal–liquid equilibria and is therefore indicative of the magmatic source, the correlation between an isotope ratio and a major or trace element can be used as a guide to the major element or trace element composition of the source. Typically, ratios of highly incompatible trace elements (Section 4.6.1 and Table 4.11) are the most useful for characterising the elemental composition of the source region. Thus, correlations between isotope ratios and ratios of highly incompatible trace elements are likely to indicate mixing between compositionally distinct sources.

Figure 6.24 shows the strontium isotope ratio plotted against Nb/U for basalts from the Society Islands (an EM2 source). Nb and U are highly incompatible elements but have similar bulk partition coefficients during mantle melting in most oceanic environments. Consequently, the limited Nb/U ratio in oceanic basalts should reflect the composition of their source. As the two axes do not share a common denominator, mixing in this diagram should define a curve rather than a straight line (Langmuir et al., 1978). Oceanic rocks (MORB and non-EM-OIB) have a Nb/U ratio of ~36–67 (Hofmann, 2014) and continental crust a ratio of Nb/U = 8 (Rudnick and Fountain, 1995); sediment has consistently higher $^{87}Sr/^{86}Sr$ ratios than MORB and OIB. Thus, OIB containing significant amounts of recycled sediment should be distinguished by high $^{87}Sr/^{86}Sr$ and low Nb/U ratios, and the observed trend towards high $^{87}Sr/^{86}Sr$ and low Nb/U is consistent with mixing between mantle and continental crust.

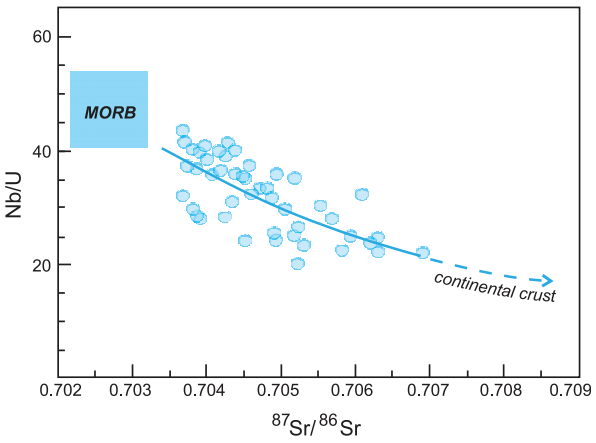

Figure 6.24 $^{87}Sr/^{86}Sr$ versus Nb/U for basalts from the Society Islands (data from White and Duncan, 1996; modified after Hofmann, 2014; with permission from Elsevier). The curved trend in the basaltic data shown here is consistent with mixing between a depleted mantle component represented by MORB and a continental crustal component.

6.3.5.4 Coupled versus Decoupled Isotope Behaviour

When covariant isotopic systems that are *expected* to behave similarly do not, they are considered to be 'decoupled'. Sm–Nd and Lu–Hf isotopes normally represent a coupled system, but early in Earth history they may have been decoupled with Lu–Hf isotopes showing supra-chondritic compositions, whereas Sm–Nd isotopes show chondritic compositions. Hoffmann et al. (2010, 2011) suggested that Eoarchean rocks in west Greenland were decoupled with respect to whole-rock Nd and Hf isotopes. Caro and Bourdon (2010) explained this observed decoupling of the Nd–Hf systems in terms of a supra-chondritic Earth model. However, Lu–Hf isotopes in meteoritic zircon (Iizuka et al., 2015) support the CHUR parameters of Bouvier et al. (2008) and recent Hf-in-zircon work does not reproduce supra-chondritic ε_{Hf} values for the same west Greenland samples (Kemp et al., 2019); therefore, invoking a supra-chondritic Hf reservoir seems unnecessary.

6.3.6 Crust–Mantle Geodynamics

The ultimate goal of defining crust and mantle isotopic reservoirs is to create geodynamic models which explain how these reservoirs have obtained their present-day compositions and how they interact.

This requires us to think about Earth processes on a global, rather than local, scale and points to a major success of isotope geology: linking reservoir compositions to the processes that govern plate tectonics. These include the subduction of oceanic crust and its associated sediment, the upwelling of mantle plumes and the recycling of continental lithosphere. We have shown in this chapter how the study of radiogenic isotopes in basalts and mantle peridotites allows us to characterize mantle end-member compositions and explore the chemical evolution of the mantle through time. These data demonstrate how the composition of the mantle has evolved in response to the processes of core formation, crust extraction and the recycling of crustal material, and it is to these themes that we now turn.

6.3.6.1 The Secular Variation of the Mantle

We showed in Section 6.3.2 that the Earth's mantle can be characterised using the isotopes of Nd, Hf, Sr, Pb and Os into four distinct reservoirs: the depleted mantle (DM), mantle with a high $^{238}U/^{204}Pb$ ratio (HIMU) and enriched mantle reservoirs (EM1 and EM2). Each of these mantle reservoirs records its own 'story' of the processes which have led to its current composition, although it is important to note that to date these 'stories' are only partially told. The DM is thought to record events which relate to crust extraction, whereas the HIMU mantle records events of U gain or Pb loss through the in-mixing of altered oceanic crust or the loss of lead to the core or through fluid processes. There are also several models for the origin of the enriched mantle (EM) which include the recycling of crustal materials, enrichment by the migration of mantle melts and the mixing of sub-continental lithosphere into the mantle.

In Section 6.3.3 we described a range of 'mantle evolution diagrams' which summarise how the composition of the mantle has evolved over time for the different isotopic systems. We proposed that the Nd and Hf systems record, at least in part, the process of crust extraction and that Os isotopes can be an important tracer of recycled ancient oceanic crust. The more complex Pb isotopes record the evolution of mantle domains with different μ values over time.

Both these approaches to the composition of the modern mantle are based upon a chondritic (CHUR) model of the Earth, although, as we have indicated, studies of Hf isotopes have sought to challenge this assumption. This leads us to the starting point for all modern geodynamic models which are the large-scale processes which took place during the early differentiation of the Earth (the reader is referred to Rollinson, 2007) and whether or not any of the Earth's primordial mantle can be recognised today.

Clues for the existence of primordial mantle come from two recent studies. A global compilation of $^{3}He/^{4}He$, Nd and Hf isotopic data from kimberlites sampling the deeper mantle identified a homogeneous, primordial reservoir (Woodhead et al., 2019). These workers showed that this reservoir was global in extent and existed until about 200 Ma ago; it represents an ancient mantle source that remained isolated from the depleted, convecting upper mantle for about 2 Ga. It is very similar in composition to CHUR and implies that bulk Earth had a composition similar to that of enstatite chondrites (Bouvier and Boyet, 2016). McCoy-West et al. (2018) also identified a primordial mantle source in 61 Ma picrites from Baffin Island, Canada. These picrites have Sr, Nd, Hf and Pb isotopes that are indistinguishable from North Atlantic MORB, but their radiogenic W and Pb isotope compositions and their stable Fe and Zn isotope compositions are consistent with ancient primordial mantle.

6.3.6.2 The Genesis of the Continental Crust

The Sr–Nd isotope correlation diagram shown in Figure 6.10 indicates that oceanic basalts are enriched in Nd isotopes and depleted in Sr isotopes relative to the BE, whereas the rocks of the continental crust show the opposite relationship. This inverse relationship suggests that the continental crust and the mantle source of oceanic basalts are complementary reservoirs of Nd and Sr isotopes. This concept forms the basis for the mass-balance modelling of the relationship between crust, mantle and the original bulk Earth composition.

In addition to compositional constraints, the timing of crustal genesis can be addressed by the combined study of U–Pb and Hf isotopes in zircon. The key issue here is identifying juvenile crust. This can be done by using the U–Pb zircon age combined with the initial $^{176}Hf/^{177}Hf$ ratio and model age of the same zircon. Where these agree, a link can be made between igneous activity and the generation of new crust.

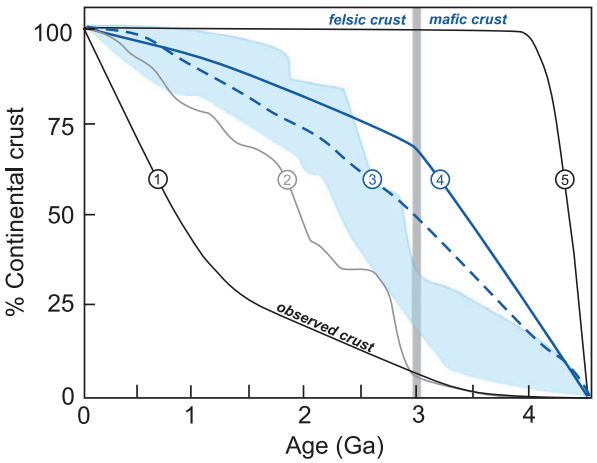

Figure 6.25 The growth of the continental crust through time. Curve 1 shows the volume of observable continental crust today (Goodwin, 1996). Curves 2–4 represent inferred crustal growth or juvenile crustal production over time (2, Condie and Aster, 2010; 3, Belousova et al., 2010; 4, Dhuime et al., 2010). Curve 5 is Armstrong's (1981) steady-state model. The shaded region represents other crustal growth curves from Viezer and Jansen (1979), McLennan and Taylor (1982), Patchet and Arndt (1986), Chase and Patchett (1988) and McCulloch and Bennett (1994). Note the change in the rate of crust production after about 3 Ga, indicated by the vertical bar, for most models in the shaded region and models 2 and 4.

Figure 6.25 summarises a number of crustal growth curves for the production of juvenile crust throughout Earth history. There are two extreme scenarios which bracket the full range of models. The first scenario suggests that crustal growth over time is represented by the amount of crust existing today (Goodwin, 1996) and the second presumes that most of the Earth's crust had been formed by about 4 Ga (Armstrong, 1981). The precise timing of the formation of the continental crust is still debated (Rollinson, 2017) and is linked to the even larger question of when precisely plate tectonics commenced on the Earth. Technological advances in mass spectrometry have driven this subject forward, and future investigations integrating microstructural, age and isotope tracer information from multiple isotope systems are likely to lead to continued advances in this field.

6.3.6.3 Crust and Mantle Mass-Balance Models

We have shown in this chapter the power of radiogenic isotopes in aiding our understanding of the large-scale processes operating in the Earth today. These lead to the development of geodynamic models for the Earth. Such models aim to set limits on the proportion of mantle involved in the formation of the continental crust, offer insights into the nature of mantle convection and seek to measure the rates of geological processes in order to understand how the composition of the Earth's mantle has changed with time.

Early models such as the plumbotectonics of Doe and Zartman (1979) were based upon a single isotope system, whereas today geochemical mass-balance calculations incorporate the findings of multiple radiogenic isotope systems as well as the results of trace element and stable isotope studies. More recent studies represent exchanges between different crust and mantle reservoirs in terms of geochemical cycles and geochemical box models. Geochemical cycles are normally developed for a single element and may show cycling over a short or long time scale. Short time-scale cycles normally incorporate the reservoirs of the Earth's surficial environment as well as the deep Earth, whereas long time-scale cycles focus on the deep Earth reservoirs. Studies of this type are augmented by geochemical box models which focus on the mass flows between the different reservoirs (see, e.g., Coltice et al., 2000). However, in order to fully understand these short- and long-term cycles we need the help of stable isotope geochemistry. This is the topic to which we now turn.

7 Using Stable Isotope Data

7.1 Introduction

Most naturally occurring elements consist of more than one stable isotope. In geochemistry the stable isotope systems of interest are those of the light elements H, C, N, O and S. These elements have been the subject of geochemical investigations for many decades and are termed the *traditional stable isotopes*. These are elements in which the mass difference between the different stable isotopes is sufficiently large to allow them to be fractionated through physical processes on the basis of their mass differences and in which the rarer isotope is of sufficient abundance to be measurable. They are often the main constituents of geologically important fluids and so provide the opportunity to study both the fluids and the effects of fluid–rock interaction.

Conventionally traditional stable isotopes are converted into a gas (usually H_2, CO_2 or SO_2) for the purposes of isotopic analysis, and the mass differences measured in a mass spectrometer. With such commonly occurring elements as H, C, N, O and S contamination during sample preparation and analysis is a particular problem and great care must be taken to ensure clean sample handling. Increasingly, ion-beam and laser technologies are being used to obtain a finer spatial resolution of isotopic compositions in small samples. Traditional stable isotope studies typically measure the isotopic composition of a molecule or compound such as H_2O or CO_2 rather than the single element. This means that there are a number of different possible isotopic combinations within a single molecule. For example, carbon dioxide can exist as $^{12}C^{16}O_2$ (mass 44), as $^{13}C^{16}O_2$ or $^{12}C^{17}O^{16}O$ (both mass 45), and there are many more possibilities. These different molecules are known as *isotopologues*; that is, they are molecules that differ from one another only in isotopic composition and may have the same or different masses. However, their abundances vary greatly. In the example given above, $^{12}C^{16}O_2$ makes up 98.4‰ of naturally occurring CO_2, whereas $^{13}C^{16}O_2$ and $^{12}C^{17}O^{16}O$ form only 1.11‰ and 748 ppm, respectively.

With the advent of multi-collector ICP-MS technology, a number of elements with higher atomic numbers, whose stable isotope variations had been regarded previously as too low to measure accurately, have been shown to have natural isotopic variations and added to the geochemical toolbox. These are often termed the *non-traditional stable isotopes*. Many occur as trace elements, some are redox sensitive, and some are biologically active, and because of their metallic nature some represent different bonding environments from the traditional covalently bonded stable isotopes. There are a large number of elements crowding into this field, with others emerging. Here we consider five of the non-traditional stable isotopes – the light elements Li, Mg and Si and the heavier elements Cr and Fe – to illustrate their diverse applications in modern geochemistry.

In this chapter we first consider in Section 7.2 some of the key principles behind interpreting stable isotope geochemistry, then in Section 7.3 there is a discussion of the application of the traditional stable isotopes H, C, N, O and S. This is followed in Section 7.4 by a discussion of the application of the non-traditional stable isotopes Li, Mg, Si, Cr and Fe. More detailed treatments of the traditional stable isotopes are given by Valley et al. (1986), Taylor et al. (1991), Sharp (2017) and Hoefs (2018), and for the non-traditional stable isotopes, Teng et al. (2017a).

7.2 Principles of Stable Isotope Geochemistry

7.2.1 Notation

7.2.1.1 Isotope Ratios: The δ Value

Stable isotope ratios are measured relative to a standard, and because the relative differences are normally very small, they are expressed in parts per thousand (informally as 'per mil'): ‰. The isotope ratio is expressed as a δ (delta) value, or del value as it is sometimes colloquially called. Using oxygen isotopes as an example, the δ value is calculated as follows:

$$\delta^{18}O‰ = \left[{}^{18}O/{}^{16}O_{(sample)} - {}^{18}O/{}^{16}O_{(standard)}/{}^{18}O/{}^{16}O_{(standard)}\right] \times 1000 \quad (7.1)$$

Thus a $\delta^{18}O$ value of +10.0‰ means that the sample is enriched in the $^{18}O/^{16}O$ ratio relative to the standard by 10 parts in thousand and is isotopically 'heavy'. Similarly, a negative value of −10.0‰ means that the sample is depleted in the $^{18}O/^{16}O$ ratio relative to the standard by 10 parts in a thousand and is isotopically 'light'.

7.2.1.2 The Fractionation Factor α

The fractionation of an isotope between two substances A and B can be defined by the fractionation factor

$$\alpha_{A-B} = \text{ratio in A}/\text{ratio in B} \quad (7.2)$$

For example, in the reaction in which ^{18}O and ^{16}O are exchanged between magnetite and quartz, the fractionation of $^{18}O/^{16}O$ between quartz and magnetite is expressed as

$$\alpha_{quartz-magnetite} = \left[\left({}^{18}O/{}^{16}O\right)_{\text{in quartz}}/\left({}^{18}O/{}^{16}O\right)_{\text{in magnetite}}\right]$$

where '$^{18}O/^{16}O$ in quartz' and '$^{18}O/^{16}O$ in magnetite' are the measured isotopic ratios in coexisting quartz and magnetite. If the isotopes are randomly distributed over all the possible atomic positions in the compounds measured, then α is related to an equilibrium constant K such that

$$\alpha = K^{1/n} \quad (7.3)$$

where n is the number of atoms exchanged. Normally, exchange reactions are written such that only one atom is exchanged, in which case $\alpha = K$, and the equilibrium constant is equivalent to the fractionation factor.

Values for α are close to unity and typically vary in the third decimal place. Most values therefore are of the form 1.00X. For example, the fractionation factor for ^{18}O between quartz and magnetite at 500°C is 1.009 (Javoy, 1977). This may be expressed as the third decimal place value – the per mil value – such that the quartz–magnetite fractionation factor is 9 (or 9.0 per mil). A useful mathematical approximation for the fractionation factor α stems from the following relationship:

$$1000 \ln (1.00X) \sim X \quad (7.4)$$

In the case cited above where $\alpha = 1.009$, $1000 \ln \alpha = 9.0$. Experimental studies have shown that $1000 \ln \alpha$ is a smooth and often linear function of $1/T^2$ for mineral–mineral and mineral–fluid pairs. This gives rise to the general relationship for the fractionation factor

$$1000 \ln \alpha_{\text{mineral 1}-\text{mineral 2}} = A\left(10^6/T^2\right) + B \quad (7.5)$$

where T is in Kelvin and A and B are constants, normally determined by experiment. In the case of the quartz–magnetite pair the values for A and B are 6.29 and 0, respectively (Chacko et al., 2001), giving the expression:

$$1000 \ln \alpha_{quartz-magnetite} = 6.29 \times 10^6/T^2$$

A further useful approximation is the relationship between $1000 \ln \alpha$ and measured isotope ratios expressed as δ values. The difference between the δ values for two minerals is expressed as Δ which approximates to $1000 \ln \alpha$, when the δ values are less than 10. In the case of oxygen isotopic exchange between quartz and magnetite,

$$\Delta_{qz-mgt} = \delta_{qz} - \delta_{mgt} \sim 1000 \ln \alpha_{qz-mgt} \quad (7.6)$$

When δ values are larger than 10, then the following expression should be used:

$$\alpha_{A-B} = (1000 + \delta_A)/(1000 + \delta_B) \quad (7.7)$$

A range of approaches is used to obtain stable isotope fractionation factors. These include theoretical calculations based upon models of atomic structure and bond strength, experimental studies, and empirical investigations based upon well-studied natural samples (see Chacko et al., 2001, for a review; Sharp 2017). These authors also provide a helpful compilation of self-consistent, experimentally determined mineral–mineral fractionation factors (values for A) for oxygen isotopes, which is summarised here in Table 7.1.

Isotopic fractionations between *minerals and melt* vary as a result of the changing composition of the melt. Mineral–melt fractionations are defined in the same way as for mineral pairs (Eq. 7.2) and these values are particularly useful when seeking to calculate the stable isotope composition of a melt from the isotopic composition of one or more refractory or phenocryst phases. Other approaches used to measure the isotopic composition of a melt include the direct measurement of the fresh glass, or to treat the melt as

Table 7.1 Oxygen isotope fractionation between mineral pairs[a]

	Cc	Ab	Ms	F-Phl	An	Phl	Ap	Zn	Alm	Di	Gr	Gh	Ttn	Fo	Ru	Mt	Pv
Qz	0.38	0.94	1.37	1.64	1.99	2.16	2.51	2.64	2.71	2.75	3.15	3.50	3.66	3.67	4.69	6.29	6.80
Cc		0.56	0.99	1.26	1.61	1.78	2.13	2.26	2.33	2.37	2.77	3.12	3.28	3.29	4.31	5.91	6.42
Ab			0.43	0.70	1.05	1.22	1.57	1.70	1.77	1.81	2.21	2.56	2.72	2.73	3.75	5.35	5.86
Ms				0.27	0.62	0.79	1.14	1.27	1.34	1.38	1.78	2.13	2.29	2.30	3.32	4.92	5.43
F-Phl					0.35	0.52	0.87	1.00	1.07	1.11	1.51	1.86	2.02	2.03	3.05	4.65	5.16
An						0.17	0.52	0.65	0.72	0.76	1.72	1.51	1.67	1.68	2.70	4.30	4.81
Phl							0.35	0.48	0.55	0.59	0.99	1.34	1.50	1.51	2.53	4.13	4.64
Ap								0.13	0.20	0.24	0.64	0.99	1.15	1.16	2.18	3.78	4.29
Zn									0.07	0.11	0.39	0.86	1.02	1.03	2.05	3.65	4.16
Alm										0.04	0.32	0.79	0.95	0.96	1.98	3.58	4.09
Di											0.28	0.75	0.91	0.92	1.94	3.54	4.05
Gr												0.47	0.63	0.64	1.66	3.26	3.77
Gh													0.16	0.17	1.19	2.79	3.30
Ttn														0.01	1.03	2.63	3.14
Fo															1.02	2.62	3.13
Ru																1.60	2.11
Mt																	0.51

[a]Values are the coefficients for Eq. 7.5, where A and B are the minerals listed along the *x* and *y* axes of the table, respectively. The values are from the experimental and empirical studies of Chacko et al. (2001) and Valley (2003).

a mixture of normative minerals with a fractionation factor calculated from the weighted average of the fractionation factors of the normative minerals (Bindeman, 2008).

7.2.2 Equilibrium Stable Isotope Fractionation

One of the most fundamental concepts behind stable isotope fractionation is that the mass of an atom affects its translational, rotational and vibrational motions and thus the strength of its chemical bonds. Most isotopic fractionations are the result of equilibrium effects and follow the rules of equilibrium thermodynamics. This means that equilibrium fractionation between two phases is based upon the differences in the bond-strength of the different isotopes of the element. The heavier isotope will form the stronger, stiffer bond. So that when an isotope is partitioned between two minerals in an exchange reaction such as

$$2Si^{16}O_2 + Fe_3{}^{18}O_4 = 2Si^{18}O_2 + Fe_3{}^{16}O_4$$

the heavier isotope will partition into the mineral with the higher ionic potential. In the case of the fractionation of ^{18}O between quartz and magnetite, it is the quartz, which contains small highly charged Si^{4+}, that is enriched in ^{18}O, and the magnetite is ^{18}O-deficient. The relationship between bond strength and isotopic fractionation was illustrated by Bindeman (2008), who gives the example of a granite at 850°C with a whole rock $\delta^{18}O$ value of 7.8‰ which shows decreasing $\delta^{18}O$ of its constituent minerals according to the increasing number of non-Si–O bonds in the mineral as follows:

$$\begin{aligned}\text{quartz}\ (8.2‰) &> \text{albite} \approx \text{Kfsp}\ (7.5‰) > \text{anorthite}\ (6.6‰)\\ &> \text{zircon}\ (6.4‰) \geq \text{pyroxene}\ (6.3‰) \approx \text{amphibole}\\ &\geq \text{biotite} \geq \text{garnet} \approx \text{olivine}\ (6.1‰) > \text{sphene}\ (5.4‰)\\ &\geq \text{ilmenite}\ (4.9‰) > \text{apatite} \geq \text{magnetite}\ (3.5‰)\end{aligned}$$

It is evident from the above that the oxygen isotope composition of plagioclase is a function of its anorthite content.

It was shown in Eq. 7.5 that there is an important temperature control on isotopic fractionation leading to an obvious application in isotopic thermometry. Relative volume changes in isotopic exchange reactions, on the other hand, are very small, except for hydrogen isotopes, and therefore there is a minimal pressure effect. Clayton (1981) showed that at pressures of less than 20 kb the effect of pressure on oxygen isotope fractionation is less than 0.1‰ and lies within the measured analytical uncertainties.

The absence of a significant pressure effect on stable isotope fractionation means that isotopic exchange reactions can be investigated at high pressures where reaction rates are fast and the results extrapolated to lower pressures.

There is also some evidence for crystallographic controls on isotope fractionation in minerals. Heavy isotopes are concentrated in more closely packed crystal structures as illustrated by the fractionation of carbon isotopes between diamond and graphite and ^{18}O between α- and β-quartz. In calcite, crystal faces from different crystallographic forms have different isotopic compositions indicating that different surfaces in the same crystal can have slightly different bonding characteristics which are sufficient to fractionate the isotopes of oxygen and carbon (Dickson, 1991).

7.2.3 Kinetic Controls on Stable Isotope Fractionation

Kinetically controlled stable isotope fractionation reflects the readiness of a particular isotope to react and can be important in identifying particular physical and biological processes. For example, in a physical process such evaporation, an isotopically light molecule will have a slightly greater velocity than an equivalent heavy molecule. Kinetic isotope effects are often associated with fast, incomplete or unidirectional processes such as evaporation, diffusion and dissociation reactions, and unlike equilibrium processes they do not follow well-understood thermodynamic rules. Typically, they are more important in low-temperature geochemistry and are rarer at high temperatures. During distillation the light isotopic species is preferentially enriched in the vapour phase according to the Rayleigh fractionation law (Section 4.2.2) as is found in the fractionation of $\delta^{18}O$ and δD in rainwater and ice.

When isotopic fractionation takes place as a result of diffusion, there is a kinetic effect whereby the light isotope is enriched relative to the heavy in the direction of transport indicating the mass dependence of this process (Watkins et al., 2017). At high temperatures diffusion-controlled isotopic fractionation can be important when interpreting the results of oxygen isotopes as thermometers or in experiments where high-temperature processes have not reached equilibrium. At lower temperatures isotopes can be fractionated by adsorption onto clay minerals in sediments. For example, isotopically lighter hydrogen, oxygen and sulphur may be preferentially adsorbed onto clay, leading to isotopic enrichments in formation waters (Ohmoto and Rye, 1979).

Kinetically controlled stable isotope fractionation is particularly important during biological processes and so is relevant to all the traditional stable isotope systems. Products from bacterial reactions tend to be enriched in in the light isotope because the dissociation energies are lower and bonds more easily broken. For example, the bacterial reduction of seawater sulphate to sulphide proceeds 2.2‰ faster for the light isotope ^{32}S than for ^{34}S. For the reactions

$$^{32}SO_4^{-2} \rightarrow H_2{}^{32}S \text{ (with a reaction rate of } k_1)$$

$$^{34}SO_4^{-2} \rightarrow H_2{}^{34}S \text{ (with a reaction rate of } k_2)$$

the rate constant k_1 is greater than the rate constant k_2 and the ratio $k_1/k_2 = 1.022$ (Rees, 1973). The effects of this fractionation in a closed system may be modelled using the Rayleigh fractionation equation (Section 4.2.2).

7.2.4 Mass-Independent Stable Isotope Fractionations

Some elements have more than two stable isotopes. For example, oxygen has three isotopes – ^{16}O, ^{17}O and ^{18}O – and sulphur has four – ^{32}S, ^{33}S, ^{34}S and ^{36}S. Given that isotope fractionations are a function of the mass difference between the isotopes, we might expect the fractionation of ^{17}O relative to ^{16}O to be half that of ^{18}O relative to ^{16}O. Broadly, this *mass-dependent* fractionation is found to be the case, although with some minor differences because of the complex way in which fractionation factors relate to isotopic mass. For this reason the fractionation of $^{17}O/^{16}O$ relative to $^{18}O/^{16}O$ is 0.52, rather than precisely 0.5. However, there are some rare circumstances in which isotopic fractionation does not follow this pattern and instead represents the process of *mass-independent fractionation.* This has been found in the case of oxygen isotopes and sulphur isotopes where they occur in the upper atmosphere.

In geochemistry the recognition of mass-independent fractionation in the sulphur isotope system has huge importance. In this system mass-independent fractionation is quantified using the Δ-notation in the expressions

$$\Delta^{33}S = \delta^{33}S - 1000\left(\left(1+\delta^{34}S/1000\right)^{0.515} - 1\right) \quad (7.8)$$

$$\Delta^{36}S = \delta^{36}S - 1000\left(\left(1+\delta^{34}S/1000\right)^{1.91} - 1\right) \quad (7.9)$$

where 0.515 represents the fractionation of ^{33}S to ^{34}S and 1.91 represents the fractionation of ^{36}S to ^{34}S. These terms may be obtained by calculating the slope for pairs of measured $\delta^{3x}S$ values in natural materials (see Farquhar and Wing, 2003, figure 2). In the modern Earth, $\Delta^{33}S$ and $\Delta^{36}S$ are zero, but in the early history of the Earth they have both positive and negative values (Farquhar and Wing, 2003). One helpful way of presenting the data is to plot a $\delta^{34}S$ versus $\Delta^{33}S$ diagram (Figure 7.24) as this shows the degree of mass-independent fractionation relative to that of mass-dependent fractionation.

Current thinking attributes the mass-independent fractionation of sulphur isotopes to photochemical reactions in the upper atmosphere (Ono, 2017); see Section 7.3.4.4. The changing pattern of mass-independent sulphur isotope evolution over time is therefore thought to relate to the chemical evolution of the Earth's atmosphere. Experimental studies show that photolysis reactions in the ultraviolet range are capable of producing large mass-independent fractionations. This observation suggests that Earth's ozone layer, which protects the planet from damaging ultraviolet radiation, was not present in the early Earth, supporting the view that the Earth's early atmosphere was not oxygenic.

7.2.5 Clumped Isotopes

A relatively recent finding in stable isotope geochemistry is that there is a tendency for isotopologues containing rare heavy isotopes to concentrate more than one rare isotope in a given molecule. These 'multiply substituted isotopologues' have been termed 'clumped isotopes', the term 'clumped' indicating that two rare isotopes are bonded together (Eiler, 2007). The concentrations of such isotopologues are extremely low and present certain analytical challenges. In the past the assumption had been that the different isotopologues of a given molecule are randomly distributed according to their abundances in nature, whereas the recent finding is that heavy isotope isotopologues are more abundant than predicted from a purely random distribution. This can be explained by the preferential bonding of heavy isotopes in a given molecule leading to the 'clumping' of heavy isotopes into multiply substituted isotopologues at the expense of singly ubstituted isotopologues (Eiler, 2007).

Clumped isotope analysis uses the Δ notation to express deviation of the measured amount from that expected from the stochastic distribution. Values may be positive or negative. One of the most commonly measured values is the Δ_{47} value for CO_2, which largely reflects variations in abundance of $^{13}C^{18}O^{16}O$ = mass 47. The Δ_{47} value of CO_2 can be calculated from the expression

$$\Delta_{47} = \left[\left(R^{47}/R^{47\times} - 1\right) - \left(R^{46}/R^{46\times} - 1\right) - R^{45}/R^{45\times} - 1)\right] \times 1000 \quad (7.10)$$

where R^{47}, R^{46} and R^{45} are the 47/44, 46/44, 45/44 ratios, respectively, for CO_2 and R^{47*}, R^{46*} and R^{45*} are the corresponding ratios if the sample had a stochastic distribution and are calculated from measured abundance ratios (see Eiler, 2007, for details). Inasmuch as clumped isotopes use the Δ notation, they might be considered similar to mass-independent isotope measurements. However, the two are very different. Clumped isotopes measure the deviation from the expected random distribution, whereas mass-independent isotope measurements record deviations from values expected from mass-dependent fractionation.

One of the main applications of clumped isotope studies is in low-temperature carbonate thermometry, giving rise to the field of '*carbonate clumped isotope thermometry*'. The formation of carbonate ions containing the heavy isotopes ^{13}C and ^{18}O is temperature-dependent but is independent of the fluid or mineralogical context in which the exchange reaction takes place. This allows, for example, foraminifera to be used to calculate former ocean temperatures (Meinicke et al., 2020). The novelty of this methodology means that it continues to develop both in the application of new technologies for the precise measurement of small isotopic difference and in the refinement of the equilibrium reaction to take account of impurities in the carbonate phases (Hill et al., 2020).

7.3 Traditional Stable Isotopes

7.3.1 Oxygen

The 'vital statistics' of oxygen isotopes, summarising the range of isotopes, the measured isotope ratio, the standards used and the range of natural compositions, are summarised in Box 7.1.

Box 7.1 Oxygen isotopes

Stable isotopes and abundances

$^{16}O = 99.763‰$

$^{17}O = 0.0375‰$

$^{18}O = 0.1995‰$

Measured isotope ratio

$$\delta^{18}O‰ = \left[\left(^{18}O/^{16}O_{(sample)} - ^{18}O/^{16}O_{(standard)}\right)/^{18}O/^{16}O_{(standard)}\right] \times 1000 \quad (7.11)$$

Standard

Vienna Standard Mean Ocean Water (VSMOW), which has an absolute $^{18}O/^{16}O$ ratio of 0.020052 (Baertschi 1976)

PDB: a belemnite from the Cretaceous Peedee formation of South Carolina (used for low-temperature carbonates)

$$\delta^{18}O_{VSMOW}‰ = 1.03091 * \delta^{18}O_{PDB}‰ + 30.91$$

Mantle value

$$\delta^{18}O‰ = 5.7 \pm 0.2$$

Variations in nature

See Figure 7.1.

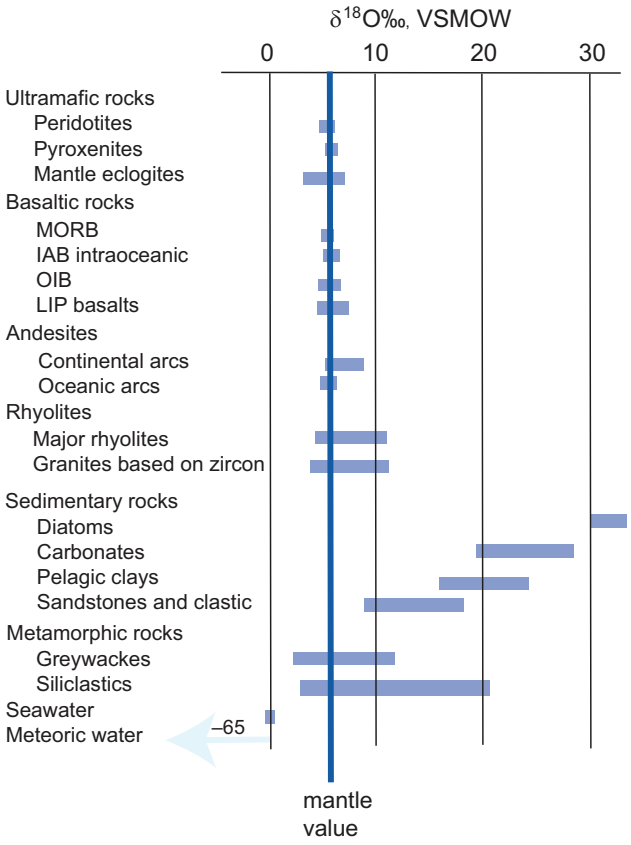

Figure 7.1 The distribution of oxygen isotopes in the major terrestrial reservoirs relative to the Earth mantle ($\delta^{18}O‰ = 5.7 \pm 0.2$ VSMOW). (After Bindeman, 2008; with permission from the Mineralogical Society of America)

Oxygen is liberated from silicates and oxides through laser-fluorination and then reduced to CO_2 at high temperature for measurement in a gas source mass spectrometer. In carbonates carbon dioxide is liberated with >103‰ phosphoric acid. When oxygen isotope ratios are determined in water, the sample is equilibrated with a small amount of CO_2 and the oxygen isotope ratio in the CO_2 is measured. From the known water–CO_2 fractionation factor the $^{18}O/^{16}O$ ratio in the water is calculated. Isotopic measurements are carried out using gas source mass spectrometry with a precision of the order of 0.1‰ (Sharp, 2017). In situ oxygen isotope analysis is also routinely carried out by ion microprobe with a precision of 0.15–0.24‰.

In this section we consider the extent to which oxygen isotopes vary in nature, their use in high-temperature and low-temperature thermometry and their application to the understanding of magmatic processes. In particular, we consider the process of crustal contamination and how it might be demonstrated on oxygen isotope–radiogenic isotope diagrams.

7.3.1.1 Variations of $\delta^{18}O$ in Nature

$\delta^{18}O$ values vary in nature by about 100‰ with about half of this range occurring in meteoric water (Figure 7.1). Evidence from the analysis of ocean basalts indicates that the mantle $\delta^{18}O$ value is 5.7 ± 0.2‰ (Bindeman, 2008), similar to the value for lunar basalts and constant over geological time (Taylor, 1980). The bulk $\delta^{18}O$ value of chondritic meteorites is similar or slightly lighter than that of the Earth's mantle. Felsic magmas show a broader and more positive range of $\delta^{18}O$ values than is found in mafic and ultramafic rocks, and, similarly, sedimentary rocks and meta-sediments are isotopically heavier than mafic rocks and the mantle. Natural waters have very variable oxygen isotope compositions, as discussed below in Section 7.3.2.3, and some water types have strongly negative values relative to the VSMOW standard.

From these observations we can infer that crustal rocks with high $\delta^{18}O$ values (i.e., those that are isotopically heavy) must have experienced some interaction with or were in part derived from high-$\delta^{18}O$ metasedimentary silicate rocks such as metapelites or greywackes. Equally, there are a smaller number of crustal rocks which have unusually low $\delta^{18}O$ values, that is, below mantle values. These are thought to represent samples which have interacted with a low-$\delta^{18}O$ reservoir, the main contender for which is meteoric water. This interaction could be through the hydrothermal alteration of the parent rocks or the metamorphism and/or re-melting of hydrothermally altered source materials (Ryan-Davis et al., 2019). In both instances it is evident that rocks which deviate significantly away from mantle values must have experienced some interaction with materials at the Earth surface, illustrating the way in which oxygen isotopes can be a useful monitor of the process of crustal assimilation and contamination. This was demonstrated by Bindeman (2008), who showed that the assimilation of high-$\delta^{18}O$ supracrustal materials and low-$\delta^{18}O$ hydrothermally altered rocks gives rise to high- and low-$\delta^{18}O$ magmas, respectively (Figure 7.2).

A particularly important means of recovering the $\delta^{18}O$ value of a magma is through the measured oxygen isotope composition of the minerals zircon and quartz. This is possible because (i) these minerals preserve their $\delta^{18}O$ even through high grades of metamorphism (Valley, 2003) and (ii) at high

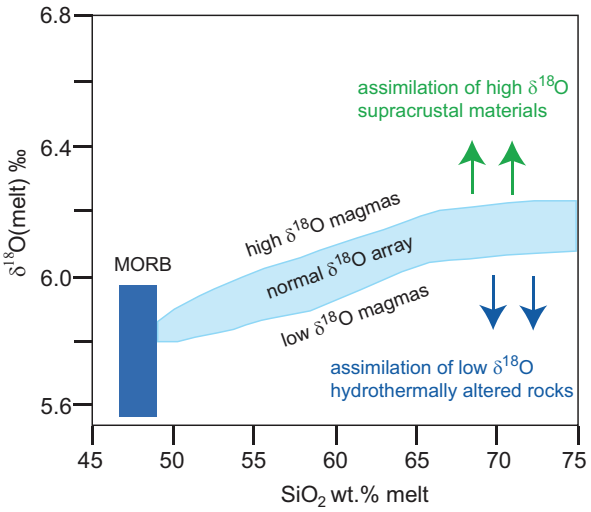

Figure 7.2 A $\delta^{18}O$ versus SiO_2 plot showing the field of mid-ocean ridge basalts (MORB) and the normal array of intermediate to felsic magmas. Also shown are the manner in which high-$\delta^{18}O$ melts are produced by the assimilation of high-$\delta^{18}O$ supracrustal materials and low-$\delta^{18}O$ melts are the product of the assimilation of low-$\delta^{18}O$ hydrothermally altered rocks. (After Bindeman, 2008; with permission from the Mineralogical Society of America)

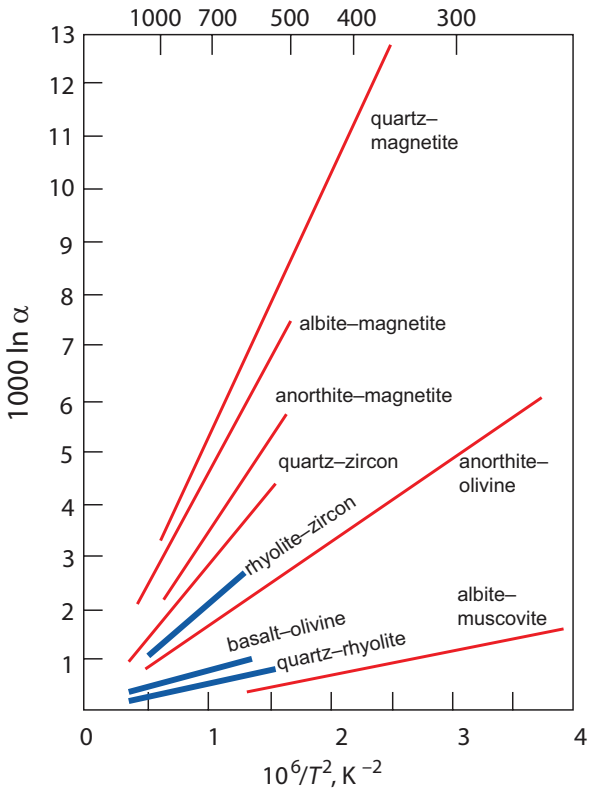

Figure 7.3 Fractionation factors expressed as 1000 ln α plotted relative to temperature shown as °C on the top axis and as $10^6/T^2$ Kelvin on the lower axis. Mineral–mineral fractionation factors are shown as red lines and mineral–melt fractionation factors as blue lines. (After Bindeman, 2008; with permission from the Mineralogical Society of America)

temperatures the fractionation of $\delta^{18}O$ between zircon or quartz and melt is small (Figure 7.3). An empirical study by Bindeman and Valley (2002) suggests that the $\delta^{18}O$ of a rhyolitic melt is about 2‰ higher than that of the zircon at ~750°C and slightly less at higher temperatures. Similarly, the $\delta^{18}O$ of quartz almost mirrors that of the melt, in particular, at temperatures >850°C (Bindeman, 2008). This approach is particularly important in the study of detrital zircons where their magmatic provenance is unknown (Valley, 2003).

7.3.1.2 Oxygen Isotope Thermometry.

One of the first applications of the study of oxygen isotopes to geological problems was to geothermometry. In 1947 Urey suggested that the enrichment of ^{18}O in calcium carbonate relative to seawater was temperature-dependent and could be used to determine the temperature of ancient ocean waters. The idea was quickly adopted, and palaeo-temperatures were calculated for the Upper Cretaceous seas of the Northern Hemisphere. Subsequently, a methodology was developed for application to higher-temperature systems based upon the distribution of ^{18}O between coexisting mineral pairs. An excellent review of the methods and applications of oxygen isotope thermometry is given by Clayton (1981).

The expression summarising the temperature dependence of oxygen isotope exchange between a mineral pair was given above as Eq. 7.5 and is summarised in the expression

$$1000 \ln \alpha_{\text{mineral 1–mineral 2}} = A\left(10^6/T^2\right) + B$$

where T is in Kelvin and A and B are constants. Often the 'B' term is zero, making the fractionation factor simply a function of $1/T^2$.

Empirical observations indicate that a graph of ln α versus $1/T^2$ is linear over a temperature range of several hundred degrees (Figure 7.3) and a plot of this type for a pair of anhydrous phases should pass through the origin. Isotopic fractionations decrease with increasing temperature, and so oxygen isotope thermometers might be expected to be less sensitive at high temperatures. However, experimental studies are most precise at high temperatures (see, e.g., Clayton et al., 1989), and so thermometers have been calibrated for use with igneous and metamorphic rocks. Temperature estimates are most reliable for mineral pairs with large 1000 ln α values, such as the mineral pair quartz–magnetite (Figure 7.3).

(a) *High-temperature applications of oxygen isotope thermometry*. Initially, it was thought that oxygen isotope thermometry in igneous and metamorphic rocks had a number of advantages over conventional cation-exchange thermometry since there was the potential for oxygen isotopic exchange to be measured between many different mineral pairs in a single rock. However, subsequent studies have shown that the re-equilibration of oxygen isotopes between mineral pairs during cooling means that peak conditions in metamorphic rocks and magmatic temperatures in igneous rocks are not always recorded. This means that for oxygen isotope thermometry to reliably record high-temperature events, the minerals examined must be primary and unaltered; they must have not experienced exchange with a fluid phase; and the

rock or magma cooled quickly so the measured isotope values are quenched and do not represent later diffusion. These conditions are rarely met for metamorphic and plutonic rocks, although they can be applied to fresh volcanic rocks containing quenched phenocrysts.

Several tests have been proposed for the reliability of oxygen isotope thermometry, the most useful of which is the concordance test and is based on the observation that there are potentially a large number of thermometers available in a single rock. The method uses mineral-pair measurements plotted on an isotherm plot in order to examine concordance between the different mineral-pair measurements and to assess the extent of isotopic equilibrium (Javoy et al., 1970; Huebner et al., 1986; Gregory et al., 1989). Isotopic equilibrium is measured relative to a straight line with a slope = 1.0, and any departure from this trend is indicative of isotopic disequilibrium.

Currently, the main application of high-temperature oxygen isotope thermometry is focused on refractory mineral pairs in which oxygen diffusion rates are low and which have seen no interaction with fluids. The selection of suitable mineral pairs therefore must be made on the basis of the expected temperature range to be determined in the light of diffusion rates and mineral closure temperatures (Valley, 2001). Suitable minerals include aluminosilicates, magnetite, garnet and rutile in quartzite, and magnetite, titanite and diopside in marble. In igneous rocks the minerals quartz and zircon may be used in silicic rocks and olivine in mafic rocks (Valley, 2001). A plot of measured and empirical mineral–mineral and mineral–melt fractionations versus temperature is shown in Figure 7.3, and a table of relevant fractionation factors is given in Table 7.1 (after Chacko et al., 2001, and Valley, 2003). A recent addition to these fractionation factors is the work of Lacroix and Vennemann (2015), who made an empirical estimate of the fractionation between quartz and Fe–Mg chlorites. They show that for the temperature range 240–550°C,

$$1000\ \ln \alpha_{\text{quartz–chlorite}} = -0.01323\ (\pm 0.002) \times T(^{\circ}\text{C}) + 10.97\ (\pm 0.92) \quad (7.12)$$

(b) *Low-temperature applications of oxygen isotope thermometry.* The earliest application of oxygen isotopes to geological thermometry was in the determination of ocean palaeotemperatures. The method assumes isotopic equilibrium between the carbonate shells of marine organisms and ocean water and uses the equation of Epstein et al. (1953). This equation is still applicable despite some proposed revisions (Friedman and O'Neill, 1977):

$$T^{\circ}\text{C} = 16.5 - 4.3(\delta_c - \delta_w) + 0.14(\delta_c - \delta_w)^2 \quad (7.13)$$

where δ_c and δ_w are respectively the $\delta^{18}O$ of CO_2 obtained from $CaCO_3$ by reaction with H_3PO_4 at 25°C and the $\delta^{18}O$ of CO_2 in equilibrium with the seawater at 25°C. The method assumes that the oxygen isotopic composition of seawater was the same in the past as today, an assumption which has frequently been challenged and which does not hold for parts of the Pleistocene when glaciation removed

Box 7.2 Example of an oxygen isotope thermometer calculation

A coexisting quartz–orthopyroxene pair from a granulite facies metapelite (Huebner et al., 1986, sample Bb25c) has the following measured compositions:

$\delta^{18}O_{\text{quartz}} = 10.2‰$

$\delta^{18}O_{\text{orthopyroxene}} = 7.9‰$

The temperature dependence on the fractionation of ^{18}O between quartz and pyroxene (we use the diopside value as an approximation) – see Table 7.1 and Eq. 7.5 – is

$$1000\ \ln \alpha_{\text{qz–pxn}} = 2.75 \times 10^6/T^2$$

Since the δ value for quartz is >10.0, in this case we use Eq. 7.7

$$\alpha_{A-B} = (1000 + \delta_A)/(1000 + \delta_B)$$

thus

$$\alpha_{\text{quartz–pyroxene}} = 1010.2/1007.9 = 1.00228$$

and

$$1000\ \ln \alpha = 2.279$$

From the thermometer equation (7.5)

$$2.279 = 2,750,000/T^2$$

$T = 1098$ K, or 825°C.

^{18}O-depleted water from the oceans (Clayton, 1981). The method also assumes that the isotopic composition of oxygen in the organism is the same as in seawater and ignores any species specific 'vital effects', and that there has not been any post-burial isotopic exchange with sediment pore water. Because the temperatures of ocean bottom waters vary as a function of depth, it is also possible to use oxygen isotope thermometry in palaeobathymetry to estimate the depth at which certain benthic marine fauna lived.

Using these methods, the careful analysis of deep sea sediment cores has allowed us to reconstruct past ocean temperatures and thus past climates over at least 800,000 years and shows the cyclicity of glacial and interglacial periods. Similarly, climatologists have recognised that continental glacial ice also preserves a long-term record of climate change, which shows the same cyclicity as seen in marine cores. In these studies both δ^{18}O and δD (see Section 7.3.2) are used as temperature proxies. δ^{18}O ice-core measurements are converted into temperature using a calibration based upon the linear relationship between annual values for δ^{18}O and mean annual temperature at the precipitation site (Jouzel et al., 1997) in which δ^{18}O becomes more negative with decreasing temperature. One such linear relationship for the Greenland Summit area gives the relationship $\delta^{18}O‰ = -148.04 + 0.46403T$ (K). While this modern analogue method works best at middle to high latitudes, there are other local (geographic) and temporal factors that must be taken into account in order to obtain an accurate temperature estimate in other areas (Jouzel et al., 1997).

7.3.1.3 Oxygen Isotope–Radiogenic Isotope Correlation Diagrams

Correlations between radiogenic and oxygen isotopes are of particular importance because variations in the two types of isotope come about through totally different mechanisms and they are particularly important in recognising processes that involve contamination and mixing.

(a) *Recognising crust and mantle reservoirs*. Oxygen isotopes are a very effective way of distinguishing between rocks which formed in equilibrium with the mantle and those which formed from the continental crust. In general, the continental crust is enriched in δ^{18}O relative to the Earth's mantle (Figure 7.1). This has come about largely as a consequence of the long interaction between the continental crust and the hydrosphere and the partitioning of ^{18}O into crustal minerals during low-temperature geological processes. Oxygen isotopes, therefore, are a valuable indicator of surface processes and a useful tracer of rocks which at some time have had contact with the Earth's surface. Radiogenic isotopes, on the other hand, show differences between crust and mantle reservoirs which are a function of long-lived differences in parent–daughter element ratios and indicate the isolation of the reservoirs from one another for long periods of Earth history. This gives rise to crustal reservoirs which generally are enriched in ^{87}Sr/^{86}Sr and in radiogenic lead isotopes but depleted in ^{143}Nd/^{144}Nd and ^{176}Hf/^{177}Hf relative to the mantle. As an example, the range of combined oxygen and strontium isotopic compositions in common rock types is shown in Figure 7.4.

(b) *Recognising crustal contamination in igneous rocks.* Many crustal materials have oxygen and strontium isotope ratios which differ from mantle values (Figure 7.4) and so have the potential to provide evidence of the interaction between mantle rocks and the continental crust. This interaction may be through the contamination of mantle-derived melts in the continental crust or through the contamination of the source region by the subduction of crustal materials into the mantle. Details of the mixing processes are given by Taylor (1980), James (1981) and Taylor and Sheppard (1986).

The calculation of mixing curves entails some assumptions about the relative proportions of the parent element of the radiogenic isotope in the end-member compositions. In the case of strontium, when the contaminant in a source region is enriched in Sr relative to the mantle and forms a relatively small proportion of the whole, then contamination on a ^{87}Sr/^{86}Sr versus δ^{18}O mixing diagram is characterised by the *convex downward* curvature of the mixing line. This arises because not only are crustal materials enriched in Sr relative to the mantle but their ^{87}Sr/^{86}Sr ratio is greater than that of the mantle and thus dominates any mixture of the two. Oxygen concentrations, however, are broadly similar in all rocks so that there is no large increase in the oxygen isotope ratio of the derivative melt. The small increase in δ^{18}O is a simple linear function of the bulk proportion of crustal to mantle materials. In the case when the melt is enriched in Sr relative to the contaminant and the relative proportion of the contaminant is high, then compositions on a Sr–O isotope plot will define a mixing curve with a *convex-up* curvature (James

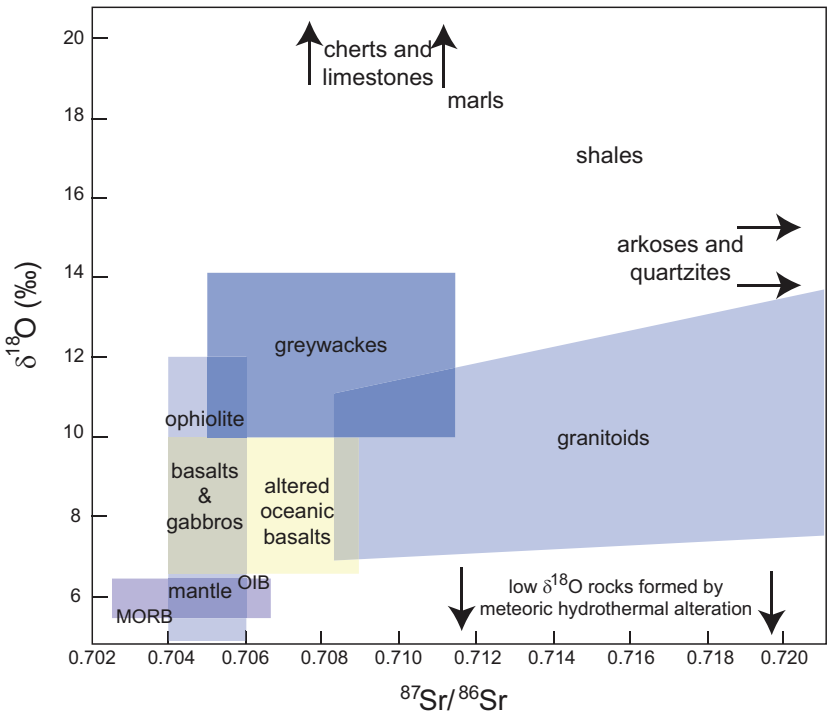

Figure 7.4 The indicative ranges of oxygen and strontium isotopes in common igneous and sedimentary rocks. (Adapted from Magaritz et al., 1978)

1981). This could be the case for a mantle-derived melt passing through the continental crust.

An example of the way in which source mixing has been inferred using oxygen and radiogenic isotopes is given by Trumbull et al. (2004). They show that 130 Ma, Cretaceous granites and related rhyolitic lavas from Namibia have a range of compositions that implies the mixing of mafic melts similar to those found in the Tristan mantle plume with a melt of lower crustal felsic rocks similar in composition to the A-type Damaran granites found in this region. A plot of $\delta^{18}O$ in quartz versus the whole-rock Nd isotope composition, expressed as ε_{Nd}, for a range of granitoids and felsic lavas lies on a mixing line between the probable mantle source and a lower crustal source (Figure 7.5a). A similar trend is seen on a plot of $\delta^{18}O$ versus the Sr isotope composition of the melt at 130 Ma (Figure 7.5b) and illustrates the convex-downward mixing curve described above.

MacPherson et al. (1998) sought to discriminate between mixing in the source region and crustal contamination in the Kermadec–Hikurangi convergent margin. Using $\delta^{18}O$ in clinopyroxene as a proxy for the composition of melts, they showed that there is a linear trend between $\delta^{18}O$ and whole-rock $^{143}Nd/^{144}Nd$ (in modern lavas this is the same as the mantle ratio). The results were compared with mixing curves for the contamination of the source region – the mixing of a depleted mantle peridotite with a fluid derived from altered subducted oceanic crust and sediment – and the contamination of basalt with crustal sediments. They showed that the shape of the curve defined by the data gave a better fit to the curves for crustal contamination than that calculated for mixing in the source (Figure 7.5c), indicating that the melts had interacted with sediments prior to eruption.

Source contamination is more easily recognisable in regions where there is no continental crust such as in oceanic basalts. This, however, has become possible only with improved resolution in oxygen isotope analysis, for the oxygen isotope variations may be small. Studies by Eiler (2001) showed that a small increase in $\delta^{18}O$ (less than 1.0‰) in olivine in ocean island basalts correlated with increasing $^{87}Sr/^{86}Sr$, implies a contaminated source.

Finally, it is important to note that crustal contamination is rarely a simple mixing process and frequently involves three components: a melt, a precipitating cumulate phase and a contaminant (Taylor, 1980; James, 1981). This is the AFC process illustrated in Figure 7.6 for mixing between $\delta^{18}O$ and

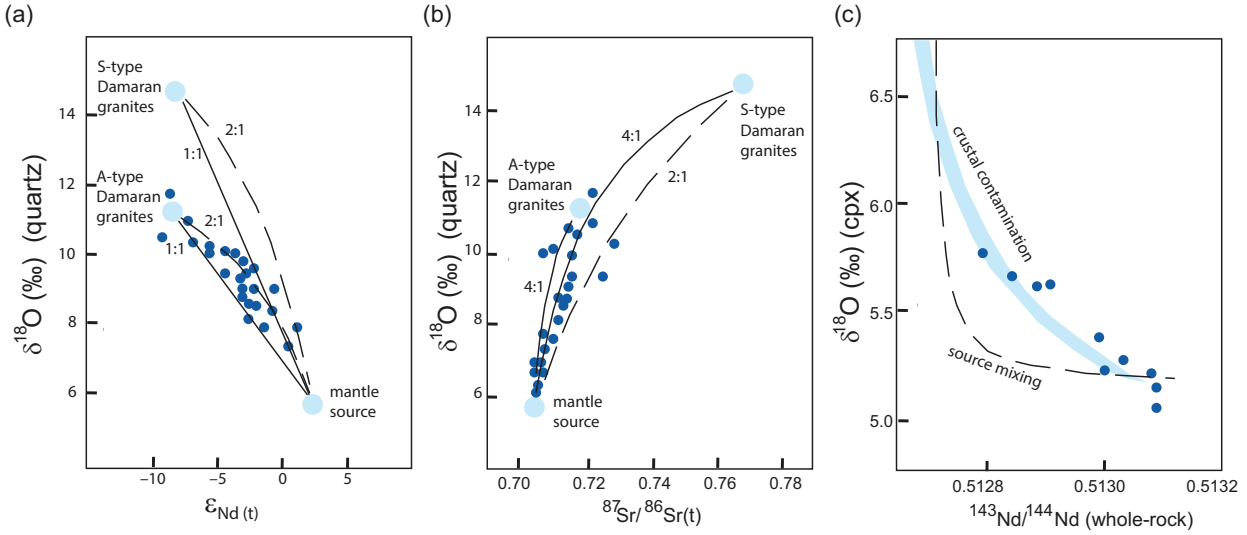

Figure 7.5 $\delta^{18}O$ versus radiogenic isotopes. (a) Plot of $\delta^{18}O_{quartz}$ versus $\varepsilon_{Nd(t)}$ for granitoids and felsic volcanic rocks (dark blue symbols) from Namibia. Source compositions for the mantle and two proxy crustal sources (Damaran granites) are shown in pale blue. Mixing lines between the mantle and crustal sources are constructed for the cases when the Nd concentrations in the crust and mantle are the same (1:1) and when the Nd concentration in the mantle is twice that in the crust (2:1). (b) Plot of $\delta^{18}O_{quartz}$ versus $(^{87}Sr/^{86}Sr)_{130Ma}$ for granitoids and felsic volcanic rocks (blue symbols) from Namibia. Source compositions for the mantle and two proxy crustal sources are shown in pale blue. Mixing lines between the mantle and crustal sources are constructed for the cases when the Nd concentrations in the mantle are twice (2:1) and four times (4:1) that in the crust. The data in panels (a) and (b) do not support mixing between the mantle source and melts of a lower crystal source similar in composition to the S-type Damaran granites (after Trumbull et al., 2004; with permission from Elsevier). (c) Plot of $\delta^{18}O_{clinopyroxene}$ versus $(^{143}Nd/^{144}Nd)_{whole\text{-}rock}$) for arc-related lavas from the Kermadec–Hikurangi margin (after MacPherson et al., 1998; with permission from Elsevier). Arc lavas are shown as blue symbols; the pale blue curve is the calculated trend for models of the magma contaminated by continental crust. The dashed line is the calculated curve for mixing between depleted upper mantle and fluids derived from subducted oceanic crust. The data support the crust-contamination model.

$^{87}Sr/^{86}Sr$ from Taylor (1980). AFC processes, as opposed to simple mixing curves, are represented by a sigmoidal curve which does not extrapolate back to the position of either the source or contaminant.

(c) *Recognising simple crystal fractionation in igneous rocks.* An igneous system which has not suffered crustal contamination will exhibit the radiogenic isotope characteristics of the source, for radiogenic isotope ratios are not altered by crystal–liquid equilibria such as crystal fractionation. Oxygen isotopes, on the other hand, do show small changes in isotope ratio with crystal fractionation as is illustrated in Figure 7.2 and show a small increase in $\delta^{18}O$ with increasing silica content. This decoupling between oxygen and strontium isotopes was documented by Chivas et al. (1982) in a study of a highly fractionated oceanic-arc plutonic suite in which oxygen isotope ratios increase from mantle values ($\delta^{18}O$ = 5.4‰) in gabbros to $\delta^{18}O$ = 7.2‰ in an aplite dyke, whereas $^{87}Sr/^{86}Sr$ ratios remain constant within the limits of error of their determination.

7.3.2 Hydrogen Isotopes and the Stable Isotope Geochemistry of Water and Hydrothermal Fluids

The element hydrogen is ubiquitous in nature in the forms H_2O, OH^-, H_2 and as hydrocarbons. There are two isotopes of hydrogen: ^1H and ^2H, normally referred to as D (deuterium); isotope ratios are measured as the ratio $D/^1H$, expressed as δD. Hydrogen isotopes show the largest relative mass difference between two stable isotopes with the result that there are large variations in measured hydrogen isotope ratios in naturally occurring materials.

The study of oxygen isotopes in conjunction with the isotopic study of hydrogen has proved to be a very powerful tool in investigating geological processes

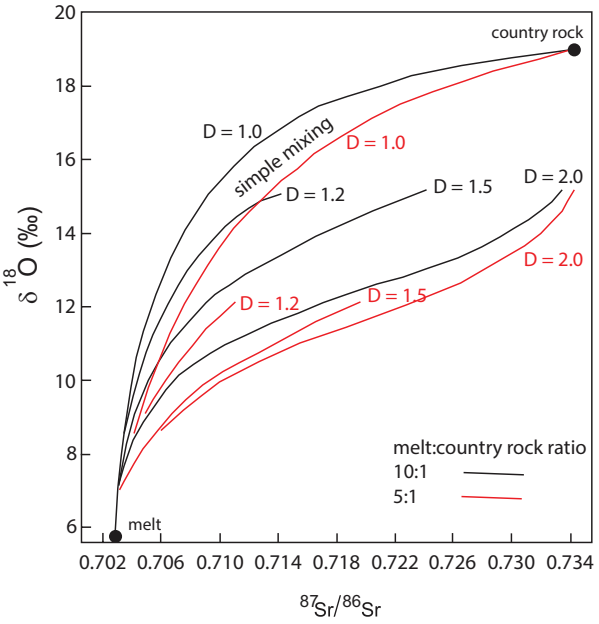

Figure 7.6 Variation in $\delta^{18}O$ with $^{87}Sr/^{86}Sr$ during assimilation and fractional crystallisation of a magma with $\delta^{18}O = 5.7$ and $^{87}Sr/^{86}Sr = 0.703$ contaminated with a crustal component (country rock) with $\delta^{18}O = 19$ and $^{87}Sr/^{86}Sr = 0.735$, for values of the partition coefficient (D) for Sr from 1 to 2. The black curves are for R = 0.1 (melt to country rock ratio = 10:1) and the red curves are for R = 0.2 (melt to country rock ratio = 5:1). The ratio of cumulates to assimilated country rock is 5:1. (After Taylor 1980)

involving water. When plotted on a bivariate δD versus $\delta^{18}O$ graph, waters from different geological environments are found to have very different isotopic signatures (Section 7.3.2.3). Hydrogen is a minor component of most rocks, and so, excepting when the fluid–rock ratio is very low, the hydrogen isotope composition of rocks and minerals is sensitive to the hydrogen isotope composition of interacting fluids. Oxygen, on the other hand, comprises 50‰ by weight (and in some cases more than 90‰ by volume) of common rocks and minerals and so is less sensitive to the oxygen isotope ratio of interacting fluids, except at very high fluid–rock ratios (Section 7.3.2.6).

7.3.2.1 Hydrogen Isotopes

The basic data for hydrogen isotopes are given in Box 7.3, and a summary of δD values for solar system bodies (Figure 7.7) and common rock types and waters (Figure 7.8) are also provided. Hydrogen is generated by heating minerals in a radio frequency (RF) induction furnace to liberate water from the mineral host. The water is then reduced to hydrogen in a furnace using zinc (Vennemann and O'Neill, 1993) or uranium.

7.3.2.2 The Distribution of Hydrogen Isotopes in the Solar System

As might be expected, given the fundamental nature of hydrogen in the solar system, the fractionation of D/H between solar system objects is of considerable interest in planetary geochemistry, in particular, in the quest to understand the origin of water on the Earth and in other planetary bodies. There are now data from a number of solar system objects obtained by direct measurement from spacecraft and from spectral studies which show that the fractionations are very large with δD from < -800 to $> +4000$ and D/H varying over two orders of magnitude (Saal et al., 2013; Clarke et al., 2019). In planetary geochemistry D/H ratios are thought to indicate where in the solar system planets and different solar system objects formed. The protosolar nebula was isotopically light with D/H about 0.25×10^{-4}, similar to the values recorded from the atmospheres of Jupiter and Saturn. Values for the inner solar system, including Earth and Mars, are higher but define a narrow range of D/H ratios of $\sim 1.5 \times 10^{-4}$. The D/H of the bulk Earth is $1.49(\pm 0.03) \times 10^{-4}$ ($\delta D = -43$) (Lécuyer et al., 1998), slightly lower than the Earth's oceans ($D/H = 1.56 \times 10^{-4}$). Outer solar system comets have higher values ranging from Earth-like values to D/H $\sim 5.0 \times 10^{-4}$. Carbonaceous chondrite meteorites have δD values in the range −197 to +133‰, although CI chondrites have a narrower range of between +77 and +133 (Eiler and Kitchen, 2004). These values are shown in Figure 7.7, using data from Eiler and Kitchen (2004), Usui et al. (2012), Saal et al. (2013), Altwegg et al. (2015) and Clarke et al. (2019).

7.3.2.3 The Distribution of Hydrogen Isotopes in Natural Waters

The isotopic composition of natural waters may be obtained either by direct measurement or by calculation from hydrous mineral phases using the method outlined in Section 7.3.2.5. Much of the work in this field was carried out in the 1960s and 1970s by Hugh Taylor's group working at Caltech and is summarised in major contributions (Taylor, 1974; 1978). Taylor (1974) identifies six types of naturally occurring water

Box 7.3 Hydrogen isotopes

Stable isotopes and abundances

$^{1}H = 99.9844‰$

$D = 0.0156‰ \ (^{2}H = \text{Deuterium})$

Measured isotope ratio

$$\delta D‰ = \left[\left(D/H_{(sample)} - D/H_{(standard)}\right)/D/H_{(standard)}\right] \times 1000 \quad (7.14)$$

In hydrology δD may be referred to as $\delta^{2}H$

In planetary studies δD may be expressed as D/H (the conversion factor uses the absolute value for D/H recorded below and Eq. 7.14)

Standard

Vienna Standard Mean Ocean Water (VSMOW); absolute D/H ratio = $1.557 * 10^{-4}$

Mantle value

δD‰ = −76 to −48‰ (average of 61‰); recommended value −60 ± 5‰ (Clog et al., 2013).
Bulk Earth δD‰ = −43

Variations in δD in the solar system

See Figure 7.7.

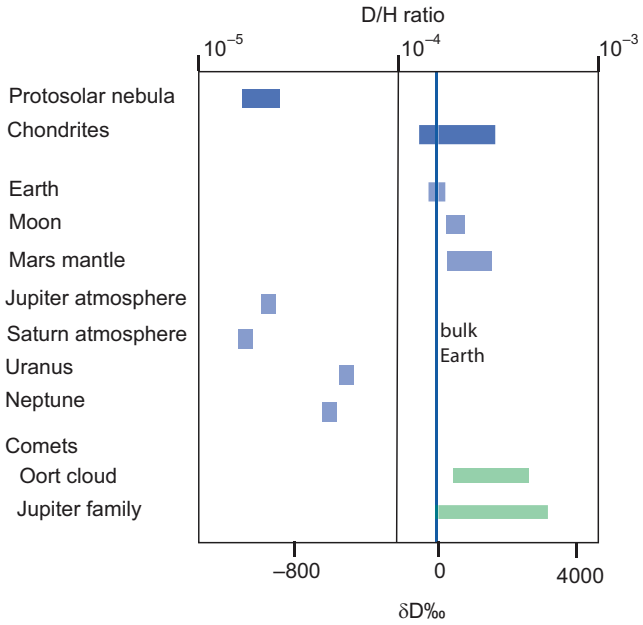

Figure 7.7 The range of hydrogen isotopes in solar system objects relative to the bulk Earth. (Data sources discussed in the text)

Box 7.3 (cont.)

Terrestrial variation of δD.
See Figure 7.8

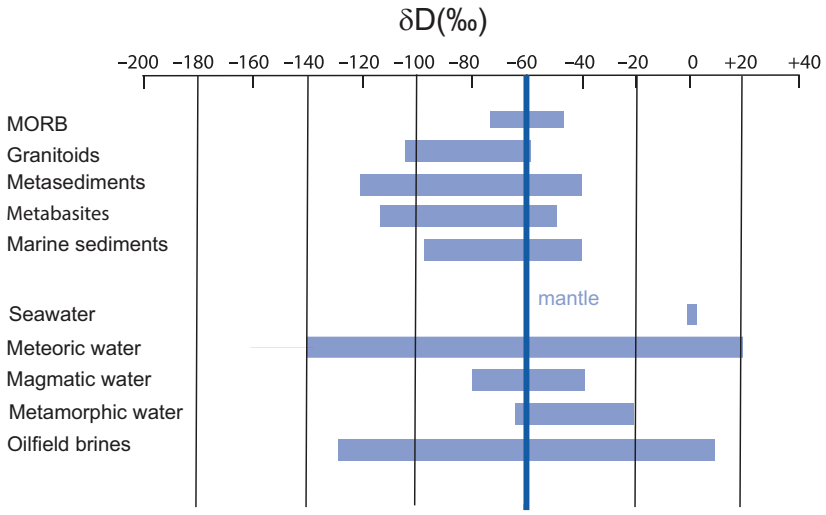

Figure 7.8 The range of hydrogen isotopes in some terrestrial reservoirs relative to the Earth's mantle. (Data sources discussed in the text)

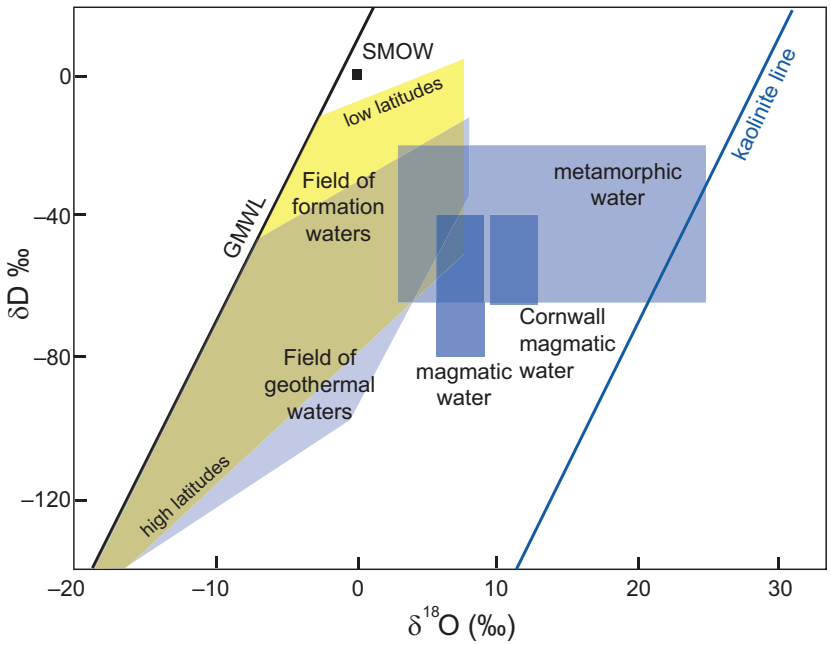

Figure 7.9 Plot of δD versus $\delta^{18}O$ diagram for different water types. The fields of magmatic water, formation waters and geothermal waters are taken from Taylor (1974). The field for magmatic water from the granites of Cornwall is from Sheppard (1977). The metamorphic water field combines the values of Taylor (1974) and Sheppard (1981). The meteoric water line is from Craig (1961) and the kaolinite line from Taylor (1974).

which have a major influence on our thinking about hydrogeological processes, the compositions of which are summarised on a δD versus $\delta^{18}O$ diagram (Figure 7.9). The isotopic character of the different types of water described here can be used to trace the origin of hydrothermal solutions.

(a) *Ocean water.* Standard Mean Ocean Water is the isotopic standard for both $\delta^{18}O$ and δD; therefore, convention dictates that ocean water has $\delta^{18}O = 0‰$ and $\delta D = 0‰$. Exceptions to this rule are from areas such as the Red Sea which has elevated values of $\delta^{18}O$ and δD created through high rates of evaporation, or from areas

where seawater is diluted with fresh water. Muehlenbachs and Clayton (1976) suggested that the oxygen isotopic composition of ocean water is buffered by exchange with the ocean crust, a view which is strongly supported by the study of Gregory and Taylor (1981) on the distribution of oxygen isotopes in the Semail ophiolite, Oman (Figure 7.12).

Less certain is the isotopic composition of seawater in the past. Lécuyer et al. (1998) and Pope et al. (2012) calculated that in the very early Earth the mass of the oceans was greater by about 20‰, that the hydrogen isotope composition of seawater was lower than the present value by 20–30‰ but that the oxygen isotope composition was comparable to that of the modern oceans. In geologically more recent times there is evidence from the oxygen isotope composition of benthic foraminifera that there were global changes in the isotopic chemistry of the oceans during the Tertiary. In addition, data from marine sediment cores show that there were also changes to the oxygen isotope composition of the oceans during the Holocene brought about by the storage of isotopically light oxygen in ice in the polar regions, giving rise to isotopically heavier ocean water.

(b) *Meteoric water.* Meteoric water shows the greatest variation in δD of all natural waters and the relationship between δD and $\delta^{18}O$ is linear and quantified by Craig (1961) as:

$$\delta D‰ = 8\delta^{18}O + 10 \quad (7.15)$$

δD and $\delta^{18}O$ values for meteoric water vary according to latitude. Values are close to zero on tropical ocean islands, whereas at high latitudes in continental areas $\delta^{18}O$ values are as low as −55‰ and δD values extend down to −440‰, although δD values below −160‰ are for polar snow and ice. Both the extreme variation and the linear relationship arise from the condensation of H_2O from the Earth's atmosphere. The extreme variation reflects the progressive lowering of ^{18}O in an air mass as it leaves the ocean and moves over a continent. The linearity of the relationship, now known as the Global Meteoric Water Line (GMWL, Figure 7.9), indicates that fractionation is an equilibrium process and that the fractionation of D/H is proportional to $^{18}O/^{16}O$. Subsequent studies identified deviations away from the GMWL, and some local meteoric water lines have slopes significantly different from the value of 8 due to local differences in temperature and humidity and kinetic effects during evaporation (Jouzel and Koster, 1996).

(c) *Geothermal water.* Modern geothermal water is meteoric in origin but isotopic compositions are transposed to higher $\delta^{18}O$ values through isotopic exchange with the country rocks. δD values are the same as in the parent meteoric water or slightly enriched due to the non-equilibrium evaporation of water vapour (Figure 7.9). In contrast, ocean-floor geothermal systems are far more complex, particularly if methane is present, for they may host microbial communities which fractionate D/H to produce extremely light hydrogen with δD values $< -400‰$ (Konn et al., 2015).

(d) *Formation water.* Formation waters from sedimentary basins are usually saline and show a wide range in $\delta^{18}O$ and δD values (Figure 7.9). The formation waters reported by Taylor (1974) are brines from oilfields. His results show that individual basins have water compositions which define specific linear trends representing mixing between meteoric water and either water from another source such as trapped seawater or the country rock. There is a decrease in the δD of formation waters at higher latitudes, further emphasising the link with surface meteoric waters.

(e) *Magmatic water.* The composition of magmatic waters is calculated from the isotopic compositions of igneous minerals (see Section 7.3.2.5). Particularly useful is the mineral muscovite, for at 800°C the isotopic composition of muscovite is the same as that of the water with which it is in equilibrium. The compositional range of magmatic water is quite well constrained for most igneous minerals and defines a very restricted field in δD–$\delta^{18}O$ space, between −40 and −80‰ and +5.5 and +9.0‰, respectively (Taylor, 1974). Sheppard (1977), however, showed that the magmatic waters associated with the Permian granites in Cornwall, southwest England, plot in a different field with δD values of −40 to −65‰, and $\delta^{18}O$ values of +9.5 to +13‰ (Figure 7.9). These granites are most probably the product of intra-crustal melting, and so the higher $\delta^{18}O$ is inherited from a crustal protolith. This example highlights one of the ongoing difficulties in interpreting δD–$\delta^{18}O$ data – that of differentiating between rocks whose source interacted with meteoric water prior to melting, that is, low-$\delta^{18}O$ magmas, and those which interacted with meteoric water during or after emplacement. New advances in our understanding in this area have come from a study of $\delta^{18}O$ in zircons; see, for example, Gilliam and Valley (1998) and Rumble et al. (2002).

(f) *Metamorphic water.* Our only access to the composition of metamorphic water is by back-calculating

from the minerals present in the rock. In order to do this accurately, the temperature of the metamorphism must be known. Estimates of the δD and $\delta^{18}O$ values of water in equilibrium with metamorphic minerals over a range of metamorphic grades have been made by Taylor (1974), Rye et al. (1976) and Sheppard (1981). A combination of these values gives a metamorphic water 'box' with $\delta^{18}O$ values between +3 and +25‰ and with δD values between −20 and −65‰ (Figure 7.9). The relatively high $\delta^{18}O$ values in some metamorphic rocks may suggest some inheritance from their sedimentary protoliths.

7.3.2.4 The Distribution of Hydrogen Isotopes in Terrestrial Reservoirs

The distribution of hydrogen isotopes from the upper mantle, the crust and clays associated with weathering is summarised in Figure 7.8 and in the discussion below.

(a) *The depleted upper mantle.* The δD value for the upper depleted mantle has been estimated from studies of magmatic water liberated from MORB. Early studies suggested a wide range of values but with the majority falling between −85 and −65‰ (Kyser and O'Neill, 1984). More recent measurements for the depleted upper mantle have revised these estimates and suggest a range between −76 and −48‰ with an average of 61‰ and a recommended value of −60 ± 5‰ (Clog et al., 2013). This value is close to that calculated by Lécuyer et al. (1998) for the bulk Earth of −40‰.

(b) *Crustal lithologies.* Other terrestrial reservoirs show a wide range of δD values, since frequently the whole-rock δD value of many terrestrial rocks is a composite value resulting from many different processes. In the case of igneous rocks, for example, processes such as magmatic degassing, crystal fractionation from a melt and sub-solidus interaction with meteoric water might all be superimposed on and thereby obscure the primary magmatic value. For this reason, the range of values for crustal lithologies shown in Figure 7.8 is not particularly useful as a discriminant.

Granitoids from the New England batholith, Australia, have δD values between −60 and −130 (O'Neill et al., 1997) and A-type granites from eastern China have δD = −59 to −145 (Wei et al., 2000). Meta-sediments have bulk rock δD values between −70 and −120 (Taylor, 1974), although lower values are recorded by Harris et al. (1997). Ultra-high-pressure (UHP) mafic rocks and felsic gneisses from the Dabie–Sulu orogenic belt in China have δD values in the range −74 to −100 (Chen et al., 2011). Lower-grade mafic and ultramafic rocks have a similar range of values (−51 to −115; Ikin and Harmon, 1983). In marine sediment δD values are in the range δD = −40 to −95 (Taylor 1974).

(c) *Clay minerals in the weathering environment.* There is strong relationship between the isotopic composition of kaolin in weathering zones and the coexisting meteoric waters such that it is possible to define a 'kaolinite line' sub-parallel to the GMWL in which, relative to meteoric waters, clays are enriched in $\delta^{18}O$ and depleted in δD (Figure 7.9). The kaolinite line may be expressed as

$$\delta D = 7.5 \times \delta^{18}O - 220 \quad (7.16)$$

The linear relationship suggests that the kaolin was formed in equilibrium with meteoric water (Taylor, 1974). In a similar way, the clay mineral smectite also forms a linear array on $\delta^{18}O$–δD diagrams, defining a 'smectite line'. However, in this case the position of the smectite line is temperature-sensitive such that the distance between the GMWL and the smectite line increases with decreasing equilibration temperature and shifts towards higher $\delta^{18}O$ values. The link between meteoric water and clay minerals means that the minerals kaolinite and smectite offer the potential to be palaeoclimatic indicators and allow for the calculation of the $\delta^{18}O$ and δD of the meteoric water in which they were in equilibrium (Mix and Chamberlain, 2014). The temperature of kaolination can be calculated from the equation of Clauer et al. (2015):

$$3.04 \times 10^6 \times T^{-2} = \delta^{18}O_k - 0.125\delta D_k + 7.04 \quad (7.17)$$

7.3.2.5 Calculating the Isotopic Composition of Hydrothermal Fluids from Mineral Compositions

Most commonly, the δD and $\delta^{18}O$ composition of a hydrothermal fluid has to be calculated from the isotopic composition of minerals which were in equilibrium with it using laboratory calibrations of equilibria between rock-forming minerals and water. More rarely, the isotopic composition of hydrothermal fluids can be measured directly as the fluid preserved in fluid inclusions (Ohmoto and Rye, 1974; de Graaf et al., 2019). Where isotopic compositions are

Box 7.4 Example of a calculation of the isotopic composition of water in equilibrium with muscovite from the Climax molybdenum deposit, Colorado (data from Hall et al. 1974, table 4, sample CL31–70).

Data
$\delta^{18}O_{muscovite} = +7.4‰$
$\delta D_{muscovite} = -91.0‰$
Temperature = 500°C (from fluid inclusion thermometry)

*Calculation of the **oxygen** isotope composition of the water*

The equation for muscovite–water (O'Neill and Taylor, 1967; see Table 7.2) is

$$1000 \ln \alpha = -3.89 + \left(2.38 \times 10^6/T^2\right) \quad [T \text{ in K}]$$

at 500°C

$$1000 \ln \alpha = 0.0931$$

Since $\Delta_{muscovite\text{-}water} = 1000 \ln \alpha$

$$\delta^{18}O_{muscovite} - \delta^{18}O_{water} = 0.0931$$
$$+7.4 - \delta^{18}O_{water} = 0.0931$$
$\delta^{18}O_{water} = 7.3‰$ (note : under these conditions, very similar to that of muscovite)

*Calculation of the **hydrogen** isotope composition of the water*

The equation for muscovite–water (Suzuoki and Epstein, 1976; see Table 7.3) is

$$1000 \ln \alpha = 19.1 - \left(22.1 \times 10^6/T^2\right) \quad [T \text{ in K}]$$

at 500°C

$$1000 \ln \alpha = -17.89$$

Since $\Delta_{muscovite\text{-}water} = 1000 \ln \alpha$

$$\delta D_{muscovite} - \delta D_{water} = -17.89$$
$$-91 - \delta D_{water} = -17.89;$$
$\delta D_{water} = -73.1‰$ (also not very different from that of the original mineral)

calculated, it is necessary to show that there was a close approach to isotopic equilibrium between a given mineral and the original hydrothermal fluid. This is not always straightforward, for the diffusion rates of hydrogen isotopes may be up to 100 times faster than those for oxygen isotopes even in the same mineral (Kyser and Kerrich, 1991).

Experimental calibrations for both oxygen and hydrogen isotopes in a range of mineral phases are given in Tables 7.2 and 7.3, respectively, allowing the isotopic composition of a hydrothermal fluid to be fully specified. This calculation requires knowledge of the temperature of equilibration which may have to be estimated or measured independently from a technique such as fluid inclusion thermometry. An example of this approach is given by Hall et al. (1974, table 4) in a study of the origin of the hydrothermal fluids involved in the formation of the Climax molybdenum deposit, Colorado. In this study the temperature of the hydrothermal fluid was already known from fluid inclusion thermometry and the $\delta^{18}O$ and δD composition of the water were calculated from the isotopic composition of muscovite and sericite using the experimental calibrations for muscovite–water. An example of the calculation is given in Box 7.4.

7.3.2.6 Quantifying Water–Rock Ratios

The geochemical effects of water–rock interaction can vary between two extremes. When the water–rock ratio is small, it is the $\delta^{18}O$ in the rock that dominates the system and it is the fluid composition which is altered. On the other hand, when the water–rock ratio is large and the $\delta^{18}O$ of the water dominates the system, then it is the $\delta^{18}O$ value of the rock that is modified. Taylor (1974, 1977) derived mass balance equations from which the water–rock ratio may be calculated from $\delta^{18}O$ values. For a closed system, from which no water is lost, the water–rock (W/R) ratio, integrated over the lifetime of the hydrothermal system, is:

$$W/R_{closed} = \left(\delta^{18}O^{final}_{rock} - \delta^{18}O^{initial}_{rock}\right)/\left(\delta^{18}O^{fluid}_{initial} - \delta^{18}O^{final}_{fluid}\right) \quad (7.18)$$

This is the effective water–rock ratio which can differ from the actual water–rock ratio depending upon the efficiency of the exchange reaction. The initial value of the rock ($\delta^{18}O^{initial}_{rock}$) is obtained from 'normal' values for the particular rock type (see Figure 7.1) or from an unaltered sample of the rock suite. The final value for the rock ($\delta^{18}O^{final}_{rock}$) is the measured value. The initial value for the fluid ($\delta^{18}O^{fluid}_{initial}$) is assumed (e.g., modern seawater) or in the case of meteoric water is calculated

Table 7.2 Constants for the fractionation of oxygen isotopes between minerals and water[a]

Mineral	T (°C)[b]	A	B	Reference
Barite	100–350	−6.79	3.00	Friedman and O'Neill (1977)
Calcite	0–700	−3.39	2.78	O'Neill et al. (1969)
Dolomite	252–295	−3.24	3.06	Matthews and Katz (1977)
Quartz	200–500	−3.4	3.38	Clayton et al. (1972)
	500–750	−1.96	2.51	Clayton et al. (1972)
	250–500	−3.31	3.34	Matsuhisa et al. (1979)
	500–800	−1.14	2.05	Matsuhisa et al.,(1979)
Alkali feldspar	350–800	−3.41	2.91	O'Neil and Taylor (1967)
	500–800	−3.7	3.13	Bottinga and Javoy (1973)
Albite	400–500	−2.51	2.39	Matsuhisa et al. (1979)
	500–800	−1.16	1.59	Matsuhisa et al. (1979)
Anorthite	350–800	−3.82	2.15	O'Neil and Taylor (1967)
	400–500	−2.81	1.49	Matsuhisa et al. (1979)
	500–800	−2.01	1.04	Matsuhisa et al. (1979)
Plagioclase	350–800	$-3.4 - 0.14 \times An$	$2.91 - 0.76 \times An$	O'Neill and Taylor (1967)
	500–800	−3.7	$3.13 - 1.04 \times An$	Bottinga and Javoy (1973)
Muscovite	400–650	−3.89	2.38	O'Neill and Taylor (1967)
	500–800	−3.1	1.9	Bottinga and Javoy (1973)
Rutile	575–775	1.46	4.1	Addy and Garlick (1974)
Magnetite	500–800	−3.7	−1.47	Bottinga and Javoy (1973)
Kaolinite	0–350	−4.05	2.76	Sheppard and Gilg (1996)
Smectite	0–350	−6.75	2.55	Sheppard and Gilg (1996)
Illite	0–350	−3.76	2.39	Sheppard and Gilg (1996)
Chlorite	66–175	For $[Mg_{2.5}Fe_{0.5}(OH)_6][Al_{1.5}Fe_{1.5}][Al, Si_3O_{10}][OH_2]$ $-11.97 + 2.67x + 2.93x^2 - 0.415x^3 + 0.037x^4$; where $x = 10^3/T$		Savin and Lee (1988)

[a] For the equation 1000 ln $\alpha_{mineral-water} = A + (B*10^6/T^2)$.
[b] Experimental range.

Table 7.3 Constants for the fractionation of hydrogen isotopes between minerals and water[a]

Mineral	T (°C)	A	B	Reference
Muscovite	450–800	19.1	−22.1	Suzuoki and Epstein (1976)
Biotite	450–800	−2.8	−21.3	Suzuoki and Epstein (1976)
Hornblende	450–800	7.9	−23.9	Suzuoki and Epstein (1976)
Ferroan pargasite	350–850	-23.1 ± 2.5		Graham et al. (1984)
Ferroan pargasite	850–950	1.1	−31	Graham et al. (1984)
Tremolite	350–650	−21.7		Graham et al. (1984)
	650–950	14.9	−31	
Actinolite	400	−29		Graham et al. (1984)
Arfedsonite	Uncertain	−52		Graham et al. (1984)
Kaolinite/Dickite	100–250	0.972-0.985		Marumo et al. (1980)
Sericite	100–250	0.973–0.977		Marumo et al. (1980)
Chlorite	100–250	0.954–0.987		Marumo et al. (1980)
Zoisite	280–650	−27.73	−15.7	Graham et al. (1980)
Epidote	<300	−138.8	29.2	Graham et al. (1980)
	300–650	$-35.9 + 2.5$		Graham et al. (1980)
All minerals	1000 ln $\alpha_{mineral-water} = 28.2 - (22.4 * 10^6/T^2)$ $+ (2X_{Al} - 4X_{Mg} - 68X_{Fe})$, where X_{Al}, etc., is the mole fraction of Al in biotite, muscovite or hornblende			Suzuoki and Epstein (1976)

[a] For the equation 1000 ln $\alpha_{mineral-water} = A + (B * 10^6/T^2)$.

from D/H ratio of the alteration assemblage and the meteoric water equation. The composition of the final fluid ($\delta^{18}O^{final}_{fluid}$) can be calculated from the mineralogy of the altered rock. This is sometimes done by using the approximation that $\delta^{18}O$ plagioclase feldspar (An_{30}) ~ $\delta^{18}O$ rock, for feldspar is generally an abundant mineral in most rocks and exhibits the greatest rate of exchange between ^{18}O and an external fluid phase. Provided that the temperature can be independently estimated, then the feldspar–water fractionation equation can be used to calculate the water composition (see the example below).

The equation for an open system in which the water makes only a single pass through the system is given by (Taylor, 1978) as

$$W/R_{open} = \ln(W/R_{closed} + 1) \quad (7.19)$$

and the contrasting effects of open and closed systems on $\delta^{18}O$ relative to the water–rock ratio are shown in Figure 7.10.

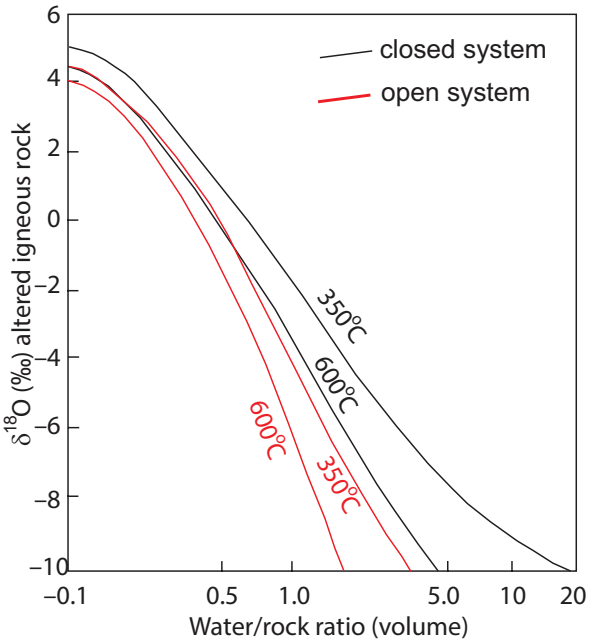

Figure 7.10 Plot of $\delta^{18}O$ values in a hydrothermally altered rock calculated from the open-system water–rock ratio equation (Eq. 7.19) and the closed-system water–rock ratio equation (Eq. 7.18) (Taylor, 1974). The model assumes an initial $\delta^{18}O$ value of +6.5 in the rock and an initial $\delta^{18}O$ value of −14 in the water and curves are shown for 350°C and 600°C.

An example of how water–rock ratios may be calculated from oxygen isotope measurements is given in Box 7.5.

Care should be taken in noting the units used for quantifying water–rock ratios, for both volume units and weight units are used. Both are shown in Figure 7.11. It is likely that any given

Box 7.5 Example of a water–rock ratio calculation using the equations of Taylor (1974, 1977).

Data

Initial rock composition: $\delta^{18}O = 6.5‰$
Final rock composition: $\delta^{18}O = -4.0‰$
Initial fluid composition: $\delta^{18}O = -14.0‰$

Calculation of final fluid composition

The equation for plagioclase (An = 0.3) –water exchange from Table 7.2 is

$$1000 \ln \alpha_{fsp-water} = (-3.41 - 0.14 \times An) + (2.91 - 0.76 \times An) \times (10^6/T^2)$$

$$1000 \ln \alpha_{fsp-water} = -3.452 + 2.682 \times (10^6/T^2)$$

at 500°C

$$1000 \ln \alpha_{fsp-water} \sim \Delta_{fsp-water} = 1.036 \text{ (see Eq.7.6)}$$

$$\Delta_{fsp-water} = \delta^{18}O_{fsp} - \delta^{18}O_{water},$$

so $\delta^{18}O_{water} = \delta^{18}O_{fsp} - \Delta_{fsp-water}$

Assuming $\delta^{18}O_{fsp} \sim \delta^{18}O_{whole\ rock}$ (final composition)

$$\delta^{18}O_{water} \sim -4.0 - 1.036 = -5.036$$

final fluid composition $\delta^{18}O = -5.036‰$

Water–rock ratio calculation

From the closed system equation (Eq. 7.18)

$$W/R_{closed} = (\delta^{18}O^{final}_{rock} - \delta^{18}O^{initial}_{rock})/(\delta^{18}O^{fluid}_{initial} - \delta^{18}O^{final}_{fluid}) = (-4 - 6.5)/(-14 - (-5.036)) = 1.17$$

From the single-pass, open-system equation (Eq. 7.19)

$$W/R_{open} = \ln(W/R_{closed} + 1) = 0.775$$

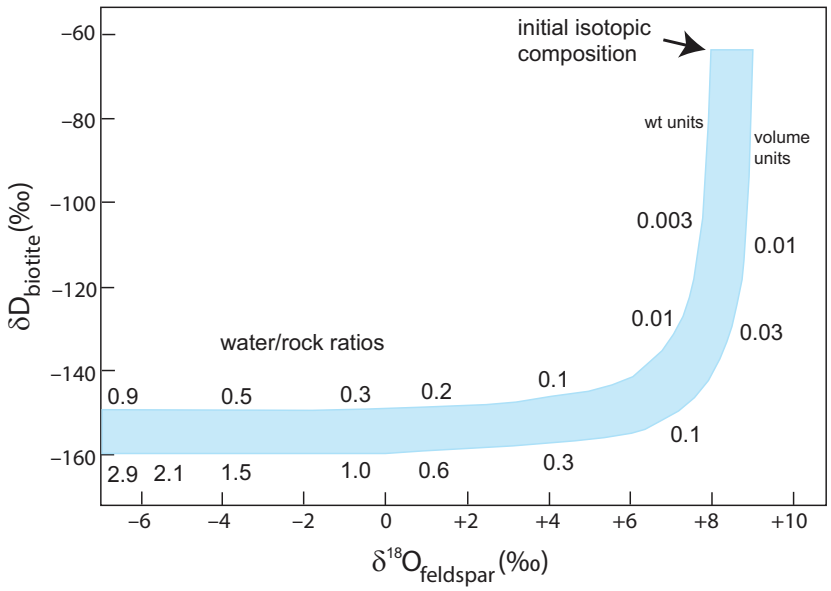

Figure 7.11 δD versus $\delta^{18}O$ diagram showing the isotopic change in D in biotite and $\delta^{18}O$ in feldspar in a granodiorite undergoing isotopic exchange with groundwater. The plotted curve shows the range of δD and $\delta^{18}O$ values with changing water–rock ratios. The curve was calculated for an initial feldspar composition of $\delta^{18}O = +8.0$ to $+9.0$, biotite $\delta D = -65.0$ and the groundwater $\delta D = -120$, $\delta^{18}O = -16$. The fractionation of D between biotite and water at 400–450 °C is given by $\Delta_{biotite-water} = -30$ and -40; the fractionation of $\delta^{18}O$ between feldspar and water at 400–450 °C is given $\Delta_{feldspar-water} = 2.0$. A small water–rock ratio has a dramatic effect on the isotopic composition of δD in biotite, whereas higher water–rock ratios affect both δD in biotite and $\delta^{18}O$ in feldspar. (Adapted from Taylor, 1978)

hydrothermal system will behave some way between the two extremes of water-dominant and rock-dominant.

The effects on the isotopic composition of a hypothetical granodiorite pluton which crystallised under conditions of increasing water–rock ratio are shown on a δD versus $\delta^{18}O$ plot in Figure 7.11, using the isotopic composition of biotite as a proxy for change in δD and the isotopic composition of feldspar as a proxy for change in $\delta^{18}O$ (Taylor, 1978). At small water–rock ratios (up to 0.1 rock volumes) oxygen isotopic compositions are virtually unchanged, while δD values are reduced by about 100‰. As the water–rock ratio increases the $\delta^{18}O$ value decreases rapidly at almost constant δD values. This is also illustrated in the study of Satir and Taubold (2001) on the Menderes gneiss complex in Turkey, who show that biotite is highly sensitive to the interaction of the gneiss with a very small amount of meteoric water and defines a trend of decreasing δD, while $\delta^{18}O$ in feldspar remains constant as predicted by Taylor (1978).

7.3.2.7 Examples of Water–Rock Interaction

There are many applications of the combined hydrogen–oxygen isotopic system to the study of water–rock interactions, and in this section a range of illustrative examples is given. As has already been shown, the sensitivity of hydrogen and oxygen isotopes to hydrothermal solutions means that they are excellent tools for detecting hydrothermal alteration in otherwise fresh rocks. Further, they may be used to identify the origin of the water and quantify its volume relative to the country rock.

(a) *Interaction between igneous intrusions and groundwater.* In a number of pioneering studies, Taylor and his co-workers showed that high-level igneous intrusions are frequently associated with hydrothermal convective systems (see review by Taylor, 1978). They found that the country rocks surrounding such intrusions are massively depleted in $\delta^{18}O$ and D relative to 'normal' values and that the minerals in both the intrusion and the country rock are isotopically out of equilibrium with magmatic values. They concluded that the isotopic effects

were due to the interaction between the magma and meteoric water and proposed that the intrusion acted as a heat engine which initiated a hydrothermal convection cell in the groundwater of the enclosing country rocks. Water–rock ratios were found to vary from $\ll 1.0$ to about 7.0. These studies brought an important insight into attempts to establish the original isotopic composition of igneous rocks, for samples showing evidence of interaction with meteoric water may not preserve primary stable and radiogenic isotopic compositions.

More recently, the examination of oxygen isotopes in zircon is leading to a re-evaluation of some claims of high-level crustal interaction between igneous intrusions and meteoric water. For example, Taylor and Forester (1971) showed that the Western Redhills granites on the Island of Skye, Scotland, were characterised by low-$\delta^{18}O$ phases, implying interaction with meteoric water during emplacement. However, subsequent zircon studies made by Gilliam and Valley (1998) show that these granites are low-$\delta^{18}O$ magmas and that any interaction with groundwater may have taken place in their source rather than during emplacement.

(b) *Interaction between ocean-floor basalt and seawater.* A large number of studies have shown that the rocks of the ocean floor, now preserved as ophiolites, have undergone massive seawater-hydrothermal exchange and alteration. In a now-classic study of the Oman ophiolite, Gregory and Taylor (1981) showed that upper layers (dykes and lavas) of the ophiolite were enriched in $\delta^{18}O$, whereas the lower gabbro and peridotite layers were depleted in $\delta^{18}O$ relative to average ocean crust (Figure 7.12). This cross-over of values, at about 250°C, is due to the temperature-dependent partitioning of oxygen isotopes between silicate minerals and seawater. Later studies showed a similar pattern of alteration in the Indian Ocean floor (Stakes et al., 1984), confirming the general applicability of the Gregory and Taylor model. Subsequent studies on hydrogen isotopes from amphibole in oceanic gabbros suggest that the hydrothermal fluid may also contain a component of magmatic water in addition to seawater (Stakes, 1991). These studies led to the important observation that the net exchange of $\delta^{18}O$ between seawater and the ocean crust in the Oman ophiolite was zero (Gregory and Taylor, 1981), suggesting that the $\delta^{18}O$ composition of seawater is buffered by the composition of the ocean floor, a view subsequently confirmed by Campbell et al. (1988).

(c) *Water–rock interaction in metamorphic rocks.* In metamorphic rocks oxygen isotopes are used to determine the patterns of fluid movement in a metamorphic sequence and establish the water–rock ratio. Fluid flow in metamorphic rocks may be pervasive, so that the fluid moves through pore spaces and establishes metamorphic equilibrium in the rocks (see, e.g., Chamberlain and Rumble, 1988), or may be channelised, migrating through cracks and fissures, in which case isotopic inhomogeneity may be preserved (see, e.g., Bottrell et al., 1990).

In addition, the combined study of hydrogen and oxygen isotopes can be used to determine the nature of the fluid originally in equilibrium with the metamorphic rock. Wickham and Taylor (1985) used this approach in their study of pelites in the French Pyrenees. They showed that the isotopic composition

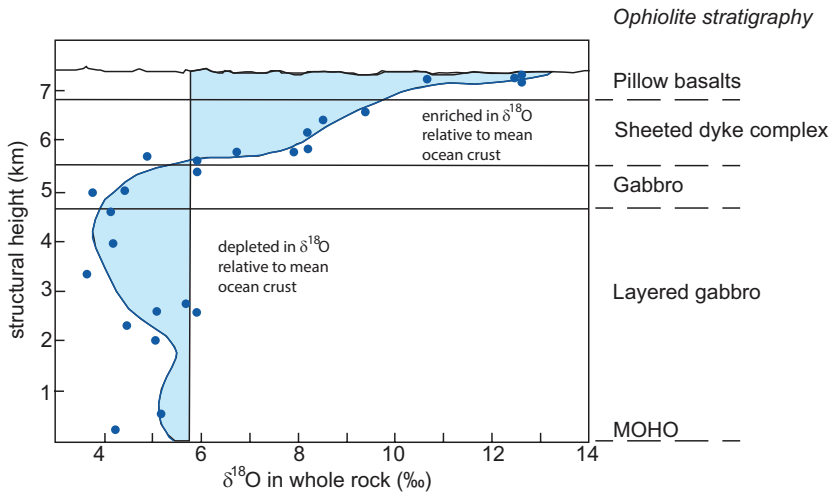

Figure 7.12 A whole-rock $\delta^{18}O$ profile through the Oman ophiolite showing the relative enrichment and depletion in $\delta^{18}O$ as a function of depth. Individual measurements are shown as solid blue circles. (Modified from Gregory and Taylor, 1981)

of muscovites had been homogenised through the influx of basinal formation waters which had exchanged their oxygen isotopes with the country rock.

(d) *Water–rock interaction during the formation of hydrothermal ore deposits*. An entire class of ore deposits is known to have formed from hydrothermal fluids. These fluids may be low or high temperature and associated with sedimentary, magmatic and, less commonly, metamorphic processes. Early studies such as that of Taylor (1974) were able to show the importance of oxygen and hydrogen isotopes in characterising these fluids and determining water–rock ratios. Indicative examples include the following:

- Porphyry copper deposits. Qiu et al. (2016) use the composition of sericites plotted on a δD–$\delta^{18}O$ diagram to show that the hydrothermal fluids in the Taiyangshan porphyry copper–molybdenum deposit of central China formed principally from magmatic fluids, with some small interaction with meteoric waters.
- Kuroko-type massive sulphide deposits. A study of fluid inclusions in pyrite and chalcopyrite in Kuroko-type massive sulphide deposits from the Hokuroku district of Japan showed that their δD–$\delta^{18}O$ compositions plot close to the composition of seawater which has experienced high-temperature isotopic exchange with the enclosing volcanic rocks (Ohmoto and Rye, 1974).
- Mississippi Valley–type Pb–Zn deposits. Carbonate-hosted Pb–Zn sulphide deposits are thought to have formed in association with oilfield brines, although the origin of the brine is sometimes uncertain. A δD–$\delta^{18}O$ study of fluid inclusions in sphalerite, fluorite and barite in the southern Appalachians showed that the brines originated as seawater but evolved to higher $\delta^{18}O$ and lower δD by mixing with water that has reacted with organic matter (Kesler et al., 1997).

7.3.3 Carbon Isotopes

Carbon occurs in nature in its oxidised form (CO_2, carbonates and bicarbonates), as reduced carbon (SiC, methane and organic carbon) and as the native element in diamond and graphite. Further, carbon is found throughout the whole solid Earth system from the core to the crust as well as in the oceans, atmosphere and biosphere.

There are two isotopes of carbon, ^{12}C and ^{13}C; isotope ratios are measured as $^{13}C/^{12}C$ and expressed as $\delta^{13}C‰$ (Eq. 7.20). In natural systems carbon isotope compositions vary over 100‰. The essential data for stable isotopes of carbon are given in Box 7.6. Figure 7.13 shows the variation in $\delta^{13}C$ in the major Earth reservoirs, and the main fractionations and their mechanisms in the global carbon cycle are shown in Figure 7.14 (after Suarez et al., 2019).

It is important to recognise the complexities of the Earth's carbon cycle (Figure 7.14) inasmuch as it includes both the short-term surficial carbon cycle which operates on a time scale of a maximum of 10,000 years and the long-term deep-Earth carbon cycle which operates on a time scale of Ga. The short-term carbon cycle is focussed on the terrestrial biosphere and is concerned with exchanges between the biosphere, the atmosphere and the oceans. The deep-Earth carbon cycle is focussed on the emission of CO_2 from volcanic sources; carbon drawdown through weathering, photosynthesis and carbonate formation; and the return of these materials to the mantle through subduction. Current estimates suggest that the present-day fluxes of CO_2 into the mantle broadly match the amount released, implying that at the present time the mantle is at a steady state with respect to carbon (Rollinson, 2007). In this section we explore the role that carbon isotopes play in elucidating the balances in and between the surfical and deep-Earth carbon cycles.

Carbon isotopes are measured as CO_2 gas, and precision is normally better than 0.1‰. CO_2 is liberated from carbonates with >103‰ phosphoric acid or by thermal decomposition. Organic compounds are normally oxidised to CO_2 at very high temperatures in a stream of oxygen or with an oxidising agent such as CuO. In situ measurements made by ion probe using secondary ion mass spectrometry (SIMS) use a focused $^{133}Cs^+$ primary beam. The impact of the $^{133}Cs^+$ atoms sputters ions off the sample surface. Sputtered ions are accelerated in the mass spectrometer and are sorted by their mass/charge ratio before reaching an array of Faraday cup and electron multiplier detectors. Analyses are made using an appropriate running standard (Denny et al., 2020).

7.3.3.1 Controls on the Fractionation of Carbon Isotopes

The fractionation of carbon isotopes is controlled by both equilibrium and kinetic processes. Equilibrium

Box 7.6 Carbon isotopes

Stable isotopes and abundances

$^{12}C = 98.89‰$
$^{13}C = 1.11‰$
^{14}C is a short-lived radioactive isotope with a half-life of 5730 years, produced by the action of cosmic rays on ^{14}N in the atmosphere. It decays to ^{14}N.

Measured isotope ratio

$$\delta^{13}C‰ = \left[\left(^{13}C/^{12}C_{(sample)} - {}^{13}C/^{12}C_{(standard)}\right)/{}^{13}C/^{12}C_{(standard)}\right] \times 1000 \quad (7.20)$$

Standard

VPDB: Vienna Peedee belemnite from the Cretaceous Peedee formation of South Carolina, USA. This standard is used because its ^{13}C and ^{18}O values are close to those of average marine limestone. The original material of the PDB standard is now exhausted and current standard materials are a carbonatite NBS-18 and marine limestone NBS-19.

Mantle value

$\delta^{13}C = -5.0‰$ (Deines 2002)

Bulk silicate Earth

$\delta^{13}C = -7.2‰$ (estimated from mean of diamond compositions, Horita and Polyakov, 2015)

Variations in nature

See Figures 7.13 and 7.14.

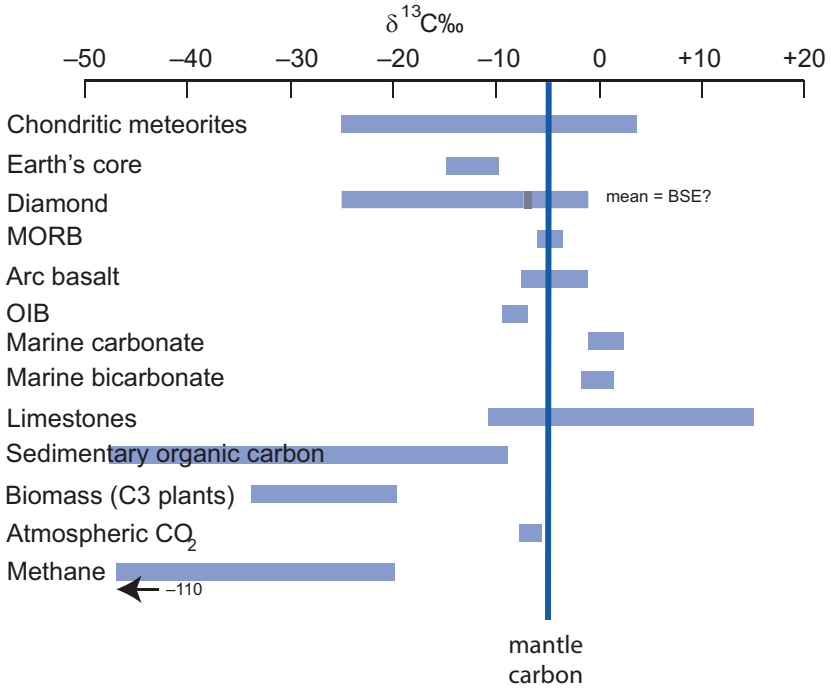

Figure 7.13 Variations in $\delta^{13}C$ in the major Earth carbon reservoirs relative to the Earth's mantle. (Data sources in the text)

Box 7.6 (cont.)

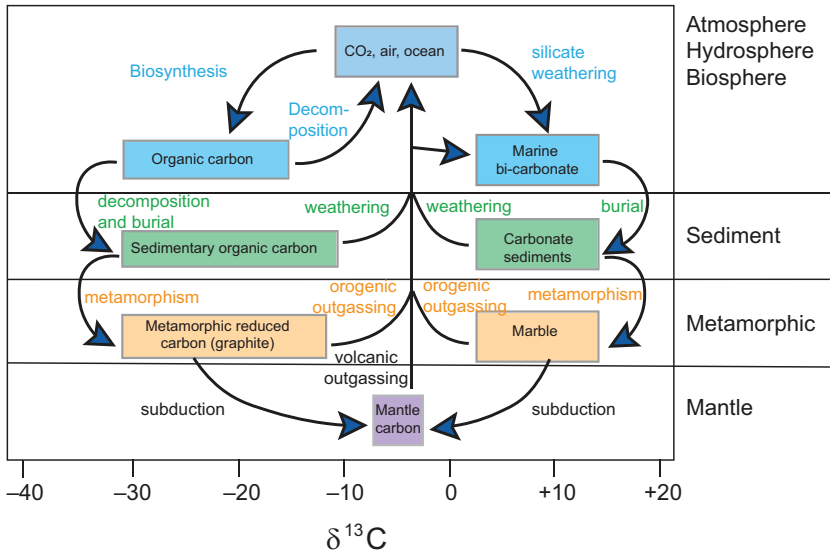

Figure 7.14 The major Earth carbon reservoirs and the processes that control carbon isotope fractionations between them. (After Suarez et al., 2019; with permission from the Mineralogical Society of America)

fractionation factors for carbon isotopes for a range of carbon-bearing species relative to CO_2 are shown in Figure 7.15. The fractionation factors (α) were obtained from both theoretical and empirical studies and are discussed by Chacko et al., 2001. It can be seen from the carbonate curves in Figure 7.15 that at relatively low temperatures carbonate precipitated from CO_2 is enriched in ^{13}C, whereas at higher temperatures the carbonate is depleted in ^{13}C. At very high temperatures the fractionation factors converge and so at mantle temperatures (~1000°C) carbon isotope fractionation between coexisting C-bearing species is small and less than 4‰ (Bottinga, 1969). Additional high-temperature fractionation curves include those for carbon-bearing species relative to carbides (Horita and Polyakov, 2015), and for atomic carbon (Deines, 2002). Fractionation factors between diamond and carbonate and diamond and carbon dioxide are given in Smit et al. (2016). At lower temperatures the fractionation of carbon isotopes between carbonates and organic carbon is such that $\delta^{13}C$ values in organic carbon are on average 25‰ lower than in co-existing carbonate carbon (see Figure 7.16).

In addition to mineral–CO_2 carbon isotope fractionation, carbon isotopes are also fractionated during volcanic degassing. $^{13}CO_2$ versus $^{12}CO_2$

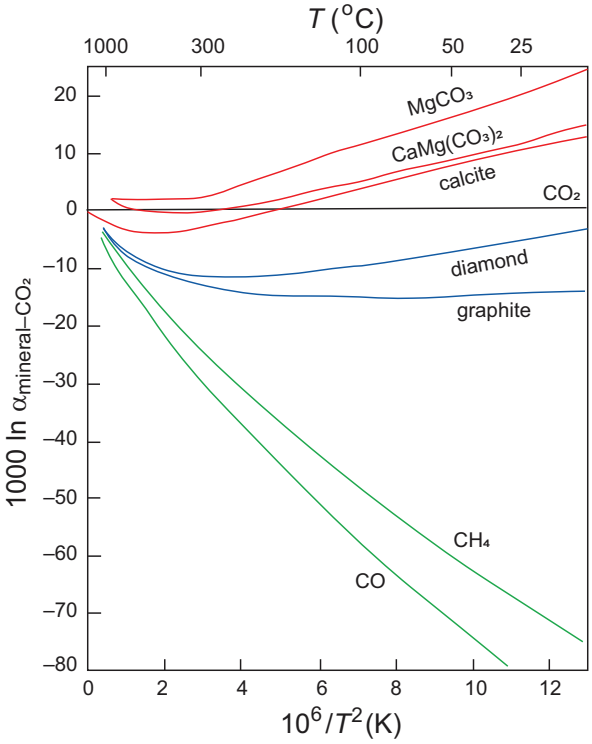

Figure 7.15 Fractionation factors shown as 1000 ln α for carbon species relative to CO_2 versus temperature – shown as degrees C on the top axis and as $10^6/T^2$ Kelvin on the lower axis. (After Chacko et al., 2001)

fractionation during degassing depends upon the fractionation factor between dissolved CO_2 in the melt and CO_2 vapour. These fractionation factors are between +2.3‰ and +4.6‰ such that there is lower $\delta^{13}C$ in the melt–CO_2 relative to the exsolved gas phase. The processes are summarised in Barry et al. (2014), who show that they include closed system, batch equilibrium degassing in which vesicles stay in contact with the melt and open system degassing when vesicles form in equilibrium with the surrounding melt but are removed during degassing. Similar principles apply to devolatisation reactions in metamorphic rocks, and Valley (1986) has calculated the differential fractionation of carbon isotopes during batch de-volatilisation and Rayleigh (fractional) devolatisation (Figure 7.18b) in metamorphic systems.

Kinetic fractionation of carbon isotopes is important in biological processes such as the fixing of CO_2 as organic carbon and the evolution of methane during the anaerobic fermentation of organic matter during diagenesis. In these cases fractionation is controlled by the greater readiness of the lighter isotope to react, and reactions can be identified which relate to specific biogenic pathways. For example, the process of photosynthesis in green plants and algae using the enzyme rubisco may lead to the fractionation of $\delta^{13}C$ of −30‰, although in detail there several different pathways and more than one version of rubisco. Similarly, the process of methanogenesis, that is, the production of methane through the reduction of CO_2 by hydrogen in methanothermobacteria, may lead to $\delta^{13}C$ fractionations in the range −22 to −58. Where the reaction involves both carbon and oxygen, the kinetic effect will influence the isotopes of both elements in a similar way, and a correlation between $\delta^{18}O$ and $\delta^{13}C$ is expected.

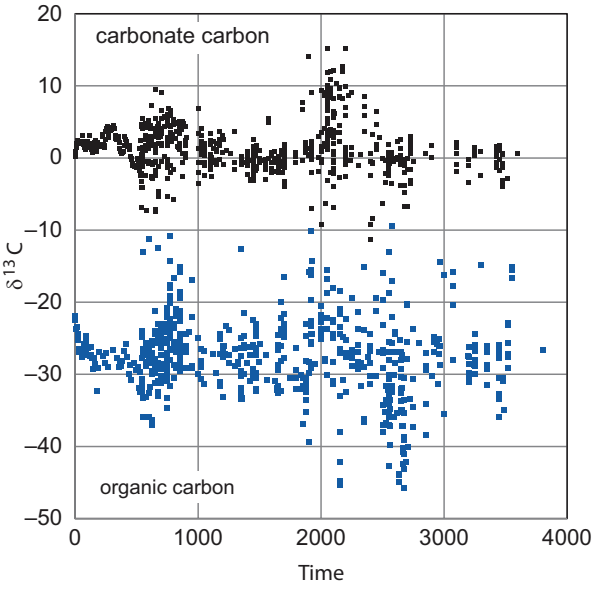

Figure 7.16 $\delta^{13}C$ measurements in carbonate rocks since ~3500 Ma, and $\delta^{13}C$ measurements in organic carbon since ~3800 Ma. (Data are the filtered data of Krissansen-Totton et al., 2015; with permission from Joshua Krissansen-Totton)

7.3.3.2 Carbon Isotopes in Meteorites

Carbon is present in chondritic meteorites in the form of organic compounds, carbonates, carbides, graphite and diamond. Grady and Wright (2003) estimate that the bulk $\delta^{13}C$ in the different chondritic meteorite groups ranges from −25 to +4‰ (Figure 7.13), although in detail the composition of individual carbon-bearing molecules and mineral species is much more variable (Simkus et al., 2019). The *solar value* for $\delta^{13}C$, based upon the bulk composition of nanodiamonds in the Allende meteorite, is $\delta^{13}C = +8 \pm 35$‰ (Lewis et al., 2018).

The presence of dissolved carbon together with graphite and carbide inclusions in iron meteorites strongly suggests that the Earth's metallic core sequestered carbon during core–mantle differentiation. Experimental and modelling studies indicate that this process would preferentially partition the lighter isotope into the metallic phase (Satish-Kumar et al., 2011; Horita and Polyakov, 2015). Although the precise $\delta^{13}C$ value of the core is not known, Horita and Polyakov (2015) estimate it to be in the range −10 to −15. Nevertheless, currently there is much uncertainty in this field, with the result that it is not possible to use a chondritic model for the isotopic composition of the Earth, and the carbon isotopic value for the bulk Earth is unknown (Mikhail and Furi, 2019).

7.3.3.3 Carbon Isotopes in the Mantle

Isotopic measurements on mid-ocean ridge basalts, carbonatites, kimberlite xenoliths and some diamonds define a mean mantle value of $\delta^{13}C \sim -5.0$‰ (Deines, 2002), although some authors place an error of ± 3‰ on this value (Cartigny, 2005). This mantle range probably represents an isotopic homogenisation event during the early differentiation of the Earth. The more varied isotopic composition of fluids in the subcontinental lithospheric mantle is revealed by the carbon isotope composition of diamonds. These show

a wide range of $\delta^{13}C$ values from ~−3.3 to −26 (Deines, 2002; Deines et al., 2009; Mikhail and Furi, 2019), and there is geochemical evidence to support the view that the isotopically light carbon was derived from subducted organic carbon (Mikhail and Furi, 2019). The mean $\delta^{13}C$ value of all diamonds worldwide is −7.2‰, and since these include diamonds from the lower mantle Horita and Polyakov (2015) suggest that this value might represent that of the *bulk silicate Earth*.

7.3.3.4 Carbon Isotopes in Igneous Rocks

CO_2 behaves highly incompatibly during mantle melting and so partitions almost entirely into the melt phase (Dasgupta and Hirschmann, 2010). This means that the CO_2 content of magmas is a function of the carbon content of the mantle source and the degree of partial melting (Black and Gibson, 2019). Measuring the original CO_2 content of volcanic rocks is difficult because of the process of degassing, although estimates can be made from trace element ratios such as CO_2/Nb and CO_2/Ba, for Nb and Ba have a similar incompatible element behaviour to that of CO_2.

Marty et al. (1999) found that the carbon isotope composition of mid-ocean ridge basalts from a range of locations around the world results in a near constant ratio, which is within the typical mantle range, of $\delta^{13}C = -5.2 \pm 0.7$‰. This value can be taken as representative of the depleted mantle. The carbon isotope composition of arc basalts is slightly lighter than that of MORB and is thought to be controlled by a mixture of mantle carbon and carbon derived from subducted carbonate sediments and is in the range $\delta^{13}C = -8$ to −2‰ (Eguchi et al., 2020). The carbon isotope composition of ocean-island basalts is also lighter than that of MORB and arc basalts and is in the range $\delta^{13}C = -9$ to −7‰ (summarised in Eguchi et al., 2020). These low values may reflect the presence of subducted organic carbon in the mantle source. Even lower values have been recorded but these are thought to reflect carbon isotope fractionation during volcanic degassing.

Carbon from degassed volcanic rocks as found in hydrothermal volcanic fluids is much more variable in composition than that in the melts themselves. This is in part due to fractionation during degassing and carbonate precipitation, but also as result of mixing with crustal rocks. Barry et al. (2014) report geothermal fluids from Iceland with $\delta^{13}C$ in the range −18.8 to +4.6 (mean -4.0 ± 3.7), thought to be the result of fractionation during degassing and carbonate precipitation. However, they calculate that the pre-eruptive value is $\delta^{13}C = -2.5 \pm 1.1$, much closer to that of the depleted mantle. Volcanic fluids from Tanzania have $\delta^{13}C$ in the range −2.3 to −6.5 (mean -3.1 ± 1.9), also close to mantle values, but in this case a $\delta^{13}C$ versus $CO_2/^3He$ plot reveals that these gases are mixtures of mantle carbon, carbon derived from limestones and an organic source (Barry et al., 2013).

7.3.3.5 Carbon Isotopes in Carbon-Bearing Sediments

The carbon isotope ratio of marine carbonates and of organic matter in the oceans is controlled by the addition of carbon to the ocean–atmosphere system. In the modern Earth a balance is maintained between the volcanic outgassing of mid-ocean ridge and arc lavas and the removal of carbon through silicate weathering and the burial of organic carbon in sediments.

Modern seawater has, by definition, a $\delta^{13}C$ value close to 0‰ and marine carbonates therefore have values close to this composition. This means that ancient limestones can be used as a proxy for the composition of seawater in the past. Figure 7.16 shows the variation in $\delta^{13}C$ in marine carbonates and marine organic carbon over geological time, indicating that there have been some major departures from modern values during Earth history. Possible mechanisms to explain these variations include episodes of extreme volcanic outgassing such as those associated with the formation of large igneous provinces (Black and Gibson, 2019). Alternatively, it has been suggested that an increase in the rate of burial of organic sediments in the oceans leads to the preferential removal of isotopically light carbon (Krissansen-Totton et al., 2015; Eguchi et al., 2020) and produces a $\delta^{13}C$ spike. A change in the rate of the burial of organic carbon may, in turn, be related to levels of oxygen in the Earth's atmosphere and therefore linked to the rise of photosynthesising organisms.

In addition to the global $\delta^{13}C$ curves discussed above, high-resolution $\delta^{13}C$ measurements can be made on specific stratigraphic sequences and used to illuminate particular geological processes. For example, Kämpf et al. (2020) use $\delta^{13}C$ in modern varved lake sediments as a proxy for flood events.

7.3.3.6 Biologically Derived (Organic) Carbon

The conversion of inorganic carbon through a CO_2-fixing mechanism into living, organic carbon entails

the preferential concentration of the light ^{12}C isotope in organic carbon. This process is chiefly controlled by reaction kinetics which favour the light isotope. At a global level the net effect of this fractionation is that relative to mantle-derived carbon ($\delta^{13}C \sim -5‰$) there are two complementary reservoirs. Biological materials are strongly depleted in $\delta^{13}C$ (−20 to −30‰), whereas seawater and marine carbonates ($\delta^{13}C \sim 0‰$) are slightly enriched (Figure 7.16). At a more detailed level the knowledge of specific fractionations in biological materials is now used in the carbon isotope fingerprinting of different plant groups and in the identification of particular biological and climatic processes (see, e.g., Kohn, 2010).

Methane is the most depleted of all carbon compounds and is commonly formed in nature either by the anaerobic fermentation of organic matter or by the thermal degradation of petroleum or kerogen at temperatures greater than 100°C. Methane of biological origin has a range of $\delta^{13}C$ values from about −30‰ to −110‰, whereas abiotic methane has $\delta^{13}C$ values between −50 and +10‰. Reeves and Fiebig (2020) helpfully classify methane of microbial and abiotic origin according to its δD and $\delta^{13}C$ composition (Figure 7.17).

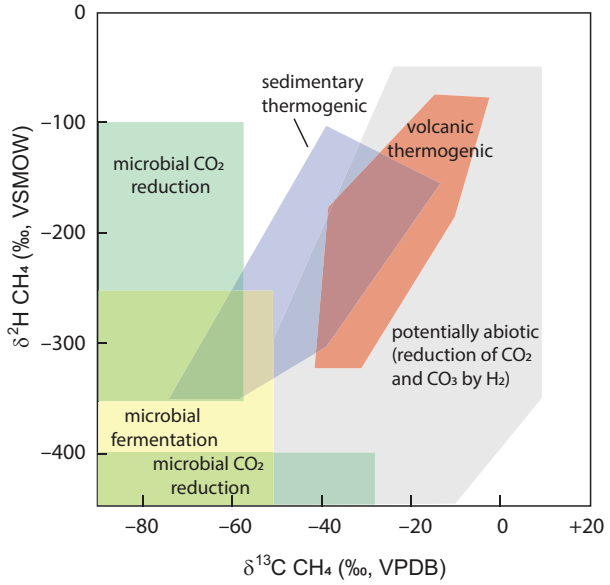

Figure 7.17 δD (δ^2H) versus $\delta^{13}C$ plot in methane showing the different types of microbial and abiotic methane. (After Reeves and Fiebig, 2020; with permission from the Mineralogical Society of America)

7.3.3.7 Carbon Isotopes and the Search for Early Life on Earth.

Schidlowski (1988) showed how the study of carbon isotopes can be used to trace ancient biological activity through the geological record. The argument is based upon the observation that isotopically light, organic carbon and isotopically heavy carbonates are complementary reservoirs which have originated from the biological fractionation of mantle carbon. Both reservoirs therefore are responsive to changes in the level of biological activity. Schidlowski (1988) showed that there is very little change in the degree of fractionation between the two reservoirs from the present day to the earliest part of the geological record at 3.8 Ga and argued for the constancy of biological activity since 3.8 Ga and presence of CO_2-fixing organisms since this time. Subsequent studies such as that of Rosing (1999) have validated the early work of Schidlowski (1988) and show that the geological record preserves very low $\delta^{13}C$ organic carbon signatures in rocks as old as 3.7 Ga (Figure 7.16). There are, however, problems in uniquely identifying biogenic signatures in the ancient sedimentary record, for there is an overlap in the degree of carbon isotope fractionation between biogenic and abiotic processes. Horita (2005) showed that abiotic reactions can produce carbon isotope fractionations that are as large as those driven by biogenic processes, and these will produce a similar degree of fractionation to that created by methanogenic bacteria.

7.3.3.8 Carbon Isotopes in Crustal Fluids

Crustal CO_2-bearing fluids can be subdivided into those which are present during metamorphism, fluids related to mineralising processes and other forms of fluid–rock interaction.

(a) *Metamorphic fluids.* The principal controls on carbon isotope fractionation during metamorphism are illustrated in Figure 7.14, and the relevant physical fractionation processes were reviewed by Valley (1986). The decarbonation of a marine limestone during metamorphism leads to lighter (more negative) $\delta^{13}C$ in calcite (Nabelek et al., 1984; Epstein et al., 2020), and the CO_2 released is correspondingly heavier in $\delta^{13}C$. The metamorphism of biogenic, non-carbonate carbon, on the other hand, leads to a loss of methane and heavier (less negative) $\delta^{13}C$ values in the residual graphite. However, this simple guide is not always applicable, for metamorphic graphite may

also be produced by the mixing of carbon-bearing fluids as in the case of hydrothermal vein graphites in the high-grade gneisses of New Hampshire (Rumble and Hoering, 1986) and in pelites from the Ivrea zone (Baker, 1988). Studies of the fractionation of carbon isotopes during subduction zone metamorphism may be used to refine models of the global carbon cycle and assess the fate of carbon-bearing sediments during the subduction process and the associated release of CO_2 (Piccoli et al., 2016; Epstein, 2020).

(b) *CO_2 in gold-mineralising fluids*. Carbonate minerals precipitated in association with Archean lode gold deposits are thought to result from the CO_2-rich nature of the auriferous fluids and as such are potentially an indicator of the source of the gold-bearing solutions (Groves et al., 1988). Early studies found that the mean $\delta^{13}C$ value of calcite carbon was between -3 and -4‰ and concluded that the CO_2-rich fluids were externally derived and of mantle origin (Burrows et al., 1986). However, in a review of orogenic gold deposits, Goldfarb and Groves (2015) show that the carbon isotope compositions of associated calcites are extremely variable and range from $\delta^{13}C = +2$ to -30, implying multiple local sources and carbon isotope fractionations during deposition. They conclude that the variability in $\delta^{13}C$ in ore fluids and for ore-related carbonates in orogenic gold deposits 'makes it very difficult to use such data to clearly define a carbon source for the ore-forming fluids'. A better approach therefore is to combine carbon isotopes measurements with measurements from another stable isotope system as discussed in Section 7.3.3.9.

(c) *CO_2 fluid–rock interaction.* The principles of fluid–rock interaction were discussed in the section on water–rock interaction (Section 7.3.2.6). When the fluid–rock ratio is small, the $\delta^{13}C$ in the rock dominates the system and the composition of the fluid is changed, whereas when the fluid–rock ratio is large and the $\delta^{13}C$ of the CO_2–fluid dominates, it is the $\delta^{13}C$ value of the rock that is modified. Mass balance calculations require a knowledge of the initial $\delta^{13}C$ values for the carbonate and the fluid, the proportions of the carbon-bearing species and the fractionation factors for ^{13}C between CO_2 and the carbon-bearing species (see Section 7.3.3.1). The shift in $\delta^{13}C$ from the original to that measured in calcite and/or graphite is used to calculate the extent of fluid–rock interaction. Examples are given by Baker (1988) and Skelton (2015). Baker (1988) found very low fluid–rock ratios in the amphibolite and granulite facies rocks of the Ivrea zone, whereas Skelton (2015) found fluid–rock ratios of more than 30:1 in carbonate rocks from Islay, Scotland.

7.3.3.9 Combined Oxygen and Carbon Isotope Studies of Carbonates: $\delta^{18}O$–$\delta^{13}C$ Plots

A combined study of carbon and oxygen isotopes in carbonates is a powerful means of distinguishing between carbonates of different origins and for understanding processes in carbonate rocks. On a $\delta^{18}O$–$\delta^{13}C$ diagram (Figure 7.18) oxygen isotope compositions are plotted relative to the VSMOW standard and carbon isotopes relative to VPDB. We focus on the signatures of limestone diagenesis, hydrothermal calcite and metamorphic rocks.

(a) *Limestone diagenesis.* The $\delta^{18}O$–$\delta^{13}C$ diagram is particularly useful in understanding the processes of limestone diagenesis and has the potential to distinguish between marine, organic and methane-related carbon (Coleman and Raiswell, 1981). Oxygen isotopes in sedimentary carbonates can be used to determine the origin of the fluids in equilibrium with the carbonates and can also provide an estimate of the temperature of carbonate formation using the Epstein et al. (1953) thermometer (Eq. 7.13), although care should be taken to establish chemical equilibrium (McConnaughey, 1989). A summary of the fractionations which can take place in carbon and oxygen isotopes in carbonate rocks during deposition, burial and exhumation is given in Figure 7.18a (after Reis et al., 2019).

A fruitful approach to understanding limestone lithification is through the isotopic analysis of the different generations of carbonate produced during this process. This allows the construction of an evolutionary pathway on a $\delta^{18}O$–$\delta^{13}C$ diagram and shows the isotopic history of the rock. Denny et al. (2020) show how combined ion-probe measurements of $\delta^{18}O$ and $\delta^{13}C$ on zoned diagenetic carbonates can be used to monitor changing fluid compositions and temperatures in different parts of the Williston basin in the northern United States.

(b) *Hydrothermal calcite.* Hydrothermal calcites formed by water–rock interaction at a mid-ocean ridge show a wide range of compositions on a $\delta^{18}O$–$\delta^{13}C$ plot, chiefly as a function of differing water–rock ratios (Stakes and O'Neill, 1982). At one extreme, calcite in a greenstone breccia has

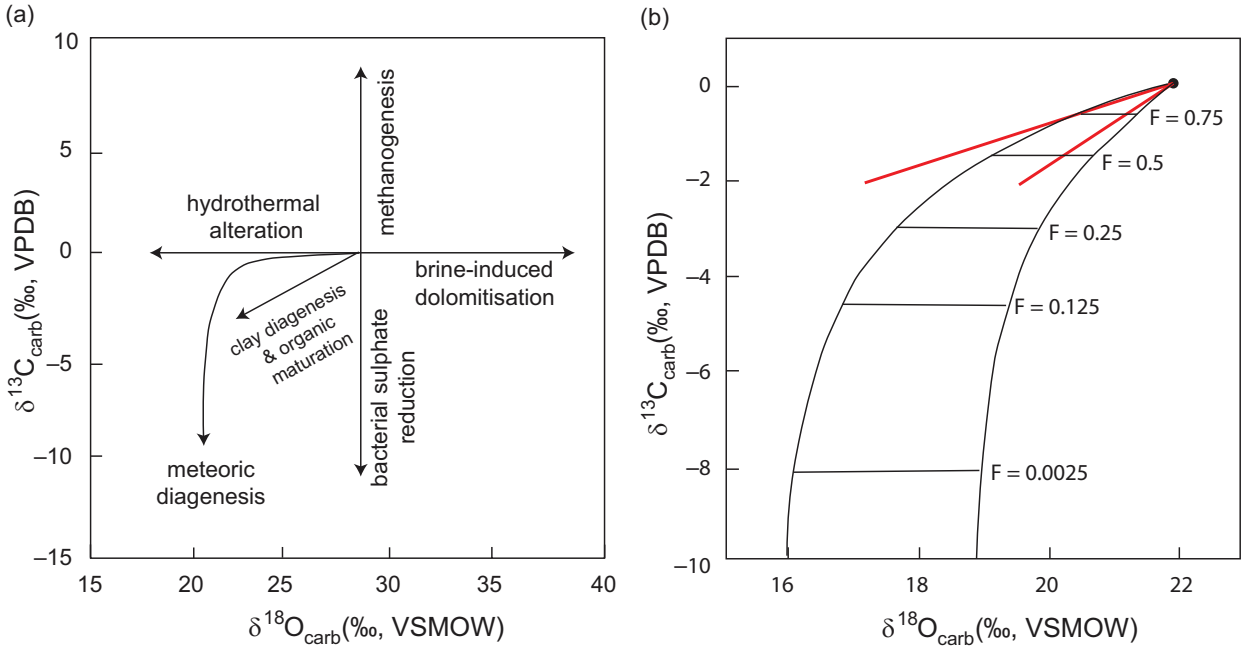

Figure 7.18 Coupled $\delta^{18}O$–$\delta^{13}C$ diagrams. (a) The effects of a range of diagenetic process on the isotopic fractionation of carbon and oxygen isotopes in carbonate sediments (after Reis et al., 2019; with permission from Elsevier). (b) $\delta^{18}O$–$\delta^{13}C$ trends which result from the devolatilisation of a calc silicate rock during batch fractionation (red lines) and Rayleigh fractionation (black lines). The curves are calculated for two values of oxygen fractionation factor ($\alpha^{18}O_{CO2\text{–}rock} = 1.012$ to 1.006) and $\alpha^{13}C_{CO2\text{–}rock} = 1.0022$. Initial values are $\delta^{18}O = +22$ and $\delta^{13}C = 0$. F values are the mole fraction of carbon which remains in the rock after fractionation. (After Valley, 1986; with permission from the Mineralogical Society of America)

mantle-like $\delta^{13}C$ values and formed in a rock-dominated environment (low water–rock ratio) at high temperature (145–170°C). In contrast, low-temperature vein calcites have seawater $\delta^{13}C$ values and represent a large volume of seawater interacting with the host basalts.

Calcites associated with Mississippi Valley–type lead–zinc mineralisation in Carboniferous limestone in Illinois show a marked decrease in $\delta^{13}C$ during their growth coupled with only a small decrease in $\delta^{18}O$. These changes indicate that early calcites were very similar to the composition of carbonates in the limestone, while late in the evolution of the hydrothermal system, fluids associated with the degradation of organic carbon become important (Richardson et al., 1988).

In carbonaceous chondrites hydrothermal calcite may form during the planetary weathering which takes place in the formation of planetesimals. In this case a plot of $\delta^{18}O$–$\delta^{13}C$ allows an estimate to be made of their temperature of formation, the composition of the gas mixture from which they were precipitated and subsequent processes of dissolution and reprecipitation (Telus et al., 2019).

(c) *Metamorphic rocks.* Valley (1986) showed how the composition of $\delta^{18}O$ and $\delta^{13}C$ varies between batch and Rayleigh fractionation during the metamorphism of carbonate rocks. Both types of fractionation lead to a similar reduction in $\delta^{18}O$, but $\delta^{13}C$ values are fractionated to much lighter values during Rayleigh fractionation (Figure 7.18b). Coupled $\delta^{18}O$ and $\delta^{13}C$ trends for many examples of contact metamorphism show a strong coupled decrease in $\delta^{18}O$ and $\delta^{13}C$ with increasing grade of metamorphism. A similar pattern is found in the subduction zone metamorphism of marine carbonates in the western Alps (Epstein et al., 2020).

7.3.3.10 Carbon Isotope Thermometry

Inspection of Figure 7.15 shows that the fractionation of ^{13}C between carbon-bearing phases is strongly temperature-dependent. Following Bottinga (1969), a number of workers have shown how these fractionations may be used as thermometers. Kueter et al.

(2019) provide an experimental calibration of the partition of carbon isotopes between carbonate phases and graphite and diamond and show how this can be used as a geothermometer. Their experiments were conducted at high temperatures (1200–1500°C) on carbonate melt and graphite and extended to lower temperatures using natural partitioning data in metamorphic rocks. They propose the following thermometer:

$$\Delta^{13}C_{carbonate-graphite} = \left(3.37\ [\pm 0.04] \times 10^6\right)/T^2 \quad (7.21)$$

in which temperature T is in K. This thermometer is calibrated in the range 610–1500°C and is applicable to carbonates which are in the solid and molten state, meaning that the thermometer is applicable to metamorphic and magmatic carbonate–graphite pairs. At mantle temperatures the fractionation of carbon isotopes between calcite and Mg–calcite and between graphite and diamond is very small, of the order of 0.1‰, which means that the carbonate–graphite thermometer may also be applied to magnesian carbonates and diamond.

In an older application, the carbon isotope composition of CO_2 in fluid inclusions and that of coexisting graphite was used as a thermometer. The exchange was calibrated by Bottinga (1969) and the method was used by Jackson et al. (1988), who obtained equilibration temperatures close to the peak of metamorphism from CO_2-rich inclusions in quartz and graphite in granulite facies gneisses from South India.

7.3.4 Sulphur Isotopes

Naturally occurring sulphur-bearing species include native sulphur, the sulphate and sulphide minerals, gaseous H_2S and SO_2 and a range of oxidised and reduced sulphur ions in solution. A summary of the isotopic compositions of some major Earth reservoirs and rock types is given in Figure 7.19.

Sulphur has four stable isotopes – ^{32}S, ^{33}S, ^{34}S and ^{36}S – and three different stable isotope ratios can be measured. Until the year 2000 most sulphur isotope studies reported only values for $\delta^{34}S$ because the two isotopes involved (^{34}S and ^{32}S) are more abundant (see Box 7.7) and relatively straightforward to measure. The lower abundances of ^{33}S and ^{36}S had meant that their measurement was more difficult, although

Box 7.7 Sulphur isotopes

Stable isotopes and abundances

$^{32}S = 95.04‰$

$^{33}S = 0.75‰$

$^{34}S = 4.20‰$

$^{36}S = 0.015‰$

Measured isotope ratios

$$\delta^{33}S‰ = \left[\left(^{33}S/^{32}S_{(sample} - {}^{33}S/^{32}S_{(standard)}\right) / {}^{33}S/^{32}S_{(standard)}\right] \times 1000 \quad (7.22a)$$

$$\delta^{34}S‰ = \left[\left(^{34}S/^{32}S_{(sample} - {}^{34}S/^{32}S_{(standard)}\right) / {}^{34}S/^{32}S_{(standard)}\right] \times 1000 \quad (7.22b)$$

$$\delta^{36}S‰ = \left[\left(^{36}S/^{32}S_{(sample} - {}^{36}S/^{32}S_{(standard)}\right) / {}^{36}S/^{32}S_{(standard)}\right] \times 1000 \quad (7.22c)$$

Delta notation (see Section 7.2.4)

$$\Delta^{33}S = d^{33}S - 1000\left(\left(1 + \delta^{34}S/1000\right)^{0.515} - 1\right) \quad (cp\ 7.8)$$

$\Delta^{33}S = \delta^{33}S - 0.515 \times \delta^{34}S$ (equilibrium curve)

$$\Delta^{36}S = \delta^{36}S - 1000\left(\left(1 + \delta^{34}S/1000\right)^{1.91} - 1\right) \quad (cp\ 7.9)$$

$\Delta^{36}S = \delta^{36}S - 1.91 \times \delta^{34}S$ (equibrium curve)

Standards

Troilite (FeS) from the Canon Diablo iron meteorite (CDT)

V-CDT is based on the reference material IAEA-S-1 (Ag_2S)

On the CDT scale ISEA-S1 has the composition $\delta^{33}S = -0.091‰$, $\delta^{34}S = -0.401‰$, $\delta^{36}S = -1.558‰$, $\Delta^{33}S = 0.116‰$, $\Delta^{36}S = -0.796‰$ (Dottin et al., 2020)

Mantle value (depleted upper mantle)

$\delta^{34}S = -0.68 \pm 0.09$ to $-1.28 \pm 0.33‰$; average $\Delta^{33}S = +0.008 \pm 0.006‰$

Continued

Box 7.7 (cont.)

Bulk silicate Earth value

$\delta^{34}S = +0.04 \pm 0.10‰$

Variations in nature

See Figure 7.19.

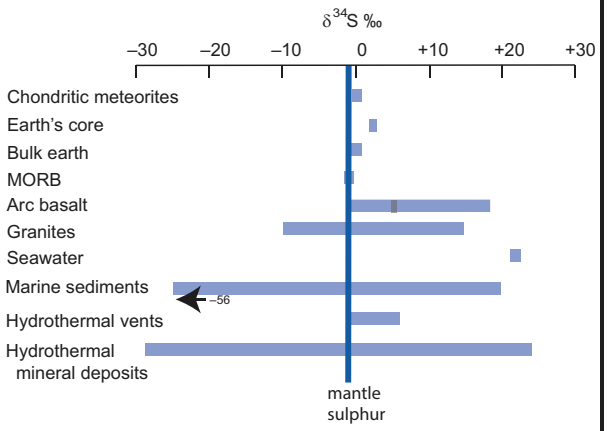

Figure 7.19 Variations in $\delta^{34}S$ (expressed relative to V-CDT) in major Earth reservoirs and rock types relative to the sulphur isotope composition of the Earth's mantle.

with technological improvements and the discovery that these isotope ratios have geological significance they are now also frequently measured.

Given that three different sulphur ratios can be determined, it is possible to discriminate between *mass-dependent* and *mass-independent fractionation* in the sulphur isotope system (see Section 7.2.4). Mass-dependent fractionation is based upon the assumption that the fractionation between the different isotopes is dependent upon their mass differences and so, for example, the fractionation of $\delta^{33}S \sim 0.5 * \delta^{34}S$. The actual value is determined from the slope of a plot of terrestrial sulphide and sulphate values for the two isotope ratios and is found to be 0.515 for equilibrium fractionation (Box 7.7). Mass-independent fractionation represents deviation from the mass-dependent fractionation line and implies that a different set of processes is operating. Mass-independent fractionation is quantified using the Δ notation and the term $\Delta^{33}S$ represents the fractionation of $\delta^{33}S$ relative to $\delta^{34}S$. In the modern Earth $\Delta^{33}S$ is zero, but in the early history of the Earth both positive and negative deviations have been recorded (Farquhar and Wing, 2003). The Δ notation is calculated following Eqs. 7.8 and 7.9 (Box 7.7) following Farquhar and Wing (2003). A slightly different calculation is given by Mishima et al. (2017), although the two definitions are almost identical where variations in $\delta^{34}S$ are less than ± 10‰.

Older sulphur isotope measurements were based upon the analysis of SO_2 gas; precision during mass spectrometry was ~0.02‰ and accuracy about 0.10‰. Modern analyses, however, require very high precision in order to measure the lower abundance isotope ratios $\delta^{33}S$ and $\delta^{36}S$, and so sulphur is now converted into SF_6 gas. This is to be preferred because fluorine has only one isotope and so the use of SF_6 reduces the number possible mass interferences from the method where multiple oxygen isotopes were involved (Ono et al., 2006). The gas chromatography–mass spectrometry fluorination method of Ono et al. (2006) can also be applied to the in situ laser ablation of samples, using a KrF laser. In this case the spatial resolution is of the order of ~150 μm in diameter.

Multiple sulphur isotopes (^{32}S, ^{33}S, ^{34}S) can be also analysed by the ion microprobe (SIMS) using simultaneous multicollection methods. The sulphur may be analysed as either positive or negative ions, although negative secondary ions give a greater yield and so typically a $^{133}Cs^+$ primary beam is used (Whitehouse et al., 2005). Precision for $\Delta^{33}S$ is between 0.2 and 0.3‰ and the spatial resolution is of the order of ~25 μm in diameter. Hauri et al. (2016) describe the high-precision analysis of sulphur isotopes using a nanoSIMS in which the spatial resolution is in the order of ~15 μm.

The primary input into the Earth's sulphur cycle comes from volcanic sulphur dioxide which in the Earth's stratosphere converts to sulphate aerosols. This returns to the Earth's surface through precipitation, weathering and riverine input into the oceans. Sulphur-rich fluids also enter the oceans through the outgassing of submarine magmas at mid-ocean ridges and their related hydrothermal systems. Sulphur is removed from the oceans primarily through pyrite precipitation, principally driven by sulphate-reducing bacteria, and to a lesser degree through sulphate–evaporite deposits. Sedimentary pyrite and sulphate are then returned either to the weathering cycle as a result of tectonic uplift or to the mantle through subduction.

These processes include a range of sulphur isotope fractionations (see Section 7.3.4.2), which give rise to

three isotopically distinct sulphur isotope reservoirs. These are the following:

(1) Mantle-derived sulphur with $\delta^{34}S$ values in the range −1 to −2‰
(2) Seawater sulphur with $\delta^{34}S$ today = +21‰, although this value has varied in the past
(3) Strongly reduced (sedimentary) sulphur with large negative $\delta^{34}S$ values.

Sulphur isotope studies today play an important role in unravelling the Earth's global sulphur cycle, both in the present and over geological time, in particular, monitoring major changes during the evolution of the Earth's atmosphere and oceans and the development of life on Earth. In addition, sulphur isotopes play a major role as geological tracers and are used to identify the sources of sulphide and sulphate in a variety of geological environments.

7.3.4.1 The Distribution of Sulphur Isotopes in Nature

Unequilibrated chondritic meteorites have a narrow range of $\delta^{34}S$ and $\Delta^{33}S$ values, close to those of the sulphur isotope standard, the mineral troilite in the Canyon Diablo iron meteorite (CDT). Primitive chondrites have $\delta^{34}S$ values averaging 0.0 ± 0.3‰ and average $\Delta^{33}S$ indistinguishable from that of CDT. Ordinary chondrites have $\delta^{34}S$ = +0.04 ± 0.10‰ and are thought to represent the bulk Earth value. Melting experiments show that the Earth's core was enriched in ^{34}S; this sulphur would have been dissolved in the alloys of the Earth's core, leading the residual mantle to be ^{34}S-deficient relative to the bulk Earth (Labidi and Cartigny, 2016, and references therein).

It has been proposed that minimal isotope fractionation takes place during mantle melting, and so estimates of the sulphur isotopic composition of the depleted upper mantle can be made from measurements on mid-ocean ridge basalts (Labidi and Cartigny, 2016). $\delta^{34}S$ values for MORB glasses range from −0.68 ± 0.09 to −1.28 ±0.33‰ and an average $\Delta^{33}S$ = +0.008 ±0.006‰, the latter indistinguishable from CDT and bulk chondrites. Slightly higher values are reported for plume basalts with $\delta^{34}S$ in the range 0 to +3.0‰ (Dottin et al., 2020), which may indicate the deep recycling of ^{34}S-enriched materials.

Arc volcanic rocks are derived from a mantle source which is enriched in $\delta^{34}S$ relative to MORB and OIB sources. Globally, they show a wide range of sulphur isotope values with $\delta^{34}S$ between −2.0 and +18.0‰, although individual arcs have a smaller range. A global average for arc volcanic rocks is $\delta^{34}S$ = +5.3 ± 4.0‰ (de Hoog et al., 2001). Li et al. (2020) have argued that the positive $\delta^{34}S$ signature of the sub-arc mantle cannot be derived from slab-derived fluids in a subduction zone and that subducted slabs return a negative $\delta^{34}S$ contribution of ~−3.7‰ to the deep mantle.

Crustal rocks show also show a wide range of $\delta^{34}S$ values. Bulk rock sulphur isotope measurements on granitoids range in composition from $\delta^{34}S$ =~ −10 to +15‰ (see, e.g., Coleman, 1977; Yang and Lentz, 2010). This variation reflects the diverse protoliths involved in granitoid genesis and varying degrees of interaction between granitic melts and their host rocks.

The average $\delta^{34}S$ value for sulphate in modern seawater is 21.24 ± 0.88‰ and the average value for $\Delta^{33}S$ value is +0.05 ± 0.014‰. Riverine $\delta^{34}S$ input varies between 5 and 15‰ depending upon the weathering source (Tostevin et al., 2014). Present-day marine sulphate evaporites are enriched in $\delta^{34}S$ by between 1 and 2‰ relative to seawater, a relationship exploited by Claypool et al. (1980) and Crockford et al. (2019) to determine the $\delta^{34}S$ value of ancient seawater. Crockford et al. (2019) summarise the changes in $\delta^{34}S$ and $\Delta^{33}S$ in sedimentary sulphate since the Archaean and show from evaporite data that there were major positive and negative excursions relative to modern values over geological time. $\delta^{34}S$ in other modern marine sediments has an extensive range with values from +20‰, reflecting the composition of seawater, down to −56‰, the product of bacterial sulphate reduction to form pyrite.

$\delta^{34}S$ in modern hydrothermal vent chimneys from mid-ocean-ridge settings have bulk rock values in the range −1.0 to 6.0‰. This range of values reflects the mixing of MORB-derived sulphur with seawater sulphate (Butler et al., 1998). Sulphides in hydrothermal mineral deposits of volcanogenic and sedimentary origin show a very wide range of $\delta^{34}S$ values, reflecting the multiple sources of the sulphur in these environments. Compare, for example, measurements for a porphyry Mo deposit ($\delta^{34}S$ = 1.5 to 3.8‰; Han et al., 2018) with findings for a shear-hosted gold deposit ($\delta^{34}S$ = −12.6 to +23.5‰; Godefroy-Rodríguez et al., 2020). In addition, recent in situ sulphide analyses show a huge variation in the $\delta^{34}S$ values of the different sulphide species within an individual mineral deposit (Li et al., 2019).

7.3.4.2 Controls on the Fractionation of Sulphur Isotopes

Inspection of Figure 7.19 shows that crustal rocks and sediments have a wide range of $\delta^{34}S$ values. These ranges of values indicate either fractionation or mixing processes. In this section we consider the main fractionation mechanisms in igneous and sedimentary rocks.

(a) *Sulphur isotope fractionation in igneous rocks.* Magmas may be rich in either SO_2 or H_2S. This is a function of the oxidation state of the melt and in part this depends upon pressure. Typically, high pressure favours H_2S, whereas at low pressures SO_2 is the dominant species (Rye, 2005). The fractionations of sulphur isotopes during igneous processes are relatively small. For example, Labidi and Cartigny (2016) in their investigation of mid-ocean ridge basalts found that there is 'negligible sulfur isotope fractionation during partial melting' of the Earth's mantle. This is an important observation for it means that the sulphur isotope composition of basaltic rocks can be taken to reflect the isotopic composition of their source.

Isotope fractionation during magmatic differentiation is more complex because a number of different processes may be operating. First, the element sulphur is sensitive to, and, depending upon its concentration may control, the redox state of the melt. Second, sulphides may segregate from the silicate melt as an immiscible sulphide melt. Variation in sulphur isotope compositions during the magmatic fractionation of the layered gabbros of the Huntley–Knock intrusion of northeast Scotland is about 2‰ under conditions of variable oxygen activity (Fletcher et al. 1989). Similarly, Ueda and Sakai (1984) report differentiated felsic and mafic sequences which record a change in $\delta^{34}S$ of 1‰ during fractionation. In the case of the segregation of an immiscible sulphide melt from a silicate melt, Labidi and Cartigny (2016) show that there is no measurable sulphur isotope fractionation between the sulphur dissolved in the silicate melt and the immiscible sulphide melt.

Volcanic rocks may lose a considerable fraction of their dissolved sulphur during volcanic degassing. It is important, therefore, to quantify the extent to which sulphur isotopes are fractionated in this process in order to estimate the primary sulphur isotope signature of the parent rock. The principal controls on sulphur isotope fractionation during volcanic degassing are the depth at which the degassing takes place, the oxidation state and temperature of magma and whether or not the degassing was as a batch or fractional process (de Hoog et al., 2001). For arc basalts, de Hoog et al. (2001) conclude that only a small amount of fractionation takes place during degassing, about 4‰, and that the isotopic shift in the melt will be normally towards lower, more negative values. Isotopic shifts towards more positive values will take place only at low pressures and temperatures (below 1000°C) and at high oxidation states, and are modest, ~1.5‰ (Fiege et al., 2015).

(b) *Sulphur isotope fractionation between sulphur species in hydrothermal systems.* At temperatures above 400°C the dominant sulphur species in hydrothermal systems are H_2S and SO_2 and the isotopic composition of the fluid is approximated by

$$\delta^{34}S_{fluid} = \delta^{34}S_{H2S} * X_{H2S} + \delta^{34}S_{SO2} * X_{SO2} \qquad (7.23)$$

where X_{H2S} etc. is the mole fraction of H_2S relative to total sulphur in the fluid (Ohmoto and Rye, 1979). At these elevated temperatures H_2S and SO_2 are assumed to behave as an ideal gas mixture. The fractionation factor is relatively large and is given in Table 7.4a; the fractionation curve is illustrated in Figure 7.20. At lower temperatures ($T < 350$°C) the dominant sulphur species in a hydrothermal system are sulphate and H_2S (Ohmoto and Rye, 1979).

There are a number of theoretical and experimental determinations of the fractionation of $\delta^{34}S$ between coexisting sulphide phases and H_2S as a function of temperature. These are given in Table 7.4a and illustrated in Figure 7.20a. From these fractionations a number of sulphide pair thermometers have been derived; see Table 7.4b and Figure 7.20b. However, these data should be used with care because of the following:

- The fractionation of ^{34}S between the different sulphur-bearing species in hydrothermal fluids is not simply controlled by temperature. Rather, it is also a function of the physico-chemical conditions of the fluid, which include oxygen activity, sulphur activity, pH and the activity of cations associated with sulphate. This means that the $\delta^{34}S$ of a hydrothermal fluid cannot be directly estimated from the $\delta^{34}S$ value of sulphide minerals unless variables such as oxygen activity and pH are also known.
- The partitioning of sulphur isotopes between sulphides is not a particularly sensitive thermometer

Table 7.4a Fractionation factors for the distribution of ^{34}S between H_2S and S compounds[a]

Mineral	A	B	T (°C)	Reference
Anhydrite/gypsum	6.463	0.56 ± 0.5	200–400	Ohmoto and Lasaga (1982)
Barite	6.5 ± 0.3		200–400	Miyoshi et al. (1984)
Molybdenite	0.45 ± 0.10		uncertain	Ohomoto and Rye (1979)
Pyrite	0.40 ± 0.08		200–700	Ohomoto and Rye (1979)
Sphalerite	0.10 ± 0.05		50–705	Ohomoto and Rye (1979)
Pyrrhotite	0.10 ± 0.05		50–705	Ohomoto and Rye (1979)
Chalcopyrite	−0.05 ± 0.08		200–600	Ohomoto and Rye (1979)
Bismuthinite	−0.67 ± 0.07		250–600	Bente and Nielsen (1982)
Galena	−0.63 ± 0.05		50–700	Ohomoto and Rye (1979)
SO_2	4.7	−0.5 ± 0.5	350–1050	Ohomoto and Rye (1979)

[a]Using the equation $1000 \ln \alpha_{mineral-H2S} = A * (10^6/T^2) + B$, temperature in Kelvin.

Table 7.4b Calibrations for sulphur isotope thermometers

Mineral pair	Thermometer equation[a]	T (°C)	Reference
Pyrite–galena	$1000 \ln \alpha = (1.03 \times 10^6)/T^2$		Ohmoto and Rye (1979)
	$1000 \ln \alpha = (1.08 \times 10^6)/T^2$	150–600	Clayton (1981)
Pyrite–sphalerite (pyrite–pyrrhotite)	$1000 \ln \alpha = (0.30 \times 10^6)/T^2)$		Ohmoto and Rye (1979)
Pyrite–chalcopyrite	$1000 \ln \alpha = (0.45 \times 10^6)/T^2)$		Ohmoto and Rye (1979)
Sphalerite–galena	$1000 \ln \alpha = (0.73 \times 10^6)/T^2)$		Ohmoto and Rye (1979)
(pyrrhotite–galena)	$1000 \ln \alpha = (0.76 \times 10^6)/T^2)$	100–600	Clayton (1981)
Sulphate–pyrite	$1000 \ln \alpha = 6.063 \times (10^6/T^2) \pm 0.56$		Ohmoto and Lasaga (1982)
Sulphate–chalcopyrite	$1000 \ln \alpha = 6.513 \times (10^6/T^2) \pm 0.56$		Ohmoto and Lasaga (1982)

[a]Temperature in Kelvin and mainly based on the fractionation factors given in Table 7.4a.

because at high temperatures the fractionation factor is small (see Figure 7.20), and so reliable sulphur isotope thermometry requires very precise isotopic determinations.

- Sulphide mineral pairs are not always in equilibrium. This can arise when the mineral pair is formed at low temperatures ($T < 200$°C), when the isotopic composition of the mineralising fluid was variable during their deposition and when there is continued isotopic exchange following the formation of the mineral phases. The attainment of isotopic equilibrium is best demonstrated by the determination of similar temperature estimates between three coexisting minerals. If this approach is not possible, then there should be clear textural evidence of equilibrium.

In contrast to the relatively small amount of sulphur isotope fractionation between sulphide mineral pairs, there is more extensive fractionation of $\delta^{34}S$ between co-existing sulphide and sulphate phases. This can be seen in the relatively large fractionation factor between H_2S and sulphate phases given in Table 7.4a and between sulphate and sulphide species listed in Table 7.4b. Rye (2005) reviewed the stable isotope geochemistry of sulphate–sulphide equilibria in igneous and fluid-related hydrothermal systems but found that there is frequently disequilibrium between coexisting sulphate and sulphide species. Rye (2005) recommends two different graphical techniques to establish equilibrium relationships. First, he uses a $1000 \ln \alpha_{SO_4-H_2S}$ versus temperature plot on which sulphide–sulphate pairs are shown relative to the H_2S–SO_2 equilibrium curve. It can be seen in this study that some sulphide–sulphate mineral pairs plot on the H_2S–SO_2 equilibrium curve, whereas others plot far away from equilibrium. A second approach is to use a $\delta^{34}S_{sulphate}$–$\delta^{34}S_{sulphide}$ plot on which the sulphate–sulphide fractionation factors are plotted for a range of temperatures (Figure 7.21).

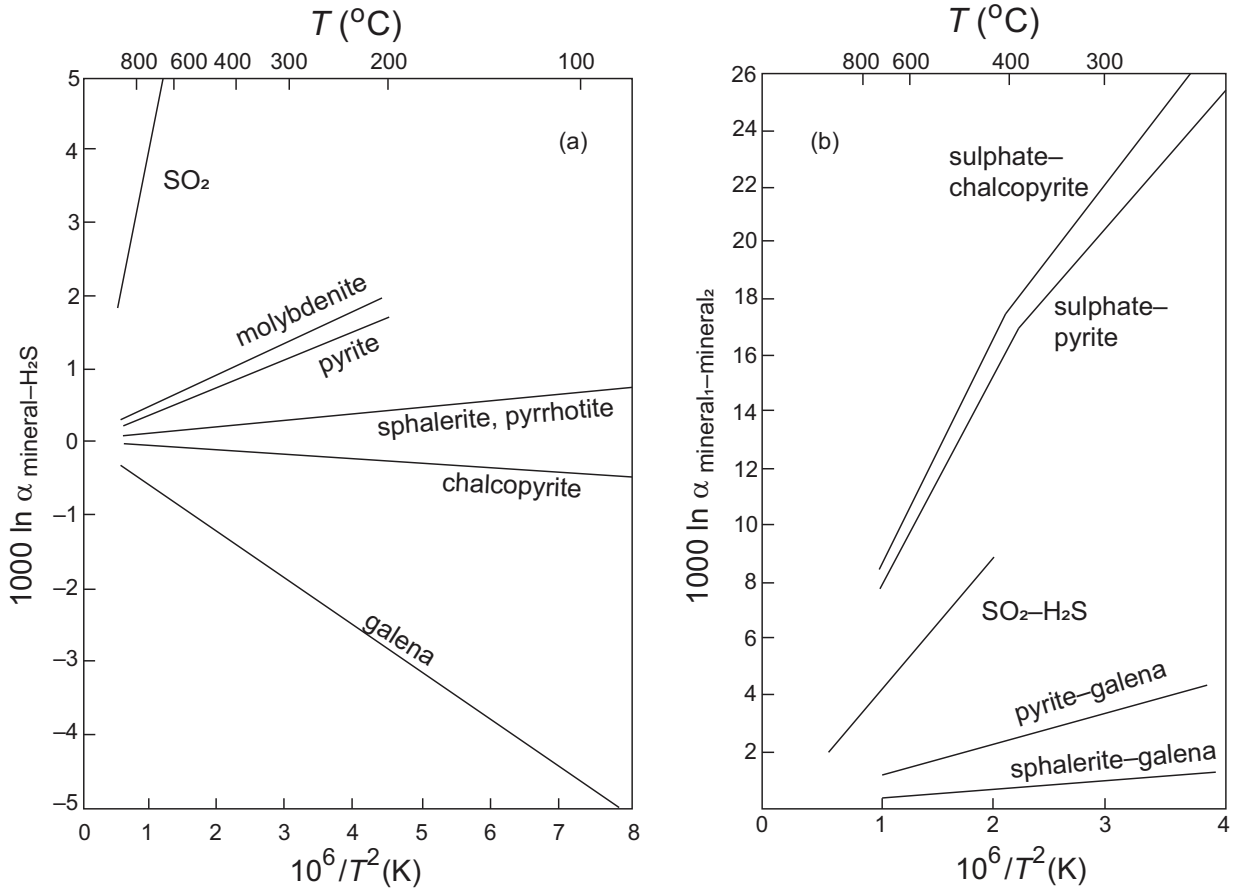

Figure 7.20 (a) Partitioning of ^{34}S between minerals and H_2S as a function of temperature. Mineral pairs with the greatest separation will be the most sensitive thermometers (data from Table 7.4a). (b) Partitioning of ^{34}S between mineral pairs and SO_2–H_2S showing that the greatest fractionations are between sulphides and sulphates.

In this plot the sulphide data should first be converted to $\delta^{34}S_{H_2S}$ values using the equations in Table 7.4a to allow for H_2S–sulphide mineral isotopic fractionation, although for sulphates this fractionation can be ignored for there is minimal fractionation between sulphate minerals and aqueous sulphate. The utility of a diagram of this type is shown in the plot of sulphide–sulphate pairs from igneous and late hydrothermal systems in the late Miocene Julcani mining district of Peru where samples plot over a range of temperatures indicative of disequilibrium (Figure 7.21; Rye, 2005).

(c) *Sulphur isotope fractionation in sedimentary rocks.* In marine sediments the sulphur cycle is driven primarily by the process of dissimilatory sulphate reduction (DSR), which is the reduction of seawater sulphate to sulphide by anaerobic microorganisms. This process can be thought of as a form of sulphate respiration. The metabolic pathway in these organisms converts sulphate into hydrogen sulphide. Much of the sulphide produced in this way is subsequently converted back into sulphate by a series of microbial and geochemical oxidation reactions, but some of the H_2S combines with iron and organic matter and is buried in the sediment. Thus, the end product of this process is the formation of sedimentary pyrite. This part of the surface sulphur cycle is closely tied to the surface oxygen and carbon cycles (Rickard et al., 2017) and has implications for the evolution of the composition of the atmosphere, the oceans and the development of life (Figure 7.22).

There are two other significant biological processes which fractionate sulphur isotopes in the sedimentary environment. Assimilatory sulphate reduction is the means by which green plants, fungi and most bacteria reduce sulphate to sulphide. In this process, sulphide is produced for biosynthesis but there is no energy gain. In addition, there is the process of microbial disproportionation of sulphur (i.e., the simultaneous

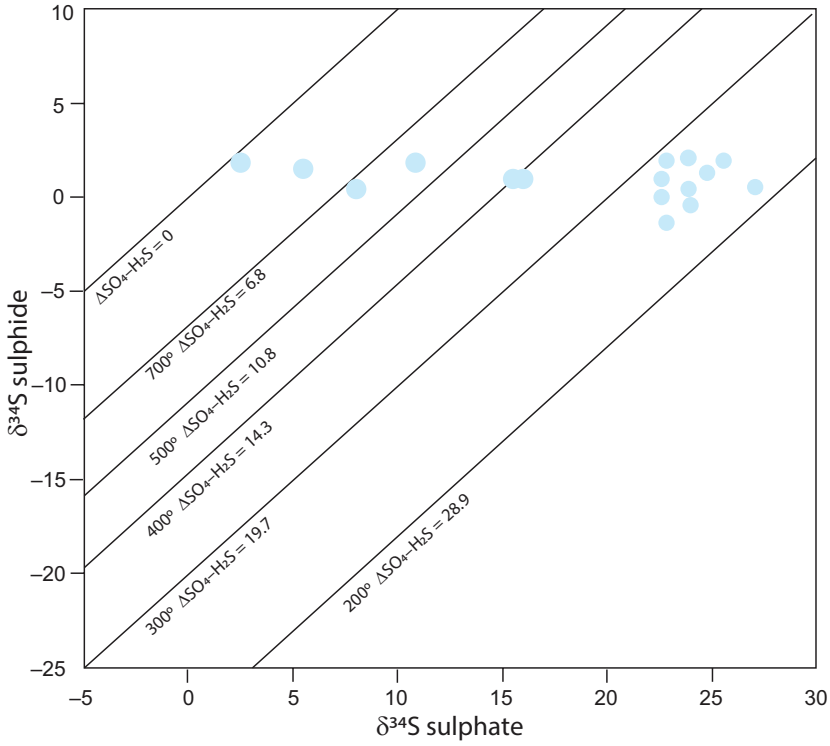

Figure 7.21 $\delta^{34}S_{sulphate}$ versus $\delta^{34}S_{sulphide}$ plot showing disequilibrium between coexisting sulphate and sulphide minerals in late Miocene magmatic and hydrothermal mineral deposits in the Julcani district of Peru.

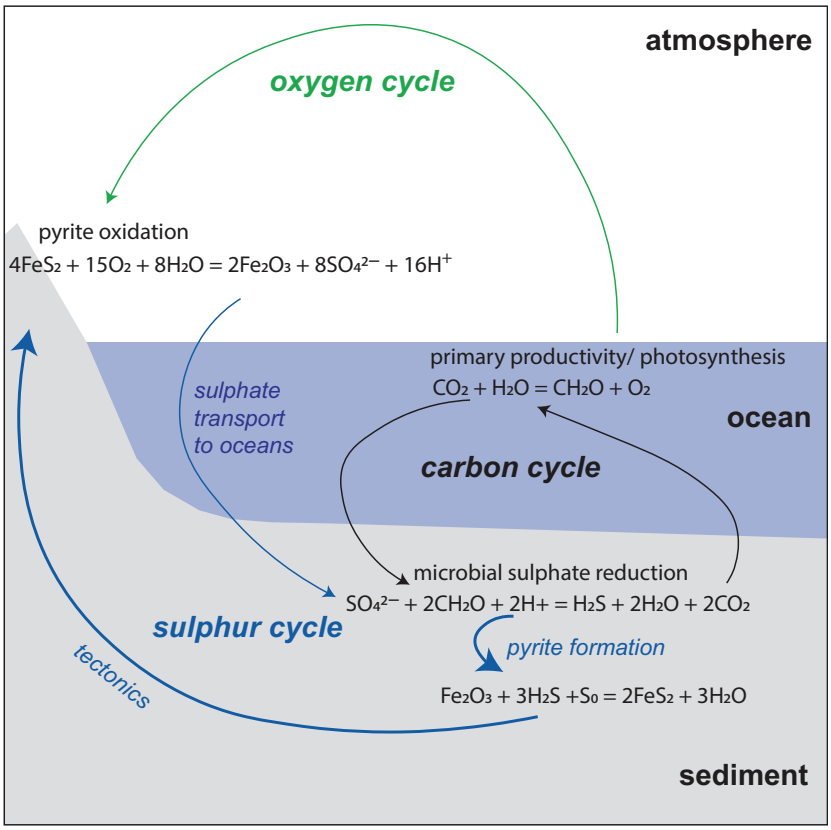

Figure 7.22 The relationship between the sulphur cycle and the surface carbon and oxygen cycles showing the principal chemical reactions. (After Rickard et al., 2017; with permission from the Mineralogical Society of America)

oxidation and reduction of sulphur) in which microbes disproportionate sulphur compounds with an intermediate oxidation state created during the re-oxidation of sedimentary sulphides, sulphites, thiosulphate and elemental sulphur.

The various redox reactions between the different sulphur species affect the isotopic composition of the resultant sulphides and sulphates. There are two main processes. First, there is kinetic fractionation, in which heavy isotopes have a reaction velocity which is slightly slower than light isotopes during the transformation of an oxidised to a reduced phase. In the conversion of sulphate to sulphide, the sulphide product is relatively enriched in the light isotope relative to the heavy isotope and so has a more negative value of $\delta^{34}S$. A second process is equilibrium fractionation, in which a heavy isotope (^{34}S) is more stable when it is part of a strong bond, such as with oxygen in sulphate, and the lighter isotope (^{34}S) is more stable when there is a weaker bond, such as with hydrogen in H_2S (Jørgensen et al., 2019). The impact of these different microbial fractionations of sulphur isotopes was summarised by Shen and Buick (2004) as follows:

- In dissimilatory sulphate reduction, sulphur isotope fractionation is relatively small; on average, the fractionation between $\delta^{34}S$ of plants and their sulphate source is about −1.5‰.
- In the case of assimilatory sulphate reduction, large fractionations have been recorded. In laboratory studies, fractionations of 70‰ are seen, although in natural populations the upper limit of fractionation is a depletion in ^{34}S of 49‰.
- During the re-oxidation of H_2S produced by microbial sulphate reduction and the disproportionation of metastable intermediate compounds, there can be depletions in ^{34}S of up to 70‰.

In addition to the microbial processes discussed, there are also abiogenic processes whereby sulphur isotopes are fractionated in the sedimentary environment. During the formation of evaporites the precipitation of sedimentary sulphate from seawater produces a relatively small $\delta^{34}S$ enrichment of 1.65 ± 0.12‰ (Thode and Monster, 1965). In addition mineral deposits show evidence of sulphate reduction at temperatures above those favourable to sulphate-reducing bacteria (Trudinger et al., 1985). For example, in ocean-ridge hydrothermal systems sulphate reduction can be achieved by reaction with Fe^{2+}-bearing minerals. It is likely that this is an equilibrium process in which the isotopic composition of sulphates in equilibrium with sulphides is isotopically heavier than that of the initial sulphate composition (Shen and Buick, 2004, and references therein).

7.3.4.3 Using Sulphur Isotopes to Identify Multiple Sources in Igneous Rocks and Hydrothermal Mineral Deposits

(a) *Igneous rocks.* The data in Figure 7.19 show that some suites of igneous rocks have a range of sulphur isotope ratios which cannot easily be explained simply by the relatively small fractionations which take place during igneous processes (Section 7.3.4.2). This is apparent in the data for arc basalts and granitoids and implies that these rock types are produced either from multiple sources with different sulphur isotope compositions or via a mixing process such as the crustal contamination of mantle-derived melts. An example of crustal contamination is given by Boztug and Arehart (2007) in their study of post-collisional granitoids from central Anatolia, Turkey. These granitoids have whole-rock sulphur isotope ratios of $\delta^{34}S = 1.9–15.3‰$ and show a positive correlation on a $\delta^{34}S$ versus $\delta^{18}O$ diagram, suggestive of mixing between mantle-derived melts (low $\delta^{34}S$ and $\delta^{18}O$) and crustal melts (high $\delta^{34}S$ and $\delta^{18}O$).

Massive sulphide ores associated with mafic and ultramafic rocks from the eastern part of the Central Asian Orogenic Belt in north-west China have $\delta^{34}S$ values in the range 0.8–8.2‰ (Tang et al., 2012). These values are higher than those found in sulphides from mantle-derived melts and are interpreted as the result of contamination of mantle-derived melts with crust-derived sulphur with a positive $\delta^{34}S$. Gabbros and associated magmatic sulphides from the Hidaka metamorphic belt in Japan also preserve a record of crustal contamination of mafic magmas, in this case through magma mixing and the assimilation of a crust-derived tonalite which has a strongly negative $\delta^{34}S$ signature. Tompkins et al. (2012) calculate that the $\delta^{34}S$ ratios in the gabbros ($\delta^{34}S = +6$ to $-7.5‰$) can be modelled with an AFC process in which 10 wt.‰ tonalite ($\delta^{34}S = -4.5$ to $-10.5‰$) was mixed with the gabbro followed by about 14 wt.‰ fractional crystallization.

An example of mixing in a mantle source region is given by Dottin et al. (2020), who show that in the magmas of the Samoan mantle plume there is evidence of the mixing of two mantle sources. Samoan basalts display a positive correlation between $\delta^{34}S$ and

$^{87}Sr/^{86}Sr$, implying a small but variable crustal component in the mantle source. They propose a model to explain the compositional variation in the melts in which there is mixing between an enriched component with slightly positive $\Delta^{33}S$ and a positive $\delta^{34}S$, which they equate with the mantle source region HIMU, and a component with $\Delta^{33}S = 0$ and negative $\delta^{34}S$, which they regard as primordial mantle.

(b) *Hydrothermal mineral deposits.* Many hydrothermal mineral deposits form as a result of mixing of fluids derived from a number of different sources with different sulphur isotope compositions. Sulphur isotope studies therefore are an important tool in constraining their origin and mechanism of deposition. This is illustrated in Figure 7.23, which shows the wide range of $\delta^{34}S$ compositions recorded in the sulphide and sulphate minerals from different types of hydrothermal mineral deposit. While this variability has been known and understood for some time, the recent application of in situ sulphur isotope measurements is opening up a much more nuanced approach to variations in the fluid chemistry (McDonald et al., 2018; Mukherjee et al., 2019).

Volcanic hosted massive sulphide deposits (VHMS), typified by modern hydrothermal vent systems forming at mid-ocean ridges and Kuroko-type deposits hosted in felsic calc-alkaline lavas, illustrate some of the end-member processes well, for at their simplest these systems represent the mixing of mantle-derived sulphur with $\delta^{34}S \sim 0‰$ and seawater sulphate with $\delta^{34}S \sim 21‰$. The $\delta^{34}S$ values recorded in the different sulphide and sulphate phases from these deposits reflect this range of values and the associated processes of bacteriological sulphate reduction (Butler et al., 1998; Luders et al., 2001; Cazanas et al., 2008; Keith et al., 2016).

The $\delta^{34}S$ values for most porphyry-type deposits are between −5.0 and +5.0‰, close to the mantle range (Han et al., 2018). In their study of the Donggebi porphyry Mo deposit in the Central Asian Orogenic Belt in China, Han et al. (2018) report a narrow range of $\delta^{34}S$ values in molybdenite and associated sulphides of between 1.5 and 3.8‰. In this instance there are no marine sediments in the vicinity, but the fact that these values are elevated above typical mantle values suggest that they have interacted with a crustal source.

Sulphides from Mississippi Valley–type (MVT) ores show a large compositional range of between $\delta^{34}S = -25$ and +25‰ (Figure 7.23); individual deposits are also quite variable with ranges of $\delta^{34}S$ up to 20–30‰. These large ranges are thought to be indicative of Rayleigh fractionation in partially closed systems where sulphate supply is the limiting factor. Deposits with negative values may result from the large fractionations produced by bacterial sulphate reduction in

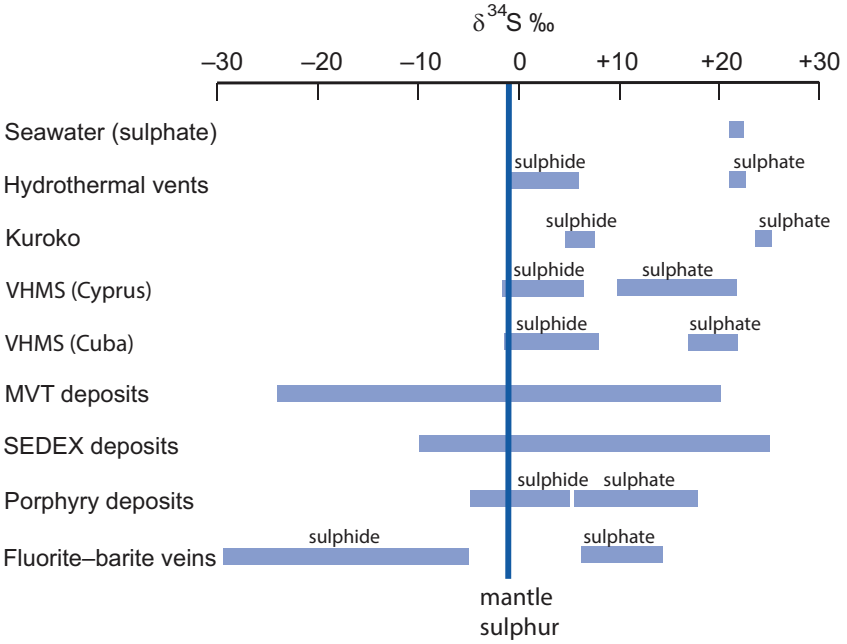

Figure 7.23 Sulphur isotope composition of sulphide and sulphate species in hydrothermal ore deposits relative to mantle sulphur. (Data from sources in the text and from the compilations in Shanks, 2013)

marine sediments. Those with positive values may reflect significant bacterial sulphate reduction in organic-rich settings or through thermochemical sulphate reduction in the subsurface (Shanks, 2013).

Sulphides in the Cretaceous fluorite–barite hydrothermal veins from the Freiberg ore district in Germany have a wide range of $\delta^{34}S$ values between −5.5 and −30.9‰. Cogenetic barites have $\delta^{34}S$ values between +6 and +14‰. This range of values is thought to indicate the mixing of two highly saline brines and the partial reduction of marine sulphate (Bauer et al., 2019).

7.3.4.4 Using Sulphur Isotopes to Understand the Evolution of the Earth's Atmosphere

The discovery of mass-independent fractionation in the sulphur isotope system was unexpected and opened up an important means of understanding the nature of the atmosphere in the early Earth. Mass-independent sulphur isotope fractionation (Section 7.2.4) is thought to reflect photochemical processes in the upper atmosphere in which SO_2 is reduced in ultraviolet radiation to elemental sulphur. The significant discovery, however, is that both the formation and the preservation of the mass-independent fractionation (MIF) signal require anoxic conditions. Experimental studies show that to create and preserve a MIF signal, oxygen concentrations have to be as low as 10^{-5} present atmospheric levels.

Early studies showed that both positive and negative $\Delta^{33}S$ signals have been preserved. This is explained in terms of two different 'channels' from the atmosphere to the sediment where the signal is preserved. In the case of elemental sulphur created by the photolysis of volcanogenic SO_2, this was transported to the Earth's oceans in rain where it continued to exist either as elemental sulphur or as thiosulphate but ultimately was preserved in sediment as sulphide with a *positive* $\Delta^{33}S$ signal. Alternatively, volcanogenic SO_2 was converted into sulphite and sulphate in the atmosphere and transferred to the oceans as sulphate with a *negative* $\Delta^{33}S$ signal. Some of this sulphate was preserved as sedimentary sulphate, while another component was converted into sedimentary sulphide with a negative $\Delta^{33}S$ signal (Farquhar and Wing, 2003). Some of the sedimentary sulphide was subsequently returned to the mantle by means of subduction and recorded for posterity in tiny sulphide inclusions in diamonds (Farquhar et al., 2002).

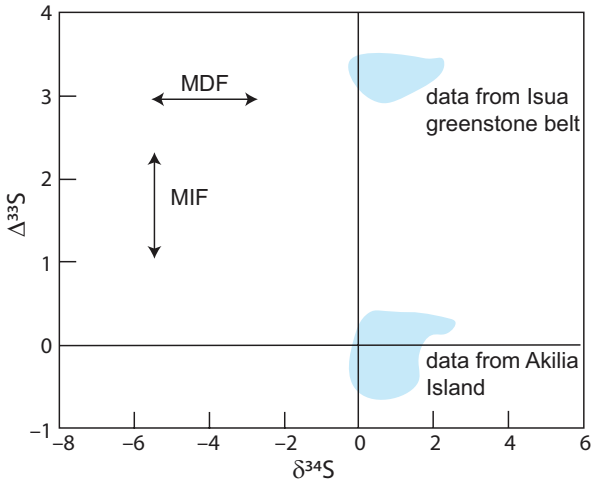

Figure 7.24 $\delta^{34}S$ versus $\Delta^{33}S$ diagram showing the composition of 3.7–3.8 Ga iron pyrites from west Greenland and the trends for mass-independent fractionation (MIF) and mass-dependent fractionation (MDF). (Data from Whitehouse et al., 2005)

Sulphur isotope data can be presented on a $\delta^{34}S$ versus $\Delta^{33}S$ diagram as a means of showing simultaneously the effects of mass-independent fractionation ($\Delta^{33}S$) relative to that of mass-dependent fractionation ($\delta^{34}S$). Ono (2017) has proposed that the Archaean reference array on this diagram has the slope $\Delta^{33}S \sim 0.9 * \delta^{34}S$. An example of a $\delta^{34}S$ versus $\Delta^{33}S$ plot is given in Figure 7.24 and shows the composition of two groups of iron pyrites from the early Archaean of west Greenland. The data from sediments of the Isua greenstone belt have a clear MIF signal, whereas the samples from high-grade metamorphic rocks from Akilia Island show no MIF signal, perhaps indicating a non-sedimentary origin (Whitehouse et al., 2005).

A plot of $\Delta^{33}S$ over geological time shows that the MIF signal is present throughout the Archaean and is particularly well represented in the Neoarchaean, but then disappears completely from the geological record after 2.33 Ga (Figure 7.25). Given that the MIF signal is an indicator of an anoxygenic atmosphere, these data imply a significant increase in the oxygenation of the Earth's atmosphere after 2.34 Ga, a finding which is consistent with other geological observations. This sharp increase in atmospheric oxygen is known as the Great Oxidation Event (GOE). It has been suggested that the plot of $\Delta^{33}S$ over geological time

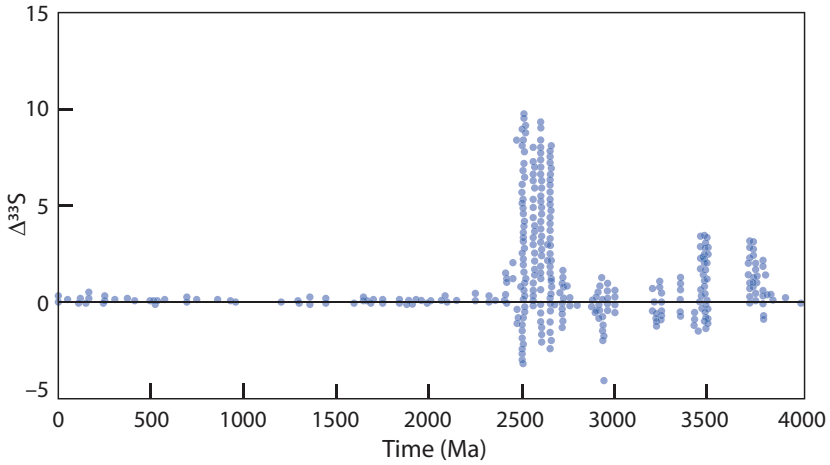

Figure 7.25 Plot of $\Delta^{33}S$ versus time showing that the mass-independent fractionation signal is restricted to rocks older than 2.3 Ga, indicating the very low concentrations of oxygen in the Earth's atmosphere before this time. (Data from the compilation of Johnston, 2011; with permission from Elsevier)

might also imply some variability of oxygen levels throughout the Archaean, although it is important to note that the data from which this diagram is constructed are based upon a limited geographic distribution of samples (Ono, 2017).

7.3.4.5 Using Sulphur Isotopes to Understand the Development of Early Life on Earth

As noted in Section 7.3.4.2, the low-temperature microbial reduction of sulphate to sulphide is accompanied by a large fractionation of sulphur isotopes such that pyrite produced by this process is strongly enriched in the light isotopes and has large negative $\delta^{34}S$ values. This means, therefore, that the recognition of large negative $\delta^{34}S$ values in the sedimentary record is a possible means of exploring the processes of microbial sulphate reduction in the geological past. This of course requires that primary biogenic signatures are preserved unmodified in the geological record. Fortuitously, sulphur is not remobilised in the sedimentary environment, for most sedimentary processes do not involve the transport of sulphur. Further, most biogenic sulphur is preserved as pyrite, and the additional isotopic fractionation associated with the conversion of microbial H_2S to pyrite is low and is less than 1‰. This means that pyrite is potentially a robust 'time capsule' for the preservation of primary microbial signatures from the geological past, even to relatively high metamorphic grades (Shen and Buick, 2004; Rickard et al., 2017).

This is evident from studies of ancient sediments from as far back as the Archaean which in some instances preserve a wide range of sulphur isotope ratios which can be taken as a signal of biological activity in the form of microbial reduction of sulphate to sulphide. An example is the ~3.47 Ga sulphate-rich sediments of the North Pole area of north-western Australia described by Shen and Buick (2004). These samples contain sulphates with $\delta^{34}S$ values between +3.2 and 5‰ and associated sulphides which show fractionations of between 7.4 and 21.1‰ relative to the sulphate. It is this fractionation which is interpreted as the signal of biological activity indicative of the process of dissimilatory sulphate reduction.

Samples from the 2.7 Ga Belingwe greenstone belt in Zimbabwe were investigated by Grassineau et al. (2005). They report a range of $\delta^{34}S$ values from −21.1 to + 16.7‰ in sulphidic sediments. These values contrast with a probable mantle value of -0.5 ± 0.9‰ from associated volcanic rocks. These authors showed that even a single sample preserved domains which showed different degrees of sulphur isotope fractionation, which they suggested reflects a diverse range of coexisting microbial colonies.

Of course, when seeking to establish a biogenic signal from sulphur isotopes in ancient rocks, it is important to consider whether the signal could have been produced through non-biological activity. Reactions such as the re-oxidation of reduced sulphur species in repeated cycles and the disproportionation of intermediate sulphites into sulphide–sulphate mixtures can give rise to significant $\delta^{34}S$ depletions. In addition, abiotic sulphur isotope fractionations can be the result of hydrothermal reactions. For this reason, establishing the validity of microbial activity in ancient sedimentary sulphide requires a full investigation of their setting using all the available geological and geochemical data.

7.3.5 Nitrogen Isotopes

Nitrogen occurs in nature as N_2 gas, a highly volatile but inert component of the Earth's atmosphere where it is present as 78‰ by volume. It also exists in multiple redox states as the reduced species NH_4^+ (ammonium), NH_3 (ammonia) and in oxidised form as NO_2^- (nitrite) and NO_3^- (nitrate). To these ionic species human activity has added NO_x (nitrogen oxides). Nitrogen is also an essential component of living organisms where it is present in amino acids, proteins and nucleic acids.

There are two naturally occurring isotopes of nitrogen: ^{14}N (99.63‰) and ^{15}N (0.37‰). Isotope ratios are measured as $^{15}N/^{14}N$ and expressed as $\delta^{15}N‰$ (Eq. 7.24) and measurements are made relative to the nitrogen isotopic composition of air (see Box 7.8). The variation in $\delta^{15}N$ of the major terrestrial reservoirs is summarised in Figure 7.26.

Nitrogen isotope measurements are determined by conventional gas source ion-ratio mass spectrometry on the N_2 molecule. Specialist sample preparation techniques are required when the sample size is very small which involve gas chromatography and dedicated combustion/reduction furnaces. In silicate rocks where concentrations are low, either static mass spectrometry or conventional ion-ratio mass spectrometry, using He as a carrier gas, allows sensitive measurements to be made (Cartigny and Marty, 2013). N-rich minerals such as nitrides and diamonds are amenable to analysis by ion-probe using a $^{133}Cs^+$ primary beam.

A large fraction (~60‰) of the Earth's nitrogen resides in the mantle (Bebout et al., 2013), and so it is important to consider the large-scale nitrogen cycle of the silicate Earth. At the Earth's surface, organic nitrogen in sediments is converted into NH_4^+ and substitutes for K^+ in clays and in detrital K-feldspar. In the crust the NH_4^+ is retained in residual mica during metamorphism and during partial melting nitrogen is retained as NH_4^+ in K-feldspar and as N_2 in cordierite (Busigny and Bebout, 2013). Ultimately, nitrogen at the Earth's surface is returned to the deep Earth by subduction; currently, there are two competing models for the mechanism whereby this takes place. It has been suggested that nitrogen is returned to the mantle via sediments in which the nitrogen is trapped in crustal minerals and bound in organic materials. More recently, Li et al. (2019) proposed that hydrothermally altered ocean crust, with positive $\delta^{15}N$ values, is a more efficient mechanism for returning nitrogen to the Earth's mantle.

At the Earth's surface the significant part of the nitrogen cycle takes place in the ocean (Figure 7.27). Here biological nitrogen fixation (diazotrophy) is the process whereby atmospheric and dissolved N_2 are converted to NH_4 using the enzyme nitrogenase. The ammonium then either is oxidised to nitrogen and returned to the atmosphere or becomes fixed in organic matter and mineralised as kerogen. This then is either incorporated into sediments or oxidised to give marine nitrate. The marine nitrate may return nitrogen to the atmosphere, be converted into kerogen via marine organisms or be biologically assimilated and converted back into ammonium. All these exchanges are controlled by microbial activities which employ the following pathways:

- Ammonification: this process includes both the fixation of nitrogen gas as ammonium and the reduction of nitrite (from nitrate) to ammonium
- Nitrification: this involves the oxidation of ammonium to either nitrite or nitrate
- Denitrification: the process whereby oxidised nitrogen species are reduced to N_2 through one or more stages
- Anammox (anaerobic ammonium oxidation): a process that simultaneously converts both ammonium and nitrite species to nitrogen (Stein and Klotz, 2016).

There are four main areas of contemporary geochemistry where the study of nitrogen isotopes is important:

- In the modern Earth to aid understanding of biogeochemical cycles and as tracers of anthropogenic activity (Hastings et al., 2013)
- In the deep Earth to improve our understanding of mantle processes from nitrogen isotopes in diamonds
- In the early Earth for developing our understanding of ancient biogeochemical cycles, in understanding the redox state of the early oceans and in the understanding of the evolution of the Earth's early atmosphere
- In the search for life on other planets (Fogel and Steele, 2013).

7.3.5.1 The Distribution of Nitrogen Isotopes in Nature

The distribution of nitrogen isotopes in the Earth's major reservoirs is summarised in Figure 7.26. It is thought that the nitrogen isotope composition of the

Box 7.8 Nitrogen isotopes

Stable isotopes and abundances

$^{14}N = 99.636‰$

$^{15}N = 0.364‰$

Measured isotope ratios

$$\delta^{15}N‰ = \left[\left({}^{15}N/{}^{14}N_{(sample)} - {}^{15}N/{}^{14}N_{(standard)}\right)/{}^{15}N/{}^{14}N_{(standard)}\right] \times 1000 \quad (7.24)$$

Standards

AIR-N_2, the nitrogen isotopic composition of air

Mantle value (depleted upper mantle)

$\delta^{15}N = -5 \pm 2‰$ (Cartigny and Marty, 2013)

Primordial mantle value

$\delta^{15}N = -40‰$ (estimated from values in diamonds; Cartigny and Marty, 2013)

Bulk silicate Earth value

$\delta^{15}N = -7 \pm 3‰$ (based on a chondritic model of the Earth's nitrogen; Jia and Kerrich, 2015)

Variations in nature

See Figure 7.26.

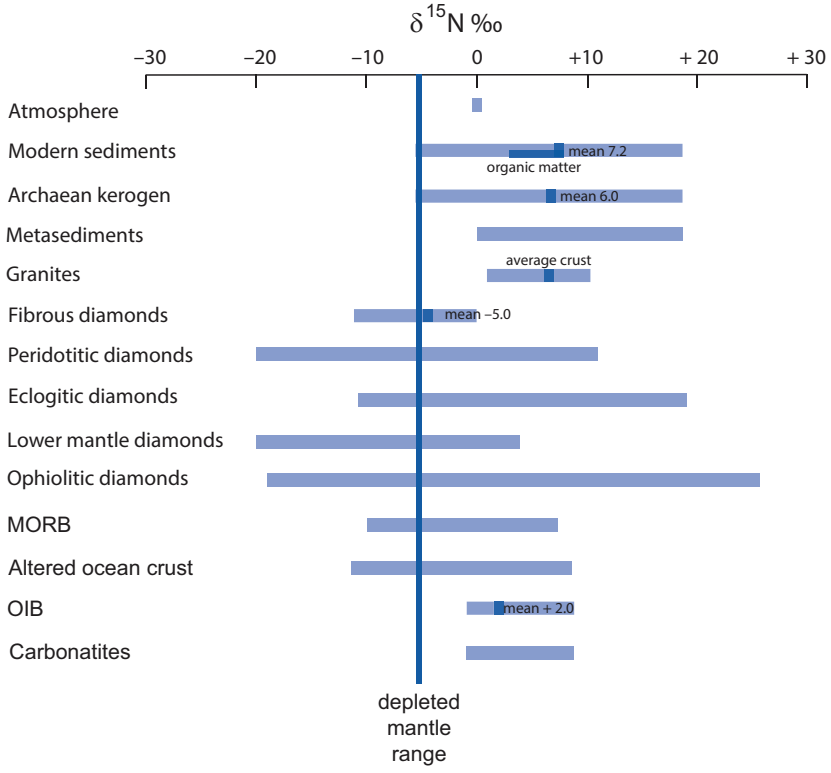

Figure 7.26 Variation in $\delta^{15}N$ in major Earth reservoirs and selected rock types shown relative to the depleted mantle range. (Data from compilation in Cartigny and Marty, 2013, and Wu et al., 2019)

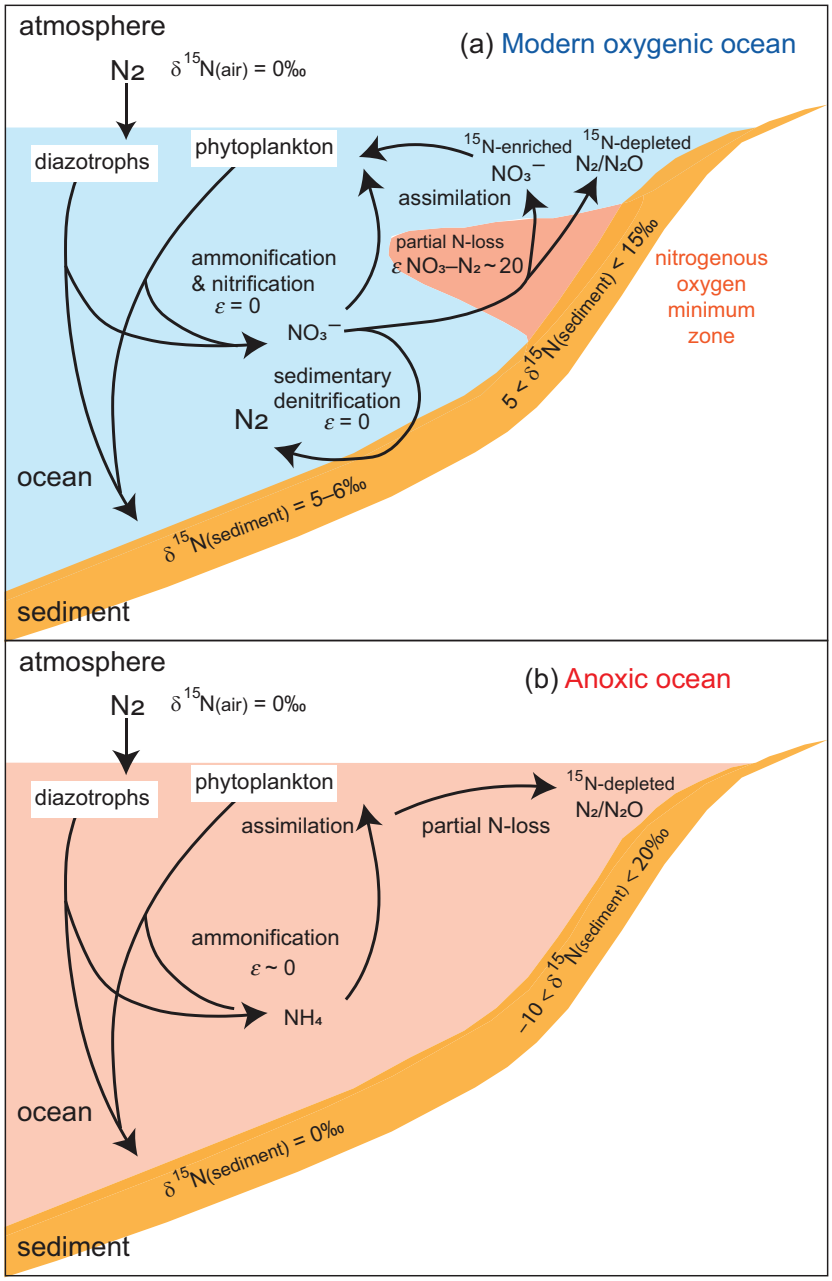

Figure 7.27 The nitrogen biogeochemical cycle in an oxygenic and an anoxic ocean; in each case the nitrogen cycle in the open ocean is shown on the left-hand side of the diagram and a zone of upwelling shown on the right-hand side of the diagram. (a) In a modern oxygenic ocean, diazotrophs and phytoplankton contribute both to organic matter in sediment and to the processes of ammonification and nitrification. In this scenario, ocean nitrate is partially denitrified and some is returned to organic matter through assimilation. In regions of upwelling through zones of low dissolved oxygen (nitrogenous oxygen minimum zone) more extreme isotopic fractionations are preserved in the sedimentary record and $\delta^{15}N$ values increase. (b) In a fully anoxic ocean, nitrogen is supplied by N-fixation and by the generation of NH_4^+. In this case there is no fractionation of nitrogen isotopes between the atmosphere and sediment. In zones of upwelling, the isotopic fractionation associated with NH_4^+ assimilation is expressed in the biomass, leading to both positive and negative fractionations and preserved in the sedimentary record. ε represents the fractionation between reactant and product ~ $(\delta_{reactant} - \delta_{product})$; where ε ~ 0‰ this indicates that the reaction is complete and there is no isotopic fractionation. (After Ader et al., 2016; with permission from Elsevier)

Earth is close to that of chondritic meteorites, for when plotted on a D/H versus $^{15}N/^{14}N$ ratio diagram the Earth has a composition which lies between that of comets and the value for the solar wind ($\delta^{15}N = -400‰$), and is close to the values of carbonaceous chondrites (Marty, 2011; Cartigny and Marty, 2013). Further support for a chondritic model for nitrogen in the primordial Earth comes from the observation that the abundance of nitrogen on Earth is close to the chondritic value. On this basis, Jia and Kerrich (2015) proposed that the $\delta^{15}N$ value for the bulk Earth can be calculated from a weighted mean of the values for enstatite chondrites ($\delta^{15}N = -20‰$ to $-30‰$) and carbonaceous chondrites ($\delta^{15}N = +16‰$ to $+52‰$) and calculated a bulk Earth value of $\delta^{15}N = -7 \pm 3‰$, a value that overlaps with the $\delta^{15}N$ value proposed for the modern mantle. In contrast to chondritic meteorites, iron meteorites have $\delta^{15}N$ values in the range $-100‰$ to $+155‰$ (Murthy et al., 2019).

Nitrogen isotope measurements in fibrous diamonds and in vesicles in fresh mid-ocean ridge basalt glass suggest that the Earth's depleted upper mantle has a value of $-5 \pm 2‰$ and so is depleted in $\delta^{15}N$ relative to the atmosphere ($\delta^{15}N = 0$). Some MORBs and OIB have higher values, indicating either that their source was contaminated with material from the Earth's surface or that the $\delta^{15}N$ values are elevated because of degassing. Nitrogen is only a minor component of volcanic gases but where measured in basaltic rocks tends to have values in the mantle range (de Moor et al., 2013).

Nitrogen substitutes for carbon in diamonds and so $\delta^{15}N$ values in diamond can provide important information about mantle processes. Most diamonds have $\delta^{15}N$ values in the range -12 to $+5‰$ with a mode of $-5 \pm 3‰$, but some samples have values as low as $\delta^{15}N = -40‰$ and as high as $+18‰$ (Figure 7.26). It has been suggested that the wide range of positive $\delta^{15}N$ values in diamonds might be evidence of the recycling of materials from the Earth's surface into the deep mantle and that those diamonds with very low values of $\delta^{15}N$ ($\sim -40‰$) could indicate the composition of the Earth's primordial mantle (Cartigny and Marty, 2013). Rare micro-diamonds found in ophiolitic chromitites have $\delta^{15}N$ values between -19 and $+26‰$ (Wu et al., 2019). A helpful way of representing the range of different diamond types is on a $\delta^{15}N$ versus $\delta^{13}C$ diagram, as illustrated in Figure 7.28.

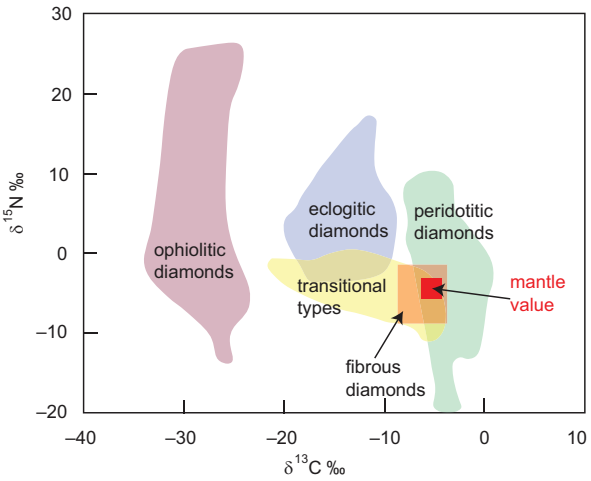

Figure 7.28 $\delta^{13}C$ versus $\delta^{15}N$ plot of diamond compositions showing the compositional range in diamond types relative to the modern (depleted) mantle value. (Modified after Wu et al., 2019)

Altered ocean crust has $\delta^{15}N$ values which are higher than those recorded in the pristine crust and mantle. In detail, measured values are very variable and increase with increasing metamorphic grade: serpentinised meta-peridotite has $\delta^{15}N = +4$ to $+15‰$, altered and metamorphosed oceanic basalts $\delta^{15}N = -11.6$ to $+8.3‰$, ophiolitic metagabbros $\delta^{15}N = +0.8$ to $+8.1‰$ and eclogitic metabasalts $\delta^{15}N = -1$ to $+8‰$ (Busigny et al., 2018). Taken together these data imply that ocean crust which is returned to the mantle via subduction is likely to have a positive $\delta^{15}N$ value.

In the Earth's continental crust the dominant nitrogen species is NH_4^+ substituting for K^+, Na^+ and Ca^{2+} in illites, micas, feldspars, clinopyroxenes and amphiboles. In granitic rocks NH_4^+ is most abundant in biotite > muscovite > K-feldspar > plagioclase. An average $\delta^{15}N$ value for the continental crust, based upon the composition of sedimentary and crystalline rocks, is $\delta^{15}N \sim +6.0‰$. This is consistent with the findings that most organic matter has $\delta^{15}N = +3$ to $+7$, that the devolatilisation of sediments during metamorphism leads to an enrichment in $\delta^{15}N$ relative to the atmosphere and that granites have $\delta^{15}N = +1$ to $+10‰$ (Busigny et al., 2018).

Sedimentary rocks are the second most important reservoir of nitrogen at the Earth's surface after the atmosphere. Nitrogen in sediments is preserved as organic nitrogen (in kerogen) and as fixed nitrogen in the form of NH_4^+ in phyllosilicates. Most

sediments have $\delta^{15}N$ values in the range −6 to +20‰ with an average value of $\delta^{15}N = +7.2 \pm 3.3$‰. Marine sediments containing organic matter have $\delta^{15}N$ values in the range +3 to +14‰ and are thought to reflect an aerobic oceanic cycle (Stüeken et al., 2016). The isotopic composition of marine nitrate is a product of the marine nitrogen cycle as illustrated in Figure 7.27 and $\delta^{15}N$ values are between ~+1.0 and +15‰ with a mode of $\delta^{15}N = +5$ to +6‰ (Ader et al., 2016).

Given that the Earth's continental crust (average $\delta^{15}N \sim +6.0$‰) and atmosphere ($\delta^{15}N = 0.0$‰) were originally extracted from the mantle, it has been suggested from mass balance calculations that the mantle should have a positive $\delta^{15}N$ value, rather than the observed $\delta^{15}N = -5.0$. Possible solutions to this paradox are that the $\delta^{15}N$ value of the mantle has changed over geological time or that there are as yet unrecognised deep mantle reservoirs with lower $\delta^{15}N$ than that of the depleted upper mantle (Cartigny and Marty, 2013).

7.3.5.2 Controls on the Fractionation of Nitrogen Isotopes

Fractionation between the different nitrogen species is not well known because the relevant fractionation factors are not yet sufficiently well determined. Some fractionation factors have been calculated theoretically (see Busigny and Bebout, 2013), although many carry a high degree of uncertainty. An empirical study by Petts et al. (2015) for diamond-bearing fluids has estimated a diamond–fluid N isotope fractionation factor ($\Delta^{15}N_{diam-fluid}$; see Eq. 7.6) of −4.0 ± 1.2‰ at 1100°C. For more complex, carbon-poor fluids this value rises to ~−5.2‰. For fluids where NH_3, N_2 and NH_4^+ are the primary N species theoretical calculations based upon these observations yield $\Delta^{15}N_{diam-fluid}$ values at 1100°C of −1.4‰, −2.1‰ and −3.6‰, respectively (Petts et al., 2015).

Nitrogen has a similar solubility to that of Ar in the mantle and is thought to be incompatible. During partial melting the fractionation of nitrogen isotopes is thought to be small and at the per mil level (Cartigny and Marty, 2013). However, there is some evidence that nitrogen isotopes are fractionated during the degassing of basaltic melts. Cartigny and Ader (2003) calculated a shift from $\delta^{15}N = -5.0$‰ in the source to +3.0‰ after the degassing of OIB melts. Under reducing conditions nitrogen behaves as siderophile element in the silicate Earth and could therefore be present in the Earth's core.

Within the modern oceanic nitrogen cycle there are a large number of different metabolic processes which give rise to a range of isotopic fractionations (Ader et al., 2016; Stüeken et al., 2016); however, given the wide range of redox states in the oceans and associated sediments, it is important to determine whether these fractionations take place under oxygenic or anoxic conditions (Figure 7.27). Denitrification and anammox are the dominant metabolic processes whereby marine nitrate is converted into atmospheric nitrogen, and these are the principal controls on the $\delta^{15}N$ composition of the oceans and modern sediment. The net effect of these reactions leads to an enrichment of $\delta^{15}N$ in the oceans of +5 to +7‰. This enrichment is then transmitted via marine organisms to sedimentary kerogen, which is then preserved in the sedimentary record with little further isotopic fractionation. Thus, under oxygenic conditions marine sediments approach the isotopic composition of NO_3^- in the overlying water column (Zerkle et al., 2017). Additional minor isotopic fractionation may occur by biological nitrogen fixation (diazotrophy) which produces a biomass with $\delta^{15}N$ between about +1.0 and −1.0‰, the diagenetic remineralisation of organic-bound ammonium to dissolved NH_4^+ which renders the residual biomass isotopically heavier by 1.4–2.3‰ (Stüeken et al., 2016), and the release of ammonium from sediment (denitrification) which leads to nitrate which is isotopically lighter than the original biomass.

Most nitrogen in the geological cycle is preserved either in kerogen or as ammonium ions in potassic minerals, and with increased burial and metamorphism $\delta^{15}N$ values in sedimentary rocks are enriched. Thomazo and Papineau (2013) suggested that values increase by 1–2‰ at greenschist facies, by 3–4‰ at amphibolite facies and up to 6–12‰ at upper amphibolite facies. Stüeken et al. (2017) show that for many metasediments the kerogen component is isotopically lighter than the silicate fraction and the bulk rock and that this difference becomes larger with increasing metamorphic grade, indicating an equilibrium isotopic separation between the kerogen-bound and silicate-bound nitrogen. These authors recommend that for samples metamorphosed up to greenschist facies and with >40‰ silicate-bound nitrogen, the primary isotopic composition of the biomass is best approximated by the bulk rock $\delta^{15}N$ value,

whereas for very kerogen-rich samples and rocks at higher metamorphic grades the $\delta^{15}N$ values of the kerogen fraction are closer to that of the original biomass.

7.3.5.3 Using Nitrogen Isotopes as a Tracer in Geological and Biological Processes

Inspection of the $\delta^{15}N$ values reported in Figure 7.26 shows that samples from the Earth's surface environment have positive values and are higher than that of the Earth's mantle. This is thought to reflect the influence of microbial processes. In contrast, some mantle-derived materials, notably, some diamonds, have highly negative $\delta^{15}N$ values indicating that some mantle fluids and/or reservoirs are highly $\delta^{15}N$-depleted. These differences therefore provide a means of discriminating between a range of geological and biological processes in the Earth. For example, the variation in $\delta^{15}N$ in sedimentary rocks can be used to track changes in the marine nitrogen biogeochemical cycle over geological time. As noted above, unaltered marine sediments that contain organic matter and have $\delta^{15}N$ values in the range +3 to +14‰ are usually interpreted as reflecting an aerobic oceanic cycle. The details of specific microbial fractionations representing particular biogeochemical reactions have been summarised by Ader et al. (2016) and Stüeken et al. (2016).

In environmental geochemistry it has been shown that anthropogenic nitrogen in the form of NOx gases, and now recorded as nitrate, has a distinctive isotopic composition. Hastings et al. (2013) show that $\delta^{15}N_{nitrate}$ values in Greenland ice cores have decreased from +11 to −1.0‰ since preindustrial times, indicating the effects of human activity in the use of fossil fuels and fertilizers. A particularly useful approach in the study of modern nitrates is to fingerprint them using the isotopes of both oxygen and nitrogen on a combined $\delta^{18}O$–$\delta^{15}N$ plot (Hastings et al., 2013).

In the Earth's mantle N isotope compositions can be combined with C isotope measurements and plotted together on a $\delta^{13}C$–$\delta^{15}N$ diagram to identify different types of diamond (Figure 7.28; Wu et al., 2019). This diagram can also be used to understand the role of carbon- and nitrogen-bearing fluids in the mantle and to evaluate their role in the formation of diamond. In this way Smit et al. (2016) showed that mixed habit diamonds from Marange in Zimbabwe formed through the mixing of two different mantle fluids, one CH_4-rich and the other CO^{2-}/CO_2-rich. The positive $\delta^{15}N$ values for these fluids suggest their derivation from a metasedimentary source and therefore imply the dehydration of a subducting slab in their genesis.

7.3.5.4 Using Nitrogen Isotopes to Understand Processes in the Early Earth

A number of authors have proposed that there is a secular trend in nitrogen isotope ratios for organic nitrogen as recorded in Archaean and Proterozoic sediments (Beaumont and Robert, 1999; Thomazo and Papineau, 2013). These authors found that kerogen in Archaean chert has average $\delta^{15}N$ values of about 0‰, whereas in the early Proterozoic these values were about +5‰, a shift which is coincident with the Great Oxidation Event at ~2.34 Ga. However, unravelling the ancient nitrogen isotope record is not straightforward, for it is always necessary to assess whether or not the measured isotopic shift is the product of biogenic processes or the effect of later metamorphism (Thomazo and Papineau, 2013).

Before the GOE at ~2.34 Ga the lack of oxygen in the atmosphere would prohibit the oxygenation of the oceans and lead to a different set of metabolic pathways from the modern (Figure 2.27b). This is illustrated by Mettam et al. (2019), who show that 2.5–2.6 Ga shallow marine carbonates preserve evidence of an anaerobic nitrogen cycle dominated by N_2 fixation and the assimilation and recycling of ammonium ($\delta^{15}N = -3.3$ to +3.2‰). In contrast, $\delta^{15}N$ values from 2.31 Ga shales from the Rooihoogte and Timeball Hill formations in South Africa, formed after the GOE, provide evidence of an aerobic marine nitrogen cycle dominated by processes of nitrogen loss. In these rocks $\delta^{15}N$ values in the upper part of the succession are 7.2 ± 1‰, close to modern marine values (Zerkle et al., 2017).

7.4 Non-traditional Stable Isotopes

Non-traditional stable isotopes are relative newcomers to the geochemical toolkit and have, for the most part, been in use for only the past two decades. Their advent has been made possible largely by the development of multi-collector inductively coupled plasma mass spectrometry (MC-ICP-MS). The development of this instrumentation has revolutionised the ability of geochemists to measure very small

differences in isotope ratios for a large number of different isotope systems and provides a level of resolution sufficient to resolve the (usually) small differences found between natural samples.

When compared with the traditional stable isotopes (H, C, N, O, S) which have a relatively low atomic mass, the non-traditional stable isotopes include both heavy and light elements, many of which are trace elements and whose properties vary from volatile to refractory. Some occur in a number of different oxidation states and some have more than two isotopes and so offer potential insights through different types of mass fractionation (Teng et al., 2017b). Because of their geochemical versatility, the non-traditional stable isotopes offer potential insights into a wide range of geological, cosmochemical and biogeochemical processes (Albarede et al., 2017).

A summary of the full range of non-traditional stable isotope systems currently being investigated by geochemists is shown on the periodic table in Figure 7.29. Here the elements are divided into those whose stable isotope geochemistry is not currently so well known – the 'emerging non-traditional isotope systems' as defined by Teng et al. (2017b) – and those stable isotope systems which are relatively well studied. Of the latter, five are selected here for more detailed discussion: Li, Mg, Si, Cr and Fe.

Some of the non-traditional stable isotope systems show only small amounts of fractionation and until the advent of precise MC-ICP-MS measurements rendered them out of reach of isotopic analysis. This is in part linked to the small relative mass differences that occur between the stable isotopes of the heavier elements. Figure 7.30 illustrates the natural terrestrial variation between isotopes in the different non-traditional isotope systems discussed here and their relative mass differences.

In addition to solution MC-ICP-MS important advances have also been made in the application of in situ techniques. These involve the use of laser ablation MC-ICPMS and MC-SIMS (ion microprobe) technologies (Chaussidon et al., 2017). The SIMS approach offers high spatial resolution (10–20 μm), high sensitivity and low background interference. The sensitivity of the LA-MC-ICPMS technique is in part dependent on the choice of laser and the ablation

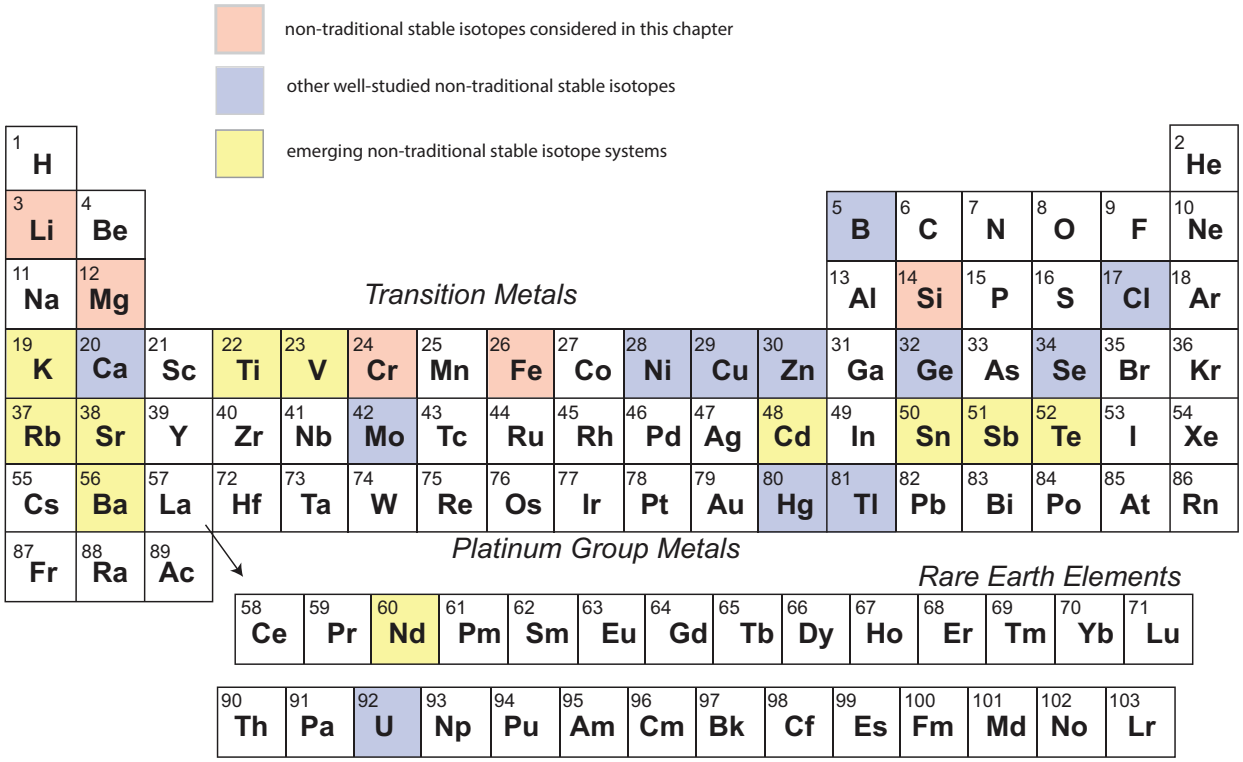

Figure 7.29 Periodic table of the elements showing the non-traditional isotope systems currently being investigated in geochemistry. The elements are identified either as having isotope systems which are relatively well-studied (blue) or as having stable isotope systems which are still emerging (yellow) (after Teng et al., 2017b). The isotope systems discussed in this section are highlighted in pink.

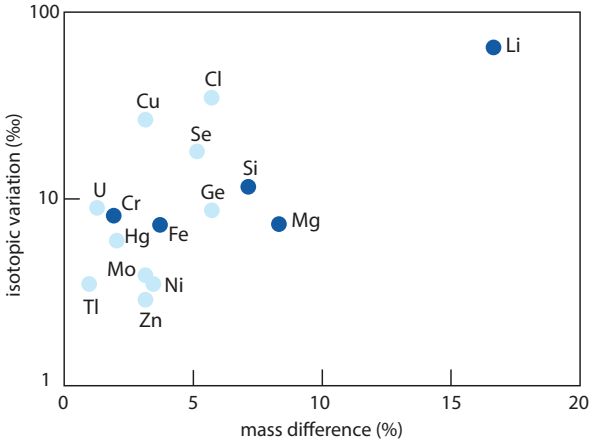

Figure 7.30 Plot of the non-traditional stable isotopes used in this section showing the extent of their natural isotopic variation (‰, log scale) versus the relative mass difference between the isotopes used in the calculation of the isotopic ratio (%). The isotopes shaded dark blue are those discussed in detail in this chapter. (After Teng et al., 2017b; with permission from the Mineralogical Society of America)

efficiency. Other analytical considerations are that the very small volume of material sputtered or ablated may limit the possible precision; the ion yield of samples may vary as a function of the composition of the sample matrix; and there can be isotopic fractionations within the instrument itself (see the review by Chaussidon et al., 2017).

For a fuller discussion of non-traditional stable isotopes the reader should consult the review volumes edited by Johnson et al. (2004), the updated version edited by Teng et al. (2017a) and the recent edition of Hoefs (2018). Titles specific to individual isotopes include the volume by Tomascak et al. (2016) on Li isotopes and Johnson et al. (2020) on Fe isotopes.

7.4.1 Lithium Isotopes

Lithium occurs most commonly as a trace element, and in octahedral coordination the Li^+ ion has a similar size to that of Mg^{2+}. For this reason Li tends to substitute for Mg in silicate minerals. There are two isotopes, ^6Li and ^7Li, and the relatively large mass difference means that there can be significant mass fractionation in excess of 50‰ (Figure 7.30). Li isotopes are measured as $^7Li/^6Li$ and expressed as δ^7Li (Eq. 7.25) relative to the synthetic standard IRMM-016. The isotope systematics of Li are summarised in Box 7.9. Li is present only as monovalent Li^+, and so its isotopic composition is not influenced by redox states. The original pioneering work in Li isotope geochemistry was carried by L.-H. Chan of Louisiana State University using thermal ionisation mass spectrometry (Chan, 1987), although this method has now been superseded by MC-ICP-MS. A fuller discussion of the application of Li isotopes is given in the recent book by Tomascak et al. (2016) and in the review article by Penniston-Dorland et al. (2017).

In low-temperature environments at the Earth's surface there are large Li isotope fractionations between minerals and an aqueous fluid phase. This means that materials from the Earth surface, such as hydrothermally altered oceanic basalts and the products of continental weathering, have distinctive isotopic compositions which have the potential to be traced through the processes of recycling back into the Earth's mantle. There appear to be no biological controls on the fractionation of Li isotopes, and so δ^7Li values in carbonate rocks offer the potential for providing a record of the Li isotopic composition of seawater. At high temperatures the differential diffusivity of the two Li isotopes is important in diffusion studies and offers the potential for studying rates of cooling in igneous rocks (Penniston-Dorland et al., 2017).

7.4.1.1 The Distribution of Lithium Isotopes in Nature

The distribution of Li isotopes in the common terrestrial and extra-terrestrial reservoirs is summarised in Figure 7.31. Chondritic δ^7Li values are between +3 and +4‰, although in situ measurements of individual chondrules show a much greater range of values, indicating significant heterogeneity both within and between samples. In other extra-terrestrial bodies Martian meteorites have δ^7Li values in the range +2.1 to +6.2‰, with an average of $+4.2 \pm 0.9$‰, thought to represent the bulk silicate composition of Mars. Lunar meteorites have δ^7Li values in the range +3.5 to +6.6‰ (Penniston-Dorland et al., 2017).

Interpreting δ^7Li values from mantle peridotites is complicated because of the effects of high-temperature diffusion in mantle minerals and later metasomatic overprinting. Bulk-rock peridotite δ^7Li values range from −9.7 to +9.6‰, but data from

Box 7.9 Lithium isotopes

Stable isotopes and abundances

$^{7}Li = 92.4‰$

$^{6}Li = 7.6‰$

Measured isotope ratios

$$\delta^{7}Li‰ = \left[\left(^{7}Li/^{6}Li_{(sample)} - {}^{7}Li/^{6}Li_{(standard)}\right)/{}^{7}Li/^{6}Li_{(standard)}\right] \times 1000 \quad (7.25)$$

Standards

Originally, L-SVEC, a Li-carbonate (NIST standard reference material 8545)
Now replaced by IRMM-016 (Penniston-Dorland et al., 2017)

Mantle value

$\delta^{7}Li = +3.5$ to $+4.0‰$

Bulk silicate Earth value

$\delta^{7}Li = +3.5$ to $+4.0‰$ (Penniston-Dorland et al., 2017)

Variations in nature
See Figure 7.31.

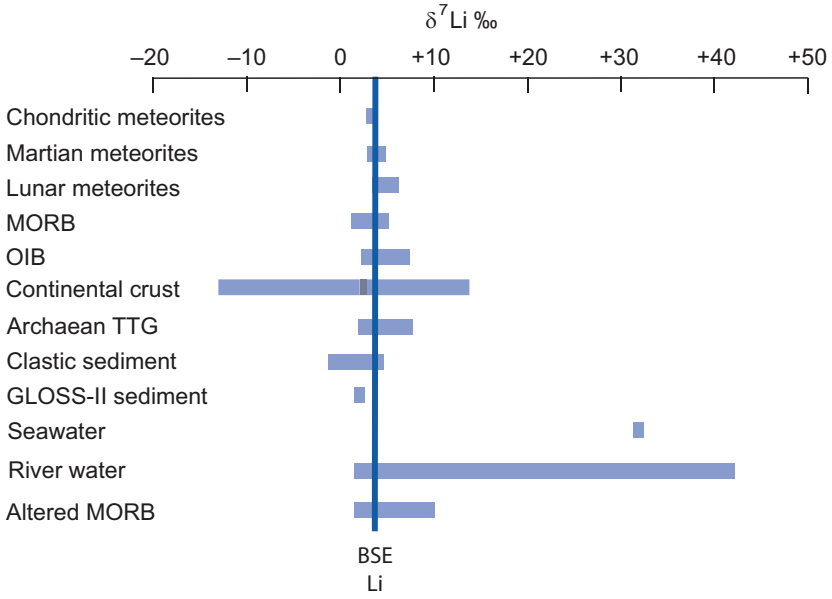

Figure 7.31 Variation in $\delta^{7}Li$ in extra-terrestrial and terrestrial reservoirs relative to the bulk silicate Earth (BSE). (After Penniston-Dorland et al., 2017). Data sources in the text

carefully selected unmetasomatised, fertile peridotites which are isotopically equilibrated show a much narrower range of $\delta^{7}Li$ values between +3.5 to +4.0‰, and this is taken to be the bulk silicate Earth value. $\delta^{7}Li$ measurements in unaltered MORB lie between +1.6 and +5.6‰ (average $\delta^{7}Li = 3.4 \pm 0.7‰$); OIB samples have a similar range $\delta^{7}Li = +2.4$ to +7.9‰ (average 3.8‰) as do arc basalts (average $\delta^{7}Li = 3.6 \pm 1.2‰$) (Penniston-Dorland et al., 2017, and references therein). The similarity in Li isotope

composition between MORB and OIB suggests that the upper and lower mantle have a similar average Li isotope composition.

The average composition of the upper continental crust, as estimated from loess, is $\delta^7Li = 0.6 \pm 0.6‰$ (Sauzeat et al., 2015). The average δ^7Li for the middle continental crust is $+4.0 \pm 1.4‰$, whereas granulites from the lower continental crust are more heterogenous; equilibrated samples are in the range $\delta^7Li = -14$ to $+14.4‰$, with an average of $\delta^7Li = 2.5‰$. Using the relative crustal proportions of Rudnick and Gao (2014) these values suggest that an average bulk crust (17 ppm Li) has a δ^7Li value of ~2.3‰. This is close to the value for average global oceanic subducted sediment (GLOSS-II), which has a value of $\delta^7Li = 2.4 \pm 0.02‰$. Archaean tonalite–trondhjemite–granodiorites (TTGs) have values in the range 2.5–7.5‰ with a mean value of 4.3‰ (Liu and Rudnick, 2011).

The Li isotopic composition of seawater is $\delta^7Li = +31 \pm 0.05‰$, isotopically much heavier than the crust and the mantle. This value is the result of inputs from the dissolve load in rivers (average $\delta^7Li = +23‰$, range $+1.0$ to $+44.0‰$), groundwater ($\delta^7Li = +15‰$) and hydrothermal vent fluids ($\delta^7Li = +7.2$ to $+8.9‰$; Foustoukos et al., 2004) and the loss of δ^7Li to clays during the hydrothermal alteration of ocean basalts. MORB altered as a result of interaction with seawater becomes isotopically heavier and has a δ^7Li value of $5.6 \pm 4.5‰$, whereas there is some evidence that mantle peridotites altered to serpentinite become isotopically lighter (Hansen et al., 2017; Penniston-Dorland et al., 2017, and references therein).

In a review of the Li isotope composition of marine sediments from a wide range of tectonic settings, Chan et al. (2006) show that the bulk δ^7Li of global sediments varies between -4.3 and $+14.5‰$ and that there are large differences between different types of sediment. For example, detrital sediments such as turbidites and clays are in the range -1.5 to $+5‰$ with clays isotopically lighter than sands because of isotopic fractionation during continental weathering. Volcanogenic marine sediments may be either heavier or lighter than the mantle value depending on the extent to which they have interacted with seawater. Biogenic sediments – carbonates and silica-rich sediments – tend to recrystallise during diagenesis, leading to isotopically heavier compositions (+6 to +14.5‰).

7.4.1.2 Controls on the Fractionation of Lithium Isotopes

In ferromagnesian minerals, lithium commonly substitutes for Fe–Mg in octahedrally coordinated sites, although in aqueous fluids it is thought to reside mostly in tetrahedrally coordinated sites. This gives rise to the preferential equilibrium partitioning of ^7Li into aqueous fluids relative to ferromagnesian minerals, so that aqueous fluids in contact with mafic rocks will be enriched in δ^7Li. Experimental studies show that at high temperatures these mineral–fluid fractionations are relatively small but at lower temperature the fractionations are large. Thus, low-temperature mineral reactions such as the formation of clays can result in large isotopic fractionations. Studies show that ^6Li is preferentially incorporated into clay, whereas the host fluid in equilibrium with the clay becomes enriched in ^7Li. In a similar way the carbonate minerals calcite and aragonite show significant isotopic fractionation relative to aqueous fluids enriching the equilibrium fluid in ^7Li. Experimentally determined mineral/rock–fluid fractionation factors for a range of geological materials are given in the review by Penniston-Dorland et al. (2017).

At high temperatures kinetic fractionations are important in the Li isotope system as a result of the more rapid diffusion of ^6Li relative to ^7Li. Large fractionations have been recorded in magmatic and metamorphic rocks (up to 20‰) and over tens of metres, although the evidence of fractionation will survive only in systems that cool rapidly (Penniston-Dorland et al., 2017, and references therein).

7.4.1.3 Using Lithium Isotopes as a Tracer in Geological Processes

Li isotopes can be used to understand igneous processes, as well as to investigate weathering processes.

(a) *Li isotopes in understanding igneous processes.* As has been noted for other stable isotope systems, the equilibrium fractionation of isotopes on the basis of their mass differences is inversely proportional to temperature, so that at high temperatures there is minimal fractionation. This principle is true for lithium isotopes and implies that for unaltered mafic rocks their isotopic composition is indicative of the composition of their mantle source. Lithium behaves as a moderately incompatible element during partial melting, and there is very little Li isotope fractionation during

this process. Further, there is no strong evidence to indicate that significant mineral–silicate melt fractionation takes place during magmatic differentiation in mafic rocks. Exceptions may be related to fluid processes such as magmatic degassing (Neukampf et al., 2019) and the exsolution of a supercritical fluid (Li et al., 2018). However, the moderately incompatible nature of Li means that it is concentrated in the crust relative to the mantle and so can be used to detect crustal contamination in mafic melts. This was demonstrated by Genske et al. (2014), who found a wide range in δ^7Li values in OIB from the Azores (+3.5 to +8.5‰) and showed using AFC modelling that their mantle source had been contaminated with hydrothermally altered oceanic crust. At high temperatures the rapid diffusivity of Li in silicate minerals coupled with significant kinetic Li isotope fractionation during diffusion means that the Li isotope system has great potential as a geo-speedometer with which rates of cooling in igneous rocks might be investigated (Richter et al., 2017; Marschall and Tang, 2020).

Given the well-established Li isotope partitioning between silicate minerals and aqueous fluids it was expected that fluids released from a subducting slab containing hydrothermally altered oceanic crust would be enriched in δ^7Li and that this signature would be imparted to the overlying mantle wedge and the resultant arc lavas. However, no obvious δ^7Li imprint on arc lavas has been found, although there is some evidence for the incorporation of subducted sediment in arc lavas. Tang et al. (2014) found that the lavas in Martinique in the Lesser Antilles are isotopically lighter than MORB with $\delta^7\text{Li values} = +1.8 \pm 1.3‰$ as are the associated sea-floor sediments ($\delta^7\text{Li} = -4.4$ to $-0.5‰$) leading them to propose that the composition of the lavas reflects a mantle source that had incorporated isotopically light subducted sediment.

In a similar way it was expected that since the Li isotope signature of hydrothermally altered crust (average $\delta^7\text{Li} = 5.6 \pm 4.5‰$) is sufficiently different from that of MORB (average $\delta^7\text{Li} = 3.4 \pm 0.7‰$), it would be possible to track subducted altered oceanic crust in the sources of MORB and OIB. In support of this view, Chan and Frey (2003) reported δ^7Li from OIB from the Hawaiian plume of between 2.5 and 5.7‰ and proposed that this variability might reflect the minor influence of recycled oceanic crust. Similarly, Elliott et al. (2006) reported δ^7Li values for fresh MORB glasses from the East Pacific Rise in the range 3.1–5.2‰, which they interpreted as coming from a mantle source which had been enriched by the incorporation of recycled mantle wedge material. However, more recently it has become clear that Li isotope data of this type must be treated with caution because of the diffusive fractionation of Li at high temperatures (Marschall and Tang, 2020).

(b) *Li isotopes in understanding the processes of continental weathering.* Empirical studies have shown that during the weathering of silicate rocks Li is soluble and that ^{6}Li partitions into the products of chemical weathering such as clays, whereas ^{7}Li partitions into the associated water. In detail, weathering is a two-step process. Initially, minerals are dissolved and then secondary phases are precipitated. Typically, Li isotopes are not fractionated during the dissolution stage but are strongly fractionated during the formation of secondary weathering products. This means that the terrestrial weathering products of the continental crust are depleted in δ^7Li but rivers are enriched in δ^7Li. This has been demonstrated in the detailed examination of weathering profiles which show that the degree of Li isotope fractionation is controlled by the type of secondary minerals formed which in turn is related to the intensity of the weathering and climatic conditions during weathering (Teng et al., 2010).

Given that Li isotopes are not fractionated by biological processes, riverine Li isotopes serve as an important record of weathering process via their dissolved and suspended loads. While rivers are complex dynamic systems and may display mixing of water from different sources (Henchiri et al., 2016), empirical studies indicate three main characteristics. First, the Li isotope signature of the dissolved load of a river reflects the degree of chemical weathering in the region. Second, the difference in δ^7Li between the dissolved and the suspended load can be related to the intensity of the weathering, with the greater δ^7Li fractionation correlated with the greater weathering intensity (Pogge von Strandmann et al., 2006). Third, a recent study of weathering in the permafrost of eastern Siberia showed that climate also exercises a weak control on river Li isotope chemistry (Murphy et al., 2019).

Using these insights, Liu and Rudnick (2011) used Li isotopes to argue that chemical weathering has played a significant role in the evolution of the composition of the continental crust over geological time

and attempted to constrain the mass of continental crust lost over time via this process. They argued that since the Li isotope composition of the continental crust is lower than that of the mantle-derived materials from which it was built, the missing δ^7Li must have been returned to the mantle as a consequence of weathering and dissolution. Using a mass balance model for the Li isotope composition of the present-day bulk continental crust, they calculated that between 15 and 70‰ (mean value 45‰) of the original juvenile crust has been lost over geological time through weathering and dissolution.

Li is well mixed in seawater and so organisms that have grown in equilibrium with seawater will preserve a record of its former composition. This has been investigated using carbonate foraminifera. Misra and Froelich (2012) show that since the Eocene–Palaeocene (60 Ma) planktonic foraminifera have increased in their δ^7Li from ~22‰ to the present-day value of 31‰. They argue this change in seawater chemistry represents a pattern of chemical weathering of continental rocks during the Eocene which is different from that in the modern, resulting in a lower riverine δ^7Li 60 Ma ago.

7.4.2 Magnesium Isotopes

Magnesium is found in silicate rocks and the oceans and is an essential element in the biosphere. It is present as a major component in ferromagnesian minerals, carbonates, sulphates and clay minerals in igneous, metamorphic and sedimentary rocks. There are three isotopes of magnesium – ^{24}Mg, ^{25}Mg and ^{26}Mg – and isotope ratios are measured as ^{26}Mg/^{24}Mg, expressed as δ^{26}Mg‰ (Eq. 7.26) relative to a synthetic standard (Box 7.10). The range of fractionation found in most terrestrial materials is between ~−6 and +2‰ (Figure 7.32); this range is small compared with other stable isotope systems (Figure 7.30).

The measurement of Mg isotopes requires very high precision and must be carried out with great care, for analytical artefacts can arise through instrumental mass fractionation during analysis and from matrix effects. A detailed discussion of Mg isotope analysis using both ion-probe and ICP-MS technologies is given by Chaussidon et al. (2017) and Fukuda et al. (2020). A comprehensive review of the geochemistry of magnesium isotopes is given by Teng (2017) and a summary of the systematics is given in Box 7.10.

7.4.2.1 The Distribution of Magnesium Isotopes in Nature

Even though there is a relatively large mass difference between the isotopes ^{24}Mg and ^{26}Mg (~8‰), the degree of magnesium isotope fractionation found in both terrestrial and extra-terrestrial reservoirs is small (Figure 7.32). Chondritic meteorites of all classes have δ^{26}Mg values in the range −0.43 to −0.15‰, with an average δ^{26}Mg = −0.27 ± 0.12‰. Lunar values, derived from lunar basalts, are similar, with an average δ^{26}Mg = −0.26 ± 0.16‰. A small difference in δ^{26}Mg between high-Ti and low-Ti lunar basalts could suggest some heterogeneity in the source, perhaps indicating some fractionation during the early differentiation of the lunar magma ocean. Bulk silicate Mars is δ^{26}Mg = −0.271 ± 0.040‰ (Magna et al., 2017). Unmodified mantle peridotite xenoliths also have a similar average value of δ^{26}Mg = −0.25 ± 0.04‰. Metasomatized samples, that is, those whose composition has been modified by the migration of mafic melts, show a wider range of values. Given the highly magnesian nature of the Earth's mantle, the mantle peridotite value is taken to be equivalent to that of the bulk silicate Earth (Figure 7.32). Taken together, the overall similarity in Mg isotope compositions of the Earth, the Moon, Mars and chondrites indicates that there was substantial Mg isotopic homogeneity in the early solar system, reflecting extensive early disc mixing (Teng, 2017).

Magnesium isotope measurements are similar in both MORB and OIB, with δ^{26}Mg between −0.31 and −0.19‰ in MORB (average = −0.25 ± 0.06‰) and δ^{26}Mg between −0.35 and −0.18‰ in OIB (average = −0.26 ± 0.07‰), indicating that the mantle is homogeneous and that there are no differences in δ^{26}Mg between upper and lower mantle sources. Altered ocean crust is isotopically much more heterogeneous, with δ^{26}Mg values between −2.76 and +0.21‰ and hydrothermally altered peridotites vary in δ^{26}Mg between −0.25 and −0.02‰. In both instances these changes are largely the result of the formation of secondary clay-rich minerals formed during the hydrothermal weathering (Teng, 2017, and references therein). Arc lavas from the Lesser Antilles have δ^{26}Mg values between −0.25 and −0.10‰, slightly heavier than in the mantle and MORB, suggesting that the sub-arc mantle source has been modified by the release of fluids enriched in δ^{26}Mg from hydrothermally altered ocean crust in the subducting slab (Teng et al., 2016).

Box 7.10 Magnesium isotopes

Stable isotopes and abundances

$^{24}Mg = 78.99‰$
$^{25}Mg = 10.00‰$
$^{26}Mg = 11.01‰$ (also used to investigate the short-lived decay of ^{26}Al in the early solar system)

Measured isotope ratios

$$\delta^{26}Mg‰ = \left[\left(^{26}Mg/^{24}Mg_{(sample)} - {}^{26}Mg/^{24}Mg_{(standard)}\right)/{}^{26}Mg/^{24}Mg_{(standard)}\right] \times 1000 \quad (7.26)$$

Standards

Dead Sea Magnesium (DSM3)
Cambridge-1 (this standard is $2.623 \pm 0.030‰$ lower than DSM3 (Teng, 2017), as solutions in nitric acid
Additional reference values for a range of silicate rocks and carbonates are given in Teng (2017).

Chondritic value

$\delta^{26}Mg = -0.27 \pm 0.12‰$ (Teng, 2017)

Mantle and bulk Earth value

$\delta^{26}Mg = -0.25 \pm 0.04‰$ (Teng, 2017)

Variations in nature

See Figure 7.32.

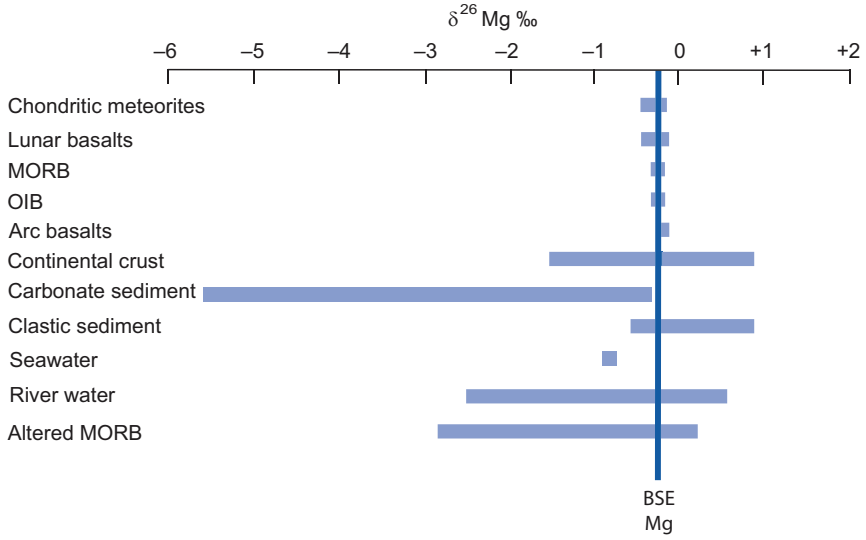

Figure 7.32 Variation in $\delta^{26}Mg$ in extra-terrestrial and terrestrial reservoirs relative to the value in the bulk silicate Earth (BSE) (after Teng, 2017). Data sources discussed in the text.

Magnesium isotope ratios in the continental crust are as follows: upper continental crust $\delta^{26}Mg = -1.64$ to $+0.92‰$, the middle crust $\delta^{26}Mg = -0.40$ to $+0.12‰$ and the lower crust $\delta^{26}Mg = 0.76$ to $-0.24‰$. The bulk continental crust average for $\delta^{26}Mg = -0.24‰$, a value that is very close to that of the mantle, reflecting the very small Mg isotope fractionations that take place during high-temperature igneous and metamorphic processes.

The magnesium isotope composition of seawater is $\delta^{26}Mg = -0.83 \pm 0.09‰$; rivers are more variable in composition, with values between $\delta^{26}Mg = -2.5$ and $+0.64‰$. Rainwater and groundwater have slightly smaller ranges than that of river water, with $\delta^{26}Mg = -1.59$ to $-0.51‰$ (average $-0.85 \pm 0.58‰$) and $\delta^{26}Mg = -1.7$ to $+0.23‰$ (average $-1.23 \pm 0.89‰$), respectively.

Carbonate-rich sediments show the largest isotopic variation in Mg isotopes of all natural materials and have $\delta^{26}Mg$ between -5.57 and $-0.38‰$. Relative to aqueous solutions abiogenic carbonates preserve fractionations of up to ~4.8‰. Dolomitic samples are at the heavy end of this range, whereas calcitic samples are lighter, indicating some mineralogical control on Mg isotope fractionation. In biogenic carbonates large fractionations of $\delta^{26}Mg > 4.5‰$ have been observed, giving rise to carbonates which are isotopically lighter than seawater. Marine sediments adjacent to subduction zones have $\delta^{26}Mg$ values in the range -3.65 to $+0.52‰$ with calcareous oozes contributing to the lighter values and clastic materials the heavier values. Clastic sediments have $\delta^{26}Mg$ between -0.57 and $+0.92‰$ (Teng 2017).

7.4.2.2 Controls on the Fractionation of Magnesium Isotopes

The data in Figure 7.32 show that the most extreme Mg isotope fractionations take place at low temperatures at the Earth's surface and that they are particularly pronounced in carbonate rocks. The similarities in $\delta^{26}Mg$ between average MORB, average OIB and average mantle peridotite suggest that there is no measurable equilibrium fractionation of magnesium isotopes during the process of the partial melting of the mantle. Further, Teng et al. (2007) showed that magnesium isotopic compositions do not change significantly during magmatic differentiation. They found that differentiated basalts and associated olivine-rich cumulates from Kīlauea Iki lava lake in Hawai'i have Mg isotope compositions similar to that of the parental magma. In metamorphic rocks Teng (2017) showed that in silicate rocks there is no measurable Mg isotopic fractionation during metamorphism. This means that even at high grades of metamorphism, silicate metamorphic rocks preserve the isotopic composition of their protolith, although this is not the case in marbles where there is evidence of Mg isotopic exchange between carbonate and silicate minerals.

Evidence of high-temperature kinetic isotopic fractionation of Mg isotopes has been observed in some olivine phenocrysts in mafic melts. Coupled Mg elemental and isotopic zoning is indicative of Mg diffusion, and fractionations of up to 0.45‰ have been reported. There is also evidence for inter-mineral Mg isotope fractionation during the sub-solidus disequilibrium exchange of Mg isotopes between olivine and chromite in disseminated mantle chromitites (Xiao et al., 2016).

At low temperatures fractionations are more pronounced, but not particularly well understood. Experimental studies on the precipitation of carbonate minerals from aqueous solutions indicate that $\Delta^{26}Mg_{aragonite-fluid}$ is between -1.1 at 25°C and -0.8 at 55°C, $\Delta^{26}Mg_{dolomite-fluid}$ between -0.93 at 130°C and -0.65 at 220°C, $\Delta^{26}Mg_{magnesite-fluid}$ between -1.2 at 150°C and -0.88 at 200°C and $\Delta^{26}Mg_{calcite-fluid}$ is ~-2.1 at 25°C. Combining theoretical with experimental studies indicates an enrichment in ^{26}Mg in carbonates in the order aragonite > dolomite > magnesite > calcite (Teng, 2017, and references therein).

The alteration of oceanic basalt in marine hydrothermal systems has been studied experimentally by Voigt et al. (2020). These authors show that isotopically heavy Mg is preferentially incorporated into basalt as the secondary clay mineral smectite, leaving a residual fluid enriched in light Mg isotopes. They calculate a smectite–liquid fractionation factor of 0.42‰ at 250°C.

7.4.2.3 Using Magnesium Isotopes as a Tracer in Geological and Biological Processes

It was shown above that there is minimal fractionation between Mg isotopes at high temperatures. This means that in igneous rocks the Mg isotope composition of basalts can be used to characterise their mantle source, and in granites Mg isotopes can be used to track the Mg isotope composition of the protolith. Similarly, the lack of fractionation in metamorphic rocks means that in silicate rocks, even at

high metamorphic grades, the Mg isotopic composition will mirror that of the protolith.

In contrast, in the low-temperature environments of the Earth's surface Mg isotopes are more extensively fractionated. A number of studies have shown that during continental weathering Mg isotopes are more variable in the dissolved and the suspended loads of the associated rivers than in the parent bedrock, indicating that isotopic fractionation takes place during the weathering process. This is evident from the study of weathering profiles. In the case of granite weathering, the fractionation is controlled principally by the formation of illite (Brewer et al., 2018), although in detail the magnitude of the Mg isotope fractionation during continental weathering depends upon the precise weathering processes involved and the clay minerals that are formed (Teng, 2017).

Magnesium is also an essential element in the biosphere, and there is evidence from laboratory experiments and in natural samples that Mg isotopes are fractionated during photosynthesis, although the extent of the fractionation depends upon both the plant species and the environmental conditions. In natural samples plants and trees prefer heavy Mg isotopes relative to their substrate, giving rise to Mg isotope fractionation during Mg transport (Teng, 2017).

The extensive isotopic fractionation of Mg isotopes in the low-temperature environments of the Earth provides an important potential tool for recognising the recycling of surficial materials into the Earth's mantle by means of subduction and provides a distinctive Mg isotope signal in the sub-arc mantle and in arc lavas. However, apart from recognising recycled carbonated oceanic crust (Chen et al., 2018), this geochemical signal is proving elusive. Hu et al. (2020) found no difference between the Mg isotope composition of xenoliths from the mantle wedge of the Kamchatka Arc and that of ambient mantle, although they did find some variability in the Mg isotope composition of the arc lavas, which might be related to the recycling of Mg isotopes from subducted oceanic crust.

7.4.3 Silicon Isotopes

Silicon is abundant in the Earth and occurs mostly in the tetravalent oxidation state bonded with oxygen in silicate minerals or silica. In solution it is found as orthosilicic acid (H_4SiO_4 or $Si(OH)_4$) and it occurs as Si^0 when alloyed with metals in planetary cores. Silicon is also an essential structural component in plants and is found in some plankton and siliceous sponges. Silicon has three naturally occurring stable isotopes: ^{28}Si, ^{29}Si and ^{30}Si. The isotope ratio measured is $^{30}Si/^{28}Si$, expressed as $\delta^{30}Si‰$ (Eq. 7.27) relative to the NBS28 standard. Mass-dependent silicon isotope fractionation on the Earth has a range of about 12‰; the isotope systematics for stable silicon isotopes are summarised in Box 7.11. Comprehensive reviews of silicon isotope geochemistry are given by Zambardi et al. (2013), Savage et al. (2014), Poitrasson (2017) and Ledevin (2019).

Silicon isotopes are analysed by high-resolution MC-ICP-MS with a long-term reproducibility of $\pm$ 0.08‰. Sample preparation includes bulk sample alkali fusion and element purification using ion-exchange chromatography. A finer spatial resolution can be obtained using the microbeam techniques SIMS and LA-MC-ICP-MS, although these methods offer slightly lower analytical precision than high-resolution MC-ICP-MS. A full discussion of analytical approaches is given in Savage et al. (2014) and Poitrasson (2017).

The largest silicon isotope fractionations are found in the Earth's surface environment (Figure 7.33), and these offer scope for deciphering past terrestrial environments and processes in the oceans. There is little silicon isotope fractionation during metamorphism, and so ancient sediments may record their primary silicon isotope compositions. In high-temperature igneous geochemistry there are important applications of silicon isotope geochemistry in the understanding of crust–mantle interactions during continent formation in the early Earth and in cosmology in the study of the processes of planetary formation.

7.4.3.1 The Distribution of Silicon Isotopes in Nature

Silicon isotope measurements in chondritic meteorites are in the range $\delta^{30}Si = -0.41$ to $-0.64‰$. $\delta^{30}Si$ values for carbonaceous chondrites (-0.41 to $-0.45‰$) and ordinary chondrites (-0.46 to $-0.49‰$) are within error of each other and together have a mean value of $-0.46 \pm 0.02‰$. Enstatite chondrites are isotopically lighter and have $\delta^{30}Si$ values between -0.59 and $-0.64‰$. In contrast to the narrow range of values within chondritic meteorites, rare pre-solar SiC grains found included in chondrites show extensive fractionation with a range of 2000‰,

Box 7.11 Silicon isotopes

Stable isotopes and abundances

$^{28}Si = 92.23‰$

$^{29}Si = 4.67‰$

$^{30}Si = 3.10‰$

Measured isotope ratios

$$\delta^{30}Si‰ = \left[\left(^{30}Si/^{28}Si_{(sample)} - {}^{30}Si/^{28}Si_{(standard)}\right)/{}^{30}Si/^{28}Si_{(standard)}\right] \times 1000 \quad (7.27)$$

Standards

RM 8546, for which $\delta^{30}Si = 0.0‰$, distributed by National Institute of Standards and Technology, NIST; also known as NBS28, sand quartz.
Formerly: Caltech Rose Quartz Standard (RQS)

Chondritic value

$\delta^{30}Si = -0.46 \pm 0.02‰$ (mean of ordinary chondrites and carbonaceous chondrites; Zambardi et al., 2013)

Bulk silicate Earth value

$\delta^{30}Si = -0.29 \pm 0.07‰$ (Savage et al., 2014; Deng et al., 2019)

Variations in nature

See Figure 7.33.

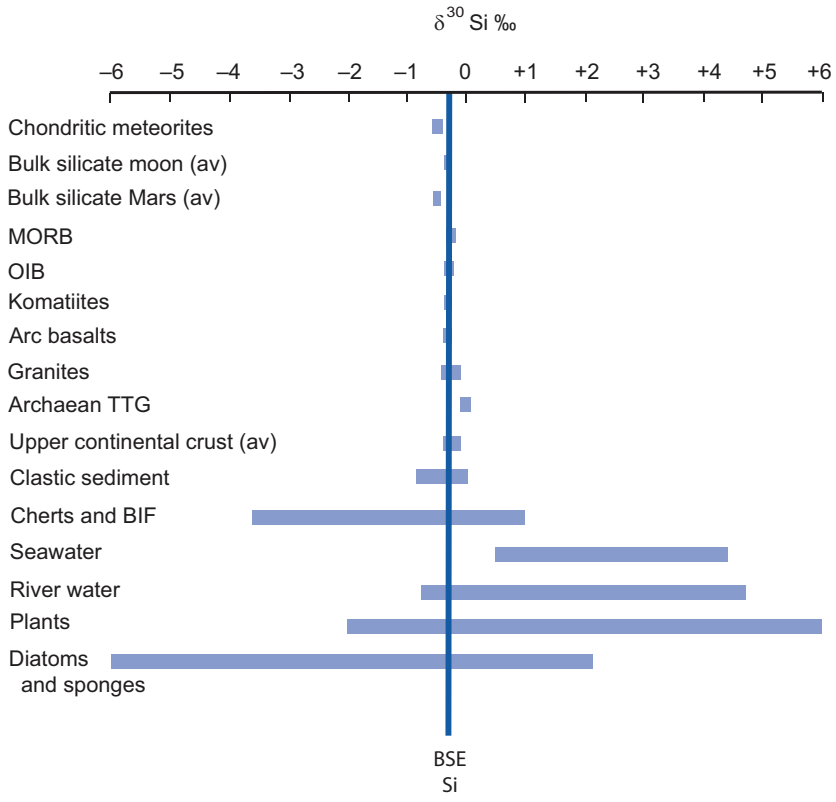

Figure 7.33 Variation in $\delta^{30}Si$ in extra-terrestrial and terrestrial reservoirs relative to the value in the bulk silicate Earth (BSE) (after Poitrasson, 2017; Ledevin, 2019). Data sources discussed in the text.

which is thought to reflect nucleosynthetic processes in the universe prior to the formation of the Sun. Basaltic samples from the Moon yield a bulk silicate moon δ^{30}Si value of -0.27 ± 0.02‰ and Martian meteorites of igneous origin have δ^{30}Si = -0.56 to -0.33‰, with a bulk silicate Mars value of -0.49 ± 0.03‰, similar to the chondritic value (Zambardi et al., 2013).

The δ^{30}Si value of the bulk silicate Earth based upon samples of mantle peridotite and basalt is -0.29 ± 0.07‰ (Savage et al., 2014; Deng et al., 2019). Averages of the samples used to calculate this value are as follows: ultramafic rocks δ^{30}Si = -0.30 ± 0.09‰, MORB δ^{30}Si = -0.27 ± 0.06‰, OIB δ^{30}Si = -0.31 ± 0.04‰, Archaean komatiite δ^{30}Si = -0.29 ± 0.02‰, and island arc basalts δ^{30}Si = -0.28 ± 0.04‰. Felsic rocks have heavier δ^{30}Si values and rhyolites from Hekla volcano in Iceland have values of ~-0.15‰. Savage et al. (2014) proposed an algorithm for igneous rocks in which δ^{30}Si is linked to the SiO_2 content of the melt, such that for mantle-derived equilibrium melts

$$\delta^{30}\text{Si‰} = 0.0056 \times \text{SiO}_2(\text{wt‰}) - 0.567\ (\pm 0.05) \tag{7.28}$$

Granites have δ^{30}Si values in the range -0.40 to -0.11‰ (average -0.23 ± 0.15‰), lighter than expected from the igneous range given above in Eq. 7.29. Deng et al. (2019) showed that the variability within the range of granite compositions may be related to the protolith composition, for there is a difference between average δ^{30}Si values for I- and A-type granites (-0.18 ± 0.02‰) and for S-type granites (-0.28 ± 0.03‰). Recent studies of Archaean granitoids of the TTG suite show average values between -0.01 ± 0.02‰ (range = -0.06 to $+0.05$‰; Deng et al., 2019) and $+0.01 \pm 0.11$‰ (range = -0.06 to $+0.15$‰; André et al., 2019). An average for the upper continental crust is -0.25 ± 0.16‰, a value which is very close to that of the BSE (Savage et al., 2014).

Sedimentary rocks show a wider range of silicon isotope values. Shales and clastic metasediments are in the range δ^{30}Si = -0.82 to $+0.01$‰, reflecting both the presence of clays formed during rock weathering and interaction with dissolved silicon in seawater. Bulk soils have δ^{30}Si = -2.7 to $+0.1$‰ and chemical sediments – cherts and banded iron formations – have δ^{30}Si = -3.7 to $+1$‰. Silicon isotope compositions in the oceans vary from $+0.5$ to $+4.4$‰. This range reflects the variable riverine input (-0.70 to $+4.66$‰), hydrothermal fluxes from and the weathering of the ocean floor, and biological activity in the shallow ocean. A global ocean average of δ^{30}Si is estimated to be ~$+1.1 \pm 0.3$‰. There is significant silicon isotope fractionation in plants through the formation of phytoliths with a compositional range of δ^{30}Si from -2.3 to $+6.1$‰ and also in the formation of diatoms and sponge spicules (Poitrasson, 2017).

7.4.3.2 Controls on the Fractionation of Silicon Isotopes

At high temperatures the equilibrium fractionation of silicon isotopes is small. The close similarity between δ^{30}Si values in the upper mantle and those of MORB and OIB show that there is minimal isotopic fractionation during partial melting. Similarly, only a very small amount of silicon isotope fractionation has been detected during magmatic differentiation and has been quantified for silicic melts by Savage et al. (2014); see Eq. 7.28. With increased differentiation towards more felsic melt compositions δ^{30}Si values become isotopically heavier. Measured fractionation factors for a number of silicate phases in mafic and felsic melts are given in Savage et al. (2014). Computed fractionation factors between silicate minerals and granites are given in Qin et al. (2016) and are understood to be a function of the mean volume of the SiO_4 tetrahedron (or average Si–O bond length) in the relevant crystalline structures. There is no evidence for high-temperature kinetic, diffusion-related fractionation of silicon isotopes in terrestrial systems.

At low temperatures calculated silicon isotope equilibrium fractionation factors between dissolved silicon as H_4SiO_4 and the phases quartz and kaolinite between 0 and 50°C are up to ~4‰. However, these calculated fractionations are in the opposite sense to those observed in nature, indicating that the reactions in natural systems are not in equilibrium but are kinetic in nature. Kinetic processes also dominate silicon isotope fractionation during weathering in which isotopically light clay minerals are produced and heavy silicon is partitioned into surface waters. This process does not appear to be strongly affected by the composition of the parent rock or by climate and weathering style, although it does reflect weathering intensity. As weathering intensity increases, as measured by the chemical index of alteration (CIA), soil δ^{30}Si becomes isotopically lighter (see review by Poitrasson, 2017).

The mechanisms of silicon isotope fractionation in biology are not well understood, although it is known that diatoms have a preference for light silicon isotopes. This fractionation is species-dependent, with fractionation factors ranging from ~−0.5 to − 2‰. Similarly, plants take up light silicon to produce opal during growth. Marine siliceous sponges also strongly fractionate silicon isotopes relative to seawater, concentrating the lighter isotope, with fractionation factors of up to −6‰ (Poitrasson, 2017, and references therein).

7.4.3.3 Using Silicon Isotopes as a Tracer in Geological and Biological Processes

The range of silicon isotope values in terrestrial reservoirs shown in Figure 7.33 demonstrates that the most extreme fractionations take place in aqueous environments at the Earth's surface and as a result of biological processes. Nevertheless, high-resolution measurements on planetary and terrestrial materials also provide an important window into high-temperature geochemical processes (Figure 7.34).

The silicon isotopic compositions of the bulk silicate Earth ($\delta^{30}Si = -0.29 \pm 0.07‰$) and the Moon ($\delta^{30}Si = -0.27 \pm 0.02‰$) are heavier than those of chondritic meteorites ($\delta^{30}Si = -0.46 \pm 0.02‰$). This difference is thought to be due to the sequestration of isotopically light silicon into the Earth's core during planetary differentiation (Savage et al., 2014). However, calculations by Zambardi et al. (2013) suggest that this mechanism may not fully explain the observed fractionation and that additional silicon isotope fractionation took place during the Moon-forming giant impact.

As already noted, the similarity between $\delta^{30}Si$ values in the upper mantle and those of MORB, OIB and Archaean komatiites indicates that the mantle is isotopically homogeneous with respect to silicon isotopes, that it has not changed in composition with time and that there is minimal isotopic fractionation during partial melting. This means that basaltic rocks may be used to trace the chemistry of their source regions. In the same way the lack of isotopic fractionation in metamorphic rocks means that they too can be used to determine the silicon isotope composition of their protolith.

During the Archaean and early Proterozoic, before biological processes regulated the silica content of the oceans, silica concentrations in the oceans were controlled by two major processes: the precipitation of siliceous sediments (cherts and banded iron formations) and by the silicic alteration of the

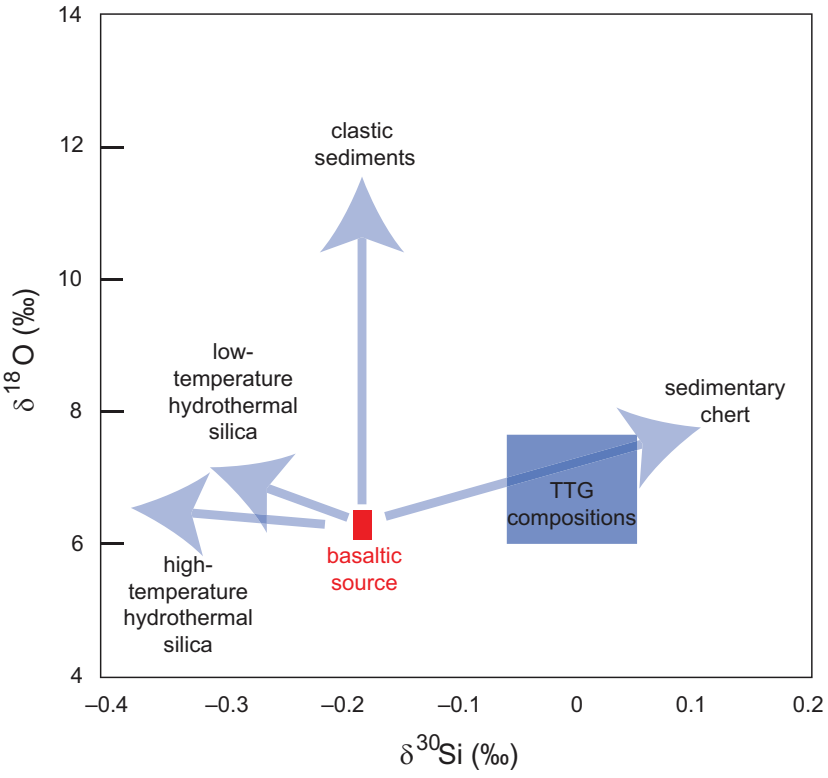

Figure 7.34 High-resolution silicon versus oxygen isotope diagram showing the likely origin of heavy $\delta^{30}Si$ enrichment in Archaean tonalite–trondhemite–granodiorite (TTG) magmas. The diagram shows the influence of different contaminants on the silicon and oxygen isotope composition of a partial melt of a basaltic source (red box) relative to the measured composition of Archaean TTGs. (Data from Deng et al., 2019)

ocean floor. Ocean crust silicification was a complex process involving first seawater percolation into a warm recharge zone in which silicon isotopes equilibrated with those of the basaltic host, followed by the diffusive ascent of warm seawater and silica precipitation during conductive cooling. During this latter stage, silicon isotopes were extensively fractionated to both heavier and lighter isotopic values (see review by Ledevin, 2019).

A number of studies have proposed that silica in ancient cherts may provide clues to the nature of the early hydrosphere (see Robert and Chaussidon, 2006). However, the fractionations that take place during seawater–chert precipitation are complex, for the fractionation factors change according to the properties of the precipitating fluid: its saturation, temperature and particulate content. Further, later isotopic changes take place during diagenesis which can lead to a shift of up to 3‰ from the initial precipitate (Ledevin, 2019). For this reason great caution must be used in seeking to interpret siliceous sediments as a monitor of the silica content and temperature of ancient oceans.

The recent recognition that Archaean TTGs are isotopically heavy ($\delta^{30}Si = -0.01$ to $+0.01$‰) relative to younger granitoids ($\delta^{30}Si = -0.23 \pm 0.15$‰) and the BSE ($\delta^{30}Si = -0.29 \pm 0.07$‰) has stimulated a revised model for the origin of Archaean felsic crust. Deng et al. (2019) and André et al. (2019) proposed that the isotopically heavy character of Archaean TTGs is inherited from their source and that they are the partial melts of a basaltic source which has incorporated sedimentary chert enriched in isotopically heavy silicon and derived from a silica-saturated Archaean ocean. The results of this model are illustrated on an oxygen–silicon isotope diagram in Figure 7.34 (after Deng et al., 2019) to show that the basaltic source was contaminated with sedimentary chert rather than other forms of sedimentary or hydrothermal silica.

7.4.4 Chromium Isotopes

Chromium is an important trace element in many igneous rocks. It is most abundant in mafic and ultramafic igneous rocks where it is compatible in ferromagnesian minerals. Cr is also present in the oxide phase chromite $(MgFe)Cr_2O_4$, an important accessory phase in mafic and ultramafic rocks and the dominant phase in cumulate chromitite rocks. Chromium is a redox-sensitive element. In most minerals it occurs in the Cr^{3+} state, although during weathering it may be oxidised to Cr^{6+}. Cr^{3+} forms oxides or hydroxides which are insoluble; in contrast, Cr^{6+} is bound with oxygen to form CrO_4^{2-} chromate, $HCrO_4^-$ bichromate or $Cr_2O_7^{2-}$ dichromate ions, all of which are water-soluble. Cr^{6+} is carcinogenic, and because of its soluble nature the anthropogenic Cr contamination of groundwater through industrial activity has led to some serious environmental problems.

There are four stable isotopes of chromium: ^{50}Cr, ^{52}Cr, ^{53}Cr and ^{54}Cr. ^{53}Cr is the daughter product of the now-extinct radionuclide ^{53}Mn. Chromium isotope ratios are measured as $^{53}Cr/^{52}Cr$, expressed as $\delta^{53}Cr$‰ (Eq. 7.29) relative to the standard SRM979. In natural systems Cr isotopes have a range of about 7‰ (Figure 7.35); the stable isotope systematics of Cr are summarised in Box 7.12. A recent review of the stable isotope geochemistry of chromium is given by Qin and Wang (2017).

High-precision chromium isotope measurements can be made using thermal ionisation mass spectrometry (TIMS) with a reported precision of up to 0.026‰ and by MC-ICP-MS techniques with a precision of between ±0.26 and 0.011‰. After acid dissolution, samples are purified using ion-exchange techniques. In situ analyses are performed by LA-ICP-MS. A full discussion of analytical approaches is given in Qin and Wang (2017).

Chromium isotopes have been used to study processes in the early solar system, in the redox evolution of the Earth's early atmosphere and oceans and in environmental geochemistry to investigate contaminated groundwater.

7.4.4.1 The Distribution of Chromium Isotopes in Nature

The average chromium isotope composition of carbonaceous chondrites is $\delta^{53}Cr = -0.128 \pm 0.043$‰ and of ordinary chondrites $\delta^{53}Cr = -0.113 \pm 0.044$‰. Measurements on two Martian meteorites give values between $\delta^{53}Cr = -0.218$ and -0.142‰ (Schoenberg et al., 2016) and the least differentiated lunar basalt of Bonnand et al. (2016) has a Cr isotopic composition of -0.222 ± 0.025‰.

The chromium isotope composition of mantle-derived rocks is in the range $\delta^{53}Cr = -0.009$ to 0.211‰. For mantle xenoliths $\delta^{53}Cr$ values $= -0.017$ to -0.167‰, for ultramafic rocks and cumulates $\delta^{53}Cr = -0.009$ to -0.211‰ and for oceanic and continental basalts $\delta^{53}Cr = -0.126$ to -0.178‰

Box 7.12 Chromium isotopes

Stable isotopes and abundances

$^{50}Cr = 4.35‰$
$^{52}Cr = 83.79‰$
$^{53}Cr = 9.50‰$ radiogenic product of extinct nuclide ^{53}Mn
$^{54}Cr = 2.36‰$

Measured isotope ratios

$$\delta^{53}Cr‰ = \left[\left(^{53}Cr/^{52}Cr_{(sample)} - {}^{53}Cr/^{52}Cr_{(standard)}\right)/{}^{53}Cr/^{52}Cr_{(standard)}\right] \times 1000 \quad (7.29)$$

Standards

SRM979, from the National Institute of Standards and Technology, often denoted as NIST 979; also SRM3112a. Both supplied in Cr^{3+} form in nitric acid.
NIST610 and NIST612 for LA-ICP-MS (Bai et al., 2019)

Chondritic value

$\delta^{53}Cr = -0.128 \pm 0.043‰$: carbonaceous chondrites
$\delta^{53}Cr = -0.113 \pm 0.044‰$: ordinary chondrites; (Schoenberg et al., 2016)

Silicate Earth

$\delta^{53}Cr = -0.124 \pm 0.101‰$ (Schoenberg et al., 2008)

Variations in nature

See Figure 7.35.

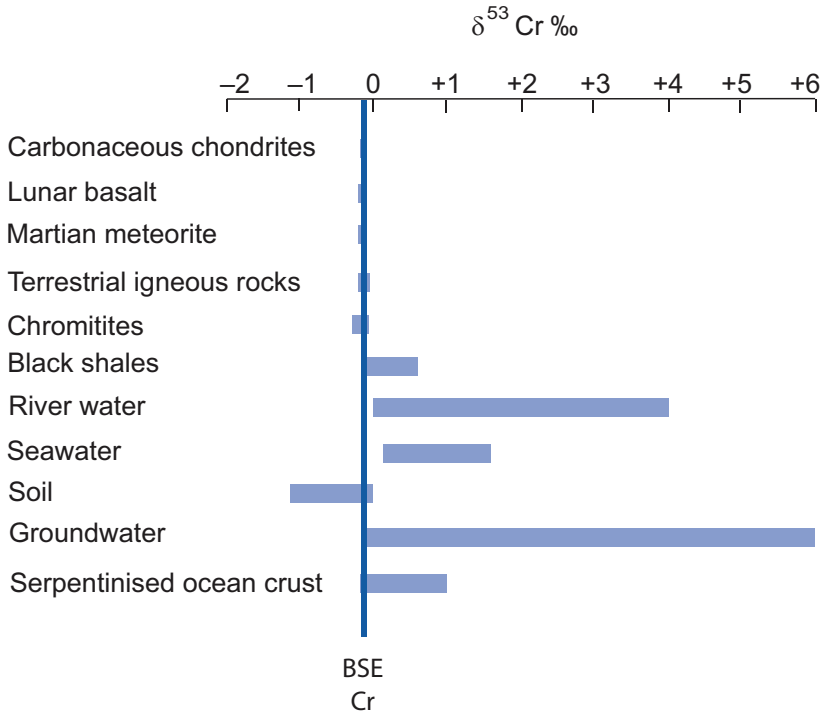

Figure 7.35 Variation in $\delta^{53}Cr$ in extra-terrestrial and terrestrial reservoirs relative to the value of the silicate Earth. Data sources discussed in the text

(average $\delta^{53}Cr = -0.151 \pm 0.050‰$). From these measurements it is possible to estimate an average value for the igneous silicate Earth of $\delta^{53}Cr = -0.124 \pm 0.101‰$ (Schoenberg et al., 2008). A single measurement on a USGS granite reference sample gives $\delta^{53}Cr = -0.177‰$, within the range of the mafic igneous rocks measured (Schoenberg et al., 2016), suggesting that an average value for the continental crust is similar to that of the silicate Earth. The similarity between the $\delta^{53}Cr$ values for the silicate Earth, Mars and chondritic meteorites suggests that contrary to earlier proposals there was no fractionation of chromium isotopes during core formation in the silicate Earth and Mars.

Farkas et al. (2013) calculated the global average Cr isotope composition for chromites as $-0.079 \pm 0.169‰$. Chromitites in layered intrusions (the Bushveld complex, the Great Dyke, the Stillwater complex) have Cr isotope compositions in the range $\delta^{53}Cr = -0.23$ to $-0.026‰$ (Schoenberg et al., 2008; Bai et al., 2019). In the Kizildag ophiolite in Turkey, Chen et al. (2019) show that podiform chromitites have slightly heavier $\delta^{53}Cr$ values (-0.22 to $-0.04‰$) than those in ophiolitic stratiform-like chromitites (-0.29 to $-0.06‰$) indicating that the range of chromium isotope compositions in ophiolitic chromitites is greater than that found in layered intrusions. Currently, all measured chromite Cr isotope compositions lie within the range of values for the silicate Earth.

Marine sediments have $\delta^{53}Cr$ values between -0.007 to $+0.009$ (mean 0.032 ± 0.065). Black shales analysed by Frank et al. (2020) have bulk $\delta^{53}Cr$ values of between $+0.02 \pm 0.15‰$ and $+0.56 \pm 0.10‰$ and a chert sample has a bulk $\delta^{53}Cr$ value of $+0.98 \pm 0.13‰$.

Chromium in modern river water is predominantly as Cr^{6+} and is derived from the weathering of the continental crust. River water has chromium isotope compositions ranging from $\delta^{53}Cr = -0.17$ to $+1.33‰$, although in source regions containing serpentinised ultramafic rocks values may be as high as $+4‰$ (Farkas et al., 2013). Seawater is not well mixed with respect to Cr isotopes and there is an inverse correlation between the Cr isotope composition and Cr concentrations in seawater (Paulukat et al., 2016). $\delta^{53}Cr$ values are between $+0.13$ and $+1.6‰$, although in surface waters the range is $+0.13$ to $+1.24‰$ (Paulukat et al., 2016; Qin and Wang, 2017).

7.4.4.2 Controls on the Fractionation of Chromium Isotopes

The reduction of Cr^{6+} to Cr^{3+} involves the breaking of Cr–O bonds because Cr^{6+} usually exists as an oxyanion. The bonds between the light Cr isotopes and oxygen are easier to break than for the heavy isotopes, and so during reducing reactions the Cr^{3+} product will be enriched in the light Cr isotopes. At low temperatures this kinetic fractionation may take place by both abiotic and biological processes. The abiotic reduction of Cr^{6+} to Cr^{3+} in laboratory experiments using a range of mineral substrates results in isotopic fractionations of the order of 2.5–3.5‰. In Fe^{2+}-rich sediments this can lead to an increase in $\delta^{53}Cr$ in the overlying water of up to 2.0‰ (Qin and Wang, 2017; Bauer et al., 2018).

Biological Cr^{6+} reduction by microbial activity is an important process in natural systems, and in the laboratory fractionations from 2.0 to 7.0‰ have been measured. In each case the reduced reaction product is isotopically lighter than the reactant. However, the transfer of three electrons from Cr^{6+} to Cr^{3+} is likely to occur in stages and so in natural systems the precise amount of fractionation will depend upon the reduction pathway and may not be as high as that predicted from laboratory experiments. The detail of metabolic pathways in thermophilic bacteria has been documented recently by Chen et al. (2019). In contrast to Cr^{6+} reduction, the processes whereby Cr^{3+} is oxidised to Cr^{6+} are less well understood, but experimental studies indicate Cr isotope fractionations of between -2.5 and $+1.0‰$ (Qin and Wang, 2017).

The very small (<0.2‰) variations in silicate rocks indicate that Cr isotopes are not extensively fractionated in high-temperature igneous systems. However, Schoenberg et al. (2016) have suggested that within this variability there are some small fractionations which reflect both partial melting and fractional crystallisation processes. This has been confirmed in a recent study by Chen et al. (2019), who demonstrated Cr isotope equilibrium fractionation during partial melting of mantle harzburgite of the Kizildag ophiolite and in the fractional crystallisation of the associated dunites and chromitites. Bai et al. (2019) have shown that during fractional crystallisation, heavy Cr isotopes are preferentially partitioned into chromite and the light isotopes into the residual melt such that equilibrium processes lead to Cr isotopic fractionation between minerals in the order $\delta^{53}Cr_{spinel} > \delta^{53}Cr_{orthopyroxene} > \delta^{53}Cr_{olivine}$.

In addition to equilibrium fractionation processes, there is also evidence of kinetic fractionation in high-temperature igneous systems. This can be seen in the Stillwater complex in the United States where the Cr isotope composition of olivines shows inter-mineral fractionations which do not follow the sequence identified above, and $\delta^{53}Cr$ diffusion profiles in these olivines indicate that kinetic factors play a role in Cr isotope fractionation (Bai et al., 2019).

7.4.4.3 Using Chromium Isotopes as a Tracer in Cosmological and Geological Processes

The isotope ^{53}Cr is produced from the decay of the short-lived isotope ^{53}Mn, which has a half-life of 3.7 Ma. Mass-independent anomalies of ^{53}Cr in meteorites have been used to provide clues about early processes in the solar nebula and the differentiation of early planetesimals. In addition, anomalies of the isotope ^{54}Cr in meteorites can be used to trace the sources and distribution of nucleosynthetic products in the early solar system (see review by Qin and Wang, 2017).

On the Earth the spread of Cr isotope values illustrated in Figure 7.35 shows that the most significant fractionations take place during low-temperature geochemical processes. One such process is the oxidative continental weathering of Cr^{3+} to Cr^{6+}, although this requires MnO_2 as a catalyst and in detail is complex. Where Cr is lost from the system during weathering, the resulting palaeosols show negative $\delta^{53}Cr$ values; currently, this weathering process is the only natural mechanism known to produce large negative Cr isotope fractionations (Frei and Polat, 2013). Other soil profiles record Cr enrichment; these have positive $\delta^{53}Cr$ values and where the weathering leads to the serpentinization of ultramafic rocks, Cr isotope compositions can be shifted to $\delta^{53}Cr$ values as high as 1.2‰ (Farkas et al., 2013).

Cr isotope fractionation in the oceans is driven by two key processes: the reduction of Cr^{6+} in surface waters and the scavenging of isotopically light Cr^{3+} to deeper water and sediment. A recent model for the mass balance of Cr isotopes in the modern oceans suggests that the principal Cr input is from rivers with an estimated $\delta^{53}Cr = +0.3$ to $+1.0$‰. Outputs include relatively minor fluxes of Cr to oxic and anoxic sediments, both with zero $\delta^{53}Cr$ fractionation and a major flux to reducing sediments with an estimated $\delta^{53}Cr$ fractionation of -0.2. This model is consistent with a Cr isotope composition for the oceans of $\delta^{53}Cr = +0.44$ to $+1.53$‰ (Qin and Wang, 2017).

In groundwater chromium isotopes can be used to understand the transport of the carcinogenic contaminant Cr^{6+}. In particular, the anaerobic reduction of Cr^{6+} can immobilise carcinogenic Cr and convert it into insoluble Cr^{3+}. The Cr isotope fractionation associated with this process can lead to elevated $\delta^{53}Cr$ values (0.7–5.2‰) and in this way the efficiency of the remediation can be monitored. In detail, the measured Cr isotope values will be very variable for they depend on the initial $\delta^{53}Cr$ value of the source and whether it is natural or anthropogenic.

A relatively recent application of Cr isotopes has been to use $\delta^{53}Cr$ values in sediments as a palaeo-redox proxy and to determine the onset of oxygenic photosynthesis. This approach has been applied to the study of banded iron formations, organic-rich shales and carbonate rocks. The logic is that in an oxygenated atmosphere Cr can be oxidised to Cr^{6+}, mobilised and isotopically fractionated. In an oxygen-free atmosphere Cr is transported as Cr-bearing minerals or as dissolved Cr^{3+} but is not fractionated. However, despite this simple theoretical framework, care must be taken to ensure that the sediments analysed faithfully record the ambient $\delta^{53}Cr$ for seawater. Consequently, corrections may need to be made for the presence of detrital material in the sediment (Frank et al., 2020) and for any biological Cr isotope fractionations. Further, geochemical controls on the oxidation of Cr require both the presence of Mn oxides, which in itself requires free oxygen, and a surface environment free of Fe^{2+}.

A compilation of $\delta^{53}Cr_{sediment}$ over geological time for selected samples shows that there is minimal $\delta^{53}Cr$ fractionation (-0.5 to $+0.5$‰) relative to the silicate Earth from the Hadean to the mid-Proterozoic. Only in the Neoproterozoic at ~1.1 Ga is there a record of extensive $\delta^{53}Cr$ fractionation (up to $+5.0$‰ in Fe-rich shales), long after the GOE at 2.34 Ga. This event at 1.1 Ga is thought to record the onset of oxidised surface environments and the deep oxygenation of ocean waters (Qin and Wang, 2017).

7.4.5 Iron Isotopes

The element iron is abundant throughout the Earth. It occurs in three oxidation states – metallic iron (Fe^0), ferrous iron (Fe^{2+}) and ferric iron (Fe^{3+}) – and these oxidation states govern its distribution. Metallic iron

is the primary constituent of the Earth's core; ferrous iron is the dominant iron species in the Earth's mantle and its derivative melts, and ferric iron is common in the oxygenated environments of the Earth's surface.

There are four stable isotopes of iron: ^{54}Fe, ^{56}Fe, ^{57}Fe and ^{58}Fe. The isotope ratio measured is ^{56}Fe/^{54}Fe, expressed as δ^{56}Fe‰ (Eq. 7.30) relative to a synthetic iron standard. The range of isotopic fractionations in natural samples is about 6.0‰, from ~ −3.5 to +2.7‰. The systematics of iron isotopes are summarised in Box 7.13, and recent reviews of the geochemistry of the stable isotopes of iron are given by Dauphas et al. (2017) and in the text by Johnson et al. (2020). Bulk samples are prepared for analysis using acid digestions followed by element purification using ion-exchange methods. The analytical method of choice is MC-ICP-MS for its precision and speed of analysis, although where high spatial resolution is required, then the in situ methods of SIMS and LA-ICP-MS can be applied. A full discussion of analytical approaches is given in Dauphas et al. (2017) and Johnson et al. (2020).

In igneous rocks only very small shifts in δ^{56}Fe are recorded, but these can be used to interpret melting and crystal fractionation processes. In contrast, in the aqueous environments of the Earth surface, the composition of some sediments and surface waters shows large iron isotope fractionations (Figure 7.36). Iron is also an essential element in living organisms; large isotopic fractionations are recorded in plants, animals and humans; and there are applications of Fe isotope chemistry in biomedical research (Albarede et al., 2017; Dauphas et al., 2017).

7.4.5.1 The Distribution of Iron Isotopes in Nature

Chondritic meteorites have a mean iron isotope value of δ^{56}Fe = −0.005 ± 0.006‰, a value which is constant throughout all chondrite types, and is coincidentally indistinguishable from that of the iron isotope standard IRMM-014, which is by definition δ^{56}Fe = 0.0. The estimated composition of the Martian mantle is δ^{57}Fe = −0.12 ± 0.04 and the primitive lunar mantle is δ^{56}Fe = −0.10 ± 0.05‰; both are slightly lighter than the chondritic value (Dauphas et al., 2017; Elardo et al., 2019).

Current estimates for the composition of the terrestrial mantle include the average for mantle peridotites of δ^{56}Fe = −0.027 ± 0.026‰ with δ^{56}Fe values ranging from −0.1 to +0.16‰ (Dauphas et al., 2017), and the estimated composition of the Earth's primitive mantle is δ^{56}Fe = +0.033 ± 0.027‰ (Sossi et al., 2016). Baffin Island picrites are in the range δ^{56}Fe = −0.025 to + 0.125‰, with a parental melt composition of 0.076 ± 0.04‰ (McCoy-West et al., 2018). MORBs have a compositional range of δ^{56}Fe = +0.06 to +0.18‰ with a mean value of +0.105 ± 0.006‰, and a calculated MORB source of +0.025 ± 0.025‰. Estimates of the iron isotope composition of the mantle source for komatiite lavas is between +0.054 to −0.093‰ (summarised in McCoy-West et al., 2018). Arc lavas from the Banda Arc are thought to be derived from a mantle source which has a lower δ^{56}Fe than that of MORB. Taken together, these variations in terrestrial mafic and ultramafic rocks lead to an emerging consensus that the Fe isotope composition of the bulk silicate Earth is chondritic (see review by Dauphas et al., 2017).

δ^{56}Fe values in silicic rocks increase with the increasing silica content of the melt. Below 70 wt.‰ SiO_2, δ^{56}Fe values are between +0.08 and +0.14‰, but above 70 wt.‰ SiO_2, values increase rapidly to +0.4‰. Poitrasson (2006) computed a mean value for the continental crust of δ^{56}Fe = +0.07 ± 0.03‰ (given as δ^{57}Fe = +0.10 ± 0.03‰).

Values for dissolved δ^{56}Fe in the world's oceans are variable but show the greatest range in the North Atlantic where they vary between −1.35 ± 0.03‰ and +0.80 ± 0.06‰ (Abadie et al., 2017). The combined dissolved and particulate δ^{56}Fe in river water varies between −1.7 and +2.7‰ (Escoube et al., 2015). High-temperature hydrothermal vent fluids have δ^{56}Fe values in the range −0.3 to −0.5‰, shifted towards lighter values relative to the composition of igneous rocks.

Modern deep-sea clays and terrigenous sediments have δ^{56}Fe values which cluster around the value for average continental crust (δ^{56}Fe = +0.07 ± 0.03‰), indicating that there is only minor iron isotope fractionation during continental weathering and transport. However, sediments formed in organic-rich reducing environments such as black shales show a much wider range with δ^{56}Fe = +1.0 to −3.5‰. Modern marine chemical sediments such as Fe–Mn crusts and nodules are enriched in the light isotopes and have δ^{56}Fe values between −0.05 and −1.13‰ (mean = −0.41 ± 0.49‰). Banded iron formations formed in the Proterozoic and Archaean preserve a wide range of compositions with δ^{56}Fe values between −2.5 and +2.0‰ (Dauphas et al., 2017).

Box 7.13 Iron isotopes

Stable isotopes and abundances

$^{54}Fe = 5.845‰$

$^{56}Fe = 91.754‰$

$^{57}Fe = 2.1191‰$

$^{58}Fe = 0.2919‰$

Measured isotope ratios

$$\delta^{56}Fe‰ = \left[\left(^{56}Fe/^{54}Fe_{(sample)} - ^{56}Fe/^{54}Fe_{(standard)}\right)/^{56}Fe/^{54}Fe_{(standard)}\right] \times 1000 \quad (7.30)$$

Standards

IRMM-014 (a synthetic metallic iron from the Institute for Reference Materials and Methods)
In practice the standard IRMM-524a is currently used; this has the same Fe isotopic value as IRMM-014

Chondritic value

$\delta^{56}Fe = -0.005 \pm 0.006‰$

Bulk silicate Earth value

$\delta^{56}Fe \sim$ chondritic (Dauphas et al., 2017)

Variations in nature

See Figure 7.36.

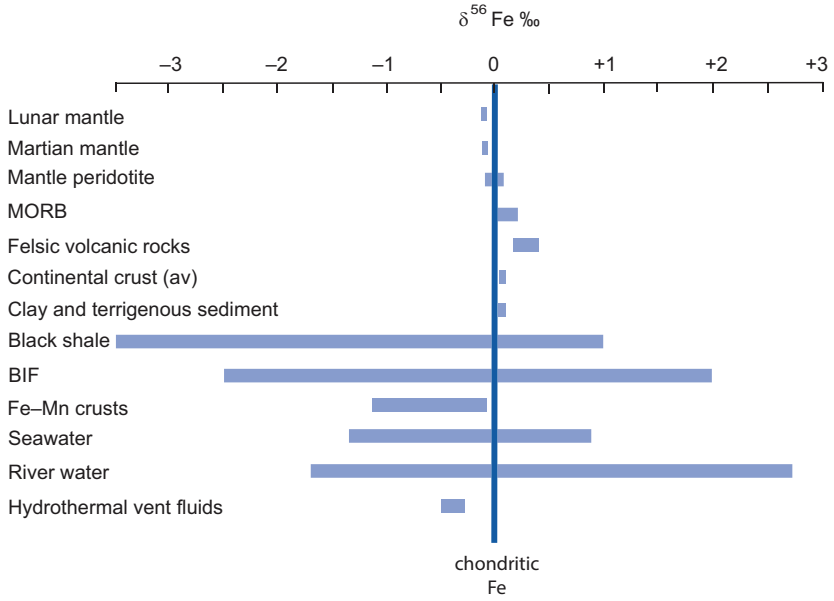

Figure 7.36 Variation in $\delta^{56}Fe$ in extra-terrestrial and terrestrial reservoirs relative to the value in chondritic meteorites, which is identical to the BSE value. Data sources discussed in the text

7.4.5.2 Controls on the Fractionation of Iron Isotopes

Evidence for kinetically controlled iron isotope fractionation at high temperatures comes from the study of diffusion in zoned minerals. Teng et al. (2011) measured δ^{56}Fe in a strongly zoned olivine from Kīlauea Iki lava lake and showed that the low-Fe core was isotopically light with δ^{56}Fe ~ −1.0‰, whereas the Fe-enriched rim was isotopically heavier with δ^{56}Fe ~ 0.0‰. Their data suggest that as the melt became more Fe-rich, Fe diffused into the olivine with the light Fe isotopes diffusing into the phenocryst more rapidly than the heavy ones, giving rise to the isotopically light mineral core. At low temperatures, examples of kinetically controlled isotope fractionations have been seen both in experimental studies and in natural systems. Examples include the biological oxidation of Fe, biological and abiotic mineral dissolution, the precipitation of Fe from seawater and the biological uptake of Fe from seawater.

Equilibrium Fe isotope fractionations are quantified using the fractionation factor β, a measure of the fractionation of a given phase relative to monatomic Fe vapour. The use of a reference material in this way allows fractionation factors to be calculated between any two coexisting phases (Dauphas et al., 2017). Experimental studies of Fe isotope fractionation between silicate and metal at high temperatures indicate that the degree of fractionation is very small, confirming the view that the composition of the BSE was little modified during core formation (Elardo et al., 2019). Other high-temperature fractionations include the mineral–melt partitioning (Δ^{56}Fe) between spinel and melt = 0.15–0.22‰ and between olivine and melt = 0.048‰ (McCoy-West et al., 2018). Mineral–mineral fractionation factors for the phases almandine, ilmenite, fayalite, chromite, hercynite and magnetite were determined by Sossi and O'Neill (2017), who showed that both the coordination environment and the oxidation state of the Fe exert important controls on Fe isotope fractionation.

In aqueous solutions the fractionation factor for Fe isotopes between Fe^{2+} and Fe^{3+} was determined experimentally by Welch et al. (2003), who showed that the ferrous component is always isotopically light relative to the ferric component. The average measured ΔFe^{3+}–Fe^{2+} fractionation was +3.57 ± 0.38‰ at 0°C, +3.00 ± 0.23‰ at 22°C and estimated to be +1.5 ± 0.6‰ at 100°C. Measured fractionations between aqueous Fe species and minerals include Fe^{3+}–haematite = −0.1 ± 0.2‰, Fe^{2+}–magnetite = −1.56 ± 0.20‰ at 22°C, Fe^{2+}–siderite = +0.48 ± 0.22‰ at 20°C and Fe^{2+}–mackinawite (FeS) = −0.33 ± 0.12‰ at 25°C (Dauphas et al., 2017, and references therein).

Leaching of Fe from basaltic rocks during hydrothermal alteration results in the release of the lighter isotope such that high-temperature vent fluids are isotopically light and the altered basalt isotopically heavy relative to fresh values by up to 1.3‰. This is due to the formation of isotopically heavy secondary minerals and the precipitation of isotopically heavy pyrite in the basalt. During continental weathering Fe isotope fractionation in soil is small, often less than ~0.5‰, indicating that weathering does not significantly fractionate iron isotopes.

In biogeochemical processes the principal controls on iron isotope fractionation include bacterial dissimilatory iron reduction (DIR) and iron oxidation. During DIR, bacteria use Fe^{3+} as an electron acceptor in anaerobic respiration – an important process in the formation of sulphide minerals. Experimental studies show that iron isotope fractionation between Fe^{2+} in solution and a ferric substrate during DIR can lead to δ^{56}Fe values that are up to 2.95‰ lower than that of the substrate, very similar to the values determined by Welch et al. (2003) for the abiotic fractionation of aqueous Fe^{2+}–Fe^{3+}. In contrast, photosynthetic Fe^{2+}-oxidising bacteria, operating under anaerobic conditions and using Fe^{2+}_{aq} as an electron donor, crystallize hydrous ferric oxide enriched in δ^{56}Fe by about 1.5‰. Plants also fractionate iron isotopes relative to soil, with an overall range in fractionation of up to 4.5‰ (see review by Dauphas et al., 2017).

7.4.5.3 Using Iron Isotopes as a Tracer in Geological and Biological Processes

The largest fractionations between the isotopes of iron are to be found in aqueous environments and as a result of biogeochemical processes (Figure 7.36). The balance of iron isotopes in the oceans is controlled by the input of isotopically heavy Fe in aerosol dust and river water, the input of isotopically light hydrothermal vent fluids and pore waters and the biological removal of heavy isotopes (Albarede et al., 2017; Dauphas et al., 2017).

Iron isotopes also serve as a useful proxy for palaeo-redox conditions, for prior to the GOE it is thought that the Earth's oceans were anoxic and rich in isotopically light δ^{56}Fe. The black shale iron isotope archive shows a wide range of values in samples

from the early Proterozoic and the Archaean ($\delta^{56}Fe = +1.0$ to -3.5‰) but a much narrower spread in rocks younger than about 2.3 Ga. This difference is thought to reflect a change in the redox state of the global oceans related to the oxygenation of the Earth's atmosphere during the GOE at 2.34 Ga. Similarly, there are large iron isotope fractionations in Archaean and Proterozoic banded iron formations (BIF) prior to 1.8 Ga ($\delta^{56}Fe = -2.5$ and $+2.0$‰), although it is unclear how much of this fractionation is primary and how much is the product of post-depositional processes (Dauphas et al. 2017).

It has been suggested that the extreme iron isotope fractionations in Archaean sediments are, in part, the product of microbial activity, although this is difficult to demonstrate unequivocally since similar fractionations can be produced by abiotic processes. Nevertheless, the recent study by Marin-Carbonne et al. (2020) argues that 3.2 Ga sedimentary pyrites from the Barberton Greenstone Belt in South Africa preserve evidence of microbial activity in the form of dissimilatory iron reduction.

In high-temperature geochemistry the difference between the average iron isotope composition of mantle peridotites ($\delta^{56}Fe = -0.027 \pm 0.026$‰) and MORBs ($\delta^{56}Fe = +0.105 \pm 0.006$‰) suggests that there is equilibrium iron isotope fractionation during the partial melting of the mantle. This is difficult to quantify, but McCoy-West et al. (2018) propose a $\delta^{56}Fe_{melt} - \delta^{56}Fe_{source}$ value of <0.04‰ for high degrees of mantle melting, although at present not all the relevant mineral–melt fractionation factors are well known (Dauphas et al., 2017). In felsic rocks the steep increase in $\delta^{56}Fe$ values with increasing silica content is most likely to be the product of fractional crystallisation, although the initial redox state of the melt and the role of Fe^{3+} should be also be taken into consideration when evaluating these isotopic fractionations (Teng et al., 2008; Dauphas et al., 2017).

Appendices

Appendix 3.1 The CIPW Norm Calculation (after Kelsey, 1965, and Cox et al., 1979)

Despite the numerous programs, macros and other tools available for calculating the CIPW norm it is helpful to use a standard form when calculating a norm by hand. This may be done by laying out the oxides (with their molecular weights and therefore the molecular proportions) as columns along the top of the page and the more common normative minerals as rows down the left-hand margin. The 'boxes' of the table are filled as the calculation is made and can be used to keep track of when an element is totally consumed. Constants used in the CIPW norm calculation are listed in Table A3.1.

The CIPW norm calculation makes a few simplifying assumptions – that the magma is anhydrous, no solid solution occurs in minerals, and the Fe/Mg ratio of ferromagnesian minerals remains constant. The whole rock chemistry is converted to molecular proportions by dividing the wt.% oxides by their respective molecular weights. At the end of the calculation the wt.% norm is generated by multiplying the proportions of normative minerals by their molecular weight.

Method

1. Divide wt.% oxides by their molecular weights to determine their molecular proportions. Use the molar oxide proportions in all subsequent calculations.
2. Add MnO to FeO.
3. Allocate CaO equal to 3.33 × P_2O_5 to apatite.
4. If FeO > TiO_2: allocate FeO equal to the amount of TiO_2 present to ilmenite.

   If FeO < TiO_2: an excess of TiO_2 is provisionally made into sphene, using an equal amount of CaO (although, only after CaO has been allocated to anorthite). If there is still an excess of TiO_2, it is allocated to rutile.

Table A3.1 Constants used in the CIPW norm calculation

Oxide	*Molecular weight*	*Normative*	*Mineral*	*Formula*	*Molecular weight*
SiO_2	60	q	Quartz	S	60
TiO_2	80	or	Orthoclase	KAS_6	556
Al_2O_3	102	ab	Albite	NAS_6	524
Fe_2O_3	160	an	Anorthite	CAS_2	278
FeO	72	lc	Leucite	KAS_4	436
MnO	71	ne	Nepheline	NAS_2	284
MgO	40	c	Corundum A		102
CaO	56	ac	Acmite	$NF^{3+}S_4$	462
Na_2O	62	wo	Wollastonite	CS	116
K_2O	94	di en	Enstatite	MS	100
P_2O_5	142	di fs	Ferrosilite	$F^{2+}S$	132
		di wo wollastonite	CS	116	
		hy en enstatite	MS	100	
		hy fs	Ferrosilite	$F^{2+}S$	132
		ol fo	Forsterite	M_2S	140
		ol fa	Fayalite	$F^{2+}S$	204
		mt	Magnetite	$F^{2+}F^{3+}$	232
		he	Hematite	F^{3+}	160
		il	Ilmenite	$F^{2+}T$	152
		ap	Apatite	$C_{3.33}P$	310

5. Provisionally allocate Al_2O_3 equal to K_2O for orthoclase.
6. Provisionally allocate to any excess Al_2O_3 equal Na_2O for albite. If there is insufficient Al_2O_3, go to step 10.
7. Any excess of Al_2O_3 over $Na_2O + K_2O$ is matched with an equal amount of CaO for anorthite.
8. If there is an excess of Al_2O_3 over CaO, it is allocated to corundum.
9. An excess of CaO over Al_2O_3 is used for diopside and wollastonite.
10. An excess of Na_2O over Al_2O_3 is used in acmite; there is no anorthite in the norm. Allocate Fe_2O_3 equal to the excess Na_2O for acmite.
11. If $Fe_2O_3 > Na_2O$, allocate an equal amount of FeO for magnetite.
12. If Fe_2O_3 is still in excess, it is calculated as hematite.
13. Sum MgO + remaining FeO. Calculate their relative proportions.
14. Any CaO unused after anorthite (step 7) allocated to diopside using an equal amount of FeO + MgO (allotted in proportion to that determined in step 13).
15. Excess CaO is provisionally allocated to wollastonite.
16. Excess MgO + FeO is provisionally allocated to hypersthene.
17. Allocate SiO_2 to sphene, acmite, provisional orthoclase, albite and anorthite, diopside, wollastonite and hypersthene in the proportions of the formulae above.
18. An excess of SiO_2 is calculated as quartz.
19. If there is insufficient SiO_2 at step 17, the SiO_2 allocated to hypersthene is omitted from the sum of SiO_2 used. If at this point there is an excess of SiO_2, the remaining SiO_2 is allocated between hypersthene and olivine using the equations

    $$x = 2S - M$$
    $$y = M - x$$

    where x is the number of hypersthene molecules and y the number of olivine molecules, M the value of available MgO + FeO, and S the amount of available SiO_2. If there is insufficient SiO_2 to match half the amount of MgO + FeO, then MgO + FeO is made into olivine (rather than hypersthene).
20. If there is still a deficiency of SiO_2 in step 19, SiO_2 allocated to sphene is subtracted from the total in step 17 and CaO and TiO_2 are calculated as perovskite.
21. If there is still a deficiency in SiO_2, the total in step 17 is calculated substituting perovskite for sphene and olivine for hypersthene. Albite is omitted and Na is distributed between albite and nepheline according to the rules

    $$x = (S - 2N)/4$$
    $$y = N - x$$

    where x is the number of albite molecules, y the number of nepheline molecules, N the amount of available Na_2O, and S the amount of available SiO_2.
22. If there is not enough SiO_2 at step 21 to equal twice the Na_2O, all the Na_2O is made into nepheline and K_2O is distributed between leucite and orthoclase, although now the total available SiO_2 is the total from step 17 when perovskite, olivine and nepheline are made and orthoclase is omitted. In this case

    $$x = (S - 4K)/2$$
    $$y = (K - x)$$

    where x is the number of orthoclase molecules and y the number of leucite molecules, K the available K_2O, and S the available SiO_2.
23. If there is still a deficiency in SiO_2, the CaO of wollastonite and diopside is distributed between these two minerals and calcium orthosilicate and the silica allocated accordingly.
24. Finally, the weight percentages of the normative minerals are calculated by multiplying the oxide amounts by the molecular weight of the minerals. An oxide is selected which appears as unity in the formulae cited above and that value (the molecular proportion) is multiplied by the molecular weights given above. This gives the normative constituents in wt.% terms. These should sum to approximately the same percentage as the original analysis.

Appendix 5.1 Discriminant Function Equations for Tectonic Discrimination Diagrams

Axes for Figure 5.5, Oceanic Basalts (Vermeesch, 2006a)

(A) $DF1 = 0.555 \ln(Al_2O_3/SiO_2) + 3.822 \ln(TiO_2/SiO_2) + 0.522 \ln(CaO/SiO_2) + 1.293 \ln(MgO/SiO_2) - 0.531 \ln(MnO/SiO_2) - 0.145 \ln(K_2O/SiO_2) - 0.399 \ln(Na_2O/SiO_2)$

$DF2 = 3.796 \ln(Al_2O_3/SiO_2) + 0.008 \ln(TiO_2/SiO_2) - 2.868 \ln(CaO/SiO_2) + 0.313 \ln(MgO/SiO_2) + 0.650 \ln(MnO/SiO_2) + 1.421 \ln(K_2O/SiO_2) - 3.017 \ln(Na_2O/SiO_2)$

(B) $DF1 = 0.016 \ln(Zr/Ti) - 2.961 \ln(Y/Ti) + 1.500 \ln(Sr/Ti)$

$DF2 = 1.474 \ln(Zr/Ti) + 2.143 \ln(Y/Ti) + 1.840 \ln(Sr/Ti)$

Axes for Figure 5.6, Ultramafic and Mafic Rocks (Verma and Agrawal, 2011)

Subscript $_A$ = adjusted to 100% and for Fe oxidation state.

(A) $DF1 = -0.6611 \times \ln(Nb/(TiO_2)_A) + 2.2926 \times \ln(V/TiO_2)_A) + 1.6774 \times \ln(Y/TiO_2)_A) + 1.0916 \times \ln(Zr/(TiO_2)_A) + 21.3603$

$DF2 = 0.4702 \times \ln(Nb/(TiO_2)_A) + 3.7649 \times \ln(V/TiO_2)_A) - 3.911 \times \ln(Y/TiO_2)_A) + 2.2697 \times \ln(Zr/(TiO_2)_A) + 4.8487$

(B) $DF1 = (-0.6146 \times \ln(Nb/(TiO_2)_A) + (2.3510 \times \ln(V/(TiO_2)_A) + (1.6828 \times \ln(Y/(TiO_2)_A) + (1.1911 \times \ln(Zr/(TiO_2)_A) + 22.7253$

$DF2 = (1.3765 \times \ln(Nb/(TiO_2)_A) + (-0.9452 \times \ln(V/(TiO_2)_A) + (4.0461 \times \ln(Y/(TiO_2)_A) + (-2.0789 \times \ln(Zr/(TiO_2)_A) + 22.2450$

(C) $DF1 = (-0.6624 \times \ln(Nb/(TiO_2)_A) + (2.24498 \times \ln(V/(TiO_2)_A) + (1.2867 \times \ln(Y/(TiO_2)_A) + (1.0920 \times \ln(Zr/(TiO_2)_A) + 18.7466$

$DF2 = (0.4939 \times \ln(Nb/(TiO_2)_A) + (3.4741 \times \ln(V/(TiO_2)_A) + (-3.8953 \times \ln(Y/(TiO_2)_A) + (2.0070 \times \ln(Zr/(TiO_2)_A) + 3.3163$

(D) $DF1 = (-0.2646 \times \ln(Nb/(TiO_2)_A) + (2.0491 \times \ln(V/(TiO_2)_A) + (3.4565 \times \ln(Y/(TiO_2)_A) + (0.8573 \times \ln(Zr/(TiO_2)_A) + 32.9472$

$DF2 = (0.01874 \times \ln(Nb/(TiO_2)_A) + (4.0937 \times \ln(V/(TiO_2)_A) + (-4.8550 \times \ln(Y/(TiO_2)_A) + (2.9900 \times \ln(Zr/(TiO_2)_A) + 0.1995$

Axes for Figure 5.7, Intermediate Rocks (Verma and Verma, 2013)

Subscript $_A$ = adjusted to 100% and for Fe oxidation state.

Major elements

(A) $DF1 = (-2.45605 \times \ln(TiO_2/SiO_2)_A) + (1.11985 \times \ln(Al_2O_3/SiO_2)_A) + (-2.22475 \times \ln(Fe_2O_3/SiO_2)_A) + (2.48861 \times \ln(FeO/SiO_2)_A) + (-0.212024 \times \ln(MnO/SiO_2)_A) + (-0.06661 \times \ln(MgO/SiO_2)_A) + (1.29066 \times \ln(CaO/SiO_2)_A) + (-0.28377 \times \ln(Na_2O/SiO_2)_A) + (-0.40211 \times \ln(K_2O/SiO_2)_A) + (0.030635 \times \ln(P_2O_5/SiO_2)_A) - 11.4309347$

$DF2 = (-0.57759 \times \ln(TiO_2/SiO_2)_A) + (-0.01121 \times \ln(Al_2O_3/SiO_2)_A) + (0.69125 \times \ln(Fe_2O_3/SiO_2)_A) + (-1.99798 \times \ln(FeO/SiO_2)_A) + (-1.72017 \times \ln(MnO/SiO_2)_A) + (0.305275 \times \ln(MgO/SiO_2)_A) + (0.816018 \times \ln(CaO/SiO_2)_A) + (-1.791727 \times \ln(Na_2O/SiO_2)_A) + (0.871298 \times \ln(K_2O/SiO_2)_A) + (0.335479 \times \ln(P_2O_5/SiO_2)_A) - 12.20158596$

(B) $DF1 = (-2.51880 \times \ln(TiO_2/SiO_2)_A) + (0.54210 \times \ln(Al_2O_3/SiO_2)_A) + (-3.790190 \times \ln(Fe_2O_3/SiO_2)_A) + (3.846277 \times \ln(FeO/SiO_2)_A) + (-0.362718 \times \ln(MnO/SiO_2)_A) + (-0.176632 \times \ln(MgO/SiO_2)_A) + (1.426496 \times \ln(CaO/SiO_2)_A) + (0.111801 \times \ln(Na_2O/SiO_2)_A) + (-0.219223 \times \ln(K_2O/SiO_2)_A) + (-0.07248 \times \ln(P_2O_5/SiO_2)_A) - 14.3151255$

DF2 = (−1.04907 × ln (TiO_2/SiO_2)$_A$) + (3.440438 × ln (Al_2O_3/SiO_2)$_A$) + (−3.43323 × ln (Fe_2O_3/SiO_2)$_A$) + (4.807165 × ln (FeO/SiO_2)$_A$) + (−3.499257 × ln (MnO/SiO_2)$_A$) + (0.373928 × ln (MgO/SiO_2)$_A$) + (−2.147775 × ln (CaO/SiO_2)$_A$) + (3.00229 × ln (Na_2O/SiO_2)$_A$) + (−0.773719 × ln (K_2O/SiO_2)$_A$) + (1.061808 × ln (P_2O_5/SiO_2)$_A$) − 13.4885545

(C) DF1 = (−2.43565 × ln (TiO_2/SiO_2)$_A$) + (1.53913 × ln (Al_2O_3/SiO_2)$_A$) + (−1.51665 × ln (Fe_2O_3/SiO_2)$_A$) + (1.45582 × ln (FeO/SiO_2)$_A$) + (0.4961937 × ln (MnO/SiO_2)$_A$) + (−0.50128 × ln (MgO/SiO_2)$_A$) + (1.258138 × ln (CaO/SiO_2)$_A$) + (−0.8274299 × ln (Na_2O/SiO_2)$_A$) + (−0.4884699 × ln (K_2O/SiO_2)$_A$) + (0.1123605 × ln (P_2O_5/SiO_2)$_A$) − 7.894955173

DF2 = (−0.736658 × ln (TiO_2/SiO_2)$_A$) + (−0.0788099 × ln (Al_2O_3/SiO_2)$_A$) + (0.065533 × ln (Fe_2O_3/SiO_2)$_A$) + (−1.130176 × ln (FeO/SiO_2)$_A$) + (−2.130889 × ln (MnO/SiO_2)$_A$) + (0.245709 × ln (MgO/SiO_2)$_A$) + (0.681694 × ln (CaO/SiO_2)$_A$) + (−1.3284307 × ln (Na_2O/SiO_2)$_A$) + (0.7709408 × ln (K_2O/SiO_2)$_A$) + (0.295664 × ln (P_2O_5/SiO_2)$_A$) − 15.24062267

(D) DF1 = (−2.32173 × ln (TiO_2/SiO_2)$_A$) + (1.97128 × ln (Al_2O_3/SiO_2)$_A$) + (−0.537435 × ln (Fe_2O_3/SiO_2)$_A$) + (0.431388 × ln (FeO/SiO_2)$_A$) + (−1.139286 × ln (MnO/SiO_2)$_A$) + (0.527984 × ln (MgO/SiO_2)$_A$) + (0.9884038 × ln (CaO/SiO_2)$_A$) + (−0.894467 × ln (Na_2O/SiO_2)$_A$) + (0.16138688 × ln (K_2O/SiO_2)$_A$) + (0.0778358 × ln (P_2O_5/SiO_2)$_A$) − 12.34961873

DF2 = (−0.40691 × ln (TiO_2/SiO_2)$_A$) + (2.60576 × ln (Al_2O_3/SiO_2)$_A$) + (0.161669 × ln (Fe_2O_3/SiO_2)$_A$) + (1.345967 × ln (FeO/SiO_2)$_A$) + (0.4457959 × ln (MnO/SiO_2)$_A$) + (−0.260127 × ln (MgO/SiO_2)$_A$) + (−0.464534 × ln (CaO/SiO_2)$_A$) + (0.9211739 × ln (Na_2O/SiO_2)$_A$) + (−1.2769499 × ln (K_2O/SiO_2)$_A$) + (−0.142884 × ln (P_2O_5/SiO_2)$_A$) + 3.501318155

Immobile trace elements

(A) DF1 = (0.1672589 × ln (La/Yb)) + (−1.2542899 × ln (Ce/Yb)) + (1.295171 × ln (Sm/Yb)) + (1.3318361 × ln (Nb/Yb)) + (0.2698636 × ln (Th/Yb)) + (1.9286976 × ln (Y/Yb)) + (0.18097357 × ln (Zr/Yb)) − 3.815745639

DF2 = (−0.2426713 × ln (La/Yb)) + (1.7265475 × ln (Ce/Yb)) + (0.4902224 × ln (Sm/Yb)) + (−1.2755648 × ln (Nb/Yb)) + (0.9602491 × ln (Th/Yb)) + (0.8511852 × ln (Y/Yb)) + (−0.4894082 × ln (Zr/Yb)) − 3.305510646

(B) DF1 = (0.0178001 × ln (La/Yb)) + (−1.2689712 × ln (Ce/Yb)) + (1.7407108 × ln (Sm/Yb)) + (1.324421438 × ln (Nb/Yb)) + (0.0288819 × ln (Th/Yb)) + (1.580888497 × ln (Y/Yb)) + (0.17161461 × ln (Zr/Yb)) − 3.3845534709

DF2 = (−2.099551 × ln (La/Yb)) + (−2.044178 × ln (Ce/Yb)) + (−0.41179008 × ln (Sm/Yb)) + (1.022466699 × ln (Nb/Yb)) + (1.2444842 × ln (Th/Yb)) + (1.87700276 × ln (Y/Yb)) + (1.07017399797 × ln (Zr/Yb)) − 0.2920468400

(C) DF1 = (0.72085 × ln (La/Yb)) + (−1.352147 × ln (Ce/Yb)) + (1.378563 × ln (Sm/Yb)) + (1.1641465 × ln (Nb/Yb)) + (−0.0423769 × ln (Th/Yb)) + (1.5584709 × ln (Y/Yb)) + (−0.1644980 × ln (Zr/Yb)) − 2.9336489118

DF2 = (0.2378909 × ln (La/Yb)) + (−2.03548886 × ln (Ce/Yb)) + (1.378563 × ln (Sm/Yb)) + (1.34733326 × ln (Nb/Yb)) + (−0.760673982 × ln (Th/Yb)) + (−0.786605747 × ln (Y/Yb)) + (0.37736968328 × ln (Zr/Yb)) + 4.15732286

(D) DF1 = (−0.977026 × ln (La/Yb)) + (−1.3886489 × ln (Ce/Yb)) + (1.36560 × ln (Sm/Yb)) + (1.8999127 × ln (Nb/Yb)) + (0.5690460 × ln (Th/Yb)) + (1.65772638 × ln (Y/Yb)) + (−0.30523813 × ln (Zr/Yb)) − 0.87680549008

DF2 = (−0.086967 × ln (La/Yb)) + (1.1636159 × ln (Ce/Yb)) + (0.3635930 × ln (Sm/Yb)) + (−0.90127239 × ln (Nb/Yb)) + (1.1257989 × ln (Th/Yb)) + (1.19149068 × ln (Y/Yb)) + (−0.39964298 × ln (Zr/Yb)) − 3.915383182

Immobile major + trace elements

(A) DF1 = (1.02293 × ln (MgO/TiO_2)$_A$) + (0.63053 × ln (P_2O5/TiO_2)$_A$) + (−0.93889 × ln (Nb/TiO_2)$_A$) + (−0.41538 × ln (Ni/TiO_2)$_A$) + (1.676898 × ln (V/TiO_2)$_A$) + (0.453813 × ln (Y/TiO_2)$_A$) + (0.5831823 × ln (Zr/TiO_2)$_A$) + 1.900726416

DF2 = (0.248529 × ln (MgO/TiO_2)$_A$) + (−0.477177 × ln (P_2O5/TiO_2)$_A$) + (−0.336281 × ln (Nb/TiO_2)$_A$) + (−0.131072 × ln (Ni/TiO_2)$_A$) + (−1.712035 × ln (V/TiO_2)$_A$) +

$(0.213840 \times \ln (Y/TiO_2)_A) + (-2.008435 \times \ln (Zr/TiO_2)_A) - 18.63750138$

(B) $DF1 = (-0.85601 \times \ln (MgO/TiO_2)_A) + (-0.300589 \times \ln (P_2O5/TiO_2)_A) + (0.861909 \times \ln (Nb/TiO_2)_A) + (0.384727 \times \ln (Ni/TiO_2)_A) + (-1.5827037 \times \ln (V/TiO_2)_A) + (-0.757282 \times \ln (Y/TiO_2)_A) + (-0.682422 \times \ln (Zr/TiO_2)_A) - 4.468550646$

$DF2 = (0.21504 \times \ln (MgO/TiO_2)_A) + (-0.503675 \times \ln (P_2O5/TiO_2)_A) + (-0.32252 \times \ln (Nb/TiO_2)_A) + (-0.122383 \times \ln (Ni/TiO_2)_A) + (-1.7097486 \times \ln (V/TiO_2)_A) + (0.426039 \times \ln (Y/TiO_2)_A) + (-1.980676 \times \ln (Zr/TiO_2)_A) - 17.04082095$

(C) $DF1 = (-1.25554 \times \ln (MgO/TiO_2)_A) + (-1.082014 \times \ln (P_2O5/TiO_2)_A) + (1.437934 \times \ln (Nb/TiO_2)_A) + (0.5454469 \times \ln (Ni/TiO_2)_A) + (-1.6196297 \times \ln (V/TiO_2)_A) + (0.3368725 \times \ln (Y/TiO_2)_A) + (-0.71359906 \times \ln (Zr/TiO_2)_A) + 5.752160917$

$DF2 = (-0.02400 \times \ln (MgO/TiO_2)_A) + (-0.054413 \times \ln (P_2O5/TiO_2)_A) + (-0.8608025 \times \ln (Nb/TiO_2)_A) + (-0.174160 \times \ln (Ni/TiO_2)_A) + (-1.6407186 \times \ln (V/TiO_2)_A) + (0.068523 \times \ln (Y/TiO_2)_A) + (-1.772088 \times \ln (Zr/TiO_2)_A) - 21.02758313$

Axes for Figure 5.9, Acid Rocks (Verma et al., 2012)

Subscript $_A$ = adjusted.

(A) $DF1 = (0.36077 \times \ln (TiO_2/SiO_2)_A) + (0.95693 \times \ln (Al_2O_3/SiO_2)_A) + (-2.09239 \times \ln (Fe_2O_3/SiO_2)_A) + (0.93391 \times \ln (FeO/SiO_2)_A) + (0.42703 \times \ln (MnO/SiO_2)_A) + (0.18732 \times \ln (MgO/SiO_2)_A) + (0.45615 \times \ln (CaO/SiO_2)_A) + (0.56098 \times \ln (Na_2O/SiO_2)_A) + (-1.65167 \times \ln (K_2O/SiO_2)_A) + (-0.15580 \times \ln (P_2O_5/SiO_2)_A) - 1.58259$

$DF2 = (0.472353 \times \ln (TiO_2/SiO_2)_A) + (-0.954629 \times \ln (Al_2O_3/SiO_2)_A) + (0.109516 \times \ln (Fe_2O_3/SiO_2)_A) + (0.699238 \times \ln (FeO/SiO_2)_A) + (0.739533 \times \ln (MnO/SiO_2)_A) + (-0.027717 \times \ln (MgO/SiO_2)_A) + (-0.244687 \times \ln (CaO/SiO_2)_A) + (0.231677 \times \ln (Na_2O/SiO_2)_A) + (0.173552 \times \ln (K_2O/SiO_2)_A) + (-0.353797 \times \ln (P_2O_5/SiO_2)_A) + 6.691035$

(B) $DF1 = (-0.4786 \times \ln (TiO_2/SiO_2)_A) + (-0.0871 \times \ln (Al_2O_3/SiO_2)_A) + (2.7433 \times \ln (Fe_2O_3/SiO_2)_A) + (-1.0663 \times \ln (FeO/SiO_2)_A) + (-0.1389 \times \ln (MnO/SiO_2)_A) + (-0.1907 \times \ln (MgO/SiO_2)_A) + (-0.8516 \times \ln (CaO/SiO_2)_A) + (-0.7139 \times \ln (Na_2O/SiO_2)_A) + (1.7166 \times \ln (K_2O/SiO_2)_A) + (0.3386 \times \ln (P_2O_5/SiO_2)_A) + 6.2573$

$DF2 = (-0.3204 \times \ln (TiO_2/SiO_2)_A) + (-1.7585 \times \ln (Al_2O_3/SiO)_A) + (-3.2046 \times \ln (Fe_2O_3/SiO_2)_A) + (1.1210 \times \ln (FeO/SiO_2)_A) + (0.2170 \times \ln (MnO/SiO_2)_A) + (-0.0745 \times \ln (MgO/SiO_2)_A) + (1.2505 \times \ln (CaO/SiO_2)_A) + (1.3142 \times \ln (Na_2O/SiO_2)_A) + (1.6616 \times \ln (K_2O/SiO_2)_A) + (0.0186 \times \ln (P_2O_5/SiO_2)_A) + 0.9984$

(C) $DF1 = (0.0226 \times \ln (TiO_2/SiO_2)_A) + (1.2877 \times \ln (Al_2O_3/SiO_2)_A) + (-2.6406 \times \ln (Fe_2O_3/SiO_2)_A) + (2.9494 \times \ln (FeO/SiO_2)_A) + (0.1970 \times \ln (MnO/SiO_2)_A) + (0.0673 \times \ln (MgO/SiO_2)_A) + (0.0620 \times \ln (CaO/SiO_2)_A) + (0.6219 \times \ln (Na_2O/SiO_2)_A) + (-2.0579 \times \ln (K_2O/SiO_2)_A) + (-0.0751 \times \ln (P_2O_5/SiO_2)_A) - 2.1790$

$DF2 = (0.2786 \times \ln (TiO_2/SiO_2)_A) + (-1.0544 \times \ln (Al_2O_3/SiO_2)_A) + (0.8267 \times \ln (Fe_2O_3/SiO_2)_A) + (0.3032 \times \ln (FeO/SiO_2)_A) + (0.4084 \times \ln (MnO/SiO2)_A) + (-0.0905 \times \ln (MgO/SiO_2)_A) + (-0.3260 \times \ln (CaO/SiO_2)_A) + (0.1518 \times \ln (Na_2O/SiO_2)_A) + (0.6698 \times \ln (K_2O/SiO_2)_A) + (-0.2261 \times \ln (P_2O_5/SiO_2)_A) + 6.5170$

Axes for Figure 5.10, Sedimentary Rocks (Verma and Armstrong-Altrin, 2013)

Subscript $_A$ = adjusted to 100% and for Fe oxidation state.

(A) $DF1 = (-0.26269 \times \ln (TiO_2/SiO_2)_A) + (0.60369 \times \ln (Al_2O_3/SiO_2)_A) + (-0.72489 \times \ln (Fe_2O_3/SiO_2)_A) + (0.66042 \times \ln (MnO/SiO_2)_A) + (2.19128 \times \ln (MgO/SiO_2)_A) + (0.14421 \times \ln (CaO/SiO_2)_A) + (-1.30432 \times \ln (Na_2O/SiO_2)_A) + (0.05449 \times \ln (K_2O/SiO_2)_A) + (-0.33002 \times \ln (P_2O_5/SiO_2)_A) + 1.58815$

$DF2 = (-1.19586 \times \ln (TiO_2/SiO_2)_A) + (1.06399 \times \ln (Al_2O_3/SiO_2)_A) + (0.30341 \times \ln (Fe_2O_3/SiO_2)_A) + (0.43567 \times \ln (MnO/SiO_2)_A) + (0.83805 \times \ln (MgO/SiO_2)_A) + (-0.40665 \times \ln (CaO/SiO_2)_A) + (1.02140 \times \ln (Na_2O/SiO_2)_A) + (-1.70582 \times \ln (K_2O/SiO_2)_A) + (-0.12643 \times \ln (P_2O_5/SiO_2)_A) - 1.06801$

(B) $DF1 = (0.60809 \times \ln (TiO_2/SiO_2)_A) + (-1.85447 \times \ln (Al_2O_3/SiO_2)_A) + (0.29904 \times \ln (Fe_2O_3/SiO_2)_A) + (-0.54964 \times \ln (MnO/SiO_2)_A) + (0.12026 \times \ln (MgO/SiO_2)_A) + (0.19377 \times \ln (CaO/SiO_2)_A) + (-1.51036 \times \ln (Na_2O/SiO_2)_A) + (1.94074 \times \ln (K_2O/SiO_2)_A) + (0.00343 \times \ln (P_2O_5/SiO_2)_A) - 0.29378$

$DF2 = (-0.55404 \times \ln (TiO_2/SiO_2)_A) + (-0.99528 \times \ln (Al_2O_3/SiO_2)_A) + (1.76467 \times \ln (Fe_2O_3/SiO_2)_A) + (-1.39149 \times \ln (MnO/SiO_2)_A) + (-1.03363 \times \ln (MgO/SiO_2)_A) + (0.22482 \times \ln (CaO/SiO_2)_A) + (0.71313 \times \ln (Na_2O/SiO_2)_A) + (0.33022 \times \ln (K_2O/SiO_2)_A) + (0.63684 \times \ln (P_2O_5/SiO_2)_A) - 3.63056$

References

Abadie, C., Lacan, F., Radic, A., Pradoux, C., Poitrasson, F., 2017. Iron isotopes reveal distinct dissolved iron sources and pathways in the intermediate versus deep Southern Ocean. *Proceedings of the National Academy of Sciences* 114, 858–863.

Acosta-Vigil, A., London, D., Morgan, G.B. VI, Cesare, B., Buick, I., Hermann, J., Bartoli, O., 2017. Primary crustal melt compositions: Insights into the controls, mechanisms and timing of generation from kinetics experiments and melt inclusions. *Lithos* 286–287, 454–479.

Addy, S.K., Garlick, G.D., 1974. Oxygen isotope fractionation between rutile and water. *Contributions to Mineralogy and Petrology* 45, 119–121.

Ader, M., Thomazo, C., Sansjofre, P., Busigny, V., Papineau, D., Laffont, R., Cartigny, P., Halverson, G.P., 2016. Interpretation of the nitrogen isotopic composition of Precambrian sedimentary rocks: Assumptions and perspectives. *Chemical Geology* 429, 93–110.

Agrawal, S., Guevara, M., Verma, S.P., 2004. Discriminant analysis applied to establish major-element field boundaries for tectonic varieties of basic rocks. *International Geology Reviews* 46, 575–594.

Ahmedali, S.T., 1989. *X-ray fluorescence analysis in the geological sciences: Advances in methodology*. Geological Association of Canada: Short course 7.

Aigner-Torres, M., Blundy, J., Ulmer, P., Pettke, T., 2007. Laser ablation ICPMS study of trace element partitioning between plagioclase and basaltic melts: An experimental approach. *Contributions to Mineralogy and Petrology* 153, 647–667.

Aitcheson, S.J., Forrest, A.H., 1994. Quantification of crustal contamination in open magmatic systems. *Journal of Petrology* 35, 461–488.

Aitchison, J., 1981. A new approach to null correlations of proportions. *Mathematical Geology* 13, 175–189.

Aitchison J., 1982. The statistical analysis of compositional data (with discussion). *Journal of the Royal Statistical Society* 44, 139–177.

Aitchison, J., 1984. The statistical analysis of geochemical compositions. *Mathematical Geology* 16, 531–564.

Aitchison, J., 1986. *The statistical analysis of compositional data*. Methuen, New York.

Aitchison, J., 2003. *The statistical analysis of compositional data*. Blackburn Press, Caldwell, NJ.

Aitchison, J., 2005. A Concise Guide to Compositional Data Analysis. www.leg.ufpr.br/lib/exe/fetch.php/pessoais:abtmartins:a_concise_guide_to_compositional_data_analysis.pdf.

Aitchison, J., Egozcue, J.J., 2005. Compositional data analysis: Where are we and where should we be heading? *Mathematical Geology* 37, 829–850.

Aitchison, J., Greenacre, M., 2002. Biplots of compositional data. *Applied Statistics* 51, 375–392.

Albarede, F., Telouk, P., Balter, V., 2017. Medical applications of isotope metallomics. *Reviews in Mineralogy and Geochemistry* 82, 851–885.

Alibert, C., McCulloch, M.T., 1993. Rare earth element and neodymium isotopic compositions of the banded iron-formations and associated shales from Hamersley, Western Australia. *Geochimica et Cosmochimica Acta* 57(1), 187–204.

Alibo, D.S., Nozaki, Y., 1999. Rare earth elements in seawater: Particle association, shale normalization, and Ce oxidation. *Geochimica et Cosmochimica Acta* 63, 363–372.

Allegre, C.J., Minster, J.F., 1978. Quantitative models of trace element behavior in magmatic processes. *Earth and Planetary Science Letters* 38, 1–25.

Allegre, C.J., Rousseau, D., 1984. The growth of the continents through geological time studied by the Nd isotopic analysis of shales. *Earth and Planetary Science Letters* 67, 19–34.

Allegre, C.J., Hart, S.R. and Minster J.-F., 1983. Chemical structure and evolution of the mantle and continents determined by inversion of Nd and Sr isotopic data, I. Theoretical models. *Earth and Planetary Science Letters* 66, 177–190.

Allegre, C.J., Treuil, M., Minster, J.F., Minster, B., Albarède, F., 1977. Systematic use of trace element in igneous process. *Contributions to Mineralogy and Petrology* 60(1), 57–75.

Al-Mishwat, A.T., 2015. CIPWFULL: A software program for calculation of comprehensive CIPW norms of igneous rocks. *International Association for Mathematical Geosciences* 47, 441–453.

Altwegg, K., et al., 2015. 67P/Churyumov-Gerasimenko, a Jupiter family comet with a high D/H ratio. *Science* 347(6220).

Amelin, Y., Lee, D.C., Halliday, A.N., 2000. Early-middle Archaean crustal evolution deduced from Lu–Hf and U–Pb isotopic studies of single zircon grains. *Geochimica et Cosmochimica Acta* 64(24), 4205–4225.

Anders, E., Grevesse, N., 1989. Abundances of the elements: Meteoritic and solar. *Geochimica et Cosmochimica Acta* 53, 197–214.

André, L., Abraham, K., Hofmann, A., Monin, L., Kleinhanns, I.C., Foley, S.F., 2019. Early continental crust generated by reworking of basalts variably silicified by seawater. *Nature Geoscience* 12, 769–773.

Anovitz, L.M., Essene, E.J., 1987. Phase equilibria in the system $CaCO_3$-$MgCO_3$-$FeCO_3$. *Journal of Petrology* 28, 389–414.

Apted, M.J., Roy S.D., 1981. Corrections to the trace element fractionation equations of Hertogen and Gijbels (1976). *Geochimica et Cosmochimica Acta* 45, 777–778.

Aranovich, L.Y., Newton, R.C., Manning, C.E., 2013. Brine-assisted anatexis: Experimental melting in the system haplogranite–H_2O–NaCl–KCl at deep-crustal conditions. *Earth and Planetary Science Letters* 374, 111–120.

Arevalo, R., 2014. Laser ablation ICP-MS and laser fluorination GS-MS. In: Holland, H.D., Turekian, K.K. (eds.), *Treatise on geochemistry*, 2nd ed. Elsevier, Oxford. 15: 425–441.

Arevalo, R., McDonough, W.F., 2010. Chemical variations and regional diversity observed in MORB. *Chemical Geology* 271, 70–85.

Arevalo R., McDonough, W.F., Luong, M., 2009. The K/U ratio of the silicate earth: Insights into mantle composition, structure and thermal evolution. *Earth and Planetary Science Letters* 278, 361–369.

Armstrong, J.T., McSwiggen, P., Nielsen, C., 2013. A thermal field-emission electron probe microanalyzer for improved analytical spatial resolution. *Microscopy and Analysis* 27, 18–22.

Armstrong, R., 1981. Radiogenic isotopes: The case for crustal recycling on a near-steady-state no-continental-growth Earth. *Philosophical Transactions of the Royal Society of London* A30, 443–472.

Arndt, N.T., Goldstein S.L., 1987. Use and abuse of crust-formation ages. *Geology* 15, 893–895.

Arndt, N.T., Jenner, G.A., 1986. Crustally contaminated komatiites and basalts from Kambalda, western Australia. *Chemical Geology* 229–255.

Arndt, N.T., Lesher, C.M., Barnes, S.J., 2008. *Komatiite*. Cambridge University Press, Cambridge.

Arth, J.G., 1976. Behavior of trace elements during magmatic processes: A summary of theoretical models and their applications. *Journal of Research US Geological Survey* 4(1), 41–47.

Asimow, P.D., Ghiorso, M.S., 1998. Algorithmic modifications extending MELTS to calculate subsolidus phase relations. *American Mineralogist* 83, 1127–1132.

Austreheim, H., Griffin, W.L. (eds.), 2000. Element partitioning in geochemistry and petrology. *Lithos* 53, 57–75.

Bacon, C.R., Druitt, T.H., 1988. Compositional evolution of the zoned calcalkaline magma chamber of Mount Mazama, Crater Lake, Oregon. *Contributions to Mineralogy and Petrology* 98, 224–256.

Baertschi, P. 1976. Absolute ^{18}O content of standard mean ocean water. *Earth and Planetary Science Letters* 1, 341–344.

Bai, Y., Su, B.-X., Xiao, Y., Chen, C., Cui, M.-M., He, X.-Q., Qin, L.-P., Charlier, B., 2019. Diffusion-driven chromium isotope fractionation in ultramafic cumulate minerals: Elemental and isotopic evidence from the Stillwater Complex. *Geochimica et Cosmochimica Acta* 263, 167–181.

Bailey, J.C., 1981. Geochemical criteria for a refined tectonic discrimination of orogenic andesites. *Chemical Geology* 32, 139–154.

Baker, A.J., 1988. Stable isotope evidence for limited fluid infiltration of deep crustal rocks from the Ivrea Zone, Italy. *Geology* 16, 492–495.

Barker, D.S., 1978. Magmatic trends on alkali-iron-magnesium diagrams. *American Mineralogist* 63, 531–534.

Barker, F., 1979. Trondhjemite: Definition, environment and hypotheses of origin. In: Barker, F. (ed.), *Trondhjemites, dacites and related rocks*. Elsevier, Amsterdam. 1–12.

Barnes, S.-J., Maier, W.D., 2002. Platinum group elements and microstructures of normal Merensky Reef, from Impala platinum mines, Bushveld Complex. *Journal of Perology* 43, 102–128.

Barrat, J.A., Zanda, B., Moynier, F., Bollinger, C., Liorzou, C., Bayon, G., 2012. Geochemistry of CI chondrites: Major and trace elements, and Cu and Zn isotopes. *Geochimica et Cosmochimica Acta* 83, 79–92.

Barry, P.H., Hilton, D.R., Fischer, T.P., de Moor, J.M., Mangasini, F., Ramirez, C., 2013. Helium and carbon isotope systematics of cold 'mazuku' CO_2 vents and hydrothermal gases and fluids from Rungwe Volcanic Province, southern Tanzania. *Chemical Geology* 339, 141–156.

Barry, P.H., Hilton, D.R., Furi, E., Halldorsson, S.A., Gronvold, K., 2014. Carbon isotope and abundance systematics of Icelandic geothermal gases, fluids and subglacial basalts with implications for mantle plume-related CO_2 fluxes. *Geochimica et Cosmochimica Acta* 134, 74–99.

Barth, T.W., 1952. *Theoretical petrology: A textbook on the origin and evolution of rocks*. Wiley, New York.

Bau, M., Schmidt, K., Koschinsky, A., Hein, J., Kuhn, T., Usui, A., 2014. Discriminating between different genetic types of marine ferro-manganese crusts and nodules based on rare earth elements and yttrium. *Chemical Geology* 381, 1–9.

Bau, M., Schmidt, K., Pack, A., Bendel, V., Kraemer, D., 2018. The European shale: An improved data set for normalisation of rare earth element and yttrium concentrations in environmental and biological samples from Europe. *Applied Geochemistry* 90, 142–149.

Bauer, K.W., Gueguen, B., Cole, D.B., Francois, R., Kallmeyer, J., Planavsky, N., Crowe, S.A., 2019. Chromium isotope fractionation in ferruginous sediments. *Geochimica et Cosmochimica Acta* 223, 198–215.

Bauer, M.E., Burisch, M., Ostendorf, J., Krause, J., Frenzel, M., Seifert, T., Gutzmer, J., 2019. Trace element geochemistry of sphalerite in contrasting hydrothermal fluid systems of the Freiberg district, Germany: Insights from LA-ICP-MS analysis, near-infrared light microthermometry of sphalerite-hosted fluid inclusions, and sulfur isotope geochemistry. *Mineralium Deposita* 54, 237–262.

Bea, F., 1996. Controls on the trace element composition of crustal melts. *Earth and Environmental Science Transactions of the Royal Society of Edinburgh* 87(1–2), 33–41.

Beattie, P., 1994. Systematics and energetics of trace-element partitioning between olivine and silicate melts: Implications for the nature of mineral/melt partitioning. *Chemical Geology* 117, 57–71.

Beaumont, V., Robert, F., 1999. Nitrogen isotope ratios of kerogens in Precambrian cherts: A record of the evolution of atmospheric chemistry? *Precambrian Research* 96, 63–82.

Bebout, G.E., Fogel, M.L., Cartigny, P., 2013. Nitrogen, highly volatile and yet surprisingly compatible. *Elements* 9, 333–338.

Beccaluva, L., Bianchini, G., Natali, C., Siena, F., 2017. The alkaline-carbonatite complex of Jacupiranga (Brazil): Magma genesis and mode of emplacement. *Gondwana Research* 44, 157–177.

Becker, A., Holz, F., Johannes, W., 1998. Liquidus temperatures and phase compositions in the system Qz-Ab-Or at 5kbar and very low water activities. *Contributions to Mineralogy and Petrology* 130, 213–224.

Bédard, J.H., 2005. Partitioning coefficients between olivine and silicate melts. *Lithos* 83, 394–419.

Bédard, J.H., 2006. Trace element partitioning in plagioclase feldspar. *Geochimica et Cosmochimica Acta* 70, 3717–3742.

Bédard, J.H., 2007. Trace element partitioning coefficients between silicate melts and orthopyroxene: Parameterizations of D variations. *Chemical Geology* 244(1–2), 263–303.

Bédard, J.H., 2014. Parameterizations of calcic clinopyroxene: Melt trace element partition coefficients. *Geochemistry, Geophysics, Geosystems* 15, doi: 10.1002/2013GC005112.

Béguelin, P., Bizimis, M., McIntosh, E.C., Cousens, B., Clague, D.A., 2019. Source vs processes: Unraveling the compositional heterogeneity of rejuvenated-type Hawaiian magmas. *Earth and Planetary Science Letters* 514, 119–129.

Belousova, E.A., Kostitsyn, Y.A., Griffin, W.L., Begg, G.C., O'Reilly, S.Y., Pearson, N.J., 2010. The growth of the continental crust: Constraints from zircon Hf-isotope data. *Lithos* 119, 457–466.

Bender, J.F., Langmuir, C.H., Hanson, G.N., 1984. Petrogenesis of basalt glasses from the Tamayo region, East Pacific Rise. *Journal of Petrology* 25, 213–254.

Bennett, S.L., Blundy, J., Elliott, T., 2004. The effect of sodium and titanium on crystal-melt partitioning of trace elements. *Geochimica et Cosmochimica Acta* 68, 2335–2347.

Bennett, V.C., Esat, T.M., Norman, M.D., 1996. Two mantle-plume components in Hawaiian picrites inferred from correlated Os–Pb isotopes. *Nature* 381(6579), 221–224.

Bente K., Nielsen H., 1982. Experimental S isotope fractionation studies between co-existing bismuthinite (Bi_2S_3) and sulphur (S_o). *Earth and Planetary Science Letters* 59, 18–20.

Berger, M., Rollinson, H., 1997. Isotopic and geochemical evidence for crust–mantle interaction during late Archaean crustal growth. *Geochimica et Cosmochimica Acta* 61, 4809–4829.

Bethke, C.M., 2012. *Geochemical and biogeochemical reaction modelling*, 2nd ed. Cambridge University Press.

Bézos, A., Humler, E., 2005. The $Fe^{3+}/\Sigma Fe$ ratios of MORB glasses and their implications for mantle melting. *Geochimica et Cosmochimica Acta* 69, 711–725.

Bézos, A., Lorand, J.P., Humler, E., Gros, M., 2005. Platinum-group element systematics in Mid-Oceanic Ridge basaltic glasses from the Pacific, Atlantic, and Indian Oceans. *Geochimica et Cosmochimica Acta* 69(10), 2613–2627.

Bhatia, M.R., 1983. Plate tectonics and geochemical composition of sandstones. *Journal of Geology* 91, 611–627.

Bhatia, M.R., 1984. Composition and classification of Paleozoic flysch mudrocks of eastern Australia: Implications in provenance and tectonic setting interpretation. *Sedimentary Geology* 41(2–4), 249–268.

Bhatia, M.R., Crook, K.A.W, 1986. Trace element characteristics of graywackes and tectonic discrimination of sedimentary basins. *Contributions to Mineralogy and Petrology* 92, 181–193.

Bickle, M.J., Arndt, N.T., Nisbet, E.G., Orpen, J.L., Martin, A., Keays, R.R., Renner, R., 1993. Geochemistry of the igneous rocks of the Belingwe greenstone belt: Alteration contamination and petro-genesis. In: Bickle, M.J., Nisbet, E.G. (eds.), *The geology of the Belingwe greenstone belt Zimbabwe*. Balkema, Rotterdam. 175–213.

Bindeman, I., 2008. Oxygen isotopes in mantle and crustal magmas as revealed by single crystal analysis. *Rev. Mineralogy and Geochemistry* 69, 445–478.

Bindeman, I.N., Davis, A.M., 2000. Trace element partitioning between plagioclase and melt: Investigation of dopant influence on partition behavior. *Geochimica et Cosmochimica Acta* 64, 2863–2878.

Bindeman, I.N., Valley, J.W., 2002. Oxygen isotope study of the Long Valley magma system, California: Isotope thermometry and convection in large silicic magma bodies. *Contributions to Mineralogy and Petrology* 144, 185–205.

Bindeman, I.N., Davis, A.M., Drake, M.J., 1998. Ion microprobe study of plagioclase-basalt partition experiments at natural concentration levels of trace elements. *Geochimica et Cosmochimica Acta* 62, 1175–1193.

Bingham, N.H., Fry, J.M., 2010. Regression: Linear models in statistics. In: *Regression*. Springer, London.

Bizimis, M., Lassiter, J.C., Salters, V.J., Sen, G., Griselin, M., 2004. Extreme Hf-Os isotope compositions in Hawaiian peridotite xenoliths: Evidence for an ancient recycled lithosphere. *AGUFM*, V51B-0550 (abstract).

Bizimis, M., Griselin, M., Lassiter, J.C., Salters, V.J., Sen, G., 2007. Ancient recycled mantle lithosphere in the Hawaiian plume: Osmium–hafnium isotopic evidence from peridotite mantle xenoliths. *Earth and Planetary Science Letters* 257, 259–273.

Black, B.A., Gibson, S.A., 2019. Deep carbon and the life cycle of large igneous provinces. *Elements* 15, 319–324.

Blackburn, T.J., Stockli, D.F., Walker, J.D., 2007. Magnetite (U–Th)/He dating and its application to the geochronology of intermediate to mafic volcanic rocks. *Earth and Planetary Science Letters* 259, 360–371.

Blichert-Toft, J., Weis, D., Maerschalk, C., Agranier, A., Albarède, F., 2003. Hawaiian hot spot dynamics as inferred from the Hf and Pb isotope evolution of Mauna Kea volcano. *Geochemistry, Geophysics, Geosystems* 4(2).

Bloch, E., Jollands, M., Devoir, A., Bouvier, A.-S., Ibañez-Mejia, M., Baumgartner, L.P., 2020. Multispecies diffusion of yttrium, rare earth elements and hafnium in garnet. *Journal of Petrology*, egaa055, https://doi.org/10.1093/petrology/egaa055.

Blundy, J., Cashman, K., 2001. Ascent-driven crystallisation of dacite magmas at Mount St Helens, 1980–1986. *Contributions to Mineralogy and Petrology* 140, 631–650.

Blundy, J.D., Wood, B.J., 1991. Crystal-chemical controls on the partitioning of Sr and Ba between plagioclase feldspar, silicate melts, and hydrothermal solutions. *Geochimica et Cosmochimica Acta* 55, 193–209.

Blundy, J.D., Wood, B.J., 1994. Prediction of crystal-melt partition coefficients from elastic moduli. *Nature* 372, 452–454.

Blundy, J.D., Wood, B.J., 2003. Partitioning of trace elements between crystals and melts. *Earth and Planetary Science Letters* 210, 383–397.

Bohrson, W.A., Spera, F.J., 2001. Energy-constrained open-system magmatic processes II: Application of energy-constrained assimilation-fractional crystallization (EC-AFC) model to magmatic systems. *Journal of Petrology* 42, 1019–1041.

Bohrson, W.A., Spera, F.J., 2007. Energy-constrained recharge, assimilation, and fractional crystallization (EC-RAXFC): A visual basic computer code for calculating trace element and isotope variations of open-system magmatic systems. *Geochemistry, Geophysics, Geosystems* 8, Q11003. https://doi.org/10.1029/2007G C001781.

Bohrson, W.A., Spera, F.J., Ghiorso, M.S., Brown, G.A., Creamer, J.B., Mayfield, A., 2014. Thermodynamic model for energy-constrained open-system evolution of crustal magma bodies undergoing simultaneous recharge, assimilation and crystallization: The magma chamber simulator. *Journal of Petrology* 55, 1685–1717.

Bolhar, R., Hofmann, A., Woodhead, J., Hergt, J., Dirks, P.H.G.M., 2002. Pb- and Nd-isotope systematics of stromatolitic limestones from the 2.7 Ga Ngezi group of the Belingwe greenstone belt: Constraints on timing of deposition and provenance. *Precambrian Research* 114(3–4), 277–294.

Bolhar, R., Whitehouse, M.J., Milani, L., Magalhães, N., Golding, S.D., Bybee, G., LeBras, L., Bekker, A., 2020. Atmospheric S and lithospheric Pb in sulphides from the 2.06 Ga Phalaborwa phoscorite-carbonatite complex, South Africa. *Earth and Planetary Science Letters* 530, 115939.

Bonnand, P., Parkinson I. J., Anand M., 2016. Mass-dependent fractionation of stable chromium isotopes in mare basalts: Implications for the formation and the differentiation of the Moon. *Geochimica et Cosmochimica Acta* 175, 208–221.

Bottinga, Y., 1969, Calculated fractionation factors between carbon and hydrogen isotope exchange in the system calcite-carbon dioxide-graphite-methane-hydrogen-water vapour. *Geochimica et Cosmochimica Acta* 33, 49–64.

Bottinga, Y., Javoy, M., 1973. Comments on oxygen isotope geothermometry. *Earth and Planetary Science Letters* 20, 250–265.

Bottrell, S.H., Greenwood, P.B., Yardley, B.W.D., Sheppard, T.J., Spiro, B., 1990. Metamorphic and post-metamorphic fluid flow in the low-grade rocks of the Harlech dome, north Wales. *Journal of Metamorphic Geology* 8, 131–143.

Bouvier, A., Boyet, M., 2016. Primitive solar system materials and Earth share a common initial ^{142}Nd abundance. *Nature* 537, 399–402.

Bouvier, A., Vervoort, J.D., Patchett, P.J., 2008. The Lu-Hf and Sm-Nd isotopic composition of CHUR: Constraints from unequilibrated chondrites and implications for the bulk composition of terrestrial planets. *Earth and Planetary Science Letters* 273(1–2), 48–57.

Bowen, N.L. 1928. *The evolution of the igneous rocks*. Princeton University Press.

Boynton, W.V., 1984. Geochemistry of the rare earth elements: Meteorite studies. In: Henderson, P. (ed.), *Rare earth element geochemistry*. Elsevier, Amsterdam. 63–114.

Boztug, D., Arehart, G.B., 2007. Oxygen and sulfur isotope geochemistry revealing a significant crustal signature in the genesis of the post-collisional granitoids in central Anatolia, Turkey. *Journal of Asian Earth Sciences* 30, 403–416.

Branson, O., Fehrenbacher, J.S., Vetter, L., Sadekov, A.Y., Eggins, S.M., Spero, H.J., 2019. LAtools: A data analysis package for the reproducible reduction of LA-ICPMS data. *Chemical Geology* 504, 83–95.

Brenan, J.M., Shaw, H.F., Ryerson, F.J., Phinney, D.L., 1995. Experimental determination of trace-element partitioning between pargasite and a synthetic hydrous andesitic melt. *Earth and Planetary Science Letters* I35, 1–11.

Brenan, J.M., Neroda, E., Lundstron, C., Shaw, H.F., Ryerson, F.J., Phinney, D.L., 1998. Behaviour of boron, beryllium, and lithium during melting and crystallization: Constraints from mineral-melt partitioning experiments. *Geochimica et Cosmochimica Acta* 62, 2129–2141.

Brewer, A., Teng, F.-Z., Dethier, D., 2018. Magnesium isotope fractionation during granite weathering. *Chemical Geology* 501, 95–103.

Brice, J.C., 1975. Some thermodynamic aspects of the growth of strained crystals. *Journal of Crystal Growth* 28, 249–253.

Brooks, C., Hart, S.R., Wendt, I., 1972. Realistic use of two-error regression treatments as applied to rubidium-strontium data. *Reviews of Geophysics* 10, 551–577.

Brophy, J.G., Ota, T., Kunihro, T., Tsujimori, T., Nakamura, E., 2011. In situ ion-microprobe determination of trace element partition coefficients for hornblende, plagioclase, orthopyroxene, and apatite in equilibrium with natural rhyolitic glass, Little Glass Mountain rhyolite, California. *American Mineralogist* 96, 1838–1850.

Brűgmann, G.E., Naldett, A.J., MacDonald, A.J., 1989. Magma mixing and constitutional zone refining in the Lac des Iles complex, Ontario: Genesis of platinum-group element mineralization. *Economic Geology* 84, 1557–1573.

Buccianti, A., Grunsky, E., 2014. Compositional data analysis in geochemistry: Are we sure to see what really occurs during natural processes? *Journal of Geochemical Exploration* 141, 1–5.

Buccianti, A., Mateu-Figueras, G., Pawlowsky-Glahn, V., 2006. *Compositional data analysis in the geosciences: From theory to practice*. Geological Society Special Publication 264. Geological Society, London.

Buccianti, A., Lima, A., Albaneses, S., De Vivo, B., 2018. Measuring the change under compositional data analysis (CoDA): Insight on the dynamics of geochemical systems. *Journal of Geochemical Exploration* 189, 100–108.

Buggle, B., Glasser, B., Hambach, U.F., Gerasimenko, N., Markovic, S., 2011. An evaluation of geochemical weathering indices in loess-palaeosol studies. *Quaternary International* 240, 12–21.

Burrows, D.R., Wood, P.C., Spooner, E.T.C., 1986. Carbon isotope evidence for a magmatic origin for Archean gold-quartz vein ore deposits. *Nature* 321, 851–854.

Busigny, V., Bebout, G., 2013. Nitrogen in the silicate Earth: Speciation and isotopic behavior during mineral–fluid interactions. *Elements* 9, 353–358.

Busigny, V., Chen, J.-B., Philippot, P., Borensztajn, S., Moynier, F., 2018. Insight into hydrothermal and subduction processes from copper and nitrogen isotopes in oceanic metagabbros. *Earth and Planetary Science Letters* 498, 54–64.

Butler, I.B., Fallick, A.E., Nesbitt, R.W., 1998. Mineralogy, sulphur isotope geochemistry and the development of sulphide structures at the Broken Spur hydrothermal vent site, 29°10′N, Mid-Atlantic Ridge. *Journal of the Geological Society, London* 155, 773–785.

Butler, J.C., 1979. Trends in ternary petrological variation diagrams: Fact or fantasy? *American Mineralogist* 64, 1115–1121.

Butler, J.C., 1981. Effect of various transformations on the analysis of percentage data. *Mathematical Geology* 13, 53–68.

Butler, J.C., 1982. Artificial isochrons. *Lithos* 15, 207–214.

Butler, J.C., 1986. The role of spurious correlation in the development of a komatiite alteration model. *Journal of Geophysical Research* 91, E275–E280.

Butler, J.C., Woronow, A., 1986. Discrimination among tectonic settings using trace element abundances of basalts. *Journal of Geophysical Research* 91, B10289–B10300.

Cabanis, B., Lecolle M., 1989. Le diagramme La/10-Y/15-Nb/8: Un outil pour la discrimination des series volcaniques et la mise en evidence des processus de melange et/ou de contamination crustale. *Comptes Rendus de l'Academie des sciences* 309(Ser. II), 2023–2029.

Campbell, A.C., et al., 1988. Chemistry of hot springs on the Mid-Atlantic Ridge. *Nature* 335, 514–519.

Carlson, R.W., 2005. Application of the Pt–Re–Os isotopic systems to mantle geochemistry and geochronology. *Lithos* 82(3–4), 249–272.

Carlson, R.W., 2014. Thermal ionisation mass spectrometry. In: Holland, H.D., Turekian, K.K. (eds.), *Treatise on geochemistry*, 2nd ed. Elsevier, Oxford. 15: 337–354.

Caro, G., Bourdon, B., 2010. Non-chondritic Sm/Nd ratio in the terrestrial planets: Consequences for the geochemical evolution of the mantle–crust system. *Geochimica et Cosmochimica Acta* 74, 3333–3349.

Carr, D.D., Rooney, L.F., 1983. Limestone and dolomite. In: Lefond, S.Y. (ed.), *Industrial minerals and rocks*, 5th ed. American Institute of Metallurgical, Mining and Petroleum Engineers, New York. 833–868.

Carr, M.J., Gazel, E., 2017. Igpet software for modelling igneous processes: Examples of application using the open educational version. *Mineralogy and Petrology* 111, 283–289.

Carr, P.F., 1985. Geochemistry of late Permian shoshonitic lavas from the southern Sydney Basin. In: Sutherland, F.L., Franklin, B.J., Waltho, A.E. (eds.), *Volcanism in Eastern Australia*. Geological Society of Australia, N.S.W. Division Publication 1, 165–183.

Cartigny, P. 2005. Stable isotopes and the origin of diamond. *Elements*, 1, 79–84.

Cartigny, P., Ader, M., 2003. A comment on 'The nitrogen record of crust–mantle interaction and mantle convection from Archean to Present' by B. Marty and N. Dauphas [Earth and Planetary Science Letters 206(2003) 397–410]. *Earth and Planetary Science Letters* 216, 425–432.

Cartigny, P., Marty, B., 2013. Nitrogen isotopes and mantle geodynamics: The emergence of life and the atmosphere–crust–mantle connection. *Elements* 9, 359–366.

Cassata, W.S., Renne, P.R., 2013. Systematic variations of argon diffusion in feldspars and implications for thermochronometry. *Geochimica et Cosmochiica Acta* 112, 251–287.

Cassata, W.S., Renne, P., Shuster, D., 2011. Argon diffusion in pyroxenes: Implications for thermochronometry and mantle degassing. *Earth and Planetary Science Letters* 304, 407–416.

Cavazzini, G., 1996. Degrees of contamination in magmas evolving by assimilation-fractional crystallization. *Geochimica et Cosmochimica Acta* 60, 2049–2052.

Cawood, P., Hawkesworth, C., Dhuime, B., 2012. Detrital zircon record and tectonic setting. *Geology* 40, 875–878.

Cazanas, X., Alfonso, P., Melgarejo, J.C., Proenza, J.A., Fallick, A.E., 2008. Geology, fluid inclusion and sulphur isotope characteristics of the El Cobre VHMS deposit, southern Cuba. *Mineralium Deposita* 43, 805–824.

Cesare, B., Acosta-Vigil, A., Bartoli, O., Ferrero, S., 2015. What can we learn from melt inclusions in migmatites and granulites? *Lithos* 239, 186–216.

Chacko, T., Cole, D.R., Horita, J., 2001. Equilibrium oxygen, hydrogen and carbon isotope fractionation factors applicable to geologic systems. In: Valley, J.W., Cole, D.R. (eds.), *Stable isotope geochemistry*. Mineralogical Society of America, Washington, DC. 1–81.

Chakhmouradian, A.R., Wall, F., 2012. Rare earth elements. *Elements* 8, 333–376.

Chakrabarti, R., Basu, A.R., Paul, D.K., 2007. Nd–Hf–Sr–Pb isotopes and trace element geochemistry of Proterozoic lamproites from southern India: Subducted komatiite in the source. *Chemical Geology* 236, 291–302.

Chamberlain, C.P., Rumble, D., 1988. Thermal anomalies in a regional metamorphic terrane: An isotopic study of the role of fluids. *Journal of Petrology* 29, 1215–1232.

Chan, L.H., 1987. Lithium isotope analysis by thermal ionisation mass-spectrometry of lithium tetraborate. *Analytical Chemistry* 59, 2662–2665.

Chan, L. H., Frey, F. A., 2003. Lithium isotope geochemistry of the Hawaiian plume: Results from the Hawaii Scientific Drilling Project and Koolau volcano. *Geochemistry Geophysics Geosystems* 4, 8707.

Chan, L.H., Leeman, W. P., Plank, T., 2006. Lithium isotopic composition of marine sediments. *Geochemistry, Geophysics, Geosystems* 7, doi: 10.1029/2005GC001202.

Chapman, J.B., Gehrels, G.E., Ducea, M.N., Giesler, N., Pullen, A., 2016. A new method for estimating parent rock trace element concentrations from zircon. *Chemical Geology* 439, 59–70.

Chappell, B.W., White, A.J.R., 1974. Two contrasting granite types. *Pacific Geology* 8, 173–174.

Chase, C., Patchett, P., 1988. Stored mafic/ultramafic crust and early Archean mantle depletion. *Earth and Planetary Science Letters* 91, 66–72.

Chaussidon, M., Deng, Z., Villeneuve, J., Moureau, J., Watson, B., Richter, F., Moynier, F., 2017. In-situ analysis of non-traditional isotopes by SIMS and LA-MC-ICP-MS: Key aspects and the example of Mg-isotopes in olivines and silicate glass. *Reviews in Mineralogy and Geochemistry* 82, 127–164.

Chauvel, C., 2018. Incompatible elements. In: White, W.M. (ed.), *Encyclopedia of geochemistry*. Springer. 719–721.

Chauvel, C., Blichert-Toft, J., 2001. A hafnium isotope and trace element perspective on melting of the depleted mantle. *Earth and Planetary Science Letters* 190(3–4), 37–151.

Chauvel, C., Rudnick, R.L., 2018. Large-ion lithophile elements. In: White, W.M. (ed.), *Encyclopedia of geochemistry*. Springer. 800–801.

Chayes, F., 1949. On ratio correlation in petrography. *Journal of Geology* 57, 239–254.
Chayes, F., 1960. On correlation between variables of constant sum. *Journal of Geophysical Research* 65, 4185–4193.
Chayes, F., 1971. *Ratio correlation*. University of Chicago Press.
Chayes, F., 1977. Use of correlation statistics with rubidium-strontium systematics. *Science* 196, 1234–1235.
Chen, C., Su, B.X., Xiao, Y., Sakyi, P.A., He, X.Q., Pang, K.N., Ibrahim, U., Erdi, A., Qin, L.P., 2019. High-temperature chromium isotope fractionation and its implications: Constraints from Kızıldag ophiolite, SE Turkey. *Lithos* 342, 361–369.
Chen, R.-X., Zheng, Y.-F., Gong, B., 2011. Mineral hydrogen isotopes and water contents in ultrahigh-pressure metabasite and metagranite: Constraints on fluid flow during continental subduction-zone metamorphism. *Chemical Geology* 281, 103–124.
Chen, Y., Huang, F., Shi, G.-H., Wu, F.-Y., Chen, X., Jin, Q.-Z., Su, B., Guo, S., Sein, K., Nyunt, T.T., 2018. Magnesium isotope composition of subduction zone fluids as constrained by jadeitites from Myanmar. *Journal of Geophysical Research: Solid Earth* 123, 7566–7585.
Chen, Y., Song, S., Niu, Y., Wei, C., 2014. Melting of continental crust during subduction initiation: A case study from the Chaidanuo peraluminous granite in the North Qilian suture zone. *Geochimica et Cosmochimica Acta* 132, 311–336.
Cherniak, D.J., 1993. Lead diffusion in titanite and preliminary results on the effects of radiation damage on Pb transport. *Chemical Geology* 110, 177–194.
Cherniak, D.J., 2000. Pb diffusion in rutile. *Contributions to Mineralogy and Petrology* 139, 198–207.
Cherniak, D.J., Watson, E.B., 1992. A study of strontium diffusion in K-feldspar, Na–K feldspar and anorthite using Rutherford backscattering spectroscopy. *Earth and Planetary Science Letters* 113, 411–425.
Cherniak, D.J., Watson, E.B., 2001. Pb diffusion in zircon. *Chemical Geology* 172, 1999–2017.
Cherniak, D.J., Hanchar, J., Watson, E., 1997. Rare earth diffusion in zircon. *Chemical Geology* 134, 289–301.
Cherniak, D.J., Lanford, W.A., Ryerson, F.J., 1991. Lead diffusion in apatite and zircon using ion implantation and Rutherford backscattering techniques. *Geochimica et Cosmochimica Acta* 55, 1663–1673.
Cherniak, D.J., Watson, E.B., Grove, M., Harrison, T.M., 2004. Pb diffusion in monazite: A combined RBS/SIMS study. *Geochimica et Cosmochimica Acta* 68, 829–840.
Chesner, C.A., Ettlinger, A.D., 1989. Composition of volcanic allanite from the TobaTuffs, Sumatra, Indonesia. *American Mineralogist* 74, 750–758.
Chivas, A.R., Andrew, A.S., Sinha, A.K., O'Neill, J.R., 1982. Geochemistry of a Pliocene-Pleistocene oceanic-arc plutonic complex, Guadalcanal. *Nature* 300, 139–143.
Clark, I., Harper, W.V., 2007. *Practical geostatistics 2000*. Ecosse North America, Columbus, OH.
Clark, R.N., Brown, R.H., Cruikshank, D.P., Swayze, G.A., 2019. Isotopic ratios of Saturn's rings and satellites: Implications for the origin of water and Phoebe. *Icarus* 321, 791–802.
Clauer, N., Fallick, A.E., Gálan, E., Aparicio, P., Miras, A., Fernández-Caliani, J.C., Aubert, A., 2015. Stable isotope constraints on the origin of kaolin deposits from Variscan granitoids of Galicia (NW Spain). *Chemical Geology* 417, 90–101.
Claypool, G.E., Holser, W.T., Kaplan, I.R., Sakai, H., Zak, I., 1980. The age curves of sulfur and oxygen isotopes in marine sulfate and their mutual interpretation. *Chemical Geology* 28, 199–260.
Clayton, R.N., 1981. Isotopic thermometry. In: Newton, R.C., Navrotsky, A., Wood, B.J. (eds.), *Thermodynamics of minerals and melts*. Springer-Verlag, New York. 85–109.
Clayton, R.N., Goldsmith, J.R., Mayeda, T.K., 1989. Oxygen isotope fractionation in quartz, albite, anorthite and calcite. *Geochimica et Cosmochimica Acta* 53, 725–733.
Clayton, R.N., O'Neill, J.R., Mayeda, T.K., 1972. Oxygen isotope exchange between quartz and water. *Journal of Geophysical Research* 77, 3057–3067.
Cliff, R.A., 1985. Isotopic dating in metamorphic belts. *Journal of the Geological Society* 142, 97–110.
Cliff, R.A., Bond, C.E., Butler, R.W.H., Dixon, J.E., 2017. Geochronological challenges posed by continuously developing tectonometamorphic systems: Insights from Rb- Sr mica ages from the Cycladic Blueschist Belt, Syros (Greece). *Journal of Metamorphic Geology* 35, 197–211.

Clog, M., Aubauda, C., Cartigny, P., Dosso, L., 2013. The hydrogen isotopic composition and water content of southern Pacific MORB: A reassessment of the D/H ratio of the depleted mantle reservoir. *Earth and Planetary Science Letters* 381, 156–165.

Cohen, A.S., Coe, A.L., Bartlett, J.M., Hawkesworth, C.J., 1999. Precise Re–Os ages of organic-rich mudrocks and the Os isotope composition of Jurassic seawater. *Earth and Planetary Science Letters* 167, 159–173.

Coleman, M.L., 1977. Sulphur isotopes in petrology. *Journal of the Geological Society* 133, 593–608.

Coleman, M.L., Raiswell, R., 1981. Carbon, oxygen and sulphur isotope variations in concretions from the Upper Lias of NE England. *Geochimica et Cosmochimica Acta* 45, 329–340.

Collerson, K.D., Kamber, B.S., 1999. Evolution of the continents and the atmosphere inferred from Th-U-Nb systematics of the depleted mantle. *Science* 283, 1519–1522.

Collerson, K.D., Campbell, L.M., Weaver, B.L., Palacz, Z.A. 1991. Evidence for extreme mantle fractionation in early Archaean ultramafic rocks from northern Labrador. *Nature* 349, 209–214.

Collins, W. J., Murphy, J.B., Johnson, T.E., Huang, H.-Q., 2020. Critical role of water in the formation of continental crust. *Nature Geoscience* 13, 331–338.

Coltice, N., Ferrachat, S., Ricard, Y., 2000. Box modelling the chemical evolution of geophysical systems: Case study of the Earth's mantle. *Geophysical Research Letters* 27, 1579–1582.

Compston, W, Williams, I.S., Meyer, C., 1984. U-Pb geochronology of zircons from lunar breccia 73217 using a sensitive high mass-resolution ion microprobe. *Journal of Geophysical Research* 89, Supplement, B525–B534.

Condie, K.C., 2005. High field strength element ratios in Archaean basalts: A window to evolving sources of mantle plumes? *Lithos* 79, 491–504.

Condie, K., 2015. Changing tectonic setting through time: Indiscriminate use of geochemical discriminant diagrams. *Precambrian Research* 266, 587–591.

Condie, K.C., Aster, R.C., 2010. Episodic zircon age spectra of orogenic granitoids: The supercontinent connection and continental growth. *Precambrian Research* 180, 227–236.

Condie, K.C., Wronkiewicz, D.J., 1990. A new look at the Archaean-Proterozoic boundary sediments and the tectonic setting constraint. In: *Developments in Precambrian Geology*. Elsevier. 8: 61–83.

Condie, K.C., Wilks, M., Rosen, D.M., Zlobin, V.L., 1991. Geochemistry of metasediments from the Precambrian Hapschan series, eastern Anabar Shield, Siberia. *Precambrian Research* 50, 37–47.

Coogan, L.A., Dosso, S.E., 2016. Quantifying parental MORB trace element compositions from eruptive prodicts of realistic magma chambers: Parental EPR MORB are depleted. *Journal of Petrology* 57, 2105–2126.

Cortés, J.A., 2009. On the Harker variation diagrams: A comment on 'The statistical analysis of compositional data. Where are we and where should we be heading? by Aitchison and Egozcue (2005). *Mathematical Geosciences* 41, 817–828.

Coryell, C.G., Chase, J.W., Winchester, J.W., 1963. A procedure for geochemical interpretation of terrestrial rare-earth abundance patterns. *Journal of Geophysical Research* 68, 559–566.

Cox, K.G., Bell, J.D., Pankhurst, R.J., 1979, *The interpretation of igneous rocks*. George, Allen and Unwin, London.

Cox, R., Lowe, D.R., Cullers, R.L., 1995. The influence of sediment recycling and basement composition on evolution of mudrock chemistry in the southwestern United States. *Geochimica et Cosmochimica Acta* 59(14), 2919–2940.

Craig, H., 1961. Isotopic variations in meteoric waters. *Science* 133, 1702–1703.

Cribb, J.-W., Barton, M., 1996. Geochemical effects of decoupled fractional crystallisation and crustal assimilation. *Lithos* 37, 293–307.

Crockford, P.W., et al., 2019. Claypool continued: Extending the isotopic record of sedimentary sulfate. *Chemical Geology* 513, 200–225.

Cross, W., Iddings, J.P., Pirsson, L.V., Washington, H.S., 1902. *Quantitative classification of igneous rocks: Based on chemical and mineral characters, with a systematic nomenclature*. University of Chicago Press.

Crow, M.J., Van Waveren, I.M., Hasibuan, F., 2019. The geochemistry, tectonic and palaeogeographic setting of the Karing Volcanic Complex and the Dusunbaru pluton, an early Permian volcanic-plutonic centre in Sumatra, Indonesia. *Journal of Asian Earth Sciences* 169, 257–283.

Cullers, R.L., 1988. Mineralogical and chemical changes of soil and stream sediment formed by intense weathering of the Danburg granite, Georgia, U.S.A. *Lithos* 21, 301–314.

Cullers, R.L., 2000. The geochemistry of shales, siltstones and sandstones of Pennsylvanian-Permian ages, Colorado, USA: Implications for provenance and metamorphic studies. *Lithos* 51, 181–203.

Cullers, R.L., Basu, A., Suttner, L.J., 1988. Geochemical signature of provenance in sand-sized material in soils and stream sediments near the Tobacco Root batholith, Montana, U.S.A. *Chemical Geology* 70, 335–348.

Dalpe, C., Baker, D.R., 2000. Experimental investigation of large-ion-lithophile-element, high-field-strength-element and rare-earth-element-partitioning between calcic amphibole and basaltic melt: The effects of pressure and oxygen fugacity. *Contributions to Mineralogy and Petrology* 140, 233–250.

Dasgupta, R., Hirschmann, M.M., 2010. The deep carbon cycle and melting in Earth's interior. *Earth and Planetary Science Letters* 298, 1–13.

Daunis-I-Estadella, J., Barcelo-Vidal, C., Buccianti, A., 2006. Exploratory compositional data analysis. In: Buccianti, A., Mateu-Figueras, G., Pawlowsky-Glahn, V. (eds.), *Compositional data analysis in the geosciences: From theory to practice*. Geological Society Special Publication 264. Geological Society, London. 161–174.

Dauphas, N., John, S., Rouxel, O., 2017. Iron isotope systematics. *Reviews in Mineralogy and Geochemistry* 82, 415–510.

Davis, F.A., Humayun, M., Hirschmann, M.M., Cooper, R.S., 2013. Experimentally determined mineral/melt partitioning of first-row transition elements (FRTE) during partial melting of peridotite at 3 GPa. *Geochimica et Cosmochimica Acta* 104, 232–260.

Davis, J.C., 2002. *Statistics and data analysis in Geology*, 3rd ed. Wiley and Sons, Hoboken, NJ.

Day, J.M.D., Brandon, A.D., Walker, R.A., 2016. Highly siderophile elements in earth, mars, the moon, and asteroids. *Reviews in Mineralogy & Geochemistry* 81, 161–238.

de Graaf, S., Nooitgedacht, C.W., Le Goff, J., van der Lubbe, J.H.J.L. Vonhof, H.B., Reijmer, J.J.G., 2019. Fluid-flow evolution in the Albanide fold-thrust belt: Insights from hydrogen and oxygen isotope ratios of fluid inclusions. *American Association of Petroleum Geologists Bulletin* 103, 2421–2445.

de Hoog, J.C.M., Taylor, B.E., van Bergen, M.J., 2001. Sulfur isotope systematics of basaltic lavas from Indonesia: Implications for the sulfur cycle in subduction zones. *Earth and Planetary Science Letters* 189, 237–252.

de la Roche, H., Leterrier, J., Grande Claude, P., Marchal, M., 1980. A classification of volcanic and plutonic rocks using R1-R2 diagrams and major element analyses: Its relationships and current nomenclature. *Chemical Geology* 29, 183–210.

de Moor, J.M., Fischer, T.P., Sharp, Z.D., Hilton, D.R., Barry, P.H., Mangasini, F., Ramirez, C., 2013. Gas chemistry and nitrogen isotope compositions of cold mantle gases from Rungwe Volcanic Province, southern Tanzania. *Chemical Geology* 339, 30–42.

Deines, P., 2002. The carbon isotope geochemistry of mantle xenoliths. *Earth Science Reviews.* 58, 247–278.

Deines, P., Gold, D.P, 1973. The isotopic composition of carbonatite and kimberlite carbonates and their bearing on the isotopic composition of deep-seated carbon. *Geochimica et Cosmochimica Acta* 37, 1709–1733.

Deines, P., Stachel, T., Harris, J.W., 2009. Systematic regional variations in diamond carbon isotopic compositions and inclusion chemistry beneath the Orapa kimberlite cluster in Botswana. *Lithos* 112, 776–784.

Delavault, H., Dhuime, B., Hawkesworth, C.J., Cawood, P.A., Marschall, H., Edinburgh Ion Microprobe Facility, 2016. Tectonic settings of continental crust formation: Insights from Pb isotopes in feldspar inclusions in zircon. *Geology* 44, 819–822.

Delbari, M., Afrasiab, P., Loiskandl, W., 2011. Geostatistical analysis of soil texture fractions on the field scale. *Soil and Water Resources* 6, 173–189.

Demetriades, A., 2014. Basic considerations: Sampling, the key for a successful applied geochemical survey for mineral exploration and environmental purposes. In: Holland, H.D., Turekian, K.K. (eds.), *Treatise on geochemistry*, 2nd ed. Elsevier, Oxford. 15: 1–31.

Demšar, U., Harris, P., Brunsdon, C., Fotheringham, S., McLoone, S., 2013. Principal component

analysis on spatial data: An overview. *Annals of the Association of American Geographers* 103, 106–128.

Deng, Z., Chaussidon, M., Guitreau, M., Puchtel, I.S., Dauphas, N., Moynier, F., 2019. An oceanic subduction origin for Archaean granitoids revealed by silicon isotopes. *Nature Geoscience* 12, 774–778.

Denny, A.C., Orland, I.J., Valley, J.W., 2020. Regionally correlated oxygen and carbon isotope zonation in diagenetic carbonates of the Bakken formation. *Chemical Geology* 531, 119327.

DePaolo, D.J., 1981a. Neodymium isotopes in the Colorado Front range and crust–mantle evolution in the Proterozoic. *Nature* 291, 193–196.

DePaolo, D.J., 1981b. Trace element and isotopic effects of combined wallrock assimilation and fractional crystallisation. *Earth and Planetary Science Letters* 53, 189–202.

DePaolo, D.J., 1988. *Neodymium isotope geochemistry: An introduction*. Springer Verlag, Berlin.

DePaolo, D.J., Wasserburg, G.J., 1976. Nd isotopic variations and petrogenetic models. *Geophysical Research Letters* 3, 249–252.

DePaolo, D.J., Wasserburg, G.J., 1979. Petrogenetic mixing models and Nd-Sr isotopic patterns. *Geochimica et Cosmochimica Acta* 43, 615–627.

Dhuime, B., Hawkesworth, C.J., Cawood, P.A., Storey, C.D., 2012. A change in the geodynamics of continental growth 3 billion years ago. *Science* 335, 1334–1336.

Dhuime, B., Wuestefeld, A., Hawkesworth, C.J., 2015. Emergence of modern continental crust about 3 billion years ago. *Nature Geoscience* 8, 552–555.

Dickson, J.A.D., 1991. Disequilibrium carbon and oxygen isotope variations in natural calcite. *Nature* 353, 842–844.

Dodson, M.H., 1973. Closure temperature in cooling geochronological and petrological systems. *Contributions to Mineralogy and Petrology* 40, 259–274.

Dodson, M.H., 1979. Theory of cooling ages. In: Jager, E., Hunziker, J.C. (eds.), *Lectures in isotope geology*. Springer-Verlag, New York. 194–202.

Dodson, M.H., 1982. On 'spurious' correlations in Rb-Sr isochron diagrams. *Lithos* 15, 215–219.

Doe, B.R., Zartman R.E., 1979. Plumbotectonics I, the Phanerozoic. In: Barnes, H.L. (ed.), *Geochemistry of hydrothermal ore deposits*, 2nd ed. Wiley-Interscience, New York. 22–70.

Dottin, J.W., Labidi, J., Lekic, V., Jackson, M.G., Farquhar, J., 2020. Sulfur isotope characterization of primordial and recycled sources feeding the Samoan mantle plume. *Earth and Planetary Science Letters* 534, 116073.

Drake, M.J., Holloway, J.R., 1981. Partitioning of Ni between olivine and silicate melt: the 'Henry's Law problem' re-examined. *Geochimica et Cosmochimica Acta* 45, 431–437.

Drake, M.J., Weill, D.F., 1975. Partition of Sr, Ba, Ca, Y, Eu^{2+}, Eu^{3+} and other REE between plagioclase feldspar and magmatic liquid: An experimental study. *Geochimica et Cosmochimica Acta* 39, 689–712.

Drummond, M.S., Defant, M.J., 1990. A model for trondhjemite-tonalite-dacite genesis and crustal growth via slab melting: Archean to modern comparisons. *Journal of Geophysical Research: Solid Earth* 95(B13), 21503–21521.

Dunham, R.J., 1962. Classification of carbonate rocks according to depositional textures. *American Association of Petroleum Geologists Memoir* 1, 108–121.

Dunn, T., 1987. Partitioning of Hf, Lu, Ti and Mn between olivine, clinopyroxene and basaltic liquid. *Contributions to Mineralogy and Petrology* 96, 476–484.

Dunn, T., Sen, C., 1994. Mineral/matrix partition coefficients for orthopyroxene, plagioclase, and olivine in basaltic to andesitic systems: A combined analytical and experimental study. *Geochimica et Cosmochimica Acta* 58, 717–733.

Dupre, B., Allegre, C.J., 1983. Pb-Sr isotope variation in Indian Ocean basalts and mixing phenomena. *Nature* 303, 142–146.

Ebadi, A., Johannes, W., 1991. Beginning of melting and composition of first melts in the system Qz-Ab-Or-H_2O-CO_2. *Contribution to Mineralogy and Petrology* 106, 286–295.

Egozcue, J.J., 2009. Reply to 'On the Harker Variation Diagrams . . .' by JA Cortes. *Mathematical Geosciences* 41, 829–834.

Egozcue, J., Pawlowsy-Glahn, V., Mateu-Figueras, G., Barcelo-Vidal, C., 2003. Isometric logratio transformations for compositional data analysis. *Mathematical Geology* 35, 279–300.

Eguchi, J., Seales, J., Dasgupta, R., 2020. Great oxidation and Lomagundi events linked by deep

cycling and enhanced degassing of carbon. *Nature Geoscience* 12, 71–76.

Eiler, J.M., 2001. Oxygen isotope variations of basaltic lavas and upper mantle rocks. *Reviews in Mineralogy and Geochemistry* 43(1), 319–364.

Eiler, J.M., 2007. 'Clumped-isotope' geochemistry: The study of naturally-occurring, multiply-substituted isotopologues. *Earth and Planetary Science Letters* 262, 309–327.

Eiler, J.M., Kitchen, N., 2004. Hydrogen isotope evidence for the origin and evolution of the carbonaceous chondrites. *Geochimica et Cosmochimica Acta* 68, 1395–1411.

Eisele, J., Sharma, M., Galer, S.J., Blichert-Toft, J., Devey, C.W., Hofmann, A.W., 2002. The role of sediment recycling in EM-1 inferred from Os, Pb, Hf, Nd, Sr isotope and trace element systematics of the Pitcairn hotspot. *Earth and Planetary Science Letters* 196, 197–212.

Eissen, J.-P., Juteau, T., Joron, J.-L., Dupre, B., Humler, E., Al'Mukhamedov, A., 1989. Petrology and geochemistry of basalts from the Red Sea axial rift at 18 deg north. *Journal of Petrology* 30, 791–839.

Elardo, S.M., Shahar, A., Mock, T.D., Sio, C.K., 2019. The effect of core composition on iron isotope fractionation between planetary cores and mantles. *Earth and Planetary Science Letters* 513, 124–134.

Elderfield, H., 1988. The oceanic chemistry of the rare-earth elements. *Philosophical Transactions of the Royal Society of London* A325, 105–126.

El-Hinnawi E., 2016a. Evaluation of boundary lines in the total alkali-silica diagram for the discrimination between subalkali and alkali basalts, and a new method to distinguish transitional basalts. *Periodico di Mineralogia* 85, 51–58.

El-Hinnawi, E., 2016b. A new method for the adjustment of Fe_2O_3/FeO ratio in volcanic rocks for the calculation of the CIPW norm. *Neues Jahrbuch für Mineralogie-Abhandlungen: Journal of Mineralogy and Geochemistry* 193, 87–93.

Elliott, T., Thomas, A., Jeffcoate, A., Niu, Y., 2006. Lithium isotope evidence for subduction-enriched mantle in the source of mid-ocean-ridge basalts. *Nature* 443, 565–568.

Elthon, D., 1983. Isomolar and isostructural pseudo-liquidus phase diagrams for oceanic basalts. *American Mineralogist* 68, 506–511.

Epstein, G.S., Bebout, G.E., Angiboust, S., Agard, P., 2020. Scales of fluid-rock interaction and carbon mobility in the deeply underplated and HP-metamorphosed schistes lustrés, western Alps. *Lithos* 354–355, 105229.

Epstein, S., Buchsbaum, R., Lowenstam, H.A., Urey, H.C., 1953. Revised carbonate–water isotopic temperature scale. *Geological Society of America Bulletin* 64, 1315–1326.

Escoube, R., Rouxel, O.J., Pokrovsky, O.S., Schroth, A., Holmes, R.M., Donard, O.F.X., 2015. Iron isotope systematics in Arctic rivers. *Comptes Rendus Geoscience* 347, 377–385.

Escrig, S., Schiano, P., Schilling, J.G., Allegre, C., 2005. Rhenium–osmium isotope systematics in MORB from the southern Mid-Atlantic Ridge (40–50 S). *Earth and Planetary Science Letters* 235, 528–548.

Evensen, N.M., Hamilton, P.J., O'Nions, R.K., 1978. Rare earth abundances in chondritic meteorites. *Geochimica et Cosmochimica Acta* 42, 1199–1212.

Ewart, A., 1982. The mineralogy and petrology of Tertiary-recent orogenic volcanic rocks with special reference to the andesitic-basaltic composition range. In: Thorpe, R.S. (ed.), *Andesites*. Wiley, Chichester. 25–87.

Falloon, T.J., Danyushevsky, L.V., Green, D.H., 2001. Peridotite melting at 1 GPa: Reversal experiments on partial melt compositions produced by peridotite–basalt sandwich experiments. *Journal of Petrology* 42, 2363–2390.

Farkas, J., Chrastny, V., Novak, M., Cadkova, E., Pasava, J., Chakrabarti, R., Jacobsen, S.B., Ackerman L., Bullen T.D., 2013. Chromium isotope variations (δ^{53}Cr) in mantle-derived sources and their weathering products: Implications for environmental studies and the evolution of δ^{53}Cr in the Earth's mantle over geologic time. *Contributions to Mineralogy and Petrology* 123, 74–92.

Farley, K.A., 2000. Helium diffusion from apatite: General behavior as illustrated by Durango fluorapatite. *Journal of Geophysical Research* 105, 2903–2914.

Farley, K.A., 2007. He diffusion systematics in minerals: Evidence from synthetic monazite and zircon structure phosphates. *Geochimica et Cosmochimica Acta* 71, 4015–4024.

Farley, K.A., Natland, J.H., Craig, H., 1992. Binary mixing of enriched and undegassed (primitive?)

mantle components (He, Sr, Nd, Pb) in Samoan lavas. *Earth and Planetary Science Letters* 111, 183–199.

Farmer, G.L., 2014. Continental basaltic rocks. In: Holland, H.D., Turekian, K.K. (eds.), *Treatise on geochemistry*, 2nd ed. Elsevier, Oxford. 4: 75–110.

Farquhar, J., Wing, B.A., 2003. Multiple sulfur isotopes and the evolution of the atmosphere. *Earth and Planetary Science Letters* 213, 1–13.

Farquhar J., Wing, B.A., McKeegan, K.D., Harris, J.W., Cartigny, P., Thiemens, M.H., 2002. Mass-independent sulfur of inclusions in diamond and sulfur recycling on early Earth. *Science* 298, 2369–2372.

Farrel, J., Clemens, S., Gromet, L.P., 1995. Improved chronostratigraphic reference curve of late Neogene seawater $^{87}Sr/^{86}Sr$. *Geology* 23, 403–406.

Fazio, G., Mendes Guimarães, E., Walde, D.W.G., do Carmo, D.A., Adorno, R.R., et al., 2019. Mineralogical and chemical composition of Ediacaran-Cambrian pelitic rocks of the Tamengo and Guaicurus formations (Corumbá Group – MS, Brazil): Stratigraphic positioning and paleoenvironmental interpretations. *Journal of South American Earth Sciences* 90, 487–503.

Fedo, C.M., McGlynn, I.O., McSween, H.Y., Jr, 2015. Grain size and hydrodynamic sorting controls on the composition of basaltic sediments: Implications for interpreting Martian soils. *Earth and Planetary Science Letters* 423, 67–77.

Fedo, C.M., Wayne Nesbitt, H., Young, G.M., 1995. Unraveling the effects of potassium metasomatism in sedimentary rocks and paleosols, with implications for paleoweathering conditions and provenance. *Geology* 23(10), 921–924.

Fiege, A., Holtz, F., Behrens, H., Mandeville, C., Shimizu, N., Crede, L.-S., Goettlicher, J., 2015. Experimental investigation of the S and S-isotope distribution between H_2O-S ± Cl fluids and basaltic melts during decompression. *Chemical Geology* 393–394, 36–54.

Fitton, J.G., 1997. X-ray fluorescence spectrometry. In: Gill, R. (ed.), *Modern analytical geochemistry: An introduction to quantitative chemical analysis for earth, environmental and material scientists*. Addison Wesley Longman, Harlow.

Fitton, J.G., Saunders, A.D., Norry, M.J., Hardarson, B.S., Taylor, R.N., 1997. Thermal and chemical structure of the Iceland plume. *Earth and Planetary Science Letters* 153, 197–208.

Fletcher, I.R., Rosman, K.J.R., 1982. Precise determination of initial e-Nd from Sm-Nd isochron data. *Geochimica et Cosmochimica Acta* 46, 1983–1987.

Fletcher, T.A., Boyce, A.J., Fallick, A.E., 1989. A sulphur isotope study of Ni-Cu mineralisation in the Huntly-Knock Caledonian mafic and ultramafic intrusions of northeast Scotland. *Journal of the Geological Society* 146, 675–684.

Floyd, P.A., Winchester, J.A., 1975. Magma-type and tectonic setting discrimination using immobile elements. *Earth and Planetary Science Letters* 27, 211–218.

Floyd, P.A., Shail, R., Leveridge, B.E., Franke, W., 1991. *Geochemistry and provenance of Rhenohercynian synorogenic sandstones: Implications for tectonic environment discrimination*. Geological Society Special Publication 57. Geological Society, London. 173–188.

Floyd, P.A., Winchester, J.A., Park, R.G., 1989. Geochemistry and tectonic setting of Lewisian clastic metasediments from the early Proterozoic Loch Maree group of Gairloch, NW Scotland. *Precambrian Research* 45, 203–214.

Fogel, M.L., Steele, A., 2013. Nitrogen in extraterrestrial environments: Clues to the possible presence of life. *Elements* 9, 367–372.

Foland, K.A., 1994. Argon diffusion in feldspars. In: Parsons, I. (ed.), *Feldspars and their reactions*. Kluwer, Amsterdam. 415–447.

Foley, S., Tiepolo, M., Vannucci, R., 2002. Growth of early continental crust controlled by melting of amphibolite in subduction zones. *Nature* 417, 837–840.

Folk, R.L., 1959. Practical petrographic classification of limestones. *American Association of Petroleum Geologists Bulletin* 43, 1–38.

Foustoukos, D.I., James, R.H., Berndt, M.E., Seyfried, W.E., 2004. Lithium isotopic systematics of hydrothermal vent fluids at the Main Endeavour Field, Northern Juan de Fuca Ridge. *Chemical Geology* 212, 17–26.

Fowler, S.J., Bohrson, W.A., Spera, F.J., 2004. Magmatic evolution of the Skye Igneous Centre, western Scotland: Modelling of assimilation, recharge and fractional crystallization. *Journal of Petrology* 45, 2481–2505.

France, L., Ouillon, N., Chazot, N, Kornprobst, J., Boivin, P., 2009. CMAS 3D, a new program to

visualize and project major elements compositions in the CMAS system. *Computers and Geosciences* 35, 1304–1310.

Frank, A.B., Klaebe, R.B., Lohr, S., Xu, L., Frei, R., 2020. Chromium isotope composition of organic-rich marine sediments and their mineral phases and implications for using black shales as a paleoredox archive. *Geochimica et Cosmochimica Acta* 270, 338–359.

Frank, M., 2002. Radiogenic isotopes: Tracers of past ocean circulation and erosional input. *Reviews of Geophysics* 40, 1–38.

Frei, R., Polat, A., 2013. Chromium isotope fractionation during oxidative weathering: Implications from the study of a Paleoproterozoic (ca. 1.9 Ga) paleosol, Schreiber Beach, Ontario, Canada. *Precambrian Research* 224, 434–453.

Friedman, I., O'Neill, J.R., 1977. Data of geochemistry: Compilation of stable isotope fractionation factors of geochemical interest. US Geological Survey Professional Paper 440-KK.

Frost, B.R., Frost, C.D., 2008. A geochemical classification for feldspathic igneous rocks. *Journal of Petrology* 49, 1955–1969.

Frost, B.R., Barnes, C.G., Collins, W.J., Arculus, R.J., Ellis, D.J., Frost, C.D., 2001. A geochemical classification for granitic rocks. *Journal of Petrology* 42, 2033–2048.

Fukuda, K., Beard, B.L., Dunlap, D.R., Spicuzzaa, M.J., Fournelle, J.H., Wadhwa, M., Kita, N.T., 2020. Magnesium isotope analysis of olivine and pyroxene by SIMS: Evaluation of matrix effects. *Chemical Geology* 540, 119482.

Gabriel, K.R., 1971. The biplot graphic display of matrices with application to principal component analysis. *Biometrika* 58, 453–467.

Gaetani, G.A, Kent, A.J.R., Grove, T.L., Hutcheon, D., Stolper, E.M., 2003. Mineral/melt partitioning of trace elements during hydrous peridotite partial melting. *Contributions to Mineralogy and Petrology* 145, 391–405.

Galy, A., France-Lanord, C., 2001. Higher erosion rates in the Himalaya: Geochemical constraints on riverine fluxes. *Geology* 29, 23–26.

Ganguly, J., Tirrone, M., Hervig, R.L., 1998. Diffusion kinetics of samarium and neodymium in garnet, and a method for determining cooling rates of rocks. *Science* 281, 805–807.

Garapić, G., Jackson, M.G., Hauri, E.H., Hart, S.R., Farley, K.A., Blusztajn, J.S., Woodhead, J.D., 2015. A radiogenic isotopic (He-Sr-Nd-Pb-Os) study of lavas from the Pitcairn hotspot: Implications for the origin of EM-1 (enriched mantle 1). *Lithos* 228, 1–11.

Garcia, M.O., Mucek, A.E., Lynn, K.J., Swanson, D.A., Norman, M.D., 2018. Geochemical evolution of Keanakāko ʻi Tephra, Kīlauea Volcano, Hawaiʻi. In: *Field volcanology: A tribute to the distinguished career of Don Swanson*. Geological Society Special Publication 538. Geological Society, London.

Garçon, M., Chauvel, C., 2014. Where is basalt in river sediments, and why does it matter? *Earth and Planetary Science Letters* 407, 61–69.

Garzanti, E., 2019. Petrographic classification of sand and sandstone. *Earth-Science Reviews* 192, 545–563.

Geng, X., Liu, Y., Zhang, W., Wang, Z., Hu, Z., Zhou, L., Liang, Z., 2020. The effect of host magma infiltration on the Pb isotopic systematics of lower crustal xenolith: An in-situ study from Hannuoba, North China. *Lithos*, doi: 10.1016/j.lithos.2020.105556.

Genske, F.S., Turner, S.P., Beier, C., Chu, M.-F., Tonarini, S., Pearson, N.J., Haase, K.M., 2014. Lithium and boron isotope systematics in lavas from the Azores islands reveal crustal assimilation. *Chemical Geology* 373, 27–36.

Gerdes, A., Zeh, A., 2006. Combined U–Pb and Hf isotope LA-(MC-) ICP-MS analyses of detrital zircons: Comparison with SHRIMP and new constraints for the provenance and age of an Armorican metasediment in Central Germany. *Earth & Planetary Science Letters* 249, 47–61.

Ghiorso, M.S., Gualda, G.A.R., 2015. An H_2O-CO_2 mixed fluid saturation model compatible with rhyolite-MELTS. *Contributions to Mineralogy and Petrology*, doi: 10.1007/s00410-015-1141-8.

Ghiorso, M.S., Sack, R.O., 1995. Chemical mass transfer in magmatic processes IV. A revised and internally consistent thermodynamic model for the interpolation and extrapolation of liquid-solid equilibria in magmatic systems at elevated temperatures and pressures. *Contributions to Mineralogy and Petrology* 119, 197–212.

Gibson, S.A., Thompson, R.N., Dickin, A.P., 2000. Ferropicrites: Geochemical evidence for Fe-rich streaks in upwelling mantle plumes. *Earth and Planetary Science Letters* 174, 355–374.

Giletti, B.J., 1974. Studies in diffusion I: Argon in phlogopite mica. In: Hofmann, A.W., Giletti, B.J.,

Yoder, H.S., Jr, Yund, R.A. (eds.), *Geochemical transport and kinetics*. Carnegie Institute, Washington Year b Publication 634, Washington, DC. 107–115.

Gill, J.B., 1981. *Orogenic andesites and plate tectonics*. Springer, Berlin.

Gill, R.C.O. (ed.), 1997. *Modern analytical geochemistry: An introduction to quantitative chemical analysis for earth, environmental and material scientists*. Addison Wesley Longman, Harlow.

Gilliam, C.E., Valley, J.W., 1998. Low $\delta^{18}O$ magma, Isle of Skye, Scotland: Evidence from zircons. *Geochimica et Cosmochimica Acta* 61, 4975–4981.

Godefroy-Rodríguez, M., Hagemann, S., LaFlamme, C., Fiorentini, M., 2020. The multiple sulfur isotope architecture of the Golden Mile and Mount Charlotte deposits, Western Australia. *Mineralium Deposita* 55, 797–822.

Goldfarb, R.J., Groves, D.I., 2015. Orogenic gold: Common or evolving fluid and metal sources through time. *Lithos* 233, 2–26.

Goldschmidt, V.M., 1937. The principles of the distribution of chemical elements in minerals and rocks. *Journal of the Chemical Society (London)* 140, 655–673.

Goldstein, S.L., 1988. Decoupled evolution of Nd and Sr isotopes in the continental crust. *Nature* 336, 733–738.

Goldstein, S.L., O'Nions, R.K., Hamilton, P.J., 1984. A Sm-Nd study of atmospheric dusts and particulates from major river systems. *Earth and Planetary Science Letters* 70, 221–236.

González-Guzmán, R., 2016. NORRRM: A free software to calculate the CIPW norm. *Open Journal of Geology* 6, 30–38. http://dx.doi.org/10.4236/ojg.2016.61004.

Goodwin, A.M., 1996. *Principles of Precambrian geology*. Academic Press, London.

Grady, M.M., Wright, I.P., 2003. Elemental and isotopic abundances of carbon and nitrogen in meteorites. *Space Science Reviews* 106, 231–248.

Graham C.M., Harmon, R.S., Sheppard, S.M.F., 1984. Experimental hydrogen isotope studies: Hydrogen isotope exchange between amphibole and water. *American Mineralogist* 69, 128–138.

Graham C.M., Sheppard, S.M.F., Heaton, T.H.E., 1980. Experimental hydrogen isotope studies I: Systematics of hydrogen isotope fractionation in the systems epidote–H_2O, zoisite–H_2O and AlO(OH)–H_2O. *Geochimica et Cosmochimica Acta* 44, 353–364.

Graham, D.J., Midgley, N.G., 2000. Graphical representation of particle shape using triangular diagrams: An Excel spreadsheet method. *Earth Surface Processes and Landforms* 25, 1473–1477.

Grandell, L., Lehtilä, A., Kivinen, M., Koljonen, T., Kihlman, S., Lauri, L.S., 2016. Role of critical metals in the future markets of clean energy technologies. *Renewable Energy* 95, 53–62.

Grant, K., Wood, B., J., 2010. Experimental study of the incorporation of Li, Sc, Al and other trace elements in olivine. *Geochimica et Cosmochimica Acta* 74, 2412–2428.

Grassineau, N.V., Appel, P.W.U., Fowler, C.M.R., Nisbet, E.G., 2005. Distinguishing biological from hydrothermal signatures via sulphur and carbon isotopes in Archaean mineralizations at 3.8 and 2.7 Ga. In: McDonald, I., Boyce, A.J., Butler, I.B., Herrington, R.J., Polya, D.A. (eds.), *Mineral deposits and Earth evolution*. Geological Society Special Publication 248. Geological Society, London. 195–212.

Green, T.H., Pearson, N.J., 1983. Effect of pressure on rare earth element partition coefficients in common magmas. *Nature* 305, 414–416.

Green, T.H., Pearson N.J., 1986. Rare-earth element partitioning between sphene and coexisting silicate liquid at high pressure and temperature. *Chemical Geology* 55, 105–119.

Green, T.H., Blundy, J.D., Adam, J., Yaxley, G.M., 2000. SIMS determination of trace element partition coefficients between garnet, clinopyroxene and hydrous basaltic liquids at 2–7.5 GPa and 1080–1200°C. *Lithos* 53, 165–187.

Greenacre, M., 2010. *Biplots in practice*. Fundcion BBVA, Bilbao.

Gregory, R.T., Taylor, H.P., 1981. An oxygen isotope profile in a section of Cretaceous oceanic crust, Semail ophiolite Oman: Evidence for $\delta^{18}O$ buffering of the oceans by deep (> 5 km) seawater-hydrothermal circulation at mid-ocean ridges. *Journal of Geophysical Research* 86, 2737–2755.

Gregory R.T., Criss, R.E., Taylor, H.P., 1989. Oxygen isotope exchange kinetics of mineral pairs in close and open systems: Applications to problems of hydrothermal alteration of igneous rocks and Precambrian iron formations. *Chemical Geology* 75, 1–42.

Gromet, L.P., Dymek, R.F., Haskin, L.A., Korotev, R.L., 1984. The 'North American Shale Composite': Its compilation, major and trace element characteristics. *Geochimica et Cosmochimica Acta* 48, 2469–2482.

Grove, M., Harrison, T.M., 1996. 40Ar* diffusion in Fe-rich biotite. *American Mineralogist* 81, 940–951.

Grove, T.L., 1993. Corrections to expressions for calculating mineral components in 'Origin of calc-alkaline series lavas at Medicine Lake Volcano by fractionation, assimilation and mixing' and 'Experimental petrology of normal MORB near the Kane Fracture Zone: 22°–25°N Mid-Atlantic Ridge'. *Contributions to Mineralogy and Petrology* 114, 422–424.

Grove, T.L., Gerlach, D.C, Sando, T.W., 1982. Origin of late calc-alkaline series lavas at Medicine Lake Volcano by fractionation, assimilation and mixing. *Contributions to Mineralogy and Petrology* 80, 160–182.

Grove, T.L., Kinzler, R.J., Bryan, W.B., 1992. Fractionation of mid-ocean ridge basalt (MORB). In: Phipps Morgan, J., Blackman, D.K., Sinton, J.M. (eds.), *Mantle flow and melt generation at mid-ocean ridges*. Geophysical Monograph, American Geophysical Union, 71, 281–310.

Groves, D.I., Golding, S.D., Rock, N.M.S., Barley, M.E., McNaughton, N.J., 1988. Archean carbon reservoirs and their relevance to the fluid source for gold deposits. *Nature* 331, 254–257.

Grunsky, E., de Caritat, P., 2019. State-of-the-art analysis of geochemical data for mineral exploration. *Geochemistry: Exploration, Environment, Analysis*, doi.org/10.1144/geochem2019–031.

Gualda, G.A.R., Ghiorso, M.S., Lemons, R.V., Carley, T.L., 2012. Rhyolite-MELTS: A modified calibration of MELTS optimized for silica-rich, fluid-bearing magmatic systems. *Journal of Petrology* 53, 875–890.

Guzman, S., Carniel, R., Caffe, P.J., 2014. AFC3D: A 3D graphical tool to model assimilation and fractional crystallization with and without recharge in the R environment. *Lithos* 190–191, 264–278.

Haase, K., Regelous, M., Schöbel, S, Gunther, T., de Wall, H., 2019. Variation of melting processes and magma sources of the early Deccan flood basalts, Malwa Plateau, India. *Earth and Planetary Science Letters* 524, 115711.

Hall, W.E., Friedman, I., and Nash, J.T., 1974. Fluid inclusion and light stable isotope study of the Climax molybdenum deposits, Colorado. *Economic Geology* 69, 884–901.

Hamilton, P.J., Evensen, N.M., O'Nions, R.K., Tarney, J., 1979a. Sm-Nd systematics of Lewisian gneisses: Implications for the origin of granulites. *Nature* 277, 25–28.

Hamilton, P.J, Evensen, N.M., O'Nions, R.K., Smith, H.S., Erlank, A.J., 1979b. Sm-Nd dating of Onverwacht group volcanics, southern Africa. *Nature* 279, 298–300.

Hammouda, T., Cherniak, D.J., 2000. Diffusion of Sr in fluorphlogopite determined by Rutherford backscattering spectrometry. *Earth and Planetary Science Letters* 178, 339–349.

Han, C., Xiao, W., Sua, B., Sayic, P.A., Aoa, S., Zhanga, J., Zhanga, Z., Wana, B., Songa, D., Wanga, Z., Zhaoal, N., 2018. Geology, Re-Os and U-Pb geochronology and sulfur isotope of the Donggebi porphyry Mo deposit, Xinjiang, NW China, Central Asian Orogenic Belt. *Journal of Asian Earth Sciences* 165, 270–284.

Hanan, B.B., Graham, D. 1996. Lead and helium isotope evidence from oceanic basalts for a common deep source of mantle plumes. *Science* 272, 991–995.

Hanchar, J., van Westrenen, W., 2007. Rare earth element behaviour in zircon-melt systems. *Elements* 3, 37–42.

Hans, U., Kleine, T., Bourdon, B., 2013. Rb-Sr chronology of volatile depletion in differentiated protoplanets: BABI, ADOR and ALL revisited. *Earth and Planetary Science Letters* 374, 204–214.

Hansen, C.T., Meixner, A., Kasemann, S.A., Bach, W., 2017. New insight on Li and B isotope fractionation during serpentinization derived from batch reaction investigations. *Geochimica et Cosmochimica Acta* 217, 51–79.

Hanski, E., Huhma, H., Rastas, P., Kamenetsky, V.S., 2001. The Palaeoproterozoic komatiite-picrite association of Finnish Lapland. *Journal of Petrology* 42, 855–876.

Hanson, G.N., 1978. The application of trace elements to the petrogenesis of igneous rocks of granitic composition. *Earth and Planetary Science Letters* 38, 26–43.

Harker, A., 1909. *The natural history of igneous rocks*. Methuen, London.

Harmer, R.E., Eglington, B.M., 1987. The mathematics of geochronometry: Equations for

use in regression calculations. National Physical research Laboratory, geochronology division, C.S.I.R., South Africa.

Harnois, L., 1988. The CIW index: A new chemical index of weathering. *Sedimentary Geology* 55, 319–322.

Harris, C., Faure, K., Diamond, R.E., Scheepers, R., 1997. Oxygen and hydrogen isotope geochemistry of S- and I-type granitoids: The Cape Granite suite, South Africa. *Chemical Geology* 143, 95–114.

Harris, N.B.W., Pearce, J.A., Tindle, A.G., 1986. Geochemical characteristics of collision-zone magmatism. In: Coward, M.P., Reis, A.C. (eds.), *Collision tectonics*. Geological Society Special Publication 19. Geological Society, London. 67–81.

Harris, P.G., 1974. Origin of alkaline magmas as a result of anatexis. In: Sorenson, H. (ed.), *The alkaline rocks*. J. Wiley & Sons, London. 427–436.

Harrison, L.N., Weis, D., Garcia, M.O., 2020. The multiple depleted mantle components in the Hawaiian-Emperor chain. *Chemical Geology* 532, 119324.

Harrison, T.M., 1981. Diffusion of ^{40}Ar in hornblende. *Contributions to Mineralogy and Petrology* 78, 324–331.

Harrison, T.M., Watson, E.B., 1984. The behaviour of apatite during crustal anatexis: Equilibrium and kinetic considerations. *Geochimica et Cosmochimica Acta* 48, 1467–1477.

Hart, S.R., 1984. A large-scale isotope anomaly in the Southern Hemisphere mantle. *Nature* 309, 753–757.

Hart, S.R., Hauri, E.H., Oschmann, L.A., Whitehead, J.A., 1992. Mantle plumes and entrainment: Isotopic evidence. *Science* 256, 517–520.

Haskin, L.A., Haskin, M.A., Frey, F.A., Wildman, T.R., 1968. Relative and absolute terrestrial abundances of the rare earths. In: Pepin, R.O., Ahrens, L.H. (eds.), *Origin and distribution of the elements*. Pergamon, Oxford. 889–911.

Hastings, M.G., Casciotti, K.L., Elliott, E.M., 2013. Stable isotopes as tracers of anthropogenic nitrogen sources, deposition, and impacts. *Elements* 9, 339–344.

Hauri, E.H., Hart, S., 1993. Re-Os isotope systematics of HIMU and EMII oceanic island basalts from the South Pacific Ocean. *Earth and Planetary Science Letters* 114, 353–371.

Hauri, E.H., Papineau, D., Wang, J., Hillion, F., 2016. High-precision analysis of multiple sulfur isotopes using NanoSIMS. *Chemical Geology* 420, 418–161.

Hawkesworth, C.J., van Calsteren, P.W.C., 1984, Radiogenic isotopes: Some geological applications. In: Henderson, P. (ed.), *Rare earth element geochemistry*. Elsevier, Amsterdam. 375–421.

Heinonen, J.S., Luttinen, A.V., Bohrson, W.A., 2016. Enriched continental flood basalts from depleted mantle melts: Modeling the lithospheric contamination of Karoo lavas from Antarctica. *Contributions to Mineralogy and Petrology* 171(1), 9.

Heinonen, J.S., Luttinen, A.V., Spera, F.J., Bohrson, W.A., 2019. Deep open storage and shallow closed transport system for a continental flood basalt sequence revealed with Magma Chamber Simulator. *Contributions to Mineralogy and Petrology* 174, 87.

Hemming, S.R., McLennan, S.M., 2001. Pb isotope compositions of modern deep sea turbidites. *Earth and Planetary Science Letters* 184, 489–503.

Henchiri, S., Gaillardet, J., Dellinger, M., Bouchez, J., Spencer, R.G.M., 2016. Riverine dissolved lithium isotopic signatures in low-relief central Africa and their link to weathering regimes. *Geophysical Research Letters* 43, 4391–4399.

Herron, M.M., 1988. Geochemical classification of terrigenous sands and shales from core or log data. *Journal of Sedimentary Petrology* 58, 820–829.

Herron, M.M., Herron, S.L., 1990. Geological applications of geochemical well logging. In: Hurst, A., Lovell, M.A., Morton, A.C. (eds.), *Geological applications of wireline logs*. Geological Society Special Publication 48. Geological Society, London. 165–175.

Hertogen, J., Gijbels, R., 1976. Calculation of trace element fractionation during partial melting. *Geochimica et Cosmochimica Acta* 40, 313–322.

Herzberg, C., 2004. Geodynamic information in peridotite petrology. *Journal of Petrology* 45, 2507–2530.

Herzberg, C., O'Hara, M.J., 2002. Plume associated ultramafic magmas of Phanerozoic age. *Journal of Petrology* 43, 1857–1883.

Herzberg, C., Asimow, P.D., Arndt, N., Niu, Y., Lesher, C.M., Fitton, J.G., Cheadle, M.J., Saunders, A.D., 2007. Temperatures in ambient

mantle and plumes: Constraints from basalts, picrites and komatiites. *Geochemistry, Geophysics, Geosystems* 8, doi: 10.1029/2006GC001390.

Herzberg, C., Condie, K., Korenaga, J., 2010. Thermal history of the Earth and its petrological expression. *Earth and Planetary Science Letters* 292(1–2), 79–88.

Hickson, C.J., Juras, S.J., 1986. Sample contamination and grinding. *Canadian Mineralogist* 24, 585–589.

Hildreth, W., 1981. Gradients in silicic magma chambers: Implications for lithospheric magmatism. *Journal of Geophysical Research* 86, B10153–B10192.

Hill, P.S., Schauble, E.A., Tripati, A., 2020. Theoretical constraints on the effects of added cations on clumped, oxygen, and carbon isotope signatures of dissolved inorganic carbon species and minerals. *Geochimica et Cosmochimica Acta* 269, 496–539.

Hinton, R.W., 1994. Ion microprobe analysis in geology. In: Potts, P.J., Bowles, J.F.W., Reed, S.J.B., Cave, M.R. (eds.), *Microprobe techniques in the Earth sciences*. 235–289.

Hoefs, J., 2018. *Stable isotope geochemistry*, 8th ed. Springer, Cham.

Hoernle, K., Tilton, G., Schmincke, H.-U., 1991. Sr-Nd-Pb isotopic evolution of Gran Canaria: Evidence for shallow enriched mantle beneath the Canary Islands. *Earth and Planetary Science Letters* 106, 44–63.

Hofer, G., Wagreich, M., Neuhuber, S., 2013. Geochemistry of fine-grained sediments of the upper Cretaceous to Paleogene Gosau Group (Austria, Slovakia): Implications for paleoenvironmental and provenance studies. *Geoscience Frontiers* 4, 449–468.

Hoffman, E.L., 1992. Instrumental neutron activation in geoanalysis. *Journal of Geochemical Exploration* 44, 297–319.

Hoffmann, J.E., Münker, C., Polat, A., König, S., Mezger, K., Rosing, M.T., 2010. Highly depleted Hadean mantle reservoirs in the sources of early Archean arc-like rocks, Isua supracrustal belt, southern West Greenland. *Geochimica et Cosmochimica Acta* 74, 7236–7260.

Hoffmann, J.E., Münker, C., Polat, A., Rosing, M.T., Schulz, T., 2011. The origin of decoupled Hf–Nd isotope compositions in Eoarchean rocks from southern West Greenland. *Geochimica et Cosmochimica Acta* 75, 6610–6628.

Hofmann, A.W., 2014. Sampling mantle heterogeneity through oceanic basalts: Isotopes and trace elements. In: Holland, H., Turekian, K.K. (eds.), *Treatise on geochemistry*, 2nd ed. Elsevier, Oxford. 3: 67–101.

Hofmann, A.W., Jochum, K.P., Seufert, M., White, W.M., 1986. Nb and Pb in oceanic basalts: New constraints on mantle evolution. *Earth and Planetary Science Letters* 79, 33–45.

Hoiland, C., Miller, E., Pease, V., 2018. Greenschist facies metamorphic zircon overgrowths as a constraint on exhumation of the Brooks Range metamorphic core, Alaska. *Tectonics*, doi: 10.1029/2018TC005006.

Hoiland, C.W., Miller, E.L., Pease, V., Hourigan, J., 2017. *Detrital zircon U–Pb geochronology and Hf isotope geochemistry of metasedimentary strata in the southern Brooks Range: Constraints on Neoproterozoic–Cretaceous evolution of Arctic Alaska*. Geological Society Special Publication 460. Geological Society, London.

Holz, F., Pichavant, M., Barbey, P., Johannes, W., 1992. Effects of H_2O on liquidus phase relations in the haplogranite system at 2 and 5 kbar. *American Mineralogist* 77, 1223–1241.

Hooker, P.J., Hamilton, P.J., O'Nions, R.K., 1981. An estimate of the Nd isotopic composition of Iapetus seawater from ca. 490 Ma metalliferous sediments. *Earth and Planetary Science Letters* 56, 180–188.

Horita, J., 2005. Some perspectives on isotope biosignatures for early life. *Chemical Geology* 218, 171–188.

Horita, J., Polyakov, V.B., 2015. Carbon-bearing iron phases and the carbon isotope composition of the deep earth. *Proceedings of the National Academy of Sciences* 112, 31–36.

Hu, Y., Teng, F.-Z., Ionov, D.A., 2020. Magnesium isotopic composition of metasomatized upper sub-arc mantle and its implications to Mg cycling in subduction zones. *Geochimica et Cosmochimica Acta* 278, 219–234.

Hu, Z., Qi, L., 2014. Sample digestion methods. In: Holland, H.D., Turekian, K.K. (eds.), *Treatise on geochemistry*, 2nd ed. Elsevier, Oxford. 15: 88–109.

Huang, F., Lundstrom, C.C., McDonough, W.F., 2006. Effect of melt structure on trace-element partitioning between clinopyroxene and silicic,

alkaline, aluminous melts. *American Mineralogist* 91(8–9), 1385–1400.

Huang, W.-L., Wyllie, P.J., 1975. Melting relations in the system $NaAlSi_3O_8$– $KAlSi_3O_8$–SiO_2 to 35 kilobars, dry and excess water. *Journal of Geology* 83, 737–748.

Huebner, M., Kyser, T.K., Nisbet, E.G., 1986. Stable-isotope geochemistry of the high-grade metapelites from the Central zone of the Limpopo belt. *American Mineralogist* 71, 1343–1353.

Hughes, H.S.R., McDonald, I., Goodenough, K.M., Ciborowsk, T.J.R., Kerr, A.C., Davies, J.H.F.L., Selby, D., 2014. Enriched lithospheric mantle keel below the Scottish margin of the North Atlantic Craton: Evidence from the Palaeoproterozoic Scourie Dyke Swarm and mantle xenoliths. *Precambrian Research* 250, 97–126.

Humphries, S.E., 1984. The mobility of the rare earth elements in the crust. In: Henderson, P. (ed.), *Rare earth element geochemistry*. Elsevier, Amsterdam. 315–341.

Iizuka, T., Yamaguchi, T., Hibiya, Y., Amelin, Y., 2015. Meteorite zircon constraints on the bulk Lu-Hf isotope composition and early differentiation of the Earth. *Proceedings of the National Academy of Sciences* 112, 5331–5336.

Ikin, N.P., Harmon, R.S., 1983. A stable isotope study of serpentinization and metamorphism in the Highland Border Suite, Scotland, U.K. *Geochimica et Cosmochimica Acta* 47, 153–167.

Ingersoll, R., 2011. Tectonics of sedimentary basins, with revised nomenclature. In: Busby, C., Azor, A. (eds.), *Tectonics of sedimentary basins: Recent advances*. Wiley, Chichester. 1–43.

Innocenti, F., Manetti, P., Mazzuuoli, R., Pasquare, G., Villari, L., 1982. Anatolia and north-western Iran. In: Thorpe, R.S. (ed.), *Andesites*. Wiley, Chichester. 327–349.

Ionov, D.A., Shirey, S.B., Weis, D., Brügmann, G., 2006. Os–Hf–Sr–Nd isotope and PGE systematics of spinel peridotite xenoliths from Tok, SE Siberian craton: Effects of pervasive metasomatism in shallow refractory mantle. *Earth and Planetary Science Letters* 241, 47–64.

Ireland, T., 2014. Ion microscopes and microprobes. In: Holland, H.D., Turekian, K.K. (eds.), *Treatise on geochemistry*, 2nd ed. Elsevier, Oxford. 15: 385–409.

Irvine, T.N., Baragar, W.R.A., 1971. A guide to the chemical classification of the common volcanic rocks. *Canadian Journal of Earth Sciences* 8, 523–548.

Irving, A.J., Frey, F.A., 1978. Distribution of trace elements between garnet megacrysts and host volcanic liquids of kimberlitic to rhyolitic composition. *Geochimica et Cosmochimica Acta* 42, 771–787.

Iveson, A.A., Rowe, M.C., Webster, J.D., Neil, O.K., 2018. Amphibole-, clinopyroxene- and plagioclase-melt partitioning of trace and economic metals in halogen-bearing rhyodacitic melts. *Journal of Petrology* 59, 1597–1604.

Jackson, D.H., Mattey, D.P., Harris, N.B.W., 1988. Carbon isotope compositions of fluid inclusions in charnockites from southern India. *Nature* 333, 167–170.

Jackson, M.G., Shirey, S.B., 2011. Re–Os isotope systematics in Samoan shield lavas and the use of Os-isotopes in olivine phenocrysts to determine primary magmatic compositions. *Earth and Planetary Science Letters* 312, 91–101.

Jackson, M.G., Hart, S.R., Koppers, A.P., Staudigel, H., Konter, J., Blusztajn, J., Kurz, M., Russell, J.A. 2007. The return of subducted continental crust in Samoan lavas. *Nature* 448, 684–687.

Jackson, M.G., Shirey, S.B., Hauri, E.H., Kurz, M.D., Rizo, H., 2016. Peridotite xenoliths from the Polynesian Austral and Samoa hotspots: Implications for the destruction of ancient ^{187}Os and ^{142}Nd isotopic domains and the preservation of Hadean ^{129}Xe in the modern convecting mantle. *Geochimica et Cosmochimica Acta* 185, 21–43.

Jacobsen, S.B., Wasserburg, G.J., 1980. Sm-Nd isotopic evolution of chondrites. *Earth and Planetary Science Letters* 50, 139–155.

Jagoutz, E., Palme, H., Baddenhausen, H., Blum, K., Cendales, M., Dreibus, G., Spottel, B., Lorenz, V., Wanke, H., 1979. The abundances of major, minor and trace elements in the Earth's mantle as derived from primitive ultramafic nodules. Proceedings of the Lunar and Planetary Science Conference 10. *Geochimica et Cosmochimica Acta Supplement* 11, 2031–2050.

James, D.E., 1981. The combined use of oxygen and radiogenic isotopes as indicators of crustal contamination. *Annual Review of Earth and Planetary Sciences* 9, 311–344.

James, R.S., Hamilton, D.L., 1969. Phase relations in the system $NaAlSi_3O_8$–$KAlSi_3O_8$–$CaAlSi_3O_8$–SiO_2 at 1 kilobar water vapour pressure.

Contributions to Mineralogy and Petrology 21, 111–141.

Janousek, V., Moyen, J.F., Martin, H., Erban, V., Farrow, C., 2016. *Geochemical modelling of igneous processes – Principles and recipes in R language: Bringing the power of R to a geochemical community*. Springer-Verlag, Berlin.

Jarvis, K.E., Williams, J.G., 1989. The analysis of geological samples by slurry nebulisation inductively coupled plasma-mass spectrometry (ICP-MS). *Chemical Geology* 77, 53–63.

Javoy, M., 1977. Stable isotopes and geothermometry. *Journal of the Geological Society* 133, 609–636.

Javoy, M., Fourcade, S., Allegre, C.J., 1970. Graphical method for examining $^{18}O/^{16}O$ fractionation in silicate rocks. *Earth and Planetary Science Letters* 10, 12–16.

Jenkin, G., 1997. Mode effects on cooling rate estimates from Rb–Sr data. *Geology* 25, 907–910.

Jenkin, G., Roger, G., Fallick, A.E., Farrow, C.M., 1995. Rb–Sr closure temperatures in bi-mineralic rocks; a mode effect and test for different diffusion models. *Chemical Geology (Isotope Geoscience)* 122, 227–240.

Jenner, F.E., O'Neill, H.St.C., 2012. Analysis of 60 elements in 616 ocean floor basaltic glasses. *Geochemistry, Geophysics, Geosystems* 13, doi: 10.1029/2011GC004009.

Jensen, L.S., 1976. A new cation plot for classifying subalkalic volcanic rocks. Ontario Division of Mines Miscellaneous Paper 66.

Jensen, L.S., Pyke, D.R., 1982. Komatiites in the Ontario portion of the Abitibi belt. In: Arndt, N.T., Nisbet, E.G. (eds.), *Komatiites*. George Allen and Unwin, London. 147–157.

Jia, Y., Kerrich, R., 2015. N-isotope composition of the primitive mantle compared to diamonds. *Lithos* 233, 131–138.

Jochum, K.P., Enzweiler, J., 2014. Reference materials in geochemical and environmental research. In: Holland, H.D., Turekian, K.K. (eds.), *Treatise on geochemistry*, 2nd ed. Elsevier, Oxford. 15: 43–70.

Jochum, K.P., Seufert, H.M., Thirlwall, M.F., 1990. High-sensitivity Nb analysis by spark source mass spectrometry (SSMS) and calibration of XRF Nb and Zr. *Chemical Geology* 81, 1–16.

Johannes, W., Holz, F., 1996. *Petrogenesis and experimental petrology of granitic rocks*. Springer, Berlin.

Johnson, C.M., Beard, B.L., Albarede, F., 2004. *Geochemistry of non-traditional stable isotopes*. Reviews in Mineralogy and Geochemistry 55. Mineralogical Society of America, Washington DC.

Johnson, C.M., Beard, B.L., Weyer, S., 2020. *Iron geochemistry: An isotopic perspective*. Springer-Nature, Cham.

Johnsson, M.J., 1993. The system controlling the composition of clastic sediments. Geological Society of America, Special Paper 284.

Johnston, D.T., 2011. Multiple sulfur isotopes and the evolution of the Earth's surface sulfur cycle. *Earth-Science Reviews* 106, 161–183.

Jørgensen, B.B., Findlay, A.J., Pellerin, A., 2019. The biogeochemical sulfur cycle of marine sediments. *Frontiers in Microbiology* 10, article 849.

Jouzel, J., Koster, R.D., 1996. A reconsideration of the initial conditions used for stable water isotope models. *Journal of Geophysical Research* D101, 22933–22938.

Jouzel, J., et al., 1997. Validity of the temperature reconstruction from water isotopes in ice cores. *Journal of Geophysical Research* 102C, 471–487.

Kamber, B.S., 2015. The evolving nature of terrestrial crust from the Hadean, through the Archaean, into the Proterozoic. *Precambrian Research* 258, 48–82.

Kamber, B.S., Webb, G.E., 2001. The geochemistry of late Archaean microbial carbonate: Implications for ocean chemistry and continental erosion history. *Geochimica et Cosmochimica Acta* 65, 2509–2525.

Kamber, B.S., Bolhar, R., Webb, G.E., 2004. Geochemistry of late Archaean stromatolites from Zimbabwe: Evidence for microbial life in restricted epicontinental seas. *Precambrian Research* 132, 379–399.

Kamber, B.S., Greig, A., Collerson, K.D., 2005. A new estimate for the composition of weathered young upper continental crust from alluvial sediments, Queensland, Australia. *Geochimica et Cosmochimica Acta* 69, 1041–1058.

Kämpf, L., Plessen, B., Lauterbach, S., Nantke, C., Meyer, H., Chapligin, B., Brauer, A., 2020. Stable oxygen and carbon isotopes of carbonates in lake sediments as a paleoflood proxy. *Geology* 48, doi: 10.1130/G46593.1.

Kanen, R., 2004. WinRock. www.geologynet.com/manuals/WinRockMan.pdf.

Keith, M., Haase, K.M., Klemd, R., Krumm, S., Strauss, H., 2016. Systematic variations of trace element and sulfur isotope compositions in pyrite with stratigraphic depth in the Skouriotissa volcanic-hosted massive sulfide deposit, Troodos ophiolite, Cyprus. *Chemical Geology* 423, 7–18.

Kelemen, P.B., 1990. Reaction between ultramafic rock and fractionating basaltic magma. I. Phase relations, the origin of calc-alkaline magma series, and the formation of discordant dunite. *Journal of Petrology* 31, 51–98.

Kelemen, P.B., Shimizu, N., Salters, V.J., 1995. Extraction of mid-ocean-ridge basalt from the upwelling mantle by focused flow of melt in dunite channels. *Nature* 375, 747–753.

Kelley, K.A., Cottrell, E., 2009. Water and the oxidation state of subduction zone magmas. *Science* 325, 605–607.

Kelsey, C.H., 1965. Calculation of the CIPW norm. *Mineralogical Magazine* 34, 276–282.

Kelsey, D.E., Clark, C., Hand, M., 2008. Thermobarometric modelling of zircon and monazite growth in melt-bearing systems: Examples using model metapelitic and metapsammitic granulites. *Journal of Metamorphic Geology* 26, 199–212.

Kemp, A., Hawkesworth, C., 2014. Growth and differentiation of the continental crust from isotope studies of accessory minerals. In: Holland, H.D., Turekian, K.K. (eds.), *Treatise on geochemistry*, 2nd ed. Elsevier, Oxford. 4: 379–421.

Kemp, A., Whitehouse, M., Vervoort, J., 2019. Deciphering the zircon Hf isotope systematics of Eoarchean gneisses from Greenland: Implications for ancient crust–mantle differentiation and Pb isotope controversies. *Geochimica et Cosmochimica Acta* 250, 76–97.

Kemp, A., Wilde, S., Hawkesworth, C., Coath, C., Nemchin, A., Pidgeon, T., Vervoort, J., DuFrane, S., 2010. Hadean crustal evolution revisited: New constraints from Pb–Hf isotope systematics of the Jack Hills zircons. *Earth and Planetary Science Letters* 296, 45–56.

Kendall, B., Creaser, R.A., Selby, D., 2006. Re-Os geochronology of postglacial black shales in Australia: Constraints on the timing of 'Sturtian' glaciation. *Geology* 34, 729–732.

Kenney, B.C., 1982. Beware spurious self-correlations! *Water Resources Research* 18, 1041–1048.

Kermack, K.A., Haldane, J.B.S., 1950. Organic correlation in allometry. *Biometrika* 37, 30–41.

Kesler, S.E., Vennemann, T.W., Frederickson, C., Breithaupt, A., Vazquez, R, Furman, F.C., 1997. Hydrogen and oxygen isotope evidence for origin of MVT-forming brines, southern Appalachians. *Geochimica et Cosmochimica Acta* 61, 1513, 1523.

Ketcham, R.A., Donelick, R.A., Carlson, W.D., 1999. Variability of apatite fission-track annealing kinetics: III. Extrapolation to geological time scales. *American Mineralogist* 84, 1235–1255.

Klein, M., Stosch, H.-G., Seck, H.A., 1997. Partitioning of high field-strength and rare-earth elements between amphibole and quartz-dioritic to tonalitic melts: An experimental study. *Chemical Geology* 138, 257–271.

Klein, M., Stosch, H.-G., Seck, H.A., Shimizu, N., 2000. Experimental partitioning of high field strength and rare earth elements between clinopyroxene and garnet in andesitic to tonalitic systems. *Geochimica et Cosmochimica Acta* 64, 99–115.

Klimm, K., Blundy, J.D., Green, T.H., 2008. Trace element partitioning and accessory phase saturation during H_2O-saturated melting of basalt with implications for subduction zone chemical fluxes. *Journal of Petrology* 49, 523–553.

Koehler, K.J., Larnz, K., 1980. An empirical investigation of goodness-of-fit statistics for sparse multinomials. *Journal of the American Statistical Association* 75, 336–344.

Koga, K.T., Kelemen, P.B., Shimizuet, N., 2001. Petrogenesis of the crust–mantle transition zone and the origin of lower crustal wehrlite in the Oman ophiolite. *Geochemisty, Geophysics, Geosystems* 2: 2000GC000132.

Kohn, M.J., 2010. Carbon isotope compositions of terrestrial C3 plants as indicators of (paleo)ecology and (paleo)climate. *Proceedings of the National Academy of Sciences* 107, 19691–19695.

Konn, C., Charlou, J.L., Holm, N.G., Mousis, O., 2015. The production of methane, hydrogen, and organic compounds in ultramafic-hosted hydrothermal vents of the Mid-Atlantic Ridge. *Astrobiology* 15, doi: 10.1089/ast.2014.1198.

Korenaga, J., 2018. Crustal evolution and mantle dynamics through Earth history. *Philosophical*

Transactions of the Royal Society A376, 20170408. http://dx.doi.org/10.1098/rsta.2017.0408.

Korotev, R. L., 1996. A self-consistent compilation of elemental concentration data for 93 geochemical reference samples. *Geostandards Newsletter* 20, 217–245.

Košler, J., Fonneland, H., Sylvester, P., Tubrett, M., Pedersen, R.B., 2002. U–Pb dating of detrital zircons for sediment provenance studies: A comparison of laser ablation ICPMS and SIMS techniques. *Chemical Geology* 182, 605–618.

Kovacs, L.O., Kovacs, G.P., Martin-Fernandez, J.A., Barcelo-Vidal, C., et al., 2006. Major-oxide compositional discrimination in Cenozoic volcanites of Hungary. In: Buccianti, A., Mateu-Figueras, G., Pawlowsky-Glahn, V. (eds.), *Compositional data analysis in the geosciences: From theory to practice*. Geological Society Special Publication 264. Geological Society, London. 11–23.

Kramers, J.D., Tolstikhin, I.N., 1997. Two terrestrial lead isotope paradoxes, forward transport modelling, core formation and the history of the continental crust. *Chemical Geology* 139(1–4), 75–110.

Krissansen-Totton, J., Buick, R., Catling, D.C., 2015. A statistical analysis of the carbon isotope record from the Archean to Phanerozoic and implications for the rise of oxygen. *American Journal of Science* 315, 275–316.

Kroner, A., Williams, I.S., Compston, W., Baur, N., Vitanage, P.W., Perera, L.R.K., 1987. Zircon ion microprobe dating of high-grade rocks in Sri Lanka. *Journal of Geology* 95, 775–791.

Kroonenberg, S.B., 1990. Geochemistry of Quaternary fluvial sands from different tectonic regimes. Geochemistry of the Earth's Surface and of Mineral Formation, 2nd International Symposium, July 2–8, Aix en Provence, France (extended abstracts), 88–91.

Kueter, N., Lilley, M.D., Schmidt, M.W., Bernasconi, S.M., 2019. Experimental carbonatite/graphite carbon isotope fractionation and carbonate/graphite thermometry. *Geochimica et Cosmochimica Acta* 253, 290–306.

Kulaksız, S., Bau, M., 2013. Anthropogenic dissolved and colloid/nanoparticle-bound samarium, lanthanum and gadolinium in the Rhine River and the impending destruction of the natural rare earth element distribution in rivers. *Earth and Planetary Science Letters* 362, 43–50.

Kuno, H., 1966. Lateral variation of basalt magma types across continental margins and island arcs. *Bulletin of Volcanology* 29, 195–222.

Kuno, H., 1968. Differentiation of basalt magmas. In: Hess, H.H., Poldervaart, A. (eds.), *Basalts: The Poldervaart treatise on rocks of basaltic composition*. Interscience, New York. 2: 623–688.

Kuritani, T., Kitgawa, H., Nakamura, E., 2005. Assimilation and fractional crystallisation controlled by transport process of crustal melt: Implications from an alkali basalt–dacite suite from Rishiri volcano, Japan. *Journal of Petrology* 46, 1421–1442.

Kurz, M.D., Jenkins, W.J., 1981. The distribution of helium in oceanic basalt glasses. *Earth and Planetary Science Letters* 53, 41–54.

Kyser, T.K., Kerrich, R., 1991. Retrograde exchange of hydrogen isotopes between hydrous minerals and water at low temperatures. In: Taylor, H.P., O'Neill, J.R., Kaplan, I.R. (eds.), *Stable isotope geochemistry: A tribute to Samuel Epstein*. Geological Society Special Publication 3. Geological Society, London. 409–422.

Kyser, T.K., O'Neill, J.R., 1984. Hydrogen isotope systematics of submarine basalts. *Geochimica et Cosmochimica Acta* 48, 2123–2133.

Labidi, J., Cartigny, P., 2016. Negligible sulfur isotope fractionation during partial melting: Evidence from Garrett transform fault basalts, implications for the late-veneer and the Hadean matte. *Earth and Planetary Science Letters* 451, 196–207.

Lacan, F., Tachikawa, K., Jeandel, C., 2012. Neodymium isotopic composition of the oceans: A compilation of seawater data. *Chemical Geology* 300, 177–184.

Lacroix, B., Vennemann, T., 2015. Empirical calibration of the oxygen isotope fractionation between quartz and Fe–Mg–chlorite. *Geochimica et Cosmochimica Acta* 149, 21–31.

Lambrecht, G., Diamond, L.W., 2014. Morphological ripening of fluid inclusions and coupled zone-refining in quartz crystals revealed by cathodoluminescence imaging: Implications for CL-petrography, fluid inclusion analysis and trace-element geothermometry. *Geochimica et Cosmochimica Acta* 141, 381–406.

Langmuir, C.H., 1989. Geochemical consequences of in situ crystallisation. *Nature* 340, 199–205.

Langmuir, C.H., Vocke, R.D., Hanson, G.N., Hart, S.R., 1978. A general mixing equation with applications to Icelandic basalts. *Earth and Planetary Science Letters* 37, 380–392.

Lassiter, J.C., Blichert-Toft, J., Hauri, E.H., Barsczus, H.G., 2003. Isotope and trace element variations in lavas from Raivavae and Rapa, Cook–Austral Islands: Constraints on the nature of HIMU- and EM-mantle and the origin of mid-plate volcanism in French Polynesia. *Chemical Geology* 202, 115–138.

Laubier, M., Grove, T.L., Langmuir, C.H., 2014. Trace element mineral/melt partitioning for basaltic and basaltic andesitic melts: An experimental and laser ICP-MS study with application to the oxidation state of mantle source regions. *Earth and Planetary Science Letters* 392, 265–278.

Leake, B.E., Hendry, G.L., Kemp, A., Plant, A.G., Harvey, P.K., Wilson, J.R., Coats, J.S., Aucott, J.W., Lunel, T., Howarth, R.J., 1969. The chemical analysis of rock powders by automated X-ray fluorescence. *Chemical Geology* 5, 7–86.

Le Bas, M.J., 2000. IUGS reclassification of the high-Mg and picritic volcanic rocks. *Journal of Petrology* 41, 1467–1470.

Le Bas, M.J., Le Maitre, R.W., Streckeisen, A., Zanettin, B., 1986. A chemical classification of volcanic rocks based on the total alkali–silica diagram. *Journal of Petrology* 27, 745–750.

Le Maitre, R.W., 1968. Chemical variation within and between volcanic rock series: A statistical approach. *Journal of Petrology* 9, 220–252.

Le Maitre, R.W., 1976. The chemical variability of some common igneous rocks. *Journal of Petrology* 17, 589–637.

Le Maitre, R.W., 1982. *Numerical petrology: Statistical interpretation of geochemical data*. Elsevier, Amsterdam.

Le Maitre, R.W., Bateman, P., Dudek, A., Keller, J., Lameyre, J., Le Bas, M.J., Sabine, P.A., Schmid, R., Sorensen, H., Streckeisen, A., Woolley, A.R., Zanettin, B., 1989. *A classification of igneous rocks and glossary of terms*. Blackwell, Oxford.

Le Maitre, R.W., Streckeisen, A., Zanettin, B., Le Bas, M., Bonin, B., Bateman, P. (eds.), 2002. *Igneous rocks: A classification and glossary of terms: Recommendations of the International Union of Geological Sciences Subcommission on the Systematics of Igneous Rocks*. Cambridge University Press, Cambridge. doi: 10.1017/CBO9780511535581.

Lechler, P.J., Desilets, M.O., 1987. A review of the use of loss on ignition as a measurement of total volatiles in whole rock analysis. *Chemical Geology* 63, 341–344.

Lécuyer, C., Gillet, P., Robert, F., 1998. The hydrogen isotope composition of seawater and the global water cycle. *Chemical Geology* 145, 249–261.

Ledevin, M., 2019. Archaean cherts: Formation, processes and palaeoenvironments. In: Van Kranendonk, M., Bennett, V.C., Hoffmann, J.E. (eds.), *Earth's oldest rocks*, 2nd ed. Elsevier. 913–944.

Lee, C.-T., 2016. Geochemical classification of elements. In: White, W.M. (ed.), *Encyclopedia of geochemistry*. Springer, Cham. 1–5.

Levasseur, S., Birck, J.L., Allegre, C.J., 1999. The osmium riverine flux and the oceanic mass balance of osmium. *Earth and Planetary Science Letters* 174, 7–23.

Lewis, J.B., Floss, C., Gyngard, F., 2018. Origin of nanodiamonds from Allende constrained by statistical analysis of C isotopes from small clusters of acid residue by NanoSIMS. *Geochimica et Cosmochimica Acta* 221, 237–254.

Li, C., Arndt, N.T., Tang, Q., Ripley, E.M., 2015. Trace element indiscrimination diagrams. *Lithos* 232, 76–83.

Li, J., Huang, X.-L., Wei, G.-J., Liu, Y., Ma, J.-L., Han, L., He, P.-L., 2018. Lithium isotope fractionation during magmatic differentiation and hydrothermal processes in rare-metal granites. *Geochimica et Cosmochimica Acta* 240, 64–79.

Li, J.-L., Schwarzenbach, E.M., John, T., Ague, J.J., Huang, F., Gao, J., Klemd, R., Whitehouse, M.J., Wang, X.-S., 2020. Uncovering and quantifying the subduction zone sulfur cycle from the slab perspective. *Nature Communications*, doi: 10.1038/s41467-019-14110-4.

Li, K., Li, L., Pearson, D.G., Stachel, T., 2019. Diamond isotope compositions indicate altered igneous oceanic crust dominates deep carbon recycling. *Earth and Planetary Science Letters* 516, 190–201.

Liegeois, J.P., Navez, J., Hertogen, J., Black, R., 1998. Contrasting origin of post-collisional high-K calc-alkaline and shoshonitic versus alkaline and

peralkaline granitoids. The use of sliding normalization. *Lithos* 45, 1–28.

Liu, B., Liang, Y., 2017. An introduction of Markov chain Monte Carlo method to geochemical inverse problems: Reading melting parameters from REE abundances in abyssal peridotites. *Geochimica et Cosmochimica Acta* 203, 216–234.

Liu, X.M., Rudnick, R.L., 2011. Constraints on continental crustal mass loss via chemical weathering using lithium and its isotopes. *Proceedings of the National Academy of Sciences* 108, 20873–20880.

Lobach-Zhuchenko, S.B., Rollinson, H.R., Chekulaev, V.P, Savatenkov, V.M., Kovalenko, A.V., Martin, H., Guseva, N.S., Arestova, N.A., 2008. Petrology of a late Archaean, highly-potassic, sanukitoid pluton from the Baltic Shield: Insights into late Archaean mantle metasomatism. *Journal of Petrology* 49, 393–420.

Lodders, K., Palme, H., Gail, H.P., 2009. 4.4 Abundances of the elements in the solar system. In: *Solar system*. Springer-Verlag, Berlin. 712–770.

Long, J.V.P., 1994. Microanalysis from the 1950 to the 1990s. In: Potts, P.J., Bowles, J.F.W., Reed, S.J.B., Cave, M.R. (eds.), *Microprobe techniques in the Earth sciences*. Cambridge University Press, Cambridge. 1–48.

Lotout, C., Poujol, M., Pitra, P., Anczkiewicz, R., Van Den Driessche, J., 2020. From burial to exhumation: Emplacement and metamorphism of mafic eclogitic terranes constrained through multimethod petrochronology: A case study from the Lévézou massif (French Massif Central, Variscan belt). *Journal of Petrology*, doi: 10.1093/petrology/egaa046.

Ludbrook, J., 1997. Comparing methods of measurement. *Clinical and Experimental Pharmacology and Physiology* 24, 193–203.

Luders, V., Pracejus, B., Halbach, P., 2001. Fluid inclusion and sulfur isotope studies in probable modern analogue Kuroko-type ores from the JADE hydrothermal field (Central Okinawa Trough, Japan). *Chemical Geology* 173, 4558.

Ludwig, K.R., 2009. *Using Isoplot/Ex, Version 4.1: A geochronological toolkit for Microsoft Excel*. Berkeley Geochronology Center Special Publication 4.

Luft, 2014. Volatiles in Earth's mantle. In: Holland, H.D., Turekian, K.K. (eds.), *Treatise on geochemistry*, 2nd ed. Elsevier, Oxford. 3: 355–391.

Lugmair, G.W., Marti, K., 1978. Lunar initial $^{143}Nd/^{144}Nd$: Differential evolution of the lunar crust and mantle. *Earth and Planetary Science Letters* 39, 349–357.

Lugmair, G.W., Scheinin, N.B., Marti, K., 1975. Search for extinct ^{146}Sm, 1. The isotopic abundance of ^{142}Nd in the Juvinas meteorite. *Earth and Planetary Science Letters* 27, 79–84.

Luhr, J.F., Carmichael, I.S.E., 1980. The Colima Volcanic Complex, Mexico. *Contributions to Mineralogy and Petrology* 71, 343–372.

Lundstrom, C., 2009. Hypothesis for the origin of convergent margin granitoids and Earth's continental crust by thermal migration zone refining. *Geochimica et Cosmochimica Acta* 73, 5709–5729.

Luth, W.C., Jahns, R.H., Tuttle, O.F., 1964. The granite system at pressures of 4–10 kbar. *Journal of Geophysical Research* 69, 759–773.

Maaloe, S., Abbott, R.N., 2005. Tetrahedral plots of the phase relations for basalts. *Mathematical Geology* 37, 869–893.

Maas, R., Kamenetsky, M.B., Sobolev, A.V., Kamenetsky, V.S., Sobolev, N.V., 2005. Sr, Nd, and Pb isotope evidence for a mantle origin of alkali chlorides and carbonates in the Udachnaya kimberlite, Siberia. *Geology* 33, 549–552.

MacDonald, G.A., 1968. Composition and origin of Hawaiian lavas. In: Coats, R.R., Hay, R.L., Anderson, C.A. (eds.), *Studies in volcanology: A memoir in honour of Howel Williams*. Geological Society of America Memoir 116, 477–522.

MacDonald, G.A., Katsura, T., 1964. Chemical composition of Hawaiian lavas. *Journal of Petrology* 5, 83–133.

Macpherson, C.G., Gamble, J.A., Mattey, D.P., 1998. Oxygen isotope geochemistry of lavas from an oceanic to continental arc transition, Kermadec–Hikurangi margin, SW Pacific. *Earth and Planetary Science Letters* 160, 609–621.

Magaritz, M., Whitford, D.J., James, D.E., 1978. Oxygen isotopes and the origin of high $^{87}Sr/^{86}Sr$ andesites. *Earth and Planetary Science Letters* 40, 220–230.

Magna, T., Hu, Y., Teng, F.-Z., Mezger, K., 2017. Magnesium isotope systematics in Martian meteorites. *Earth and Planetary Science Letters* 474, 419–426.

Mallmann, G., O'Neill, H.St-C., 2007. The effect of oxygen fugacity on the partitioning of Re

between crystals and silicate melt during mantle melting. *Geochimica et Cosmochimica Acta* 71, 2837–2857.

Mallmann, G., O'Neill, H.St-C., 2009. The crystal/melt partitioning of V during mantle melting as a function of oxygen fugacity compared with some other elements (Al, P, Ca, Sc, Ti, Cr, Fe, Ga, Y, Zr and Nb). *Journal of Petrology* 50, 1765–1794.

Mallmann, G., O'Neill, H.St-C., 2013. Calibration of an empirical thermometer and oxybarometer based on the partitioning of Sc, Y and V between olivine and silicate melt. *Journal of Petrology* 54, 933–949.

Mallmann, G., O'Neill, H.St-C., 2014. Corrections to 'Calibration of an empirical thermometer and oxybarometer based on the partitioning of Sc, Y and V between olivine and silicate melt'. *Journal of Petrology* 55, 1241.

Mangold, N., Baratoux, D., Arnalds, O., et al., 2011. Segregation of olivine grains in volcanic sands in Iceland and implications or Mars. *Earth and Planetary Science Letters* 310, 233–243.

Manning, D.A.C., 1981. The effect of fluorine on liquidus phase relationships in the system Qz–Ab–Or with excess water at 1 kb. *Contributions to Mineralogy and Petrology* 76, 206–215.

Marin-Carbonne, J., Busigny, V., et al., 2020. In situ Fe and S isotope analyses in pyrite from the 3.2 Ga Mendon Formation (Barberton Greenstone Belt, South Africa): Evidence for early microbial iron reduction. *Geobiology* 18, 306–325.

Marschall, H.R., Tang, M., 2020. High-temperature processes: Is it time for lithium isotopes? *Elements* 16, 247–252.

Marshall, B.D., DePaolo, D.J., 1982. Precise age determinations and petrogenetic studies using the K–Ca method. *Geochimica et Cosmochimica Acta* 46, 2537–2545.

Marty, B., 2011. The origins and concentrations of water, carbon, nitrogen and noble gases on Earth. *Earth and Planetary Science Letters* 313–314, 56–66.

Marty, B., Zimmermann, L., 1999. Volatiles (He, C, N, Ar) in mid-ocean ridge basalts: Assessment of shallow-level fractionation and characterization of source composition. *Geochimica et Cosmochimica Acta* 63, 3619–3633.

Marumo K., Nagasawa, K., Kuroda, Y., 1980. Mineralogy and hydrogen isotope chemistry of clay minerals in the Ohunuma geothermal area, NE Japan. *Earth and Planetary Science Letters* 47, 255–262.

Masuda, A., 1962. Regularities in variation of relative abundances of lanthanide elements and an attempt to analyse separation-index patterns of some minerals. *Journal of Earth Sciences (Nagoya University)* 10, 173–187.

Matsuhisa, Y., Goldsmith, J.R., Clayton, R.N., 1979. Oxygen isotope fractionation in the systems quartz–albite–anorthite–water. *Geochimica et Cosmochimica Acta* 43, 1131–1140.

Matthews, A., Katz, A., 1977. Oxygen isotope fractionation during the dolomitisation of calcium carbonate. *Geochimica et Cosmochimica Acta* 41, 1431–1438.

McConnaughey, T., 1989, ^{13}C and ^{18}O isotopic disequilibrium in biological carbonates: I. Patterns. *Geochimica et Cosmochimica Acta* 53, 151–162.

McCoy-West, A.J., Fitton, J.G., Pons, M.-L., Inglis, E. C., Williams, H.M., 2018. The Fe and Zn isotope composition of deep mantle source regions: Insights from Baffin Island picrites. *Geochimica et Cosmochimica Acta* 238, 542–562.

McCulloch, M.T., Bennett, V., 1994. Progressive growth of the Earth's continental crust and depleted mantle: Geochemical constraints. *Geochimica et Cosmochimica Acta* 58, 4717–4738.

McCulloch, M.T., Black, L.P., 1984. Sm–Nd isotopic systematics of Enderby Land granulites and evidence for the redistribution of Sm and Nd during metamorphism. *Earth and Planetary Science Letters* 71, 46–58.

McCulloch, M.T., Chappell, B.W., 1982. Nd isotopic characteristics of S- and I-type granites. *Earth and Planetary Science Letters* 58, 51–64.

McCulloch, M.T., Jaques, A.L., Nelson, D.R., Lewis, J.D., 1983. Nd and Sr isotopes in kimberlites and lamproites from western Australia: An enriched mantle origin. *Nature* 302, 400–403.

McDermott, F., Hawkesworth C.J., 1991. Th, Pb and Sr isotopic variations in young island arc volcanics and oceanic sediments. *Earth and Planetary Science Letters* 104, 1–15.

McDonald, M. J., Piercey, S.J., Lyne, J.D., Pigage, L.C., Piercey, G., 2018. Mineral assemblages, textures and in situ sulphur isotope geochemistry of sulphide mineralization from the Cyprus-type ice volcanogenic massive sulphide (VMS) deposit,

Yukon, Canada. *Minerals* 8, 501. doi: 10.3390/min8110501.

McDonough, W.F., 1990. Constraints on the composition of the continental lithospheric mantle. *Earth and Planetary Science Letters* 101, 1–18.

McDonough, W.F., 2014a. Compositional model for the Earth's core. In: Holland, H.D., Turekian, K.K. (eds.), *Treatise on geochemistry*, 2nd ed. Elsevier, Oxford. 3: 559–577.

McDonough, W.F. (ed.), 2014b. *Treatise on geochemistry*, 2nd ed., vol. 15. Elsevier, Oxford.

McDonough, W.F., Sun, S.-S., 1995. The composition of the Earth. *Chemical Geology* 120, 223–253.

McIntire, W.L., 1963, Trace element partition coefficients: A review of theory and applications to geology. *Geochimica et Cosmochimica Acta* 27, 1209–1264.

McKenzie, D., 1985. The extraction of magma from the crust and mantle. *Earth and Planetary Science Letters* 74, 81–91.

McKenzie, D., O'Nions, R.K., 1991. Partial melt distributions from inversion of rare earth element concentrations. *Journal of Petrology* 32, 1021–1092.

McLennan, S.M., 1989. Rare earth elements in sedimentary rocks: Influence of provenance and sedimentary processes. In: Lipin, B.R., McKay, G.A. (eds.), *Geochemistry and mineralogy of rare earth elements*. Mineralogical Society of America, Washington, DC. 169–200.

McLennan, S.M., 2018. Lanthanide rare earths. In: White, W.M. (ed.), *Encylopedia of geochemistry*. Springer, Cham. 792–799.

McLennan, S., Taylor, S., 1982. Geochemical constraints on the growth of continental crust. *Journal of Geology* 9, 342–354.

McLennan, S.M., Taylor, S.R., 1991. Sedimentary rocks and crustal evolution revisited: Tectonic setting and secular trends. *Journal of Geology* 99, 1–21.

McLennan, S. M., Taylor, S.R., 2012. Geology, geochemistry and natural abundances of the rare earth elements. In: Atwood, D.A. (ed.), *The rare earth elements: Fundamentals and applications.* Wiley, Chichester. 1–19.

Meibom, A., Sleep, N.H., Chamberlain, C.P., Coleman, R.G., Frei, R., Hren, M.T., Wooden, J.L., 2002. Re–Os isotopic evidence for long-lived heterogeneity and equilibration processes in the Earth's upper mantle. *Nature* 419, 705–708.

Meinicke, N., Ho, S.L., Hannisdal, B., Nurnberg, D., Tripati, A., Schiebel, R., Mecklerl, A.N., 2020. A robust calibration of the clumped isotopes to temperature relationship for foraminifers. *Geochimica et Cosmochimica Acta* 270, 160–183.

Meisch, A.T., 1969. The constant sum problem in geochemistry. In: Merriam, D.F. (ed.), *Computer applications in the earth sciences*. Springer, Boston. 161–176.

Merrill, R.B., Robertson, J.K., Wyllie, P.J., 1970. Melting reactions in the system $NaAlSi_3O_8$–$KAlSi_3O_8$–SiO_2–H_2O to 20 kilobars compared with results for other feldspar–quartz–H_2O and rock–H_2O systems. *Journal of Geology* 78, 558–569.

Meschede, M., 1986. A method of discriminating between different types of mid-ocean ridge basalts and continental tholeiites with the Nb–Zr–Y diagram. *Chemical Geology* 56, 207–218.

Mettam, C., Zerkle, A.L., Claire, M.W., Pravea, A.R., Poulton, S.W., Junium, C.K., 2019. Anaerobic nitrogen cycling on a Neoarchaean ocean margin. *Earth and Planetary Science Letters* 527, 115800.

Michard, A., Gurriet, P., Soudant, M., Albarede, F., 1985. Nd isotopes in French phanerozoic shales: External vs internal aspects of crustal evolution. *Geochimica et Cosmochimica Acta* 49, 601–610.

Middlemost, E.A.K., 1985. *Magmas and magmatic rocks*. Longman, London.

Middlemost, E.A.K., 1989. Iron oxidation ratios, norms and the classification of volcanic rocks. *Chemical Geology* 77, 19–26.

Mikhail, S., Furi, E., 2019. On the origins(s) and evolution of the Earth's carbon. *Elements* 15, 307–312.

Miller, R.G., O'Nions, R.K., 1985. Source of Precambrian chemical and clastic sediments. *Nature* 314, 325–330.

Millero, F.J., 2014. Physico-chemical controls on seawater. In: Holland, H.D., Turekian, K.K. (eds.), *Treatise on geochemistry*, 2nd ed. Elsevier, Oxford. 8: 1–18.

Milliken, K.L., 2014. A compositional classification for grain assemblages in fine-grained sediments and sedimentary rocks. *Journal of Sedimentary Research* 84, 1185–1199.

Minster, J.F., Allegre, C.J., 1978. Systematic use of trace elements in igneous processes. Part III: Inverse problem of batch partial melting in

volcanic suites. *Contributions to Mineralogy and Petrology* 68, 37–52.

Minster, J.F., Minster, J.B., Treuil, M., Allegre, C.J., 1977. Systematic use of trace elements in igneous processes. Part II. Inverse problem of the fractional crystallisation process in volcanic suites. *Contributions to Mineralogy and Petrology* 61, 49–77.

Mishima, K., Yamazaki, R., Satish-Kumar, M., Ueno, Y., Hokada, T., Toyoshima, T., 2017. Multiple sulfur isotope geochemistry of Dharwar Supergroup, Southern India: Late Archean record of changing atmospheric chemistry. *Earth and Planetary Science Letters* 464, 69–83.

Misra, S., Froelich, P.N., 2012. Lithium isotope history of Cenozoic seawater: Changes in silicate weathering and reverse weathering. *Science* 335, 818–823.

Mix, H.T., Chamberlain, C.P., 2014. Stable isotope records of hydrologic change and paleotemperature from smectite in Cenozoic western North America. *Geochimica et Cosmochimica Acta* 141, 532–546.

Miyashiro, A., 1974. Volcanic rock series in island arcs and active continental margins. *American Journal of Science* 274, 321–355.

Miyoshi T., Sakai, H., Chiba, H., 1984. Experimental study of sulphur isotope fractionation factors between sulphate and sulphide in high temperature melts. *Geochemical Journal* 18, 75–84.

Mongelli, G., Critelli, S., Perri, F., Sonnino, M, Perrone, V., 2006. Sedimentary recycling, provenance and paleoweathering from chemistry and mineralogy of Mesozoic continental red-bed mudrocks, Peloritani mountains, southern Italy. *Geochemical Journal* 40, 197–209.

Montgomery, D., Peck, E., Vining, G., 2012. *Introduction to linear regression analysis*, 5th ed. Wiley & Sons, Hoboken, NJ.

Moss, R.L., Tzimas, E., Kara, H., Willis, P., Kooroshy, J., 2011. Critical metals in strategic energy technologies. JRC scientific and technical reports. European Commission.

Moyen, J., Champion, D., Smithies, R., 2009. The geochemistry of Archaean plagioclase-rich granites as a marker of source enrichment and depth of melting. *Earth and Environmental Science Transactions of the Royal Society of Edinburgh* 100, 35–50.

Muehlenbachs, K., Clayton, R.N., 1976. Oxygen isotope composition of the oceanic crust and its bearing on seawater. *Journal of Geophysical Research* 81, 4365–4369.

Muenow, D.W., Garcia, M.O., Aggrey, K.E., Bednarz, U., Schmincke, H.U., 1990. Volatiles in submarine glasses as a discriminant of tectonic origin: Application to the Troodos ophiolite. *Nature* 343, 159–161.

Mukherjee, I., Large, R.R., Bull, S., Gregory, D.G., Stepanov, A.S., Avila, J., Ireland, T.R., Corkrey, R., 2019. Pyrite trace-element and sulfur isotope geochemistry of Paleo-Mesoproterozoic McArthur Basin: Proxy for oxidative weathering. *American Mineralogist* 104, 1256–1272.

Mullen, E.D., 1983. $MnO/TiO_2/P_2O_5$: A minor element discriminant for basaltic rocks of oceanic environments and its implications for petrogenesis. *Earth and Planetary Science Letters* 62, 53–62.

Mullen, E.K., Weiss, D., 2013. Sr–Nd–Hf–Pb isotope and trace element evidence for the origin of alkalic basalts in the Garibaldi Belt, northern Cascade arc. *Geochemistry, Geophysics, Geosystems* 14, 3126–3155.

Murphy, M.J., Porcelli, D., Pogge von Strandmann, P.A.E., Hirst, C.A., Kutscher, L., Katchinoff, J.A., Morth, C.M., Maximov, T., Andersson, P.S., 2019. Tracing silicate weathering processes in the permafrost-dominated Lena River watershed using lithium isotopes. *Geochimica et Cosmochimica Acta* 245, 154–171.

Murthy, S.V.S., Ghosh, S., Ray, D., 2019. Noble gases and nitrogen in Raghunathpura (IIAB) and Nyaung (IIIAB) iron meteorites. *Meteoritics and Planetary Science* 54, 90–103.

Mysen, B.O, 1988. *Developments in geochemistry, vol. 4: Structures and properties of silicate melts*. Elsevier, Amsterdam.

Nabelek, P.I., Labotka, T.C., O'Neill, J.R., Papike, J.J., 1984. Contrasting fluid/rock interaction between Notch Peak granite intrusion and argillites and limestones in western Utah: Evidence from stable isotopes and phase assemblages. *Contributions to Mineralogy and Petrology* 86, 25–34.

Nagasawa, H., 1966. Trace element partition coefficient in ionic crystals. *Science* 152, 767–769.

Nägler, T.F., Kramers, J.D., 1998. Nd isotopic evolution of the upper mantle during the Precambrian: Models, data and the uncertainty of both. *Precambrian Research* 91(3–4), 233–252.

Nakayama, K., Nakamura, T., 2014. X-ray fluorescence spectroscopy for geochemistry.

In: Holland, H.D., Turekian, K.K. (eds.), *Treatise on geochemistry*, 2nd ed. Elsevier, Oxford. 15: 181–194.

Nash, W.P., Crecraft, H.R., 1985. Partition coefficients for trace elements in silicic magmas. *Geochimica et Cosmochimica Acta* 49, 2309–2322.

Neal, C.R., Davidson, J.P. 1989. An unmetasomatized source for the Malaitan alniiite (Solomon Islands): Petrogenesis involving zone refining, megacryst fractionation, and assimilation of oceanic lithosphere. *Geochimica et Cosmochimica Acta* 53, 1975–1990.

Nebel, O., Scherer, E.E., Mezger, K., 2011. Evaluation of the ^{87}Rb decay constant by age comparison against the U–Pb system. *Earth and Planetary Science Letters* 301, 1–8.

Neilson, R.L., Ustunisik, G., Weinsteiger, A.B., Tepley, F.J., III, Johnston, A.D., Kent, A.J.R., 2017. Trace element partitioning between plagioclase and melt: An investigation of the impact of experimental and analytical procedures. *Geochemistry, Geophysics, Geosystems* 18, doi: 10.1002/2017GC007080.

Nesbitt, H.W., 1979. Mobility and fractionation of rare earth elements during weathering of a granodiorite. *Nature* 279, 206–210.

Nesbitt, H.W., Young, G.M., 1982. Early Proterozoic climates and plate motions inferred from major element chemistry of lutites. *Nature* 299, 715–717.

Nesbitt, H.W., Young, G.M., 1984. Prediction of some weathering trends of plutonic and volcanic rocks based upon thermodynamic and kinetic considerations. *Geochimica et Cosmochimica Acta* 48, 1523–1534.

Nesbitt, H.W., Young, G.M., 1989. Formation and diagenesis of weathering profiles. *Journal of Geology* 97, 129–147.

Nesbitt, H.W., Young, G.M., 1996. Petrogenesis of sediments in the absence of chemical weathering: Effects of abrasion and sorting on bulk composition and mineralogy. *Sedimentology* 43, 341–358.

Nesbitt, H.W., MacRae, N.D., Kronberg, B.I., 1990. Amazon deep-sea fan muds: Light REE enriched products of extreme chemical weathering. *Earth and Planetary Science Letters* 100, 118–123.

Neukampf, J., Ellis, B.S., Magna, T., Laurent, O., Bachmann, O., 2019. Partitioning and isotopic fractionation of lithium in mineral phases of hot, dry rhyolites: The case of the Mesa Falls tuff, Yellowstone. *Chemical Geology* 506, 175–186.

Nicholls, J., 1988. The statistics of Pearce element diagrams and the Chayes closure problem. *Contributions to Mineralogy and Petrology* 99, 11–24.

Nicholls, J., Russell, J.K., 2016. Igneous rock associations 20. Pearce element ratio diagrams: Linking geochemical data to magmatic processes. *Geoscience Canada* 43, 133–146.

Nicolescu, S., Reiners, P., 2005. (U–Th)/He dating of epidote and andradite garnet. *Geochimica et Cosmochimica Acta* 69, A26.

Nielsen, R.L., Drake, M.J., 1979. Pyroxene–melt equilibria. *Geochimica et Cosmochimica Acta* 43, 1259–1272.

Nielsen, R.L., Dungan, M.A., 1983. Low pressure mineral–melt equilibria in natural anhydrous mafic systems. *Contributions to Mineralogy and Petrology* 84(4), 310–326.

Nisbet, E.G., Deitrich, V. J., Esenwein, A., 1979. Routine trace element determination in silicate minerals and rocks by X-ray fluorescence. *Forschritte der Mineralogie* 57, 264–279.

Nishimura, K., 2012. A mathematical model of trace element and isotopic behavior during simultaneous assimilation and imperfect fractional crystallization. *Contributions to Mineralogy and Petrology* 164, 427–440.

Nishimura, K., 2013. AIFCCalc: An Excel spreadsheet for modelling simultaneous assimilation and imperfect fractional crystallization. *Computers and Geosciences* 51, 410–414.

Nishimura, K., 2019. Chemical mass balance equations for open-system magma chamber processes that result in crystal zoning. *Journal of Volcanology and Geothermal Research* 374, 181–196.

Niu, Y., 2004. Bulk-rock major and trace element compositions of abyssal peridotites: Implications for mantle melting, melt extraction and post-melting processes beneath mid-ocean ridges. *Journal of Petrology* 45, 2423–2458.

Niu, Y., Batiza, R., 1997. Trace element evidence from seamounts for recycled oceanic crust in the eastern Pacific mantle. *Earth and Planetary Science Letters* 148, 471–483.

Norman, M.D., De Deckker, P., 1990. Trace metals in lacustrine and marine sediments: A case study

from the Gulf of Carpentaria, northern Australia. *Chemical Geology* 82, 299–318.

Norman, M.D., Leeman, W.P., 1990. Open-system magmatic evolution of andesites and basalts from the Salmon Creek volcanics, southwest Idaho, U.S.A. *Chemical Geology* 81, 167–189.

Norman, M.D., Leeman, W.P., Blanchard, D.P., Fitton, J.G., James, D., 1989. Comparison of major and trace element analyses by ICP, XRF, INAA and ID methods. *Geostandards Newsletter*, 13283–13290.

Norrish, K., Chappell, B.W., 1977. X-ray fluorescence spectrometry. In: Zussman, J. (ed.), *Physical methods in determinative mineralogy*, 2nd ed. Academic Press, New York. 201–272.

O'Connor, J.T., 1965. A classification for quartz-rich igneous rock based on feldspar ratios. U.S.G.S. Professional Paper 525B, B79–B84.

O'Hara, M.J., 1968. The bearing of phase equilibria studies on the origin and evolution of basic and ultrabasic rocks. *Earth Science Reviews* 4, 69–133.

O'Hara, M.J., 1977. Geochemical evolution during fractional crystallisation of a periodically refilled magma chamber. *Nature* 266, 503–507.

O'Hara, M.J., Matthews, R.E., 1981. Geochemical evolution in an advancing, periodically replenished, periodically tapped, continuously fractionated magma chamber. *Journal of the Geological Society* 138, 237–277.

Ohmoto, H., Lasaga, A.C., 1982. Kinetics of reactions between aqueous sulphates and sulphides in hydrothermal systems. *Geochimica et Cosmochimica Acta* 46, 1727–1745.

Ohmoto, H., Rye, R.O., 1974. Hydrogen and oxygen isotopic compositions of fluid inclusions in the Kuroko deposits, Japan. *Economic Geology* 69, 947–953.

Ohmoto, H., Rye, R.O., 1979. Isotopes of sulfur and carbon. In: Barnes, H.L. (ed.), *Geochemistry of hydrothermal ore deposits*. Wiley, New York. 509–567.

Olesik, J.W., 2014. Inductively coupled plasma mass spectrometers. In: Holland, H.D., Turekian, K.K. (eds.), *Treatise on geochemistry*, 2nd ed. Elsevier, Oxford. 15: 309–336.

O'Neill, H.St-C., 2016. The smoothness and shapes of chondrite-normalized rare earth element patterns in basalts. *Journal of Petrology* 57, 1463–1508.

O'Neill, J.R., Taylor, H.P., 1967. The oxygen isotope and cation exchange chemistry of feldspars. *American Mineralogist* 52, 1414–1437.

O'Neill, J.R., Clayton, R.N., Mayeda, T.K., 1969. Oxygen isotope fractionation in divalent metal carbonates. *Journal of Physical Chemistry* 51, 5547–5558.

O'Neill, J.R., Shaw, S.E., Flood, R.H., 1997. Oxygen and hydrogen isotope compositions as indicators of granite genesis in the New England Batholith, Australia. *Contributions to Mineralogy and Petrology* 62, 313–328.

O'Nions, R.K., McKenzie, D.P., 1988. Melting and continent generation. *Earth Planetary Science Letters* 90, 449–456.

O'Nions, R.K., Carter, S.R., Evensen, N.M., Hamilton, P.J., 1979. Geochemical and cosmochemical applications of Nd isotope analysis. *Annual Review of Earth and Planetary Sciences* 7, 11–38.

O'Nions, R.K., Hamilton, P.J., Evensen, N.M., 1977. Variations in $^{143}Nd/^{144}Nd$ and $^{87}Sr/^{86}Sr$ in oceanic basalts. *Earth and Planetary Science Letters* 34, 13–22.

O'Nions, R.K., Hamilton, P.J., Hooker, P.J., 1983. A Nd isotope investigation of sediments related to crustal development in the British Isles. *Earth and Planetary Science Letters* 63, 229–240.

Ono, S., 2017. Photochemistry of sulfur dioxide and the origin of mass-independent isotope fractionation in Earth's atmosphere. *Annual Review of Earth and Planetary Sciences* 45, 301–329.

Ono, S., Wing, B., Rumble, D., Farquhar, J., 2006. High precision analysis of all four stable isotopes of sulfur (^{32}S, ^{33}S, ^{34}S and ^{36}S) at nanomole levels using a laser fluorination isotope-ratio-monitoring gas chromatography–mass spectrometry. *Chemical Geology* 225, 30–39.

Onuma, N., Higuchi, H., Wakita, H., Nagasawa, H., 1968. Trace element partitioning between two pyroxenes and the host lava. *Earth and Planetary Science Letters* 5, 47–51.

Oonk, P.B.H., Mason, P.R.D., Tsikos, H., Bau, M., 2018. Fraction-specific rare earth elements enable the reconstruction of primary seawater signatures from iron formations. *Geochimica et Cosmochimica Acta* 238, 102–122.

Owen-Smith, T.M., Ashwal, L.D., Sudo, M., Trumbull, R.B., 2017. Age and petrogenesis of the

Doros Complex, Namibia, and implications for early plume-derived melts in the Paraná–Etendeka LIP. *Journal of Petrology* 58, 423–442.

Palin, R.M., White, R.W., Green, E.C.R., 2016. Partial melting of metabasic rocks and the generation of tonalitic–trondhjemitic–granodioritic (TTG) crust in the Archaean: Constraints from phase equilibrium modelling. *Precambrian Research* 287, 73–90.

Palme, H., Nickel, K.G., 1985. Ca/Al ratio and composition of the Earth's upper mantle. *Geochimica et Cosmochimica Acta* 49, 2123–2132.

Palme, H., O'Neill, H., 2014. Cosmochemical estimates of mantle composition. In: Holland, H.D., Turekian, K.K. (eds.), *Treatise on geochemistry*, 2nd ed. Elsevier, Oxford. 3: 1–39.

Parkinson, I.J., Hawkesworth, C.J., Cohen, A.S., 1998. Ancient mantle in a modern arc: Osmium isotopes in Izu–Bonin–Mariana forearc peridotites. *Science* 281, 2011–2013.

Patchett, P., Arndt, N., 1986. Nd isotopes and tectonics of 1.9–1.7 Ga crustal genesis. *Earth and Planetary Science Letters* 78, 329–338.

Patchett, P.J., Tatsumoto, M., 1980. Lu–Hf total-rock isochron for eucrite meteorites. *Nature* 288, 571–574.

Patino Douce, A.E., 1999. What do experiments tell us about the relative contributions of crust and mantle to the origin of granitic magmas? In: Castro, A., Fernandez, C., Vigneresse, J.L. (eds.), *Understanding granites: Integrating new and classical techniques*. Geological Society Special Publication 168. Geological Society, London. 55–75.

Patino Douce, A.E., 2005. Vapor-absent melting of tonalite at 15–32 kbar. *Journal of Petrology* 46, 275–290.

Patino Douce, A.E., Beard, J.S., 1995. Dehydration-melting of biotite gneiss and quartz amphibolite from 3 to 15 kbar. *Journal of Petrology* 36, 707–738.

Patino Douce, A.E., Harris, N., 1998. Experimental constraints on Himalayan anatexis. *Journal of Petrology* 39, 689–710.

Paulukat, C., Gilleaudeau, G.J., Chernyavskiy, P., Frei, R., 2016. The Cr-isotope signature of surface seawater: A global perspective. *Chemical Geology* 444, 101–109.

Pawlowsky-Glahn, V., Egozcue, J. J., 2006. Compositional data and their analysis: An introduction. In: Buccianti, A., Mateu-Figueras, G., Pawlowsky-Glahn, V. (eds.), *Compositional data analysis in the Geosciences: From theory to practice*. Geological Society Special Publication 264. Geological Society, London. 1–10.

Pawlowsky-Glahn, V., Egozcue, J.J., 2016. Spatial analysis of compositional data: A historical review. *Journal of Geochemical Exploration* 164, 28–32.

Pawlowsky-Glahn, V., Olea, R.A., 2004. *Geostatistical analysis of compositional data*, vol. 7. Oxford University Press, New York.

Peacock, M A., 1934. Classification of igneous rock series. *Journal of Geology* 39, 689–710.

Pearce, J.A., 1976. Statistical analysis of major element patterns in basalts. *Journal of Petrology* 17, 15–43.

Pearce, J.A., 1982. Trace element characteristics of lavas from destructive plate boundaries. In: Thorpe, R.S. (ed.), *Andesites, orogenic andesites and related rocks*. Wiley, Chichester. 525–548.

Pearce, J.A., 1983. Role of the sub-continental lithosphere in magma genesis at active continental margins. In: Hawkesworth, C.J., Norry, M.J. (eds.), *Continental basalts and mantle xenoliths*. Shiva, Nantwich. 230–249.

Pearce, J.A., 1987. An expert system for the tectonic characterisation of ancient volcanic rocks. *Journal of Volcanology and Geothermal Research* 32, 51–65.

Pearce, J.A., 2008. Geochemical fingerprinting of oceanic basalts with applications to ophiolite classification and the search for Archaean ocean floor. *Lithos* 100, 14–48.

Pearce, J.A., Cann, J.R., 1971. Ophiolite origin investigated by discriminant analysis using Ti, Zr and Y. *Earth and Planetary Science Letters* 12, 339–349.

Pearce, J.A., Cann, J.R., 1973. Tectonic setting of basic volcanic rocks determined using trace element analyses. *Earth and Planetary Science Letters* 19, 290–300.

Pearce, J.A., Gale, G.H., 1977. Identification of ore-deposition environment from trace element geochemistry of associated igneous host rocks. In: *Volcanic processes in ore genesis*. Geological Society Special Publication 7. Geological Society, London. 14–24.

Pearce, J.A., Norry, M.J., 1979. Petrogenetic implications of Ti, Zr, Y and Nb variations in volcanic rocks. *Contributions to Mineralogy and Petrology* 69, 33–47.

Pearce, J.A., Harris, N.B., Tindle, A.G., 1984. Trace element discrimination diagrams for the tectonic interpretation of granitic rocks. *Journal of Petrology* 25, 956–983.

Pearce, J.A., Kempton, P.D., Nowell, G.M., Noble, S.R., 1999. Hf–Nd element and isotope perspective on the nature and provenance of mantle and subduction components in Western Pacific arc-basin systems. *Journal of Petrology* 40, 1579–1611.

Pearce, T.H., 1968. A contribution to the theory of variation diagrams. *Contributions to Mineralogy and Petrology* 19, 142–157.

Pearce, T.H., 1970. Chemical variations in the Palisades Sill. *Journal of Petrology* 11, 15–32.

Pearce, T.H., Stanley, C.R., 1991. The validity of Pearce element ratio analysis in petrology: An example from the Uwekahuna laccolith, Hawaii. *Contributions to Mineralogy and Petrology* 108, 212–218.

Pearson, D.G., 1999. Evolution of cratonic lithospheric mantle: An isotopic perspective. In: Fei, Y., Bertka, C.M., Mysen, B.O. (eds.), *Mantle petrology: Field observations and high-pressure experimentation*. Geochemical Society Special Publication 6. Geochemical Society, Houston, TX. 57–78.

Pearson, D.G., Wittig, N., 2014. The formation and evolution of the cratonic mantle lithosphere: Evidence from mantle xenoliths. In: Holland, H.D., Turekian, K.K. (eds.), *Treatise on geochemistry*, 2nd ed. Elsevier, Oxford. 3: 255–292.

Pearson, D.G., Canil, D., Shirey, S.B., 2014. Mantle samples included in volcanic rocks: Xenoliths and diamonds. In: Holland, H.D., Turekian, K.K. (eds.), *Treatise on geochemistry*, 2nd ed. Elsevier, Oxford. 3: 169–253.

Pearson, K., 1896. On a form of spurious self-correlation which may arise when indices are used in the measurement of organs. *Proceedings of the Royal Society of London* 60, 489–502.

Pease, V., Kuzmeichev, A., Danukalova, M., 2015. The New Siberian Island and evidence for the continuation of the Uralides, Arctic Russia. *Journal of the Geological Society* 172, 1–4.

Peccerillo, R., Taylor, S.R., 1976. Geochemistry of Eocene calc-alkaline volcanic rocks from the Kastamonu area, northern Turkey. *Contributions to Mineralogy and Petrology* 58, 63–81.

Penniston-Dorland, S., Liu, X.M., Rudnick, R.L., 2017. Lithium isotope geochemistry. *Reviews in Mineralogy and Geochemistry* 82, 165–217.

Pernet, C.R., Wilcox, R., Rousselet, G.A., 2013. Robust correlation analyses: False positive and power validation using a new open source Matlab toolbox. *Frontiers in Psychology* 3, article 606, doi: 10.3389/fpsyg.2012.00606.

Petrelli, M., Poli, G., Perugini, D., Peccerillo, A., 2005. PetroGraph: A new software to visualize, model, and present geochemical data in igneous petrology. *Geochemistry, Geophysics, Geosystems* 6, doi: 10.1029/2005GC000932.

Pettijohn, F.J., Potter, P.E., Siever, R., 1972. *Sand and sandstones*. Springer-Verlag, New York.

Petts, D.C., Stern, R.A., Chacko, T., Stachel, T., Heaman, L.M., 2015. A nitrogen isotope fractionation factor between diamond and its parental fluid derived from detailed SIMS analysis of a gem diamond and theoretical calculations. *Chemical Geology* 410, 188–200.

Peucat, J.J., Vidal, P., Bernard-Griffiths, J., Condie, K.C., 1988. Sr, Nd and Pb isotopic systematics in the Archaean low- to high-grade transition zone of southern India: Syn-accretion vs. post-accretion granulites. *Journal of Geology* 97, 537–550.

Peucker-Ehrenbrink, B., Ravizza, G., 2000. The marine osmium isotope record. *Terra Nova* 12, 205–219.

Philpotts, J.A., Schneztler, C.C., 1970. Phenocryst–matrix partition coefficients for K, Rb, Sr and Ba with applications to anorthosite and basalt genesis. *Geochimica et Cosmochimica Acta* 34, 307–322.

Piccoli, F., Brovarone, A.V., Beyssac, O., Martinez, I., Ague, J.J., Chaduteau, C., 2016. Carbonation by fluid–rock interactions at high-pressure conditions: Implications for carbon cycling in subduction zones. *Earth and Planetary Science Letters* 445, 146–159.

Plank, T., 2014. The chemical composition of subducting sediments. In: Holland, H., Turekian, K.K. (eds.), *Treatise on geochemistry*, 2nd ed. Elsevier, Oxford. 4: 607–639.

Plank, T., Kelley, K.A., Zimmer, M.M., Hauri, E.H., Wallace, P.J. 2013. Why do mafic arc magmas contain ~4 wt.% water on average? *Earth and Planetary Science Letters* 364, 168–179.

Pogge von Strandmann, P.A.E., Burton, K.W., James, R.H., van Calsteren, P., Gislason, S.R., Mokadem, F., 2006. Riverine behaviour of uranium and lithium isotopes in an actively glaciated basaltic terrain. *Earth Planetary Science Letters* 251, 134–147.

Poitrasson, F., 2006. On the iron isotope homogeneity level of the continental crust. *Chemical Geology* 235, 195–200.

Poitrasson, F., 2017. Silicon isotope geochemistry. *Reviews in Mineralogy and Geochemistry* 82, 289–344.

Pope, E., Bird, D.K., Rosing, M.T., 2012. Isotope composition and volume of Earth's early ocean. *Proceedings of the National Academy of Sciences*, www.pnas.org/cgi/doi/10.1073/pnas.1115705109.

Potts, P.J., Webb, P.C., Watson, J.S., 1990. Exploiting energy dispersive X-ray fluorescence spectrometry for the determination of trace elements in geological samples. *Analytical Proceedings* 27, 67–70.

Pourmand, A., Dauphas, N., Ireland, T.J., 2012. A novel extraction chromatography and MC-ICPMS technique for rapid analysis of REE, Sc and Y: Revising CI-chondrite abundances and post-Archean Australian shale (PAAS). *Chemical Geology* 291, 38–54.

Powell, R., 1984. Inversion of the assimilation and fractional crystallisation (AFC) equations; characterisation of contaminants from isotope and trace element relationships in volcanic suites. *Journal of the Geological Society* 141, 447–452.

Powell, R., Holland, T.J.B., 1988. An internally consistent dataset with uncertainties and correlations: 3. Application to geobarometry, worked examples and a computer programme. *Journal of Metamorphic Geology* 6, 173–204.

Presnall, D.C., Hoover, J.D., 1984. Composition and depth of origin of primary mid-ocean ridge basalts. *Contributions to Mineralogy and Petrology* 87, 170–178.

Presnall, D.C., Dixon, J.R., O'Donnell, T.H., Dixon, S.A., 1979. Generation of mid-ocean ridge tholeiites. *Journal of Petrology* 20, 3–35.

Presnall, D.C., Gudfinnsson, G.H., Walter, M.J., 2002. Generation of mid-ocean ridge basalts at pressures from 1 to 7 GPa. *Geochimica et Cosmochimica Acta* 66, 2073–2090.

Price, W.J., 1972. *Analytical atomic absorption spectrometry*. Heyden, London.

Prowatke, S., Klemme, S., 2005. Effect of melt composition on the partitioning of trace elements between titanite and silicate melt. *Geochimica et Cosmochimica Acta* 69, 695–709.

Prowatke, S., Klemme, S., 2006. Rare earth element partitioning between titanite and silicate melts: Henry's law revisited. *Geochimica et Cosmochimica Acta* 70, 4997–5012.

Puchtel, I.S., Walker, R.J., Touboul, M., Nisbet, E.G., Byerly, G.R., 2014. Insights into early Earth from the Pt–Re–Os isotope and highly siderophile element abundance systematics of Barberton komatiites. *Geochimica et Cosmochimica Acta* 125, 394–413.

Qin, L., Wang, X., 2017. Chromium isotope geochemistry. *Reviews in Mineralogy and Geochemistry* 82, 379–414.

Qin, T., Wu, F., Wu, Z., Huang, F. 2016. First-principles calculations of equilibrium fractionation of O and Si isotopes in quartz, albite, anorthite, and zircon. *Contributions to Mineralogy and Petrology* 171, article 91.

Qiu, K.-F., Taylor, R.D., Song, Y.-H., Yua, H.-C., Song, K.-R., Li, N., 2016. Geologic and geochemical insights into the formation of the Taiyangshan porphyry copper–molybdenum deposit, Western Qinling Orogenic Belt, China. *Gondwana Research* 35, 40–58.

Rahimi, E., Maghsoudi, A., Hezarkhani, A., 2016. Geochemical investigation and statistical analysis on rare earth elements in Lakehsiyah deposit, Bafq district. *Journal of African Earth Sciences* 124, 139–150.

Rahn, M.K., Brandon, M.T., Batt, G.E., Garver, J.I., 2004. A zero-damage model for fission-track annealing in zircon. *American Mineralogist* 89, 473–484.

Ramsay, M.H., 1997. Sampling and sample preparation. In: Gill, R. (ed.), *Modern analytical geochemistry: An introduction to quantitative chemical analysis for earth, environmental and material scientists*. Addison Wesley Longman, Harlow. 12–28.

Rao, N.C., Creaser, R.A., Lehmann, B., Panwar, B.K., 2013. Re–Os isotope study of Indian kimberlites and lamproites: Implications for mantle source regions and cratonic evolution. *Chemical Geology* 353, 36–47.

Reed, S.J., 1994. Electron microprobe microanalysis. In: Potts, P.J., Bowles, J.F.W., Reed, S.J.B., Cave, M.R. (eds.), *Microprobe techniques in the Earth sciences*. Cambridge University Press, Cambridge. 49–90.

Rees, C.E., 1973. A steady-state model for sulphur isotope fractionation in bacterial reduction processes. *Geochimica et Cosmochimica Acta* 37, 1141–1162.

Reeves, E.P., Fiebig, J., 2020. Abiotic synthesis of methane and organic compounds in Earth's lithosphere. *Elements* 16, 25–31.

Rehkamper, M., Halliday, A.N., Fitton, J.G., Lee, D.-C., Wieneke, M., Arndt, N.T., 1999. Ir, Ru, Pt, and Pd in basalts and komatiites: New constraints for the geochemical behaviour of the platinum-group elements in the mantle. *Geochimica et Cosmochimica Acta* 63, 3915–3934.

Reimann, C., Filzmoser, P, Garrett, R., Dutter, R., 2008. *Statistical data analysis explained: Applied environmental statistics with R*. Wiley & Sons, Chichester.

Reimink, J.R., Davies, J.H.F.L., Chacko, T., Stern, R.A., Heaman, L.M., Sarkar, C., Schaltegger, U., Creaser, R., Pearson, D.G., 2016. No evidence for Hadean continental crust within Earth's oldest evolved rock unit. *Nature Geoscience* 9, 777–780.

Reiners, P., 2009. Nonmonotonic thermal histories and contrasting kinetics of multiple thermochonometers. *Geochimica et Cosmchimica Acta* 73, 3612–3629.

Reiners, P., Farley, K., 1999. He diffusion and (U–Th)/He thermochronometry of titanite. *Geochimica et Cosmochimica Acta* 63, 3845–3859.

Reiners, P., Carlson, R., Renne, P., Cooper, K., Granger, D., McLean, N., Schoene, B., 2018. *Geochronology and thermochronology*. John Wiley & Sons., Chichester.

Reiners, P., Spell, T., Nicolescu, S., Zanetti, K.A., 2004. Zircon (U–Th)/He thermochronometry: He diffusion and comparison with $^{40}Ar/^{39}Ar$ dating. *Geochimica et Cosmochimica Acta* 68, 1857–1887.

Reinhard, A.A., Jackson, M.G., Koornneef, J.M., Rose-Koga, E.F., Blusztajn, J., Konter, J.G., Koga, K.T., Wallace, P.J., Harvey, J., 2018. Sr and Nd isotopic compositions of individual olivine-hosted melt inclusions from Hawai'i and Samoa: Implications for the origin of isotopic heterogeneity in melt inclusions from OIB lavas. *Chemical Geology* 495, 36–49.

Reis, A., Erhardt, A.M., McGluea, M.M., Waite, L., 2019. Evaluating the effects of diagenesis on the $\delta^{13}C$ and $\delta^{18}O$ compositions of carbonates in a mud-rich depositional environment: A case study from the Midland Basin, USA. *Chemical Geology* 524, 196–212.

Renne, P.R., Mundil, R., Balco, G., Min, K., Ludwig, K.R., 2010. Joint determination of ^{40}K decay constants and $^{40}Ar/^{40}K$ for the Fish Canyon sanidine standard, and improved accuracy for $^{40}Ar/^{39}Ar$ geochronology. *Geochimica et Cosmochimica Acta* 74(18), 5349–5367.

Rezaei, M., Nikbakht, M., Shakeri, A., 2017. Geochemistry and sources of fluoride and nitrate contamination of groundwater in Lar area, south Iran. *Environmental Science and Pollution Research* 24(18), 15471–15487.

Richardson, C.K., Rye, R.O., Wasserman, M.D., 1988. The chemical and thermal evolution of the fluids in the Cave-in-Rock fluorspar district, Illinois: Stable isotope systematics at the Deardorff mine. *Economic Geology* 83, 765–783.

Richter, D.H., Moore, J.G., 1966. Petrology of the Kilauea Iki lava lake, Hawaii. USGS Professional Paper 537-B.

Richter, F., Chaussidon, M., Watson, E.B., Mendybaev, R., Homolova, V., 2017. Lithium isotope fractionation by diffusion in minerals. Part 2: Olivine. *Geochimica et Cosmochimica Acta* 219, 124–142.

Rickard, D., Mussmann, M., Steadman, J.A., 2017. Sedimentary sulfides. *Elements* 13, 117–122.

Rickli, J., Frank, M., Halliday, A.N., 2009. The hafnium–neodymium isotopic composition of Atlantic seawater. *Earth and Planetary Science Letters* 280, 118–127.

Rickli, J., Gutjahr, M., Vance, D., Fischer-Gödde, M., Hillenbrand, C.D., Kuhn, G., 2014. Neodymium and hafnium boundary contributions to seawater along the West Antarctic continental margin. *Earth and Planetary Science Letters* 394, 99–110.

Rickwood, P.C., 1989. Boundary lines within petrologic diagrams which use oxides of major and minor elements. *Lithos* 22, 247–263.

Righter, K., Campbell, A.J., Humayun, M., Hervif, R.L., 2004. Partitioning of Ru, Rh, Pd, Re, Ir, and Au between Cr-bearing spinel, olivine, pyroxene and silicate melts. *Geochimica et Cosmochimica Acta* 68, 867–880.

Rink, W.J., Thompson, J.W. (eds.), 2015. *Encyclopedia of scientific dating methods*. Springer Netherlands, Dordrecht.

Rizo, H., Boyet, M., Blichert-Toft, J., Rosing, M., 2011. Combined Nd and Hf isotope evidence for deep-seated source of Isua lavas. *Earth and Planetary Science Letters* 312, 267–279.

Rizo, H., Boyet, M., Blichert-Toft, J., Rosing, M.T., 2013. Early mantle dynamics inferred from ^{142}Nd

variations in Archean rocks from southwest Greenland. *Earth and Planetary Science Letters* 377, 324–335.

Rizo, H., Walker, R.J., Carlson, R.W., Touboul, M., Horan, M.F., Puchtel, I.S., Boyet, M., Rosing, M.T., 2016. Early Earth differentiation investigated through ^{142}Nd, ^{182}W, and highly siderophile element abundances in samples from Isua, Greenland. *Geochimica et Cosmochimica Acta* 175, 319–336.

Robbins, G.A., 1972. Radiogenic argon diffusion in muscovite under hydrothermal conditions. MS thesis, Brown University.

Robert, F., Chaussidon, M., 2006. A palaeotemperature curve for the Precambrian oceans based on silicon isotopes in cherts. *Nature* 443, 969–972.

Robinson, F.A., Toro, J., Pease, V., 2019, U-Pb and oxygen isotope characteristics of Timanian- and Caledonian-age detrital zircons from the Brooks Range, Arctic Alaska, USA. Geological Society of America Bulletin, https://doi.org/10.1130/B35036.1.

Rocha-Júnior, E.R., Puchtel, I.S., Marques, L.S., Walker, R.J., Machado, F.B., Nardy, A.J., Babinski, M., Figueiredo, A.M., 2012. Re–Os isotope and highly siderophile element systematics of the Paraná continental flood basalts (Brazil). *Earth and Planetary Science Letters* 337, 164–173.

Rocha-Júnior, E.R., Marques, L.S., Babinski, M., Nardy, A.J., Figueiredo, A.M., Machado, F.B., 2013. Sr–Nd–Pb isotopic constraints on the nature of the mantle sources involved in the genesis of the high-Ti tholeiites from northern Paraná continental flood basalts (Brazil). *Journal of South American Earth Sciences* 46, 9–25.

Rock, N.M.S., 1987. The need for standardization of normalised multi-element diagrams in geochemistry: A comment. *Geochemical Journal* 21, 75–84.

Rock, N.M.S., 1988. Summary statistics in geochemistry: A study of the performance of robust estimates. *Mathematical Geology* 20, 243–275.

Rock, N.M.S., 1989. Reply to Aitchison. *Mathematical Geology* 21, 791–793.

Rollinson, H.R., 1992. Another look at the constant sum problem in geochemistry. *Mineralogical Magazine* 56, 469–475.

Rollinson, H.R., 1999. Petrology and geochemistry of metamorphosed komatiites and basalts from the Sula Mountains greenstone belt, Sierra Leone. *Contributions to Mineralogy and Petrology* 134, 86–101.

Rollinson, H.R., 2007. *Early Earth systems: A geochemical approach*. Blackwell, Oxford.

Rollinson, H.R., 2009. New models for the genesis of plagiogranites in the Oman ophiolite. *Lithos* 112, 603–614.

Rollinson, H. R., 2014. Plagiogranites from the mantle section of the Oman ophiolite: Models for early crustal evolution. In: Rollinson, H.R., Searle, M.P., Abbasi, I.A., Al-Lazki, A.I., Al Kindi, M.H. (eds.), *Tectonic evolution of the Oman mountains: An introduction*. Geological Society Special Publication 392. Geological Society, London. 247–261.

Rollinson, H.R., 2015. Slab and sediment melting during subduction initiation: Granitoid dykes from the mantle section of the Oman ophiolite. *Contributions to Mineralogy and Petrology* 170, doi: 10.1007/s00410-015-1177-9.

Rollinson, H. R., 2017. There were no large volumes of continental crust in the early Earth. *Geosphere (GSA)*, doi: 10.1130/GES01437.1.

Rollinson, H.R., Roberts, C.R., 1986. Ratio correlation and major element mobility in altered basalts and komatiites. *Contributions to Mineralogy and Petrology* 93, 89–97.

Rose, J., Koppers, A.A., 2019. Simplifying age progressions within the Cook–Austral Islands using ARGUS-VI high-resolution ^{40}Ar/^{39}Ar incremental heating ages. *Geochemistry, Geophysics, Geosystems* 20, https://doi.org/10.1029/2019GC008302.

Roser, B.P., Korsch R.J., 1986. Determination of tectonic setting of sandstone–mudstone suites using SiO_2 content and K_2O/Na_2O ratio. *Journal of Geology* 94, 635–650.

Roser, B.P., Cooper, R.A., Nathan, S., Tulloch, A.J., 1996. Reconnaissance sandstone geochemistry, provenance, and tectonic setting of the lower Paleozoic terranes of the West Coast and Nelson, New Zealand. *New Zealand Journal of Geology and Geophysics* 39(1), 1–16.

Rosing, M.T., 1999. ^{13}C-depleted carbon microparticles in > 3700-Ma sea-floor sedimentary rocks from west Greenland. *Science* 283, 674–676.

Rouessac, F., Rouessac, A., 2007. *Chemical analysis: Modern instrumentation methods and techniques*. Wiley, Chichester.

Rowe, H., Hughes, N., Robinson, K., 2012. The quantification and application of handheld energy-dispersive X-ray fluorescence (ED-XRF) in mudrock chemostratigraphy and geochemistry. *Chemical Geology* 324–325, 122–131.

Rudnick, R.L., Fountain, D., 1995. Nature and composition of the continental crust: A lower crustal perspective. *Reviews of Geophysics* 33, 267–309.

Rudnick, R.L., Gao, S., 2014. Composition of the continental crust. In: Holland, H., Turekian, K.K. (eds.), *Treatise on geochemistry*, 2nd ed. Elsevier, Oxford. 4: 1–51.

Rudnick, R.L., Walker, R.J., 2009. Interpreting ages from Re–Os isotopes in peridotites. *Lithos* 112, 1083–1095.

Rumble, D., Hoering, T.C., 1986. Carbon isotope geochemistry of graphite vein deposits from New Hampshire, USA. *Geochimica et Cosmochimica Acta* 50, 1239–1247.

Rumble, D., Giorgis, D., Ireland, T., Zhang, Z., Xu, H., Yui, T.F., Yang, J., Xu, Z., Liou, J.G., 2002. Low $\delta^{18}O$ zircons, U-Pb dating, and the age of the Qinglongshan oxygen and hydrogen isotope anomaly near Donghai in Jiangsu Province, China. *Geochimica et Cosmochimica Acta* 66, 2299–2306.

Ruscitto, D.M., Wallace, P.J., Cooper, L.B., Plank, T. 2012. Global variations in H_2O/Ce: 2. Relationships to arc magma geochemistry and volatile fluxes. *Geochemistry, Geophysics, Geosystems* 13, http://dx.doi.org/10.1029/2011GC003887.

Russell, J.K., Nicholls, J., 1988. Analysis of petrological hypotheses with Pearce element ratios. *Contributions to Mineralogy and Petrology* 99, 25–35.

Rutherford, E., Soddy, F., 1903. Radioactive change. *Philosophical Magazine* 6, 576–591.

Ryan-Davis, J., Lackey, J.S., Gevedon, M., Barnes, J.D., Lee, C.A., Kitajima, K., Valley, J.W., 2019. Andradite skarn garnet records of exceptionally low δ^{18} O values within an Early Cretaceous hydrothermal system, Sierra Nevada, CA. *Contributions to Mineralogy and Petrology* 174(8), 68.

Rye, R.O., 2005. A review of the stable-isotope geochemistry of sulfate minerals in selected igneous environments and related hydrothermal systems. *Chemical Geology* 215, 5–36.

Rye, R.O., Ohmoto H., 1974. Sulfur and carbon isotopes and ore genesis. A review. *Economic Geology* 69, 826–842.

Rye, R.O., Schuiling, R.D., Rye, D.M., Jansen, J.B.H., 1976. Carbon hydrogen and oxygen isotope studies of the regional metamorphic complex at Naxos, Greece. *Geochimica et Cosmochimica Acta* 40, 1031–1049.

Ryerson, F.J., Hess, P.C., 1978. Implications of liquid–liquid distribution coefficients to mineral–liquid partitioning. *Geochimica et Cosmochimica Acta* 42, 921–932.

Saal, A.E., Hauri, E.H., Langmuir, C.H., Perfit, M.R., 2002. Vapour undersaturation in primitive mid-ocean-ridge basalt and the volatile content of Earth's upper mantle. *Nature* 419, 451–455.

Saal, A.E., Hauri, E.H., Van Orman, J.A., Rutherford, M.J., 2013. Hydrogen isotopes in lunar volcanic glasses and melt inclusions reveal a carbonaceous chondrite heritage. *Science* 340, 1317–1320.

Saccani, E., 2015. A new method of discriminating different types of post-Archean ophiolitic basalts and their tectonic significance using Th–Nb and Ce–Dy–Yb systematics. *Geoscience Frontiers* 6(4), 481–501.

Sachs, L., 1984. *Applied statistics: A handbook of techniques*, 2nd ed. Springer-Verlag, New York.

Salters, V.J., Stracke, A., 2004. Composition of the depleted mantle. *Geochemistry, Geophysics, Geosystems* 5, Q05B07.

Salters, V.J., Mallick, S., Hart, S.R., Langmuir, C.E., Stracke, A., 2011. Domains of depleted mantle: New evidence from hafnium and neodymium isotopes. *Geochemistry, Geophysics, Geosystems* 12, Q08001.

Sano, Y., Terada, K., Fukuoka, T., 2002. High mass resolution ion microprobe analysis of rare earth elements in silicate glass, apatite and zircon: Lack of matrix dependency. *Chemical Geology* 184, 217–230.

Satir, M., Taubold, H., 2001. Hydrogen and oxygen isotope evidence for fluid–rock interactions in the Menderes Massif, western Turkey. *International Journal of Earth Sciences* 89, 812–821.

Satish-Kumar, M., So, H., Yoshino, T., Kato, M., Hiroi, Y., 2011. Experimental determination of carbon isotope fractionation between iron carbide melt and carbon: ^{12}C-enriched carbon in the Earth's core? *Earth and Planetary Science Letters* 310, 340–348.

Sato, J., Hirose, T., 1981. Half-life of ^{138}La. *Radiochemical and Radioanalytcal Letters* 46, 145–152.

Sauzeat, L., Rudnick, R.L., Chauvel, C., Garcon, M., Tang, M., 2015. New perspectives on the Li isotopic composition of the upper continental crust and its weathering signature. *Earth and Planetary Science Letters* 428, 181–192.

Savage, P.S., Armytage, R.M.G., Georg, R.B., Halliday, A.E., 2014. High temperature silicon isotope geochemistry. *Lithos* 190–191, 500–519.

Savin, S.M., Lee, M., 1988. Isotopic study of phyllosicates. In: Bailey, S.W. (ed.), *Hydrous phyllosilicates (exclusive of muscovite)*. Mineralogical Society of America Reviews in Mineralogy 19, 189–223.

Schairer, J.F., Bowen, N.L., 1935. Preliminary report on equilibrium relations between feldspathoids, alkali feldspars and silica. Transactions of the American Geophysical Union, 16th Annual Meeting, 325–328.

Scherer, E., Cameron, K., Blichert-Toft, J., 2000. Lu–Hf garnet geochronology: Closure temperature relative to the Sm–Nd system and the effects of trace mineral inclusions. *Geochimica et Cosmochimica Acta* 64, 3413–3432.

Schidlowski, M, 1988. A 3,800-million-year isotopic record of life from carbon in sedimentary rocks. *Nature* 333, 313–318.

Schijf, Y., Christenson, E.A., Byrne, R.H., 2015. YREE scavenging in seawater: A new look at an old model. *Marine Chemistry* 177, 460–471.

Schiller, D., Finger, F., 2019. Application of Ti-in-zircon thermometry to granite studies: Problems and possible solutions. *Contributions to Mineralogy and Petrology* 174, article 51.

Schmidt, M.W., Connolly, A.D., Gunther, D., Bogaerts, M., 2006. Element partitioning: The role of melt structure and composition. *Science* 312, 1646–1650.

Schoenberg, R., Kamber, B.S., Collerson, K.D., Eugster, O., 2002. New W-isotope evidence for rapid terrestrial accretion and very early core formation. *Geochimica et Cosmochimica Acta* 66, 3151–3160.

Schoenberg, R., Merdian, A., Holmden, C., Kleinhanns, I.C., Hasler, K., Wille, M., Reitter, E., 2016. The stable Cr isotopic compositions of chondrites and silicate planetary reservoirs. *Geochimica et Cosmochimica Acta* 183, 14–30.

Schoenberg, R., Zink, S., Staubwasser, M., Von Blanckenburg, F., 2008. The stable Cr isotope inventory of solid Earth reservoirs determined by double spike MC-ICP-MS. *Chemical Geology* 249, 294–306.

Schomberg, A.C., Wemmer, K., Warr, L., Grathoff, G., 2019. K–Ar age determinations on the fine fractions of clay mineral 'crystallinity index standards' from the Palaeozoic mudrocks of southwest England. *Clay Minerals* 54, 15–26.

Severs, M.J., Beard, J.S., Fedele, L., Hanchar, J.M., Mutchler, S.R., Bodnar, R.J., 2009. Partitioning behavior of trace elements between dacitic melt and plagioclase, orthopyroxene, and clinopyroxene based on laser ablation ICPMS analysis of silicate melt inclusions. *Geochimica et Cosmochimica Acta* 73, 2123–2141.

Shand, S. J., 1947. *The eruptive rocks*, 3rd ed. John Wiley, New York.

Shanks, W.C.P., III, 2013. Stable isotope geochemistry of mineral deposits. In: Holland, H.D., Turekian, K.K. (eds.), *Treatise on geochemistry,* 2nd ed. Elsevier, Oxford. 13, 59–85.

Shannon, R.D., 1976. Revised effective ionic radii and systematic studies of interatomic distances in halides and chalcogenides. *Acta Crystallography (Sect. A)* 32, 751–767.

Shao, J., Yang, S., Li, C., 2012. Chemical indices (CIA and WIP) as proxies for integrated chemical weathering in China: Inferences from analysis of fluvial sediments. *Sedimentary Geology* 265–266, 110–120.

Sharp, Z.D., 2014. Stable isotope techniques for gas source mass spectrometry. In: Holland, H.D., Turekian, K.K. (eds.), *Treatise on geochemistry*, 2nd ed. Elsevier, Oxford. 15: 291–307.

Sharp, Z.D., 2017. *Principles of stable isotope geochemistry*, 2nd ed. doi: https://doi.org/10.25844/h9q1-0p82. Downloaded from https://digitalrepository.unm.edu/unm_oer/1/.

Shaw, D.M., 2000. Continuous (dynamic) melting theory revisited. *Canadian Mineralogist* 38, 1041–1063.

Shaw, D.M., 2006. *Trace elements in magmas: A theoretical treatment*. Cambridge University Press.

Shen, Y., Buick, R., 2004. The antiquity of microbial sulfate reduction. *Earth-Science Reviews* 64, 243–272.

Sheppard, S.M.F., 1977. The Cornubian batholith, SW England: D/Hand ^{18}O/^{16}O studies of kaolinite

and other alteration minerals. *Journal of the Geological Society* 133, 573–591.

Sheppard, S.M.F., 1981. Stable isotope geochemistry of fluids. *Physics and Chemistry of the Earth* 13–14, 419–445.

Sheppard, S.M.F., Gilg, H.A., 1996. Stable isotope geochemistry of clay minerals: 'The story of sloppy, sticky, lumpy and tough' Cairns-Smith (1971). *Clay Minerals* 31, 1–24.

Shervais, J.W., 1982. Ti–V plots and the petrogenesis of modern and ophiolitic lavas. *Earth and Planetary Science Letters* 59, 101–118.

Sheth, H.C., 2008. Do major oxide tectonic discrimination diagrams work? Evaluating new log-ratio and discriminant-analysis–based diagrams with Indian Ocean mafic volcanics and Asian ophiolites. *Terra Nova* 20, 229–236.

Shimura, T., Kemp, A.I.S., 2015. Tetrahedral plot diagram: A geometrical solution for quaternary systems. *American Mineralogist* 100, 2545–2547.

Shragge, J., Snow, C.A., 2006. Bayesian geochemical discrimination of mafic volcanic rocks. *American Journal of Science* 306, 191–209.

Shuster, D.L., Farley, K.A., 2005. Diffusion kinetics of proton induced ^{21}Ne, ^{3}He, and ^{4}He in quartz. *Geochimica et Cosmochimica Acta* 69, 2349–2359.

Shuster, D.L., Vasconcelos, P.M., Heim, J.A., Farley, K.A., 2005. Weathering geochronology by (U–Th)/He dating of goethite. *Geochimica et Cosmochimica Acta* 69, 659–673.

Shuster, D.L., Flowers, R.M., Farley, K.A., 2006. The influence of natural radiation damage on helium diffusion kinetics in apatite. *Earth and Planetary Science Letters* 249, 148–161.

Simkus, D.N., Aponte, J.C., Hilts, R.W., Elisila, J.E., Herd, C.D.K., 2019. Compound-specific carbon isotope compositions of aldehydes and ketones in the Murchison meteorite. *Meteoritics and Planetary Science* 54, 142–156.

Sims, K.W.W., DePaolo, D.J., 1997. Inferences about mantle magma sources from incompatible element concentration ratios in oceanic basalts. *Geochimica et Cosmochimica Acta* 61, 765–784.

Sio, C.K.I., Dauphas, N., Teng, F.-Z., Chaussidon, M., Helz, R.T., Roskosz, M., 2013. Discerning crystal growth from diffusion profiles in zoned olivine by in situ Mg–Fe isotopic analyses. *Geochmica et Cosmochimica Acta* 123, 302–321.

Skelton, A., Lewerentz, A., Kleine, B., Webster, D., Pitcairn, I., 2015. Structural channelling of metamorphic fluids on Islay, Scotland: Implications for paleoclimatic reconstruction. *Journal of Petrology* 56, 2145–2172.

Smit, K.V., Shirey, S.B., Stern, R.A., Steele, A., Wang, W., 2016. Diamond growth from C–H–N–O recycled fluids in the lithosphere: Evidence from CH_4 micro-inclusions and $\delta^{13}C$–$\delta^{15}N$–N content in Marange mixed-habit diamonds. *Lithos* 265, 68–81.

Smith, P.M., Asimow, P.D., 2005. Adiabat_1ph: A new public front-end to the MELTS, pMELTS, and pHMELTS models. *Geochemistry Geophysics Geosystems* 6, Q02004.

Smith, S.E., Humphries, S.E., 1998. Geochemistry of basaltic rocks from the TAG hydrothermal mound (26°08′ N), Mid-Atlantic Ridge. In: Herzig, P.M., Humphries, S.E., Miller, D.J., and Zierenberg, R.A. (eds.), *Proceedings of the Ocean Drilling Program, scientific results* 158. Texas A & M University Press, College Station. 213–229.

Smoliar, M.I., Walker, R.J., Morgan, J.W., 1996. Re–Os isotope constraints on the age of Group IIA, IIIA, IVA, and IVB iron meteorites. *Science* 271, 1099–1102.

Sobolev, A.V., Hofmann, A.W., Jochum, K.P., Kuzmin, D.V., Stoll, B., 2011. A young source for the Hawaiian plume. *Nature* 476, 434–437.

Söderlund, U., Patchett, P.J., Vervoort, J.D., Isachsen, C.E., 2004. The ^{176}Lu decay constant determined by Lu–Hf and U–Pb isotope systematics of Precambrian mafic intrusions. *Earth and Planetary Science Letters* 219, 311–324.

Soesoo, A., 1997. A multivariate statistical analysis of clinopyroxene composition: Empirical coordinates for the crystallisation PT-estimations. *GFF* 119, 55–60.

Sossi, P.A., O'Neill, H.StC., 2017. The effect of bonding environment on iron isotope fractionation between minerals at high temperature. *Geochimica et Cosmochimica Acta* 196, 121–143.

Sossi, P.A., Nebel, O., Foden, J., 2016. Iron isotope systematics in planetary reservoirs. *Earth and Planetary Science Letters* 452, 295–308.

Spera, F.J., Bohrson, W.A., 2001. Energy-constrained open-system magmatic processes I: General model and energy constrained assimilation and fractional crystallization (EC-AFC) formulation. *Journal of Petrology* 42, 999–1018.

Stacey, J.S., Kramers, J.D., 1975. Approximation of terrestrial lead isotope evolution by a two-stage

model. *Earth and Planetary Science Letters* 26, 207–221.

Stakes, D.S., 1991. Oxygen and hydrogen isotope compositions of oceanic plutonic rocks: High-temperature deformation and metamorphism of oceanic layer 3. In: Taylor, H.P., O'Neill, J.R., Kaplan, I.R. (eds.), *Stable isotope geochemistry: A tribute to Samuel Epstein*. Geochemical Society Special Publication 3, 77–90.

Stakes, D.S., O'Neill, J.R., 1982. Mineralogy and stable isotope geochemistry of hydrothermally altered oceanic rocks. *Earth and Planetary Science Letters* 57, 285–304.

Stakes, D.S., Taylor, H.P., Fisher, R.L., 1984. Oxygen isotope and geochemical characterization of hydrothermal alteration in ophiolite complexes and modern oceanic crust. In: Gass, I.G., Lippard, S.J., Shelton, A.W. (eds.), *Ophiolites and oceanic lithosphere*. Blackwell Scientific Publications, Oxford. 199–214.

Stanley, C.R., 1993. Effects of non-conserved denominators on Pearce element ratio diagrams. *Mathematical Geology* 25, 1049–1070.

Stanley, C.R., Russell, J.K., 1989. Petrologic hypothesis testing with Pearce element ratio diagrams: Derivation of diagram axes. *Contributions to Mineralogy and Petrology* 103, 78–89.

Staudigel, H., Bryan, W.B., 1981. Contrasted glass–whole rock compositions and phenocryst redistribution, IPOD sites 417 and 418. *Contributions to Mineralogy and Petrology* 78, 255–262.

Steiger, R.H., Jager, E., 1977. Subcommission on geochronology: Convention of the use of decay constants in geo- and cosmo-chronology. *Earth and Planetary Science Letters* 36, 359–362.

Stein, L.Y., Klotz, G., 2016. The nitrogen cycle. *Current Biology* 26, R83–R101.

Steiner, J.C., Jahns, R.H., Luth, W.C., 1975. Crystallisation of alkali feldspars and quartz in the haplogranite system $NaAlSi_3O_8$–$KAlSi_3O_8$–SiO_2–H_2O at 4 kb. *Geological Society of America Bulletin* 86, 83–98.

Stepanov, A.S., Hermann, J., Rubatto, D., Rapp, R.P., 2012. Experimental study of monazite/melt partitioning with implications for the REE, Th and U geochemistry of crustal rocks. *Chemical Geology* 300–301, 200–220.

Stern, R.A., Hanson, G.N., Shirey, S.B., 1989. Petrogenesis of mantle-derived, LILE-enriched Archean monzodiorites and trachyandesites (sanukitoids) in southwestern Superior Province. *Canadian Journal of Earth Sciences* 26, 1688–1712.

Stichel, T., Frank, M., Rickli, J., Haley, B.A., 2012. The hafnium and neodymium isotope composition of seawater in the Atlantic sector of the Southern Ocean. *Earth & Planetary Science Letters* 317, 282–294.

Stimac, J., Hickmott, D., 1994. Trace-element partition-coefficients for ilmenite, orthopyroxene and pyrrhotite in rhyolite determined by micro-PIXE analysis. *Chemical Geology* 117, 313–330.

Stracke, A., 2016. Mantle geochemistry. In: White, W.M. (ed.), *Encyclopedia of geochemistry*. Springer, Cham. 867–877.

Stracke, A., Hofmann, A.W., Hart, S.R., 2005. FOZO, HIMU, and the rest of the mantle zoo. *Geochemistry, Geophysics, Geosystems* 6(5). doi:10.1029/2004GC000824.

Stracke, A., Scherer, E.E., Reynolds, B.C., 2014. Application of isotope dilution in geochemistry. In: Holland, H.D., Turekian, K.K. (eds.), *Treatise on geochemistry*, 2nd ed. Elsevier, Oxford. 15: 71–86.

Streck, M.J., Grunder, A.L., 1997. Compositional gradients and gaps in high-silica rhyolites of the Rattlesnake tuff, Oregon. *Journal of Petrology* 38, 133–163.

Stüeken, E.E., Kipp, M.A., Koehler, M.C., Buick, R., 2016. The evolution of Earth's bio-geochemical nitrogen cycle. *Earth-Science Reviews* 160, 220–239.

Stüeken, E.E., Zaloumis, J., Meixnerová, J., Buick, R., 2017. Differential metamorphic effects on nitrogen isotopes in kerogen extracts and bulk rocks. *Geochimica et Cosmochimica Acta* 217, 80–94.

Suarez, C.A., Edmonds, M., Jones, A.P., 2019. Earth catastrophes and their impact on the carbon cycle. *Elements* 15, 301–306.

Sun, C., Liang, Y., 2013. The importance of crystal chemistry on REE partitioning between mantle minerals (garnet, clinopyroxene, orthopyroxene, and olivine) and basaltic melts. *Chemical Geology* 358, 23–36.

Sun, C., Graff, M., Liang, Y., 2017. Trace element partitioning between plagioclase and silicate melt: The importance of temperature and plagioclase composition, with implications for terrestrial and lunar magmatism. *Geochimica et Cosmochimica Acta* 206, 273–295.

Sun, S.S., McDonough, W.F., 1989. Chemical and isotopic systematics of oceanic basalts: Implications for mantle composition and processes. In: Saunders, A.D., Norry, M.J. (eds.), *Magmatism in ocean basins*. Geological Society Special Publication 42. Geological Society, London. 313–345.

Sun, X.-L., Wu, Y.-J., Wang, H.-L-, Zhao, Y.-G., Zhang, G.-L., 2014. Mapping soil particle size fractions using compositional kriging, cokriging and additive log-ratio cokriging in two case studies. *Mathematical Geosciences* 46, 429–443.

Sutton, S.R., Newville, M., 2014. Synchrotron X-ray spectroscopic analysis. In: Holland, H.D., Turekian, K.K. (eds.), *Treatise on geochemistry*, 2nd ed. Elsevier, Oxford. 15: 213–230.

Suzuoki T., Epstein S., 1976. Hydrogen isotope fractionation between OH-bearing minerals and water. *Geochimica et Cosmochimica Acta*, 40, 1229–1240.

Tang, D.-M., Qin, K.-Z., Sun, H., Su, B.-X., Xiao, Q.-H., 2012. The role of crustal contamination in the formation of Ni–Cu sulfide deposits in Eastern Tianshan, Xinjiang, Northwest China: Evidence from trace element geochemistry, Re–Os, Sr–Nd, zircon Hf–O, and sulfur isotopes. *Journal of Asian Earth Sciences* 49, 145–160.

Tang, M., Chen, K., Rudnick, R.L., 2016. Archean upper crust transition from mafic to felsic marks the onset of plate tectonics. *Science* 351, 372–375.

Tang, M., Rudnick, R.L., Chauvel, C., 2014. Sedimentary input to the source of Lesser Antilles lavas: A Li perspective. *Geochimica et Cosmochimica Acta* 144, 43–58.

Tanimizu, M., 2000. Geophysical determination of the ^{138}La β-decay constant. *Physical Review C* 62, 017601.

Tatsumoto, M., Knight, R.J., Allegre, C.J., 1973. Time difference in the formation of meteorites as determined from the ratio of lead-207 to lead-206. *Science* 180, 1279–1283.

Taylor, H.P., 1974. The application of oxygen and hydrogen isotope studies to problems of hydrothermal alteration and ore deposition. *Economic Geology* 69, 843–883.

Taylor, H.P., 1978. Oxygen and hydrogen isotope studies of plutonic granitic rocks. *Earth and Planetary Science Letters* 38, 177–210.

Taylor, H.P., Forester, R.W., 1971. Low-O-18 igneous rocks from the intrusive complexes of Skye, Mull, and Ardnamurchan, western Scotland. *Journal of Petrology* 12, 465–497.

Taylor, H.P., Sheppard, S.M.F., 1986. Igneous rocks: I: Processes of isotopic fractionation and isotope systematics. In: Valley, J.W., Taylor, H.P., Jr, O'Neill, J.R. (eds.), *Stable isotopes in high-temperature geological processes*. Reviews in Mineralogy 16. Mineralogical Society of America. 277–271.

Taylor, H.P., O'Neill, J.R., Kaplan, I.R. (eds.), 1991. *Stable isotope geochemistry: A tribute to Samuel Epstein*. Geochemical Society Special Publication 3.

Taylor, P.N., Moorbath, S., Goodwin, R., Petrykowski, A.C., 1980. Crustal contamination as an indicator of the extent of early Archaean continental crust: Pb isotopic evidence from the late Archaean gneisses of west Greenland. *Geochimica et Cosmochimica Acta* 44, 1437–1453.

Taylor, R.P., Fryer, B.J., 1980. Multiple-stage hydrothermal alteration in porphyry copper systems in northern Turkey: The temporal interplay of potassic, propylitic, and phyllic fluids. *Canadian Journal of Earth Sciences* 17(7), 901–926.

Taylor, S.R., McLennan, S.M., 1981. The composition and evolution of the continental crust: Rare earth element evidence from sedimentary rocks. *Philosophical Transactions of the Royal Society A* 301, 381–399.

Taylor, S.R., McLennan, S.M., 1985. *The continental crust: Its composition and evolution*. Blackwell, Oxford.

Taylor, S.R., McLennan, S.M., 2009. *Planetary crusts: Their composition, origin and evolution*. Cambridge University Press, Cambridge.

Telus, M., Alexander, C.M.O'D., Hauri, E.H., Wang, J., 2019. Calcite and dolomite formation in the CM parent body: Insight from in situ C and O isotope analyses. *Geochimica et Cosmochimica Acta* 260, 275–291.

Teng, F.-Z., 2017. Magnesium isotope geochemistry. *Reviews in Mineralogy and Geochemistry* 82, 219–287.

Teng, F.-Z., Dauphas, N., Helz, R.T., 2008. Iron isotope fractionation during magmatic differentiation in Kilauea Iki lava lake. *Science* 320, 1620–1622.

Teng, F.-Z., Dauphas, N., Helz, R.T., Gao, S., Huang, S., 2011. Diffusion driven magnesium and iron isotope fractionation in Hawaiian olivine. *Earth and Planetary Science Letters* 308, 317–324.

Teng, F.-Z., Hu, Y., Chauvel, C., 2016. Magnesium isotope geochemistry in arc volcanism. *Proceedings of the National Academy of Sciences* 113, 7082–7087.

Teng, F.-Z., Li, W.-Y., Rudnick, R.L., Gardner, L.R., 2010. Contrasting lithium and magnesium isotope fractionation during continental weathering. *Earth and Planetary Science Letters* 300, 63–71.

Teng, F.-Z., Wadhwa, M., Helz, R.T., 2007. Investigation of magnesium isotope fractionation during basalt differentiation: Implications for a chondritic composition of the terrestrial mantle. *Earth and Planetary Science Letters* 261, 84–92.

Teng, F.-Z., Watkins, J.M., Dauphas, N., 2017a. Non-traditional stable isotopes. *Reviews in Mineralogy and Geochemistry*, 82, 885.

Teng, F.-Z., Watkins, J.M., Dauphas, N., 2017b. Non-traditional stable isotopes: Retrospective and prospective. *Reviews in Mineralogy and Geochemistry*, 82, 1–26.

Tepley, F.J., III, Lundstrom, C.C., McDonough, W.F., Thompson, A., 2010. Trace element partitioning between high-An plagioclase and basaltic to basaltic andesite melt at 1 atmosphere pressure. *Lithos* 118, 82–94.

Thode, H.G., Monster, J., 1965. Sulfur isotope geochemistry of petroleum, evaporites and ancient seas. *American Association of Petroleum Geologists Memoir* 4, 367–377.

Thomas, C.W., Aitchison, J., 2006. Log-ratios and geochemical discrimination of Scottish Dalradian limestones: A case study. In: Buccianti, A., Mateu-Figueras, G., Pawlowsky-Glahn, V. (eds.), *Compositional data analysis in the geosciences: From theory to practice*. Geological Society Special Publication 264. Geological Society, London. 161–174.

Thomas, J.B., Bodnar, R.J., Shimizu, N., Sinha, A.K., 2002. Determination of zircon/melt trace element partition coefficients from SIMS analysis of melt inclusions in zircon. *Geochimica et Cosmochimica Acta* 66, 2887–2901.

Thomazo, C., Papineau, D., 2013. Biogeochemical cycling of nitrogen on the early Earth. *Elements* 9, 345–351.

Thompson, M., Walsh, J.N., 1983. *A handbook of inductively coupled plasma spectrometry*. Blackie, Glasgow.

Thompson, R.N., 1984. Dispatches from the basalt front. 1. Experiments. *Proceedings of the Geological Association* 95, 249–262.

Thompson, R.N., Morrison, M.A., Dickin, A.P., Hendry, G.L., 1983. Continental flood basalts . . . Arachnids rule OK? In: Hawkesworth, C.J., Norry, M.J. (eds.), *Continental basalts and mantle xenoliths*. Shiva, Nantwich. 158–185.

Thy, P., Esbensen, K.H., 1993. Seafloor spreading and the ophiolitic sequences of the Troodos complex: A principal component analysis of lava and dike compositions. *Journal of Geophysical Research* 98(B7), 11799–11805.

Tiepolo, M., Bottazzi, P., Foley, S.F., Oberti, R., Vannucci, R., Zanetti, A., 2001. Fractionation of Nb and Ta from Zr and Hf at mantle depths: The role of titanian pargasite and kaesutite. *Journal of Petrology* 42, 221–232.

Tiepolo, M., Oberti, R., Zanetti, A., Vannucci, R., Foley, S.F., 2007. Trace-element partitioning between amphibole and silicate melt. *Reviews in Mineralogy and Geochemistry* 67, 417–452.

Till, R., 1974. *Statistical methods for the earth scientist: An introduction*. Macmillan International Higher Education, London.

Tilton, G.R., 1973. Isotopic lead ages of chondritic meteorites. *Earth and Planetary Science Letters* 19, 321–329.

Tofallis, C., 2015. Fitting equations to data with the perfect correlation relationship. Hertfordshire Business School Working Paper, http://dx.doi.org/10.2139/ssrn.2707593.

Tomascak, P.B., Magna, T.S., Dohmen, R., 2016. *Advances in lithium isotope geochemistry*. Springer International Publishing, Cham.

Tompkins, A.G., Rebryna, K.C., Weinberg, R.F., Schaffer, B.F., 2012. Magmatic sulfide formation by reduction of oxidized arc basalt. *Journal of Petrology* 53, 1537–1567.

Tostevin, R., Turchyn, A.V., Farquhar, J., Johnston, D.T., Eldridge, D.L., Bishop, J.K.B., McIlvin, M., 2014. Multiple sulfur isotope constraints on the modern sulfur cycle. *Earth and Planetary Science Letters* 396, 14–21.

Totten, M.W., Hanan, M.A., 2007. Heavy minerals in shales. *Developments in Sedimentology* 58, 323–341.

Totten, M.W., Hanan, M.A., Weaver, B.L., 2000. Beyond whole-rock geochemistry of shales: The importance of assessing mineralogic controls for

revealing tectonic discriminants of multiple sediment sources for the Ouachita Mountain flysch deposits. *Geological Society of America Bulletin* 112, 1012–1022.

Trudinger, P.A., Chambers, L.A., Smith, J.W., 1985. Low-temperature sulphate reduction: Biological vs abiological. *Canadian Journal of Earth Sciences* 22, 1910–1918.

Trumbull, R.B., Harris, C., Frindt, S., Wigand, M., 2004. Oxygen and neodymium isotope evidence for source diversity in Cretaceous anorogenic granites from Namibia and implications for A-type granite genesis. *Lithos* 73, 21–40.

Turner, S., Langmuir, C., Dungan, M., Escrig, S., 2017. The importance of mantle wedge heterogeneity to subduction zone magmatism and the origin of EM1. *Earth and Planetary Science Letters* 472, 216–228.

Tuttle, O.F., Bowen, N.L., 1958. The origin of granite in the light of experimental studies in the system $NaAlSi_3O_8$–$KAlSi_3O_8$–SiO_2–H_2O. *Geological Society of America Memoir* 74.

Ueda, A., Sakai, H., 1984. Sulfur isotope study of Quaternary volcanic rocks from the Japanese islands arc. *Geochimica et Cosmochimica Acta* 48, 1837–1848.

Urey, H.C., 1947. The thermodynamic properties of isotopic substances. *Journal of the Chemical Society*, 562–581.

Usui, T., Alexander, C.M.O'D., Wang, J., Simon, J.I., Jones, J.H., 2012. Origin of water and mantle–crust interactions on Mars inferred from hydrogen isotopes and volatile element abundances of olivine-hosted melt inclusions of primitive shergottites. *Earth and Planetary Science Letters* 357–358, 119–129.

Valley, J.W., 1986. Stable isotope geochemistry of metamorphic rocks. In: Valley, J.W., Taylor, H.P., O'Neill, J.R. (eds.), *Stable isotopes in high temperature geological processes*. Reviews in Mineralogy 16. Mineralogical Society of America, Washington, DC. 445–490.

Valley, J.W., 2001. Stable isotope thermometry at high temperatures. *Reviews in Mineralogy and Geochemistry* 43, 365–413.

Valley, J.W., 2003. Oxygen isotopes in zircon. *Zircon: Reviews in Mineralogy and Geochemistry* 53, 343–385.

Valley, J.W., Taylor, H.P., O'Neill, J.R. (eds.), 1986. *Stable isotopes and high temperature geological processes*. Reviews in Mineralogy 16. Mineralogical Society of America, Washington, DC.

Van Acken, D., Brandon, A.D., Humayun, M., 2011. High-precision osmium isotopes in enstatite and Rumuruti chondrites. *Geochimica et Cosmochimica Acta* 75, 4020–4036.

Van Breemen, O., Aftalion, M., Pankhurst, R.J., Richardson, S.W., 1979. Age of the Glen Dessary syenite, Invernessshire: Diachronous Palaeozoic metamorphism across the Great Glen. *Scottish Journal of Geology* 15, 49–62.

Van den Boogaart, K.G., Tolosana-Delgado, R., 2013. *Analyzing compositional data with R*, vol. 122. Springer, Heidelberg.

Veizer, J., Ala, D., et al., 1999. $^{87}Sr/^{86}Sr$, $\delta^{13}C$ and delta $\delta^{18}O$ evolution of Phanerozoic seawater. *Chemical Geology* 161, 59–88.

Vennemann, T.W., O'Neill, J.R., 1993. A simple and inexpensive method of hydrogen isotope and water analyses of minerals and rocks based on zinc reagent. *Chemical Geology (Isotope Geoscience Section)* 103, 227–234.

Verma, S.K., Pandarinath, K., Verma, S.P., 2012. Statistical evaluation of tectono-magmatic discrimination diagrams for granitic rocks and proposal of new discriminant-function–based multi-dimensional diagrams for acid rocks. *International Geology Review* 54, 325–347.

Verma, S.P., 2010. Statistical evaluation of bivariate, ternary and discriminant function tectonomagmatic discrimination diagrams. *Turkish Journal of Earth Sciences* 19, 185–238.

Verma, S.P., 2020. *Road from geochemistry to geochemometrics*. Springer, Singapore.

Verma, S.P., Agrawal, S., 2011. New tectonic discrimination diagrams for basic and ultrabasic volcanic rocks through log-transformed ratios of high field strength elements and implications for petrogenetic processes. *Revista Mexicana de Ciencias Geológicas* 28, 24–44.

Verma, S.P., Armstrong-Altrin, J.S., 2013. New multi-dimensional diagrams for tectonic discrimination of siliciclastic sediments and their application to Precambrian basins. *Chemical Geology* 355, 117–133.

Verma, S.P., Verma, S.-K., 2013. First 15 probability-based multidimensional tectonic discrimination diagrams for intermediate magmas and their robustness against post-emplacement

compositional changes and petrogenetic processes. *Turkish Journal of Earth Sciences* 22, 931–995.

Verma, S.P., Pandarinath, K., Verma, S.K., Agrawal, S., 2013. Fifteen new discriminant-function-based multi-dimensional robust diagrams for acid rocks and their application to Precambrian rocks. *Lithos* 168–169, 113–123.

Verma, S.P., Rivera-Gomez, M.A., Diaz-Gonzalez, L., Quiroz-Ruiz, A., 2016. Log-ratio transformed major element based multidimensional classification for altered high-Mg igneous rocks. *Geochemistry, Geophysics, Geosystems* 17, 4955–4972, doi: 10.1002/2016GC006652.

Vermeesch, P., 2006a. Tectonic discrimination diagrams revisited. *Geochemistry, Geophysics, Geosystems* 7, Q06017, doi: 10.1029/2005GC001092.

Vermeesch, P., 2006b. Tectonic discrimination of basalts with classification trees. *Geochimica et Cosmochimica Acta* 70, 1839–1848.

Vermeesch, P., 2012. On the visualisation of detrital age distributions. *Chemical Geology* 312–313, 190–194.

Vermeesch, P., 2013. Multi-sample comparison of detrital age distributions. *Chemical Geology* 341, 140–146.

Vermeesch, P., 2018a. Dissimilarity measures in detrital geochronology. *Earth-Science Reviews* 178, 310–321.

Vermeesch, P., 2018b. IsoplotR: A free and open toolbox for geochronology. *Geoscience Frontiers*, doi: 10.1016/j.gsf.2018.04.001.

Vermeesch, P., Garzanti, E., 2015. Making geological sense of 'Big Data' sedimentary provenance. *Chemical Geology* 409, 20–27.

Vervoort, J.D., Blichert-Toft, J., 1999. Evolution of the depleted mantle: Hf isotope evidence from juvenile rocks through time. *Geochimica et Cosmochimica Acta* 63(3–4), 533–556.

Vervoort, J.D., Patchett, P.J., Blichert-Toft, J., Albarède, F., 1999. Relationships between Lu–Hf and Sm–Nd isotopic systems in the global sedimentary system. *Earth and Planetary Science Letters* 168, 79–99.

Villiger, S., Ulmer, P., Muntener, O., Thompson, A.B., 2004. The liquid line of descent of anhydrous, mantle-derived, tholeiitic liquids by fractional and equilibrium crystallization: An experimental study at 1.0 GPa. *Journal of Petrology* 45, 2369–2388.

Voigt, M., Pearce, C.R., Fries, D.M., Baldermann, A., Oelkers, E.H., 2020. Magnesium isotope fractionation during hydrothermal seawater–basalt interaction. *Geochimica et Cosmochimica Acta* 272, 21–35.

von Blanckenburg, F., O'Nions, R.K., Heinz, J.R., 1996. Distribution and sources of pre-anthropogenic lead isotopes in deep ocean water from FeMn crusts. *Geochimica et Cosmochimica Acta* 60, 4957–4963.

Wakita, H., Rey, P., Schmitt, R.A., 1971. Abundances of the 14 rare-earth elements and 12 other trace elements in Apollo 12 samples: Five igneous and one breccia rocks and four soils. *Lunar and Planetary Science Conference Proceedings* 2, 1319.

Walker, D., Shibata, T., DeLong, S.E., 1979. Abyssal tholeiites from the Oceanographer Fracture Zone III. Phase equilibria and mixing. *Contributions to Mineralogy and Petrology* 70, 111–125.

Walker, R.J., Carlson, R., Shirey, S., Boyd, F., 1989. Os, Sr, Nd, and Pb isotope systematics of southern African peridotite xenoliths: Implications for the chemical evolution of the subcontinental mantle. *Geochimica et Cosmochimica Acta* 53, 1583–1595.

Walker, R.J., Horan, M.F., Morgan, J.W., Becker, H., Grossman, J.N., Rubin, A.E., 2002. Comparative ^{187}Re–^{187}Os systematics of chondrites: Implications regarding early solar system processes. *Geochimica et Cosmochimica Acta* 66, 4187–4201.

Walsh, J.N., Howie, R.A., 1980. An evaluation of the performance of an inductively coupled plasma source spectrometer for the determination of major and trace constituents of silicate rocks and minerals. *Mineralogical Magazine* 47, 967–974.

Walter, M.J., 1998. Melting of garnet peridotite and the origin of komatiite and depleted lithosphere. *Journal of Petrology* 39, 26–60.

Waltham, D., 2000. *Mathematics: A simple tool for geologists*, 2nd ed. Wiley-Blackwell, Oxford.

Ward, C., Mueller, U., 2012. Multivariate estimation using log ratios: A worked alternative. In: Abrahamsen, P., Hauge, R., Kolbjørnsen, O. (eds.), *Geostatistics Oslo 2012.* Quantitative Geology and Geostatistics 17. Springer, Dordrecht.

Warren, C.J., Kelley, S.P., Sherlock, S.C., McDonald, C.S., 2012. Metamorphic rocks seek meaningful cooling rate: Interpreting ^{40}Ar/^{39}Ar

ages in an exhumed ultra-high-pressure terrane. *Lithos* 155, 30–48.

Wartho, J.-A., Kelley, S.P., Brooker, R.A., Carroll, M.R., Villa, I.M., Lee, M.R., 1999. Direct measurement of Ar diffusion profiles in a gem-quality Madagascar K-feldspar using the ultra-violet laser ablation microprobe (UVLAMP). *Earth and Planetary Science Letter* 170, 141–153.

Wasserburg, G.J., Jacobsen, S.B., DePaolo, D.J., McCulloch, M.T., Wen J., 1981. Precise determinations of Sm/Nd ratios, Sm and Nd isotopic abundances in standard solutions. *Geochimica et Cosmochimica Acta* 45, 2311–2323.

Watkins, J.M., DePaolo, D.J., Watson, E.B., 2017. Kinetic fractionation of non-traditional stable isotopes by diffusion and crystal growth reactions. In: Teng, F.-Z., Watkins, J.M., Dauphas, N. (eds.), *Reviews in mineralogy and geochemistry* 82, 85–125.

Watson, E.B., 1976. Two-liquid partition coefficients: Experimental data and geochemical implications. *Contributions to Mineralogy and Petrology* 56, 119–134.

Watson, E.B., Wark, D.A., Thomas, J.B., 2006. Crystallization thermometers for zircon and rutile. *Contributions to Mineralogy and Petrology* 151, 413–433.

Wei, C.-S., Zheng, Y.-F., Zhao, Z.-F., 2000. Hydrogen and oxygen isotope geochemistry of A-type granites in the continental margins of eastern China. *Tectonophysics*, 328, 205–227.

Weinberg, R.F., Hasalova, P., 2015. Water-fluxed melting of the continental crust: A review. *Lithos* 212–215, 158–188.

Weiss, B.P., Shuster, D.L., Stewart, S.T., 2002. Temperature on Mars from $^{40}Ar/^{39}Ar$ thermochronology of ALH84001. *Earth and Planetary Science Letters* 201, 465–472.

Welch, S.A., Beard, B.L., Johnson, C.M., Braterman, P.S., 2003. Kinetic and equilibrium Fe isotope fractionation between aqueous Fe(II) and Fe(III). *Geochimica et Cosmochimica Acta* 67, 4231–4250.

White, W.M., 2010. Oceanic island basalts and mantle plumes: The geochemical perspective. *Annual Review of Earth and Planetary Sciences* 38, 133–160.

White, W.M., 2013. *Geochemistry*. Wiley-Blackwell, Chichester.

White, W.M., 2015. *Isotope geochemistry*. Wiley, Chichester.

White, W.M., Duncan, R., 1996. Geochemistry and geochronology of the Society Islands: New evidence for deep mantle recycling. In: Basu, A., Hart, S.R. (eds.), *Earth processes: Reading the isotopic code*. Geophysical Monograph Series 95. American Geophysical Union, Washington, DC. 183–206.

White, W.M., Klein, E.M., 2014. Composition of the oceanic crust. In: Holland, H., Turekian, K.K. (eds.), *Treatise on geochemistry*, 2nd ed. Elsevier, Oxford. 4: 457–496.

Whitehouse, M.J., Platt, J., 2003. Dating high-grade metamorphism: Constraints from rare-earth elements in zircon and garnet. *Contributions to Mineralogy and Petrology* 145, 61–74.

Whitehouse, M.J., Kamber, B.S., Fedo, C.M., Lepland, A., 2005. Integrated Pb- and S-isotope investigation of sulphide minerals from the early Archaean of southwest Greenland. *Chemical Geology* 222, 112–131.

Whitten, E.H.T., 1995. Open and closed compositional data in petrology. *Mathematical Geology* 27, 789–806.

Wickham, S.M., Taylor, H.P., 1985. Stable isotope evidence for large-scale seawater infiltration in a regional metamorphic terrane: The Trois Seigneurs Massif, Pyrenees, France. *Contributions to Mineralogy and Petrology* 91, 122–137.

Wieler, R. 2014. Noble gas mass spectrometry. In: Holland, H.D., Turekian, K.K. (eds.), *Treatise on geochemistry*, 2nd ed. Elsevier, Oxford. 15: 355–373.

Willbold, M., Stracke, A., 2006. Trace element composition of mantle end-members: Implications for recycling of oceanic and upper and lower continental crust. *Geochemistry, Geophysics, Geosystems* 7, doi: 10.1029/2005GC001005.

Willbold, M., Stracke, A., 2010. Formation of enriched mantle components by recycling of upper and lower continental crust. *Chemical Geology* 276, 188–197.

Wilson, A.H., Zeh, A., Gerdes, A., 2017. In situ Sr isotopes in plagioclase and trace element systematics in the lowest part of the eastern Bushveld Complex: Dynamic processes in an evolving magma chamber. *Journal of Petrology* 58, 327–360.

Wilson, M., 1989. *Igneous petrogenesis*. Unwin Hyman, London.

Winchester, J.A., Floyd, P.A., 1976. Geochemical magma type discrimination: Application to altered

and metamorphosed basic igneous rocks. *Earth and Planetary Science Letters* 28, 459–469.

Windrim, D.P., McCulloch, M.T., 1986. Nd and Sr isotopic systematics of central Australian granulites: Chronology of crustal development and constraints on the evolution of the lower continental crust. *Contributions to Mineralogy and Petrology* 94, 289–303.

Wolff, J.A., Ramos, F.C, 2014. Processes in caldera-forming high-silica rhyolite magma: Rb-Sr and Pb isotope systematics of the Otowi member of the Bandelier tuff, Valles Caldera, New Mexico, USA. *Journal of Petrology* 55, 345–375.

Wolff, J.A., Ramos, F.C., Hart, G.L., Patterson, J.D., Brandon, A.D., 2008. Columbia River flood basalts from a centralized crustal magmatic system. *Nature Geoscience* 1, 177–180.

Wood, B.J., Blundy, J.D., 1997. A predictive model for rare earth element partitioning between clinopyroxene and anhydrous silicate melt. *Contributions to Mineralogy and Petrology* 129, 166–181.

Wood, B.J., Blundy, J.D., 2014. Trace element partitioning: The influences of ionic radius, cation charge, pressure, and temperature. In: Holland, H., Turekian, K.K. (eds.), *Treatise on geochemistry*, 2nd ed. Elsevier, Oxford. 3: 421–448.

Wood, D.A., 1979. Dynamic partial melting: Its application to petrogenesis of basalts erupted in Iceland, the Faeroe Islands, the Isle of Skye (Scotland) and the Troodos Massif (Cyprus). *Geochimica et Cosmochimica Acta* 43, 1031–1046.

Wood, D.A., 1980. The application of a Th–Hf–Ta diagram to problems of tectono-magmatic classification and to establishing the nature of crustal contamination of basaltic lavas of the British Tertiary volcanic province. *Earth and Planetary Science Letters* 50, 11–30.

Wooden, J.L., Czamanske, G.K., Fedorenko, V.A., Arndt, N.T., Chauvel, C., Bouse, R.M., King, B.W., Knight, R.J., Siem, D.F., 1993. Isotopic and trace-element constraints on mantle and crustal contributions to Siberian continental flood basalts, Noril'sk area, Siberia. *Geochimica et Cosmochimica Acta* 57, 3677–3704.

Woodhead, J., Hergt, J., Giuliani, A., Maas, R., Phillips, D., Pearson, D.G., Nowell, G., 2019. Kimberlites reveal 2.5-billion-year evolution of a deep, isolated mantle reservoir. *Nature* 573, 578–581.

Woodhouse, O., Ravizza, G., Kenison Falkner, K., Statham, P., Peucker-Ehrenbrink, B., 1999. Osmium in seawater: Vertical profiles of concentration and isotopic composition in the eastern Pacific Ocean. *Earth and Planetary Science Letters* 173, 223–233.

Workman, R.K., Hart, S., 2005. Major and trace element composition of the depleted MORB mantle (DMM). *Earth and Planetary Science Letters* 231, 53–72.

Workman, R.K., Hart, S.R., Jackson, M., Regelous, M., Farley, K.A., Blusztajn, J., Kurz, M., Staudigel, H., 2004. Recycled metasomatized lithosphere as the origin of the Enriched Mantle II (EM2) end-member: Evidence from the Samoan volcanic chain. *Geochemistry, Geophysics, Geosystems* 5(4) 2003GC000623.

Woronow, A., 1990. Methods for quantifying, statistically testing and graphically displaying shifts in compositional abundances across data suites. *Computers and Geosciences* 16, 1209–1233.

Woronow, A., Love, K.M., 1990. Quantifying and testing differences among means of compositional data. *Mathematical Geology* 22, 837–852.

Wright, T.L., Marsh, B., 2016. Quantification of the intrusion process at Kīlauea volcano, Hawai'i. *Journal of Volcanology and Geothermal Research* 328, 34–44.

Wu, W., Yang, J., Wirth, R., Zheng, J., Lian, D., Qiu, T., Milushi, I., 2019. Carbon and nitrogen isotopes and mineral inclusions in diamonds from chromitites of the Mirdita ophiolite (Albania) demonstrate recycling of oceanic crust into the mantle. *American Mineralogist*, 104, 485–500.

Xiao, Y., Teng, F.-Z., Su, B.-X., Hu, Y., Zhou, M.-F., Zhu, B., Shi, R.-D., Huang, Q.-S., Gong, X.-H., He, Y.-S., 2016. Iron and magnesium isotopic constraints on the origin of chemical heterogeneity in podiform chromitite from the Luobusa ophiolite, Tibet. *Geochemistry, Geophysics, Geosystems* 17, doi: 10.1002/2015GC006223.

Yang, A.Y., Zhao, T.P., Zhou, M.F., Deng, X.G., Wang, G.Q., Li, J., 2013. Os isotopic compositions of MORBs from the ultra-slow spreading Southwest Indian Ridge: Constraints on the assimilation and fractional crystallization (AFC) processes. *Lithos* 179, 28–35.

Yang, X.-M., Lentz, D., 2010. Sulfur isotopic systematics of granitoids from southwestern New Brunswick, Canada: Implications for magmatic-

hydrothermal processes, redox conditions, and gold mineralization. *Mineralium Deposita* 45, 795–816.

Yarbrough, L., Engle, R., Easson, G., 2019. Chemostratigraphy of the Upper Jurassic (Oxfordian) Smackover Formation for Little Cedar Creek and Brooklyn Fields, Alabama. *Geosciences* 9, doi: 10.3390/geosciences9060269.

Yoder, H.S., Tilley, C.E., 1962. Origin of basalt magmas: An experimental study of natural and synthetic rock systems. *Journal of Petrology* 3, 342–532.

York, D., 1966. Least-squares fitting of a straight line. *Canadian Journal of Physics* 44, 1079–1086.

York, D., 1967. The best isochron. *Earth and Planetary Science Letters* 2, 479–482.

York, D., 1969. Least squares fitting of a straight line with correlated errors. *Earth and Planetary Science Letters* 5, 320–324.

York, D., Evensen, N., Lopez Martinex, M., de Basabe Delgado, J., 2004. Unified equations for the slope, intercept, and standard errors of the best straight line. *American Journal of Physics* 72, 367–375.

Yuan, B., Yu, H., Yang, Y., Zhao, Y., Yang, J., Xu, Y., Lin, Z., Tang, X., 2018. Zone refinement related to the mineralization process as evidenced by mineralogy and element geochemistry in a chimney fragment from the Southwest Indian Ridge at 49.6°E. *Chemical Geology* 482, 46–60.

Zambardi, T., Poitrasson, F., Corgne, A., Meheut, M., Quitte, G., Anand, M., 2013. Silicon isotope variations in the inner solar system: Implications for planetary formation, differentiation and composition. *Geochimica et Cosmochimica Acta* 121, 67–83.

Zen, E.A., 1988. Phase relations of peraluminous granitic rocks and their petrogenetic implications. *Annual Review of Earth and Planetary Sciences* 16, 21–51.

Zerkle, A.L., Poulton, S.W., Newton, R.J., Mettam, C., Claire, M.W., Bekker, A., Junium, C.K., 2017. Onset of the aerobic nitrogen cycle during the Great Oxidation Event. *Nature* 542, 465–467.

Zhang, J., Lin, Y., Yang, W., Shen, W., Hao, J., Hu, S., Cao, M., 2014. Improved precision and spatial resolution of sulfur isotope analysis using NanoSIMS. *Journal of Analytical Atomic Spectrometry* 29, 1934–1943.

Zhang, Q., Liu, X., 2019. Big data: New methods and ideas in geological scientific research. *Big Earth Data* 3, 1–7.

Zhang, W., Roberts, D., Pease, V., 2015. Provenance characteristics and regional implications of Neoproterozoic, Timanian-margin successions and a basal Caledonian nappe in northern Norway. *Precambrian Research* 268, 153–167.

Zhang, W., Roberts, D., Pease, V., 2016. Provenance of sandstones from Caledonian nappes in Finnmark, Norway: Implication for Neoproterozoic-Cambrian palaeogeography. *Tectonophysics* 691, 198–205.

Zhang, X., Omma, J., Pease, V., Scott, R., 2013. Provenance study of late Paleozoic-Mesozoic sandstones from the Taimyr Peninsula, Arctic Russia. In: Schmidt, J. (ed.), Sedimentary basins and orogenic belts. *Geosciences* 3, 502–527.

Zhao, J., Chen, S., Zuo, R., 2017. Identification and mapping of litho-geochemical signatures using staged factor analysis and fractal/multifractal models. *Geochemistry: Exploration, Environment, Analysis* 17, 239–251.

Zheng, Y.F., Wang, Z.R., Li, S.G., Zhao, Z.F., 2002. Oxygen isotope equilibrium between eclogite minerals and its constraints on mineral Sm–Nd chronometer. *Geochimica et Cosmochimica Acta* 66, 625–634.

Zhou, D., 1987. Robust statistics and geochemical data analysis. *Mathematical Geology* 19, 207–218.

Zhou, H., Hoernle, K., Geldmacher, J., Hauff, F., Homrighausen, S., Garbe-Schönberg, D., Jung, S., 2020. Geochemistry of Etendeka magmatism: Spatial heterogeneity in the Tristan–Gough plume head. *Earth and Planetary Science Letters* 535, 116123.

Zindler, A., Hart, S.R., 1986. Chemical geodynamics. *Annual Review of Earth and Planetary Sciences* 14, 493–571.

Zou, H., 1997. Inversion of partial melting through residual peridotites or clinopyroxenes. *Geochimica et Cosmochimica Acta* 61, 4571–4582.

Zou, H., Reid, M.R., 2001. Quantitative modelling of trace element fractionation during incongruent dynamic melting. *Geochimica et Cosmochimica Acta* 65, 153–162.

Index